Cumhuriyet

Science

Journal

C

S

J

Cumhuriyet Science Journal (CSJ)

Derginin Eski Adı: Cumhuriyet Üniversitesi Fen-Edebiyat Fakültesi Fen Bilimleri Dergisi

Eski ISSN: 1300-1949

CUMHURİYET SCIENCE JOURNAL

CONTENTS

PAGES

NATURAL SCIENCES

ENGINEERING SCIENCES

On a Fuzzy Boundary Value Problem with an Eigenvalue Parameter Contained in the Boundary Condition

Hülya GÜLTEKİN ÇİTİL iD

Giresun University, Faculty of Arts and Sciences, Department of Mathematics, Giresun, TURKEY

Abstract. A fuzzy boundary value problem with an eigenvalue parameter contained in the boundary condition is investigated in this paper. The examination is made under the approach of Hukuhara differentiability. The effect on the eigenvalue and the eigenfunction of the problem of the eigenvalue in the boundary condition is shown.

*Keywords***:** Fuzzy Boundary Value Problem, Hukuhara Differentiability, Eigenvalue, Eigenfunction.

Sınır Koşulunda bir Özdeğer Parametre Bulunan bir Fuzzy Sınır Değer Problemi Üzerine

Özet. Bu çalışmada sınır koşulunda bir özdeğer parametre içeren bir fuzzy sınır değer problemi araştırıldı. Bu araştırma Hukuhara diferansiyellenebilirlik yaklaşımı altında yapıldı. Sınır koşulundaki özdeğer parametrenin problemin özdeğer ve özfonksiyonu üzerindeki etkisi gösterildi.

*Anahtar Kelimeler***:** Fuzzy Sınır Değer Problem, Hukuhara Diferansiyellenebilirlik, Özdeğer, Özfonksiyon.

1. INTRODUCTION

The fuzzy differential equation can be examined several approaches. The first approach is Hukuhara differentiability and for this, firstly the existence and uniqueness of the solution of a fuzzy differential equation are examined [1, 2]. Gültekin and Altınışık [3] have investigated the existence and uniqueness of solutions of two-point fuzzy boundary value problems using the Hukuhara differentiability. Gültekin Çitil and Altınışık [4] have defined the fuzzy Sturm-Liouville equation and they have examined eigenvalues and eigenfunctions of the problem under the approach of the Hukuhara differentiability.

The second approach is generalized derivative. The generalized derivative was presented in [5] and examined in [6-10]. Khastan and Nieto [11] have studied the fuzzy boundary value problem using the generalized derivative and introduced a new notion of the solution.

The third approach is to generate the fuzzy solution from the crips solution. In this approach offered by Gasilov at al. [12], a differential equation with fuzzy boundary values is investigated and the problem is interpreted as a set of crips problems.

This paper is on the eigenvalues and the eigenfunctions of the fuzzy boundary value problem with an eigenvalue parameter contained in the boundary condition under the approach Hukuhara differentiability. The drawn figures are plotted using the mathematica program.

Definition 1.1

A function $u \colon \mathbb{R} \to [0,1]$ satisfying the following properties is a fuzzy number:

u is normal, u is convex fuzzy set, u is upper semi-continuous on $\mathbb{R}$ and $cl\{x \in \mathbb{R}|u(x) > 0\}$ is compact, where cl denotes the closure of a subset [9].
Let $\mathbb{R}_F$ be the space of fuzzy numbers.

Definition 1.2

Let $u \in \mathbb{R}_F$. The α-level set of u is $[u]^\alpha = \{x \in \mathbb{R}|u(x) \geq \alpha\}$, $0 < \alpha \leq 1$. If $\alpha = 0$, the support of u is $[u]^0 = cl\{x \in \mathbb{R}|u(x) > 0\}$. $[u]^\alpha = [\underline{u}_\alpha, \overline{u}_\alpha]$ shows the α-level set of u. $\underline{u}_\alpha$ and $\overline{u}_\alpha$ denote the lower and upper branches of $[u]^\alpha$, respectively [11].

Remark 1.1

$[\underline{u}_\alpha, \overline{u}_\alpha]$ satisfying the following properties is the valid α-level set:

     1) $\underline{u}_\alpha$ is bounded monotonic increasing (nondecreasing) left-continuous function on $(0,1]$ and right-continuous for $\alpha = 0$,

     2) $\overline{u}_\alpha$ is bounded monotonic decreasing (nonincreasing) left-continuous function on $(0,1]$ and right-continuous for $\alpha = 0$,

     3) $\underline{u}_\alpha \leq \overline{u}_\alpha$, $0 \leq \alpha \leq 1$ [9].

Definition 1.3

The α-level set of A which is a symmetric triangular number with support $[\underline{a}, \overline{a}]$ is

$$[A]^\alpha = \left[\underline{a} + \left(\frac{\overline{a} - \underline{a}}{2}\right)\alpha, \overline{a} - \left(\frac{\overline{a} - \underline{a}}{2}\right)\alpha\right]$$ [14].

Definition 1.4

The sum $u + v$ and the product λu are defined by $[u + v]^\alpha = [u]^\alpha + [v]^\alpha$, $[\lambda u]^\alpha = \lambda[u]^\alpha$, $\forall \alpha \in [0,1]$, for $u, v \in \mathbb{R}_F$ and $\lambda \in \mathbb{R}$ [2].

The metric structure is given by the Hausdorff distance

$$D \colon \mathbb{R}_F \times \mathbb{R}_F \to \mathbb{R}_+ \cup \{0\},$$

by

$$D(u, v) = \sup_{\alpha \in [0,1]} \max\left\{\left|\underline{u}_\alpha - \underline{v}_\alpha\right|, \left|\overline{u}_\alpha - \overline{v}_\alpha\right|\right\}$$ [9].

Definition 1.5

Let $u, v \in \mathbb{R}_F$. w which is $u = v + w$, $w \in \mathbb{R}_F$ is called the H-difference of u and v and it is denoted $u \underset{H}{-} v$ [14].

Definition 1.6

Let $I = (a, b)$, for $a, b \in \mathbb{R}_F$, and $F: I \to \mathbb{R}_F$ be a fuzzy function. If there exist an element $F'(t_0) \in \mathbb{R}_F$ and the limits

$$\lim_{h \to 0^+} \frac{F(t_0+h) - F(t_0)}{h} = \lim_{h \to 0^+} \frac{F(t_0) - F(t_0+h)}{h} = F'(t_0),$$

then F is Hukuhara differentiable at $t_0 \in I$ [9].

Theorem 1.1

Let $f: I \to \mathbb{R}_F$ be a function and show $[f(t)]^\alpha = \left[\underline{f_\alpha}(t), \overline{f}_\alpha(t)\right]$, for each $\alpha \in [0,1]$. If f is Hukuhara differentiable, $\underline{f_\alpha}$ and $\overline{f}_\alpha$ are differentiable functions and $[f'(t)]^\alpha = \left[\underline{f_\alpha}'(t), \overline{f}_\alpha'(t)\right]$ [13].

2. RESULTS AND DISCUSSION

Consider the fuzzy Sturm-Liouville problem

$$y'' + \lambda y = 0, \quad x \epsilon (a, b) \tag{2.1}$$

$$\beta_1 y(a) + \beta_2 \lambda y'(a) = 0, \tag{2.2}$$

$$\beta_3 y(b) + \beta_4 y'(b) = 0, \tag{2.3}$$

where $\lambda > 0$, $\beta_1, \beta_2, \beta_3, \beta_4 \geq 0$, $\beta_1^2 + \beta_2^2 \neq 0$ and $\beta_3^2 + \beta_4^2 \neq 0$. Let $\lambda = k^2, k > 0$,

$$\phi(x, \lambda) = \left(k^2 \beta_2 Cos(ka) + \frac{\beta_1}{k} Sin(ka)\right) Cos(kx) +$$

$$+ \left(-\frac{\beta_1}{k} Cos(ka) + k^2 \beta_2 Sin(ka)\right) Sin(kx)$$

and

$$\psi(x, \lambda) = \left(\beta_4 Cos(kb) + \frac{\beta_3}{k} Sin(kb)\right) Cos(kx) + \left(-\frac{\beta_3}{k} Cos(kb) + \beta_4 Sin(kb)\right) Sin(kx)$$

be the solutions of the classical differential equation $y'' + \lambda y = 0$ satisfying the conditions $y(a) = \lambda \beta_2$, $y'(a) = -\beta_1$ and $y(b) = \beta_4$, $y'(b) = -\beta_3$, respectively. Then,

$$[\phi(x, \lambda)]^\alpha = \left[\underline{\phi}_\alpha(x, \lambda), \overline{\phi}_\alpha(x, \lambda)\right] = [\alpha, 2 - \alpha]\phi(x, \lambda) \tag{2.4}$$

and

$$[\psi(x, \lambda)]^\alpha = \left[\underline{\psi}_\alpha(x, \lambda), \overline{\psi}_\alpha(x, \lambda)\right] = [\alpha, 2 - \alpha]\psi(x, \lambda) \tag{2.5}$$

are the solutions of the fuzzy differential equation (2.1) satisfying the conditions (2.2) and (2.3), respectively. The eigenvalues of the fuzzy Sturm-Liouville problem (2.1)-(2.3) if and only if are consist of the zeros of Wronskian functions

$$\underline{W}_\alpha(\lambda) = W\left(\underline{\phi}_\alpha, \underline{\psi}_\alpha\right)(x, \lambda) = \underline{\phi}_\alpha(x, \lambda)\underline{\psi}_\alpha'(x, \lambda) - \underline{\psi}_\alpha(x, \lambda)\underline{\phi}_\alpha'(x, \lambda), \tag{2.6}$$

$$\overline{W}_\alpha(\lambda) = W(\overline{\phi}_\alpha, \overline{\psi}_\alpha)(x, \lambda) = \overline{\phi}_\alpha(x, \lambda)\overline{\psi}'_\alpha(x, \lambda) - \overline{\psi}_\alpha(x, \lambda)\overline{\phi}'_\alpha(x, \lambda) \text{ [4].} \tag{2.7}$$

Then,

$$\underline{\phi}_\alpha(x, \lambda) = \alpha\left\{\left(k^2\beta_2 Cos(ka) + \frac{\beta_1}{k}Sin(ka)\right)Cos(kx) + \right.$$

$$\left. +\left(-\frac{\beta_1}{k}Cos(ka) + k^2\beta_2 Sin(ka)\right)Sin(kx)\right\} \tag{2.8}$$

$$\underline{\phi}'_\alpha(x, \lambda) = \alpha\{(-k^3\beta_2 Cos(ka) - \beta_1 Sin(ka))Sin(kx) +$$

$$+(-\beta_1 Cos(ka) + k^3\beta_2 Sin(ka))Cos(kx)\} \tag{2.9}$$

$$\underline{\psi}_\alpha(x, \lambda) = \alpha\left\{\left(\beta_4 Cos(kb) + \frac{\beta_3}{k}Sin(kb)\right)Cos(kx) + \right.$$

$$\left. +\left(-\frac{\beta_3}{k}Cos(kb) + \beta_4 Sin(kb)\right)Sin(kx)\right\} \tag{2.10}$$

$$\underline{\psi}'_\alpha(x, \lambda) = \alpha\{(-\beta_4 k Cos(kb) - \beta_3 Sin(kb))Sin(kx) +$$

$$+(-\beta_3 Cos(kb) + \beta_4 k Sin(kb))Cos(kx)\} \tag{2.11}$$

substituing to in (2.6) and making the necessary operations yields

$$\underline{W}_\alpha(\lambda) = \alpha^2\left((\beta_1\beta_4 - k^2\beta_2\beta_3)Cos(k(a-b)) + \left(\frac{\beta_1\beta_3}{k} + k^3\beta_2\beta_4\right)Sin(k(b-a))\right)$$

and

$$\overline{W}_\alpha(\lambda) = (2-\alpha)^2\left((\beta_1\beta_4 - k^2\beta_2\beta_3)Cos(k(a-b)) + \left(\frac{\beta_1\beta_3}{k} + k^3\beta_2\beta_4\right)Sin(k(b-a))\right).$$

Then,

$$\underline{W}_\alpha(\lambda) = \overline{W}_\alpha(\lambda) = 0 \Longrightarrow \left((\beta_1\beta_4 - k^2\beta_2\beta_3)Cos(k(a-b)) + \right.$$

$$\left. +\left(\frac{\beta_1\beta_3}{k} + k^3\beta_2\beta_4\right)Sin(k(b-a)) = 0.\right.$$

Showing $k = k_n$ the above equation satisfying the values k and substituing to in (2.4), (2.5),

$$[\phi(x, \lambda)]^\alpha = [\alpha, 2-\alpha]\left(k_n{}^2\beta_2 Cos(k_n a) + \frac{\beta_1}{k_n}Sin(k_n a)\right)Cos(k_n x) +$$

$$+\left(-\frac{\beta_1}{k_n}Cos(k_n a) + k_n{}^2\beta_2 Sin(k_n a)\right)Sin(k_n x)$$

$$[\psi(x, \lambda)]^\alpha = [\alpha, 2-\alpha]\left(\beta_4 Cos(k_n b) + \frac{\beta_3}{k_n}Sin(k_n b)\right)Cos(k_n x) +$$

$$+\left(-\frac{\beta_3}{k_n}Cos(k_nb)+\beta_4Sin(k_nb)\right)Sin(k_nx)$$

is obtained. If $[\phi(x,\lambda)]^\alpha$ and $[\psi(x,\lambda)]^\alpha$ are valid α-level sets, they are eigenfunctions. Therefore, $[\phi(x,\lambda)]^\alpha$ and $[\psi(x,\lambda)]^\alpha$ must be valid α-level sets. Consequently, for k_n making $[\phi(x,\lambda)]^\alpha$ is a valid α-level set, $[\phi(x,\lambda)]^\alpha$ is eigenfunction with associated the eigenvalues $\lambda_n = k_n^2$. Similarly, for k_n making $[\psi(x,\lambda)]^\alpha$ is a valid α-level set, $[\psi(x,\lambda)]^\alpha$ is eigenfunction with associated the eigenvalues $\lambda_n = k_n^2$.

Example 2.1

Consider the fuzzy boundary value problem

$$y'' + \lambda y = 0, \quad y(0) + \lambda y'(0) = 0, \quad y(1) = 0 . \tag{2.12}$$

Let $\lambda = k^2, k > 0$ and

$$\phi(x,\lambda) = k^2Cos(kx) - \frac{1}{k}Sin(kx),$$

$$\psi(x,\lambda) = SinkCos(kx) - CoskSin(kx)$$

be the solutions of the classical differential equation $y'' + \lambda y = 0$ satisfying the conditions $y(0) = k^2$, $y'(0) = 1$ and $y(1) = 1$, respectively. Then,

$$[\phi(x,\lambda)]^\alpha = \left[\underline{\phi}_\alpha(x,\lambda), \overline{\phi}_\alpha(x,\lambda)\right]$$

$$= [\alpha, 2-\alpha]\left(k^2Cos(kx) - \frac{1}{k}Sin(kx)\right) \tag{2.13}$$

and

$$[\psi(x,\lambda)]^\alpha = \left[\underline{\psi}_\alpha(x,\lambda), \overline{\psi}_\alpha(x,\lambda)\right]$$

$$= [\alpha, 2-\alpha]\big(SinkCos(kx) - CoskSin(kx)\big) \tag{2.14}$$

are the solutions of the fuzzy differential equation $y'' + \lambda y = 0$ satisfying the first and the second boundary conditions, respectively. Because of the eigenvalues of the fuzzy boundary value problem (2.12) are zeros of the functions $\underline{W}_\alpha(\lambda)$ and $\overline{W}_\alpha(\lambda)$, $\underline{W}_\alpha(\lambda)$ and $\overline{W}_\alpha(\lambda)$ are obtained as

$$\underline{W}_\alpha(\lambda) = \alpha^2\left(-k^2Cos(k) + \frac{1}{k}Sin(kx)\right),$$

$$\overline{W}_\alpha(\lambda) = (2-\alpha)^2\left(-k^2Cos(k) + \frac{1}{k}Sin(kx)\right).$$

From this we get

$$-k^3Cos(kx) + Sin(kx) = 0.$$

Computing the values k satisfying the above equation , we have

$$k_1 = 4.70277, k_2 = 7.85192, k_3 = 10.9948, k_4 = 14.1368, k_5 = 17.2786, \dots$$

Let show this values $k_n, n = 1,2, ...$ and substitute in (2.13), (2.14). Then, we obtain

$$[\phi_n(x)]^\alpha = \left[\underline{\phi_n}_\alpha(x), \overline{\phi_n}_\alpha(x)\right] = [\alpha, 2 - \alpha]\left(k_n{}^2 Cos(k_n x) - \frac{1}{k_n} Sin(k_n x)\right)$$

$$[\psi_n(x)]^\alpha = \left[\underline{\psi_n}_\alpha(x), \overline{\psi_n}_\alpha(x)\right] = [\alpha, 2 - \alpha]\left(Sink_n Cos(k_n x) - Cosk_n Sin(k_n x)\right)$$

When $\left(k_n{}^2 Cos(k_n x) - \frac{1}{k_n} Sin(k_n x)\right) > 0$ and $\left(Sink_n Cos(k_n x) - Cosk_n Sin(k_n x)\right) > 0$, $[\phi_n(x)]^\alpha$

and $[\psi_n(x)]^\alpha$ are valid α-level sets. Let be $k_n x \in [(n-1)\pi, n\pi]$, $n = 1,2, ...$.

For $[\phi_n(x)]^\alpha$,

    i)   If n is odd, $Sink_n x \geq 0$. From here,

$$k_n{}^3 Cot(k_n x) \geq 1 \Longrightarrow Cot(k_n x) \geq \frac{1}{k_n{}^3}$$

$$\Longrightarrow k_n x \leq cot^{-1}\left(\frac{1}{k_n{}^3}\right) \Longrightarrow x \leq \frac{1}{k_n} cot^{-1}\left(\frac{1}{k_n{}^3}\right).$$

Since the above inequality must be for all $0 \leq x \leq 1$, it must be

$$\frac{1}{k_n} cot^{-1}\left(\frac{1}{k_n{}^3}\right) - 1 \geq 0.$$
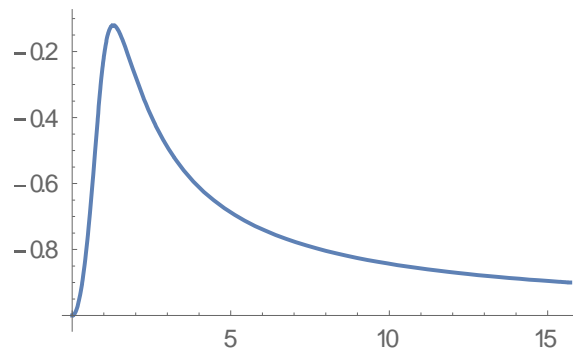
Figure 1. The graphic of the function $\frac{1}{k} cot^{-1}\left(\frac{1}{k^3}\right) - 1$

ii) If n is even, $Sink_n x \leq 0$. Then,

$$k_n{}^3 Cot(k_n x) \leq 1 \Longrightarrow Cot(k_n x) \leq \frac{1}{k_n{}^3}$$

$$\Longrightarrow k_n x \geq cot^{-1}\left(\frac{1}{k_n{}^3}\right) \Longrightarrow x \geq \frac{1}{k_n} cot^{-1}\left(\frac{1}{k_n{}^3}\right).$$

Since the above inequality must be for all $0 \leq x \leq 1$, it must be

$$\frac{1}{k_n} cot^{-1}\left(\frac{1}{k_n{}^3}\right) \leq 0$$
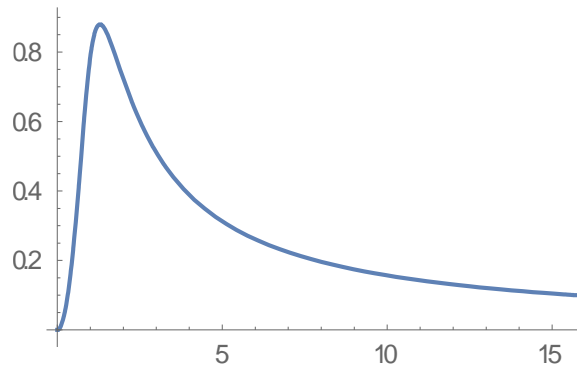
Figure 2. The graphic of the function $\frac{1}{k}cot^{-1}\left(\frac{1}{k^3}\right)$

According to Figure 1 and Figure 2, $[\phi_n(x)]^\alpha$ is not a valid α-level set.

For $[\psi_n(x)]^\alpha$,

    i)   If n is odd, $Sin k_n x \geq 0$. Then,

$$Sin k_n Cos(k_n x) - Cos k_n Sin(k_n x) \geq 0$$

$$Cot(k_n x) \geq Cot k_n \implies k_n x \leq k_n \implies x \leq 1.$$

    ii)   If n is even, $Sin k_n x \leq 0$ and $Sin k_n \leq 0$. Then,

$$Sin k_n Cos(k_n x) - Cos k_n Sin(k_n x) \geq 0$$

$$Cot(k_n x) \geq Cot k_n \implies k_n x \leq k_n \implies x \leq 1.$$

Consequently; the eigenvalues are $\lambda_n = k_n^2$, with associated eigenfunctions

$$[y_n(x)]^\alpha = [\alpha, 2 - \alpha]\big(Sin k_n Cos(k_n x) - Cos k_n Sin(k_n x)\big).$$

Example 2.2

Consider the fuzzy problem

$$y'' + \lambda y = 0, \quad y(0) + \lambda y'(0) = 0, \quad y'(1) = 0 \tag{2.15}$$

Similar to example 2.1,

$$[\phi(x,\lambda)]^\alpha = \left[\underline{\phi}_\alpha(x,\lambda), \overline{\phi}_\alpha(x,\lambda)\right]$$

$$= [\alpha, 2 - \alpha]\left(k^2 Cos(kx) - \frac{1}{k}Sin(kx)\right) \tag{2.16}$$

and

$$[\psi(x,\lambda)]^\alpha = \left[\underline{\psi}_\alpha(x,\lambda), \overline{\psi}_\alpha(x,\lambda)\right]$$

$$= [\alpha, 2 - \alpha]\big(Cos k Cos(kx) + Sin k Sin(kx)\big) \tag{2.17}$$

are the solutions of the fuzzy differential equation $y'' + \lambda y = 0$ satisfying the first condition and the second condition, respectively. $\underline{W}_\alpha(\lambda)$ and $\overline{W}_\alpha(\lambda)$ are obtained as

$$\underline{W}_\alpha(\lambda) = \alpha^2\big(Cos(k) + k^3 Sin(kx)\big),$$

$$\overline{W}_\alpha(\lambda) = (2-\alpha)^2\big(Cos(k) + k^3 Sin(k)\big).$$

From this we get

$$Cos(kx) + k^3 Sin(kx) = 0.$$

Computing the values k satisfying the above equation , we have

$$k_1 = 0.505503, k_2 = 3.10831, k_3 = 6.27915, k_4 = 9.42358, k_5 = 12.5659, \dots$$

Substituing this values in (2.16), (2.17), we obtain

$$[\phi_n(x)]^\alpha = \Big[\underline{\phi_n}_\alpha(x), \overline{\phi_n}_\alpha(x)\Big] = [\alpha, 2-\alpha]\left(k_n{}^2 Cos(k_n x) - \frac{1}{k_n} Sin(k_n x)\right),$$

$$[\psi_n(x)]^\alpha = \Big[\underline{\psi_n}_\alpha(x), \overline{\psi_n}_\alpha(x)\Big] = [\alpha, 2-\alpha]\big(Cosk_n Cos(k_n x) + Sink_n Sin(k_n x)\big).$$

When $\left(k_n{}^2 Cos(k_n x) - \frac{1}{k_n} Sin(k_n x)\right) > 0$ and $\big(Cosk_n Cos(k_n x) + Sink_n Sin(k_n x)\big) > 0,$ $[\phi_n(x)]^\alpha$ and $[\psi_n(x)]^\alpha$ are valid α-level sets. From the example 2.1, $[\phi_n(x)]^\alpha$ is not a valid α-level set. For $[\psi_n(x)]^\alpha$,

Let be $k_n x \in \left(\frac{2(n-1)-1}{2}\pi, \frac{2(n-1)+1}{2}\pi\right), n = 1,3,5, \dots$ Then, $Cos(k_n x) \geq 0$ and

$$Cosk_n Cos(k_n x) + Sink_n Sin(k_n x) \geq 0 \implies tan(k_n) tan(k_n x) \geq -1.$$

i) If $k_n x \in \left(\frac{2(n-1)-1}{2}\pi, (n-1)\pi\right), n = 1,3,5, \dots ,$ $tan(k_n x) \leq 0$.

$$tan(k_n x) \leq -\frac{1}{tan(k_n)} \implies k_n x \leq tan^{-1}\left(-\frac{1}{tan(k_n)}\right),$$

$$x \leq \frac{1}{k_n} tan^{-1}\left(-\frac{1}{tan(k_n)}\right).$$

Since the above inequality must be for all $0 \leq x \leq 1$, it must be

$$\frac{1}{k_n} tan^{-1}\left(-\frac{1}{tan(k_n)}\right) - 1 \geq 0.$$
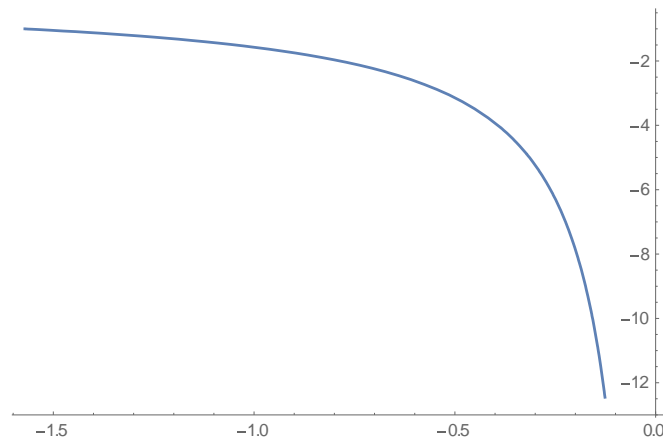
Figure 3. The graphic of the function $\frac{1}{k_n} tan^{-1}\left(-\frac{1}{tan(k_n)}\right) - 1$

ii) If $k_n x \in \left((n-1)\pi, \frac{2(n-1)+1}{2}\pi \right), n = 1,3,5,\dots,\ tan(k_n x) \geq 0$.

$$tan(k_n x) \geq -\frac{1}{tan(k_n)} \Longrightarrow k_n x \geq tan^{-1}\left(-\frac{1}{tan(k_n)} \right),$$

$$x \geq \frac{1}{k_n} tan^{-1}\left(-\frac{1}{tan(k_n)} \right).$$

Since the above inequality must be for all $0 \leq x \leq 1$, it must be

$$\frac{1}{k_n} tan^{-1}\left(-\frac{1}{tan(k_n)} \right) \leq 0.$$
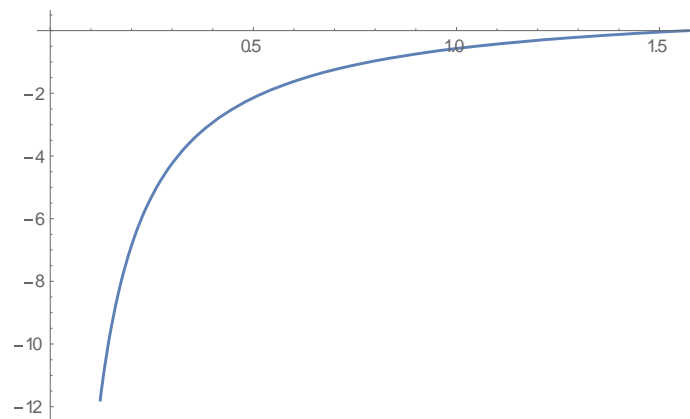
Figure 4. The graphic of the function $\frac{1}{k_n} tan^{-1}\left(-\frac{1}{tan(k_n)} \right)$.

Consequently;

$k_n x \in \left((n-1)\pi, \frac{(2n-1)\pi}{2} \right)$, n=1,3,5,…. the eigenvalues are $\lambda_n = k_n^2$, with associated eigenfunctions

$$[y_n(x)]^\alpha = [\alpha, 2-\alpha]\big(Sin k_n Cos(k_n x) - Cos k_n Sin(k_n x) \big).$$

3. CONCLUSION

A fuzzy Sturm-Liouville problem with an eigenvalue parameter contained in the boundary condition is investigated in this paper. The examination is made using the Hukuhara differentiability. The effect on the eigenvalue and the eigenfunction of the problem of the eigenvalue in the boundary condition is shown. Two examples are solved. It is shown that function that provides boundary condition with eigenvalue parameter of the differential equation does not define eigenfunction. But examples can be multiplied. Also, different studies can be made. This is a new area and these results will be useful for other mathematicians.

REFERENCES

[1]. Buckey J.J. and Feuring T., Fuzzy Differential Equations, Fuzzy Sets and Systems, 110 (2000) 43-54.

[2]. Kaleva O., Fuzzy Differential Equations, Fuzzy Sets and Systems, 24 (1987) 301-317.

[3]. Gültekin H. and Altınışık N., On Solution of Two-Point Fuzzy Boundary Value Problems, The Bulletin of Society for Mathematical Services and Standarts, 11 (2014) 31-39.

[4]. Gültekin Çitil H. and Altınışık N., On the Eigenvalues and the Eigenfunctions of the Sturm-Liouville Fuzzy Boundary Value Problem, Journal of Mathematical and Computational Science, 7(4) (2017) 786-805.

[5]. Bede B. and Gal S.G., Almost Periodic Fuzzy-Number-Valued Functions, Fuzzy Sets and Systems, 147 (2004) 385- 403.

[6]. Bede B. and Gal S.G., Generalizations of the Differentibility of Fuzzy Number Value Functions with Applications to Fuzzy Differential Equations, Fuzzy Sets and Systems, 151 (2005) 581-599.

[7]. Bede B., Rudas I.J and Bencsik A.L., First Order Linear fuzzy Differential Equations Under Generalized Differentiability, Inform. Sci., 177 (2007) 1648-1662.

[8]. Chalco-Cano Y. and Roman-Flores H., On New Solutions of Fuzzy Differential Equations, Chaos, Solitons & Fractals, 38 (2008) 112-119.

[9]. Khastan A., Bahrami F. and Ivaz K., New Results on Multiple Solutions for Nth-Order Fuzzy Differential Equations under Generalized Differentiability, Boundary Value Problems, (2009) doi:10.1155/2009/395714. Article ID 395714, 13 pages.

[10]. Nieto J.J., Khastan A. and Ivaz K., Numerical Solution of Fuzzy Differential Equations under Generalized Differentiability, Nonlinear Analysis: Hybrid Systems, 3 (2009) 700-707.

[11]. Khastan A. and Nieto J.J., A Boundary Value Problem for Second Order Fuzzy Differential Equations, Nonlinear Analysis, 72 (2010) 3583-3593.

[12]. Gasilov N.A., Amrahov Ş.E. and Fatullayev A.G., A Geometric Approach to Solve Fuzzy Linear Systems of Differential Equations, Appl. Math. Inf. Sci., 5 (2011) 484-495.

[13].Fard O.S., Esfahani A. and Kamyad A.V., On Solution of a Class of Fuzzy BVPs, Iranian of Fuzzy Systems, 9-1 (2012) 49-60.

[14].Liu H.K., Comparation Results of Two-Point Fuzzy Boundary Value Problems, International Journal of Computational and Mathematical Sciences, 5-1 (2011) 1-7.

Electrochemical Investigation of Carbon Nanotube Modified Surfaces Based on Ferricyanide and Guanine Signals for DNA Biosensor Applications

Dilşat ARIKSOYSAL [iD]

Ege University, Department of Analytical Chemistry, Faculty of Pharmacy, Izmir, TURKEY

Abstract. This study was designed to investigate the performance of carbon nanotubes (CNT) modified carbon paste and carbon printed electrodes (SPE) produced in laboratory conditions. The effect of carbon nanotube use on signal enrichment was determined by using cyclic voltammetry (CV), square wave voltammetry (SWV) or differential pulse voltammetry (DPV) techniques based on potassium ferricyanide/ ferrocyanide or guanine signal. The application of different activation procedures to the electrode surface such as chemical (H_2SO_4, acetone, N,N-Dimethylformamide or NaOH) or electrochemical (different potential applications) were presented in this study. It was observed that the activation procedure applied to the nanotube modified electrode has strong effects on signal enrichment. From these procedures it was determined that the guanine signal obtained in activation with NaOH increased about 62-fold. It was also found that different nanotube species gave different responses to the activation processes. The optimum conditions of the nanotube-based biosensor were also presented.

Keywords: Electrochemical techniques, DNA, biosensor, carbon nanotubes, screen printed electrode(SPE), Nucleic Acid Hybridization.

DNA Biyosensör Uygulamaları İçin Karbon Nanotüp Modifiye Yüzeylerin Ferrisiyanür ve Guanin Sinyallerine Dayalı Olarak Elektrokimyasal İncelenmesi

Özet. Bu çalışmada karbon nanotüpler (CNT) ile modifiye edilmiş karbon pastası (CPE) ve laboratuvar koşullarında basılarak üretilen perde baskılı karbon (SPE) elektrotların performansı karşılaştırılmış ve dönüşümlü voltametri(CV), kare dalga voltametri (SWV) veya diferansiyel puls voltametri (DPV) teknikleri kullanılarak elde edilen potasyum ferri / ferrosiyanür veya guanin sinyallerindeki artış miktarı tayin edilmiştir. Bu çalışmada elektrotlara kimyasal (H_2SO_4, aseton, N, N-Dimetilformamid veya NaOH) veya elektrokimyasal (farklı potansiyel uygulamaları) gibi farklı aktivasyon prosedürleri uygulanmıştır. Nanotüp modifiye elektrota uygulanan aktivasyon prosedürünün sinyal zenginleşmesi üzerine güçlü etkileri olduğu gözlenmiştir. Bu prosedürlerden NaOH ile aktivasyonda elde edilen guanin sinyalinin yaklaşık 62 kat arttığı tespit edilmiştir. Bu çalışmada ayrıca farklı nanotüp türlerinin aktivasyon proseslerine farklı yanıtlar verdiği de bulunmuştur. Nanotüp bazlı biyosensörün optimum şartları da ayrıca sunulmuştur.

Anahtar Kelimeler: Elektrokimyasal teknikler, DNA, biyosensör, karbon nanotüpler, perde baskılı elektrot (SPE), Nükleik asit hibridizasyonu.

1. INTRODUCTION

New generation DNA biosensor systems, including simple, precise, fast and easy-to-use methods, continue to be developed for routine medical applications such as genetic diagnosis along with the advancements in nanotechnology. These bio-devices designed for the specification of many genetic disorders include various nanomaterial-based assay methodologies. Among them electrochemical DNA biosensors, which were developed as an alternative to classical test methods and other biosensor systems, have some powerful benefits such as the monitoring of signals are more rapid and direct [1] than other i.e. optical or piezoelectric biosensor systems. However, in all cases, DNA detection with these nanosystems is usually based on signal enrichment. In fact, the aim of using nanomaterials in biosensor systems is to provide more biomaterial binding to the sensor surface. In this case, when the signal is enhanced, the limit of detection can be reduced considerably. Carbon nanotube(CNT) contained electrochemical biosensors have still received considerable interest from researchers because of their rapid electron transport and high biomolecule binding capacity via self-assemble strategies [2-6]. They have been used for many of detection purposes up to now such as drug-DNA interactions [7, 8], DNA hybridization sensing [9, 10], biomolecular interactions by hybrid assemblies [11-13] etc.

Hexagonal graphitic sheets-based CNTs are divided into two groups as single-walled carbon nanotubes (SWCNT) and multi-walled carbon nanotubes (MWCNT). They both have a very high surface area with nanometers range and their lengths can be micron levels. CNTs have still been used for preparation of a sensitive sensing layers in the field of biosensor design technologies due to amplifying recognition events. However, in order to increase the sensing signal, it is necessary to find some optimum conditions. Because the amount of signal increase, arising from the nanomaterial is influenced by experimental conditions as well as nanomaterial characteristics. For example, SWCNTs-modified electrode gave lover detection limit than MWCNTs modified one for the amperometric determination of hydrogen peroxide and phenolic compounds that was reported by Chekin et al. [14] Another example was presented by Erdem et al. related to CNTs-based biosensor design for the detection of Microcystis spp gene sequences. In their work, higher oxidation signals of guanine and adenine were obtained using MWCNTs-modified screen printed electrode in comparison to the SWCNTs-contained one[15]. Jeong et al. was developed the thrombin sensor by using bare(unmodified), gold nano particle (GNP), SWCNT or MWCNT modified electrodes in order to investigate the surface effect on SWV signals in that work [16].

On the other hand, in electrode systems carrying microchip substructure such as screen printed or pencil graphite electrodes, polymers are used in both commercial and hand-made electrodes to hold the powdery materials (i.e. gold particles, graphite, carbon nanotubes, etc.) together and to adhere them to the solid surface. This causes decrease in electron transfer kinetics and thus low signal acquisition from sensor surfaces. In electrochemical studies, application of the activation process to the electrode surface is very important in order to obtain reproducible results. The activation of the aforementioned disposable, nanomaterial-containing electrodes prior to use is also important for obtaining both reproducible and enriched signals. In addition, pretreatment of the electrodes helps to form -COOH groups on the SPE surface which increase the hydrophilicity of the surface and its reproducibility, thereby remove possible contaminants from the sensor [17]. In other words, there is an increment for active sites on the working electrode.

In this study, suitable experimental conditions for the use of nanotube modified electrodes in biosensor systems were investigated. It is aimed to obtain the highest electrochemical response with handmade carbon paste (CPE) and screen printed carbon electrode (SPE) containing bamboo or hollow type carbon nanotubes. As known, it is very important in electrochemical biosensor systems to reduce the detection limit of the sensor

depending on the level of the signal obtained because of biochemical interaction. Here, the contribution of the nanomaterial to reducing the detection limit of the biosensor (or contribution to enhancing the signal obtained from the sensor) was explored using different experimental conditions. Basically, the disposable electrodes were prepared in the laboratory using a screen printed electrode machine to contain certain percentages of nanotubes firstly. Electrodes were then chemically or electrochemically activated by chemical treatment or applying positive potential onto the surface of the working electrodes in order to increase sensitivity and stability of the device. Electrochemical responses of potassium feri/ferrocyanide or guanine were measured and evaluated based on cyclic, square wave or differential puls voltammetry techniques. To our knowledge, optimum parameters (or operating conditions) of nanomaterial modified electrodes should be determined before the biosensor designs so that the developed biosensors can have features such as low detection limit, rapid analysis capability which are requirements of medical DNA tests. Advantages and disadvantages of these electrodes were evaluated in the following sections.

2. MATERIAL AND METHODS

2.1. Apparatus, Chemicals and Sample Preparation

AUTOLAB 12 potatiostat/galvanostat device (Eco Chemie, Netherlands) containing the software package GPES 4.9 (General Purpose Electrochemical System) was used for electrochemical measurements. Savitzky and Golay filter (level 2) of the software was preferred to smooth raw DPV voltammograms.

Disposable screen-printed electrodes (SPE) were prepared in the Firenze University, biosensor laboratory, Florence, Italy. They consisted of a silver (pseudo) reference electrode, a graphite working electrode ($\emptyset$ = 3 mm) and a graphite auxiliary electrode as similarly reported in Carpini et al. [18] (Scheme 1). The carbon SPEs were printed by using a screen-printer machine (Model 248, DEK, Weimouth, UK). A Electrodag 423 SS model graphite ink and a Electrodag 410 PF model silver ink purchased from Acheson (Milan, Italy), a Vinyl fast 36-100 model insulating ink was obtained from Argon, Lodi, (Milan, Italy). An Autostat CT5 type polyester film purchased from Autotype (Milan, Italy) for the printing substrate. The silver ink was also used to serve as the conductive tracks. The thin sheet was fixed to the polycarbonate support so that the desired electrode thickness could be obtained. The SPE connector was used as the interface in all measurements.
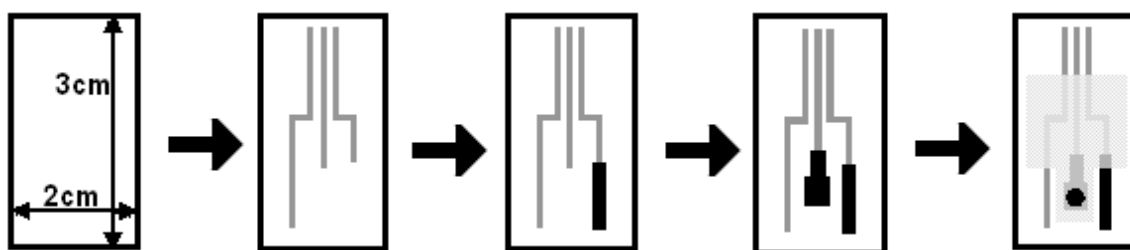
Scheme 1. 2 cm wide and 3 cm long electrode printing process contains printing of silver ink for pseudo-reference electrode and electrical contact layers (a), printing of counter(b) and working(c) electrodes by using carbon ink, and printing of insulating layer(d) by using the insulating ink respectively. Carbon ink of the working electrode contained 1%, 2% or 5% ratio of carbon nanotubes.

Graphite powder and all types of CNTs (SWCNTs, hollow/bamboo structure of MWCNTs) purchased from Sigma-Aldrich.

The other three electrode system used in this study consisted of the surface-renewable carbon paste electrode (CPE) as the working electrode, a

reference electrode (Ag/AgCl), and a counter electrode (platinum wire). A 3 mm i.d. of glass tube was used as the body of the CPE and the mixture of carbon paste was packed in it. The electrical conductivity was provided using copper wire passed through the paste-filled tube. Carbon paste mixture composed of graphite powder (Fisher) and mineral oil (Acheson 38) in a 70:30 mass ratio. The CPE surface was polished by using a weighing paper before use.

2.1. Synthetic DNA materials

Double-stranded (ds) calf thymus DNA was purchased from Sigma-Aldrich (Milan, Italy). The stock solution of dsDNA (1000μg/ml) was prepared with Tris-EDTA buffer (10mM Tris–HCl, 1mM EDTA, pH 8.00) and store at freezer. More diluted solutions of DNA were prepared with 0.50M acetate buffer (pH 4.80) (ABS).

2.3. Chemicals

Sodium dihydrogen phosphate, disodium hydrogen phosphate, and acetic acid were obtained from Sigma (Milan, Italy). All reagents were of analytical grade and ultrapure water (18Ω) was used in all preparations of solutions (Elgastat, England). All experiments were carried out at room temperature provided by air condition (22.0-25.0 °C).

2.2. Methods

Scheme 2 shows the experimental details of the CNT-based biosensor. In the first part of the study, a 20μg/ml fish sperm double stranded DNA(dsDNA) was immobilized to various percentages such as 1%, 2%, 5% of SWCNT-containing CPE electrode. The increase in guanine oxidation signal was monitored by square wave and compared to the bare electrode. Guanine, which is an electroactive DNA base, is oxidized at about +1.0V potential at acetate buffer (pH:4.80) medium. In the second part, 20μg/ml dsDNA was attached to the surface of the SPEs that had been printed to contain SWCNTs/MWCNTs and the resulting of the electron transfer in the Nernst difussion layer was measured based on potassium ferri/ferrocyanide by cyclic voltammetry or

guanine signal by differential pulse voltammetry. CNT-related signal enhancement was observed at different pretreatment conditions.
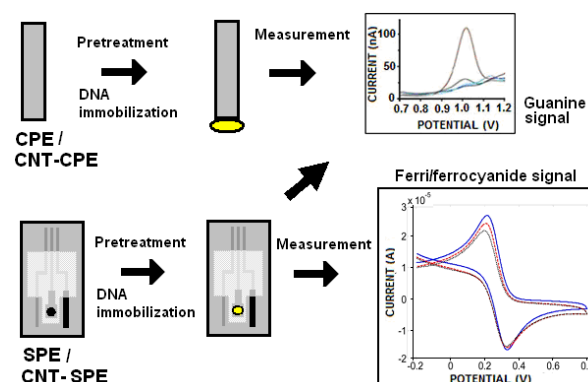
Scheme 2. Schematic diagrams illustrating the experimental steps of bare/CNTs-modified CPE and SPE electrodes and the detection of CNT-related signal enhancement based on guanine or ferri/ferrocyanide signals.

2.2.1. The preparation of sensor surfaces.

The pretreatment of SWCNTs-modified CPE was made by applying a potential of +1.70 V vs. reference electrode for 20s or 0 V(open circuit potential) for 20sec. in acetate buffer solution (0.50 M ABS; pH 4.80) without stirring. The 20μg/mL of dsDNA prepared in ABS was subsequently modified onto the activated surface of CPE by applying a fixed potential of +0.20 V for 5 min. The dsDNA immobilized CPE was then rinsed with ABS twice.

On the other hand, a 100 μL of ABS droplet was put on SWCNTs-contained SPEs for the pretreatment of their carbon working electrode surfaces. The different pretreatment and DNA immobilization conditions are as follows:

Table 1. The table showing the electrochemical activation processes applied in biosensor experiments with screen printed carbon electrode for guanine signal measurements.

Pretreatment (in ABS)	DNA immobilization
1.2V for 60s.	Passive adsorption for 2min.
1.6V for 60 s.	Passive adsorption for 2min.
1.8V for 60 s.	Passive adsorption for 2min.
1.6V, 120 s.+ 1.8V, 60 s.	Passive adsorption for 2min.
2.0V for 60 s.	Passive adsorption for 2min.
1.8V for 60 s.	+0.50 V for 120s. with stirring (200rpm.)

After pretreatment SPEs were then rinsed with 100 μL of blank ABS two times using micropipette. Each electrode strip was covered with a droplet including 20 μg/ml of dsDNA in ABS. After 2 min. of DNA immobilization under open circuit potential application (~0V), they were washed with the same buffer for 30s. with 200 rpm stirring. The electrodes were then coated with 100 μL of new drop of ABS so that their surfaces were not dry, and were left to stand until measurement.

2.2.2.   Different pretreatment applications

Various activation techniques were applied to MWCNTs-modified SPEs (carbon ink contained 2% ratio of hollow or bamboo structure of MWCNTs) to achieve optimal signal enrichment. For example;

i. H_2SO_4 pretreatment: 2 CV scans (from -1.0 to +1.0V) in 0.2 M H_2SO_4
ii.   Acetone pretreatment: 10 μL drop (acetone/water 1:1) on the working electrode surface for 10 min.
iii. N,N-Dimethylformamide pretreatment: 10 μL drop on the surface till dryness.
iv.   NaOH pretreatment: +1.5V for 2min in 1M NaOH.

2.2.3.   Electrochemical Measurements

The electrochemical transduction of the oxidation and reduction peaks of $Fe(CN)_6^{3-/4-}$ were recorded with cyclic voltammetry(CV) technique scanning from -0.25V to +0.65V potential range, 50mV scan rate and 3mV step potential. The oxidation signal of guanine was measured directly by square wave voltammetry scanning from +0.20 to +1.35V potential range versus Ag/AgCl reference electrode (or Ag-Pseudo-reference electrode) in the ABS aliquot at 40 mV pulse amplitude, 15mV step potential and 200 Hz frequency. The oxidation signal of guanine was also measured in blank ABS by DPV by scanning from +0.70 to +1.45 V with the amplitude of 50 mV at 16 mV/s scan rate. If necessary, the raw curve was treated by using the software program of GPES "Savitzky and Golay fitler" (level 2) with moving average

baseline correction, using a "peak width" of 0.01 V.

Each procedure explained above was repeated at least three times and repetitive measurements were performed by refreshing the surface by using both electrochemical transducers.

3.   RESULTS AND DISCUSSION

In theese studies, increased $Fe(CN)_6^{3-/4-}$ or guanine signals in the presence of CNTs were evaluated.

3.1.   DNA detection based on guanine signal by using SWCNTs-modified CPE

First, the effect of the pretreatment applied to CPE surface on guanine signals was investigated and the results are shown in Figure 1. The peak currents of the guanine signal obtained from the unpretreated and pretreated electrodes by SWV technique are shown below. The oxidation of the guanine was obtained at about +1.00V in the absence and presence of SWCNTs modification.
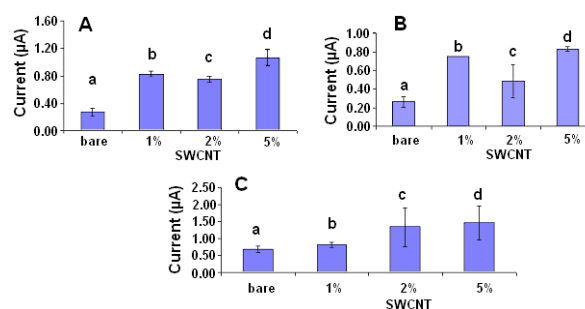
Figure 1. Graphs show the magnitude of guanine oxidation signals obtained from dsDNA immobilized surfaces (A) unpretreated CPE, (B) only 20s. ABS pretreated CPE (without potential application) (C) pretreated CPE applying at +1.7V potential during 20sec. and each column presents (a) bare electrode in the absence of carbon nanotube, (b) CNT-contained electrode in the presence of 1% SWCNTs, (c) 2% of SWCNTs and (d) 5% of SWCNTs modification onto CPEs.

The magnitude of guanine peak observed with dsDNA modified unpreated (Figure 1A, a) and ABS pretreated (Figure 1B, a) CPEs in the absence of CNTs were about the same (main averege responses ~0.30μA). However, the electrochemically pretreated CPE (Figure 1C, a) gave the highest signal after dsDNA immobilization onto the CNTs-free electrode

surface. All of these results indicated that the activation process with potential application (+1.70V during 20sec.) enhances DNA binding onto the sensor surface.

On the other hand, guanine signal obtained from dsDNA modified SWCNTs electrodes were higher (Figure 1A; b,c and d, Figure 1B; b, c and d) than that obtained CNTs-free electrode (Figure 1A, a and Figure 1B, a) in the absence of potential application for pretreatment. When these increased signals are evaluated, it is seen that the electrode with different ratios of CNT has approximately 3-4 times more response than CNTs-free electrode (Figure 1A; b,c and d, Figure 1B; b, c and d). The highest guanine signal was obtained with 5% SWCNTs modified

unpretreated electrode (Figure 1A; c). But when the pretreatment process is applied to the CNTs-contained electrode surface, only two fold signal enhancement was obtained from CPE with 2% and 5% SWCNTs without reproducibility.

A series of three repetitive DPV measurements of the guanine signal at 20 μg/ml concentration level of fish-sperm dsDNA modified unpretreated electrode with 5% SWCNTs resulted in reproducible results such as a mean response about 1.10μA with a relative standard deviation of 9.8% was calculated. As unsatisfactory and non-reproducible responses were obtained with DNA modified CPE, further studies were continued with SPE.

3.2. SWCNT-based studies by using SPE
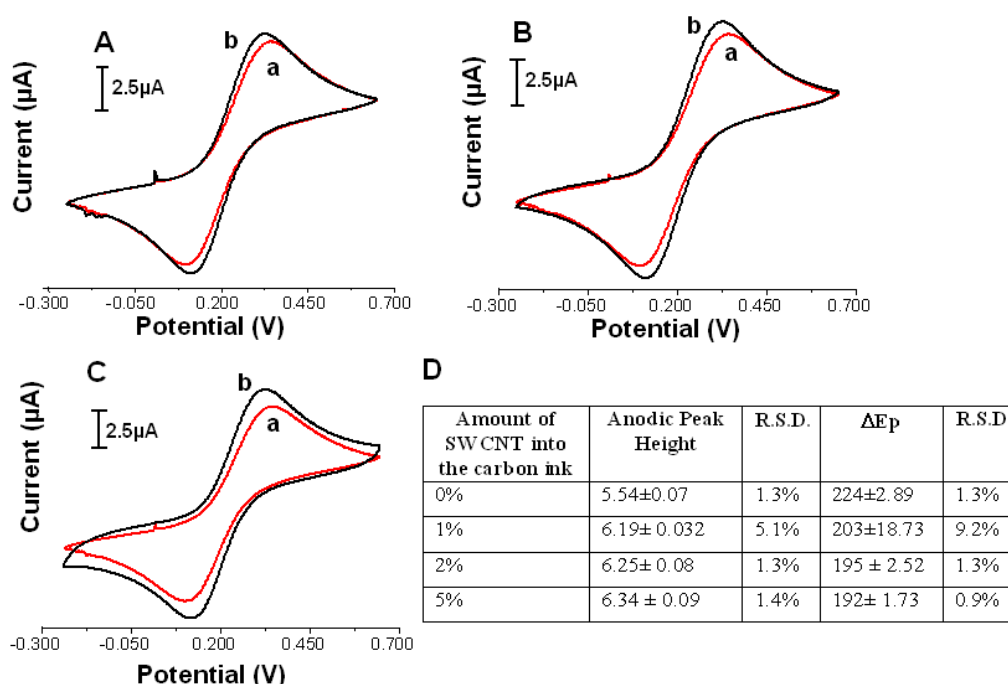
Figure 2. Cyclic voltammogram of 10 mM $K_4[Fe(CN)_6]/K_3[Fe(CN)_6]$ (1 : 1) containing 1M KCl obtained from unpretreated bare (a) and SWCNTs-modified (b) SPE surfaces. The modification rates of SWCNTs in SPE are 1%(A), 2% (B) and 5%(C), respectively. The comparison of the electron transfer features of modified SPEs was also showed in the inset Table (D).

Amount of SWCNT into the carbon ink	Anodic Peak Height	R.S.D.	ΔEp	R.S.D.
0%	5.54±0.07	1.3%	224±2.89	1.3%
1%	6.19± 0.032	5.1%	203±18.73	9.2%
2%	6.25± 0.08	1.3%	195 ± 2.52	1.3%
5%	6.34 ± 0.09	1.4%	192± 1.73	0.9%

SWCNTs were simply mixed into the carbon ink of the SPE transducer with different rates as 1%, 2% and 5% as explained in the experimental part, and the electron transfer rate of modified electrodes was monitored using CV as shown in

Figure 2. The differentiations in CV measurements were showed between the CNTs-free and CNTs-modified SPEs. According to the results, CNTs-contained electrode gave higher signal than bare electrode in each modification

conditions and the height of the anodic peak showed negative shift (approximately 21mV(1%), 29mV(2%) and 32mV (5%) respectively) in the Epa of Fe(CN)6 $3^-/4^-$ (Figure 2A, B and C). Figure 2D also presents anodic peak heights and ΔEp values of bare and modified electrodes with relative standard deviation values. The results indicated that the SWCNTs modified electrodes provide enhanced electron transfer rate (Figure 2A, B and C; approximately 11.7%, 12.8% and

14.4% of signal enhancement respectively) in comparison to the bare electrode. This result can be explained by carbon nanotube modified surfaces have better conductivity than simple carbon surfaces.

The effect of SWCNTs modification on intrinsic guanine response in different electrochemical pretreatment conditions by using SPE was showed in Figure 3.
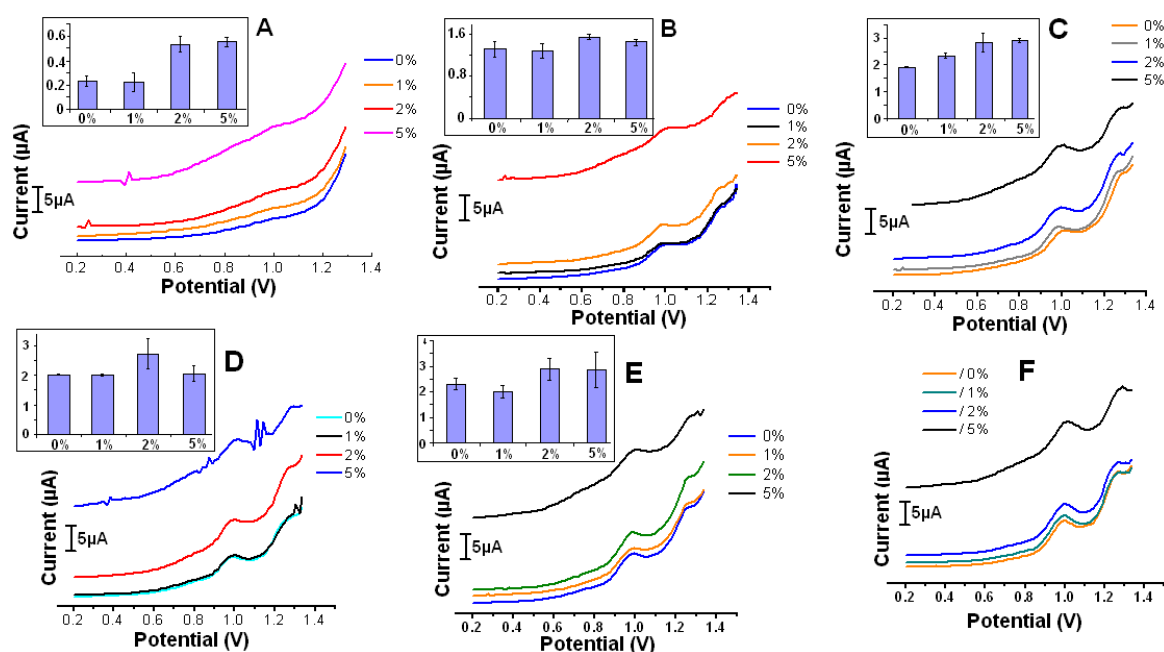
Figure 3. Voltammetric signal of guanine related to dsDNA modified sensor obtained by different pretreatment conditions such as (A) 1.2V for 60s.; (B) 1.6V for 60 s.; (C) 1.8V for 60 s.; (D) 1.6V, 120 s. and 1.8V, 60 s. together; (E) 2.0V for 60 s.; (F) 1.8V, 60s. respectively. dsDNA concentration was used as 20μg/mL and it was immobilized onto the surface of SPE by passive adsorption for 2 min. (A, B, C, D, and E) or potential application (+0.50 V for 120sec. with 200rpm. stirring, F). SWV parameters were described in the experimental section and Table 1.

The first thing to notice when looking at all the raw results obtained from figure 3A, B, C, D, E and F is that the baseline of 5% modification is higher than unmodified (0%) and other rate of CNTs modifications (1% or 2%). Another point is that the peaks obtained from the +1.2V potential applied electrodes for the pretreatment (Figure 3A, 0%, 1%, 2%, 5%) are much lower than the other electrochemically pretreated electrodes. (Figures 3B, C, D, E and F). However, the signal difference between bare and CNT-coated electrodes activated by applying the +1.2V potential (Figure 3A) is grater than more positive potential applied SPEs (Figure 3B, C, D, E and F).

In Figure 3A, it is seen that approximately 0.23μA of guanine signals were obtained with both the unmodified (0%) and the modified electrode with 1% CNT. However, in the presence of 2% or 5% of CNTs modification onto SPE, about 2.4 times higher guanine signal (average response ~0.55μA) was measured in comparison to the unmodified or 1% ratio of CNTs modified sensor. The relative standard deviation (RSD) of three repetitive measurements was calculated as 10% in the presence of 2% CNTs modification and 7% in the presence of 5% CNTs modification onto the SPE. Acording to the Figure 3A, it is proved that more sensitive DNA analysis was achieved by using

CNTs-modified (2% or 5%) screen printed electrodes.

On the other hand, the expected increase at guanine signal could not be achieved with 1.6V potential applied CNT-contained electrodes (Figure 3B). In figure 3C, when compared the detection performance of modified electrodes with unmodified electrodes, it was observed that there was an approximately 1.5-fold increase in the presence of CNT (2% and 5% ratios). However, the reproducibility of the results was not good especially for 2% of CNTs modified transducer.

When the pretreatment potential or time is further increased (Figure 3D and E) or if DNA immobilization is carried out under potential application (Figure 3F), it was observed that the CNTs modified and unmodified electrodes gave similar guanine responses (The average peak potential of all electrodes was obtained as 3-3.5µA). In other words, the signal increase expected with the modified electrodes could not be observed. This situation did not change with the extension of the DNA immobilization time (data not shown).

3.3. MWCNTs-based studies by using SPE.

Electrode type	Anodic Peak Height	R.S.D.	ΔEp	R.S.D.
Normal CSPE	5.02± 0.48	9.6%	0.25± 0.023	9.2%
bamboo type CNT	6.78± 0.01	0.2%	0.15± 0.002	1.3%
hollow type CNT	5.57±0.14	2.5%	0.21± 0.004	2.5%
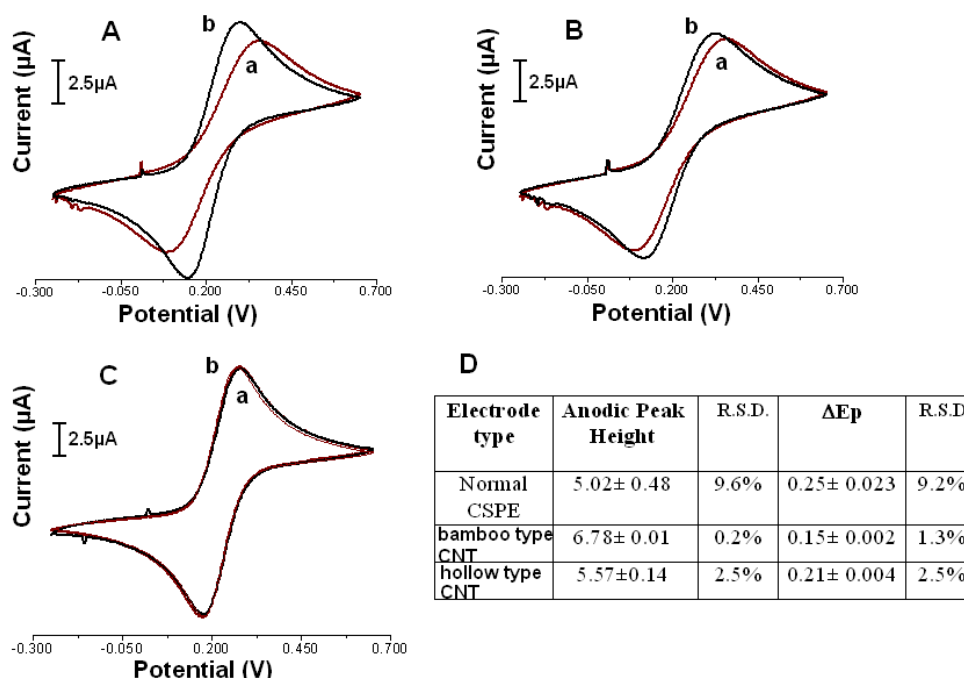
Figure 4. Voltammograms obtained from bare (a) and MWCNTs-modified (b) SPE surfaces with the solution of 10 mM $K_4[Fe(CN)_6]/K_3[Fe(CN)_6]$ (1 : 1) containing 1M KCl. The modifications of 2% ratio of MWCNTs in SPE are bamboo structure (A and C), hollow structure (B) and the surface of the SPEs were unpretreated (A and B) or pretreated (C). CV measurement parameters as explained in Figure 2. The comparison of the electron transfer features of modified SPEs was also showed in the inset Table (D).

As explained in the experimental part, MWCNTs were simply mixed into the carbon ink of the SPE transducer with 2% ratio (In the direction of the previously obtained results from DNA-based studies, 2% CNT modification was performed on the electrodes.). Differentiations in CV measurements performed in $Fe(CN)_6^{3-/4-}$ solution were presented in Figure 4. In this experiment, CNTs-free and different types of MWCNTs-modified SPEs were used to to measure the effect

of CNT modification on conductivity. Figure 4A and 4C show the responses obtained from bamboo-type MWCNTs modified SPE and Figure 4B presents the CV of hollow-type CNT-contained electrode. Red lines of each figure show the response of unmodified (CNTs-free) electrode. The most increase at the signals of ferri/ferro cyanide (~ 3.2 folds) was obtained with bamboo-structure MWCNTs modified and unpretreated SPE (Figure 4A, black line), in contrast to to the

signals observed using hollow-structure CNT modified (Figure 4C, black line) and pretreated bamboo-type CNT-modified SPEs (black line of Figure 4B). The electrochemical pretreatment (1.6V for 2min and 1.8V for 1min in acetate buffer) protocol for SPE destroyed the signal enhancement obtained by bamboo-type MWCNT modification (Figure 4C, black line). Since pretreatment was required for electrode surface optimization, it was decided to apply different pretreatment procedures in subsequent experiments. When all the results obtained using 2% bamboo-type MWCNT-modified SPEs were evaluated (Figure 4A and D), it was observed that these electrodes gave about 35% more $Fe(CN)_6^{3-/4-}$ signal than the bare electrode(Figure 4A, black line) and 22% more than the SPE containing SWCNT(Figure 2B and D) under the same experimental conditions.

On the other hand, if hollow-type MWCNT(Figure 4B and D) is used for the modification of SPE, only 11% increase in signal was observed compared to bare electrode. Thus, the high level increment at $Fe(CN)_6^{3-/4-}$ signal (Figure 4A) indicate that bamboo-type MWCNTs can provide enhanced electron transfer rate and higher surface area on the SPE. The comparison of the electron transfer features of modified SPEs based on ΔEp values were also showed in the Table (D).

Different pretreatment conditions

Different pretreatment procedures were applied [19-22] to the sensor surface to obtain the highest and reproducible responses from the CNT modified electrode. All these procedures were used for the analysis of different target molecules such as organophosphates [22].

Figure 5 shows the average signals of ferri/ferrocyanide obtained after the different

pretreatment applications on MWCNT-contained SPE surface such as (A and B) H_2SO_4 pretreatment: 2 CV scans (from -1.0 to +1.0V) in 0.2 M H_2SO_4 for bamboo type CNT(A) and hollow-type CNT(B) modified electrodes; (C and D) Acetone pretreatment: 10 μL drop (acetone/water 1:1) on the working electrode surface for 10 min. for bamboo type CNT(C) and hollow-type CNT(D) modified electrodes; (E) N,N-Dimethylformamide pretreatment: 10 μL drop on the surface till dryness for bamboo-type CNT modified electrode; (F) NaOH pretreatment: +1.5V for 2min in 1M NaOH for bamboo-type CNT modified electrode respectively. CV parameters were described in the experimental section and Figure 2.

According to the Figure 5, when NaOH(1M) pretreatment was applied to the SPE by using +1.5V potential for 2min. or diluted acetone solution (1:1) was used for pretreatment of the SPE for 10 min duration better results were obtained with them when compared to the H_2SO_4 or dimethyl formamide activated electrode surfaces based on ferri/ferrocyanide signal.

The signal increment ratio about 70% was found to be the best result obtained with the acetone pretreated and bamboo-structure CNT modified SPE (Figure 5C). However, with other H_2SO_4 (Figure 5A) and NaOH(Figure 5F) pretreatment conditions, a signal increase of about 30% was obtained with the bamboo-structure CNT modified electrode.

On the other hand, no sufficient increase in DNA signals could be obtained with pretreatment procedures at acidic pH throughout the study. For this reason, further studies were carried out with acetone and NaOH-activated electrodes for label-free biosensor applications. The studies based on guanine signal measurement performed with dsDNA are shown in Figure 6.
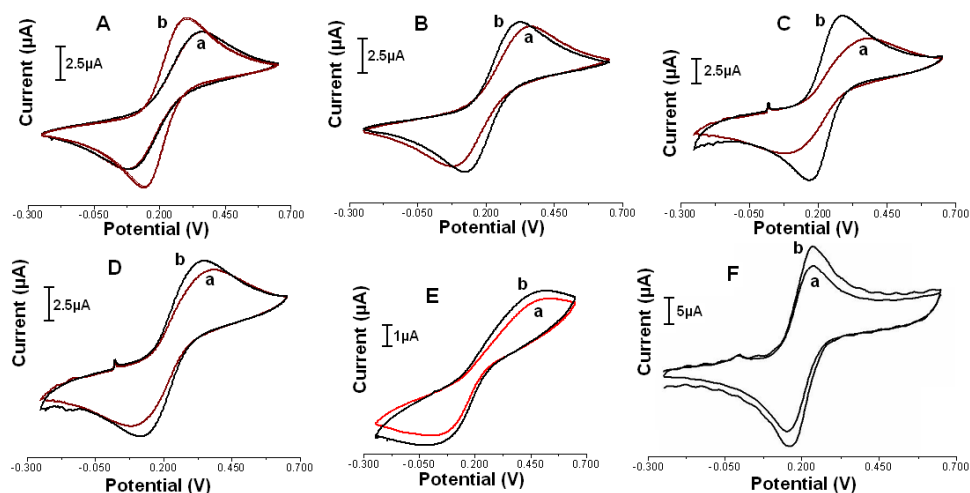
Figure 5. Voltammograms obtained from bare (a) and MWCNTs-contained (b) SPE surfaces with the solution of 10 mM $K_4[Fe(CN)_6]/K_3[Fe(CN)_6]$ (1: 1) containing 1M KCl. The modifications of 2% ratio of bamboo(A,C, E and F) or hollow-structure(B and D) MWCNTs in SPE the surface of the SPEs were pretreated with H_2SO_4 (A, B), acetone (C,D), Dimethylformamide(E) or NaOH (F). CV measurement parameters as similarly with the Figure 2.

SPEs were pretreated with H_2SO_4 (A, B), acetone (C,D), Dimethylformamide(E) or NaOH (F). CV measurement parameters as similarly with the Figure 2.

In label-free DNA biosensor studies it is expected that the guanine signal increase is obtained with the nanomaterial modified electrodes. For this purpose, 20 ppm dsDNA was immobilized in acetone(Figure 6A) or NaOH(Figure 6B) activated surfaces for 1 hour. After washing, guanine and adenine signals obtained from bare SPE or bamboo-structure CNT-modified SPE measured by DPV method were examined.
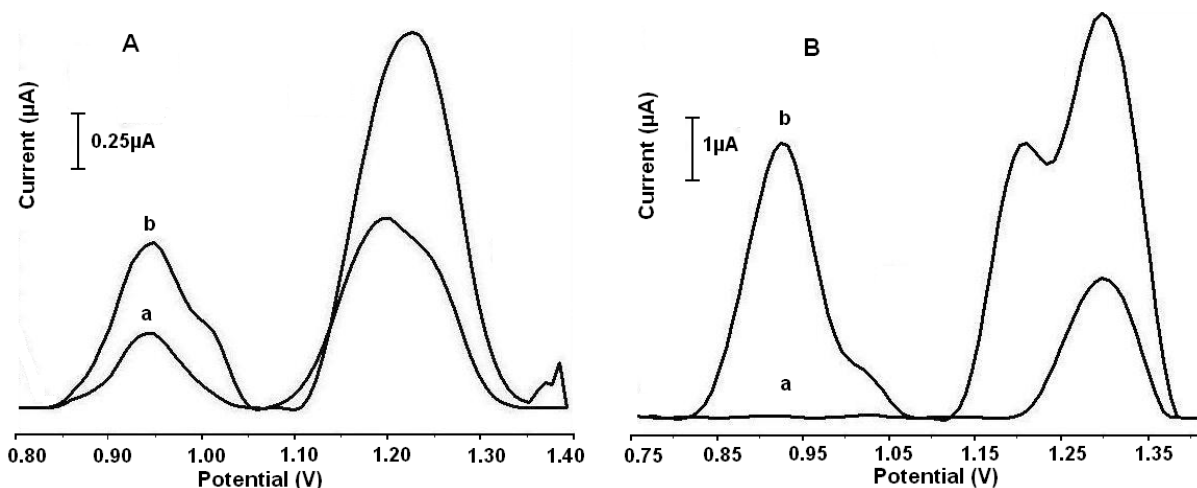
Figure 6. Influence of acetone (A) and NaOH(B)-based pretreatment process on the sensitivity of biosensor by using guanine-contained double stranded DNA. DPV of guanine oxidation signals obtained from DNA-modified bare (a) and bamboo-structured MWCNTs modified (b) electrodes.

The average guanine signal was observed as 332nA with bare electrode and 731nA with nanomaterial modified SPE by using acetone pretreatment method (Figure 6A). The CNT-modified electrode (Figure 6A,b) showed nearly two times increase at guanine response when compared to the bare electrode(Figure 6A,a). On the other hand, the average guanine response was

obtained as 4.36μA with NaOH-pretreated and CNT-contained SPE (Figure 6B,b). In comparison to the responses observed by using 20 μg/mL dsDNA immobilized bare electrode (Figure 6B,a), approximately 62 folds increment at the guanine peak was obtained by using DNA modified CNT-included SPE (Figure 6B, b). This huge signal enhancement originated from bamboo-type carbon nanotubes. The results of this experiment showed that carbon nanotubes could be used successfully to reduce the detection limit in biosensor design studies. On the other hand, in adenine signals obtained at about 1.25V(second peaks of Figure 6A and B at about 1.25V), significant signal increases were obtained with nanotube modified electrodes.

If the acetone and NaOH pretreatment techniques are compared in terms of ferricyanide/ferrocyanide signal increase between bare and CNT-modified electrode, acetone-based method showed 3.2 times more increase (Figure 5C) than NaOH pretreatment technique(Figure 5F). However, when the obtained guanine signals are evaluated, the signal obtained by the NaOH based pretreatment is much more than the acetone based method. This demonstrates the importance of pretreatment in biosensor studies. As a result, the guanine signal obtained after DNA immobilization on the electrode should be carefully examined after a certain increase in the electron transfer rate to be observed by the activation of the nanomaterial modified electrode.

There are also numerous conditions for pretreatment of SPEs in the literature for different research purposes [23]. For example, Morrin et al applied an electrochemical pretreatment based on CV method scanning between +1.2 V and +1.5 V in 0.2M H_2SO_4 solution [24]. Lee et al. also used CV technique scanning from -0.5V to +0.2V for 20 min in 0.1M $NaNO_3$[25.]. In another work, screen printed carbon electrodes were activated in saturated Na_2CO_3 solution at +1.2V for 5 min [17]. Patris et al. pretreated SPEs for 1.5 min in H_2SO_4 under +1.6V potential application [26]. When we compared our simple NaOH pretreatment protocol with these studies, it has advantages such as shorter activation time (2 min) and potential application (+1.5 V). In addition, it is the first time that NaOH pretreatment method and bamboo-type CNTs modification have been shown to increase the DNA signal by nearly 62 times.

4. CONCLUSION

The bamboo-type MWCNTs structure was modified to the SPE surface which is suitable for measuring intrinsic guanine oxidation signal directly. The main advantage of the applied protocol is its effective pretreatment step applied on CNTs-contained SPE providing highly enhanced signal with high sensitivity. The effect of bamboo-type carbon nanotubes on guanine signal enrichment was shown for the first time in this study. The modification of SPEs and its pretreatment with NaOH provide enhanced adsorption of DNA on the surface of the sensor, and thus they offer nearly 62 times increased sensitivity besides low detection limit when compared with CNTs-free sensor. In the new biosensor systems to be designed, if the method in this sensor based on label-free measurement is used, a new and strong alternative will be introduced to the traditional methods. Because indicator-free detection is greatly simplify the sensing methodology by eliminating the use of label and the need for the additional time-consuming process for indicator-DNA interaction. Future plan for this laboratory will be the development of hybridization-based DNA biosensors that can be converted into microchips.

REFERENCES

[1]. Lazerges M., Bedioui F. Analysis of the evolution of the detection limits of electrochemical DNA biosensors. Anal. Bioanal. Chem. 405 (2013) 3705–3714.

[2]. Liu Z., Tabakman S., Welsher K., Dai H.J. Carbon nanotubes in biology and medicine: In vitro and in vivo detection, imaging and drug delivery. Nano Res. 2 (2009) 85–120.

[3]. Trojanowicz M. Analytical applications of carbon nanotubes: a review. TrAC Trends Anal. Chem. 25 (2006) 480–489.

[4]. Wang J., Lin Y.H. Functionalized carbon nanotubes and nanofibers for biosensing applications. TrAC Trends Anal. Chem. 27 (2008) 619–626.

[5]. Li F., Peng J., Wang J., Tang H., Tan L., Xie Q., Yao S. Carbon nanotube-based label-free electrochemical biosensor for sensitive detection of miRNA-24. Biosens. Bioelectron. 54 (2014) 158–164.

[6]. Zhu X., Li J., He H., Huang M., Zhang X., Wang S. Application of nanomaterials in the bioanalytical detection of diseaserelated genes yayinindan Biosensors and Bioelectronics 74 (2015) 113–133.

[7]. Erdem A., Kuralay F., Cubukcu H.E., Congur G., Karadeniz H., Canavar E. Sensitive sepiolite-carbon nanotubes based disposable electrodes for direct detection of DNA and anticancer drug–DNA interactions. Analyst 137 (2012) 4001–4004.

[8]. Sengiz C., Congur G., Eksin E., Erdem A. Multiwalled Carbon Nanotubes-Chitosan Modified Single-Use Biosensors for Electrochemical Monitoring of Drug-DNA Interactions. Electroanal. 27 (2015) 1855 – 1863.

[9]. Zhang Q.D., Piro B., Noël V., Reisberg S., Pham M.C. Functionalization of single-walled carbon nanotubes for direct and selective electrochemical detection of DNA. Analyst 136 (2011) 1023–1028.

[10]. Lee A.C., Du D., Chen B., Heng C.K., Lim T.M., Lin, Y. Electrochemical detection of leukemia oncogenes using enzyme-loaded carbon nanotube labels. Analyst 139 (2014) 4223–4230.

[11]. Thuy N.T., Tama P.D., Tuan M.A., Le A.-T., Tama L.T., Thu V.V., Hieu N.V., Chien N.D., Detection of pathogenic microorganisms using biosensor based on multi-walled carbon nanotubes dispersed in DNA solution. Curr. Appl. Phys. 12 (2012) 1553–1560.

[12]. Zhang X., Jiao K., Liu S., Hu Y. Readily reusable electrochemical DNA hybridization biosensor based on the interaction of DNA with single-walled carbon nanotubes. Anal. Chem. 81 (2009) 6006–6012.

[13]. Ozkan-Ariksoysal D., Kayran Y.U., Yilmaz F.F., Ciucu A.A., David I.G., David V., Hosgor-Limoncu M., Ozsoz M. DNA-wrapped multi-walled carbon nanotube modified electrochemical biosensor for the detection of Escherichia coli from real samples. Talanta 166 (2017) 27–35.

[14]. Chekin F., Gorton L., Tapsobea I. Direct and mediated electrochemistry of peroxidase and its electrocatalysis on a variety of screen-printed carbon electrodes: amperometric hydrogen peroxide and phenols biosensor. Anal. Bioanal. Chem. 407 (2015) 439–446.

[15]. Erdem A., Karadeniz H., Canavar P.E., Congur G. Single-Use Sensor Platforms Based on Carbon Nanotubes for Electrochemical Detection of DNA Hybridization Related to Microcystis spp. Electroanal. 24 (2012) 502 – 511.

[16]. Jeong S.H., Kim C.S., Yang J. Comparison of the sensitivity of thiolated aptamer based biosensor according to the condition of electrode substrates. BioChip J. 4 (2010) 141-147.

[17]. Cui G., Yoo J.H., Lee J.S., Yoo J., Uhm J.H., Cha G.S., Nam H. Effect of pre-treatment on the surface and electrochemical properties of screen-printed carbon paste electrodes. Analyst 126 (2001) 1399–1403.

[18]. Carpini G., Lucarelli F., Marrazza G., Mascini M. Oligonucleotide-modified screen-printed gold electrodes for enzyme-

amplified sensing of nucleic acids. Biosens. Bioelectron. 20 (2004) 167–175.

[19]. Trojanowicz M., Mulcandani A., Mascini M. Carbon nanotubes-modified screen-printed electrodes for chemical sensors and biosensors. Anal. Lett.,37 (2004) 3185- 3204

[20]. Wen J.G., Li W. Z., Huang Z. P., Tu Y., Wang D. Z., Chen J. H., Yang S. X., Ren Z. F. Microstructural Studies on CVD grown multiwall carbon nanotubes and their breaking behaviors by TEM., 199th meeting of The electrochemical Society, March 25-30, 2001, Washington, DC.

[21]. Williams K.A., Veenhuizen P.T.M. de la Torre BG., Eritja R., Dekker C. Nanotechnology: carbon nanotubes with DNA recognition. Nature, 420 (2002), 761.

[22]. Lin Y., Lu F., Wang J. Disposable carbon nanotube modified screen printed biosensor for amperometric detection of organophosphorus pesticides and verve agents. Electroanal., 16 (2004) 145-149.

[23]. Topkaya S.N., Ozkan-Ariksoysal D. Prostate Cancer Biomarker Detection with Carbon Nanotubes Modified Screen Printed Electrodes Electroanal. 28 (2016) 1077 – 1084.

[24]. Morrin A., Killard A.J., Smyth M. R. Electrochemical characterization of commercial and home-made Screen-Printed Carbon electrodes. Anal. Lett. 36 (2003), 2021–2039.

[25]. Lee P.T., Lowinsohn D., Compton R. G. The Use of Screen-Printed Electrodes in a Proof of Concept Electrochemical Estimation of Homocysteine and Glutathione in the Presence of Cysteine Using Catechol. Sensors 14 (2014), 10395–10411.

[26]. Patris S., De Pauw P., Vandeput M., Huet J., Van Antwerpen P., Muyldermans S., Kauffmann J.M. Nanoimmunoassay onto a screen printed electrode for HER2 breast cancer biomarker determination. Talanta 130 (2014), 164–170.

Selfadjointness and Positiveness of the Differential Operators Generated by New Type Sturm-Liouville Problems

Hayati OLĞAR

Gaziosmanpasa University, Faculty of Science Department of Mathematics, Tokat, TURKEY

Abstract. It is purpose of this paper to investigate Sturm-Liouville equation $-u''(x) + q(x)u(x) = \lambda u(x)$ on many-interval $[\alpha, \gamma_1^-) \cup (\gamma_1^+, \gamma_2^-) \cup (\gamma_2^+, \beta]$ with the eigenvalue parameter appearing linearly in the boundary conditions and with two supplementary transmission conditions. The classical Sturmian theory did not cover such type of many-interval boundary value transmission problems. For the classical Sturm-Liouville problems it is guaranteed that the problem is self-adjoint with compact resolvent, the spectrum is disctrete and consist of eigenvalues and the corresponding eigenfunctions form an orthogonal basis in the well-known Hilbert space $L_2[\alpha, \beta]$. But the boundary-value-transmission problems are not self-adjoint and the system of eigenfunctions did not form a basis in the classical Hilbert space $L_2[\alpha, \beta]$ in general. Taking in view this fact we suggest a new approach for self-adjoint realization of such type transmission problems. Moreover, we define some new Hilbert spaces to establish positiveness of corresponding operator-pencil. At first we define a concept of generalized eigenfunctions for this kind of spectral problems. In particular it is shown that if the potential $q(x)$ is continuous then the generalized eigenfunctions satisfies the considered problem is the classical sense. Then we introduce to the consideration some compact operators such a way that the considered boundary-value-transmission problem can be reduced to the appropriate operator-pencil equation. Finally, we prove that this operator-pencil is self-adjoint and positive definite for sufficiently large negative values of the eigenparameter. It is important to note that the obtained results extends classical results associated with regular Sturm-Liouville problems.

Keywords: Boundary value problems, eigenfunctions, boundary and transmission conditions, positive operators.

Yeni Tipten Sturm-Liouville Problemlerinin Ürettiği Diferansiyel Operatörlerin Kendine Eşlenikliği ve Pozitivliği

Özet. Bu makalenin amacı $[\alpha, \gamma_1^-) \cup (\gamma_1^+, \gamma_2^-) \cup (\gamma_2^+, \beta]$ çok-aralığında tanımlı olan, özdeğer parametresini doğrusal olarak sınır şartlarında bulunduran ve iki tane ek geçiş şartı içeren $-u''(x) + q(x)u(x) = \lambda u(x)$ Sturm-Liouville problemini araştırmaktır. Klasik Sturm-Liouville teorisi bu tipten çok-aralıklı sınır-değer-geçiş problemlerini kapsamaktadır. Klasik Sturm-Liouville problemleri için kendine-eşleniklik, rezolventin kompaktlığı, spektrumun diskretliği ve uygun özfonksiyonların iyi bilinen $L_2[\alpha, \beta]$ Hilbert uzayında ortogonal baz oluşturma özelliği sağlanmaktadır. Genellikle sınır-değer-geçiş problemleri kendine-eşlenik değildir ve özfonksiyonlar sistemi klasik $L_2[\alpha, \beta]$ Hilbert uzayında baz oluşturmuyor. Bunu dikkate alarak, bu tipten geçiş problemlerinin kendine-eşlenik biçimde sonuçlanabilmesi için yeni bir yaklaşım önermişiz.

* Corresponding author. *Email address:*   *hayati.olgar@gop.edu.tr*

Bunun dışında uygun operatör-demetinin pozitivliğini gösterebilmek için bazı yeni Hilbert uzayları tanımladık. İlk olarak bu türden spektral problemlerin genelleştirilmiş özfonksiyonları kavramını tanımladık. Özel olarak gösterdik ki, eğer $q(x)$ potansiyeli sürekli ise, o halde genelleşmiş özfonksiyonlar incelediğimiz problemi klasik anlamda da sağlıyor. Daha sonra bazı kompakt operatörleri öyle tanımladık ki araştırılan sınır-değer-geçiş problemlerini uygun operatör demetine dönüştürmek mümkün olsun. Son olarak özdeğer parametresinin mutlak değerce yeteri kadar büyük negatif değerleri için bu operatör demetinin kendine eşlenik ve pozitif olduğunu ispat ettik. Elde edilen sonuçların düzgün Sturm-Liouville problemlerinin sağladığı klasik sonuçları genelleştirmesi önem arz etmektedir.

Anahtar Kelimeler: Sınır değer problemleri, özfonksiyonlar, sınır ve geçiş şartları, pozitif operatörler.

1. INTRODUCTION

In the present work we consider a Sturm-Liouville equation

$$-u''(x)+q(x)u(x)= \lambda u(x) \tag{1}$$

on $[\alpha,\gamma_1^-)\cup(\gamma_1^+,\gamma_2^-)\cup(\gamma_2^+,\beta]$, together with eigendependent boundary conditions at the end-points $x=\alpha$ and $x=\beta$, given by

$$\kappa_1 u(\alpha)-\kappa_3 u'(\alpha)-\lambda\kappa_2 u'(\alpha)=0 \tag{2}$$
$$u'(\beta)=0 \tag{3}$$

and with transmission conditions at two interior points $x=\gamma_1$ and $x=\gamma_2$, given by

$$u(\gamma_1^+)-\tau_1 u(\gamma_1^-)=0 \tag{4}$$

$$u'(\gamma_1^+)-\frac{1}{\tau_1}u'(\gamma_1^-)-u(\gamma_1^-)=0 \tag{5}$$

$$u(\gamma_2^+)-\tau_2 u(\gamma_2^-)=0 \tag{6}$$

$$u'(\gamma_2^+)-\frac{1}{\tau_2}u'(\gamma_2^-)-u(\gamma_2^-)=0 \tag{7}$$

where $q(x)$ is a real valued function which is continuous in $\eth_1=(\alpha,\gamma_1^-)$, $\eth_2=(\gamma_1^+,\gamma_2^-)$ $\eth_3=(\gamma_2^+,\beta)$ and has finite limits $q(\alpha+0),q(\gamma_1^\pm\pm0),q(\gamma_2^\pm\pm0),q(\beta-0),\lambda$ is a complex spectral parameter, κ_i,τ_j ($i=1,2,3$ and $j=1,2$) are real numbers and $\rho=\kappa_1\kappa_2>0$, $\tau_j>0$.

Some properties of the Sturm-Liouville Problem (1)-(3) has been studied by many authors (see, e.g., [1-4]). The main goal of those papers is the analysis of the spectrum and justification of the eigenfunction expansion. The considerations of [2, 4] are based on the operator-theoretic formulation of the Sturm-Liouville problem (1)-(3). The discrete version of this problem was dealt with by Harmsen and Li [5], Atkinson [6]. The boundary value problem with the parameter appearing nonlinearly in the boundary conditions is also important and has a variety of applications. The continuous version of this problem was dealt with by Binding et al. [7-8], Greenberg and Babuska [9]. Oscillation and comparison results have been obtained in [7]. The completeness of the eigenfunctions and eigenfunction expansions in various function spaces for the Sturm-Liouville problems with spectral parameter in the boundary conditions have been considered in [10-16]. Problems with various singularities have been analyzed in [17-19, 20-30].

In different areas of applied mathematics and physics many problems arise in the form of boundary value problems involving transmission conditions at the interior singular points. Such problems are called boundary-value-transmission problems. This kind of problems arise in various problems of mathematics and physics as well as in applications. For example, some boundary value problems with transmission conditions arise in heat and mass transfer problems [31], in vibrating string problems [32], in diffraction problems [33] and etc. The basis properties and eigenfunction expansions in various function spaces of the eigenfunction of the Sturm-Liouville problems with spectral parameter in the boundary conditions have been considered in [10-13, 31, 34]. The concept of generalized solutions in a Hilbert space (see, [34]) allows the eigenvalue problem to be reduced to an operator-pencil equation. In suitable Hilbert space Belinskiy and Dauer in [10, 11] have considered the generalized eigenfunctions of a regular Sturm-Liouville problem on a finite interval with the eigenvalue parameter appearing linearly in the boundary conditions.

It is the aim of this paper is to reduce the boundary-value-transmission problem (1)-(7) to an operator pencil equation

$$L(\lambda)\psi = 0, \quad L(\lambda) := \sum_{i=0}^{n} \lambda^{i} A_{i}$$

in a corresponding Hilbert space. We introduce to the consideration some compact operators such a way that the considered boundary-value problem can be reduced to the appropriate operator-pencil equation and prove that this operator-pencil is self-adjoint and positive definite for sufficiently large negative values of the eigenparameter.

2. SOME AUXILIARY FACTS

We use the standard notations for the Hilbert spaces $\bigoplus_{i=1}^{3} L_2(\mho_i), \bigoplus_{i=1}^{3} H^1(\mho_i)$. The inner products in those spaces are given by

$$\langle u, \vartheta \rangle_0 = \int_{\alpha}^{\gamma_1^-} u(x)\overline{\vartheta}(x)dx + \int_{\gamma_1^+}^{\gamma_2^-} u(x)\overline{\vartheta}(x)dx + \int_{\gamma_2^+}^{\beta} u(x)\overline{\vartheta}(x)dx$$

and

$$\langle u, \vartheta \rangle_1 = \int_{\alpha}^{\gamma_1^-} \left\{ u'(x)\overline{\vartheta'}(x) + u(x)\overline{\vartheta}(x) \right\} dx$$

$$+ \int_{\gamma_1^+}^{\gamma_2^-} \left\{ u'(x)\overline{\vartheta'}(x) + u(x)\overline{\vartheta}(x) \right\} dx$$

$$+ \int_{\gamma_2^+}^{\beta} \left\{ u'(x)\overline{\vartheta'}(x) + u(x)\overline{\vartheta}(x) \right\} dx$$

with the corresponding norms are

$$\|u\|_0 = \sqrt{\langle u, u \rangle_0}$$

and

$$\|u\|_1 = \sqrt{\langle u, u \rangle_0} \tag{8}$$

respectively. According to the embedding theorems for the Sobolev spaces ([35]) the functions in $\bigoplus_{i=1}^{3} H^1(\mho_i)$ are continuous on $\mho_i$, but their (generalized) derivatives can only be assumed to be elements of $\bigoplus_{i=1}^{3} L_2(\mho_i)$.

In below we shall use the following inequalities which can be derived from the well-known embedding theorems for Sopbolev spaces (see, for example ([34])). For any $u \in \bigoplus_{i=1}^{3} H^1(\mho_i)$, the following inequalities hold

$$\left| u(x_j) \right|^2 \le d_j \|u'\|_0^2 + \frac{2}{d_j} \|u\|_0^2, \tag{9}$$

where $j = 1, 2, 3, 4$, $x_1 = \alpha$, $x_2 = \gamma_1^{\pm} \pm 0$, $x_3 = \gamma_2^{\pm} \pm 0$, $x_4 = \beta$ and d_j ($j = 1, 2, 3, 4$) are any positive real numbers are small enough. Moreover, for any $\xi \in \mho = \mho_1 \cup \mho_2 \cup \mho_3$ the inequality

$$\left| u(\xi) \right| \le C(\xi) \|u\|_1 \tag{10}$$

holds, where the constant $C(\xi)$ is independent of the function u, i.e. is dependent only of ξ.

Remark 1 Note, the normal derivative of a function $u \in \bigoplus_{i=1}^{3} H^1(\mho_i)$, might not be defined as an element of $\bigoplus_{i=1}^{3} L_2(\mho_i)$.

Remark 2 Without loss of generality the function $q(x)$ can be assumed to be positive on $\mho$. In fact, after the shift of the spectral parameter $\lambda \to \lambda - h$, where $h = \max q(x)$ for $x \in \mho$, the function $q(x)$ can be asumed to be positive eveywhere on $\mho$.

3. THE CONCEPT OF GENERALIZED EIGENFUNCTION

Let us introduce to the consideration a new Hilbert space Ξ which is the main Hilbert space considered in the remainder of this article.

Definition 1 *The inner product in the Hilbert space* $\Xi = \bigoplus_{i=1}^{3} H^1(\mho_i) \oplus \mathbb{C}$ *is defined by*

$$\langle U, V \rangle_{\Xi} = \langle u(x), \vartheta(x) \rangle_{\bigoplus_{i=1}^{3} H^1(\mho_i)} + u_1 \overline{\vartheta_1} \tag{11}$$

for $U, V \in \Xi$, *where* $u(x), \vartheta(x) \in \bigoplus_{i=1}^{3} H^1(\mho_i)$ *and* $u_1, \vartheta_1 \in \mathbb{C}$.

For further investigation we shall introduce a new inner product on the same linear space $\overset{3}{\underset{i=1}{\oplus}} H^1(\mho_i)$ as follows:

$$\langle u, \vartheta \rangle_{\overset{3}{\underset{i=1}{\oplus}} H_q^1(\mho_i)} = \langle u, q\vartheta \rangle_0 + \langle u', \vartheta' \rangle_0.$$

Since $q(x)$ is bounded, positively defined and measurable function, there exist constants $m > 0$ and $M > 0$ such that

$$m \| u \|_1 < \| u \|_{\overset{3}{\underset{i=1}{\oplus}} H^1(\mho_i)} < M \| u \|_1$$

for all $u(x) \in \overset{3}{\underset{i=1}{\oplus}} H^1(\mho_i)$.

Consequently the inner product (11) generates a norm that is equivalent to the standard norm produced by (8) and therefore the inner product space $\overset{3}{\underset{i=1}{\oplus}} H^1(\mho_i)$ is also Hilbert space.

Now we shall define a concept of generalized solution which is fundamental to this work. The definition of a generalized solutions of the Sturm-Liouville problem (1)-(7) follows by the known procedure (see [34], [36]). Multiplying equation (1) by a conjugate to an arbitrary function $\vartheta(x) \in \overset{3}{\underset{i=1}{\oplus}} H^1(\mho_i)$ and integrate by parts over the intervals $\mho_i (i = 1, 2, 3)$ and applying the boundary and transmission conditions (2)-(7), we can reduce it to the integral form

$$\int_{\mho_1} \left\{ u'(x)\overline{\vartheta'}(x) + q(x)u(x)\overline{\vartheta}(x) \right\} dx + \int_{\mho_2} \left\{ u'(x)\overline{\vartheta'}(x) + q(x)u(x)\overline{\vartheta}(x) \right\} dx$$
$$+ \int_{\mho_3} \left\{ u'(x)\overline{\vartheta'}(x) + q(x)u(x)\overline{\vartheta}(x) \right\} dx + \tau_1 u(\gamma_1^-)\overline{\vartheta}(\gamma_1^-) + \tau_2 u(\gamma_2^-)\overline{\vartheta}(\gamma_2^-) + u'(\alpha)\overline{\vartheta}(\alpha) \quad (12)$$
$$= \lambda \left\{ \int_{\mho_1} u(x)\overline{\vartheta}(x)dx + \int_{\mho_2} u(x)\overline{\vartheta}(x)dx + \int_{\mho_3} u(x)\overline{\vartheta}(x)dx \right\}.$$

According to the structure of the space $\overset{3}{\underset{i=1}{\oplus}} H^1(\mho_i)$ the values of derivatives at a point should be excluded from the idntity (12).

Denoting $\omega := \kappa_2 u'(\alpha)$ and taking in view the boundary condition (2), we have $u'(\alpha) = \dfrac{\omega}{\kappa_2}$. Then the boundary condition (2) can be written in the following form: $\kappa_1 u(\alpha) - \kappa_3 u'(\alpha) = \lambda \omega$.

Taking in view the last relation it is easy to see that the first boundary condition (2) takes the form

$$\frac{u(\alpha)}{\kappa_2} - \frac{\kappa_3}{\kappa_2} \frac{\omega}{\rho} = \lambda \frac{\omega}{\rho}. \quad (13)$$

Putting $u'(\alpha) = \dfrac{\omega}{\kappa_2}$ in the integral identity (17), we obtain

$$\langle u,\vartheta\rangle_{\underset{i=1}{\overset{3}{\oplus}} H^1(\mho_i)} + \tau_1 u(\gamma_1^-)\overline{\vartheta}(\gamma_1^-) + \tau_2 u(\gamma_2^-)\overline{\vartheta}(\gamma_2^-) + \frac{\omega}{\kappa_2}\overline{\vartheta}(\alpha) = \lambda\langle u,\vartheta\rangle_0 . \tag{14}$$

Thus the integro-differential equation (12) is transformed into the system of equalities (13)-(14) all terms of which are defined for the $u,\vartheta \in \underset{i=1}{\overset{3}{\oplus}} H^1(\mho_i)$.

Now we are ready to introduce a concept of generalized solution for the problem under consideration.

Definition 2 *The two-component element* $(u(x),\omega)$ *of the Hilbert space* Ξ *is said to be a generalized solution of the Sturm-Liouville problem (1)-(7), if this element satisfy the equations (13) and (14) for any* $\vartheta \in \underset{i=1}{\overset{3}{\oplus}} H^1(\mho_i)$.

The concept of the generalized solution is based on the following result.

Lemma 1 *Let the function* u *is twice continuously differentiable and the function* q *continuously on* $\mho$. *Then the generalized solution of the Sturm-Liouville problem satisfies equations (1)-(7) in the classical sense.*

Consequently the concept of generalized solution is an extension of a classical solution.

4. OPERATOR-PENCIL REALIZATION OF THE PROBLEM

The reduction of identities (13)-(14) to an operator-pencil equation is based on the following result.

Lemma 2 *For the bilinear functionals*

$$\ell_1(u,\vartheta) := \tau_1 u(\gamma_1^-)\overline{\vartheta}(\gamma_1^-) + \tau_2 u(\gamma_2^-)\overline{\vartheta}(\gamma_2^-) , \tag{15}$$

$$\ell_2(u,\vartheta) := \langle u,\vartheta\rangle_0 , \tag{16}$$

and

$$\ell_3(\omega,\vartheta) := \frac{\omega}{\kappa_2}\overline{\vartheta}(\alpha) \tag{17}$$

there are such bounded linear operators $\mathrm{T}_1,\mathrm{T}_2$ *and* T_3 *respectively such that*

$$\ell_k(u,\vartheta) = \langle \mathrm{T}_k u,\vartheta\rangle_{\underset{i=1}{\overset{3}{\oplus}} H^1(\mho_i)} \ \text{for}\ k = 1,2$$

and

$$\ell_3(\omega,\vartheta) = \langle \mathrm{T}_3\omega,\vartheta\rangle_{\underset{i=1}{\overset{3}{\oplus}} H^1(\mho_i)} \ \text{for}\ k = 3. \tag{18}$$

Moreover the operators $\mathrm{T}_1,\mathrm{T}_2 : \underset{i=1}{\overset{3}{\oplus}} H^1(\mho_i) \to \underset{i=1}{\overset{3}{\oplus}} H^1(\mho_i)$ *and* $\mathrm{T}_3 : \mathbb{C} \to \underset{i=1}{\overset{3}{\oplus}} H^1(\mho_i)$ *are compact, the operators* T_1 *and* T_2 *are selfadjoint and positive.*

Proof. The functionals ℓ_k $(k = 1, 2, 3)$ allows the following obvious estimates:

$$\left|\ell_1(u, \vartheta)\right| \le C_1 \left\{ |\tau_1| \; \left|u(\gamma_1^-)\right| \left|\overline{\vartheta}(\gamma_1^-)\right| + |\tau_2| \; \left|u(\gamma_2^-)\right| \left|\overline{\vartheta}(\gamma_2^-)\right| \right\},$$

$$\left|\ell_2(u, \vartheta)\right| \le C_2 \|u\| \|\vartheta\|,$$

and

$$\left|\ell_3(\omega, \vartheta)\right| \le C_3 |\omega| |\vartheta(\alpha)|.$$

Here and below C_k $(k = 1, 2, ...)$ denote different positive constant whose exact values are not important for the proof.

The inequality (9)-(10) imply

$$\|u\| \le C_4 \|u\|_{\underset{i=1}{\overset{3}{\oplus}} H_q^1(\mho_i)}$$

and

$$|u(d)| \le C_5 \|u\|_{\underset{i=1}{\overset{3}{\oplus}} H_q^1(\mho_i)} \; for \; any \; d \in \mho_i.$$

Hence, the functionals ℓ_k $(k = 1, 2, 3)$ alllows the following estimate:

$$\left|\ell_1(u, \vartheta)\right| \le C_6 \|u\|_{\underset{i=1}{\overset{3}{\oplus}} H_q^1(\mho_i)} \|\vartheta\|_{\underset{i=1}{\overset{3}{\oplus}} H_q^1(\mho_i)},$$

$$\left|\ell_2(u, \vartheta)\right| \le C_7 \|u\|_{\underset{i=1}{\overset{3}{\oplus}} H_q^1(\mho_i)} \|\vartheta\|_{\underset{i=1}{\overset{3}{\oplus}} H_q^1(\mho_i)},$$

$$\left|\ell_3(\omega, \vartheta)\right| \le C_8 |\omega| \|\vartheta\|_{\underset{i=1}{\overset{3}{\oplus}} H_q^1(\mho_i)}.$$

Thefore, ℓ_k $(k = 1, 2, 3)$ are linear functionals in $\vartheta \in \underset{i=1}{\overset{3}{\oplus}} H^1(\mho_i)$ for any given $u \in \underset{i=1}{\overset{3}{\oplus}} H^1(\mho_i), k = 1, 2$, and $\omega \in \mathbb{C}, k = 3$, respectively. The Riesz representation theorem shows that the representations (15)-(17) are valid for some bounded operators T_k $(k = 1, 2, 3)$. The selfadjointness and positiveness of the operators T_1 and T_2 are obvious. The compactness of T_2 is well-known fact (see, [34]). The proof of the compactness of T_1 can be found by using the same arguments, as in [10, 11] and [13].

Now the compactness of the operator T_3 will be proven. It is easy to verify that the adjoint operator of T_3 is defined on whole $\underset{i=1}{\overset{3}{\oplus}} H^1(\mho_i)$ with equality $T_3^* u = \dfrac{1}{\kappa_2} u(\alpha)$. From this representation it follows that , the operator T_3^* from $\underset{i=1}{\overset{3}{\oplus}} H^1(\mho_i)$ to $\mathbb{C}$ are bounded, i.e

$$\left|T_3^* u\right| \le C_9 \|u\|_{\underset{i=1}{\overset{3}{\oplus}} H_q^1(\mho_i)}.$$

Consequently the operator T_3^* is bounded linear operator with finite dimensional range and therefore is compact.

Then by virtue of well-known theorem of Functional Analysis (see, for example [37]) the operator T_3 is also compact. The proof is complete.

Lemma 3 *The generalized eigenfunctions of the Sturm-Liouville problem (1)-(7) satisfy the following operator polynomial equation in* Ξ

$$L(\lambda)\Phi = 0, \quad L(\lambda) = L_1 - \lambda L_2,$$

$$L_1 = \begin{pmatrix} I + T_1 & T_3 \\ T_3^* & -\dfrac{\kappa_3}{\kappa_2 \rho} I \end{pmatrix}, \quad L_2 = \begin{pmatrix} T_2 & 0 \\ 0 & \dfrac{1}{\rho} I \end{pmatrix}. \tag{19}$$

Here I *is the identity operator and the space* Ξ *is described in Definition1 and* $\Phi = (u(x) \quad \omega)$.

Proof. By using Lemma 2 the identities (13)-(14) can be rewritten as follows

$$\langle u, \vartheta \rangle_{\underset{i=1}{\overset{3}{\oplus}} H_q^1(\mho_i)} + \langle T_1 u, \vartheta \rangle_{\underset{i=1}{\overset{3}{\oplus}} H_q^1(\mho_i)} + \langle T_3 \omega, \vartheta \rangle_{\underset{i=1}{\overset{3}{\oplus}} H_q^1(\mho_i)} = \lambda \langle T_2 u, \vartheta \rangle_{\underset{i=1}{\overset{3}{\oplus}} H_q^1(\mho_i)},$$

$$T_3^* u - \frac{\kappa_3}{\kappa_2} \frac{\omega}{\rho} = \lambda \frac{\omega}{\rho}.$$

The arbitrariness of $\vartheta \in \underset{i=1}{\overset{3}{\oplus}} H^1(\mho_i)$ implies

$$u + T_1 u + T_3 \omega = \lambda T_2 u$$

and hence, the proof is complete.

5. SELFADJOINTNESS AND POSITIVENESS OF THE CORRESPONDING OPERATOR-PENCIL

Theorem 1 *The operators* L_1 *and* L_2 *are self-adjoint in the Hilbert space* Ξ .

Proof. Let $\Phi_1 = (u(.), \omega)$ and $\Phi_2 = (v(.), \omega')$ be any two element of Ξ . Then making use of the representation $T_3^* u = \dfrac{1}{\kappa_2} u(\alpha)$ from (15)-(18) and (19) we have

$$\langle L_1 \Phi_1, \Phi_2 \rangle_{\Xi} = \langle u + T_1 u + T_3 \omega, v \rangle_{\underset{i=1}{\overset{3}{\oplus}} H_q^1(\mho_i)} + \left(T_3^* u - \frac{\kappa_3}{\kappa_2} \frac{\omega}{\rho} \right) \overline{\omega'} \tag{20}$$

$$\langle \Phi_1, L_1 \Phi_2 \rangle_{\Xi} = \overline{\langle L_1 \Phi_2, \Phi_1 \rangle_{\Xi}} = \overline{\langle v + T_1 v + T_3 \omega', u \rangle_{\underset{i=1}{\overset{3}{\oplus}} H_q^1(\mho_i)}} + \overline{\left(T_3^* v - \frac{\kappa_3}{\kappa_2} \frac{\omega'}{\rho} \right) \overline{\omega}} . \tag{21}$$

Substracting (21) from (20) and realizing that

$$\langle T_i \omega, v \rangle_{\underset{i=1}{\overset{3}{\oplus}} H_q^1(\mho_i)} = \omega \overline{\left(T_i^* v \right)} \quad \text{and} \quad T_i^* u \overline{\omega'} = \langle u, T_i \omega' \rangle_{\Xi}$$

by definition of the adjoint operator, we see that

$$\left\langle L_1 \Phi_1, \Phi_2 \right\rangle_\Xi - \left\langle \Phi_1, L_1 \Phi_2 \right\rangle_\Xi = 0$$

so the operator L_1 is self-adjoint in the Hilbert space Ξ . Similarly we have

$$\left\langle L_2 \Phi_1, \Phi_2 \right\rangle_\Xi = \left\langle T_2 u, v \right\rangle_{\underset{i=1}{\overset{3}{\oplus}} H_q^1(\mho_i)} + \frac{\omega \overline{\omega'}}{\rho^2},$$

$$\left\langle \Phi_1, L_2 \Phi_2 \right\rangle_\Xi = \overline{\left\langle L_2 \Phi_2, \Phi_1 \right\rangle_\Xi} = \overline{\left\langle T_2 v, u \right\rangle}_{\underset{i=1}{\overset{3}{\oplus}} H_q^1(\mho_i)} + \overline{\frac{\omega' \overline{\omega}}{\rho^2}} = \left\langle T_2 u, v \right\rangle_{\underset{i=1}{\overset{3}{\oplus}} H_q^1(\mho_i)} + \frac{\omega \overline{\omega'}}{\rho^2}.$$

Consequently,

$$\left\langle L_2 \Phi_1, \Phi_2 \right\rangle_\Xi - \left\langle \Phi_1, L_2 \Phi_2 \right\rangle_\Xi = 0$$

so the operator L_2 is self-adjoint in the Hilbert space Ξ . The operators L_1 and L_2 are also compact in the Hilbert space Ξ , which completes the proof.

Corollary 1 *The operator* $L(-\lambda) = L_1 + \lambda L_2$ *is self-adjoint for each real* λ .

Remark 3 *Let* $\lambda \in \mathbb{C}$ *be any eigenvalue with the generalized eigenfunction* $\tilde{u}(x, \lambda) := \left(u(x, \lambda), \omega \right)$. *Then the operator polynomial equation* $L(-\lambda)\, \tilde{u}(., \lambda) = 0$ *is hold in the Hilbert space* Ξ .

Lemma 4 *The inequality*

$$2 \left| \text{Re} \left(\int_\mho u(x) \overline{\vartheta}(x) dx \right) \right| \leq \|u\|^2 + \|\vartheta\|^2 \tag{22}$$

is hold for any $u, \vartheta \in \underset{i=1}{\overset{3}{\oplus}} L_2(\mho_i)$.

Proof. The inequality (22) is a direct consequence of the polar identity.

Now, making use the Lemma 2, Theorem 1 and inequality (22) we have the following important result.

Theorem 2 There exists $\mu > 0$ such that for each real $\lambda_0 > \mu$, the operators $L(-\lambda_0)$ is positive defined in the Hilbert space Ξ , that is for real positive λ_0 large enough, there exists a constant $C = C(\lambda_0) > 0$ depending only of parameter λ_0 , such that

$$\left\langle L(-\lambda_0) \Phi, \Phi \right\rangle_\Xi \geq C(\lambda_0) \|\Phi\|_\Xi^2$$

for all $\Phi \in \Xi$.

REFERENCES

[1]. C. T. Fulton, Two-point boundary value problems with eigenvalue parameter contained in the boundary conditions, Proc. R. Soc. Edinburgh, A77(1977), 293-308.

[2]. D. B. Hinton, An expansion theorem for an eigenvalue problem with eigenvalue parameter contained in the boundary condition, Quart. J. Math. Oxford, 30(1979), 33-42.

[3]. A. Schneider, A Note on Eigenvalue Problems with Eigenvalue Parameter in the Boundary Conditions, Math. Z., 136(1974) 163-167.

[4]. J. Walter, Regular eigenvalue problems with eigenvalue parameter in the boundary conditions. Math. Z. 133(1973), 301-312.

[5]. B. Harmsen, A. Li, Discrete Sturm-Liouville problems with parameter in the boundary conditions, Journal of Difference Equations and Applications, 8(11)(2002), 969-981.

[6]. F. V. Atkinson, Discrete and Continuous Boundary Problems, Academic Press, New York, 1964.

[7]. P. A. Binding, P. J. Browne, Oscillation theory for indefinite Sturm-Liouville problems with eigenparameter dependent boundary conditions, Proc. Roy. Soc. Edinburgh Sect., A 127(1997), 1123-1136.

[8]. P. A. Binding, P. J. Browne and K. Seddighi, Sturm-Liouville problems with eigenparameter dependent boundary conditions, Proc. Edinburgh Math. Soc., 37(2)(1993), 57-72.

[9]. L. Greenberg, I. Babuska, A continuous analogue of Sturm sequences in the context of Sturm-Liouville problems, SIAM Journal on Numerical Analysis, 26(1989), 920-945.

[10]. B. P. Belinskiy, J. P. Dauer, On a regular Sturm-Liouville problem on a finite interval with the eigenvalue parameter appearing linearly in the boundary conditions, Spectral theory and computational methods of Sturm-Liouville problem. Eds. D. Hinton and P. W. Schaefer, 1997.

[11]. B. P. Belinskiy, J. P. Dauer, Eigenoscillations of mechanical systems with boundary conditions containing the frequency, Quarterly of Applied Math., 56(1998), 521-541.

[12]. N. B. Kerimov, R. Kh. Mamedov, On a boundary value problem with Spectral parameter in the boundary conditions, (Russian) Sibirsk. Mat. Zh. 40, no 2, (1999) pp. 325-335.

[13]. H. Olğar, O. Sh. Mukhtarov, Weak Eigenfunctions Of Two-Interval Sturm-Liouville Problems Together With Interaction Conditions, Journal of Mathematical Physics, 58, 042201 (2017), DOI: 10.1063/1.4979615.

[14]. E. M. Russakovskii, Sturm-Liouville problem with parameter in the boundary conditions, Trudy Seminara imeni I. G. Petrovskogo, 18, 1993.

[15]. A. M. Sarsenbi, A. A. Tengaeva, On the basis properties of root functions of two generalized eigenvalue problems, ISSN 0012-2661, Differential Equations, 2012, Vol. 48, No. 2, pp. 306-308.

[16]. A. A. Shkalikov, On the Basis Problem of the Eigenfunctions of an Ordinary Differential Operators, Uspekhi Mat. Nauk, 34:5 (209)(1979), 235-236.

[17]. R. Kh. Amirov, A. S. Ozkan and B. Keskin, Inverse problems for impulsive Sturm-Liouville operator with spectral parameter linearly contained in boundary conditions, Integral Transforms and Special Functions, 20(8)(2009), 607-618.

[18]. R. Amirov, N. Topsakal, On inverse problem for singular Sturm-Liouville operator with discontinuity conditions, Bull. Iranian Math. Soc. Vol. 40(2014), No. 3, pp. 585–607.

[19]. B. P. Allahverdiev, E. Bairamov and E. Ugurlu, Eigenparameter dependent Sturm Liouville problems in boudary conditions with transmission conditions, J. Math. Anal. Appl. 401(2013), 388-396.

[20]. K. Aydemir, H. Olğar, O. Sh. Mukhtarov and F. S. Muhtarov, Differential operator equations with interface conditions in modified direct sum spaces, Filomat, 32:3(2018), 921-931.

[21]. K. Aydemir, O. Mukhtarov, A Class of Sturm-Liouville Problems with Eigenparameter Dependent Transmission Conditions, Numerical Functional Analysis and Optimization, (2017), Doi:10.1080/01630563.2017.1316995.

[22]. K. Aydemir, O. Sh. Mukhtarov, Second-order differential operators with interior singularity, Advances in Difference Equations, (2015), 2015:26 DOI 10.1186/s13662-015-0360-7.

[23]. Y. Güldü, R. Kh. Amirov and N. Topsakal, On impulsive Sturm–Liouville operators with singularity and spectral parameter in boundary conditions , Ukrainian Mathematical Journal, Vol. 64, No. 12, May,2013 (Ukrainian Original Vol. 64, No. 12, December, 2012), 1816-1838.

[24]. M. Kandemir, O. Sh. Mukhtarov, Nonlocal Sturm-Liouville Problems with Integral Terms in the Boundary Conditions, Electronic Journal of Differential Equations, Vol. 2017 (2017), No. 11, pp. 1-12.

[25]. O. Sh. Mukhtarov, K. Aydemir, Eigenfunction expansion for Sturm-Liouville problems with transmission conditions at one interior point, Acta Mathematica Scientia, 35B(3)(2015), 639-649.

[26]. O. Sh. Mukhtarov, K. Aydemir, The Eigenvalue Problem with Interaction Conditions at One Interior Singular Point, Filomat 31:17(2017), 5411-5420.

[27]. O. Sh. Mukhtarov, H. Olğar and K. Aydemir, Resolvent Operator and Spectrum of New Type Boundary Value Problems, Filomat, 29:7(2015), 1671-1680.

[28]. O. Sh. Mukhtarov, M. Kandemir, Asymptotic behaviour of eigenvalues for the discontinuous boundary-value problem with Functional-Transmissin conditions, Acta Mathematica Scientia, 22B(3)(2002), pp.335-345.

[29]. A. S. Ozkan, B. Keskin and Y. Cakmak, Double discontinuous inverse problems for Sturm-Liouville operator with parameter-dependent conditions, Abstract and Applied Analysis, 2013, Article ID 794262, P.7.

[30]. E. S. Panakhov, T. Gulsen, On discontinuous Dirac systems with eigenvalue dependent boundary conditions, AIP Conference Proceeding, 1648, 260003(2015), 1-4, https://doi.org/10.1063/1.4912520.

[31]. A. V. Likov, Yu. A. Mikhailov, The Theory Of Heat And Mass Transfer, Qosenergaizdat (Russian), 1963.

[32]. A. N. Tikhonov, A. A. Samarskii, Equations Of Mathematical Physics, Oxford and New York, Pergamon, 1963.

[33]. N. N. Voitovich, B. Z. Katsenelbaum and A. N. Sivov, Generalized Method Of Eigen-Vibration In The Theory Of Diffraction, Nakua, Moskow (Russian), 1997.

[34]. O. A. Ladyzhenskaia, The Boundary Value Problems of Mathematical Physics, Springer-Verlag, New York, 1985.

[35]. I. C. Gohberg, M. G. Krein, Introduction to The Theory of Linear Non-Selfadjoint Operators, Translation of Mathematical Monographs, vol. 18, Amer. Math. Soc., Providence, Rhode Island, 1969.

[36]. D. Gilbarg, N. S. Trudinger, Elliptic partial differential equations of second order, 2nd ed. Springer-Verlag, Berlin, 1983.

[37]. E. Kreyszig, Introductory Functional Analysis With Application, New-York, 1978.

Histopathological Effects of Fonofos on Gills of Zebrafish *(Danio rerio)*

*Sezgi ARMAN[1]** ID , *Sema İŞİSAĞ ÜÇÜNCÜ[2]* ID

[1]Sakarya University, Faculty of Arts and Sciences, Department of Biology, Sakarya, TURKEY

[2]Ege University, Faculty of Science, Department of Biology, Izmir, TURKEY

Abstract. Organophosphate pesticides are commonly used to increase agricultural efficiency worldwide. However, it has been proved that these chemicals generally do not show target specificity and non-target vertebrate organisms are adversely affected by pesticide exposure. The aim of the present study was to examine the potential harmful effects of fonofos, an organophosphate insecticide, on the gill tissues of zebrafish (*Danio rerio*). Adult zebrafish were exposed to 1, 2 and 4 mg/L fonofos for 96 hours. Gill tissues were removed, fixed with Bouin's fluid and embedded in paraffin. 5 µm serial sections were stained with hematoxylin-eosin, Gomori trichrome or periodic acid-Schiff. Samples were investigated by light microscopy and histological alterations were compared with the 0.1% dimethyl sulfoxide (DMSO) exposed solvent control samples. Fonofos caused epithelial lifting, curling of secondary lamellae, desquamation, epithelial hyperplasia, and lamellar fusion in the gills. Gills showed distinct histopathological changes through fonofos exposure. It was determined that fonofos is a threat to non-target organisms living in aquatic ecosystems.

*Keywords***:** Fonofos, insecticide, gill, histopathology, zebrafish, *Danio rerio*

Fonofos'un Zebra Balığı (*Danio rerio*) Solungaçlarındaki Histopatolojik Etkileri

Özet. Organofosfatlı pestisitler dünya çapında tarımsal verimliliği artırmak için yaygın olarak kullanılmaktadır. Ancak, bu kimyasalların genel olarak hedef özgüllüğü göstermediği ve hedef dışındaki omurgalı canlıların da pestisit maruziyetinden etkilendikleri ortaya konmuştur. Bu çalışmanın amacı, organofosfatlı bir insektisit olan fonofosun zebra balığının (*Danio rerio*) solungaç dokularındaki potansiyel zararlı etkilerini araştırmaktır. Ergin zebra balıkları 96 saat boyunca 1, 2 ve 4 mg/L fonofosa maruz bırakıldı. Solungaçlar çıkartılarak Bouin sıvısında tespit edildi ve parafine gömüldü. 5 µm kalınlıktaki kesitler hematoksilen eozin, Gomori trikrom veya periyodik asit Schiff boyaları ile boyandı. Örnekler ışık mikroskobunda incelenerek histolojik değişimleri %0,1 dimetilsülfoksit (DMSO) uygulanan çözücü kontrol grubu örnekleriyle karşılaştırıldı. Fonofos solungaçlarda, epitel dokuda kalkma, sekonder lamellerde kıvrılma, deskuamasyon, epitelyal hiperplazi ve lamellar füzyona yol açtı. Solungaçlar fonofos maruziyeti ile belirgin histopatolojik farklılıklar gösterdi. Fonofosun sucul ekosistemlerde yaşayan hedef dışı organizmalar için bir tehdit oluşturduğu belirlenmiştir.

*Anahtar Kelimeler***:** Fonofos, insektisit, solungaç, histopatoloji, zebra balığı, *Danio rerio.*

1. INTRODUCTION

It is an essential concern to develop agricultural productivity to support the food requirement of the increased human population. Pesticides are being commonly used worldwide for this purpose and manufacturing industry progresses to satisfy the demand. There are various classes of pesticides based on their chemical structures such as organochlorines, organophosphates and more

---

recently developed carbamates, pyrethroids, and neonicotinoids. Persistent organochlorines have substantially fallen into disuse; however, it is predicted that organophosphates (OP) will be used widely in the near future due to their low cost, low cumulative ability, and short-term persistence in nature [1,2]. On the other hand, low- persistence obliges farmers to do repeated applications, and this case makes OP pesticides get through to water sources [3]. It is pointed out that OPs are harmful to fish [4-6]. Researches focusing on the investigations of adverse effects of OP pesticides on teleost fish have been conducting for a long time.

Fonofos (*O*-ethyl *S*-phenyl ethylphosphonodithioate) is an OP insecticide applied directly to soil to control various worms that are hazardous for corn, sugarcane, peanuts, and tobacco [7,8].

Zebrafish (*Danio rerio*) is a model organism for many research areas such as developmental biology, genetics, and toxicology. Small size, diversified adaptability, and low cost make zebrafish a useful experimental material [9,10].

Teleost gills are responsible for the gas transfer, osmoregulation, acid-base balance, and ionic regulation. In toxicological studies, gills are helpful tools to observe the effects of environmental pollutants [11].

The aim of this study is to examine the harmful effects of fonofos on gills of zebrafish by histological techniques.

2. MATERIALS AND METHODS

The experiment was conducted in accordance with the guidelines for animal research established by the Local Ethics Committee of Animal Experiments at Ege University (the date and the number of the document: 2016-090).

Adult zebrafish were obtained from a commercial fish dealer in Izmir. They were acclimated under laboratory conditions for two weeks before the treatment. They were maintained in a glass aquarium with dechlorinated tap water at 26±2 ºC and natural photoperiod regime. They were fed with artemia twice a day.

Fonofos (99.5%) (CAS No: 944-22-9) and DMSO (≥99.5%) were purchased from Sigma-Aldrich. The stock solution was freshly prepared before the experiment by solving fonofos in DMSO (0.1%). Treatment concentrations (1, 2 and 4 mg/L fonofos) were diluted from the stock solution. The control group samples were treated with the same concentration of DMSO (0.1%) of the stock solution. Five fish were used for each treatment and the control groups. They were exposed to the chemical for 96 h. Fish were anaesthetized with MS222 (tricaine methanesulfonate), gill tissues were removed, fixed with Bouin's fluid [12] for 24 h and embedded in paraffin. 5 µm serial sections were stained with Mayer's hematoxylin-eosin (H-E), Gomori trichrome (GT) or periodic acid-Schiff (PAS) [13]. Histological alterations were investigated by light microscopy. Micrographs were taken with Zeiss Axio Scope A1 (Carl Zeiss, Germany) equipped with Zeiss Axiocam ERc5s.

3. RESULTS

No histological anomaly was observed in the control samples. Gill filaments were rich in blood vessels consisted of primary lamellae that had central cartilage axis and secondary lamellae which were covered by squamous epithelium. Supportive pillar cells were observed. Additionally, central veins were noticed clearly (Fig. 1.).

1 mg/L fonofos treatment group samples showed slightly curled secondary lamellae and epithelial hyperplasia (Fig. 2.).
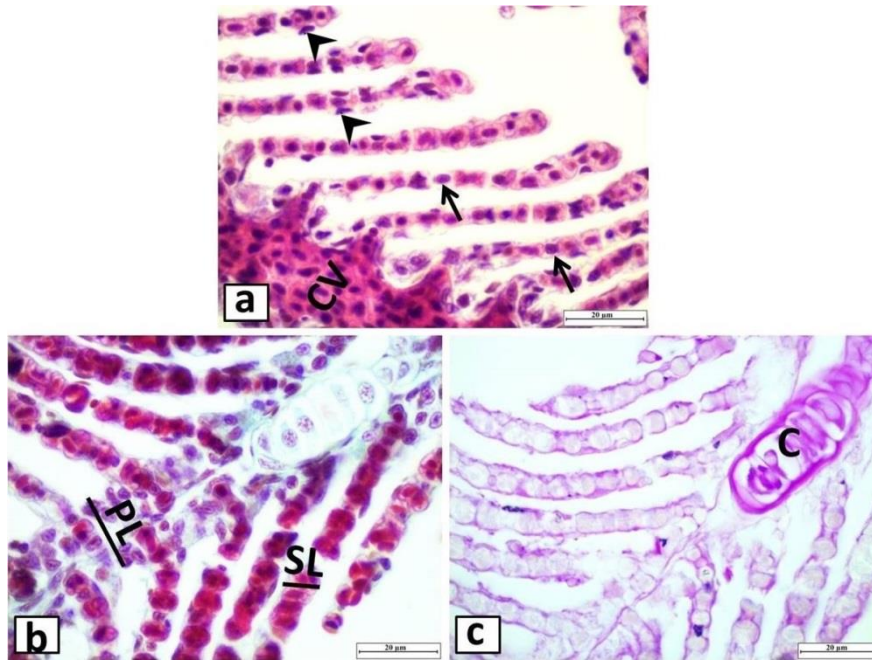
Figure 1. Gill sections of zebrafish from the control group. **a)** Central vein (CV), pillar cells (arrows), and epithelial cells (arrowheads), H-E, X100. **b)** Primary lamella (PL), and secondary lamella (SL), GT, X100. **c)** Cartilage (C), PAS, X100.
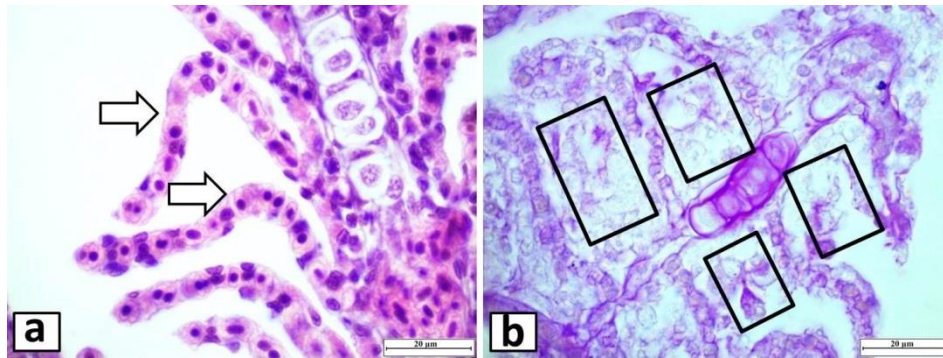
Figure 2. 1 mg/L fonofos treatment group. **a)** Curling of secondary lamellae (white arrows), H-E, X100. **b)** Epithelial hyperplasia (rectangles), PAS, X100.

2 mg/L fonofos exposed group exhibited severe curling of secondary lamellae, epithelial hyperplasia, desquamation, and epithelial lifting (Fig. 3.).
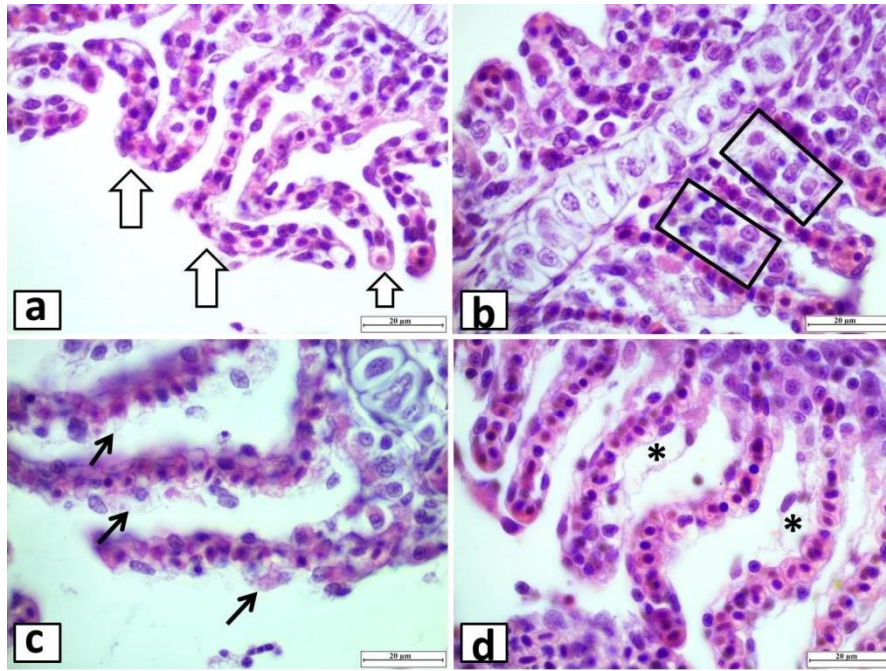
Figure 3. 2 mg/L fonofos treatment group. **a)** Curling of secondary lamellae (white arrows), H-E, X100. **b)** Epithelial hyperplasia (rectangels), H-E, X100. **c)** Desquamation (arrows), H-E, X100. **d)** Epithelial lifting (asterisks), H-E, X100.

4 mg/L fonofos treatment caused curling of secondary lamellae, epithelial lifting, progressive epithelial hyperplasia, and lamellar fusion (Fig. 4.).
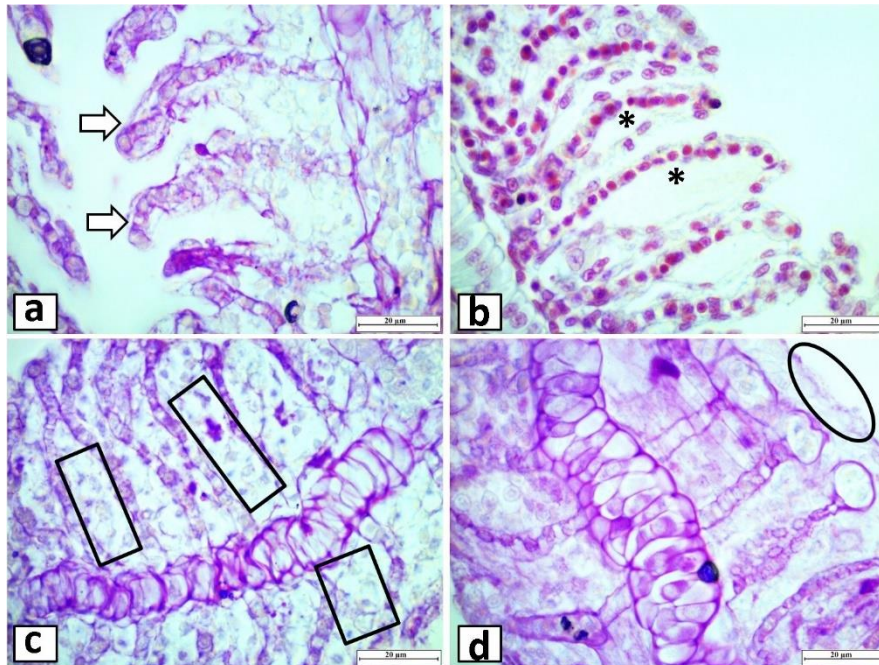
Figure 4. 4 mg/L fonofos treatment group. **a)** Curling of secondary lamellae (white arrows), PAS, X100. **b)** Epithelial lifting (asterisks), GT, X100. **c)** Epithelial hyperplasia (rectangles), PAS, X100. **d)** Lamellar fusion (ellipse), PAS, X100.

4. DISCUSSION

This is the first study that revealed fonofos caused histopathological alterations in the gills of non-target zebrafish. Fish are sensitive organisms that are directly affected by environmental contaminants or pollutants, so they are useful indicators for monitoring the effects of chemicals in aquatic environments [14,15]. Histopathological observations have been widely used to prove the damage of xenobiotics to a specific tissue rapidly. Various staining methods could be used to mark or highlight the special departments of the tissue, so in this study we performed GT and PAS methods in addition to H-E staining in parallel with the study of Adalı and Koca [16]. However, no significant pathology was noted in particular structures just as in red blood cells indicated by GT or in cartilage reacted with PAS, thus only general gill morphology was evaluated after fonofos exposure. Several reports are examining the histopathological alterations in teleost fish gills caused by various OP pesticides. Malathion exposure gave rise to necrosis and desquamation of secondary lamellar epithelium, epithelial lifting, intraepithelial edema, a fusion of adjacent secondary lamellae, disorganization, and rupture in secondary lamellae, hypertrophy and hyperplasia of epithelial cells in the gills of *Gambusia affinis* [17]. *Oreochromis mossambicus* gills were also affected by malathion treatment. The authors noted thickening of secondary lamellae, hemorrhage at primary lamellae, epithelial lining in the tips, lamellar aneurysm, lifting up of epithelium, deformation of the cartilage core, erosion and curling of secondary lamellae in *O. mossambicus* [18]. *Cirrhinus mrigala* gills exhibited epithelial hyperplasia, aneurysm, epithelial necrosis, desquamation, epithelial lifting, edema, lamellar fusion, and curling of secondary lamellae after monocrotophos exposure [19]. Dichlorvos caused hyperplasia, desquamation, necrosis, epithelial lifting, edema, lamellar fusion, collapsed secondary lamellae, and aneurysm in the secondary lamellae of *C. mrigala* [3]. Trichlorfon treatment gave rise to hyperplasia, swelling of blood sinuses in the secondary lamellae, subepithelial edema, lamellar fusion, and blood congestion in the gills of *Piaractus mesopotamicus* [20]. *Labeo rohita* gills showed epithelial lifting, lamellar fusion, and epithelial necrosis after profenofos treatment [15]. Chlorpyrifos exposure caused hyperplasia, hemorrhage and necrosis at primary lamellae, intraepithelial edema, destruction of epithelial lamella and epithelial lifting in *Salmo trutta caspius* gills [21].

In the present study fonofos adversely affected the gills of zebrafish and the alterations were noted as epithelial lifting, curling of secondary lamellae, desquamation, epithelial hyperplasia, and lamellar fusion. All histopathological changes observed in the gills were in a concentration-dependent manner.

In conclusion, fonofos caused acute toxic effects in zebrafish gills. Gills have critical roles in the metabolism of fish and fonofos exposure may destroy the function of gills. It is evident that fonofos is a threat to non-target organisms living in aquatic ecosystems.

Acknowledgment

REFERENCES

[1]. Fairchild, J. F., Little, E. E., Huckins, J. N. Aquatic hazard assessment of the organophosphate insecticide fonofos. Archives of Environmental Contamination and Toxicology, 22-4 (1992) 375-379.

[2]. Costa, L.G. Current issues in organophosphate toxicology. Clinica Chimica Acta, 366-1 (2006) 1-13.

[3]. Velmurugan, B., Selvanayagam, M., Cengiz, E.I., Unlu, E. Histopathological changes in the gill and liver tissues of freshwater fish, *Cirrhinus mrigala* exposed to dichlorvos. Brazilian Archives of Biology and Technology, 52-5 (2009) 1291–1296.

[4]. Murthy, K. S., Kiran, B. R., Venkateshwarlu, M. A review on toxicity of pesticides in fish. International Journal of Open Scientific Research, 1-1, (2013) 15-36.

[5]. Deb, N., Das, S. Chlorpyrifos toxicity in fish: A Review. Current World Environment, 8-1, (2013) 77-84.

[6]. Ullah, S., Zorriehzahra, M. J. Ecotoxicology: a review of pesticides induced toxicity in fish. Advances in Animal and Veterinary Sciences, 3-1, (2015) 40-57.

[7]. U.S. EPA. (2008). Health Effects Support Document For Fonofos. Washington, DC: US Environmental Protection Agency. Available: https://www.epa.gov/sites/production/files/2014-09/documents/health_effects_support_document_for_fonofos.pdf [accessed 16 May 2018].

[8]. Mahajan, R., Blair, A., Lynch, C.F., Schroeder, P., Hoppin, J.A., Sandler, D.P., Alavanja, M.C. Fonofos exposure and cancer incidence in the agricultural health study. Environmental Health Perspectives, 114-12 (2006) 1838-1842.

[9]. Lele, Z., Krone, P.H. The zebrafish as a model system in developmental, toxicological and transgenic research. Biotechnology Advances, 14-1 (1996) 57–72.

[10]. Dai, Y.J., Jia, Y.F., Chen, N., Bian, W.P., Li, Q.K., Ma, Y.B., Chen, Y.L., Pei, D.S. Zebrafish as a model system to study toxicology. Environmental Toxicology and Chemistry, 33-1 (2014) 11–7.

[11]. Machado, M.R., Fanta, E. Effects of the organophosphorous methyl parathion on the branchial epithelium of a freshwater fish *Metynnis roosevelti*. Brazilian Archives of Biology and Technology, 46-3 (2003) 361–372.

[12]. Gröner, F., Höhne, C., Kleiner, W., Kloas, W. Chronic diclofenac exposure affects gill integrity and pituitary gene expression and displays estrogenic activity in nile tilapia (*Oreochromis niloticus*). Chemosphere, 166, (2017) 473-481.

[13]. Presnell, J.K., Schreibman, M.P. and Humason, G.L., Humason's animal tissue techniques. Johns Hopkins University Press. 1997

[14]. Lakra, W.S., Nagpure, N.S. Genotoxicological studies in fishes: a review. Indian Journal of Animal Sciences, 79-1 (2009) 93-97.

[15]. Nataraj, B., Hemalatha, D., Rangasamy, B., Maharajan, K., Ramesh, M. Hepatic oxidative stress, genotoxicity and histopathological alteration in fresh water fish *Labeo rohita* exposed to organophosphorus pesticide profenofos. Biocatalysis and Agricultural Biotechnology, 12 (2017) 185–190.

[16]. Adali, Y., Koca, Y.B. Effects of pollution on some tissues of fish collected from different regions of Büyük Menderes river: A histopathological study. Journal of Environmental Protection and Ecology, 17-2 (2016) 477-487.

[17]. Cengiz, E.I., Ünlü, E. Histopathology of gills in mosquitofish, *Gambusia affinis* after long-term exposure to sublethal concentrations of malathion. Journal of Environmental Science and Health - Part B Pesticides, Food Contaminants, and Agricultural Wastes, 38-5 (2003) 581–589.

[18]. Subburaj, A., Jawahar, P., Jayakumar, N., Srinivasan, A., Ahilan, B. Acute toxicity bioassay of Malathion (EC 50%) on the fish, *Oreochromis mossambicus* (Tilapia) and associated histological alterations in gills. Journal of Entomology and Zoology Studies, 6-1 (2018) 103–107.

[19]. Velmurugan, B., Selvanayagam, M., Cengiz, E.I., Unlu, E. The effects of monocrotophos to different tissues of freshwater fish *Cirrhinus mrigala*. Bulletin of Environmental Contamination and Toxicology, 78-6 (2007) 450–454.

[20]. Mataqueiro, M.I., Nakaghi, L.S.O., De Souza, J.P., Da Cruz, C., De Oliveira, G.H., Urbinati, E.C. Histopathological changes in the gill, liver and kidney of pacu (*Piaractus*

mesopotamicus, Holmberg, 1887) exposed to various concentrations of trichlorfon. Journal of Applied Ichthyology, 25-1 (2009) 124–127.

[21]. Adel, M., Dadar, M., Khajavi, S.H., Pourgholam, R., Karimí, B., Velisek, J. Hematological, biochemical and histopathological changes in Caspian brown trout (*Salmo trutta caspius* Kessler, 1877) following exposure to sublethal concentrations of chlorpyrifos. Toxin Reviews, 36-1 (2017) 73-79.

Some New Properties of The Real Quaternion Matrices and Matlab Applications

Kemal Gökhan NALBANT[1]* iD *, Salim YÜCE[2]* iD

[1]Beykent University, Faculty of Engineering and Architecture, Software Engineering Department, Istanbul, TURKEY

[2]Yildiz Technical University, Faculty of Arts and Sciences, Department of Mathematics, Istanbul, TURKEY

Abstract. In this study, firstly, it was shown that the set of real quaternion matrices $M_n\left(H_\mathbb{R}\right)$ is a 4-dimensional module over the real matrix ring $M_n\left(\mathbb{R}\right)$ and 2-dimensional module over the complex matrix ring $M_n\left(\mathbb{C}\right)$. Moreover, some new properties of the real quaternion matrices were described. Then, matrix representations of the real quaternion matrices were found easily by Matlab. These matrices were also applied to find the inverse of the real quaternion matrices and inverse matrices were obtained easily with these matrices. In addition, some new properties for matrix representations of the real quaternion matrices were found. Also, the inverse of the 2×2 real quaternion block matrices was obtained by new methods. Finally, a new method to calculate the determinant of the 2×2 real quaternion matrices was found and the determinant of these matrices was calculated easily with Matlab application.

Keywords: Quaternions, real quaternions, real quaternion matrices, real matrix representation, determinant, block matrices.

Reel Kuaterniyon Matrislerinin Bazı Yeni Özellikleri ve Matlab Uygulamaları

Özet. Bu çalışmada, ilk olarak, $M_n\left(H_\mathbb{R}\right)$ reel kuaterniyon matrislerin kümesinin $M_n\left(\mathbb{R}\right)$ reel matris halkası üzerinde 4 boyutlu bir modül olduğu ve $M_n\left(\mathbb{C}\right)$ kompleks matris halkası üzerinde 2 boyutlu bir modül olduğu gösterilmiştir. Ayrıca, reel kuaterniyon matrislerin bazı yeni özellikleri tanımlanmıştır. Daha sonra, reel kuaterniyon matrislerin matris temsilleri Matlab uygulamaları ile kolayca elde edilmiştir. Bu matrisler reel kuaterniyon matrislerin tersini bulmak için de uygulanmış ve bu matrislerle ters matrisler kolaylıkla elde edilmiştir. Buna ek olarak, reel kuaterniyon matrislerin matris temsilleri için bazı yeni özellikler bulunmuştur. Ayrıca, 2×2 tipindeki reel kuaterniyon blok matrislerin tersi yeni yöntemlerle elde edilmiştir. Son olarak, 2×2 tipindeki reel kuaterniyon matrislerin determinantını hesaplamak için yeni bir yöntem bulunmuş ve Matlab uygulaması ile bu matrislerin determinantı kolayca hesaplanmıştır.

Anahtar Kelimeler: Kuaterniyonlar, reel kuaterniyonlar, reel kuaterniyon matrisler, reel matris temsili, determinant, blok matrisler.

1. INTRODUCTION

The set of quaternions can be represented as

$$H_{\mathbb{R}} = \left\{ q = q_0 + i q_1 + j q_2 + k q_3 \ \big| \ q_0, q_1, q_2, q_3 \in \mathbb{R} \right\} \tag{1}$$

where

$$i^2 = j^2 = k^2 = -1, \ i\,j = -j\,i = k, \quad j\,k = -k\,j = i, \quad k\,i = -i\,k = j,$$

which given by Hamilton [1], in 1843. From these rules one can see that multiplication of quaternions is not commutative.

Several authors worked on algebraic properties of quaternion matrices [2-8]. In 1997, Zhang [8] gave a brief survey on quaternions and matrices of quaternions. In his study, properties such as addition, multiplication, conjugate, transpose, conjugate transpose, inverse were examined and adjoint of a quaternion matrix was defined and eigenvalues, determinants of quaternion matrices were discussed. Moreover, properties such as equality, rank, inverse, transpose, conjugate transpose and determinant of quaternion matrices were investigated in [9]. The eigenvalues and properties of quaternion matrices were investigated in [10, 11].

Calculating the inverse of real and complex matrices are great importance. In [12], the Study determinant and q - determinant were used. Moreover, they saw that it is very difficult to generalize inverse method of adjoint matrix to quaternion matrices. The details can be found in [13]. Aslasken investigated many different definitions of determinant (Cayley determinant, Study determinant, Dieudonne determinant and Moore determinant) [13]. Gelfand et al. [14] others investigated Moore determinants of Hermitian quaternion matrices and Quasideterminants, Study determinants of quaternion matrices. Moreover, Lewis mentioned relation between the Bagazgoitia's identity [15] and the Dieudonné determinant [16].

Jiang and Wei [17] defined the real representation of the quaternion matrix and gave their properties. Then, they studied the solution of the quaternion matrix equation by means of real representation. Song and others used real representation method for solving Yakubovich-j-conjugate quaternion matrix equation in [18]. Two types of universal factorization equalities for real quaternions and matrices of real quaternions were presented in [19] and real representation of the quaternion matrix was used in this study. In [20], determinants based on real matrix representations of quaternion matrices and linear matrix equations with quaternion coefficients are studied.

Lin and Wang [21] completed a 2×2 block matrix of real quaternions with a partially specified inverse. Also in [22], the general partitioned linear representation form of matrix quaternions are obtained. Localization theorems are discussed for the left and right eigenvalues of block quaternion matrices in [23]. In [24], some sufficient conditions for two, three and four quaternion matrices are block independent in the least squares inverse, the minimum norm inverse and the 1,3,4-inverse are derived respectively.

2. REAL QUATERNIONS

A set of real quaternions is denoted by

$$H_{\mathbb{R}} = \{ q = a + bi + c\,j + d\,k \,|\, a,b,c,d \in \mathbb{R}, i, j, k \notin \mathbb{R} \}$$

where the basis elements i, j, k satisfy the following multiplication rules [25]:

$$i^2 = j^2 = k^2 = -1, \quad ij = -ji = k, jk = -kj = i, ki = -ik = j.$$

A real quaternion may be defined as a pair (S_q, V_q), where $S_q = a \in \mathbb{R}$ is scalar part and $V_q = bi + cj + dk \in \mathbb{R}^3$ is the vector part of q. If $a = 0$, then q is called pure real quaternion. Addition of any real quaternions $q = a + bi + cj + dk$ and $p = a_2 + b_2 i + c_2 j + d_2 k$ is defined as

$$\begin{aligned}
q + p &= (a + bi + cj + dk) + (a_2 + b_2 i + c_2 j + d_2 k) \\
&= (a + a_2) + (b + b_2)i + (c + c_2)j + (d + d_2)k \\
&= (S_q + S_p) + (V_q + V_p).
\end{aligned}$$

The addition rule preserves the associativity and commutativity properties of addition. The product of scalar $(\mu \in \mathbb{R})$ and a real quaternion are defined as

$$\mu q = (\mu a)1 + (\mu b)i + (\mu c)j + (\mu d)k = (\mu S_q) + (\mu V_q).$$

The real quaternion product of two quaternions $q = a + bi + cj + dk$ and $p = a_2 + b_2 i + c_2 j + d_2 k$ is defined as:

$$\begin{aligned}
qp &= aa_2 - (bb_2 + cc_2 + dd_2) + a(b_2 i + c_2 j + d_2 k) + a_2(bi + cj + dk) \\
&\quad + (cd_2 - dc_2)i + (-bd_2 + db_2)j + (bc_2 - cb_2)k \\
&= S_q S_p - \langle V_q, V_p \rangle + S_q V_p + S_p V_q + V_q \wedge V_p.
\end{aligned}$$

The conjugate of a real quaternion is denoted by $\bar{q}$ and norm of a real quaternion is denoted by $\|q\|$ as follows:

$$\bar{q} = a - (bi + cj + dk) = S_q - V_q.$$
$$\|q\| = \sqrt{q\bar{q}} = \sqrt{\bar{q}q} = \sqrt{a^2 + b^2 + c^2 + d^2}.$$

If $\|q\| = 1$, then q is called unit real quaternion. The inverse of the real quaternion q is

$$q^{-1} = \frac{\bar{q}}{\|q\|^2}, \quad \text{if } \|q\| \neq 0.$$

The set $H_{\mathbb{R}}$ is a 4-dimensional vector space on $\mathbb{R}$ and its basis is the set $\{1, i, j, k\}$ [8, 26].

Theorem 2.1. Let $p, q \in H_{\mathbb{R}}$ and $\mu, \eta \in \mathbb{R}$. The conjugate, norm and inverse of real quaternions satisfy the following properties [8];

(i) $\bar{\bar{q}} = q$,

(ii) $\overline{pq} = \bar{q}\,\bar{p}$,

(iii) $\|qp\| = \|q\|\|p\|$,

(iv) $\left\|q^{-1}\right\| = \dfrac{1}{\|q\|}$.

2.1. Real Matrix Representations of Real Quaternions

Let $q = a + bi + cj + dk \in H_{\mathbb{R}}$ be a real quaternion. The left linear map $L_q : H_{\mathbb{R}} \to H_{\mathbb{R}}$ is defined by $L_q(p) = pq$ for all $p \in H_{\mathbb{R}}$. Then the left real matrix representation of real quaternion q is

$$L_q = \begin{pmatrix} a & -b & -c & -d \\ b & a & d & -c \\ c & -d & a & b \\ d & c & -b & a \end{pmatrix}.$$

Furthermore $det(L_q) = \|q\|^4$. Here $det(L_q)$ is usual determinant of L_q. The right linear map $R_q : H_{\mathbb{R}} \to H_{\mathbb{R}}$ is defined by $R_q(p) = qp$ for all $p \in H_{\mathbb{R}}$. Then the right real matrix representation of real quaternion q is

$$R_q = \begin{pmatrix} a & -b & -c & -d \\ b & a & -d & c \\ c & d & a & -b \\ d & -c & b & a \end{pmatrix}.$$

Furthermore $det(R_q) = \|q\|^4$ [26]. Here $det(R_q)$ is usual determinant of R_q.

3. COMPLEX BLOCK QUATERNIONS

The determinant of a 2×2 complex block matrix can be calculated by

$$det\begin{pmatrix} A & B \\ C & D \end{pmatrix} = det(A - BD^{-1}C)det(D). \tag{2}$$

where $A, B, C, D \in M_n(\mathbb{C})$ and D is invertible [27, 28]. If D^{-1} does not exist, then the determinant of a 2×2 block matrix can be calculated by

$$det\begin{pmatrix} A & B \\ C & D \end{pmatrix} = det(D - CA^{-1}B)det(A). \tag{3}$$

where $A, B, C, D \in M_n(\mathbb{C})$ and A is invertible [27, 29]. If neither inverse exists, then generalized inverses must be used [30-32].

The inverse of a 2×2 complex block matrix can be calculated by

$$\begin{pmatrix} A & B \\ C & D \end{pmatrix}^{-1} = \begin{pmatrix} A^{-1} + A^{-1}B(D - CA^{-1}B)^{-1}CA^{-1} & -A^{-1}B(D - CA^{-1}B)^{-1} \\ -(D - CA^{-1}B)^{-1}CA^{-1} & (D - CA^{-1}B)^{-1} \end{pmatrix}. \tag{4}$$

where $A, B, C, D \in M_n(\mathbb{C})$. If A and the 2×2 block matrix are nonsingular. Then, the Schur complement $D - CA^{-1}B$ is nonsingular, too [29, 33]. This formula is called the Banachiewicz inversion formula for the inverse of a nonsingular matrix [34].

The inverse of a 2×2 complex block matrix can be calculated by

$$
\begin{pmatrix} A & B \\ C & D \end{pmatrix}^{-1} = \begin{pmatrix} (A - BD^{-1}C)^{-1} & -(A - BD^{-1}C)^{-1}BD^{-1} \\ -D^{-1}C(A - BD^{-1}C)^{-1} & D^{-1} + D^{-1}C(A - BD^{-1}C)^{-1}BD^{-1} \end{pmatrix}. \tag{5}
$$

where $A, B, C, D \in M_n(\mathbb{C})$ [27, 29, 35]. If D and the 2×2 block matrix are nonsingular. Then, the Schur complement $A - BD^{-1}C$ is nonsingular, too [29, 33].

If A, D and the 2×2 block matrix are nonsingular. Then, the Schur complements $A - BD^{-1}C$ and $D - CA^{-1}B$ nonsingular, too. The inverse of a 2×2 complex block matrix can be calculated by

$$
\begin{pmatrix} A & B \\ C & D \end{pmatrix}^{-1} = \begin{pmatrix} (A - BD^{-1}C)^{-1} & -A^{-1}B(D - CA^{-1}B)^{-1} \\ -(D - CA^{-1}B)^{-1}CA^{-1} & (D - CA^{-1}B)^{-1} \end{pmatrix}.
$$

where $A, B, C, D \in M_n(\mathbb{C})$ [36, 37].

4. REAL QUATERNION MATRICES

The set of real quaternion matrices can be defined as

$$
M_{m \times n}(H_{\mathbb{R}}) = \{\tilde{A} = A + Bi + Cj + Dk \,|\, A, B, C, D \in M_{m \times n}(\mathbb{R})\}
$$

where $A = (a_{rs}), B = (b_{rs}), C = (c_{rs}), D = (d_{rs})$ and

$$
i^2 = j^2 = k^2 = -1, \; ij = -ji = k, \quad jk = -kj = i, \quad ki = -ik = j.
$$

If $m = n$, then the set of real quaternion matrices is denoted by $M_n(H_{\mathbb{R}})$ [16-19].

Let $\tilde{A} = A\tilde{1} + B\tilde{I} + C\tilde{J} + D\tilde{K}$ be a quaternion matrix. We will define the right linear map $\Re_{\tilde{A}}$ as $\Re_{\tilde{A}} : M_n(H_{\mathbb{R}}) \to M_n(H_{\mathbb{R}})$ such that $\Re_{\tilde{A}}(\tilde{B}) = \tilde{A}\tilde{B}$. Using this operator and the basis $\{\tilde{1}, \tilde{I}, \tilde{J}, \tilde{K}\}$ of the module $M_n(H_{\mathbb{R}})$, we can write

$$
\Re_{\tilde{A}}(\tilde{1}) = \tilde{A}\tilde{1} = A\tilde{1} + B\tilde{I} + C\tilde{J} + D\tilde{K},
$$
$$
\Re_{\tilde{A}}(\tilde{I}) = \tilde{A}\tilde{I} = -B\tilde{1} + A\tilde{I} + D\tilde{J} - C\tilde{K},
$$
$$
\Re_{\tilde{A}}(\tilde{J}) = \tilde{A}\tilde{J} = -C\tilde{1} - D\tilde{I} + A\tilde{J} + B\tilde{K},
$$
$$
\Re_{\tilde{A}}(\tilde{K}) = \tilde{A}\tilde{K} = -D\tilde{1} + C\tilde{I} - B\tilde{J} + A\tilde{K}.
$$

Then, the following right real matrix representation can be found as

$$\Re_{\tilde{A}} = \begin{pmatrix} A & -B & -C & -D \\ B & A & -D & C \\ C & D & A & -B \\ D & -C & B & A \end{pmatrix}_{4n \times 4n} \in S_{4n}(\mathbb{R}) \tag{6}$$

where $S_{4n}(\mathbb{R}) \subset M_{4n}(\mathbb{R})$ [17-19, 38, 39].

Example 4.1. The real matrix representations of $\tilde{1}, \tilde{I}, \tilde{J}, \tilde{K}$ are

$$\Re_{\tilde{1}} = \begin{pmatrix} I_n & 0_n & 0_n & 0_n \\ 0_n & I_n & 0_n & 0_n \\ 0_n & 0_n & I_n & 0_n \\ 0_n & 0_n & 0_n & I_n \end{pmatrix}_{4n \times 4n} , \Re_{\tilde{I}} = \begin{pmatrix} 0_n & -I_n & 0_n & 0_n \\ I_n & 0_n & 0_n & 0_n \\ 0_n & 0_n & 0_n & -I_n \\ 0_n & 0_n & I_n & 0_n \end{pmatrix}_{4n \times 4n} ,$$

$$\Re_{\tilde{J}} = \begin{pmatrix} 0_n & 0_n & -I_n & 0_n \\ 0_n & 0_n & 0_n & I_n \\ I_n & 0_n & 0_n & 0_n \\ 0_n & -I_n & 0_n & 0_n \end{pmatrix}_{4n \times 4n} , \Re_{\tilde{K}} = \begin{pmatrix} 0_n & 0_n & 0_n & -I_n \\ 0_n & 0_n & -I_n & 0_n \\ 0_n & I_n & 0_n & 0_n \\ I_n & 0_n & 0_n & 0_n \end{pmatrix}_{4n \times 4n} ,$$

where $\tilde{1}, \tilde{I}, \tilde{J}, \tilde{K} \in M_n(H_{\mathbb{R}}), \Re_{\tilde{1}}, \Re_{\tilde{I}}, \Re_{\tilde{J}}, \Re_{\tilde{K}} \in S_{4n}(\mathbb{R})$ [38]. Furthermore, these real representation matrices satisfy [38]:

$$\Re_{\tilde{1}}^2 = I_{4n}, \Re_{\tilde{I}}^2 = \Re_{\tilde{J}}^2 = \Re_{\tilde{K}}^2 = -I_{4n},$$
$$\Re_{\tilde{I}} \Re_{\tilde{J}} = -\Re_{\tilde{J}} \Re_{\tilde{I}} = \Re_{\tilde{K}},$$
$$\Re_{\tilde{J}} \Re_{\tilde{K}} = -\Re_{\tilde{K}} \Re_{\tilde{J}} = \Re_{\tilde{I}},$$
$$\Re_{\tilde{K}} \Re_{\tilde{I}} = -\Re_{\tilde{I}} \Re_{\tilde{K}} = \Re_{\tilde{J}}.$$

Then, left real matrix representation can be found in the same way as follows:

$$\mathcal{L}_{\tilde{A}} = \begin{pmatrix} A & B & C & D \\ -B & A & -D & C \\ -C & D & A & -B \\ -D & -C & B & A \end{pmatrix}_{4n \times 4n} \in S_{4n}(\mathbb{R}) \tag{7}$$

where $S_{4n}(\mathbb{R}) \subset M_{4n}(\mathbb{R})$ [16].

Example 4.2. The real matrix representations of $\tilde{1}, \tilde{I}, \tilde{J}, \tilde{K}$ are

$$\mathcal{L}_{\tilde{1}} = \begin{pmatrix} I_n & 0_n & 0_n & 0_n \\ 0_n & I_n & 0_n & 0_n \\ 0_n & 0_n & I_n & 0_n \\ 0_n & 0_n & 0_n & I_n \end{pmatrix}_{4n \times 4n} , \mathcal{L}_{\tilde{I}} = \begin{pmatrix} 0_n & I_n & 0_n & 0_n \\ -I_n & 0_n & 0_n & 0_n \\ 0_n & 0_n & 0_n & -I_n \\ 0_n & 0_n & I_n & 0_n \end{pmatrix}_{4n \times 4n} ,$$

$$\mathcal{L}_{\tilde{J}} = \begin{pmatrix} 0_n & 0_n & I_n & 0_n \\ 0_n & 0_n & 0_n & I_n \\ -I_n & 0_n & 0_n & 0_n \\ 0_n & -I_n & 0_n & 0_n \end{pmatrix}_{4n \times 4n} \quad , \mathcal{L}_{\tilde{K}} = \begin{pmatrix} 0_n & 0_n & 0_n & I_n \\ 0_n & 0_n & -I_n & 0_n \\ 0_n & I_n & 0_n & 0_n \\ -I_n & 0_n & 0_n & 0_n \end{pmatrix}_{4n \times 4n}$$

where $\tilde{1}, \tilde{I}, \tilde{J}, \tilde{K} \in M_n(H_{\mathbb{R}}), \mathcal{L}_{\tilde{1}}, \mathcal{L}_{\tilde{I}}, \mathcal{L}_{\tilde{J}}, \mathcal{L}_{\tilde{K}} \in S_{4n}(\mathbb{R})$.

Furthermore, these real representation matrices satisfy [38]:

$$\mathcal{L}_{\tilde{1}}^2 = I_{4n}, \mathcal{L}_{\tilde{I}}^2 = \mathcal{L}_{\tilde{J}}^2 = \mathcal{L}_{\tilde{K}}^2 = -I_{4n},$$
$$\mathcal{L}_{\tilde{I}} \mathcal{L}_{\tilde{J}} = -\mathcal{L}_{\tilde{J}} \mathcal{L}_{\tilde{I}} = \mathcal{L}_{\tilde{K}},$$
$$\mathcal{L}_{\tilde{J}} \mathcal{L}_{\tilde{K}} = -\mathcal{L}_{\tilde{K}} \mathcal{L}_{\tilde{J}} = \mathcal{L}_{\tilde{I}},$$
$$\mathcal{L}_{\tilde{K}} \mathcal{L}_{\tilde{I}} = -\mathcal{L}_{\tilde{I}} \mathcal{L}_{\tilde{K}} = \mathcal{L}_{\tilde{J}}.$$

Corollary 4.1. $S_{4n}(\mathbb{R})$ is a special subset of $M_{4n}(\mathbb{R})$.

4.1. Determinant of 2×2 Real Quaternion Matrices

In practice, the determinant of a 2×2 real quaternion matrix is defined by

$$det \begin{pmatrix} \tilde{a}_{11} & \tilde{a}_{12} \\ \tilde{a}_{21} & \tilde{a}_{22} \end{pmatrix} = \tilde{a}_{11}\tilde{a}_{22} - \tilde{a}_{12}\tilde{a}_{21} \tag{8}$$

In the above definition the so-called rule "multiplication from above to down below" rule is used [9].

5. SOME NEW PROPERTIES OF REAL QUATERNION MATRICES

In this Section, we will investigate some new properties of quaternion matrices and their real matrix representations. After that we will give some relations between quaternion matrices and their real matrix representations. In addition, matlab applications on this subject will be done.

Definition 5.1. For $\tilde{A} = (\tilde{a}_{rs}) = A + Bi + Cj + Dk \in M_{m \times n}(H_{\mathbb{R}})$,

$\tilde{B} = (\tilde{b}_{rs}) = A_2 + B_2 i + C_2 j + D_2 k \in M_{m \times n}(H_{\mathbb{R}})$, the ordinary matrix addition is defined by

$$\tilde{A} + \tilde{B} = (\tilde{a}_{rs} + \tilde{b}_{rs}) \in M_{m \times n}(H_{\mathbb{R}}),$$

or

$$\tilde{A} + \tilde{B} = (A + A_2) + (B + B_2)i + (C + C_2)j + (D + D_2)k.$$

Definition 5.2. For $\tilde{A} = (\tilde{a}_{rs}) = A + Bi + Cj + Dk \in M_{m \times n}(H_{\mathbb{R}})$ and

$\tilde{B} = (\tilde{b}_{so}) = A_2 + B_2 i + C_2 j + D_2 k \in M_{n \times p}(H_{\mathbb{R}})$, the ordinary matrix multiplication is defined by

$$\tilde{A}\tilde{B} = (\sum_{s=1}^{n} \tilde{a}_{rs} \tilde{b}_{so}) \in M_{m \times p}(H_{\mathbb{R}}),$$

or

$$\tilde{A}\tilde{B} = AA_2 - (BB_2 + CC_2 + DD_2) + (AB_2 + BA_2 + CD_2 - DC_2)i$$
$$+ (AC_2 + CA_2 - BD_2 + DB_2)j + (AD_2 + DA_2 + BC_2 - CB_2)k.$$

Corollary 5.1. $\tilde{A}\tilde{B} \neq \hat{B}\hat{A}$ (in general), for suitable real quaternion matrices $\tilde{A}$ and $\tilde{B}$.

5.1. Module $M_n(H_{\mathbb{R}})$ Structure Over the Ring $M_n(\mathbb{C})$

Definition 5.3. For $Q = (q_{tr}) \in M_n(\mathbb{C})$ and $\tilde{A} = (\tilde{a}_{rs}) = A + Bi + Cj + Dk \in M_n(H_{\mathbb{R}})$, the left multiplication of a real quaternion matrix and a real matrix is defined as

$$Q\tilde{A} = (\sum_{r=1}^{n} q_{tr} \tilde{a}_{rs}) \in M_n(H_{\mathbb{R}})$$

or

$$Q\tilde{A} = QA + QBi + QCj + QDk. \qquad (9)$$

The right multiplication can be defined in the same way.

Lemma 5.1. The left multiplication has the following properties:

for $\tilde{A}, \tilde{B} \in M_n(H_{\mathbb{R}}), Q_1, Q_2 \in M_n(\mathbb{C})$,

(i) $(Q_1 + Q_2)\tilde{A} = Q_1\tilde{A} + Q_2\tilde{A}$,

(ii) $(Q_1 Q_2)\tilde{A} = Q_1(Q_2\tilde{A})$,

(iii) $Q_1(\tilde{A} + \tilde{B}) = Q_1\tilde{A} + Q_1\tilde{B}$,

(iv) $I_n(\tilde{A}) = \tilde{A}$,

(v) $(Q_1\tilde{A})\tilde{B} = Q_1(\tilde{A}\tilde{B})$,

(vi) $(\tilde{A}Q_1)\tilde{B} = \tilde{A}(Q_1\tilde{B})$.

Proof. (ii), (iii), (iv), (v) and (vi) can be easily shown. Now we will prove (i): Let

$\tilde{A} = A + Bi + Cj + Dk \in M_n(H_{\mathbb{R}})$ and $Q_1, Q_2 \in M_n(\mathbb{C})$. From (9) we get

$$
\begin{aligned}
(Q_1 + Q_2)\tilde{A} &= (Q_1 + Q_2)A + (Q_1 + Q_2)Bi + (Q_1 + Q_2)Cj + (Q_1 + Q_2)Dk \\
&= (Q_1 A + Q_2 A) + (Q_1 B + Q_2 B)i + (Q_1 C + Q_2 C)j + (Q_1 D + Q_2 D)k \\
&= (Q_1 A + Q_1 Bi + Q_1 Cj + Q_1 Dk) + (Q_2 A + Q_2 Bi + Q_2 Cj + Q_2 Dk) \\
&= Q_1 \tilde{A} + Q_2 \tilde{A}.
\end{aligned}
$$

The properties of the right multiplication can be shown in the same way. With the properties above, the following theorems can be given without the proof.

Theorem 5.1. $M_n(H_{\mathbb{R}})$ is a 4-dimensional module left (right) module over $M_n(\mathbb{R})$.

For all $\tilde{A} = A + Bi + Cj + Dk \in M_n(H_{\mathbb{R}})$ we can write

$$
\tilde{A} = A\tilde{1} + B\tilde{I} + C\tilde{J} + D\tilde{K}
$$

where $\tilde{1} = I_n, \tilde{I} = iI_n, \tilde{J} = jI_n, \tilde{K} = kI_n$. So, the span of $M_n(H_{\mathbb{R}})$ module over the ring $M_n(\mathbb{R})$ is

$$
S_1 = \{\tilde{1}, \tilde{I}, \tilde{J}, \tilde{K}\}
$$

where

$$
\tilde{1} = \begin{pmatrix} 1 & 0 & \dots & 0 \\ 0 & 1 & \dots & 0 \\ \dots & \dots & \ddots & \vdots \\ 0 & 0 & \dots & 1 \end{pmatrix}, \tilde{I} = \begin{pmatrix} i & 0 & \dots & 0 \\ 0 & i & \dots & 0 \\ \dots & \dots & \ddots & \vdots \\ 0 & 0 & \dots & i \end{pmatrix}, \tilde{J} = \begin{pmatrix} j & 0 & \dots & 0 \\ 0 & j & \dots & 0 \\ \dots & \dots & \ddots & \vdots \\ 0 & 0 & \dots & j \end{pmatrix}, \tilde{K} = \begin{pmatrix} k & 0 & \dots & 0 \\ 0 & k & \dots & 0 \\ \dots & \dots & \ddots & \vdots \\ 0 & 0 & \dots & k \end{pmatrix} \in M_n(H_{\mathbb{R}})
$$

and

$$
\tilde{1}^2 = \tilde{I}_n, \tilde{I}^2 = \tilde{J}^2 = \tilde{K}^2 = -\tilde{I}_n, \tilde{I}\tilde{J} = -\tilde{J}\tilde{I} = \tilde{K}, \tilde{J}\tilde{K} = -\tilde{K}\tilde{J} = \tilde{I}, \tilde{K}\tilde{I} = -\tilde{I}\tilde{K} = \tilde{J}.
$$

Theorem 5.2. $M_n(H_{\mathbb{R}})$ is a 2-dimensional module module over $M_n(\mathbb{C})$.

For all $\tilde{A} = A + Bi + Cj + Dk \in M_n(H_{\mathbb{R}})$ we can write

$$
\tilde{A} = Z_1 + Z_2 \tilde{J}
$$

where $Z_1 = A\tilde{1} + B\tilde{I}, Z_2 = C\tilde{1} + D\tilde{I} \in M_n(\mathbb{C})$ and $\tilde{1} = I_n, \tilde{I} = iI_n, \tilde{J} = jI_n, \tilde{K} = kI_n$. So, the span of $M_n(H_{\mathbb{R}})$ module over the ring $M_n(\mathbb{C})$ is

$$
S_2 = \{\tilde{1}, \tilde{J}\}
$$

where

$$
\tilde{1}^2 = \tilde{I}_n, \tilde{I}^2 = \tilde{J}^2 = \tilde{K}^2 = -\tilde{I}_n, \tilde{I}\tilde{J} = -\tilde{J}\tilde{I} = \tilde{K}, \tilde{J}\tilde{K} = -\tilde{K}\tilde{J} = \tilde{I}, \tilde{K}\tilde{I} = -\tilde{I}\tilde{K} = \tilde{J}.
$$

Definition 5.4. Let $\tilde{A} = A + Bi + Cj + Dk \in M_n(H_{\mathbb{R}})$ and $Q \in M_n(\mathbb{R})$ where $A,B,C,D \in M_n(\mathbb{R})$. We define the Kronecker product of a $n \times n$ real quaternion matrix with $4n \times 4n$ real matrix as follows:

$$Q \otimes \mathfrak{R}_{\tilde{A}} = Q \otimes \begin{pmatrix} A & -B & -C & -D \\ B & A & -D & C \\ C & D & A & -B \\ D & -C & B & A \end{pmatrix} = \begin{pmatrix} QA & -QB & -QC & -QD \\ QB & QA & -QD & QC \\ QC & QD & QA & -QB \\ QD & -QC & QB & QA \end{pmatrix} = \mathfrak{R}_{Q\tilde{A}}. \tag{10}$$

Let $\tilde{A}, \tilde{B} \in M_n(H_{\mathbb{R}})$, $Q \in M_n(\mathbb{R})$ and $\mathfrak{R}_{\tilde{A}}, \mathfrak{R}_{\tilde{B}}, \mathfrak{R}_Q \in S_{4n}(\mathbb{R})$. Then the following properties are satisfied;

(i) $Q \otimes \mathfrak{R}_{\tilde{A}} = \mathfrak{R}_{Q\tilde{A}} = \mathfrak{R}_Q \mathfrak{R}_{\tilde{A}}$,

(ii) $Q \otimes (\mathfrak{R}_{\tilde{A}} + \mathfrak{R}_{\tilde{B}}) = Q \otimes \mathfrak{R}_{\tilde{A}} + Q \otimes \mathfrak{R}_{\tilde{B}}$,

(iii) $(Q_1 + Q_2) \otimes \mathfrak{R}_{\tilde{A}} = Q_1 \otimes \mathfrak{R}_{\tilde{A}} + Q_2 \otimes \mathfrak{R}_{\tilde{A}}$, for $Q_1, Q_2 \in M_n(\mathbb{R})$,

(iv) $(Q_1 Q_2) \otimes \mathfrak{R}_{\tilde{A}} = Q_1 \otimes (Q_2 \otimes \mathfrak{R}_{\tilde{A}})$, for $Q_1, Q_2 \in M_n(\mathbb{R})$.

Note 5.1. The real matrix representation of quaternion matrix obtained as a result of this external operation is equal to Kronecker product of $Q \in M_n(\mathbb{R})$ and $\mathfrak{R}_{\tilde{A}}$.

Now, we will investigate some new properties of the real matrix representation of a quaternion matrix.

Example 5.1. Let $\tilde{A} = \begin{pmatrix} 1+2i-4j+5k & 2-i+2j+k \\ 2+5i+j-2k & 3+4i-3j+k \end{pmatrix}$ be a real quaternion matrix.

Then the right real matrix representation of $\tilde{A}$ is

$$\mathfrak{R}_{\tilde{A}} = \begin{pmatrix} 1 & 2 & -2 & 1 & 4 & -2 & -5 & -1 \\ 2 & 3 & -5 & -4 & -1 & 3 & 2 & -1 \\ 2 & -1 & 1 & 2 & -5 & -1 & -4 & 2 \\ 5 & 4 & 2 & 3 & 2 & -1 & 1 & -3 \\ -4 & 2 & 5 & 1 & 1 & 2 & -2 & 1 \\ 1 & -3 & -2 & 1 & 2 & 3 & -5 & -4 \\ 5 & 1 & 4 & -2 & 2 & -1 & 1 & 2 \\ -2 & 1 & -1 & 3 & 5 & 4 & 2 & 3 \end{pmatrix}.$$

and the left real matrix representation of $\tilde{A}$ is

$$
\mathcal{L}_{\tilde{A}} = \begin{pmatrix}
1 & 2 & 2 & -1 & -4 & 2 & 5 & 1 \\
2 & 3 & 5 & 4 & 1 & -3 & -2 & 1 \\
-2 & 1 & 1 & 2 & -5 & -1 & -4 & 2 \\
-5 & -4 & 2 & 3 & 2 & -1 & 1 & -3 \\
4 & -2 & 5 & 1 & 1 & 2 & -2 & 1 \\
-1 & 3 & -2 & 1 & 2 & 3 & -5 & -4 \\
-5 & -1 & 4 & -2 & 2 & -1 & 1 & 2 \\
2 & -1 & -1 & 3 & 5 & 4 & 2 & 3
\end{pmatrix}.
$$

We can find the real representation of real quaternion matrix in Example 5.1 with Matlab. The Matlab command, followed by the output, is shown in the box below.

```
>> m=2; A=[1 2; 2 3]; B=[2 -1; 5 4]; C=[-4 2; 1 -3]; D=[5 1; -2 1];
Re1=vertcat(A, B, C, D); Re2=vertcat(-B, A, D, -C);
Re3=vertcat(-C, -D, A, B); Re4=vertcat(-D, C, -B, A);
Re=horzcat(Re1, Re2, Re3, Re4)
Re =
 1  2 -2  1  4 -2 -5 -1
 2  3 -5 -4 -1  3  2 -1
 2 -1  1  2 -5 -1 -4  2
 5  4  2  3  2 -1  1 -3
-4  2  5  1  1  2 -2  1
 1 -3 -2  1  2  3 -5 -4
 5  1  4 -2  2 -1  1  2
-2  1 -1  3  5  4  2  3
Le1=vertcat(A, -B, -C, -D); Le2=vertcat(B, A, D, -C);
Le3=vertcat(C, -D, A, B); Le4=vertcat(D, C, -B, A);
Le=horzcat(Le1, Le2, Le3, Le4)
Le =
 1  2  2 -1 -4  2  5  1
 2  3  5  4  1 -3 -2  1
-2  1  1  2 -5 -1 -4  2
-5 -4  2  3  2 -1  1 -3
 4 -2  5  1  1  2 -2  1
-1  3 -2  1  2  3 -5 -4
-5 -1  4 -2  2 -1  1  2
 2 -1 -1  3  5  4  2  3
```

Theorem 5.3. Let $\tilde{A}, \tilde{B} \in M_n(H_{\mathbb{R}})$. Then the followings are satisfied;

    (i) $\Re_{\tilde{I}_n} = I_{4n}$,

    (ii)   Let $\tilde{A} \in M_n(H_{\mathbb{R}})$. Then $\tilde{A}$ is Hermitian, anti-Hermitian, unitary or normal if and only if $\Re_{\tilde{A}}$ is symmetric, anti-symmetric, orthogonal or normal, respectively,

(iii)   Let $\tilde{A} \in M_n(H_\mathbb{R})$ be an invertible matrix. If the inverse of the $4n \times 4n$ real matrix is

$$(\Re_{\tilde{A}})^{-1} = \begin{pmatrix} A_2 & -B_2 & -C_2 & -D_2 \\ B_2 & A_2 & -D_2 & C_2 \\ C_2 & D_2 & A_2 & -B_2 \\ D_2 & -C_2 & B_2 & A_2 \end{pmatrix} = \Re_{\tilde{A}^{-1}}$$

where $A_2, B_2, C_2, D_2 \in M_n(\mathbb{R})$ then

$$\tilde{A}^{-1} = A_2 + B_2 i + C_2 j + D_2 k,$$

(iv)   Let $\tilde{A} \in M_n(H_\mathbb{R})$ be an invertible matrix. If the inverse of the $4n \times 4n$ real matrix is

$$(\mathcal{L}_{\tilde{A}})^{-1} = \begin{pmatrix} A_2 & B_2 & C_2 & D_2 \\ -B_2 & A_2 & -D_2 & C_2 \\ -C_2 & D_2 & A_2 & -B_2 \\ -D_2 & -C_2 & B_2 & A_2 \end{pmatrix} = \mathcal{L}_{\tilde{A}^{-1}}$$

where $A_2, B_2, C_2, D_2 \in M_n(\mathbb{R})$ then

$$\tilde{A}^{-1} = A_2 + B_2 i + C_2 j + D_2 k .$$

Proof. (i) and (iv) can be easily shown. Now we will prove one condition of (ii):

Let $\tilde{A} \in M_n(H_\mathbb{R})$. Firstly, $\tilde{A}$ is Hermitian matrix. Then we get

$$A = A^T, B = -B^T, C = -C^T, D = -D^T. \tag{11}$$

and

$$(\Re_{\tilde{A}})^T = \begin{pmatrix} A^T & B^T & C^T & D^T \\ -B^T & A^T & D^T & -C^T \\ -C^T & -D^T & A^T & B^T \\ -D^T & C^T & -B^T & A^T \end{pmatrix}. \tag{12}$$

If we use (11) in (12), we get

$$(\Re_{\tilde{A}})^T = \Re_{\tilde{A}} .$$

Thus we find, if $\tilde{A}$ is Hermitian matrix, then $\Re_{\tilde{A}}$ is symmetric matrix. Secondly, if $\Re_{\tilde{A}}$ is symmetric matrix, we get (11). By using (11) in $\tilde{A}$, we obtain

$$\tilde{A}^* = -\tilde{A} .$$

So we find, if $\Re_{\tilde{A}}$ is symmetric matrix, then $\tilde{A}$ is Hermitian matrix. Consequently, $\tilde{A}$ is Hermitian if and only if $\Re_{\tilde{A}}$ is symmetric.

The other conditions can be done in the same way. Then, we will prove (iii):

If $\tilde{A}$ is invertible then $\tilde{A}\tilde{A}^{-1} = \tilde{A}^{-1}\tilde{A} = I_n$. By property (i), we get

$$I_{4n} = \Re_{\tilde{I}_n} = \Re_{\tilde{A}\tilde{A}^{-1}} = \Re_{\tilde{A}}\Re_{\tilde{A}^{-1}} \, .$$

Thus, we obtain

$$(\Re_{\tilde{A}})^{-1} = \Re_{\tilde{A}^{-1}} \, .$$

Hence, we may find inverse of $\tilde{A}$ by using Theorem 5.3 / (iii), (iv). Following example will show us how to find the inverse of a dual quaternion matrix by using inverse of its real matrix representation.

Example 5.2. Let $\tilde{A} = \begin{pmatrix} i & j \\ 0 & k \end{pmatrix} \in M_2(H_{\mathbb{R}})$. The right real matrix representation of $\tilde{A}$ is

$$\Re_{\tilde{A}} = \begin{pmatrix} 0 & 0 & -1 & 0 & 0 & -1 & 0 & 0 \\ 0 & 0 & 0 & 0 & 0 & 0 & 0 & -1 \\ 1 & 0 & 0 & 0 & 0 & 0 & 0 & 1 \\ 0 & 0 & 0 & 0 & 0 & -1 & 0 & 0 \\ 0 & 1 & 0 & 0 & 0 & 0 & -1 & 0 \\ 0 & 0 & 0 & 1 & 0 & 0 & 0 & 0 \\ 0 & 0 & 0 & -1 & 1 & 0 & 0 & 0 \\ 0 & 1 & 0 & 0 & 0 & 0 & 0 & 0 \end{pmatrix} .$$

Here $det(\Re_{\tilde{A}}) = 1 \neq 0$. Hence, $\tilde{A}$ is invertible.

The inverse of $(\Re_{\tilde{A}})^{-1}$ is found by using Matlab as follows:

$$(\Re_{\tilde{A}})^{-1} = \begin{pmatrix} 0 & 1 & 1 & 0 & 0 & 0 & 0 & 0 \\ 0 & 0 & 0 & 0 & 0 & 0 & 0 & 1 \\ -1 & 0 & 0 & 1 & 0 & 0 & 0 & 0 \\ 0 & 0 & 0 & 0 & 0 & 1 & 0 & 0 \\ 0 & 0 & 0 & 0 & 0 & 1 & 1 & 0 \\ 0 & 0 & 0 & -1 & 0 & 0 & 0 & 0 \\ 0 & 0 & 0 & 0 & -1 & 0 & 0 & 1 \\ 0 & -1 & 0 & 0 & 0 & 0 & 0 & 0 \end{pmatrix} .$$

By using the inverse of $\Re_{\tilde{A}}$ we find

$$\tilde{A}^{-1} = \begin{pmatrix} -i & 1 \\ 0 & -k \end{pmatrix} .$$

Moreover, the left real matrix representation of $\tilde{A}$ is

$$\mathcal{L}_{\tilde{A}} = \begin{pmatrix} 0 & 0 & 1 & 0 & 0 & 1 & 0 & 0 \\ 0 & 0 & 0 & 0 & 0 & 0 & 0 & 1 \\ -1 & 0 & 0 & 0 & 0 & 0 & 0 & 1 \\ 0 & 0 & 0 & 0 & 0 & -1 & 0 & 0 \\ 0 & -1 & 0 & 0 & 0 & 0 & -1 & 0 \\ 0 & 0 & 0 & 1 & 0 & 0 & 0 & 0 \\ 0 & 0 & 0 & -1 & 1 & 0 & 0 & 0 \\ 0 & -1 & 0 & 0 & 0 & 0 & 0 & 0 \end{pmatrix}.$$

Here $det(\mathcal{L}_{\tilde{A}}) = 1 \neq 0$. Hence, $\tilde{A}$ is invertible.

The inverse of $(\mathcal{L}_{\tilde{A}})^{-1}$ is found by using Matlab as follows:

$$(\mathcal{L}_{\tilde{A}})^{-1} = \begin{pmatrix} 0 & 1 & -1 & 0 & 0 & 0 & 0 & 0 \\ 0 & 0 & 0 & 0 & 0 & 0 & 0 & -1 \\ 1 & 0 & 0 & 1 & 0 & 0 & 0 & 0 \\ 0 & 0 & 0 & 0 & 0 & 1 & 0 & 0 \\ 0 & 0 & 0 & 0 & 0 & 1 & 1 & 0 \\ 0 & 0 & 0 & -1 & 0 & 0 & 0 & 0 \\ 0 & 0 & 0 & 0 & -1 & 0 & 0 & 1 \\ 0 & 1 & 0 & 0 & 0 & 0 & 0 & 0 \end{pmatrix}.$$

By using the inverse of $\mathcal{L}_{\tilde{A}}$ we find

$$\tilde{A}^{-1} = \begin{pmatrix} -i & 1 \\ 0 & -k \end{pmatrix}.$$

Corollary 5.2. Each real quaternion matrix can be factorized. The number of elementary row (column) operations for a real matrix representation of a quaternion matrix is four times than the number of elementary row (column) operations for this quaternion matrix.

6. THE INVERSE OF 2×2 REAL QUATERNION MATRICES

We will find the inverse of 2×2 real quaternion block matrices.

Theorem 6.1. The inverse of a 2×2 real quaternion block matrix can be calculated by

$$\begin{pmatrix} \tilde{A} & \tilde{B} \\ \tilde{C} & \tilde{D} \end{pmatrix}^{-1} = \begin{pmatrix} (\tilde{A} - \tilde{B}\tilde{D}^{-1}\tilde{C})^{-1} & -(\tilde{A} - \tilde{B}\tilde{D}^{-1}\tilde{C})^{-1}\tilde{B}\tilde{D}^{-1} \\ -\tilde{D}^{-1}\tilde{C}(\tilde{A} - \tilde{B}\tilde{D}^{-1}\tilde{C})^{-1} & \tilde{D}^{-1} + \tilde{D}^{-1}\tilde{C}(\tilde{A} - \tilde{B}\tilde{D}^{-1}\tilde{C})^{-1}\tilde{B}\tilde{D}^{-1} \end{pmatrix}. \tag{13}$$

where $\tilde{A}, \tilde{B}, \tilde{C}, \tilde{D} \in M_n(H_{\mathbb{R}})$ if $\tilde{D}$ is invertible.

Proof.

$$\begin{pmatrix} \tilde{A} & \tilde{B} \\ \tilde{C} & \tilde{D} \end{pmatrix}\begin{pmatrix} x \\ y \end{pmatrix} = \begin{pmatrix} c \\ d \end{pmatrix}.$$

where $\tilde{A}, \tilde{B}, \tilde{C}, \tilde{D} \in M_n(H_\mathbb{R})$, $x, y, c, d \in H_\mathbb{R}$. Namely,

$$\tilde{A}x + \tilde{B}y = c$$
$$\tilde{C}x + \tilde{D}y = d$$

If $\tilde{D}$ is invertible, we solve for y getting

$$y = \tilde{D}^{-1}(d - \tilde{C}x)$$

and using y in the first equation, we get

$$(\tilde{A} - \tilde{B}\tilde{D}^{-1}\tilde{C})x = c - \tilde{B}\tilde{D}^{-1}d.$$

If the quaternion matrix $(\tilde{A} - \tilde{B}\tilde{D}^{-1}\tilde{C})^{-1}$ is invertible, then we can get

$$x = (\tilde{A} - \tilde{B}\tilde{D}^{-1}\tilde{C})^{-1}(c - \tilde{B}\tilde{D}^{-1}d)$$
$$y = \tilde{D}^{-1}(d - \tilde{C}(\tilde{A} - \tilde{B}\tilde{D}^{-1}\tilde{C})^{-1}(c - \tilde{B}\tilde{D}^{-1}d)).$$

Then, we get the inverse of $\begin{pmatrix} \tilde{A} & \tilde{B} \\ \tilde{C} & \tilde{D} \end{pmatrix}$ as

$$\begin{pmatrix} \tilde{A} & \tilde{B} \\ \tilde{C} & \tilde{D} \end{pmatrix}^{-1} = \begin{pmatrix} (\tilde{A} - \tilde{B}\tilde{D}^{-1}\tilde{C})^{-1} & -(\tilde{A} - \tilde{B}\tilde{D}^{-1}\tilde{C})^{-1}\tilde{B}\tilde{D}^{-1} \\ -\tilde{D}^{-1}\tilde{C}(\tilde{A} - \tilde{B}\tilde{D}^{-1}\tilde{C})^{-1} & \tilde{D}^{-1} + \tilde{D}^{-1}\tilde{C}(\tilde{A} - \tilde{B}\tilde{D}^{-1}\tilde{C})^{-1}\tilde{B}\tilde{D}^{-1} \end{pmatrix}. \tag{14}$$

We can write (14) as

$$\begin{pmatrix} \tilde{A} & \tilde{B} \\ \tilde{C} & \tilde{D} \end{pmatrix}^{-1} = \begin{pmatrix} \tilde{I}_n & \tilde{0}_n \\ -\tilde{D}^{-1}\tilde{C} & \tilde{I}_n \end{pmatrix}\begin{pmatrix} (\tilde{A} - \tilde{B}\tilde{D}^{-1}\tilde{C})^{-1} & \tilde{0}_n \\ \tilde{0}_n & \tilde{D}^{-1} \end{pmatrix}\begin{pmatrix} \tilde{I}_n & -\tilde{B}\tilde{D}^{-1} \\ \tilde{0}_n & \tilde{I}_n \end{pmatrix}$$

and we obtain

$$\begin{pmatrix} \tilde{A} & \tilde{B} \\ \tilde{C} & \tilde{D} \end{pmatrix} = \begin{pmatrix} \tilde{I}_n & \tilde{B}\tilde{D}^{-1} \\ \tilde{0}_n & \tilde{I}_n \end{pmatrix}\begin{pmatrix} (\tilde{A} - \tilde{B}\tilde{D}^{-1}\tilde{C}) & \tilde{0}_n \\ \tilde{0}_n & \tilde{D} \end{pmatrix}\begin{pmatrix} \tilde{I}_n & \tilde{0}_n \\ \tilde{D}^{-1}\tilde{C} & \tilde{I}_n \end{pmatrix}$$

The above expression shows that only the inverse of $\tilde{D}$ is needed.

Theorem 6.2. The inverse of a 2×2 real quaternion block matrix can be calculated by

$$\begin{pmatrix} \tilde{A} & \tilde{B} \\ \tilde{C} & \tilde{D} \end{pmatrix}^{-1} = \begin{pmatrix} \tilde{A}^{-1} + \tilde{A}^{-1}\tilde{B}(\tilde{D} - \tilde{C}\tilde{A}^{-1}\tilde{B})^{-1}\tilde{C}\tilde{A}^{-1} & -\tilde{A}^{-1}\tilde{B}(\tilde{D} - \tilde{C}\tilde{A}^{-1}\tilde{B})^{-1} \\ -(\tilde{D} - \tilde{C}\tilde{A}^{-1}\tilde{B})^{-1}\tilde{C}\tilde{A}^{-1} & (\tilde{D} - \tilde{C}\tilde{A}^{-1}\tilde{B})^{-1} \end{pmatrix}. \tag{15}$$

where $\tilde{A}, \tilde{B}, \tilde{C}, \tilde{D} \in M_n(H_{\mathbb{R}})$ if $\tilde{A}$ is invertible.

Example 6.1. Let $\tilde{Q} = \begin{pmatrix} i & j & 0 & k \\ 0 & k & j & 0 \\ 1 & 0 & i & j \\ 0 & k & 0 & k \end{pmatrix} \in M_4(H_{\mathbb{R}})$ be a real quaternion matrix.

We can write $\tilde{Q}$ as 2×2 real quaternion block matrix.

$$\tilde{Q} = \begin{pmatrix} \tilde{A} & \tilde{B} \\ \tilde{C} & \tilde{D} \end{pmatrix}$$

where $\tilde{A}, \tilde{B}, \tilde{C}, \tilde{D} \in M_2(H_{\mathbb{R}})$. $\tilde{D}$ is invertible. Then by using Theorem 6.1, we get

$$\tilde{Q}^{-1} = \begin{pmatrix} \frac{1}{2} - \frac{1}{2}i - \frac{1}{2}j + \frac{1}{2}k & \frac{1}{2} - \frac{1}{2}i + \frac{1}{2}j + \frac{1}{2}k & \frac{1}{2} - \frac{1}{2}i - \frac{1}{2}j - \frac{1}{2}k & i \\ -\frac{1}{2}i - \frac{1}{2}j & \frac{1}{2} - \frac{1}{2}k & -\frac{1}{2} - \frac{1}{2}k & 0 \\ \frac{1}{2} - \frac{1}{2}k & \frac{1}{2}i - \frac{1}{2}j & -\frac{1}{2}i + \frac{1}{2}j & 0 \\ \frac{1}{2}i + \frac{1}{2}j & -\frac{1}{2} + \frac{1}{2}k & \frac{1}{2} + \frac{1}{2}k & -k \end{pmatrix}.$$

7. THE DETERMINANT OF 2×2 REAL QUATERNION MATRICES

We now discuss the determinant of 2×2 real quaternion matrices. We will find (8) by a different method. The determinant of a 2×2 real quaternion matrix $\tilde{A}$ is a real quaternion number and denoted by $det(\tilde{A})$.

Theorem 7.1. Let $\tilde{A} = A + Bi + Cj + Dk \in M_2(H_{\mathbb{R}})$. Then,

$$det(\tilde{A}) = det(A) - det(B) - det(C) - det(D) + (\sum_{s=1}^{2} \{det([A|B]_s) + det([C|D]_s^*)\})i$$

$$+ (\sum_{s=1}^{2} \{det([A|C]_s) + det([D|B]_s^*)\})j + (\sum_{s=1}^{2} \{det([A|D]_s) + det([B|C]_s^*)\})k. \tag{16}$$

Proof. Let $\hat{A} = A + Bi + Cj + Dk \in M_2(H_{\mathbb{R}})$. By $det([A|B]_s), det([A|C]_s), det([A|D]_s),$ $det([C|D]_s^*), det([D|B]_s^*), det([B|C]_s^*)$ and usual determinant of A, B, C, D, we can obtain (16), easily.

Note 7.1. The matrices $[A|B]_S, [A|C]_S$ and $[A|D]_S$ mean changing $s.$ column components of the matrices B, C and D instead of $s.$ column components of matrix A. The matrices $[C|D]_S^*$ mean changing $s.$ column components of the matrices D instead of $s.$ column components of matrix C. The matrices $[D|B]_S^*$ mean changing $s.$ column components of the matrices B instead of $s.$ column components of matrix D. The matrices $[B|C]_S^*$ mean changing $s.$ column components of the matrices C instead of $s.$ column components of matrix B.

$*$ means product $s.$ component of the second column with minus one.

Example 7.1. Let $\tilde{A} = \begin{pmatrix} 2+i+2j+k & -1-i+2j+k \\ 3+2i-j+k & 1+2i+j+2k \end{pmatrix} \in M_2(H_{\mathbb{R}})$. Then we get the determinant of $\tilde{A}$ as

$$det(\tilde{A}) = -4 + 10i - 6j + 3k.$$

We can find determinant of real quaternion matrix on Example 7.1 by (16) with Matlab. The Matlab command, followed by the output, is shown in the box below.

```
>> A=[2 -1;3 1]; B=[1 -1;2 2]; C=[2 2;-1 1]; D=[1 1;1 2]; Aoriginal=A; Boriginal=B;
Coriginal=C; Doriginal=D; X1=det(A)-det(B)-det(C)-det(D); X2=0; X3=0; X4=0;
for r = 1:2
B(:,r) = A(:,r);
D(:,r) = C(:,r);
D(2,r) = -D(2,r);
X2 = X2+det(B)+det(D);
B=Boriginal;
D=Doriginal;
end
for r = 1:2
C(:,r) = A(:,r);
B(:,r) =D(:,r);
B(2,r)= -B(2,r);
X3 = X3+det(C)+det(B);
B=Boriginal;
C=Coriginal;
end
for r = 1:2
D(:,r) = A(:,r);
C(:,r) = B(:,r);
C(2,r)= -C(2,r);
X4 = X4+det(C)+det(D);
C=Coriginal;
D=Doriginal;
end
disp(['Det= 'num2str(X1) ' + 'num2str(X2) ' i 'num2str(X3) ' j +'num2str(X4) ' k ' ])
Det= -4 + 10i - 6j + 3k
```

Note 7.2. It is difficult to directly calculate the determinant of the real quaternion matrix, the determinant of the 2×2 real quaternion matrices can be easily calculated by this method with Matlab.

REFERENCES

[1]. Hamilton W.R., Elements of Quaternions, London: Longmans, Green & Company, 1866.
[2]. Brenner J.L., Matrices of Quaternions, Pacific Journal of Mathematics, 1 (1951) 329-335.
[3]. Erdoğdu M. and Özdemir M., On Complex Split Quaternion Matrices, Advances in Applied Clifford Algebras, 23-3 (2013) 625-638.
[4]. Erdoğdu M. and Özdemir M., Split Quaternion Matrix Representation of Dual Split Quaternions and Their Matrices, Advances in Applied Clifford Algebras, 25-4 (2015) 787-798.
[5]. Kösal H. H. and Tosun, M., Commutative Quaternion Matrices, Advances in Applied Clifford Algebras, 24-3 (2014) 769-779.
[6]. Wiegmann N.A., Some Theorems on Matrices with Real Quaternion Elements, Canadian Journal of Mathematics, 7 (1955) 191-201.
[7]. Wolf L.A., Similarity of Matrices in which the Elements are Real Quaternions, Bulletin of the American Mathematical Society, 42-10 (1936) 737-743.
[8]. Zhang F., Quaternions and Matrices of Quaternions, Linear Algebra and Its Applications, 251 (1997) 21-57.
[9]. Morais J.P., Georgiev S. and Sprößig W., Real Quaternionic Calculus Handbook, Birkhäuser, Springer Basel, 2014.
[10]. Huang L. and So W., On Left Eigenvalues of a Quaternionic Matrix, Linear Algebra and Its Applications, 323 (2001) 105-116.
[11]. Zhang F., Geršgorin Type Theorems for Quaternionic Matrices, Linear Algebra and Its Applications, 424 (2007) 139-153.
[12]. Cohen N. and De Leo S., The Quaternionic Determinant, Electronic Journal of Linear Algebra, 7 (2000) 100-111.
[13]. Aslaksen H., Quaternionic Determinants, The Mathematical Intelligencer, 18-3 (1996) 57-65.
[14]. Gelfand I., Retakh V. and Wilson R.L., Quaternionic Quasideterminants and Determinants, Translations of the American Mathematical Society-Series 2, 210 (2003) 111-124.
[15]. Bagazgoitia A., A Determinantal Identity for Quaternions, In Proceedings of 1983 Conference on Algebra Lineal y Aplicaciones, Vitoria-Gasteiz, Spain, (1984) 127-132.
[16]. Lewis D., A Determinantal Identity for Skewfields, Linear algebra and its applications, 71 (1985) 213-217.
[17]. Jiang T. S. and Wei M. S., On a Solution of the Quaternion Matrix Equation $X - A\tilde{X}B = C$ and Its Application, Acta Mathematica Sinica, 21-3 (2005) 483-490.
[18]. Song C., Feng J.-e, Wang X. and Zhao J., A Real Representation Method for Solving Yakubovich-j-Conjugate Quaternion Matrix Equation, Abstract and Applied Analysis, Hindawi, (2014).
[19]. Tian Y., Universal Factorization Equalities for Quaternion Matrices and Their Applications, Mathematical Journal of Okayama University, 41 (1999) 45-62.
[20]. Rodman L., Topics in Quaternion Linear Algebra, Princeton: Princeton University Press, 2014.
[21]. Lin Y. and Wang Q.-W., Completing a Block Matrix of Real Quaternions with a Partial Specified Inverse, Journal of Applied Mathematics, (2013).
[22]. Al-Zhour Z., Some New Linear Representations of Matrix Quaternions with Some Applications, Journal of King Saud University-Science, (2017).
[23]. Ahmad S.S. and Ali I., Bounds for Eigenvalues of Matrix Polynomials over Quaternion Division Algebra, Advances in Applied Clifford Algebras, 26-4 (2016) 1095-1125.

[24]. Song G. and Zhou Y., Block Independence in Various Generalized Inverses of Partitioned Quaternion Matrices, Iranian Journal of Science and Technology, Transactions A: Science, (2018) 1-10.

[25]. Hamilton W.R., Lectures on Quaternions, Dublin: Hodges and Smith, 1853.

[26]. Ward J., Quaternions and Cayley Numbers: Algebra and Applications, Mathematics and Its Applications, Dordrecht: Kluwer, 1997.

[27]. Powell P.D., Calculating Determinants of Block Matrices, arXiv:1112.4379 (2011).

[28]. Silvester J.R., Determinants of Block Matrices, The Mathematical Gazette, 84 (2000) 460-467.

[29]. Tian Y. and Takane Y., More on Generalized Inverses of Partitioned Matrices with Banachiewicz-Schur forms, Linear Algebra and its Applications, 430 (2009) 1641-1655.

[30]. Meyer Jr C.D., Generalized Inverses and Ranks of Block Matrices, SIAM Journal on Applied Mathematics, 25-4 (1973) 597-602.

[31]. Moors E., On the Reciprocal of the General Algebraic Matrix, Bull. Amer. Math. Soc., 26 (1920) 394-395.

[32]. Penrose R., A Generalized Inverse for Matrices, Mathematical Proceedings of the Cambridge Philosophical Society, Cambridge University Press, 51 (1955) 406-413.

[33]. Zhang F., The Schur Complement and Its Applications, Springer Science & Business Media, 2006.

[34]. Banachiewicz T., Zur Berechnung der Determinanten, wie auch der Inversen und zur darauf basierten Auflosung der Systeme linearer Gleichungen, Acta Astronom. Ser. C, 3 (1937) 41-67.

[35]. Frazer R.A., Duncan W.J. and Collar A. R., Elementary Matrices and Some Applications to Dynamics and Differential Equations, Cambridge: Cambridge University Press, 1938.

[36]. Gallier J., The Schur Complement and Symmetric Positive Semidefinite (and definite) Matrices, Penn Engineering, (2010).

[37]. Horn R.A. and Johnson C.R., Matrix Analysis, Cambridge: Cambridge University Press, 1990.

[38]. De Leo S., Scolarici G. and Solombrino L., Quaternionic Eigenvalue Problem, Journal of Mathematical Physics, 43-11 (2002) 5815-5829.

[39]. Jiang T. and Ling S., On a Solution of the Quaternion Matrix Equation $A\tilde{X} - XB = C$ and Its Applications, Advances in Applied Clifford Algebras, 23-3 (2013) 689-699.

Assessment of Gluten-Free Food Sourced Heavy Metal Accumulation for Celiac People

Mustafa SOYLAK[1] [iD] *, Ali DURAN[2]* [iD] *, Erkan YILMAZ[3,4]** [iD]

[1]*Erciyes University, Faculty of Science, Department of Chemistry, Kayseri, TURKEY*

[2]*Abdullah Gul University, Faculty of Engineering, Department of Materials Science and Nanotechnology Engineering, Kayseri, TURKEY*

[3]*Erciyes University, Faculty of Pharmacy, Department of Analytical Chemistry, Kayseri, TURKEY*

[4]*Erciyes University, Nanotechnology Research Center (ERNAM), Kayseri, TURKEY*

Abstract. This paper shows an evaluation to the study of some heavy metals in certain gluten-free foods for celiac people marketed in Kayseri, Turkey. The concentration values of Cu, Mn, Co, Pb, Cr, Zn, Ni, Cd and Fe in eleven different gluten-free food samples are reported. The determinations were carried out by flame atomic absorption spectrometry after wet digestion method. The average metal concentrations of all the analyzed samples were determined in the range of 0.45-5.12, 1.84-12.2, 1.29-22.5, 0.60-3.01, 0.08-0.18, and 4.61-79.6 mg kg^{-1} for Cu, Mn, Zn, Ni, Cd and Fe, respectively. The accuracy of the method was confirmed by the analysis of a standard reference material (SRM 1570a Spinach Leaves). Metal pollution index was also calculated to examine the overall heavy metal levels in all analyzed samples. The concentrations of the analyzed metals are equivalent to 7.55-35.3% compared to the daily intake offered by international decision authorities. For this reason, the nutritional quality index for gluten-free food products with respect to all the metals seems to be relatively low.

*Keywords***:** Heavy metals, gluten-free foods, celiac disease, flame atomic absorption spectrometry.

Çölyak Hastaları için Glütensiz Gıda Kaynaklı Ağır Metal Birikiminin Değerlendirilmesi

Özet. Bu çalışma, Kayseri'de satışa sunulan çölyak hastaları için bazı glütensiz gıdalarda belirli ağır metallerin çalışılmasına ilişkin bir değerlendirme sunmaktadır. On bir farklı glutensiz gıda numunesinde Cu, Mn, Co, Pb, Cr, Zn, Ni, Cd ve Fe konsantrasyon değerleri rapor edilmiştir. Tespit çalışmaları yaş yakma yöntemini takiben alevli atomik absorpsiyon spektrometresi ile yapılmıştır. Analiz edilen tüm numunelerin ortalama metal konsantrasyonları Cu, Mn, Zn, Ni, Cd ve Fe için sırasıyla 0,45-5,12, 1,84-12,2, 1,29-22,5, 0,60-3,01, 0,08-0,18 ve 4,61-79,6 mg kg^{-1} olarak belirlenmiştir. Yöntemin doğruluğu, standart referans materyalin (SRM 1570a Ispanak Yaprakları) analizi ile teyit edilmiştir. Analiz edilen tüm numunelerde toplam ağır metal seviyelerini incelemek için metal kirliliği endeksi de hesaplanmıştır. Analiz edilen metallerin konsantrasyonları uluslararası karar makamları tarafından önerilen günlük alım miktarı ile karşılaştırıldığında %7,55 ile 35,3'lük kısma denk gelmektedir. Bu nedenle, tüm metallere göre glütensiz gıda ürünlerinin beslenme kalite endeksi nispeten düşük görünmektedir.

*Anahtar Kelimeler***:** Ağır metaller, glütensiz gıdalar, çölyak hastalığı, atomik absorpsiyon spektrometresi.

1. INTRODUCTION

Celiac disease is a genetically mediated autoimmune disease in which gluten causes gastral inflammation or damage [1]. Gluten refers to the proteins in cereal grains, such as wheat, rye, barley and derivatives. Among other negative effects, celiac disease could cause some problems with absorption of some nutrients including micro and macro elements, and vitamins [2-4]. Recent studies indicate that celiac disease has a high rate and that the prevalence of celiac disease is approximately 2% in the general world population [5,6]. The prevalence of celiac disease in Turkey is 1:100, similar to several European countries and United States [1,7,8]. Historically, celiac disease has been under diagnosed; however, the rate of diagnosis is increasing day by day [1]. Today, the only available and effective treatment for celiac people is a lifelong strict gluten-free diet. Additionally, with the help of novel therapy methods for celiac disease, the gluten detoxification through enzymatic cures come into question [9,10].

Celiac disease was a difficult diagnosis to live with 20 years ago. This was probably due to the limited range of gluten-free products as well as the guided to high quality products. Over the years, the increased prevalence of celiac disease guides to a high demand of gluten-free products and this made a dramatic increase of the gluten-free market. However, it has become easier to find and consume gluten-free products with high amounts and desired quality. There are too many similar gluten-free products in the market all around the world including breads, cereal bars, pastas, crusts, desserts and more.

Currently, there are limited studies available focused on the heavy metal contents in gluten-free foods [2,5,11-14]. In addition, the manufacturers attach the only available information about mineral composition on the label. The World Health Organization (WHO) and some other international authorities have determined and published acceptable levels in food [15,16]. Using these publications and the label data, not only health professionals but also the researchers and celiac people are having chance to compare the right products they need. As they are not synthesized in the body, heavy metals have an important role in human beings life. Trace amounts of some metals are essential micronutrients and have a range of different biochemical functions in human beings. On the other hand, some mineral trace elements are toxic and can cause negative effects in human health even at trace levels. Many analytical techniques have been developed in order to determine heavy metal contents of food and environmental samples such as atomic absorption spectrometry, inductively coupled plasma mass spectrometry and inductively coupled plasma optical emission spectrometry [17-20]. In particular, atomic absorption spectrometry has been a widely used technique due to its simplicity and economy [21].

The purpose of this study was to obtain data on the heavy metal (Cu, Mn, Zn, Ni, Cd and Fe) concentrations in selected gluten-free food samples (Black Wheat, Burger Pasta, Bread, Flour, Noodle, Spaghetti, White cookie, Cocoa cookie, Cake, Plane Pasta, Lasagna) marketed in Kayseri, Turkey. Also, intake levels and percentage of contribution to dietary reference intakes are assessed. There is a lot of study for the intake levels of non-celiac people in literature, however there is limited information for the celiac ones [22-25].

2. EXPERIMENTAL

a. Instrumentation

The metal contents of the digested gluten-free samples were determined by using a Perkin Elmer A 800 flame atomic absorption spectrometer (FAAS) equipped with hollow cathode lamps. Operation conditions of FAAS for each metal are shown in Table 1. A Millipore water purification system was used to acquire purified reverse osmosis water ($18.2\,\mathrm{M\Omega\,cm}$ resistivity (Millipore, Bedford, MA, USA). A Hettich Universal 320 centrifuge (Tuttlingen, Germany)

was utilized for the separation of undissolved parts from aqueous sample phase.

Table 1. FAAS settings.

Element	Wavelength (nm)	Lamp Current (mA)	Slit width (nm)	Calibration range (mg L^{-1})
Cu	324.8	15	0.7	0.5-5
Ni	232.0	30	0.2	0.5-5
Mn	279.5	20	0.2	0.1-2.5
Zn	213.9	10	0.7	0.1-1.0
Cd	228.8	8	0.7	0.1-1.0
Fe	248.3	30	0.2	0.5-5
Co	240.7	30	0.2	0.5-5
Pb	283.3	4	0.7	1-10
Cr	357.9	30	0.7	1-10

b.   Reagents and Solutions

Analytical reagent-grade chemicals were preferred for all stages of the developed procedure. Analytical reagent-grade of hydrochloric acid, nitric acid and hydrogen peroxide were obtained from Merck Company (E. Merck, Darmstadt, Germany). All glassware and the plastic laboratory equipments were kept in %10 (v/v) of nitric acid solution bath for 24 hours and rinsed with reverse osmosis water prior to use. The standard solutions of increasing concentration were prepared for each element by diluting their stock solutions of 1000 mg L^{-1} (Sigma Aldrich, St. Louis, MO, USA). Calibration curves for each element were obtained by measuring of absorbance values of the prepared standart solutions. Concentration range of calibration curve is shown in Table 1.Certified reference material (SRM 1570a spinach leaves) was used in the experiments in order to check the accuracy of the digestion procedure.

c.   Sampling, digestion and determination

Gluten-free samples were obtained from local markets in Kayseri. The obtained samples were dried at 90 °C for 10 h. homogenized by using an agate homogenizer and stored in sampling bottles. Wet digestion procedure was carried out for the digestion of the samples and extraction of metal ions from food matrix to acidic solution phase. The suggested wet digestion procedure was carried out on the heater plate at ~ 90 °C. For this purpose, 10 mL of analytical grade concentrated HNO$_3$ was added on the 1.0 g of SRM 1570a spinach leaves or each of the collected samples and the mixture was evaporated until dryness. After cooling, a solution consist of analytical grade 3 mL of H$_2$O$_2$ and 10 mL of HNO$_3$ was added on the same samples. Then they were again evaporated to near dryness. The resulting mixture was taken with ultra-pure water, centrifuged and filtered through a blue-band filter paper. Last volume of the filtrate was completed to 10 mL with 1 M HNO$_3$ solution. The suggested digestion method was also applied to blank samples. Concantration of metal ions in last phase were analyzed by using flame atomic absorption spectrometer.

3.   RESULTS AND DISCUSSION

Accuracy of the developed digestion and measurement procedure was checked by using the certified reference material SRM 1570a spinach leaves. The obtained results for the studied elements in the certified reference material were within or near the certified values. The results shown in Table 2 proved that our method is free from the interference of matrix components in the food samples. The combined wet digestion and flame atomic absorption spectrometry procedure was preferred due to its accuracy, simple and short sample preparation and analysis time.

Table 2. Analysis of SRM 1570a spinach leaves standard reference material (N=3).

Element	Certified value, (mg kg^{-1})	Found value (mg kg^{-1})
Cu	12.2±0.86	12.1±0.4[a]
Ni	2.14±0.10	UDL[b]
Mn	76.0±1.2	75.4±2.4
Zn	82.3±3.9	79.0±3.0
Cd	2.89±0.07	3.01±0.09

a: mean±standart deviation.
b: Under of the detection limit.

The metal concentrations in the studied gluten-free samples are shown in Table 3. All measurements and calculations were carried out on a dry weight basis. All analysis were conducted in triplicate. The obtained results are calculated and given as mean±standard deviation. Concentrations of cobalt, chromium and lead were found to be under of the detection limits of FAAS.

Table 3. Metal concentrations in analyzed gluten-free food samples (mg kg^{-1}, N=3).

Sample	Cu	Mn	Zn	Ni	Cd	Fe
Black Wheat	1.57±0.11	7.20±0.46	6.83±0.06	1.83±0.21	0.08±0.03	12.0±0.22
Burger Pasta	0.74±0.09	3.72±0.15	1.29±0.13	0.60±0.17	0.12±0.03	44.5±0.66
Bread	1.41±0.11	4.37±0.15	2.58±0.19	1.68±0.42	0.13±0.04	5.79±0.22
Flour	1.25±0.11	5.89±0.15	22.5±1.25	2.42±0.21	0.18±0.03	46.3±0.66
Noodle	0.45±0.05	1.84±0.06	1.61±0.09	0.77±0.10	0.10±0.04	4.61±0.11
Spaghetti	2.63±0.23	4.41±0.13	8.43±0.31	3.01±0.21	0.18±0.03	36.5±0.44
White cookie	0.63±0.09	3.68±0.13	4.93±0.25	1.83±0.21	0.18±0.03	79.6±5.07
Cocoa cookie	5.12±0.34	12.2±0.50	16.3±0.18	3.01±0.21	0.17±0.03	24.6±2.20
Cake	3.18±0.12	6.53±0.23	10.2±0.97	1.36±0.10	0.14±0.01	26.8±0.88
Plane Pasta	0.53±0.05	3.36±0.06	6.71±0.29	0.62±0.10	0.16±0.01	10.1±0.66
Lasagna	0.62±0.06	3.25±0.06	10.0±0.28	1.06±0.10	0.17±0.02	19.7±1.65
Mean	**1.65±0.12**	**5.13±0.19**	**8.30±0.36**	**1.65±0.19**	**0.14±0.03**	**28.2±1.06**

Copper is one of the most important element for living cells and has important roles on the nervous system, lipid and carbohydrate metabolisms and so on [26-28]. Lack of copper to be taken with daily diets, copper deficiency can cause dangerous diseases for living cells [29-31]. Hence accurate analysis of copper concentrations in the consumed diatery samples is an important task for analytical chemists. In our study, copper concentrations in collected gluten-free samples were found between 0.45 and 5.12 mg kg^{-1} (Table 3). In a different experiment conducted on the Gluten-free Foods From Saudi Arabia, the mean concentration of copper was found between 1.4–10.5 mg kg^{-1} [5]. According to The Brasilian Ministry of Health, copper levels should be lower than 10 mg kg^{-1} [32]. Copper concentration in all of the our samples was lower than this recommedation value. World Health Organization (WHO) recommends daily 2-5 mg copper intake for adults [33] and moreover it is difficult to say that food-based copper intake is a health problem because there are no limitation.

Manganese also plays important role in different metabolisms as an essential element in living cells such as protein, fat, nitrogen and inorganic acid metabolism. Moreover it has an important task on the activation of many enzymes used in metabolic processes [29, 31]. The minimum and maximum levels of manganese were 1.84 mg kg^{-1} for dried noodle and 12.2 mg kg^{-1} for dried cocoa cookie samples, respectively (Table 3). According to the National Research Council, the daily adequate intake of manganese from dietary supplements, water, and food should be between 2–5 mg and lower than 11 mg [34].

Zinc is one of the most important essential trace elements for living cells and has a role in the biochemical reactions in the most of the cells and enzymes. For example, Zinc is an important element for growth and development, cell-mediated immunity, neurosensory functions and DNA synthesis and act as the active center of approximately 300 enzymes. As low levels of zinc in humans can cause serious discomfort such as immunological abnormalities, anorexia, skin

changes and. growth retardation. High level of zinc can show toxic effects [29, 31, 35]. The mean concentration of zinc in studied samples were found in the range of 1.29 and 16.3 mg kg^{-1}. As the burger pasta sample has the lowest zinc concentration, the cocoa cookies sample has the highest zinc concentration (Table 3). Turkish Food Codex announced that the permitted maximum amount of zinc in foods is 5 mg kg^{-1}. According to WHO, the tolerable daily intake of zinc is 0.3–1.0 mg kg^{-1} [36]. Zinc levels in some of the studied gluten-free samples were higher than these suggested values.

Trace level of nickel is both essential and toxic for living organisms. Nickel plays a important role on the glucose and adrenaline metabolism and production of the red blood cells. But high level of nickel can cause serious health problems such as respiratory system cancer, skin disorder known as nickel-eczema, lung, kidney and cardiovascular diseases [29, 31, 37, 38]. A Ni-poor nutrition of <0.1 mg kg^{-1} dry matter cause Ni deficiency symptoms. Food and water are the main possible sources of nickel for humans. Hence accurate and sensitive analysis of nickel in food samples is a important task. The minimum and maximum levels of nickel were 0.60 mg kg^{-1} for burger pasta and 3.01 mg kg^{-1} for dried spaghetti pasta and cocoa cookie samples, respectively (Table 3). According to The Turkish Official Gazette for Turkish standards, the maximum permitted nickel amounts in some food samples are 0.2 mg kg^{-1} [36]. Nickel levels in all of the studied gluten-free samples were higher than these permitted values.

Cadmium is known as highly toxic element even in low concentrations and has a biological half-life in the range of 10–30 years. It causes adverse effects on the important organs such as kidneys, liver and lungs, even at its very low amounts [39-41]. The World Health Organization has suggested that the provisional allowable intake of cadmium not exceed 0.4–0.5 mg per week or 0.057–0.071 mg per day [42]. Food and water intake are the main possible sources of cadmium for living cells. As can be seen from Table 3, as

the highest level of cadmium were in flour, spaghetti pasta and white cookie samples (0.18 mg kg^{-1}), the lowest level was in Black wheat (0.08 mg kg^{-1}) (Table 3).

Iron, which is primarily involved in a wide range of metabolic processes, including oxygen transport, DNA synthesis and electron transport, is vital to the survival of life. However iron levels in different parts of the body should be kept under constant control and regulated tightly because the excess iron in the living structure causes tissue damage as a result of the formation of free radicals. Metabolic diseases born of the high or low amount of iron are among the most common disorders in people. It covers a wide spectrum of diseases with various clinical manifestations ranging from anemia to iron overload and possibly to neurodegenerative diseases [39, 31, 43, 44]. The mean iron concentration in studied gluten-free foods were found in range of 4.61 and 79.6 mg kg^{-1}. As the noodle has the lowest iron concentration, the white cookie has the highest iron concentration (Table 3).

To determine the overall heavy metal concentrations in all analyzed gluten-free samples, metal pollution index (MPI) was calculated (Figure 1). This index was obtained by calculating the geometrical mean of concentrations of all the metals in the samples

$$MPI=(C_1*C_2*C_3*\dots\dots*C_n)\wedge(1/n)$$

where C_n is the concentration of single metal in the sample. Among different gluten-free food analyzed, cocoa cookie showed the highest value of MPI (4.83) followed by flour (3.85) and the spaghetti (3.52) respectively. As compared to the previous products, noodle sample showed lower value of MPI (0.88).
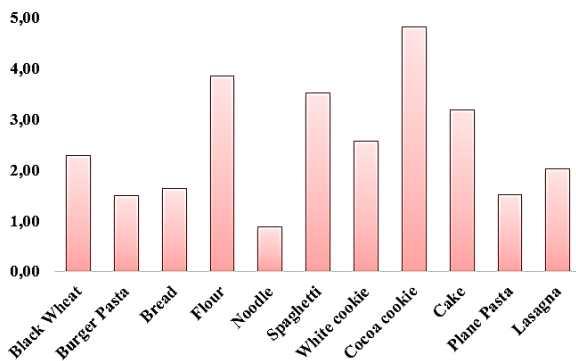
Figure 1. Metal pollution index for analyzed gluten-free food samples.

4. CONCLUSION

In this reported study, the concentration values of Cu, Mn, Co, Pb, Cr, Zn, Ni, Cd and Fe in eleven different gluten-free food samples, which consumed by celiac patients from Turkey, are reported. After wet digestion procedure, concentrations of the analytes in the final phase were measured by FAAS. While the Cd amounts of samples were the lowest for all samples, Fe levels were the highest. Analyzed levels of the trace elements in the gluten-free foods were compared with the recommended values or maximum corresponding levels suggested by the National NAS/NRC, WHO, the Turkish Food Codex, the Brasilian Ministry of Health, the Turkish standards and the EC. The obtained results showed that the amounts of Ni, Zn and Cd in the analyzed samples were higher than the recommended or maximum values.

REFERENCES

[1]. Dennis M., Anne R.L., Tara M., Nutritional Considerations of the Gluten-Free Diet, Gastroenterol. Clin. N., 48 (1) (2019) 53-72.

[2]. Melisa J.H., Roxana N.V., Sonia C.S, Eduardo J.M., Roberto G.P., Toxic Trace Element Contents in Gluten-free Cereal Bars Marketed in Argentina, International Journal of Celiac Disease, 3(1) (2015) 12-16.

[3]. Mlyneková Z., Chrenková M., Formelová Z., Cereals and Legumes in Nutrition of People with Celiac Disease, International Journal of Celiac Disease, 2(3) (2014) 105-109.

[4]. Litwinek D., Ziobro R., Gambus H., Sikora M., Gluten Free Bread in a Diet of Celiacs, International Journal of Celiac Disease, 2(1) (2014) 11-16.

[5]. Mehder A.O., Yilmaz E., Sungur A., Soylak M., Alothman Z.A., Assessment of Cr, Mn, Fe, Co, Ni, Cu, Zn, As, Cd, and Pb Concentrations in Gluten-free Foods From Saudi Arabia by Inductively Coupled Plasma Mass Spectrometry, Atom. Spectrosc., 36 (6) (2015) 254-260.

[6]. Munera-Picazo S., Burló F., Carbonell-Barrachina Á.A., Arsenic Speciation In Rice-Based Food For Adults With Celiac Disease, Food Addit. Contam. A., 31 (8) (2014) 1358-1366.

[7]. Sarı H., Gökdağ H., Kızılkaya A.E., Çölyak Hastalığına Sahip İlkokul Öğrencilerinin Okulda Sosyo-Biyolojik İhtiyaçlarının Karşılanmasında Yaşadıkları Problemlerin İncelenmesi: Bir Vaka Çalışması Yöntemi, Sosyal Politika Çalışmaları Dergisi. 18 (40) (2018) 121-134.

[8]. Harmancı Ö., Erişkin Yaş Grubunda Çölyak Hastalığının Klinik Özellikleri (Yan Dal Uzmanlık Tezi), Ankara, 2008 (in Turkish).

[9]. Rizzello C.G., Montemurro M., Gobbetti M., Characterization of the Bread Made with Durum Wheat Semolina Rendered Gluten Free by Sourdough Biotechnology in Comparison with Commercial Gluten-Free Products, J. Food Sci., 81(9) (2016) H2263-H2272.

[10]. Gobbetti M., Rizzello C.G., Di Cagno R., De Angelis M., How the sourdough may affect the functional features of leavened baked goods, Food Microbiol., 37 (2014) 30-40.

[11]. Melisa J.H., Sonia C.S., José M.C., Eduardo J.M., Roberto G.P., Trace element concentrations in commercial gluten-free amaranth bars, Journal of Food Measurement and Characterization, 9(3) (2015) 426-434.

[12]. Halina G., Dorota P., Florian G., Paulina W., Rafał Z., Mickowska B., Sikora M., Nutritional and dietary value of gluten-free rolls enriched in amaranth flour, Journal of Pre-Clinical and Clinical Research, 4(2) (2010) 126-130.

[13].Santino O., Diana A., Maria R., Salvatore B., Claudia L., Francesca D.G., Determination of trace elements in gluten-free food for celiac people by ICP-MS, Microchem. J., 116 (2014) 163-172.

[14].Yalçın G., Trace Element Content and Antioxidant Capacity of Gluten-Free Snacks Produced for Coeliac Disease Patients, Marmara Pharmaceutical Journal, 21(3) (2017) 598-602.

[15].EC, Commission Regulation (EC) No 1881/2006 of 19 December 2006 setting maximum levels for certain contaminants in foodstuffs, Off. J. Eur. Union L364 (2006) 0005-0024.

[16].FAO/WHO, Food Balance Sheet, http://www.fao.org/faostat/en/#data/FBS 2007.

[17].Pourreza N., Naghdi T., Silicon carbide nanoparticles as an adsorbent for solid phase extraction of lead and determination by flame atomic absorption spectrometry, J. Ind. Eng. Chem., 20 (5) (2014) 3502-3506.

[18].Saracoglu S., Soylak M., Cabuk D., Topalak Z., Karagozlu Y., Determination of some trace elements in food and soil samples by atomic absorption spectrometry after coprecipitation with holmium hydroxide, J. AOAC Int., 95 (2012) 892-896.

[19].Bressy F.C., Brito G.B., Barbosa I.S., Teixeira L.S.G., Korn M.G.A., Determination of trace element concentrations in tomato samples at different stages of maturation by ICP OES and ICP-MS following microwave-assisted digestion, Microchem. Journal., 109 (2013) 145-149.

[20].Nardi E.P., Evangelista F.S., Tormen L., Pierre T.D.S., Curtius A.J., de Souza S.S., Jr F.B., The use of inductively coupled plasma mass spectrometry (ICP-MS) for the determination of toxic and essential elements in different types of food samples, Food Chem.,112 (3) (2009) 727-732.

[21].Erbas Z., Karatepe A., Soylak M., Heavy metal contents of play dough, face and finger paint samples sold in turkish markets, Talanta 170 (2017) 377-383.

[22].Beccaloni E., Vanni F., Beccaloni M., Carere M., Concentrations of arsenic, cadmium, lead and zinc in homegrown vegetables and fruits: estimated intake by population in an industrialized area of Sardinia, Italy, Microchem. J., 107 (2013) 190-195.

[23].Radwan M.A., Salama A.K., Market basket survey for some heavy metals in Egyptian fruit and vegetables, Food Chem. Toxicol., 44 (2006) 1273-1278.

[24].Ysart G., Miller P., Crews H., Robb P., Baxter M., De L'Argy C., Lofthouse, S., Sargent C., Harrison N., Dietary exposure estimates of 30 elements from the UK total diet study, Food Add. Contam., 16 (1999) 391-403.

[25].Orecchio S., Papuzza V., Levels, fingerprint and daily intake of polycyclic aromatic hydrocarbons (PAHs) in bread baked using wood as fuel, J. Hazard. Mater., 164 (2-3) (2009) 876-883.

[26].SternB. R., Essentiality and toxicity in copper health risk assessment: overview, update and regulatory considerations, J. Toxicol. Env. Heal. A, 73(2-3) (2010) 114-127.

[27].Enjalbert F., Lebreton P., Salat, O., Effects of copper, zinc and selenium status on performance and health in commercial dairy and beef herds: retrospective study, J. Anim. Physiol. An. N., 90(11-12) (2006) 459-466.

[28].Barceloux D.G., Barceloux D., Copper, Journal of toxicology: clinical Toxicology, 37(2) (1999) 217-230.

[29].Fraga C.G., Relevance, essentiality and toxicity of trace elements in human health, Mol. Aspects Med., 26(4-5) (2005) 235-244.

[30].Milne D.B., Johnson P. E., Assessment of copper status: effect of age and gender on reference ranges in healthy adults, Clin. Chem., 39(5) (1993) 883-887.

[31].Maggio A., Orecchio S., Barreca S., Review on chemical composition of gluten-free food for celiac people, Integr Food Nutr Metab, 6 (1) (2019) 1-11.

[32].Brasilian Ministry of Health, Ministério da Saúde, Secretaria de Vigilância Sanitária. Portaria. Diário Oficial da República Federativa do Brasil, 685 (1998).

[33]. World Health Organization [WHO], Quality Directive of Potable Water. WHO, Geneva 197 (1994).

[34]. National Research Council, Food, Nutrition Board, National Academy of Sciences Recommended Dietary Allowances, 10th edn. Washington, DC: National Academy Press (1989).

[35]. Walsh C.T., Sandstead H.H., Prasad A.D.S., Newberne P.M., Fraker P.J., Zinc: health effects and research priorities for the 1990s, Environ. Health Persp., 102 (1994) 5-46.

[36]. Anonymous Regulation of setting maximum levels for certain conta minants in foodstuffs Turkish Official Gazette, 24908 (2002).

[37]. Barceloux D.G., Barceloux, D., Nickel, Journal of Toxicology: Clinical Toxicology, 37(2) (1999) 239-258.

[38]. Denkhaus E., Salnikow K., Nickel essentiality, toxicity, and carcinogenicity, Crit. Rev. Oncol. Hemat., 42(1) (2002) 35-56.

[39]. Piscator M., Dietary exposure to cadmium and health effects: impact of environmental changes, Environ. Health Persp., 63 (1985) 127.

[40]. Klaassen C.D., Liu J., Diwan B.A., Metallothionein protection of cadmium toxicity, Toxicol. Appl. Pharm., 238(3) (2009) 215-220.

[41]. Nawrot T.S., Staessen J.A., Roels H.A., Munters E., Cuypers A., Richart T., Vangronsveld, J., Cadmium exposure in the population: from health risks to strategies of prevention, Biometals, 23(5) (2010) 769-782.

[42]. Es'haghi Z., Khalili M., Khazaeifar A., Rounaghi, G.H., Simultaneous extraction and determination of lead, cadmium and copper in rice samples by a new pre-concentration technique: Hollow fiber solid phase microextraction combined with differential pulse anodic stripping voltammetry, Electrochim. Acta, 56(9) (2011) 3139-3146.

[43]. Allen L. H. Anemia and iron deficiency: effects on pregnancy outcome, Am. J. Clin. Nutr., 71(5) (2000) 1280-1284.

[44]. Tenenbein M., Kowalski S., Sienko A., Bowden D.H., Adamson I.Y.R., Pulmonary toxic effects of continuous desferrioxamine administration in acute iron poisoning, The Lancet, 339 (8795) (1992) 699-701.

AES Encryption and A Cryptosystem Obtained with Soft Set II

Emin AYGÜN ⓘD

Erciyes University, Faculty of Sciences, Department of Mathematics, Kayseri, TURKEY

Abstract. In this paper, a new cryptographic algorithm was created with the soft sets, symmetric groups, soft matrices representing soft sets, and AES. In 1999, by Molodtsov proposed soft set theory as a new mathematical tool to deal with uncertainties. This theory which has been applied to many fields which contain uncertainties received much attention since proposed. The inverse product and characteristic product defined on soft matrices was used in soft encryption and soft decryption. In order to make the encryption more secure, symmetric groups included in the algorithm.

Keywords: Soft Set, AES, Inverse Product, Characteristic Product.

AES Şifreleme ve Esnek Kümeler Yardımıyla Elde Edilen Kriptosistem II

Özet. Bu çalışmada, esnek kümeler, esnek kümeleri temsil eden esnek matrisler, simetrik gruplar ve AES ile yeni bir şifreleme algoritması oluşturulmuştur.1999'da Molodtsov tarafından esnek küme teorisi belirsizlikleri ortadan kaldırabilmek için yeni bir matematiksel yöntem olarak kullanılmaya başlandı. Belirsizlikleri içeren birçok alana uygulan bu teori önerildiğinden bu yana çok dikkat çekmiştir. Esnek matrisler üzerinde tanımlanan invers çarpım ve karakteristik çarpım esnek şifrelemede ve esnek deşifrelemede kullanılmıştır. Şifrelemenin daha güvenli olması için simetrik gruplar algoritmaya dahil edilmiştir.

Anahtar Kelimeler: Esnek Küme, AES, İnvers Çarpım, Karakteristik Çarpım.

1. INTRODUCTION

The soft set theory introduced by Molodtsov[1] is seen as an effective mathematical tool as composed to other existing methods that were used to deal with uncertainties. The advantage of soft set theory over other theories is that researchers can select any parameters when they needed, since it does not impose any restriction while defining an object.

By using soft set theory Molodtsov worked in many fields such as Riemann integration, game theory, continuous differentiable functions, probability theory and measure theory[1-3].

Roy et. al. [4] investigated soft set theory for decision making problems. Many researches studied on soft set theory. For exampleFeng et al. [5] defined various concepts such as intersection, union, difference on soft sets. Sezgin and Atagün [6] introduced intersection, extended intersection, limited union, and limited difference on soft sets and examined the relationship with others. Aktaş and Çağman[7] compared soft sets with related concept of fuzzy sets and rough sets. In addition to, they introduced concept of soft group that has been launched in many new works. They also defined concepts of soft subgroup, normal soft subgroup and soft homomorphism on soft groups. Atagün and

Sezgin [8] worked on ring, field and soft algebraic modul. Sezgin and Atagün [9] defined soft near-ring. Atagun and Aygun proved that the set of all soft sets over a universe U is an abelian group under the each operations and called "the inverse group of soft sets" and "the characteristic group of soft sets" [10].

AES(Advanced Encryption Standard) is a subset of the Rijndael block cipher developed by two Belgian cryptographers, Vincent Rijmen and Joan Daemen, who submitted a proposal to NIST during the AES selection process. Rijndael is a family of ciphers with different key and block sizes [11]. AES which still maintains its reliability today, is used for security in the computing world. Today, fast and small size product are required in techonology's preferred features. Therefore, AES and speed need to have as few memories as possible. In our study [12], we did this with the charahteristic product. In this paper, a new cryptographic algorithmusing the inverse product is proposed for soft sets, soft matrices, symmetric groups and using the row shift method in AES cryptosystem.

2.   PRELIMINARIES

Definition 2.1. Let U be a universal set, $P(U)$ be power set of U , E be a parameter set and $A \subseteq E$. Then, $f_A : E \to P(U)$ defined as follows:

$$(f_A, E) = \{(e, f_A(e)) : e \in E, f_A(e) \in P(U) \mid e \notin A \text{ ise } f_A(e) = \varnothing\}$$

 The pair (f_A, E) is called soft set on U [13]. Where, f_A is approximate function of (f_A, E) and $f_A(e)$ is called ε-approach set. (f_A, E) can be represented as (F, A) or F_A. Moreover, (f_A, E) can be written as $(f_A, E) = \{f_A(e) \mid e \in A\}$[2].

Definition 2.2. Let (f_A, E) be a soft set on U .

i_1) If for all $e \in A$, $(f_A, E) = \emptyset$, then (f_A, E) is called empty soft set and it is denoted by $(f_A, E) = \Phi$.

i_2) If for all $e \in A$, $(f_A, E) = U$, then (f_A, E) is called absolute soft set and it is shown as $(f_A, E) = (f_{\tilde{A}}, E)$ [1].

Definition 2.3. Let (f_A, E) be a soft set on U .The complement of (f_A, E) denoted by $(f_A, E)^c$, $\forall e \in E$, $f^c{}_A(e) = U / f_A(e)$ [1].

Proposition 2.4. Let (f_A, E) be a soft set on U . Then,

i_1) $(f^c{}_A, E)^c = (f_A, E)$,

i_2) $\Phi^c = (f_E, E)$ [2].

Definition 2.5. The algorithm that uses the same key for encryption and decryption is called secret keyed algorithm [14].

Definition 2.6. The algorithms in which different keys are used for the encryption and decryption operations, decryption key can't be obtained from encryption key are called open keyed algorithm [14].

Definition 2.7. (Advanced Encryption Standard **)** The AES encryption algorithm is a block encryption algorithm that encrypts 128-bit data blocks with 128, 192 or 256-bit key operations. The information of

128 bits in size is separated into (4x4) square matrices and included in the encryption algorithm. The obtained matrix is named as "state" and every row of this matrix is named as "word" [14].

Definition 2.8. (Loop Structure)
Once state matrix is established, algorithm come into operation. The length of key determines the number of loops. The process of using columns is not needed in the final loops, a coded block is obtained by doing addition with the type key. The inverse of these sub-operation is used to solve encrypted text. In loops of state matrix, the four operations, given in [14] are used.

Definition 2.8.1. (Bit Changing)
Matrix named as state matrix will have a change in its elements. These changes are made according the previously calculated S-box. In S-box, the elements of the state matrices can be 16x16 matrix since they are based on the hexadecimal basis [14].

Definition 2.8.2. (Row Shifting)
This operation is done on new state matrix. The first row of the matrix remains fixed, the second, third and fourth rows are shifted by 1, 2 and 3 rows to the loft respectively [14].

Definition 2.8.3. (Column Shuffling)
The shuffling of columns is achieved by matrix multiplication of each column of the state matrix obtained by shifting rows in previous stage equation

$$a(x) = \{03\}\, x^3 + \{01\}\, x^2 + \{01\}\, x + \{02\}$$

independently. The new column is replaced by the old column [14].

Definition2.8.4. (Adding Loop Key)
According to AES algorithm, the key material is added at th end of each loop. This is the key index originally generated by the key generation block [14].

Definition 2.9.
The AES decryption algorithm is an algorithm used for decrypting the encrypted text. Similar steps used to decrypt the encrypted text, but operations are inversed. The conversions applied to encrypt the text are translated in the opposite direction and start in the inverse order of encryption [14].

Definition 2.9.1. (Inverse Row Shifting)
The state matrix is shifting to the right rather than to the left as applied in encryption. The second, third and fourth row are shifted by 1, 2 and 3 rows to the right respectively [14].

Definition 2.9.2.(Inverse Byte Changing)
In the encryption process, S- box has been used to change the byte. Similarly, S-box is also used for decryption. However, this S-box is the inverse of the S-box used for encryption [14].

Definition 2.9.3. (Inverse Coloumn Changing)
Every coloumn is multiplied with the equation $a^{-1}(x) = \{0B\}x^3 + \{0D\}x^2 + \{09\}x + \{0E\}$ and replaced with the old column [14].

Definition 2.9.4. (Adding Loop Key)
The loop key has a symmetrical structure and the opposite of the loop key is itself. The AES algorithm uses the same key to encrypt and decrypt the text [14].

Definition 2.10. The one-to-one and onto function defined on a non-empty set A is called permutation. It is a group with respect to composition of functions, and named as permutation group. It is shown as S_n [16].

3. SOFT MATRICES

Definition 3.1. Let (f_A, E) be a soft set on U. The subset $R_A = \{(u,e): e \in A, u \in f_A(e)\}$ of $U \times E$ is called relation form of (f_A, E).

$$X_{R_A}: U \times E \to \{0,1\}, \quad X_{R_A}(u,e) = \begin{cases} 1, & (u,e) \in R_A \\ 0, & (u,e) \notin R_A. \end{cases}$$

where R_A is called characteristic function [15].

If $a_{ij} = X_{R_A}(u_i, e_j)$,

$[a_{ij}] = \begin{bmatrix} a_{11} & \cdots & a_{1n} \\ \vdots & \ddots & \vdots \\ a_{m1} & \cdots & a_{mn} \end{bmatrix}$ is called soft matrix of (f_A, E) on U. The all soft matrix of U are denoted by SM_{mxn}.

Example 3.2. Let $U = \{u_1, u_2, u_3, u_4, u_5\}$ be the universal set, $E = \{e_1, e_2, e_3, e_4\}$ be parameter set, $A = \{e_1, e_3, e_4\}$ and $(f_A, E) = \{(e_1, \{u_2, u_4\}), (e_3, \{u_1, u_3, u_5\}), (e_4 \, U)\}$. The relation form of (f_A, E) $R_A = \{(u_2, e_1), (u_4, e_1), (u_1, e_3), (u_3, e_3), (u_5, e_3) \, (u_1, e_4), (u_2, e_4), (u_3, e_4), (u_4, e_4), (u_5, e_4)\}$. Then soft matrix

$$[a_{ij}] = \begin{bmatrix} 0 & 0 & 1 & 1 \\ 1 & 0 & 0 & 1 \\ 0 & 0 & 1 & 1 \\ 1 & 0 & 0 & 1 \\ 0 & 0 & 1 & 1 \end{bmatrix}$$

Definition 3.3. Let $[a_{ij}] \in SM_{mxn}$.

i_1) If $a_{ij} = 0$ for all i and j, $[a_{ij}]$ is called zero soft matrix and it is shown with [0].

i_2) If $a_{ij} = 1$ for all $j \in I_A = \{j: e_j \in A\}$ and i , $[a_{ij}]$ is called A-universal soft matrix and it is shown with $[\tilde{a}_{ij}]$.

i_3) If $a_{ij} = 1$ for all i and j , $[a_{ij}]$ is called universal soft matrix and it is shown with [1]. [10]

Definition 3.4. Let $[a_{ij}], [b_{ij}] \in SM_{m \times n}$. Then "$\cdot_i$" inverse product of $[a_{ij}]$ and $[b_{ij}]$ is

$[a_{ij}] \cdot_i [b_{ij}] = [c_{ij}]$, for each i, j

it is defined as $c_{ij} = \begin{cases} 1, & a_{ij} \neq b_{ij} \\ 0, & a_{ij} = b_{ij} \end{cases}$ [10].

Definition 3.5. Let $[a_{ij}]$, $[b_{ij}] \in SM_{m \times n}$. Then "$\cdot_c$" characteristic product of $[a_{ij}]$ and $[b_{ij}]$ is $[a_{ij}] \cdot_c$ $[b_{ij}] = [c_{ij}]$, for each i, j

it is defined as $c_{ij} = \begin{cases} 1, & a_{ij} = b_{ij} \\ 0, & a_{ij} \neq b_{ij} \end{cases}$ [10].

4. SOFT ENCRYPTION

The numbers corresponding to the letters in the alphabet for the cryptosystem are as follows:

$$\begin{array}{ccccccccccccccccccc} HARFLER & A & B & C & D & E & F & G & H & I & J & K & L & M & N & O & P & Q & R \\ NUMARALAR & 0 & 1 & 2 & 3 & 4 & 5 & 6 & 7 & 8 & 9 & 10 & 11 & 12 & 13 & 14 & 15 & 16 & 17 \end{array}$$

$$\begin{array}{ccccccccccccc} S & T & U & V & W & X & Y & Z & Ç & Ğ & İ & Ö & Ş & Ü \\ 18 & 19 & 20 & 21 & 22 & 23 & 24 & 25 & 26 & 27 & 28 & 29 & 30 & 31 \end{array}$$

The 5-bit counterpart of each letter in binary system:

A	B	C	…	Ş	Ü
00000	00001	00010	…	00100	11111

Due to binary system 6 letters are added to obtain 32: Ç,Ğ,İ,Ö,S,Ü.

Definition 4.1. While any $S \in SM_{5 \times 5}$ soft matrix is arranged according to any $\pi \in S_5$ permutation group, the elements in each row of the soft matrix are displaced according to the given π. Obtained matrix will be shown with S_π. This paper, soft matrix will be shown with S, message with M, ciphertext with C.

Example 4.2. Let $S = \begin{bmatrix} 1 & 0 & 1 & 0 & 1 \\ 1 & 0 & 1 & 0 & 1 \\ 0 & 1 & 1 & 1 & 0 \\ 0 & 1 & 0 & 0 & 0 \\ 1 & 1 & 1 & 0 & 0 \end{bmatrix}$ and $\pi =(13542)$. The elements of each row of soft matrix

are displaced according to $1 \rightarrow 3 \rightarrow 5 \rightarrow 4 \rightarrow 2 \rightarrow 1$ to arrange soft matrix according to π permutation. The first row arranged is 00111. If the same operation applied to each row

$$S_\pi = \begin{bmatrix} 0 & 0 & 1 & 1 & 1 \\ 0 & 0 & 1 & 1 & 1 \\ 1 & 1 & 0 & 0 & 1 \\ 1 & 0 & 0 & 0 & 0 \\ 0 & 0 & 1 & 0 & 1 \end{bmatrix}$$

matrix is obtained.

Theorem 4.3. Let $S, M, C \in SM_{5x5}$ and $\pi \in S_5$. Then,

$i_1) \ S_\pi \cdot_i M = C$

$i_2) \ S_\pi \cdot_c M = C$

$i_3) \ (S_\pi \cdot_i M) \cdot_c S_\pi = C$

Proof: Theorem 4.3. Soft Encryption Algorithm with i_1)

1. Any soft set is taken.
2. A soft matrix is obtained which corresponds to the soft set.
3. The message is divide into blocks and found counterpart in binary system.
4. The first row of the soft matrix remains fix, the second, third and fourth row is shifted by 1, 2 and 3 rows to the left respectively.
5. Each row of the soft matrix is rearrange according to π and S_π key is obtained.
6. Makes "$\cdot_i$" product S_π and message.
7. Each row of the matrix which obtained letter and sends to receiver.

The other matters of the theorem can be done in similar way only changing the type of product.

Theorem 4.4. Let $S, M, C \in SM_{5x5}$ and $\pi \in S_5$. Different decryption methods are given as follows according to Theorem 4.3.

i_1) $C \cdot_i S_\pi = M$

i_2) $C \cdot_c S_\pi = M$

i_3) $S_\pi \cdot_i (C \cdot_c S_\pi) = M$

Proof: Theorem 4.4. Soft Decryption Algorithm with i_1)

1. The soft set used for encryption is taken.
2. The soft matrix corresponding to the soft set is obtained.
3. Ciphertext is divided into blocks and found corresponding in the binary system.
4. The first row of the soft matrix remains fix, the second, third and fourth row is shifted by 1, 2 and 3 rows to the left respectively.
5. Each row of the soft matrix is rearrange according to π and S_π key is obtained.
6. Makes "$\cdot_i$" product S_π and ciphertext.
7. Each row of the matrix which obtained letter and the message is decrypted.

The other matters of the theorem can be done in similar way only changing the type of product.

5. APPLICATION OF SOFT ENCRYPTION AND DECRYPTION

Example 5.1. Soft Encryption

1) Let (f_A ,E) = { $(e_1 , \{u_1 , u_3, u_5\})$, $(e_3 , \{u_2 , u_4 , u_5\})$, $(e_5 , \{u_3 , u_4\})$ } be soft set on U Let " SOFT ENCRYPTION " is the message.

2) The soft matrix corresponding to the soft set:

$$ S = \begin{bmatrix} 1 & 0 & 0 & 0 & 0 \\ 0 & 0 & 1 & 0 & 1 \\ 1 & 0 & 0 & 0 & 0 \\ 0 & 0 & 1 & 0 & 1 \\ 1 & 0 & 1 & 0 & 0 \end{bmatrix} $$

3) The message is divided into blocks. SOFTE / NCRYP / TIONA
Found counterpart in binary system and each row create a matrix. Here, to the last of the message is appended with a letter to complete the block.

SOFTE - 10010 , 01110 , 00101 , 10011 , 00100

$$M_1 = \begin{bmatrix} 1 & 0 & 0 & 1 & 0 \\ 0 & 1 & 1 & 1 & 0 \\ 0 & 0 & 1 & 0 & 1 \\ 1 & 0 & 0 & 1 & 1 \\ 0 & 0 & 1 & 0 & 0 \end{bmatrix}$$

NCRYP   - 01101, 00010, 10001, 11000, 01111

$$M_2 = \begin{bmatrix} 0 & 1 & 1 & 0 & 1 \\ 0 & 0 & 0 & 1 & 0 \\ 1 & 0 & 0 & 0 & 1 \\ 1 & 1 & 0 & 0 & 0 \\ 0 & 1 & 1 & 1 & 1 \end{bmatrix}$$

TIONA - 10011, 01000, 01110, 01101, 00000

$$M_3 = \begin{bmatrix} 1 & 0 & 0 & 1 & 1 \\ 0 & 1 & 0 & 0 & 0 \\ 0 & 1 & 1 & 1 & 0 \\ 0 & 1 & 1 & 0 & 1 \\ 0 & 0 & 0 & 0 & 0 \end{bmatrix}$$

4) Other rows obtained the first row of the soft matrix are shifted as defined in the algorithm.

$$S = \begin{bmatrix} 1 & 0 & 0 & 0 & 0 \\ 0 & 1 & 0 & 1 & 0 \\ 0 & 0 & 0 & 1 & 0 \\ 0 & 1 & 0 & 0 & 1 \\ 0 & 1 & 0 & 1 & 0 \end{bmatrix}$$

5) Let $\pi = (14235) \in S_5$. Soft matrix is arranged according to π.

$$S_\pi = \begin{bmatrix} 0 & 0 & 0 & 1 & 0 \\ 0 & 1 & 1 & 0 & 0 \\ 0 & 1 & 0 & 0 & 0 \\ 1 & 0 & 1 & 0 & 0 \\ 0 & 1 & 1 & 0 & 0 \end{bmatrix}$$

$$6)\ S_\pi \cdot_i M_1 = C_1 = \begin{bmatrix} 1 & 0 & 0 & 0 & 0 \\ 0 & 0 & 0 & 1 & 0 \\ 0 & 1 & 1 & 0 & 1 \\ 0 & 0 & 1 & 1 & 1 \\ 0 & 1 & 0 & 0 & 0 \end{bmatrix}$$

Similarly, $C_2 = \begin{bmatrix} 0 & 1 & 1 & 1 & 1 \\ 0 & 1 & 1 & 1 & 0 \\ 1 & 1 & 0 & 0 & 1 \\ 0 & 1 & 1 & 0 & 0 \\ 0 & 0 & 0 & 1 & 1 \end{bmatrix}$, $C_3 = \begin{bmatrix} 1 & 0 & 0 & 0 & 1 \\ 0 & 0 & 1 & 0 & 0 \\ 0 & 0 & 1 & 1 & 0 \\ 1 & 1 & 0 & 0 & 1 \\ 0 & 1 & 1 & 0 & 0 \end{bmatrix}$ is obtained.

7) Turns from soft matrix of message the letter. the ciphertext is obtaind as

" QCNHIPOZMDREGZM" and is sent to receiver.

Soft Decryption

1) The soft set used for encryption is taken.
$(f_A , E) = \{ (e_1 , \{u_1 , u_3, u_5\}) , (e_3 , \{u_2 , u_4 , u_5\}) , (e_5 , \{u_3 , u_4\}) \}$

2) The soft matrix corresponding to the soft set:

$$S = \begin{bmatrix} 1 & 0 & 0 & 0 & 0 \\ 0 & 0 & 1 & 0 & 1 \\ 1 & 0 & 0 & 0 & 0 \\ 0 & 0 & 1 & 0 & 1 \\ 1 & 0 & 1 & 0 & 0 \end{bmatrix}$$

3) The ciphertext is divided into blocks "QCNHI- POZMD- REGZM" soft matrices of the ciphertext respectively:

$$C_1 = \begin{bmatrix} 1 & 0 & 0 & 0 & 0 \\ 0 & 0 & 0 & 1 & 0 \\ 0 & 1 & 1 & 0 & 1 \\ 0 & 0 & 1 & 1 & 1 \\ 0 & 1 & 0 & 0 & 0 \end{bmatrix}, C_2 = \begin{bmatrix} 0 & 1 & 1 & 1 & 1 \\ 0 & 1 & 1 & 1 & 0 \\ 1 & 1 & 0 & 0 & 1 \\ 0 & 1 & 1 & 0 & 0 \\ 0 & 0 & 0 & 1 & 1 \end{bmatrix}, C_3 = \begin{bmatrix} 1 & 0 & 0 & 0 & 1 \\ 0 & 0 & 1 & 0 & 0 \\ 0 & 0 & 1 & 1 & 0 \\ 1 & 1 & 0 & 0 & 1 \\ 0 & 1 & 1 & 0 & 0 \end{bmatrix}$$

4) Other rows except the first row of the soft matrix are shifted as defined in the algorithm.

$$S = \begin{bmatrix} 1 & 0 & 0 & 0 & 0 \\ 0 & 1 & 0 & 1 & 0 \\ 0 & 0 & 0 & 1 & 0 \\ 0 & 1 & 0 & 0 & 1 \\ 0 & 1 & 0 & 1 & 0 \end{bmatrix}$$

5) $\pi = (14235) \in S_5$ was taken as. Soft matrix is arranged according to π.

$$S_\pi = \begin{bmatrix} 0 & 0 & 0 & 1 & 0 \\ 0 & 1 & 1 & 0 & 0 \\ 0 & 1 & 0 & 0 & 0 \\ 1 & 0 & 1 & 0 & 0 \\ 0 & 1 & 1 & 0 & 0 \end{bmatrix}$$

6) $C \cdot_i S_\pi = M_1 = \begin{bmatrix} 1 & 0 & 0 & 1 & 0 \\ 0 & 1 & 1 & 1 & 0 \\ 0 & 0 & 1 & 0 & 1 \\ 1 & 0 & 0 & 1 & 1 \\ 0 & 0 & 1 & 0 & 0 \end{bmatrix}$, $M_2 = \begin{bmatrix} 0 & 1 & 1 & 0 & 1 \\ 0 & 0 & 0 & 1 & 0 \\ 1 & 0 & 0 & 0 & 1 \\ 1 & 1 & 0 & 0 & 0 \\ 0 & 1 & 1 & 1 & 1 \end{bmatrix}$, $M_3 = \begin{bmatrix} 1 & 0 & 0 & 1 & 1 \\ 0 & 1 & 0 & 0 & 0 \\ 0 & 1 & 1 & 1 & 0 \\ 0 & 1 & 1 & 0 & 1 \\ 0 & 0 & 0 & 0 & 0 \end{bmatrix}$

7) Turns from soft matrix of message the letter. SOFTE / NCRYP / TIONA the message is decrypted. "SOFT ENCRYPTION" obtains the message. Similarly, other theorems can be used for encryption and decryption.

6. CONCLUSION

In this paper, a new cryptographic algorithm was created based on the soft sets, symmetric groups and AES. Precise selection of universal set and soft set elements improves the security of encryption. The soft encryption created with $\pi \in S_5$ similarly can be applied for $\pi \in S_6$, S_7. Then, the size of the soft matrix changes. Furthermore, we can also do the operations in the rows instead of the columns.

Acknowledgements

REFERENCES

[1]. Molodtsov, D., Soft set theory-first results, Computers and Mathematics with Applications, 37 (1999) 19–31.

[2]. Molodtsov, D. , The Theory of Soft Sets, URRS Puplishers. , Moscow, (in Russian) 2004.

[3]. Rivest, R. , Adleman, L. and Dertouzos, M., On data banks and privacy homomorphisms, In Foundations of Secure Computation, (1978) 169–180.

[4]. Roy, A.R. and Maji, P.K., A fuzzy soft set theoretic approach to decision making problem, Journal of Computational and Applied Mathematics , 203 (2007) 412–418.

[5]. Feng, F., Jun, Y. B. and Zhao X., Soft semirings, Computers and Mathematics with Applications, 56 (2008) 2621–2628.

[6]. Sezgin, A. and Atagün, A.O., On operations of soft sets, Computers and Mathematics with Applications, 61 (2011) 1457–1467.

[7]. Aktas H., Çagman N., Soft sets and soft groups, Inform. Sci. , 177 (2007) 2726-2735.

[8]. Atagün, A.O. and Sezgin, A., Soft substructures of rings, fields and modules, Comput. Math. Appl., 61 (3) (2011) 592-601.

[9]. Sezgin, A .Atagün, O. and Aygün, E., A note on soft near-rings and idealistic soft near-rings, Filomat, 25-1 (2011) 53–68.

[10]. Atagün, A.O. and Aygün, E., Groups of soft sets, Journal of Intelligent and Fuzzy Sys., 30 (2016) 729-733.

[11]. Miller, F.P., Vandome, A.V., McBrewster, J., Advanced Encryption Standard, Alpha Press, London, 243s. 2009.

[12]. Aygun, E. and Akbulut, S. AES Şifreleme ve Esnek Kümeler Yardımıyla Elde Edilen Yeni Bir Kriptosistem, Erciyes University Journal of the Institute of Science and Technology, 35-1 (2019)

[13]. Maji, P.K., Biswas , R. and Roy, A.R., Soft set theory. Computers & Mathematics with Applications, 45 (2003) 555-562.

[14]. Daeman, J., Rijmen, V. The design of Rijndael: AES: the Advanced Encryption Standard.Berlin Heidelberg: Springer-Verlag 128s, 2002.

[15]. Çağman, N. and Enginoğlu S., Soft matrix theory and its decions making, Computers and Mathemetics with Applications, 59 (2010) 3308-3314.

[16]. Stinson, D., Cyrptography: Theory and Practice , CRC Press, New Jersey 573s. 1995.

Cumhuriyet Science Journal

CSJ

Amplitude of Elastic Scattering for the Region of Large Impact Parameters

Sajida G. ABDULVAHABOVA * ⓘD *, N.Sh. BARKHALOVA, T.O. BAYRAMOVA*

Baku State University, Baku, Azerbaijan

Abstract. The work is dedicated to consequences of analyticity and unitarity of the scattering amplitude. Using the Gaussian quasipotential an equation for the scattering amplitude matrix is obtained and formula is derived for the cross sections. The dependence of the cross section and ratio of the real part of the amplitude in the forward scattering to its imaginary part of on the momentum are discussed. The steep Gaussian peak for cross section at small angles is followed by the exponential (Orear) regime. Results from theoretical approach are compared with experimental data.

Keywords: Quasipotential, scattering amplitude, unitarity, cross section, impact parameter.

Büyük Etki Parametreleri Bölgesi İçin Elastik Saçılma Genliği

Özet. Bu çalışmada, saçılma genliğinin analitikliğinin ve uniterliğinin gerekliliği incelenmiştir. Gaussiyen yarı-potential kullanılarak, saçılma genliği matrisi için bir denklem elde edilmiş ve tesir kesitleri için bir formül elde edilmiştir. Tesir kesitin bağımlılığı ve ileri saçılmadaki genliğin gerçel bölümünün momentum üzerindeki sanal kısmına oranı tartışılmıştır. Küçük açılarda tesir kesiti için dik Gaussiyen zirveyi üstel (Orear) rejim takip eder. Teorik yaklaşımdan elde edilen sonuçlar deneysel veriler ile karşılaştırılmıştır.

Anahtar Kelimeler: Yarı potansiyel, saçılma genliği, üniterlik, tesir kesiti, etki parametresi.

1. INTRODUCTION

A theoretical analysis of the angular distribution of the fragments arising from the break-up of the projectile by the nuclear and interaction with the target is very useful and necessary for the experimental investigations. More useful would be the exclusive experiments where the scattering process of the projectile is separated from the background of other reactions by means of the coincidence detection of the two outgoing fragments together with a simultaneous measurement of their energies [1].

In the theory of diffraction, the reaction is considered as a quantum mechanical process due to the fact that different components of the wave function of the incident hadron have a different probability of interaction with the target [2]. As a result, the wave function is distorted. If we expand it over a complete set of functions, after collision, it contains not only the initial hadron function and other states of the incident particle. In this case we are talking about those components of the wave function for which the probability of interaction with the target is small, i.e. In the course of the collision, only a small part of the target is excited (an elastic collision with only one of its constituent particles). Since other wise the quark wave function of the target will lose its coherence and the

---

target will decay into a large number of secondary hadrons. To do this, we must use the "point" component of the wave function of the incident hadron. This is possible in the following cases: - quarks and gluons are at a small distance from each other and the scattering cross section is very small; - go into the field of large impact parameters. In particular, has been the touchstone of the theory since its first derivation, showing a remarkable agreement between the predicted and experimental structure of the angular scattering distribution. The analysis of hadron-nucleus cross sections in the diffraction approximation can be used to extract information on the scatering amplitude parameters. For this it will be necessary to measure the hadron-nucleus cross sections at various incident-hadron energies.

According to the model developed in [3], when the de Broil wavelength of the incident particle is much smaller than the size of the target nucleus, the interaction of each incident particle with the nucleus can be considered as a process of interaction along a narrow tube inside the nucleus, whose distance from

the center of the nucleus is determined by the impact parameter b. In this paper, we discuss the cross section of elastic scattering for the region of large impact parameters b.

2. THE AMPLITUDE OF ELASTIC SCATTERING

We will discuss some aspects of nucleon-nucleon collisions without physical overlap, i.e. collisions with impact parameters, b, larger than the sum of the nuclear radii, R, i.e. $b > 2R$. Particles can be produced in these collisions through an interaction of the fields of the nuclei. The interactions can involve both the electromagnetic and nuclear fields, but because of the short range of the nuclear force, purely nuclear processes are suppressed for $b > 2R$.

If the momentum transfers from the nuclei are small enough (q<kc/R), the fields both nuclei couple coherently to all nucleons. This enhances the cross sections and gives the events a unique

signature, which can be used for identification. The restrictions on the momentum transfer do not prevent the production of heavy systems, however, in high-energy collisions.

The scattering of hadrons at high energies is a multiparticle process, as a result of which the unitarity condition reduces to an unsolvable infinite chain of interlocking equations. One of the methods that would allow us to construct an elastic scattering amplitude that satisfies at least the two-particle unitarity condition is the use of a quasipotential [4].

The quasipotential in space configuration depends on the velocity and is nonlocal. In addition, it depends on the total energy of the system and is a complex function. Choosing a quasipotential in the form of a smooth, local (in configurational space) function that depends on energy, with a positive definite imaginary part, it is possible to correctly describe the basic properties of hadron scattering at small and large angles [5,6].

The potential description of scattering with a given quasipotential permits a description region of the phase shifts of individual iteration which are essential in the transition from the description region of momentum transfer to the Orear region. The probability description can be considered as a justification for the introduction of smooth quasipotentials into field theory, and in addition it appears to be more promising for describing scattering with momentum transfers comparable with energy.

As a concrete example, we choose a quasipotential in the form of a Gaussian

$$V(s,r) = is\left(\frac{\pi}{a}\right)^{3/2} \exp\left(-r^2/4a\right), \qquad (1)$$

corresponding to a purely imaginary amplitude of diffraction scattering. In (1) the parameter a characterizes the effective interaction radius, which depends on the energy. With increasing energy, the parameter a increases logarithmically: $a = a_0 + lns$. The local quasipotential (1) has a positive definite imaginary part and is a smooth non-singular

function of *r* which satisfies all of the principles enumerated above and also the requirement of diffractive behaviour at small transferred momenta. The advantage of Gaussian Potential is that it is very flexible. In contrast to analytic potentials, the accuracy of Gaussian potential can be improved by adding more quantum mechanical data at various points in configurational space without changing the fit globally. The flexibility of the fit ensures that the best possible fit is achieved for any given data [7].

In the representation of invariant variables (Mandelstam variables) the standard relationship of the scattering amplitude f with the differential cross section of elastic scattering has the following form

$$\frac{d\sigma_{el}(s,t)}{dt} = |f(s,t)|^2, \qquad s = 4(k^2 + m^2) = 4E^2,$$

$$t = -(\mathbf{p} - \mathbf{k})^2. \tag{2}$$

The scattering amplitude is analytic not only in the *s* plane, but also in the *t* plane.

In the description of elastic diffraction, it is convenient to use the eikonal model, the advantage lies in the fact that in an explicit form it leads to the observance of the unitarity condition for the scattering amplitude. If the energy of the incident particle is sufficiently large, so that the wavelength $\Box = \kappa^{-1}$ is small in comparison with the characteristic dimensions of the interaction region *R* (where *R* is the nucleus radius), i.e. *kR >> 1*, the so-called high-energy approximation is well-suited to explain the scattering of such particles.

The high-energy or eikonal approximation is widely and successfully used to describe the scattering of particles also in complex nuclei as scattering in a certain optical continuous medium. In this approximation, instead of the law of conservation of energy, the law of conservation of the momentum projection on the direction **k** takes place: **pk** = const. This means that the movement in the transverse directions is completely neglected. In addition, in this approximation, no restrictions are imposed on the masses and coordinates of the particles, both the finite radius and the recoil are considered exactly. Therefore, the eikonal approximation can be used to calculate the differential cross sections for both direct and exchange processes. In addition, in the eikonal approximation, the effect of distortions is taken into account only in the phase of a plane wave. Therefore, the high-energy approximation can be used to calculate the angular distributions of scattered particles.

For the hadron scattering amplitude at high energies, it is very convenient to pass from expansion in partial waves to the representation of the impact parameter *b*:

$$f(s,b) = i \int b\, db \left(1 - \exp\left[-\frac{i}{m} \int_{-\infty}^{z} V(b^2 + z'^2)\, dz' \right] \right) \tag{3}$$

Such a recording of the amplitude in the high-energy region is not based on a specific mechanism of interaction. The entire dynamics of the process in the eikonal models should be introduced by specifying a specific kind of eikonal [8]:

$$\chi(s,b) = i\left(exp(-\mu\sqrt{b^2 + a^2}) - exp(-2\mu\sqrt{b^2 + a^2}) \right)$$

(4)

here the parameters μ_0 and a_0 have the meaning of the reduced mass and the interaction radius:

$$\mu = \mu_0 / \sqrt{1 + \ln s - i\pi/2} \;;$$
$$a = a_0 / \sqrt{1 - \ln s - i\pi/2} \tag{5}$$

In the eikonal approximation, the characteristic scattering angle is determined by the quantity $\theta \le \lambdabar / b$.

(3) can be expressed in terms of the eikonal

$$f(s,t) = i \int b\, db \left(1 - \exp[i\chi(s,b)] \right) J_0(b\sqrt{-t})$$
(6)

where J_0 is the Bessel function.

We note that the function $f(s,b)$, which determines the amplitude for purely nuclear scattering according to Eq. (6), is virtually equal to unity within the nucleus, both in the case of antinucleon scattering, and in that of nucleon scattering. This means that for these particles the nucleus acts as an absolutely black sphere (in the central region) with a diffuse boundary.

At high energies, each value of b corresponds to its partial wave $l = b\sqrt{s/2}$ and the unitarity condition has the form

$$2\,\mathrm{Im}\,f(s,b) = |f(s,b)|^2 + \varphi_{in}(s,b),\qquad (7)$$

here $\varphi_{in}(s,b)$ is the contribution of inelastic channels, i.e. probability of inelastic interaction at a point b.

The total collision cross section and the inelastic scattering cross section are determined as follows

$$\sigma_{tot} = 4\pi \int \mathrm{Im}\,f(s,b)bdb$$
$$\sigma_{in} = 2\pi \int \varphi_{in}(s,b)bdb \qquad (8)$$

The differential cross section for elastic scattering is related to the amplitude as follows

$$\frac{d\sigma(s)}{dt} = \left[\mathrm{Re}\,f(s,t)^2 + \mathrm{Im}\,f(s,t)^2\right] \qquad (9)$$

The elastic scattering amplitude must satisfy the general principles of analyticity and unitarity.

After simple calculations for the differential cross section for elastic scattering, we obtain

$$\frac{d\sigma}{dt} = \left(\frac{d\sigma}{dt}\right)_{t=0} \exp\{2[a(t)-1]\ln(s/s_0)\} \qquad (10)$$

The differential cross sections of binary processes (in particular, the elastic pp scattering reactions), according to formula (10), are concentrated in a narrow region of transmitted momentum |t|, whose width decreases logarithmically with increasing energy. This phenomenon in elastic processes is usually called the reduction of the diffraction cone. Reduction of the cone of the angular distribution was observed experimentally in all binary reactions.

The total cross section is related to the imaginary part of the scattering amplitude according to the optical theorem.

$$\sigma_{tot} = 4\pi \int \mathrm{Im}\,f(s,b)bdb = \frac{\mathrm{Im}\,f(0)}{s} \qquad (11)$$

In the b representation the total cross section increases with increasing s as

$$\sigma_{tot} \propto \ln^2 s. \qquad (12)$$

Due to the fact that with increasing energy the cross section grows in the logarithmic approximation, as s increases, it is necessary to noted that the distance at which the collision probability is not yet small increases with increasing according to the law

$$r(\ln s) = a\ln s + d - c\ln s \qquad (13)$$

where a, d, c are constants. The cross section with amplitude $f(s,b)$ and with radius (13) is a disc with radius $r \propto \ln s$. Inside the disk ($b < r$) $Im\,f \square 1$, and at the periphery of the disk ($b > r$) $f \propto \exp(-2m_\pi(b-r))$. This behaviour ensures the correct position of the nearest feature of the t channel $t = 4m^2$.

The amplitude can be expanded in a series b containing only even powers of the regularity condition for the Fourier-Bessel transform of the function (6):

$$f(s,t) = is\sum_{n=1}^{\infty} \frac{\exp(a|t|n)}{n!\cdot n}\left(-\frac{4\pi^2\mu}{a}\right)^{n-1}. \qquad (14)$$
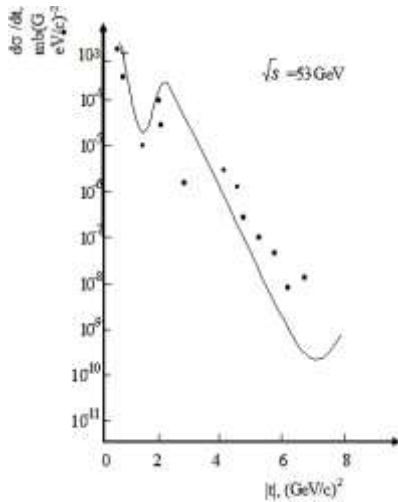
Figure 1. Dependence of the differential cross section of an elastic *pp* scattering from. Points-experimental data from [9,10].

On the basis of the obtained formulas, we first consider proton-proton scattering.

For
$$t \approx -\frac{2}{a} \ln\left(\frac{a}{\pi^2}\right)$$
the contribution of the second term in the expansion (14) is comparable with the first term. Therefore, a second minimum must appear in the differential cross section. This fact is confirmed by the known experimental data [9,10] for measuring the differential cross section for elastic *pp* scattering at $\sqrt{s}$ =53GeV. The parameters are adjusted to experimental data. As can be seen from Fig.1, the model predicts the first minimum at ~1.2 (GeV/c)^2 and the second minimum at ~7.0 (GeV/c)^2. There are three minimums for the cross section in the experiment. The first and third coincide with the theoretical values, but the second minimum does not exist on the theoretical curve. Undoubtedly, the imaginary part of the elastic scattering amplitude dominates at small angles in the diffraction cone and the problem of the behaviour of the real part of the amplitude of elastic scattering for nonzero momentum transfers becomes very relevant.

One might think that the discrepancy is due to the fact that at high energies because of intense meson formation, all phases become complex and the nuclear amplitude - forward scattering is almost completely imaginary. In this case, the scattering can be represented as due to the action of the one-pion exchange potential. In the paper [11], proton-proton elastic scattering was studied in the framework of one pion exchange model and a scalar theory in an attempt to simulate nucleon-nucleon interactions covering a large energy range. When the models were compared with the available total cross-sectional data, it was found that the scalar theory best fits the data below the below labotary momentum of 0,5 GeV. However, compliance with high-energy data is not as good as it was found in a very low momentum region.

In Fig. 2 compares the results of calculations using formula (11) with experimental data for the scattering cross section *p*^{9}Be [12]. The solid line corresponds to the cross-section calculated from equation (11), the points correspond to the experimental data.
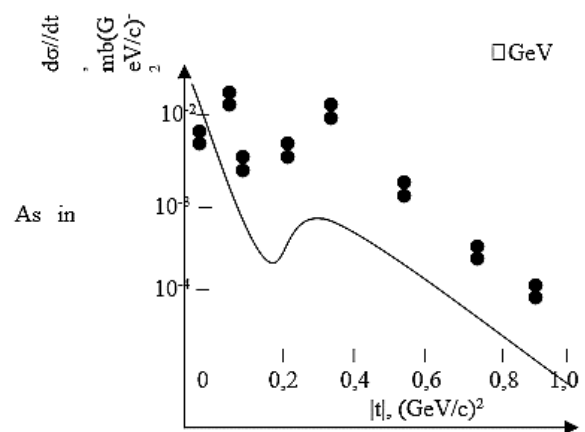
Figure 2. Differential cross section for *p*^{9}Be scattering. The solid line corresponds to the cross-section calculated from equation (11), the points correspond to the experimental data from [12].

It can be seen from Fig. 2 that the model of a composite nucleon leads to a satisfactory agreement between the calculated cross section and its t-dependence and experimental data. As in the usual eikonal approach, at large $|t|$ values are predicted $d\sigma/dt$ (Fig.1. and Fig.2) that are significantly smaller than in the experiment. In addition, there is no pronounced minimum in the experiment. The experimental cross section has a slight inflection at | t | = 0.4 (GeV / c) ^{2}. The unitarity condition predicts an exponential fall for the differential cross section with additional substructure to occur exactly between the low momentum transfer diffraction cone and high momentum transfer. As can be seen from the Fig.2, the steep Gaussian peak at small angles is followed by the exponential (Orear) regime with some shoulders and dips and then by the power-law drop.

It is known that the ^{9}Be nucleus does not have spherical symmetry, and one of the reasons may be a significant deformation of the nucleus, which has a significant quadrupole moment Q = 53 mb. We made very simple assumptions about the structure of the nuclei and indicated the main theoretical considerations for detailed calculations. Depending on the number of nucleons, the number of channels influencing the decay channel increases. If deformed nucleus, the deformation also affects the process. Other reasons are an increase in the ratio of the real part of the elementary scattering amplitude to the imaginary one and the presence of some incoherent scattering channels. Accounting for all of these factors sharply increases the complexity of the calculations. Therefore, this article did not take into account the role of deformation and number of channels.

It follows from (9) that the ratio of the real part of the amplitude in the forward scattering to its imaginary part

$$A(s,t) = \frac{\operatorname{Im} f(s,t)}{\operatorname{Re} f(s,t)} \qquad (15)$$

must tend to zero in the asymptotic as *s* increases. A definite relation between the real and imaginary parts of the amplitude is valid for a certain energy interval.

The dependence of the $A(s,t)$ on *t* for E>150 GeV is shown in Fig.3. The ratio $A(t)$ becomes zero for $|t|^2 \approx 0{,}42$ and for large values of *t* it tends to ≈ -9. The result, shown in Fig.3, must be considered as follows from the unitarity condition. This decrease shows that it is more difficult for particles to dissipate with larger transverse momenta, preserving their integrity. As we can see, the real part of the amplitude can overexceed at large momentum transfers, according to the unitarity condition. In this region, the real part of the amplitude can be large and negative in comparison with its imaginary part. We note that $A(t)$ vanishes and becomes negative. This result agrees with the general theorem on the change in the sign of the real part of the elastic scattering amplitude at high energies [13]. But on the other hand, the decrease in $A(t)$ with an increase in *t* is unsatisfactory. $A(t)$ is very sharply decreasing in the region 0.4-0.7 GeV^2. More peripheral interactions with large A(*t*) are characterized by small momentum transfers. The result given in Fig.3 should be considered as one more extreme approximation to the true solution of the equation expressing the unitarity condition.
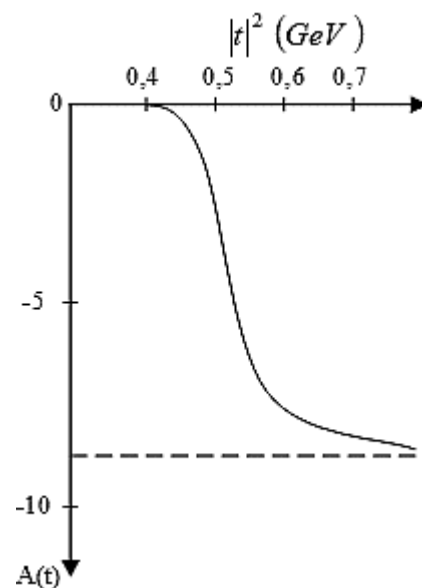
Figure 3. Dependence of the *A*(t) of an ||t|^2.

general theorem on the change in the sign of the real part of the elastic scattering amplitude at high energies [13]. But on the other hand, the decrease in $A(t)$ with an increase in t is unsatisfactory. $A(t)$ is very sharply decreasing in the region 0.4-0.7 GeV^2. More peripheral interactions with large $A(t)$ are characterized by small momentum transfers. The result given in Fig.3 should be considered as one more extreme approximation to the true solution of the equation expressing the unitarity condition.

In explaining the energy dependence of the hadron-hadron scattering cross section, the *t*-channel exchange picture is more adequate, which for high energies was formulated in the form of the Regge model. Diffraction scattering in the Regge model is described by the exchange of a pomeron-a vacuum moving pole in the complex plane of the angular momentum. But this model also can not explain all the data. (s, t) -dependence of the differential cross sections and the ratio A(t) in a wide energy range and momentum transfers can not be solved without introducing fitting parameters.

3. CONSCLUSION

In this paper we carried out a study on the basis of the continued unitarity method in which the main equation for the scattering amplitude is the elastic unitarity condition, analytically continued to the region above the first inelastic threshold. Here we considered only the Gaussian potential. Nevertheless, the physical interpretation of the results suggests [14], that the qualitative scattering pattern described in the main features is valid for a larger class of strong potentials that decrease rapidly at infinity.

We have made very simple assumptions regarding the structure of the nuclei and pointed out the main theoretical considerations for detailed calculations. More specific structure effects, such as e.g. resonances, are expected to appear on a background parameterized by the above equations. The availability of experimental data in the near future will certainly arouse interest on the detailed investigation of such effect. Such experiments would give valuable information on disintegration

reactions and about the distribution of the nuclear density in the nuclear surface. At high energies both the electromagnetic and the nuclear interaction between projectile and target will be important. Far from being a drawback, this can be of utility to extract complementary information about these different reaction mechanisms in the peripheral collisions. A decomposition of these mechanisms from the analysis of angular distribution of the fragments or from the dependence of the cross sections on the energy, charge and mass parameters is possible in accurate measurements.

There are many models, but it is still difficult to give preference to any one of them. Most models are successful at the introduction of different assumptions. It is essential how to achieve improvement of existing models: by avoiding simplifying assumptions or looking for new physical arguments that would make the model more realistic and save it from simplifications. It is from this point of view that one should approach the analysis of the further development of the model of hadron scattering, caused by new experimental facts.

REFERENCES

[1]. C.A. Bertulani and G. Baur, Coincidence cross sections for the dissociation of light ions in high-energy collisions, Nuclear. Physics, A 480 (1988) 615- 628.

[2]. N. P. *Zotov*, V. A. *Tsarev*, Diffraction dissociation: 35 years on, *Sov. Phys.Uspekhi*, 31-2 (1988) 119–139.

[3]. D. Kiang, S.H Ling, K.Young, C.S. Lam, Multiplicity distribution in hadron-nucleus scattering, Phys.Rev. D, 31-1 (1985) 31-35.

[4]. A.A. Logunov and A.N. Tavkhelidze, Quasi-Optical Approach in Quantum Field Theory, Nuovo Cim., 29-2 (1963) 380-399.

[5]. Yu.D. Chernichenko, Form factor for a two-particle system within a relativistic quasipotential approach: Case of arbitrary masses and of a vector current, Physics of Atomic Nuclei, 78-2 (2015) 201–214.

[6]. W. Ulmer, A new calculation formula of nuclear cross-section of therapeutic protons, Jour Proton Therapy, 1-1 (2015) 1-11.

[7]. Bartók-Pártay, The Gaussian Approximation Potential, Doctoral Thesis accepted by University of Cambridge, UK, Springer-Verlag Berlin Heidelberg, 2010, p. 83. DOI 10.1007/978-3-642-14067-9.

[8]. S.G. Abdulvahabova, E.A. Rasulov, Proceeding of International workshop "Quantum particles, fields and strings" Fizika, 3 (2002) 83- 85.

[9]. H.S. Hans. Nuclear Physics: Experimental and Theoretical. New Age Pulisher, 2001, p.787.

[10].N. P. Zotov, S.V. Rusakov,V. A. Tsarev, Uprugoye rasseyaniye protonov na protonax

pri visokix energiyax i bolshix peredannix impulsax. PEPAN, 11-5 (1980) 1160-12230.

[11].Ryan B. Norman, Frank Dick, John W. Norbury and Steve R. Blattnig, Differential Cross Sections for Proton-Proton Elastic Scattering NASA/TP, 215565 (2009), 215565, p. 87.

[12].G.D. Alkhazov, S.L. Belostotsky, A.A. Vorobiev. Scattering of protons by light nuclei. Preprint LINP-449, (1978) p. 11.

[13].A. Martin, Froissart bound for inelastic cross sections, Phys. Rev. D, 80-6 (2009) 1-5.

[14].I. M. Dremin, Elastic scattering of hadrons, Uspekhi Fizicheskikh Nauk, 183-1 (2013) 3-32.

On Razzaboni Transformation of Surfaces in Minkowski 3-Space

Melek ERDOĞDU[1]* iD, Mustafa ÖZDEMİR[2] iD

[1]Necmettin Erbakan University, Faculty of Science, Department of Mathematics-Computer Science, Konya, TURKEY

[2]Akdeniz University, Faculty of Science, Department of Mathematics, Antalya, TURKEY

Abstract. In this paper, we investigate the surfaces generated by binormal motion of Bertrand curves, which is called Razzaboni surface, in Minkowski 3-space. We discussed the geometric properties of these surfaces in $\mathbb{M}^3$ with respect to the character of Bertrand geodesics. Then, we define the Razzaboni transformation for a given Razzaboni surface. In other words, we prove that there exists a dual of Razzaboni surface for each case. Finally, we show that Razzaboni transformation maps the surface σ, which has Bertrand geodesic with constant curvature, to the surface σ^* whose Bertrand geodesic also has constant curvature with opposite sign.

*Keywords***:** Razzaboni surface, Minkowski space.

Minkowski-3 Uzayında Yüzeylerin Razzaboni Dönüşümü Üzerine

Özet. Bu çalışmada, Minkowski-3 uzayında, Bertrand eğrilerin binormal hareketi ile meydana gelen, Razzaboni yüzeyi adı verilen yüzeyler incelenmiştir. Minkowski-3 uzayındaki bu yüzeylerin geometrik özelliklerini Bertrand geodeziklerin karakterine bağlı olarak tartıştık. Daha sonra, verilen bir Razzaboni yüzeyi için Razzaboni dönüşümünü tanımladık. Diğer bir deyişle, her durum için Razzaboni yüzeyinin bir duali olduğunu ispatladık. Son olarak, Razzaboni dönüşümlerinin; sabit eğrilikli Bertrand geodeziğe sahip σ yüzeyini; işareti ters olmak üzere aynı sabit eğrilikli Bertrand geodeziğe sahip $\sigma *$ yüzeyine dönüştürdüğünü gösterdik.

*Anahtar Kelimeler***:** Razzaboni yüzeyi, Minkowski uzayı.

1. INTRODUCTION

Bertrand curves are well-studied classical curves in Euclidean space and Lorentzian space [1, 2]. Curves of constant curvature or torsion constitute particular Bertrand curves; and Bertrand curve shares its principal normals with another Bertrand curve, which is called Bertrand mate. The surfaces, which admit geodesic embedding of Bertrand curves, were deeply studied by Amilcare Razzaboni [3]. Then the class of surfaces with Bertrand geodesics came to be called Razzaboni surfaces [4]. In particular, Razzaboni surfaces, which have Bertrand geodesics with constant curvature or torsion, were discussed in earlier work of Razzaboni [5, 6].

The Razzaboni surface can be considered as a surface which is generated by binormal motion of Bertrand curve [4]. The binormal motion of curves with constant curvature and torsion is discussed in [7, 8]. On the other hand, motion of timelike surfaces in timelike geodesic coordinates is examined in the study [9].

In this study, we investigate the Razzaboni surfaces in Minkowski 3-space in three different cases. The geometric properties of Razzaboni surfaces in geodesic coordinates are stated for each case. And, we define Razzaboni transformation for a given Razzaboni surface in $\mathbb{M}^3$. Then, we examine the curvature and torsion of the Bertrand geodesics of dual Razzaboni surface. Moreover, the Gaussian curvature of Razzaboni surface is given for each case. Finally, the dual Razzaboni surfaces are examined which have geodesics with constant torsion or curvature, respectively.

2.   PRELIMINARIES

In this part, we give a brief summary of Razzaboni surface in Euclidean 3- Space, [4]. Then, some essential properties of curves in Minkowski 3-space are given to provide the necessary background [10, 11].

Definition 1 Two curves which, at any point, have a common principal normal vector are called Bertrand curves. Moreover, curves for which there exists constants A and B such that

$$A\kappa + B\tau = 1$$

are also known as Bertrand curves. Here κ is the curvature and τ is the torsion of the curve.

We know that a curve is a geodesic on a surface σ if and only if the principal normal of the curve is parallel to the normal N of the surface. This means that if the surface σ is spanned by one parameter family of geodesic Bertrand curves α with the same constants A and B then the Bertrand mate α^* form a parallel surface σ^* on which they are likewise geodesics [4].

Let $\sigma = \sigma(u,v)$ be a one parameter family of geodesics with geodesic coordinates. Then the first fundamental form of the surface is of the form

$$I = du^2 + \lambda^2 dv^2.$$

Here, $u -$ parameter curves are unit speed geodesics and $v -$ parameter curves form the orthogonal parallels. Since $\sigma_u \perp \sigma_v$ and principal normal n of the geodesics is orthogonal to the surface, then the tangent vectors of coordinate line should be of the form

$$\sigma_u = t, \sigma_v = \lambda b$$

where b denotes the binormal vector field of the geodesics. The surface σ is generated by the motion of a inextensible curve in binormal direction with the speed λ. Thus, a Razzaboni surface can be considered as a surface which is generated by binormal motion of Bertrand curve with the same constants A and B. The variation of Frenet Frame $\{t, n, b\}$ of the geodesics in $u -$ direction is given by Serret Frenet equations;

$$\begin{bmatrix} t \\ n \\ b \end{bmatrix}_u = \begin{bmatrix} 0 & \kappa & 0 \\ -\kappa & 0 & \tau \\ 0 & -\tau & 0 \end{bmatrix} \begin{bmatrix} t \\ n \\ b \end{bmatrix}.$$

The variation of $\{t, n, b\}$ in $v -$ direction should be of the form

$$\begin{bmatrix} t \\ n \\ b \end{bmatrix}_v = \begin{bmatrix} 0 & \alpha & \beta \\ -\alpha & 0 & \gamma \\ -\beta & -\gamma & 0 \end{bmatrix} \begin{bmatrix} t \\ n \\ b \end{bmatrix}.$$

By using the compatibility condition $\sigma_{uv} = \sigma_{vu}$, we get

$$\alpha n + \beta b = -\tau\lambda n + \lambda_u b.$$

Thus, the variation of $\{t, n, b\}$ in $v-$ direction becomes

$$\begin{bmatrix} t \\ n \\ b \end{bmatrix}_v = \begin{bmatrix} 0 & -\tau\lambda & \lambda_u \\ \tau\lambda & 0 & \gamma \\ -\lambda_u & -\gamma & 0 \end{bmatrix} \begin{bmatrix} t \\ n \\ b \end{bmatrix}.$$

The compatibility conditions $t_{uv} = t_{vu}$, $n_{uv} = n_{vu}$ and $b_{uv} = b_{vu}$ gives the following undetermined system

$$\kappa_v = -2\tau\lambda_u - \tau_u\lambda,$$

$$\tau_v = \gamma_u + \kappa\lambda_u,$$

$$\lambda_{uu} = \tau^2\lambda + \kappa\gamma.$$

The above system can be considered as the Gauss-Minardi-Codazzi equations for the surface with geodesic coordinates. If the constraint

$$A\kappa + B\tau = 1$$

is imposed then the system is well determined and the surface is guaranteed to be a Razzaboni surface [4].

In the case of $A = 0$, the geodesics have constant torsion. Choosing $B = \tau = 1$ without loss of generality, the system becomes

$$\kappa_v = -2\lambda_u,$$

$$0 = \gamma_u + \kappa\lambda_u,$$

$$\lambda_{uu} = \lambda + \kappa\gamma.$$

This integrable system may be regarded as an extension of the sine-Gordon equation;

$$\Psi_{uv} = \sin\Psi.$$

A single equation is obtained as follows:

$$\left(\frac{\theta_{vuu} - \theta_v}{\theta_u}\right)_u + \theta_u\theta_{vu} = 0$$

by setting $\kappa = \theta_u$ and $\lambda = -\frac{\theta_v}{2}$.

In the case of $B = 0$, the geodesics have constant curvature. Without loss of generality, choosing $A = \kappa = 1$, the system becomes

$$0 = -2\tau\lambda_u - \tau_u\lambda,$$

$$\tau_v = \gamma_u + \lambda_u,$$

$$\lambda_{uu} = \tau^2 \lambda + \gamma.$$

If we set $\lambda = \frac{1}{\sqrt{\tau}}$, then the system reduces to

$$\tau_v = \left[(\frac{1}{\sqrt{\tau}})_{uu} - \tau\sqrt{\tau} + \frac{1}{\sqrt{\tau}} \right]_u$$

which represents an extension of the Dym equation

$$\tau_v = (\frac{1}{\sqrt{\tau}})_{uuu}.$$

It can be noted that, the extended Dym equation is generated by binormal motion of an inextensible curve with the speed $\frac{1}{\sqrt{\tau}}$. For further discussions about the Razzaboni surfaces, the readers are referred to [4].

The Minkowski 3-space, denoted by $\mathbb{M}^3$, is Euclidean 3-space equipped with Lorentzian inner product

$$\langle u, v \rangle_{\mathbb{L}} = -u_1 v_1 + u_2 v_2 + u_3 v_3$$

where $u = (u_1, u_2, u_3)$, $v = (v_1, v_2, v_3) \in \mathbb{M}^3$. Lorentzian inner product characterizes the elements $u = (u_1, u_2, u_3)$ of $\mathbb{M}^3$.

if $\langle u, u \rangle_{\mathbb{L}} > 0$ or $u = 0$ then u is called spacelike,

if $\langle u, u \rangle_{\mathbb{L}} < 0$ then u is called timelike,

if $\langle u, u \rangle_{\mathbb{L}} = 0$ and $u \neq 0$ then u is called lightlike or null.

The norm of $u = (u_1, u_2, u_3) \in \mathbb{M}^3$ is defined by $\|u\| = \sqrt{|\langle u, u \rangle|}$. Lorentzian vector product of $u = (u_1, u_2, u_3)$ and $v = (v_1, v_2, v_3) \in \mathbb{M}^3$ is defined by

$$u \times_{\mathbb{L}} v = \begin{vmatrix} -e_1 & e_2 & e_3 \\ u_1 & u_2 & u_3 \\ v_1 & v_2 & v_3 \end{vmatrix}.$$

For details, see [12-14].

A curve α in $\mathbb{M}^3$ is called timelike, spacelike or null if and only if tangent vector field t of α is timelike, spacelike or null, respectively. Let $\alpha(s)$ be a unit speed nonlightlike curve in $\mathbb{M}^3$, i,e., $\langle \alpha', \alpha' \rangle_{\mathbb{L}} = \varepsilon_1 = \pm 1$. The constant ε_1 is called the casual character of α. Frenet frame field $\{t, n, b\}$, which is an orthonormal field along α, satisfies the Serret-Frenet equation:

$$\begin{bmatrix} t \\ n \\ b \end{bmatrix}_s = \begin{bmatrix} 0 & \varepsilon_2 \kappa & 0 \\ -\varepsilon_1 \kappa & 0 & -\varepsilon_3 \tau \\ 0 & \varepsilon_2 \tau & 0 \end{bmatrix} \begin{bmatrix} t \\ n \\ b \end{bmatrix}. \tag{1}$$

The functions $\kappa \geq 0$ and τ are called the curvature and torsion, respectively. The constants $\varepsilon_2 = \langle n, n \rangle_{\mathbb{L}}$ and $\varepsilon_3 = \langle b, b \rangle_{\mathbb{L}}$ are called the second casual character and third casual character of α, respectively [10-12].

3.   RAZZABONI TRANSFORMATION OF SURFACES IN MINKOWSKI 3-SPACE

In this part, Razzaboni surfaces in Minkowski 3-space are investigated in three different cases.

Case 1: Geodesic Bertrand curves of Razzaboni surface have timelike principal normal.

Let $\sigma = \sigma(u, v)$ be a one parameter family of geodesic Bertrand curve with timelike principal normals in $\mathbb{M}^3$. And let u and v be the geodesic coordinates of the Razzaboni surface σ. Then the first fundamental form of the surface is of the form

$$I = du^2 + \lambda^2 dv^2.$$

Here $u -$ parameter curves are unit speed spacelike Bertrand geodesics and $v -$ parameter curves form orthogonal spacelike parallels. Since $\langle \sigma_u, \sigma_v \rangle_{\mathbb{L}} = 0$ and the principal normal n of geodesics are normal to the surface, then the tangent vectors of coordinate curves are given as

$$\sigma_u = t \text{ and } \sigma_v = \lambda b$$

where b denotes the binormal vector field of geodesics. The variation of the Frenet Frame $\{t, n, b, \}$ of Bertrand geodesics in $u -$ direction is obtained as follows:

$$\begin{bmatrix} t \\ n \\ b \end{bmatrix}_u = \begin{bmatrix} 0 & -\kappa & 0 \\ -\kappa & 0 & -\tau \\ 0 & -\tau & 0 \end{bmatrix} \begin{bmatrix} t \\ n \\ b \end{bmatrix}$$

by setting $(\varepsilon_1, \varepsilon_2, \varepsilon_3) = (1, -1, 1)$ in Equation 1. The variation of $\{t, n, b\}$ in $v -$ direction must be in the following form:

$$\begin{bmatrix} t \\ n \\ b \end{bmatrix}_v = \begin{bmatrix} 0 & \alpha & \beta \\ \alpha & 0 & \gamma \\ -\beta & \gamma & 0 \end{bmatrix} \begin{bmatrix} t \\ n \\ b \end{bmatrix}.$$

The compatibility condition $\sigma_{uv} = \sigma_{vu}$ implies that

$$\alpha n + \beta b = (-\lambda \tau)n + \lambda_u b.$$

So, we get $\alpha = -\lambda \tau$ and $\beta = \lambda_u$. Then the variation of $\{t, n, b\}$ in $v -$ direction becomes

$$\begin{bmatrix} t \\ n \\ b \end{bmatrix}_v = \begin{bmatrix} 0 & -\lambda\tau & \lambda_u \\ -\lambda\tau & 0 & \gamma \\ -\lambda_u & \gamma & 0 \end{bmatrix} \begin{bmatrix} t \\ n \\ b \end{bmatrix}.$$

On the other hand, the compatibility condition $t_{uv} = t_{vu}$ implies that

$$t_{uv} = (-\kappa n)_v = (\lambda\kappa\tau)t + (-\kappa_v)n + (-\kappa\gamma)b,$$

$$t_{vu} = (-\lambda\tau n + \lambda_u b)_u = (\lambda\kappa\tau)t + (-\lambda\tau_u - 2\lambda_u\tau)n + (-\kappa\gamma)b.$$

So we get

$$\kappa_v = \lambda \tau_u + 2\lambda_u \tau.$$

And by the compatibility condition $n_{uv} = n_{vu}$, we obtain

$$n_{uv} = (-\kappa t - \tau b)_v = (-\kappa_v + \lambda_u \tau)t + (\kappa \lambda \tau - \tau \gamma)n + (-\lambda_u \kappa - \tau_v)b,$$

$$n_{vu} = (-\lambda \tau t + \gamma b)_u = (-\lambda_u \tau - \lambda \tau_u)t + (\kappa \lambda \tau - \tau \gamma)n + (\gamma_u)b.$$

Thus, we get

$$\tau_v = -\lambda_u \kappa - \gamma_u.$$

Finally, the compatibility condition $b_{uv} = b_{vu}$ gives that

$$b_{uv} = (-\tau n)_v = (\lambda \tau^2)t + (-\tau_v)n + (-\tau \gamma)b,$$

$$b_{vu} = (-\lambda_u t + \gamma n)_u = (-\lambda_{uu} - \kappa \gamma)t + (\lambda_u \kappa + \gamma_u)n + (-\tau \gamma)b.$$

Then, we get

$$\lambda_{uu} = -\lambda \tau^2 - \kappa \gamma.$$

The system

$$\kappa_v = \lambda \tau_u + 2\lambda_u \tau,$$

$$\tau_v = -\lambda_u \kappa - \gamma_u,$$

$$\lambda_{uu} = -\lambda \tau^2 - \kappa \gamma$$

may be regarded as the Gauss-Minardi-Codazzi equations for the surface. If the constraint

$$A\kappa + B\tau = 1$$

is imposed then the system is well determined and the surface σ is guaranteed to be a Razzaboni surface.

Now, let's suppose that φ is a transformation between two Razzaboni surfaces in $\mathbb{M}^3$ defined as $\sigma^* = \varphi(\sigma)$. And let $\{t^*, n^*, b^*\}$ be the Frenet Frame of Bertrand geodesics of Razzaboni surface σ^*. Then the $u^* -$ parameter curves are unit speed spacelike Bertrand geodesics and $v^* -$ parameter curves form orthogonal spacelike parallels. If the following properties are satisfied

  i) $|\sigma - \sigma^*| = $ constant;

  ii) $\sigma - \sigma^* \perp b$;

  iii) $\sigma - \sigma^* \perp b^*$;

  iv) $\langle b, b^* \rangle_{\mathbb{L}} = $ constant,

then φ is called a Razzaboni transformation and the surface σ^* is called dual Razzaboni surface of σ. By the first property, the distance between corresponding points of the surfaces is constant. So, we can write

$$\sigma^*(u,v) = \varphi(\sigma(u,v)) = \sigma(u,v) + An(u,v).$$

Since the geodesics of the Razzaboni surfaces σ and σ^* are Bertrand mates, we have $n = n^*$. Also we get

$$\sigma_u^* = \sigma_u + An_u = (1 - A\kappa)t - A\tau b = \tau(Bt - Ab).$$

That is

$$t^* = \frac{1}{\sqrt{A^2+B^2}}(Bt - Ab).$$

Since $b^* = -t^* \times_{\mathbb{L}} n^*$, we obtain

$$b^* = \frac{1}{\sqrt{A^2+B^2}}(At + Bb).$$

And

$$du^* = \sqrt{A^2 + B^2}\,\tau du.$$

Then, we have

$$\langle \sigma^* - \sigma, b \rangle_{\mathbb{L}} = \langle An, b \rangle_{\mathbb{L}} = 0,$$

$$\langle \sigma^* - \sigma, b^* \rangle_{\mathbb{L}} = \frac{1}{\sqrt{A^2 + B^2}} \langle An, At + Bb \rangle_{\mathbb{L}} = 0,$$

$$\langle b, b^* \rangle_{\mathbb{L}} = \frac{1}{\sqrt{A^2+B^2}} \langle b, At + Bb \rangle_{\mathbb{L}} = \frac{B}{\sqrt{A^2+B^2}}.$$

Thus, the properties ii), iii) and iv) are also satisfied which means that $\varphi: \sigma \to \sigma^*$ is a Razzaboni transformation. On the other hand, we have

$$t_{u^*}^* = \frac{B}{(A^2 + B^2)\tau}t_u - \frac{A}{(A^2 + B^2)\tau}b_u = \frac{-\kappa B + A\tau}{(A^2 + B^2)\tau}n.$$

Then, the curvature of Bertrand geodesic of dual Razzaboni surface is found as

$$\kappa^* = \langle t_{u^*}^*, n^* \rangle_{\mathbb{L}} = \frac{-\kappa B + A\tau}{(A^2 + B^2)\tau} \langle n, n \rangle_{\mathbb{L}} = \frac{B\kappa - A\tau}{(A^2 + B^2)\tau}.$$

Moreover, we have

$$b_{u^*}^* = \frac{A}{(A^2 + B^2)\tau}t_u + \frac{B}{(A^2 + B^2)\tau}b_u = \frac{-A\kappa - B\tau}{(A^2 + B^2)\tau}n = \frac{-1}{(A^2 + B^2)\tau}n.$$

Then, we get

$$\tau^* = \langle b_{u^*}^*, n^* \rangle_{\mathbb{L}} = \frac{-1}{(A^2 + B^2)\tau} \langle n, n \rangle_{\mathbb{L}} = \frac{1}{(A^2 + B^2)\tau}.$$

Thus, we have proved the following theorem.

Theorem 1. Let $\sigma = \sigma(u, v)$ be Razzaboni surface with geodesic Bertrand curve having timelike principal normal. Then, the curvature and torsion of Bertrand geodesic of dual Razzaboni surface σ^* are found as

$$\kappa^* = \frac{B\kappa - A\tau}{(A^2 + B^2)\tau'},$$

$$\tau^* = \frac{1}{(A^2 + B^2)\tau'},$$

respectively.

Case 2: Geodesic Bertrand curves of the Razzaboni surface have timelike binormals.

Let $\sigma = \sigma(u, v)$ be a one parameter family of geodesic Bertrand curve with timelike binormals in $\mathbb{M}^3$. And let u and v be the geodesic coordinates of the Razzaboni surface σ. Then the first fundamental form of the surface is of the form

$$I = du^2 - \lambda^2 dv^2.$$

Here the curves $u -$ parameter curves are unit speed spacelike Bertrand geodesics and $v -$ parameter curves form orthogonal timelike parallels. Since $\langle \sigma_u, \sigma_v \rangle_{\mathbb{L}} = 0$ and the principal normal n of geodesics are normal to the surface, then the tangent vectors of coordinate curves are given as

$$\sigma_u = t \text{ and } \sigma_v = \lambda b$$

where b denotes the binormal vector field of geodesics. The variation of the Frenet Frame $\{t, n, b,\}$ of Bertrand geodesics in $u -$ direction is obtained as follows:

$$\begin{bmatrix} t \\ n \\ b \end{bmatrix}_u = \begin{bmatrix} 0 & \kappa & 0 \\ -\kappa & 0 & \tau \\ 0 & \tau & 0 \end{bmatrix} \begin{bmatrix} t \\ n \\ b \end{bmatrix}$$

by setting $(\varepsilon_1, \varepsilon_2, \varepsilon_3) = (1,1,-1)$ in Equation 1. The variation of $\{t, n, b\}$ in $v -$ direction must be in the following form:

$$\begin{bmatrix} t \\ n \\ b \end{bmatrix}_v = \begin{bmatrix} 0 & \alpha & \beta \\ -\alpha & 0 & \gamma \\ \beta & \gamma & 0 \end{bmatrix} \begin{bmatrix} t \\ n \\ b \end{bmatrix}.$$

The compatibility condition $\sigma_{uv} = \sigma_{vu}$ implies that

$$\alpha n + \beta b = (\lambda\tau)n + \lambda_u b.$$

So, we get $\alpha = \lambda\tau$ and $\beta = \lambda_u$. Then the variation of $\{t, n, b\}$ in $v -$ direction becomes

$$\begin{bmatrix} t \\ n \\ b \end{bmatrix}_v = \begin{bmatrix} 0 & \lambda\tau & \lambda_u \\ -\lambda\tau & 0 & \gamma \\ \lambda_u & \gamma & 0 \end{bmatrix} \begin{bmatrix} t \\ n \\ b \end{bmatrix}.$$

On the other hand, the compatibility condition $t_{uv} = t_{vu}$ implies that

$$t_{uv} = (\kappa n)_v = (-\lambda\kappa\tau)t + (\kappa_v)n + (\kappa\gamma)b,$$

$$t_{vu} = (\lambda\tau n + \lambda_u b)_u = (-\lambda\kappa\tau)t + (\lambda\tau_u + 2\lambda_u\tau)n + (\kappa\gamma)b.$$

So we get

$$\kappa_v = \lambda\tau_u + 2\lambda_u\tau.$$

And by the compatibility condition $n_{uv} = n_{vu}$, we obtain

$$n_{uv} = (-\kappa t + \tau b)_v = (-\kappa_v + \lambda_u\tau)t + (-\kappa\lambda\tau + \tau\gamma)n + (-\lambda_u\kappa + \tau_v)b,$$

$$n_{vu} = (-\lambda\tau t + \gamma b)_u = (-\lambda_u\tau - \lambda\tau_u)t + (-\kappa\lambda\tau + \tau\gamma)n + (\gamma_u)b.$$

Thus, we get

$$\tau_v = \lambda_u\kappa + \gamma_u.$$

Finally, the compatibility condition $b_{uv} = b_{vu}$ gives that

$$b_{uv} = (\tau n)_v = (-\lambda\tau^2)t + (\tau_v)n + (\tau\gamma)b,$$

$$b_{vu} = (\lambda_u t + \gamma n)_u = (\lambda_{uu} - \kappa\gamma)t + (\lambda_u\kappa + \gamma_u)n + (\tau\gamma)b.$$

Then, we get

$$\lambda_{uu} = -\lambda\tau^2 + \kappa\gamma.$$

The system

$$\kappa_v = \lambda\tau_u + 2\lambda_u\tau,$$

$$\tau_v = \lambda_u\kappa + \gamma_u,$$

$$\lambda_{uu} = -\lambda\tau^2 + \kappa\gamma$$

can be considered as the Gauss-Minardi-Codazzi equations for the surface. By the constraint

$$A\kappa + B\tau = 1,$$

the system is well determined and the surface σ is guaranteed to be a Razzaboni surface.

Similar to case 1, we can define Razzaboni transformation $\varphi: \sigma \to \sigma^*$ as

$$\sigma^*(u, v) = \sigma(u, v) + An(u, v).$$

It is easily seen that the transformation φ satisfies all properties of Razzaboni transformation. Here u^* and v^* are the geodesic coordinates of dual Razzaboni surface σ^*. And let $\{t^*, n^*, b^*\}$ be the Frenet Frame of Bertrand geodesics of dual Razzaboni surface σ^*. Then the $u^* -$ parameter curves are unit speed

spacelike Bertrand geodesics and $v^* -$ parameter curves forms orthogonal timelike parallels. Since the geodesics of the Razzaboni surface and its dual are Bertrand mates, we have $n = n^*$. Also we have

$$\sigma_u^* = \sigma_u + An_u = (1 - A\kappa)t + A\tau b = \tau(Bt + Ab).$$

That is

$$t^* = \frac{Bt + Ab}{\sqrt{B^2 - A^2}}.$$

Since $b^* = -t^* \times_{\mathbb{L}} n^*$, we obtain

$$b^* = \frac{-At + Bb}{\sqrt{B^2 - A^2}}.$$

And

$$du^* = \sqrt{B^2 - A^2}\,\tau du.$$

Moreover, we have

$$t_{u^*}^* = \frac{B}{(B^2 - A^2)\tau} t_u + \frac{A}{(B^2 - A^2)\tau} b_u = \frac{\kappa B + A\tau}{(B^2 - A^2)\tau} n,$$

$$\kappa^* = \langle t_{u^*}^*, n^* \rangle_{\mathbb{L}} = \frac{\kappa B + A\tau}{(B^2 - A^2)\tau} \langle n, n \rangle_{\mathbb{L}} = \frac{\kappa B + A\tau}{(B^2 - A^2)\tau},$$

$$b_{u^*}^* = -\frac{A}{(B^2 - A^2)\tau} t_u + \frac{B}{(B^2 - A^2)\tau} b_u = \frac{-A\kappa + B\tau}{(B^2 - A^2)\tau} n,$$

$$\tau^* = \langle b_{u^*}^*, n^* \rangle_{\mathbb{L}} = \frac{-A\kappa + B\tau}{(B^2 - A^2)\tau} \langle n, n \rangle_{\mathbb{L}} = \frac{-A\kappa + B\tau}{(B^2 - A^2)\tau}.$$

Theorem 2. Let $\sigma = \sigma(u, v)$ be Razzaboni surface with geodesic Bertrand curve having timelike binormal. Then, the curvature and torsion of Bertrand geodesic of dual Razzaboni surface σ^* are found as

$$\kappa^* = \frac{\kappa B + A\tau}{(B^2 - A^2)\tau},$$

$$\tau^* = \frac{-A\kappa + B\tau}{(B^2 - A^2)\tau},$$

respectively.

Case 3: Geodesic Bertrand curves of the Razzaboni surface are timelike.

Let $\sigma = \sigma(u,v)$ be a one parameter family of timelike geodesic Bertrand curve in $\mathbb{M}^3$. And let u and v be the geodesic coordinates of the Razzaboni surface σ. Then the first fundamental form of the surface is of the form

$$I = -du^2 + \lambda^2 dv^2.$$

Here the $u-$ parameter curves are unit speed timelike Bertrand geodesics and $v-$ parameter curves form orthogonal spacelike parallels. Since $\langle \sigma_u, \sigma_v \rangle_{\mathbb{L}} = 0$ and the principal normal n of geodesics are normal to the surface, then the tangent vectors of coordinate curves are given as

$$\sigma_u = t \quad \text{and} \quad \sigma_v = \lambda b$$

where b denotes the binormal vector field of geodesics. The variation of the Frenet Frame $\{t,n,b,\}$ of Bertrand geodesics in $u-$ direction is obtained as follows:

$$\begin{bmatrix} t \\ n \\ b \end{bmatrix}_u = \begin{bmatrix} 0 & \kappa & 0 \\ \kappa & 0 & -\tau \\ 0 & \tau & 0 \end{bmatrix} \begin{bmatrix} t \\ n \\ b \end{bmatrix}$$

by setting $(\varepsilon_1, \varepsilon_2, \varepsilon_3) = (-1,1,1)$ in Equation 1. The variation of $\{t,n,b\}$ in $v-$ direction must be in the following form:

$$\begin{bmatrix} t \\ n \\ b \end{bmatrix}_v = \begin{bmatrix} 0 & \alpha & \beta \\ \alpha & 0 & \gamma \\ \beta & -\gamma & 0 \end{bmatrix} \begin{bmatrix} t \\ n \\ b \end{bmatrix}.$$

The compatibility condition $\sigma_{uv} = \sigma_{vu}$ implies that

$$\alpha n + \beta b = (\lambda \tau) n + \lambda_u b.$$

So, we get $\alpha = \lambda \tau$ and $\beta = \lambda_u$. Then the variation of $\{t,n,b\}$ in $v-$ direction becomes

$$\begin{bmatrix} t \\ n \\ b \end{bmatrix}_v = \begin{bmatrix} 0 & \lambda \tau & \lambda_u \\ \lambda \tau & 0 & \gamma \\ \lambda_u & -\gamma & 0 \end{bmatrix} \begin{bmatrix} t \\ n \\ b \end{bmatrix}.$$

On the other hand, the compatibility condition $t_{uv} = t_{vu}$ implies that

$$t_{uv} = (\kappa n)_v = (\lambda \kappa \tau) t + (\kappa_v) n + (\kappa \gamma) b,$$

$$t_{vu} = (\lambda \tau n + \lambda_u b)_u = (\lambda \kappa \tau) t + (\lambda \tau_u + 2\lambda_u \tau) n + (\kappa \gamma) b.$$

So we get

$$\kappa_v = \lambda \tau_u + 2\lambda_u \tau.$$

And by the compatibility condition $n_{uv} = n_{vu}$, we obtain

$$n_{uv} = (\kappa t - \tau b)_v = (\kappa_v - \lambda_u \tau) t + (\kappa \lambda \tau + \tau \gamma) n + (\lambda_u \kappa - \tau_v) b,$$

$$n_{vu} = (\lambda \tau t + \gamma b)_u = (\lambda_u \tau + \lambda \tau_u) t + (\kappa \lambda \tau + \tau \gamma) n + (\gamma_u) b.$$

Thus, we get

$$\tau_v = \lambda_u \kappa - \gamma_u.$$

Finally, the compatibility condition $b_{uv} = b_{vu}$ gives that

$$b_{uv} = (\tau n)_v = (\lambda \tau^2)t + (\tau_v)n + (\tau \gamma)b,$$

$$b_{vu} = (\lambda_u t - \gamma n)_u = (\lambda_{uu} - \kappa \gamma)t + (\lambda_u \kappa - \gamma_u)n + (\tau \gamma)b.$$

Then, we get

$$\lambda_{uu} = \lambda \tau^2 + \kappa \gamma.$$

The system

$$\kappa_v = \lambda \tau_u + 2\lambda_u \tau,$$

$$\tau_v = \lambda_u \kappa - \gamma_u,$$

$$\lambda_{uu} = \lambda \tau^2 + \kappa \gamma$$

may be regarded as the Gauss-Minardi-Codazzi equations for the surface. If the constraint

$$A\kappa + B\tau = 1$$

is imposed then the system is well determined and the surface σ is guaranteed to be a Razzaboni surface.

Again, we define the Razzaboni transformation $\varphi: \sigma \to \sigma^*$ as follows;

$$\sigma^*(u, v) = \sigma(u, v) + An(u, v).$$

Let u^* and v^* be the geodesic coordinates of dual Razzaboni surface σ^*. And let $\{t^*, n^*, b^*\}$ be the Frenet Frame of Bertrand geodesics of dual Razzaboni surface σ^*. Then the $u^* -$ parameter curves are unit speed timelike Bertrand geodesics and $v^* -$ parameter curves form orthogonal spacelike parallels. Since the geodesics of the Razzaboni surface and its dual are Bertrand mates, we have $n = n^*$. Also we have

$$\sigma_u^* = \sigma_u - An_u = (1 - A\kappa)t + A\tau b = \tau(Bt + Ab).$$

That is

$$t^* = \frac{1}{\sqrt{B^2 - A^2}}(Bt + Ab).$$

Since $b^* = -t^* \times_{\mathbb{L}} n^*$, we obtain

$$b^* = \frac{1}{\sqrt{B^2 - A^2}}(-At + Bb).$$

And

$$du^* = \sqrt{B^2 - A^2}\,\tau du.$$

On the other hand, we have

$$t_{u^*}^* = \frac{B}{(B^2 - A^2)\tau}t_u + \frac{A}{(B^2 - A^2)\tau}b_u = \frac{B\kappa + A\tau}{(B^2 - A^2)\tau}n,$$

$$\kappa^* = \langle t_{u^*}^*, n^* \rangle_{\mathbb{L}} = \frac{B\kappa + A\tau}{(B^2 - A^2)\tau}\langle n, n \rangle_{\mathbb{L}} = \frac{B\kappa + A\tau}{(B^2 - A^2)\tau},$$

$$b_{u^*}^* = \frac{-A}{(B^2 - A^2)\tau}t_u + \frac{B}{(B^2 - A^2)\tau}b_u = \frac{-A\kappa + B\tau}{(B^2 - A^2)\tau}n,$$

$$\tau^* = \langle b_{u^*}^*, n^* \rangle_{\mathbb{L}} = \frac{-A\kappa + B\tau}{(B^2 - A^2)\tau}\langle n, n \rangle_{\mathbb{L}} = \frac{-A\kappa + B\tau}{(B^2 - A^2)\tau}.$$

Theorem 3. Let $\sigma = \sigma(u, v)$ be Razzaboni surface with timelike geodesic Bertrand curve. Then, the curvature and torsion of Bertrand geodesic of dual Razzaboni surface σ^* are found as

$$\kappa^* = \frac{B\kappa + A\tau}{(B^2 - A^2)\tau},$$

$$\tau^* = \frac{-A\kappa + B\tau}{(B^2 - A^2)\tau},$$

respectively.

4. CONCLUSION

In the first case, we obtain that the solutions κ, τ, λ and γ of the system

$$\kappa_v = \lambda\tau_u + 2\lambda_u\tau,$$

$$\tau_v = -\lambda_u\kappa - \gamma_u,$$

$$\lambda_{uu} = -\lambda\tau^2 - \kappa\gamma,$$

$$A\kappa + B\tau = 1$$

constitute the spacelike Razzaboni surfaces in $\mathbb{M}^3$. In the second case we obtain that the solutions κ, τ, λ and γ of the system

$$\kappa_v = \lambda\tau_u + 2\lambda_u\tau,$$

$$\tau_v = \lambda_u\kappa + \gamma_u,$$

$$\lambda_{uu} = -\lambda\tau^2 + \kappa\gamma$$

$$A\kappa + B\tau = 1$$

constitutes the timelike Razzaboni surfaces with timelike $v -$ parameter curves in $\mathbb{M}^3$.

For first and second cases, the second fundamental form of the surface σ is of the form

$$II = -\kappa du^2 - 2\lambda\tau dudv + \frac{\lambda}{\kappa}(-\lambda_{uu} - \lambda\tau^2)dv^2.$$

Then the Gaussian curvature of the surface is obtained as

$$K = -\frac{\lambda_{uu}}{\lambda}.$$

In the last case, we obtain that the solutions κ, τ, λ and γ of the system

$$\kappa_v = \lambda\tau_u + 2\lambda_u\tau,$$

$$\tau_v = \lambda_u\kappa - \gamma_u,$$

$$\lambda_{uu} = \lambda\tau^2 + \kappa\gamma$$

$$A\kappa + B\tau = 1$$

constitute the timelike Razzaboni surfaces with timelike $u -$ parameter curves in $\mathbb{M}^3$. In this case, the second fundamental form of the surface is of the form

$$II = -\kappa du^2 - 2\lambda\tau dudv + \frac{\lambda}{\kappa}(-\lambda_{uu} + \lambda\tau^2)dv^2.$$

Then Gaussian curvature of the surface is obtained as

$$K = \frac{\lambda_{uu}}{\lambda}.$$

In the case of $A = 0$, which means that Bertrand geodesics of the surface σ must have constant torsion

$$\tau = \frac{1}{B},$$

then Razzaboni transformation of the surface coincides to the main Razzaboni surface. That is

$$\varphi(\sigma) = \sigma.$$

In the case of $B = 0$, which means that Bertrand geodesics of the surface σ must have constant curvature, we have

$$\kappa = \frac{1}{A}.$$

Thus, Razzaboni transformation is defined as

$$\varphi(\sigma(u, v)) = \sigma^*(u, v) = \sigma(u, v) + \frac{1}{\kappa}n(u, v).$$

Since

$$\kappa^* = -\frac{1}{A} = -\kappa,$$

then Razzaboni transformation maps the surface σ, whose Bertrand geodesics have constant curvature, to the surface σ^*, whose Bertrand geodesics also have constant curvature with the opposite sign. Moreover, the torsions of Bertrand geodesics of the surfaces satisfy the relation

$$\tau\tau^* = \frac{1}{A^2}.$$

REFERENCES

[1]. Eisenhart L.P., A Treatise on the Differential Geometry of Curves and Surfaces. Dover, New York (1960).

[2]. Lopez R. Differential Geometry of Curves and Surfaces in Lorentz-Minkowski Space, arXiv:0810.3351v1, (2008).

[3]. Razzaboni A., Delle superficie nelle quali un sistema di geodetiche sono curve del Bertrand. Bologna Mem., 10 (1903) 539-548.

[4]. Schief W.K., On the Integrability of Bertrand curves and Razzaboni surfaces, Journal of Geometry and Physics, 45 (2002) 130-150.

[5]. Fibbi C., Sulle superficie che contengono un sistema di geodetiche a torsione constante, Pisa Ann., 5 (1888) 79-164.

[6]. Razzaboni A., Delle superficie nelle quali un sistema di geodetiche sono curve del Bertrand. Bologna, Tipografia Gamberini e Parmeggiani (1998).

[7]. Rogers C. and Schief W.K., Backlund and Darboux Transformations, Geometry of Modern Applications in Soliton Theory, Cambridge University Press, (2002).

[8]. Schief W.K. and Rogers C., Binormal Motion of Curves of Constant Curvature and Torsion, Generation of Soliton Surfaces, Proc. R. Soc. Lond. A., 455 (1999) 3163-3188.

[9]. Gürbüz N., The Motion of Timelike Surfaces in Timelike Geodesic Coordinates, Int. Journal of Math. Analysis, 4 (2010) 349-356.

[10]. Ding Q.and Inoguchi J., Schrödinger flows, binormal motion for curves and second AKNS-hierarchies, Chaos Solitons and Fractals, 21 (2004) 669-677.

[11]. Inoguchi J., Biharmonic curves in Minkowski 3-space, International Journal of Mathematics and Mathematical Sciences, 21 (2003) 1365-1368.

[12]. Erdoğdu M. and Özdemir M., Geometry of Hasimoto Surfaces in Minkowski 3-space. Mathematical Physics, Analysis and Geometry, 17 (2014) 169-281.

[13]. Inoguchi J. Timelike surfaces of constant mean curvature in Minkowski 3-space, Tokyo Journal of Mathematics, 21 (1998) 141-152.

[14]. Özdemir M. and Ergin A.A., Parallel Frames of Non-Lightlike Curves. Missouri Journal of Mathematical Sciences, 20 (2008) 127-137.

Determination of Outdoor Absorbed Gamma Dose Rates of Kahramanmaraş Province, Turkey

Muhammet KARATAŞLI 🆔

Cukurova University, Faculty of Arts and Sciences, Department of Physics, Adana, TURKEY

Abstract. Outdoor absorbed gamma dose rates were measured in 118 different regions at a height of 1 m above the ground in the gonad (genitals) level in humans in Kahramanmaraş province and its vicinity using Eberline portable detector. Outdoor gamma dose rates varied from 32.7 nGy/h and 96.4 nGy/h with an arithmetic average of 64.8 nGy/h. The average value of the corresponding annual effective dose rate was estimated as 79.5 µSv/y. Lifetime cancer risk values estimated according to ICRP 103, BEIR VII and ICRP 60 were found to be 0.032, 0.036 and 0.040 respectively.

Keywords: Cancer risk, effective dose, gamma dose.

Türkiye'nin Kahramanmaraş İlinde Soğurulan Gama Doz Seviyesinin Belirlenmesi

Özet. Kahramanmaraş İli ve çevresinde 118 farklı bölgede açık havada soğurulan gama radyasyon doz düzeyini belirlemek için insanlarda gonad (üreme organları) hizasında yerden yaklaşık 1m yükseklikte Eberline marka portatif dedektörle ölçümler alınmıştır. Her bölgede ölçümler alınırken 5 metre yarıçapında üç farklı okuma yapılmış ve bu üç değerin ortalaması alınarak her bir ölçüm bölgesi için gama doz değerleri belirlenmiştir. Kahramanmaraş ili geneli için gama dozu ölçümlerinin değeri 32,7 nGy/s ile 96,4 nGy/s arasında bulunmuş olup, aritmetik ortalaması 64,8 nGy/s olarak hesaplanmıştır. Soğurulan gama radyasyon dozu kullanılarak hesaplanan yıllık etkin doz eşdeğerinin ortalama değeri ise 79,5 µSv/y olarak hesaplanmıştır. Kahramanmaraş ilinde yaşam boyu kanser risk değerleri ICRP 103, BEIR VII ve ICRP 60 için yüzdelik ortalamaları sırasıyla 0,032, 0,036 ve 0,040 olarak bulunmuştur. Elde edilen sonuçlarla Türkiye'de diğer illerde yapılan benzer çalışmaların sonuçları ve dünya ortalamaları ile karşılaştırılmıştır.

Anahtar Kelimeler: Kanser riski, etkindoz, gama doz.

1. INTRODUCTION

During the life of the people, they live inthe environment in which they live, depending on their environment and quality of life significantly natural radiation, nuclear weapons experiments, nuclear plant accidents, nuclear power plant emissions and leaks as a result of artificial radiation sources and internal and external irradiation as a result of radiation under the influence of [1].

Radionuclides with higher half-life such as ^{238}U an ^{232}Th radioactive uranium series and radioactive potassium (^{40}K) are naturally present from the formation of the earth's crust. The gamma rays that they broadcast form a large part of the environmental radiation. Their effect on these gamma rays depends on the concentration of radioactive elements in their territory. The activity concentrations of ^{238}U, ^{232}Th and ^{40}K vary with

soil and rock types. Therefore, the absorbed gamma dose rate measured in the outdoor air is closely related to the concentrations of radio-nuclei in the soil [2, 3].

The main purpose of environmental radiation measurements is to determine the radiation type and dose of people from environmental sources and to evaluate the risk they will generate. In this, the environmental concentrations of radionuclides, which constitute the sources of natural radiation, and the effects of radiation on biological systems, especially in humans, need to be determined. In addition, the relationship between the radionuclides in the environment and the radiation dose that people receive from these sources should also be determined. However, after such research, it can be decided whether a region is suitable for natural radiation or not. The difference in the concentration of radioactivity in the earth crust is one of the most important factors affecting the level of radiation. The differentiation of the radioactivity concentration varies depending on the geographic and geological structure of the region, the mineralogical structure of the rock and its soils and the elevation above sea level [4].

In addition to the dose and type of radiation in the world and Turkey as human research for assessing the risk they might have on health it is made. After the Chernobyl nuclear accident in 1986, a number of studies aimed at determining the level of natural background radiation in Turkey, especially in regions affected by this accident could have been made [5, 6].

However, despite the majority in Turkey take place in the Mediterranean region, located in the northern and northeastern parts of Eastern Anatolia Region does not have a sufficient number of studies to determine the gamma dose levels of Kahramanmaras. For this reason, this study was conducted to measure, evaluate and understand. This data will also be useful in assessing possible future environmental pollution.

2. MATERIALS & METHODS

Geology of the survey area

Kahramanmaraş, 37º 11' and 38º 36' north latitude of 36º 15' and 37º 42' east longitude is between 14 457 km² area in terms of area size and Turkey's 12 largest cities. As seen in Figure 1, although the majority of the Kahramanmaraş province is located in the Mediterranean Region, some parts of the north and northeast are in Eastern Anatolia. The eastern parts of the Çağlayancerit and Pazarcık districts are within the borders of the Southeastern Anatolia Region. In terms of land structure and altitude, flatness, pit and mountainous areas are numerous [7]. Most of the landforms consist of collapsed areas between the mountains, which are the extensions of the Southeast Taurus Mountains and these mountains. The vast majority of the plains are located around the Ceyhan Valley. The plateaus are located between the mountainous areas and the plains. 59.7% of the province of Kahramanmaraş consists of mountains, 24% plateaus and 16.3% plains. The altitude ranges from 350 meters to 3090 meters [8].

Figure 1. Research Region of Kahramanmaraş.

Gamma Scintillation Detector

In this study, Eberline Smart Portable (ESP-2) model, portable microcomputer and a SPA-6 plastic scintillation detector connected device were used to determine the external gamma radiation levels. ESP-2 is a device specially designed for radiation measurements, which can record the measured information and then transfer the information recorded to a connected printer. Allows multiple reads (over 500) and subsequently a computer can be connected to the printer. The SPA-6 detector is highly sensitive to the detection of radiation emitted from low-activity radionuclides descending into the ground with fallout with measurements of natural gamma radiation. The ESP-2 has seven multi-function opening switches and a liquid crystal display (LCD), designed as an interface for the user. The data can be given either as scientific or motion point recording and in selectable measurement units [9].

Scintillation detectors consist of a substance used as a scintillator and a photon amplifier tube connected directly behind it. Ionizing radiation interacts with some of the solid, liquid or gaseous substances, called scintillation phosphorus, resulting in ionization and stimulation. When the energy given to the electron is not enough to detach it from the environment, the electron is emitted and the visible light is released as it returns to its original state. The light emitted by the scintillation phosphors is collected by photon multiplier tubes and converted into voltage pulses. The amplitude of the pulse is proportional to the energy of the radiation. These detectors are used for counting and also for energy separation. Although scintillation phosphors may be in liquid or crystalline form, only crystal ones are still used in radiation control work [9].

In order to minimize measurement errors during the determination of gamma dose values, three readings were made at each measurement point and the mean of these three values were determined and the gamma dose values for each measurement region were determined. The results include contributions from both terrestrial radionuclides and cosmic rays. The portable detector used in the measurements shows the measurement results in µR/h. After getting the average of three different measurements, results were recorded in µR/h and then the conversion factor of 8.7 nGy µ/Rwas used to change the unit of µR/ h to the nGy/h[10].

Determination of outdoor gamma dose rates

After getting the average of three different measurements, results were recorded in µR h^{-1} and then the conversion factor of 8.7 nGy µR^{-1} was used to change the unit of µR h^{-1} to the nGy h^{-1}. To obtain the annual effective dose equivalent (AEDE), the following equation was used [11,12].

$$AEDE = ADRA \times DCF \times OF \times T \tag{1}$$

In this equation, the environmental gamma dose conversion factor is determined as 0.7 Sv/Gy and this value does not change for measurements both inside and outside the home. Another factor that should be known in this equation is the Busy Factor, that is, the time that people are exposed to these rays. In the calculations made in this study, it is considered that people spend 20% of their time in open areas and 80% in closed areas (occupancy factor is taken as 0.8 for home and 0.2 for outside house). Time is the number of hours in a year (8760 s/y). Lifetime cancer risk (ELCR) was calculated using equation 2 [11,13].

$$ELCR = AEDE \times DL \times RF \tag{2}$$

Here AEDE is the annual effective dose equivalent, DL, mean life expectancy (mean 70 years) and RF is the fatal cancer risk factor in Sv^{-1}, and in this study, the RFs of ICRP 103, BEIRVII [14] and ICRP 60 for the public as 0.057, 0.064 and 0.072, respectively, have been used [15].

3. RESULTS AND DISCUSSION

The absorbed dose rate in air (ADRA) 1 m above the ground consisting of the terrestrial and the cosmic gamma components was determined as 64,8 nGy h^{-1} for the entire region. Thereadingsrangedfrom 32,7 to 96,4 nGy/ h. The measured outdoor gamma exposure dose rates (GEDR) in µR/h and absorbed gamma dose rates in air (ADRA) in nGy/h are presented for each distinct of the Kahramanmaraş in Table 1.

Table 1. Gamma Exposure Dose Rate and Absorbed dose rate for each distinct of the Kahramanmaraş.

Distinct	GEDR (Gamma Exposure Dose Rate) (µR/h)			ADRA (Absorbed Dose Rate in Air) (nGy/h)		
	Minimum	Maximum	Mean	Minimum	Maximum	Mean
KahramanmaraşMerkez	3.75	7.90	6.44	32.7	68.8	56
Türkoğlu	5.65	6.86	6.09	49.2	59.7	53
Pazarcık	6.27	9.60	7.07	54.6	83.6	61.5
Çağlayancerit	7.06	10.97	7.97	61.5	95.5	69.4
Andırın	6.60	10.39	7.96	57.5	90.4	67.3
Afşin	7.40	10.88	8.81	64.4	94.7	76.7
Elbistan	7.52	10.32	8.32	65.5	89.8	72.5
Göksun	7.05	10.18	7.85	61.4	88.6	68.3
Ekinözü	7.11	10.80	8.12	61.9	94.3	70.7
Nurhak	6.40	11.08	9.22	55.7	96.4	80.3
Region	3.75	11.08	7.45	32.7	96.4	64.8

The absorbed gamma dose map obtained as a result of the measurements in Kahramanmaraş province and its districts was drawn. Figure 2 shows the general distribution of the absorbed gamma dose rate throughout the province in the form of an isodose map. Red areas represent areas where Kahramanmaras province and overall absorbed gamma dose doses are high.

Table 2 presents the radiation doses (yearly effective dose equivalents) of people exposed to one year during the year and the risk factors for life-long cancer caused by environmental gamma radiation for a year by using absorbed gamma dose values in Kahramanmaras province.
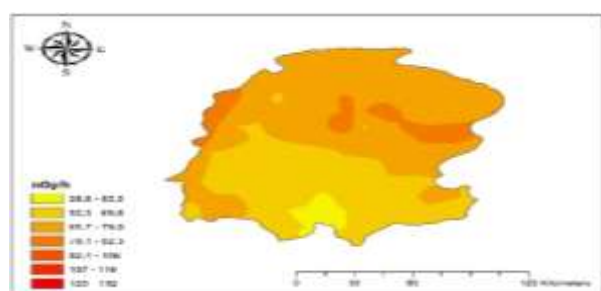
Figure 2. ADRA in Kahramanmaraş.

Table 2. The average annual effective dose values and Lifetime cancer risk.

	AEDE Annual effective dose (µSv/y)	Lifetime cancer risk %		
		ICRP 103	BEIR VII	ICRP 60
Kahramanmaraş Merkez	68.7	0.027	0.031	0.035
Türkoğlu	65	0.026	0.030	0.033
Pazarcık	75.4	0.030	0.034	0.038
Çağlayancerit	85	0.034	0.038	0.042
Andırın	83	0.033	0.037	0.042
Afşin	94	0.038	0.042	0.048
Elbistan	89	0.036	0.040	0.045
Göksun	84	0.034	0.038	0.042
Ekinözü	87	0.035	0.039	0.044
Nurhak	98.5	0.039	0.044	0.050
Region	79.5	0.032	0.036	0.040

The annual effective dose equivalent calculated using the absorbed gamma dose measurement varies between 40.1 μSv/y and 11.2 μSv/y, but the average value was found to be 79.5 70 μSv/y. As can be seen in Table 3, the annual effective dose equivalent is 79.5 μSv/y, the world average is greater than 70 μSv/y [12].

Table 3. Absorbed Dose Rates in Air (ADRA) in close cities to region and worldwide averages.

	ADRA (AbsorbedDose Rate) (nGy/h)	AEDE (Annualeffectivedose) (μSv/y)
İstanbul [16].	65	79.7
Kastamonu [17].	54.81	67.21
Şanlıurfa [18].	60.9	74.7
Kırklareli [19].	118	144.7
Tekirdağ [20].	43.85	53.77
Çanakkale [21].	66.4	81.4
Çankırı [22].	69.6	87.7
Trabzon [23].	59	72.4
Yalova [24].	84	103
Balıkesir [25].	127	155.8
Kahramanmaraş	64.8	79.5
Worldwide [12].	60	70

REFERENCES

[1]. Karataşlı, M., Özer, T., Investigation of Radiation Activity Growing Peanuts in Osmaniye, Süleyman Demirel University, Journal of Natural and Applied Sciences, 21, 3 (2017) 1017-1023.

[2]. Beck, H.L., The Natural Radiation Environment II. USERDA Conf.-720805-P2, The Physics of Environmental Gamma Radiation Fields, (1982), 101-104.

[3]. National Council on Radiation Protection and Measurements, Environmental Radiation Measurement, NCRP Report No. 50, ISBN. 0- 913392-32-4, (1977).

[4]. Eisenbud, M., Environmental Radioactivity, Third Edition, ISBN. 0-12-235153, Academic Pres, Inc., London, 1987.

[5]. TAEK, Post-Chernobyl Radiation and Radioactivity measurements in Turkey, Atomic Energy Agency Ankara, 1998.

[6]. TAEK, Post-Chernobyl Radiation and Radioactivity measurements in Turkey. Turkey Atomic Energy Agency, Ankara, 2006.

[7]. Tursun, N., Tursan, A. Ö., Kaçan, K., Determination of Weeds in Cotton Fields in Kahramanmaraş, Turkey, KSU Journal of Science and Engineering 7-1 (2004) 92-95.

[8]. Gürbüz,M., Yıldırım,U., Belli A., Metropolitan Municipality Analysis on Scale of Kahramanmaraş. Adnan Menderes University, Journal of Institute of Social Sciences, 1-1, Special Issue, (2014) 102-135.

[9]. Değerlier, M., Determination of Enviromental Natural Radioactivity of Adana and The Annual Effective Dose Equivalent Due to Natural Radiation, Ph.D. Thesis, Department Of Physics Institute Of Natural And Applied Sciences University of Çukurova, Adana, 2007.

[10].Baykara, O. The determinations of natural radioactivity in the intersect zone of the North Anatolian Fault and East Anatolian. PhD thesis, Fault, Firat University Graduate School of Natural and Applied Science, Physics Department, Elazig, Turkey (in Turkish) 2005.

[11].Karataşlı, M., Turhan, Ş., Varinlioğlu, A., Yeğingil, Z.: Natural and fallout radioactivity levels and radiation hazard evaluation in soil samples. Environ. Earth Sci., 75-5 (2016) 1-9.

[12].UNSCEAR Report of the United Nations Scientific Committee on the Effects of Atomic Radiation, Sources, Effects, and Risks of Ionizing Radiation. United Nations sales publication, New York. United Nations, 2000.

[13].UNSCEAR UNSCEAR, Report of the United Nations Scientific Committee on the Effects of Atomic Radiation, Sources, Effects, and Risks of Ionizing Radiation. United Nations sales publication, New York. United Nations, 2008.

[14].NCR, National Academy of Sciences. National Research Council Committee to

Assess Health Risks from Exposure to Low Levels of Ionizing Radiation. Report of VII, 2006

[15].ICRP Publication 103 Recommendations of the ICRP: Annals of the ICRP (International Commission on Radiological Protection), 37 (2007).2-4

[16].Karahan, G.,Bayulken, A., Assesment of Gamma Dose Rates Around Istanbul. Journal of Envrionmental Radioactivity, 47-2 (2000) 213-221.

[17].Kam, E., Bozkurt, A., Environmental radioactivity measurements in Kastamonu region of northernTurkey. Applied Radiation and Isotopes, 65 (2007) 440–444.

[18].Bozkurt, A., Yorulmaz, N., Kam, E., Karahan, G. And Osmanlıoğlu, A. E., Assessment of environmental radioactivity for Şanliurfa region of Southeastern Turkey. Radiation Measurements, 42-8 (2007) 1387-1391.

[19].Taskin, H. Karavus, M., Ay, P., Topuzoglu, A., Hidiroglu, S, Karahan, G., Radionuclide concentrations in soil and lifetime cancer risk due to gamma radioactivity in Kirklareli, Turkey, Journal of Environmental Radioactivity, 100 (2009) 49–53.

[20].Kam, E., Yarar, Y., Bozkurt, A., A study of background radioactivity level for Tekirdag. Turk Radiat Prot Dosimetry, 138 (2010) 40–44.

[21].Kam, E., Bozkurt, A., Ilgar, R., A study of background radioactivity level for Canakkale, Turkey. Environ. Monit. Assess, 168 (2010) 685–690.

[22].Kapdan, E., Taşkın, H., Kam, E., Osmanlıoğlu, A.E., Karahan, G., Bozkurt A., 2011. A study of environmental radioactivity measurements for Cankiri, Turkey. Radiation Protection Dosimetry, 150-3 (2010) 398–404.

[23].Kurnaz, A., Kucukomeroglu, B., Damla, N., Cevik, U., Radiological maps for Trabzon, Turkey. J. Environ. Radioactiv. 102 (2011) 393–399.

[24].Kapdan, E. , Varinlioglu , A. Karahan, G., Radioactivity Levels and Health Risks due to Radionuclides in the Soil of Yalova, Northwestern Turkey, 5-4 (2011) 837-846.

[25].Kapdan, E., Varinlioglu , A. Karahan, G., Outdoor radioactivity and health risks in Balikesir, Northwestern Turkey, Radiation Protection Dosimetry, 148-3 (2012) 301–309.

[26].ICRP, The International Commission on Radiological Protection, ICRP Publication 60. Recommendations of the International Commission on the Radiological Protection, Pergamon Press Inc., ICRP 1990, USA.

Cumhuriyet Science Journal
CSJ

On Mochizuki-Trooshin Theorem for Sturm-Liouville Operators

İbrahim ADALAR

Sivas Cumhuriyet University Zara Veysel Dursun Colleges of Applied Sciences Zara/Sivas, TURKEY

Abstract. In this paper, the inverse spectral problems of Sturm-Liouville operators are considered. Some new uniqueness theorems and analogies of the Mochizuki-Trooshin Theorem are proved.

2010 Mathematics Subject Classification. Primary 34A55, 34B24; Secondary 34L05.

Keywords: Inverse spectral problem, Sturm-Liouville equation.

Sturm-Liouville Operatörleri için Mochizuki-Trooshin Teoremi Üzerine

Özet. Bu makalede, Sturm-Liouville operatörlerinin ters spektral problemleri ele alınmıştır. Bazı yeni teklik teoremleri ve Mochizuki-Trooshin teoreminin benzetimleri ispatlanmıştır.

Anahtar Kelimeler: Ters spektral problem, Sturm-Liouville denklemi.

1. INTRODUCTION

We consider the classical Sturm-Liouville problem $L = L(q(x), h, H)$

$$-y'' + q(x)y = \lambda y \tag{1}$$

$$y'(0) - hy(0) = 0 \tag{2}$$

$$y'(1) + Hy(1) = 0 \tag{3}$$

where $h, H \in \mathbb{R}$, λ is a spectral parameter and $q(x) \in L_1(0,1)$. The spectrum of such problems consists of countable many real eigenvalues, which have no finite limit point.

The inverse spectral problem for L is to determine the potential function $q(x)$ from some given data. The first result on this area is given by Ambarzumian [1]. Borg [2] showed that generally a single spectrum is insufficient to determine the potential. Levinson [9] showed that if the potential $q(x)$ is symmetric, $q(x) = q(1-x)$, then it is determined uniquely by a single spectrum. Later Gelfand and Levitan [3] proved that the eigenvalues and normalizing coefficients uniquely determine the potential $q(x)$. Hochstadt and Lieberman [7] proved that a single spectra and the potential on the interval $[1/2,1]$ uniquely determine the potential $q(x)$ on the whole interval $[0,1]$.

In 2001, Mochizuki and Trooshin [5] proved a uniqueness theorem for interior spectral data of the Sturm-Liouville operator. They used similar techniques in [7]. This kind of problems for the Sturm-Liouville operator were formulated and studied in [12-19].

Together with L, we consider a boundary value problem $\widetilde{L} = L(\widetilde{q}(x), h, H)$ of the same form but with a different coefficient $\widetilde{q}$. We agree that if a certain symbol s denotes an object related to L, then $\widetilde{s}$ will denote an analogous object related to $\widetilde{L}$. The eigenvalues and the corresponding eigenfunctions of the problem L are denoted by λ_n and $\varphi_n(x) = \varphi(x, \lambda_n)$, respectively.

The statement of Mochizuki and Trooshin theorem is as following:

Theorem 1.1. [5] *If for every $n = 0, 1, 2, \ldots$ we have*

$$\lambda_n = \widetilde{\lambda_n}, \quad \frac{\varphi'_n(1/2)}{\varphi_n(1/2)} = \frac{\widetilde{\varphi}'_n(1/2)}{\widetilde{\varphi}_n(1/2)} \tag{4}$$

then $q(x) = \widetilde{q}(x)$ almost everywhere on $[0,1]$.

The purpose of the present study is to prove some analogies of this theorem and new uniqueness theorems for inverse Sturm-Liouville problems.

In the second section, we give some preliminaries. Section 3 contains new uniqueness theorems and alternative proofs for Mochizuki-Trooshin theorem and Levinson's theorem.

2. PRELIMINARIES

We shall first mention some known results which will be needed later. Let $\varphi(x, \lambda)$ be the solution of equation (1) satisfying the initial conditions,

$$\varphi(0, \lambda) = 1, \quad \varphi'(0, \lambda) = h. \tag{5}$$

We need specifically to focus on the properties of $\varphi(1/2, \lambda)$. It is known that, [4,8,17,18] for each $x \in [0,1]$, $\varphi(x, \lambda)$ and $\varphi'(x, \lambda)$ are entire functions of λ and there exist some constants $c_1, c_2 > 0$ such that $\varphi(1/2, \lambda)$ and $\varphi'(1/2, \lambda)$ are all bounded by $c_1 \exp(c_2 |\lambda|^{1/2})$. For $|\lambda| \to \infty$ uniformly with respect to $x \in [0,1]$,

$$\varphi(x, \lambda) = \cos \rho x + O(\frac{\exp \tau x}{\rho})$$
$$\varphi'(x, \lambda) = -\rho \sin \rho x + O(\exp \tau x). \tag{6}$$

Here $\rho = \sqrt{\lambda}$ and $\tau = |\mathrm{Im}\, \rho|$. The function

$$\omega(\lambda) = \varphi'(1, \lambda) + H\varphi(1, \lambda)$$

is entire in λ and it has an at most countable set of zeros, $\{\lambda_n\}$. Denote

$$G_\delta = \{\rho : |\rho - k\pi| \ge \delta, k = 0, \pm 1, \pm 2, \ldots\}, \delta > 0.$$

We have that [8]

$$|\omega(\lambda)| \geq C_\delta |\rho| \exp \tau \tag{7}$$

for $\rho \in G_\delta$, $|\rho| \geq \rho^*$ and sufficiently large ρ^*. The Weyl m_- function is defined by:

$$m_-(a,\lambda) = -\frac{\varphi(a,\lambda)}{\varphi'(a,\lambda)}$$

where $a \in [0,1]$. The following Marchenko's uniqueness theorem [6] is also necessary for our analysis.

Theorem 2.1. [6] *The Weyl $m_-(a,\lambda)$ function uniquely determines h as well as $q(x)$ almost everywhere on $[0,a]$.*

3. UNIQUENESS THEOREMS

Here we provide an alternative proof for Mochizuki and Trooshin theorem.

Proof of the Theorem 1.1. Consider the initial-value problems:

$$-\varphi'' + q(x)\varphi = \lambda\varphi$$
$$\varphi(0) = 1, \varphi'(0) = h \tag{8}$$

and

$$-\tilde{\varphi}'' + \tilde{q}(x)\tilde{\varphi} = \lambda\tilde{\varphi}$$
$$\tilde{\varphi}(0) = 1, \tilde{\varphi}'(0) = h. \tag{9}$$

The functions $\varphi(x,\lambda)$ and $\varphi'(x,\lambda)$ satisfy

$$\tilde{\varphi}(0,\lambda)\varphi'(0,\lambda) - \varphi(0,\lambda)\tilde{\varphi}'(0,\lambda) = 0.$$

Multiplying (8) by $\tilde{\varphi}(x,\lambda)$ and (9) by $\varphi(x,\lambda)$, subtracting, and integrating from 0 to $1/2$, we obtain

$$f(\lambda) = \int_0^{1/2} \left(q(x) - \tilde{q}(x)\right)\varphi(x,\lambda)\tilde{\varphi}(x,\lambda)dx = \tilde{\varphi}(1/2,\lambda)\varphi'(1/2,\lambda) - \varphi(1/2,\lambda)\tilde{\varphi}'(1/2,\lambda). \tag{10}$$

The conditions of the theorem imply

$$f(\lambda_n) = 0.$$

Define $h(\lambda) = \dfrac{f(\lambda)}{\omega(\lambda)}$, which is an entire function. From the asymptotics (6) and (7) for $f(\lambda)$ and $\omega(\lambda)$, we see that

$$h(\lambda) = O\left(\frac{1}{|\rho|}\right)$$

for large $|\rho|$. Thus, by Liouville's theorem, we obtain for all λ,

$$h(\lambda) = 0$$

or

$$f(\lambda) = 0.$$

From (10), we have that

$$\frac{\varphi(1/2,\lambda)}{\varphi'(1/2,\lambda)} = \frac{\widetilde{\varphi}(1/2,\lambda)}{\widetilde{\varphi}'(1/2,\lambda)}$$

and hence

$$m_-(1/2,\lambda) = \widetilde{m_-}(1/2,\lambda).$$

By Theorem 2.1, we prove $q(x) = \widetilde{q}(x)$ almost everywhere on $[0,1/2]$.

To prove that $q(x) = \widetilde{q}(x)$ almost everywhere on $[1/2,1]$, we will consider the supplementary problem $\overline{L}$:

$$-y'' + q(1-x)y = \lambda y$$

$$y'(0) - Hy(0) = 0$$

$$y'(1) + hy(1) = 0.$$

Since $\varphi_n(1-x) = \overline{\varphi}_n(x)$, the assumption conditions in Theorem 1.1 are still satisfied. If we repeat the above arguments then this yields $q(1-x) = \widetilde{q}(1-x)$ on $[0,1/2]$, that is $q(x) = \widetilde{q}(x)$ almost everywhere on $[1/2,1]$. This completes the proof. $\square$

By the remark to proof of Theorem 1, we have proved the following result:

Corollary 3.1. *Let* $f(\lambda) = 0$ *for all* λ. *If for every* $n = 0,1,2,\ldots$ *we have*

$$\lambda_n = \widetilde{\lambda}_n,$$

then $q(x) = \widetilde{q}(x)$ *almost everywhere on* $[0,1]$.

Let L_0:

$$-y'' + q(x)y = \lambda y$$

$$y'(0) - hy(0) = 0$$

$$y'(1) + hy(1) = 0.$$

Here we provide an alternative proof for the following Levinson's theorem [9].

Theorem 3.2. [9] *If* $q(x) = q(1-x)$ *then the function* $q(x)$ *and* h *are uniquely determined by the spectrum of problem* L_0.

Proof. Applying the same arguments as that in the proof of Theorem 1.1, we can see that

$$f(\lambda) = 2 \int_0^{1/2} \left(q(x) - \tilde{q}(x) \right) \varphi(x, \lambda) \tilde{\varphi}(x, \lambda) dx = 0$$

and hence

$$f(\lambda_n) = 2 \int_0^{1/2} \left(q(x) - \tilde{q}(x) \right) \varphi(x, \lambda_n) \tilde{\varphi}(x, \lambda_n) dx = 0.$$

We obtain for all λ,

$$f(\lambda) = \tilde{\varphi}(1/2, \lambda) \varphi'(1/2, \lambda) - \varphi(1/2, \lambda) \tilde{\varphi}'(1/2, \lambda) = 0$$

Thus we arrive at

$$m_-(1/2, \lambda) = \widetilde{m_-}(1/2, \lambda).$$

By Theorem 2.1, the proof is complete. □

Let us consider the following Sturm-Liouville problems

$$-y'' + q(x)y = \lambda y \tag{11}$$

$$y(0) = y(1/2) = 0 \tag{12}$$

$$y(0) = y'(1/2) = 0. \tag{13}$$

Let $\{\mu_n\}_{n=0}^{\infty}$ and $\{\upsilon_n\}_{n=0}^{\infty}$ be the spectra of the problems (11), (12) and (11), (13), respectively. Consider the problem: given three spectra $\{\lambda_n\}_{n=0}^{\infty}$, $\{\mu_n\}_{n=0}^{\infty}$ and $\{\upsilon_n\}_{n=0}^{\infty}$ determine $q(x)$. Knowledge of $\{\mu_n\}_{n=0}^{\infty}$ and $\{\upsilon_n\}_{n=0}^{\infty}$ is equivalent to the knowledge of $q(x)$ on $[0, 1/2]$. Thus this problem is the Hochstadt-Lieberman problem in [7]. Now consider the problem: given $\{\lambda_n\}_{n=0}^{\infty} \subset \left\{ \{\upsilon_n\}_{n=0}^{\infty} \bigcup \{\mu_n\}_{n=0}^{\infty} \right\}$ determine $q(x)$. In this case, only spectra $\{\lambda_n\}_{n=0}^{\infty}$ uniquely determine the potential $q(x)$ on the whole $[0,1]$. We can give the following uniqueness theorem.

Theorem 3.3. *Let* $\{\lambda_n\}_{n=0}^{\infty} \subset \left\{ \{\upsilon_n\}_{n=0}^{\infty} \bigcup \{\mu_n\}_{n=0}^{\infty} \right\}$ *and* $\{\widetilde{\lambda}_n\}_{n=0}^{\infty} \subset \left\{ \{\widetilde{\upsilon}_n\}_{n=0}^{\infty} \bigcup \{\widetilde{\mu}_n\}_{n=0}^{\infty} \right\}$. *If for every* $n = 0, 1, \dots$ *we have*

$$\lambda_n = \widetilde{\lambda}_n,$$

then $q(x) = \tilde{q}(x)$ *almost everywhere on* $[0,1]$.

Proof. As in the proof of Theorem 1.1, we can show that

$$f(\lambda) = \int_0^{1/2} \left(q(x) - \tilde{q}(x) \right) \varphi(x, \lambda) \tilde{\varphi}(x, \lambda) dx = \tilde{\varphi}(1/2, \lambda) \varphi'(1/2, \lambda) - \varphi(1/2, \lambda) \tilde{\varphi}'(1/2, \lambda).$$

To prove, as in the Corollary 3.1, it suffices to show that $f(\lambda) = 0$ for all λ. The assumptions of the theorem imply that

$$\varphi_n(1/2, \lambda_n) = 0 \text{ or } \varphi'_n(1/2, \lambda_n) = 0 \text{ and } \tilde{\varphi}_n(1/2, \lambda_n) = 0 \text{ or } \tilde{\varphi}'_n(1/2, \lambda_n) = 0.$$

Hence, we have

$$f(\lambda_n) = 0.$$

Thus, repeating the proof Theorem 1.1, we arrive at

$$f(\lambda) = 0,$$

which implies that

$$m_-(1/2,\lambda) = \widetilde{m}_-(1/2,\lambda)$$

and $q(x) = \tilde{q}(x)$ almost everywhere on $[0,1/2]$. The supplementary problem $\overline{L}$ in proof of Theorem 1.1 completes the proof. $\qquad\square$

Let us define

$$g(\rho) = \int_0^{1/2} \left(q(x) - \tilde{q}(x)\right)\varphi(x,\lambda)\widetilde{\varphi}(x,\lambda)dx = \widetilde{\varphi}(1/2,\lambda)\varphi'(1/2,\lambda) - \varphi(1/2,\lambda)\widetilde{\varphi}'(1/2,\lambda) \tag{14}$$

where $\rho = \sqrt{\lambda}$. The asymptotics (6) imply that the entire function $g(\rho)$ is a function of exponential type ≤ 1. As shown by the above discussion, let $g(\rho) = 0$ then only spectra $\{\lambda_n\}_{n=0}^{\infty}$ uniquely determine the potential $q(x)$ on $[0,1]$. We now consider the problem: If the zeros of an entire function of exponential type are known to include a given sequence of positive real numbers what can be said about growth of the function. The first result of this type is given by Carlson's Theorem. This theorem [11, p.153] says, if g is entire function of exponential type $< \pi$ and vanishes on the positive integers then g vanishes everywhere. This

idea has been further developed by Rubel [10, p.422]:

Theorem 3.4. [10] *Let* $\rho = t + i\tau$ *and* $\Omega = \left\{\rho_n : \rho_{n+1} - \rho_n \geq \gamma > 0, \rho_n > 0, n \in \mathbb{Z}^+\right\}$. *In order to each entire function* $g(\rho)$ *satisfying*

$$g(\rho) = O(1)\exp(a|\rho|), \quad a < \infty \tag{15}$$

$$g(i\tau) = O(1)\exp(b|\tau|), \quad b < \delta \tag{16}$$

$$g(\rho_n) = 0 \tag{17}$$

vanish identically, it is sufficient that

$$\inf_{\rho>1} \limsup_{k\to\infty} (\ln\rho)^{-1} \sum_{\rho_n \leq pk} \frac{1}{\rho_n} = L(\Omega) \geq \frac{\delta}{\pi}. \tag{18}$$

Here, $L(\Omega)$ is the logarithmic block density of Ω.

We turn repeat that equation (14). From asymptotics (6), the entire function

$$g(\rho) = \int_0^{1/2} \left(q(x) - \tilde{q}(x)\right)\varphi(x,\lambda)\widetilde{\varphi}(x,\lambda)dx$$

satisfies (15) and (16). Also we have that

$$\rho_{n+1} - \rho_n > 0$$

where $\sqrt{\lambda_n} = \rho_n$. In this case, we can give a uniqueness theorem by using Theorem 3.4.

Theorem 3.5. *Let $\Lambda \subset \mathbb{N} \cup \{0\}$ be a subset of nonnegative integer numbers and let $\Omega := \{\lambda_n\}_{n \in \Lambda}$ be a part of the spectrum of L such that the numbers $\sqrt{\lambda_n} = \rho_n$ satisfy (18) for function $g(\rho)$. If for $n \in \Lambda$, we have*

$$\lambda_n = \widetilde{\lambda_n}, \quad \frac{\varphi'_n(1/2)}{\varphi_n(1/2)} = \frac{\widetilde{\varphi}'_n(1/2)}{\widetilde{\varphi}_n(1/2)}$$

then $q(x) = \tilde{q}(x)$ almost everywhere on $[0,1]$.

Proof. As in the proof of Theorem 1, we obtain

$$g(\rho) = \int_0^{1/2} \left(q(x) - \tilde{q}(x) \right) \varphi(x,\lambda) \widetilde{\varphi}(x,\lambda) dx = \widetilde{\varphi}(1/2,\lambda) \varphi'(1/2,\lambda) - \varphi(1/2,\lambda) \widetilde{\varphi}'(1/2,\lambda).$$

The assumptions of the theorem imply

$$g(\rho_n) = 0, \quad n \in \Lambda.$$

By the Theorem 3.4, we have that

$$g(\rho) = 0$$

on the whole ρ-plane. Thus, $\varphi(x,\lambda)$ and $\widetilde{\varphi}(x,\lambda)$ satisfy

$$\widetilde{\varphi}(1/2,\lambda)\varphi'(1/2,\lambda) - \varphi(1/2,\lambda)\widetilde{\varphi}'(1/2,\lambda) = 0$$

and hence

$$m_-(1/2,\lambda) = \widetilde{m}_-(1/2,\lambda).$$

By the Theorem 2.1, we prove $q(x) = \tilde{q}(x)$ almost everywhere on $[0,1/2]$. Repeating the supplementary problem in the last part of proof of Theorem 1.1, we can show that $g(\rho) = 0$ on the whole ρ-plane, which implies that $q(x) = \tilde{q}(x)$ on $[1/2,1]$ and consequently, $q(x) = \tilde{q}(x)$ almost everywhere on $[0,1]$. This completes the proof.   □

Let us consider the Sturm-Liouville problem L for $q(x) \in L_2(0,1)$. Horvath [15, 19, p.268] proved Hochstadt-Lieberman type an uniqueness theorem by using simple closedness properties of the exponential system corresponding to the known eigenvalues. We can give the following uniqueness theorem with same arguments in [15] for Mochizuki-Trooshin type theorem.

Theorem 3.6. *Let* $\Lambda \subset \mathbb{N} \cup \{0\}$ *be a subset of nonnegative integer numbers and let* $\Omega := \{\lambda_n\}_{n \in \Lambda}$ *be a part of the spectrum of* L *such that the system of functions* $\{\cos 2\rho_n x\}_{n \in \Lambda}$ *is complete in* $L_2(0,1/2)$. *If for* $n \in \Lambda$, *we have*

$$\lambda_n = \widetilde{\lambda_n}, \quad \frac{\varphi'_n(1/2)}{\varphi_n(1/2)} = \frac{\widetilde{\varphi}'_n(1/2)}{\widetilde{\varphi}_n(1/2)}$$

then $q(x) = \widetilde{q}(x)$ *almost everywhere on* $[0,1]$.

Proof. As in the proof of Theorem 1, we can show that

$$f(\lambda) = \int_0^{1/2} \left(q(x) - \widetilde{q}(x) \right) \varphi(x,\lambda) \widetilde{\varphi}(x,\lambda) dx = \widetilde{\varphi}(1/2,\lambda)\varphi'(1/2,\lambda) - \varphi(1/2,\lambda)\widetilde{\varphi}'(1/2,\lambda).$$

Hence, we have that

$$f(\lambda_n) = 0, \quad n \in \Lambda. \tag{19}$$

The following representation holds [4,6,8]

$$\varphi(x,\lambda) = \cos \rho x + \int_0^x K(x,t) \cos \rho t \, dt$$

where $K(x,t)$ is a continuous function which does not depend on λ. Hence,

$$\varphi(x,\lambda)\widetilde{\varphi}(x,\lambda) = \frac{1}{2}\left(1 + \cos 2\rho x + \int_0^x K_1(x,t) \cos \rho t \, dt \right) \tag{20}$$

where $K_1(x,t)$ is a continuous function which does not depend on λ. From (19) and (20), we have

$$\int_0^{1/2} \left[\phi(x) + \int_x^{1/2} K_1(x,t)\phi(t) dt \right] \cos 2\rho_n x \, dx + \int_0^{1/2} \phi(x) dx = 0, \quad n \in \Lambda,$$

where $\phi(x) = q(x) - \widetilde{q}(x)$. By the Riemann-Lebesgue lemma,

$$\int_0^{1/2} \phi(x) dx = 0.$$

By the completeness of the functions $\{\cos 2\rho_n x\}_{n \in \Lambda}$ we have

$$\phi(x) + \int_x^{1/2} K_1(x,t)\phi(t) dt = 0.$$

Since this homogeneous integral equation has only the trivial solution it follows that and $q(x) = \tilde{q}(x)$ almost everywhere on $[0, 1/2]$. The supplementary problem $\overline{L}$ in proof of Theorem 1.1 completes the proof. □

REFERENCES

[1]. Ambarzumyan, V.A., Uber eine Frage der Eigenwerttheorie, Z. Phys. 53 (1929) 690-695.

[2]. Borg, G., Eine umkehrung der Sturm-Liouvillesehen eigenwertaufgabe, Acta Math. 78 (1946) 1-96.

[3]. Gelfand, L.M., Levitan, B.M., On the determination of a differential equation from its spectral function, Izv. Akad. Nauk SSR. Ser. Mat. 15 (1951) 309-360 (in Russian), English transl. in Amer. Math. Soc.. Transl. Ser. 2 (1) (1955) 253-304.

[4]. Levitan B.M., Sargsjan I.S., Sturm-Liouville and Dirac Operators. Dordrecht: Kluwer; 1991.

[5]. Mochizuki, K., Trooshin, I., Inverse problem for interior spectral data of Sturm-Liouville operator, J. Inverse Ill-posed Probl. 9 (2001) 425-433.

[6]. Marchenko V., Some questions in the theory of one-dimensional linear differential operators of the second order. I. Tr.Mosk. Mat. Obs. (1952) 1:327-420. (Russian). English transl. in Am.Math. Soc. Trans. (1973) 2:1-104.

[7]. Hochstadt, H., Lieberman, B., An inverse Sturm-Liouville problem with mixed given data, SIAM J. Appl. Math. 34 (1978) 676-680.

[8]. Freiling, G., Yurko, V.A., Inverse Sturm-Liouville Problems and Their Applications, NOVA Science Publishers, New York, 2001.

[9]. Levinson, N., The inverse Sturm-Liouville problem, Math. Tidsskr, 13 (1949), 25- 30.

[10]. Rubel, L.A., Necessary and suffcient conditions for Carison's theorem on entire functions, Trans. Amer. Math. Soc. vol. 83 (1956) 417-429.

[11]. Boas, R.P., Entire functions, New York, Academic Press, 1954.

[12]. Mochizuki, K., Trooshin, I., Inverse problem for interior spectral data of the Dirac operator on a finite interval, Publ. RIMS, Kyoto Univ. 38 (2002) 387-395.

[13]. Sat, M., Panakhov, E., A uniqueness theorem for Bessel operator from interior spectral data. Abstr. Appl. Anal., Volume 2013, Article ID 713654, 6 pages.

[14]. Ozkan, A.S., Amirov, R. Kh., An interior inverse problem for the impulsive Dirac operator, Tamkang Journal of Mathematics, 42 (2011) 259-263.

[15]. Horvath, M., Inverse spectral problems and closed exponential systems, Ann. of Math. 162 (2005) 885-918.

[16]. Panakhov, E., Sat, M., Inverse problem for the interior spectral data of the equation of hydrogen atom, Ukrainian Mathematical Journal, 64 (2013), no.11.

[17]. Guo, Y., Wei, G., Inverse Sturm-Liouville problems with the potential known on an interior subinterval, Appl. Anal., 94 (5) (2015) 1025-1031.

[18]. Gesztesy F., Simon B., Inverse spectral analysis with partial information on the potential. II. The case of discrete spectrum. Trans. Am. Math. Soc. 352 (6) (2000) 2765-2787.

[19]. Shieh, C.T., Yurko, V.A., Inverse nodal and inverse spectral problems for discontinuous boundary value problems. J. Math. Anal. Appl. 347 (2008) 266-272.

Investigation on L_i ($i = l$, β, and γ)–to-$L_α$ X-ray Intensity Ratios of Tl in Thallium Compounds

Erhan CENGİZ

Alanya Alaaddin Keykubat University, Faculty of Engineering, Fundamental Science Department, Antalya, TURKEY

Abstract. The L_i ($i = l$, β, and γ)–to-$L_α$ X-ray intensity ratios of Tl in some thallium compounds were measured by EDXRF spectrometer. These compounds were excited by 59.5 keV gamma-rays from a [241]Am annular radioactive source. L X-rays emitted by the compounds were counted using an Ultra-LEGe detector with a resolution of 150 eV at 5.9 keV. L_i –to-$L_α$ X-ray intensity ratios of Tl in these compounds are compared with that of the pure Tl calculated theoretically. While the values of $L_l/L_α$ and $L_γ/L_α$ intensity ratios are compatible with the theoretically calculated value, the values of $L_β/L_α$ intensity ratios have differences.

Keywords: Thallium, intensity ratio, EDXRF, chemical effect, multiple ionization effect.

Talyum Bileşiklerindeki Tl $L_i/L_α$ ($i = l$, β ve γ) X-ışını Şiddet Oranlarının Araştırılması

Özet. Bazı talyum bileşiklerindeki talyumun $L_i/L_α$ ($i = l$, β and γ) X-ışını şiddet oranları EDXRF spektrometresi yardımıyla ölçüldü. Bu bileşikler [241]Am halka radyoaktif kaynağından yayımlanan 59.5 keV enerjili gama ışınları ile uyarıldı. Bileşiklerden yayımlanan L X-ışınları rezülasyonu 5.9 keV'ta 150 eV olan Ultra-LEGe dedektör ile sayıldı. Bu bileşiklerdeki talyumun $L_i/L_α$ X-ışını şiddet oranları saf talyum için teorik olarak hesaplanan değer ile karşılaştırıldı. $L_l/L_α$ ve $L_γ/L_α$ değerleri teorik olarak hesaplanan değer ile uyumlu iken, $L_β/L_α$ X-ışını şiddet oranı değerleri farklılıklara sahiptir.

Anahtar Kelimeler: Talyum, şiddet oranı, EDXRF, kimyasal etki, çoklu iyonizasyon etkisi.

1. INTRODUCTION

Thallium is a soft and ductile heavy metal found in the sulphide ores of heavy metals such as lead, copper and zinc, and in coal. The burning of fossil fuels, oil refining, metal smelting and some industrial operations will cause the thallium to accumulate in soil and water. The increase in the amount of thallium will cause it to be taken by plants and livestock. Thallium is a non-essential metal present in low concentrations in human tissues and is a highly toxic element. Thallium has been once used in medical treatment such as ringworm of the scalp, tuberculosis, venereal diseases and malaria, and used as a rodenticide against rats and squirrels, and used as an insecticide. Besides, thallium is used in the electrical and electronics industries, scintillation counters, low-temperature thermometers, mixed crystals for infrared instruments and laser

equipment and etc. Radioactive isotopes of thallium are used in physics for measurement of exact time periods, in industry for measuring the thickness of material, and in medicine for scintigraphy of heart, liver, thyroid and testes, and for the diagnosis of melanoma [1, 2].

Increasing the complexity of materials used in industrial and scientific applications has increased the importance of physical and chemical analysis of these materials. For this purpose, ED-XRF method has been successfully used for qualitative and quantitative analysis of element compounds in a sample [3]. Besides, the correct determination of the atomic parameters of the elements such as fluorescence cross-section, intensity ratios and fluorescence yield using ED-XRF method is particularly important in atomic, molecular and radiation physics, in medical physics. The fluorescence parameters of the K, L and M shells of the elements are used in scientific researches especially in nuclear power plants, radiation protection, storage of radioactive materials, space studies etc. Moreover, a comparison of the fluorescence parameters with theoretical estimates provides a check on the validity of various physical parameters in the evaluation of theoretical estimation [4]. When looked at the literature, the L X-ray intensity ratios of the samples have been studied by a number of researchers using different detectors and sources [5-19].

The aim of this study is to investigate the L_i ($i = l$, β, and γ)–to-L_α X-ray intensity ratios of Tl in thallium compounds occurred with different ligands, and interpret the differences between the experimental values of these compounds and the theoretical value of the pure thallium.

2.   EXPERIMENTAL PROCEDURE

The measurement geometry between detector, radioactive source and sample are shown in Figure 1. Thallium compounds were obtained commercially and their purities were better than 99%. The compounds were exposed to 59.5 keV photons emitted by an annular 50 mCi ^{241}Am radioactive source. The fluorescence L X-rays from each compound were detected by an Ultra-LEGe detector having a thickness of 5 mm and energy resolution 150 eV at 5.96 keV. The output from the preamplifier, with a pulse pile-up rejection capability, was fed to a multi-channel analyzer interfaced with a personal computer provided with suitable software for data acquisition and peak analysis. For determining peak intensity, the X-ray spectra were analyzed with the use of the Origin program. The L X-ray spectra of Tl for Tl_2SO_4 are shown in Figure 2.
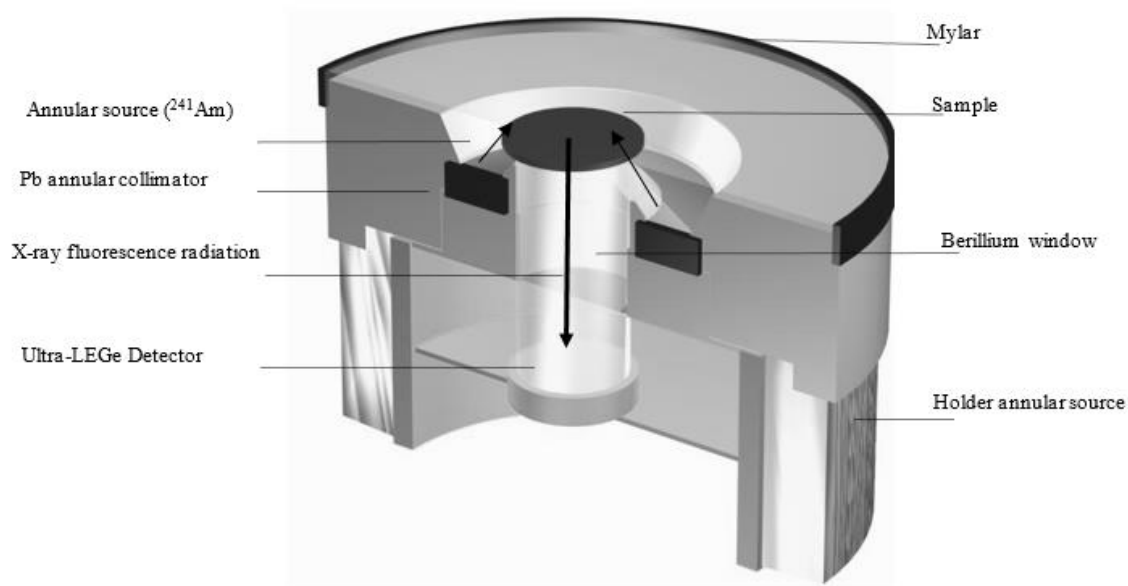
Figure 1. The measurement geometry.

The experimental L_i ($i = l$, β, and γ)–to-L_α X-ray intensity ratios were evaluated using the following equation [7]:

$$\frac{I_{L_i}}{I_{L_\alpha}} = \frac{N_{L_i}}{N_{L_\alpha}} \frac{\beta_{L_\alpha}}{\beta_{L_i}} \frac{\varepsilon_{L_\alpha}}{\varepsilon_{L_i}} \tag{1}$$

where N_{L_i} and N_{L_α} are the ratios of the counting rates under the L_i and L_α peaks; β_{L_α} and β_{L_i} are the ratios of self-absorption correction factors of the target that accounts for the absorption of incident photons and emitted L X-ray photons; and ε_{L_α} and ε_{L_i} represent the ratios of the detector efficiency values for L_α and L_i X-rays, respectively.
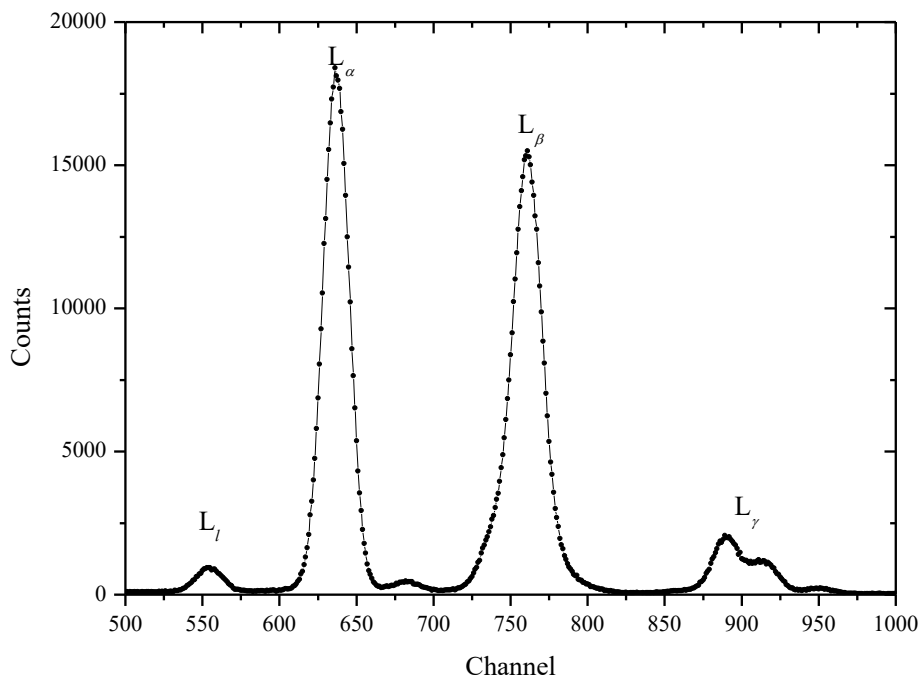
Figure 2. The K X-ray spectra of Tl in Tl$_2$SO$_4$

The self-absorption correction was calculated as below:

$$\beta_{K_X} = \frac{1 - \exp\{[-(\mu_{inc} \csc\theta_1 + \mu_{emt} \csc\theta_2)t]\}}{(\mu_{inc} \csc\theta_1 + \mu_{emt} \csc\theta_2)t} \tag{2}$$

where μ_{inc} and μ_{emt} are the mass attenuation of incident photons and emitted characteristic X-rays, respectively [20]; the angles of incident photons and emitted X-rays with respect to the sample surface, θ_1 and θ_2, were equal to 45^0 and 90^0, respectively. t is the target thickness in g/cm^2.

The product $I_0 G \varepsilon$ that contains the incident photon flux, a geometrical factor and absolute efficiency of the X-ray detector, was determined for this study by collecting K_α and K_β X-ray spectra of samples of Cr, Fe, Zn, As, Se, Sr, Zr, Ru, and Cd in the same geometry using the equation:

$$I_0 G \varepsilon_{K_x} = \frac{N_{K_x}}{\sigma_{K_x} \beta_{K_x} m_i} \qquad (x=\alpha \text{ and } \beta) \qquad (3)$$

where the terms N_{K_x} and β_{K_x} are the same meaning in Eq. (1). m_i is the elemental concentration (g/cm^2). σ_{K_x} X-ray production cross-section was calculated using the following equation [7]:

$$\sigma_{K_x} = \sigma_K(E)\omega_K F_{K_x} \qquad (4)$$

where $\sigma_K(E)$ is the K-shell photoionization cross-section of the given element for the excitation energy E [21], ω_K is the K-shell fluorescence yield [22], and F_{K_x} is the emission rate of the fractional X-ray for K_α and K_β X-rays [23].

The factor $I_0 G \varepsilon_{K_x}$ was fitted as a function of energy using the polynomials:

$$I_0 G \varepsilon_{K_x} = A_0 + A_1 E_i + A_2 E_i^2 + A_3 E_i^3 \qquad (\text{1st part}) \qquad (5)$$

$$I_0 G \varepsilon_{K_x} = B_0 + B_1 E_i + B_2 E_i^2 \qquad (\text{2nd part}) \qquad (6)$$

where E_i is the K_α or K_β X-ray energy. The variation $I_0 G \varepsilon_{K_x}$ as a function of the K X-ray energy is shown in Figure 3. The Equations 5 and 6 correspond to the left-hand side and right-hand side of Figure 3, respectively.
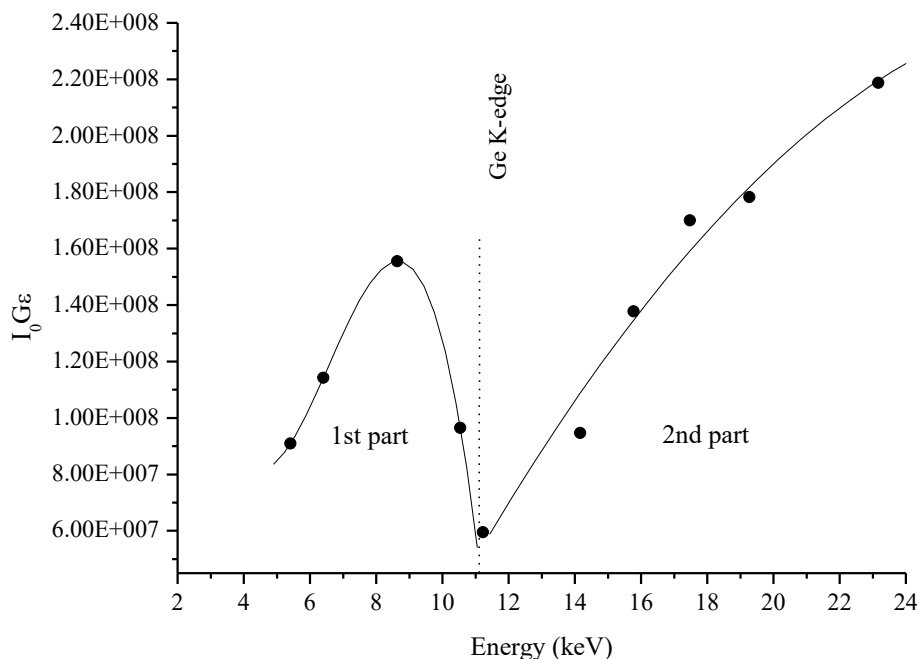
Figure 3. The variation of $I_0 G \varepsilon$ as a function of K X-ray energy.

The theoretical L-shell X-ray intensity ratios L_i/L_α were determined using the following equation:

$$\frac{I_{Li}}{I_{L\alpha}} = \frac{\sigma_{Li}}{\sigma_{L\alpha}} \qquad (i = l, \beta \text{ and } \gamma) \qquad (7)$$

where σ_{Ll}, $\sigma_{L\alpha}$, $\sigma_{L\beta}$ and $\sigma_{L\gamma}$ are the production cross-sections calculated theoretically using the following equations [7]:

$$\sigma_{L\ell} = \left[\sigma_{L1}^{P}\left(f_{12}f_{23} + f_{13}\right) + \sigma_{L2}^{P}f_{23} + \sigma_{L3}^{P}\right]\omega_{3}F_{3l} \tag{8}$$

$$\sigma_{L\alpha} = \left[\sigma_{L1}^{P}\left(f_{12}f_{23} + f_{13}\right) + \sigma_{L2}^{P}f_{23} + \sigma_{L3}^{P}\right]\omega_{3}F_{3\alpha} \tag{9}$$

$$\sigma_{L\beta} = \sigma_{L1}^{P}\omega_{1}F_{1\beta} + \left[\left(\sigma_{L1}^{P}f_{12}\right) + \sigma_{L2}^{P}\right]\omega_{2}F_{2\beta} + \left[\sigma_{L1}^{P}\left(f_{12}f_{23} + f_{13}\right) + \sigma_{L2}^{P}f_{23} + \sigma_{L3}^{P}\right]$$
$$\omega_{3}F_{3\beta} \tag{10}$$

$$\sigma_{L\gamma} = \sigma_{L1}^{P}\omega_{1}F_{1\gamma_{2,3}} + \left[\left(\sigma_{L1}^{P}f_{12}\right) + \sigma_{L2}^{P}\right]\omega_{2}F_{2\gamma_{1}} \tag{11}$$

where σ_{Li}^{P} (i=1,2,3) is the sub-shell photoionization cross-section of the given elements at 59.5 keV [21]. ωi (i=1,2,3) is the L sub-shell fluorescence yield and fij (i≠j=1,2,3) is the Coster- Kronig transition probability [22]. F_{ny} ($F_{3\alpha}$, F_{3l} etc.) is the fraction of the L X-rays originating from the L_n (n = 1, 2 and 3) transition that contributes to Ly (y = l, α, β and γ) peak [23].

3. RESULTS AND DISCUSSION

The experimental results for the L_i ($i = l$, β, and γ)–to-L_α X-ray intensity ratios of Tl in thallium compounds are presented in Table 1. The overall error in the present measurement is estimated to be 6%. This error is the quadrature sum of the uncertainties in the different parameters used to evaluate the K-shell fluorescence parameters, i.e. target thickness (2%), the evaluation of the peak area (3%), the detector efficiency $I_0G\varepsilon K_x$ (3%) and the absorption correction factor (3%).

Table 1. The experimental $I_{Li}/I_{L\alpha}$ (i=l, β and γ) intensity ratio values.

Compounds	IL_l/IL_α		IL_β/IL_α		IL_γ/IL_α	
	Exp.	Theo.	Exp.	Theo.	Exp.	Theo.
Tl_2CO_3	0.0508±0.0028	0.0518	1.2842±0.0719	1.0914	0.1699±0.0095	0.1802
Tl_2SO_4	0.0512±0.0029		1.3000±0.0728		0.1710±0.0096	
Tl_2O_3	0.0517±0.0029		1.2424±0.0696		0.1748±0.0098	
TlCl	0.0532±0.0030		1.2677±0.0710		0.1810±0.0101	
TlI	0.0518±0.0029		1.2651±0.0708		0.1873±0.0105	
$TlNO_3$	0.0511±0.0029		1.3024±0.0729		0.1743±0.0098	
Tl_2O	0.0497±0.0028		1.1472±0.0642		0.1727±0.0097	

The experimental values of the Li ($i = l$, β, and γ)–to-L_α X-ray intensity ratios of Tl in thallium compounds were compared with the theoretically calculated value of pure thallium. While the values of L_l/L_α and L_γ/L_α intensity ratios are good agreement with the theoretically calculated value of pure Tl within the experimental error, the values of L_β/L_α X-ray intensity ratios have differences. One of the reasons of the differences is the chemical effect. It is well known that the chemical effects on the energy levels and electronic transitions of the atom in a molecule can be interpreted according to the change in characteristic X-ray intensity released from the atom. The individual characteristics of the molecular structures (polarity, valence, the electronegativity of atoms, coordination number, bond type, etc.) significantly affect the positions of atomic lines.

The addition of an atom to chemical bond will result in a significant change in the electron density, particularly in the electron density of the valence. Electron density decreases or increases in the molecule, crystal or complex depending on the type of binding with the adjacent atom. In addition, the inner shell energies are strongly dependent on the change in the electron density of the atom [24]. Removal of a valence electron of the atom in the bond formation will change both the density and the shielding of the valence electrons. A reduction in the shielding effect will be observed and the remaining electrons will bind more tightly to the atom. Thus, a shift will be observed in the binding energies of the inner shell electrons. The change in these binding energies will increase with the increase in the number of valance electrons involved in the bond formation [25]. This will cause changes in X-ray peak shape and intensity. The valence states of thallium consist of 6s and 6p electrons. These electrons determine the chemical properties of the elements. L_β and L_γ transitions may be most affected by chemical effects. Because these transitions take place from the shells close to the valence shell.

Another reason for the difference between experimental and theoretical values of L_β/L_α X-ray intensity ratios may be the effect of electron removal from the shells above the L shell. Multiple ionization processes occur as a result of collisions of energetic particles with atoms or ions, or by reorganization of atomic shells after the an initial inner-shell vacancy has been filled [26]. For ionized atoms, very different configurations are possible depending on the number of electrons extracted from the different shell or subshell [27]. Multiple ionization of atoms can be a source of observed deviations. Because the additional ionizations generated on the worked shell can change the possibilities of Auger, Coster-Kronig, Super Coster-Kronig and radiative transition probabilities [28]. In the case of multi-ionized atoms, the shielding of the inner shell electrons is changed, so that the electrons' bonding energy also changes. This changes the life time of situations, and the X-ray peak shape and peak intensity are modified. The change in peak intensity and peak shape is strongly associated with non-radiative transitions. The non-radiative transitions for Tl were presented by Cooper [29]. These transitions may be affected by the reorganization process of the atomic shells. Consequently, the L X-ray intensity ratios can be affected. Therefore, the observed deviations on the L shell fluorescence parameters may also arise from the multiple ionization effect.

Acknowledgments

REFERENCES

[1]. Kazantzis G., Thallium in the Environment and Health Effects, Environ. Geochem. Health, 22 (2000) 275-280.

[2]. Frattini P., Thallium Proporties and Behaviour-A Litterature Study, Geological Survey of Finland, (2005).

[3]. Unterumsberger R., Hönicke P., Pollakowski-Hermann B., Müller M. and Beckhoff B., Relative L3 transition probabilities of titanium compounds as a function of the oxidation state using high-resolution X-ray emission spectrometyry, Spectrochim. Acta B 145 (2018) 71-78.

[4]. Apaydın G., Aylıkcı V., Kaya N., Cengiz E. and Tıraşoğlu E., Measurement of L Shell X-ray Production and Average L Shell Fluorescence Yields for Some Heavy Elements at 123.6 keV, Acta Phys. Pol. A 113 (2008) 1629-1638.

[5]. Doğan M., Cengiz E., Nas A, Tıraşoğlu E., Kantekin H. And Aylıkcı V., L Shell X-ray Fluorescence Parameters of Pb in phyhalocyanine complexes, Appl. Radiat. Isot., 104 (2015) 43-48.

[6]. Kaçal M.R., Durak R., Akman F., Turhan M.F. and Han, I., Measurement of L Subshell Fluorescence Cross Sections and Intensity Ratios of Heavy Elements at 22.6 keV, Rad. Phys. Chem., 80 (2011) 692-700.

[7]. Cengiz E., Tıraşoğlu E., Aylıkcı V. and Apaydın G., The investigations on K and L X-ray fluorescence parameters of gold compounds, Rad. Phys. Chem., 79 (2010) 809-815.

[8]. Kumar A., Chauhan Y. and Puri S., Incident Photon Energy and Z Dependence of L X-ray Relative Intensities, Atom. Data Nucl. Data, 96 (2010) 567-585.

[9]. Cengiz E., Tıraşoğlu E., Aylıkcı V., Apaydın G. and Küp Aylıkcı N., Investigation on L-shell X-ray fluorescence parameters of heavy elements and compounds, Chem. Phys. Lett., 498 (2010) 107-112.

[10]. Cipolla S.J., L X-ray Intensity Ratios for Proton Impact on Selected Rare-earth Elements, Nucl. Instr. and Meth. B, 261 (2007) 153-156.

[11]. Karabulut A. and Gürol A., Measurement of L X-ray Fluorescence Cross Sections and Relative Intensity Ratios for Some Elements in the Atomic Range 72≤ Z≤92, Nucl. Instr. and Meth. B, 244 (2006) 303-306.

[12]. Salah W. and Al-Jundi J., Measurement of L X-ray Cross Sections and Relative Intensities of Heavy Elements by 15.2 keV Photons, J. Quant. Spectrosc. Rad. Trans., 94 (2005) 325-333.

[13]. Kurmaev E.Z., Ankudinov A.L., Rehr J.J., Finkelstein L.D., Karimov P.F. and Moewes A., The L2:L3 Intensity Ratio in Soft X-ray Emission Spectra of 3d Elements, J. Electron Spectrosc., 148 (2005) 1-4.

[14]. Liu Z., Yuge K. and Kawai J., High Resolution X-ray Fluorescence Spectra of Palladium Compounds, Spectrochim. Acta B, 59 (2004) 93-99.

[15]. Ramakrishna Y., Rao K.R., Nagu Raju G., Rao K.B., Rao V.S., Venkateswarlu P. and Reddy S.B., L X-ray Energy Shifts and Intensity Ratios in Tantalum with C and N Ions-multiple Vacancies in M, N and O Shells, Pramana J. Phys., 59 (2002) 685-691.

[16]. Ismail A.M. and Malhi N.B., L Shell X-ray Relative Intensities of Some Heavy Elements Excited by 20.48 keV X-rays, X-ray Spectrom., 29 (2000) 317-319.

[17]. Raghavaiah C.V., Rao N.V., Reddy S.B., Satyanarayana G. and Sastry D.L., Lα/ Ll X-ray Intensity Ratios for Elements in the Region 55≤Z≤80, J. Phys. B: At. Mol. Phys., 20 (1987) 5647-5651.

[18]. Verma H.R. Pal D., Garg M.L. and Trehan P.N., Photon Induced L Shell X-ray Intensity Ratios for 74W and 80Hg in the Energy Range 17≤E≤47 keV, J. Phys. B: At. Mol. Phys., 18 (1985) 1133-1138.

[19]. Shadendra K., Allawadhi K.L. and Sood B.S., Energy Dependence of Photon-induced L Shell X-ray Intensity Ratios in Some High Z Elements, J. Phys. B: At. Mol. Phys., 16 (1983) 4313-4322.

[20]. Berger, M. J., Hubbell, J. H., Seltzer, S. M., Chang, J., Coursey, J. S., Sukumar, R and Zucker, D. S., 2005. XCOM: Photon Cross Section Database (version 1.3) [Online] (Gaithersburg, MD: National Institute of Standards and Technology), available at http://physics.nist.gov/xcom.

[21]. Scofield J.H., Theoritical Photoionization Cross Sections from 1 to 1500 keV, Lawrence Livermore Laboratory (UCRL), No: 513626 (1973).

[22]. Krause M.O., 1979. Atomic Radiative and Radiotionless Yields for K and L Shells, J. Phys. Chem. Ref. Data 8 (1979) 307-327.

[23]. Scofield J.H., Relativistic Hartree-Slater Values for K and L Shell X-ray Emission Rates, Atom. Data and Nucl. Data, 14 (1974) 121-137.

[24]. Mazalov, N. ve Treiger, B.A., Chemical Bonding Effects in X-ray Spectral Analysis, Struct. Chem., 24 (1983) 276-305.

[25]. Agarwal, B.K., X-ray Spectroscopy: An Introduction, Springer-Verlag, Berlin, New York, (1979).

[26]. Zschornack, G., Handbook of X-ray Data. Springer Berlin Heidelberg Press, Newyork, (2007).

[27]. Carlen, M.W., Polasik, M., Boschung, B., Dousse, J.-Cl., Gasser, M., Halabuka, Z., Hoszowska, J., Kern, J., Perny, B. ve Rheme, Ch., M- and L-shell Ionization in Near-central Collisions of 5.5 MeV/amu 16O Ions with Mo Atoms Deduced from Theoretical Analysis of High Resolution K X-ray Spectra, Phys. Rev. A, 46 (1992) 3893-3903.

[28]. Pajek, M., Banas, D., Semaniak, J., Braziewiez, J., Majewska, U., Chojnacki, S., Czyzewski, T., Fijal, I., Jaskola, M., Glombik, A., Kretscmer, W., Trautmann, D., Lapicki, G. ve Mukoyama, T., Multiple Ionization and Coupling Effects in L-subshell Ionization of Heavy Atoms by Oxygen Ions, Phys. Rev. A, 68 (2003) 022705-022722.

[29]. Cooper J.N., Auger Transitions and Widths of X-ray Energy Levels, Phys. Rev. 65 (1944) 155-161.

Cumhuriyet Science Journal
CSJ

Curcumin-Loaded Bio-Based Electrospun Polyurethane Scaffolds

Nesrin HORZUM POLAT[1,2] iD , Nehir Arık KINALI[2] iD

[1]*Izmir Katip Celebi University, Faculty of Engineering and Architecture, Department of Engineering Sciences, Izmir, TURKEY*

[2]*Izmir Katip Celebi University, Graduate School of Natural and Applied Sciences, Department of Biocomposite Engineering Graduate Program, Izmir, TURKEY*

Abstract. Polymeric electrospun fibers present well-design scaffolds for wound healing applications. Here, the fabrication of biobased polyurethane (PU) blend fibers containing curcumin (Cur) was reported. Not only polymer concentration but also curcumin concentration affects the morphology, diameter, and contact angle values of the fibers. Morphological investigations revealed that the diameter and hydrophilicity of the PU fibers increased upon addition of curcumin. Effect of process parameters (applied voltage, flow rate, and tip-to-collector distance) on the average diameter and the hydrophilicity of the PU and PU/Cur fibers were examined. Optimum conditions to obtain uniform and bead-free PU/Cur fibers were determined as 12.5 kV, 1 mL/h, and 17 cm. This study demonstrates that the electrospinning process provides a simple way of obtaining bioactive agent loaded fibrous scaffolds, as well as contributing to a better understanding of the effect of process variables in the fabrication of PU/Cur blend fibers for wound healing applications.

*Keywords***:** Biomaterials, bio-based polyurethane, curcumin, electrospinning, fibers, wound healing.

Kurkumin Yüklü Biyo-Bazlı Elektroeğirme Poliüretan Yapılar

Özet. Polimerik elektroeğirme lifler, yara iyileşme uygulamaları için iyi tasarımlı iskeleler sunmaktadır. Burada, kurkumin (Cur) içeren biyobazlı poliüretan (PU) karışım liflerin üretimi rapor edilmektedir. Yalnızca polimer konsantrasyonu değil, aynı zamanda kurkumin konsantrasyonu, fiberlerin morfolojisi, çapı ve temas açısı değerlerini etkilemiştir. Morfolojik araştırmalar, PU liflerinin çapının ve hidrofilikliğinin kurkumin ilavesi üzerine arttığını ortaya koymuştur. Proses parametrelerinin (uygulanan voltaj, akış hızı ve uçtan toplayıcıya mesafe) PU ve PU/Cur liflerinin ortalama çap ve hidrofilikliği üzerindeki etkileri incelenmiştir. Homojen ve boncuksuz PU/Cur lif elde etmek için optimum koşullar 12.5 kV, 1 mL/s ve 17 cm olarak belirlenmiştir. Bu çalışma, elektroeğirme işleminin, biyoaktif madde yüklü lifli iskeleleri elde etmenin basit bir yolunu sağlamasının yanı sıra, PU/Cur karışım liflerinin imalatında yara iyileşmesi uygulamaları için işlem değişkenlerinin etkisinin daha iyi anlaşılmasına katkıda bulunduğunu göstermektedir.

*Anahtar Kelimeler***:** Biyomalzemeler, biyo-tabanlı poliüretan, kurkumin, elektroeğirme, lifler, yara iyileşmesi

1. INTRODUCTION

Along with the increased role of nanotechnology in multidisciplinary research, electrospinning technique has become a significant step in the fabrication of nano/microfibers. This technique provides the fabrication of fibrous mats from both organic and/or inorganic materials and finds their potential applications in the field of biosensors, drug delivery, tissue engineering, and wound dressing. Electrospun scaffolds mimic extracellular matrix (ECM) since it has a fiber-like structure with a highly effective surface for

adhesion and cell growth. It is well known that an ideal scaffold should act like an ECM, as structural and biological functions, which is responsible of regulating cellular activities and mechanical support.

Many biomaterials such as alginate, cellulose, chitosan, collagen, and poly (ε-caprolactone) are promising for biomedical applications [1]. Medicinal plant extracts, spices, and essential oils have also been used as biologically active agents for personal care, pharmaceuticals, and food-processing applications [2-4]. Curcumin (Cur) is one of the most widely used spices for the treatment of many inflammatory wounds and other diseases [5]. Cur, which is obtained from the rhizomes of *Curcuma longa*, has most of the pharmaceutical properties such as antioxidant [6], anti-inflammatory [7], hypoglycemic effect [8], antitumor [9], anti-HIV [10], induces apoptosis of damaged hepatocytes[11] and wound healing activities [12].

There are many researchers working on electrospun nanofibers to develop scaffolds for wound dressing and tissue engineering [13-15]. Dhurai et al. [16, 17] fabricated the Cur-loaded chitosan and chitosan/PLA nanofibers, and tested their suitability for wound healing. The results showed the reduction of wound area due to the presence of both Cur and chitosan. Cur-incorporated electrospun nanofibers of a blend of poly (lactic acid) (PLA) and hyperbranched polyglycerol (HPG) were used for a potential wound patch dressing for acute and chronic wound dressing [18]. Fabrication of Cur-loaded poly(3-hydroxy butyric acid-*co*-3-hydroxy valeric acid) (PHBV) nanofiber-based wound dressing materials was reported by Mutlu et al. [19], who found that PHBV and PHBV/Cur nanofibers enhanced the cell attachment and proliferation. Shababdoust et. al. [20] described the fabrication of Cur-loaded polycaprolactone (PCL) (with two different molecular weights; 2000 and 530 Da)-based polyurethane (PU) substrate. They demonstrated that Cur-loaded PU synthesized by PCL with a molecular weight of 2000 Da showed better mechanical properties as

well as better antibacterial properties for wound dressing applications. Sedhgi et.al. [21] fabricated electrospun nanofibers with using graphene oxide (GO) and Zn-Cur complex, and they investigated the capacity of the Zn-Cur scaffolds for bone regeneration. They reported that the Zn-Cur composite nanofibers with advanced osteogenic capacity and cytocompatibility were promising for bone tissue engineering. In a very recent work, Li et. al [22] have presented the formation of the sandwich structure composite (SSC) membranes which have three layers, including polyvinylidene fluoride fibrous layer (bottom), Cur/PLA microsphere layer (middle), and the enrofloxacin/PLA fibrous layer (top), respectively. The drug-loaded SSC membranes showed a precise antioxidant activity against •OH and diphenyl picryl hydrazinyl (DPPH) free radicals, and antibacterial activity against *Staphylococcus aureus, Escherichia coli, Streptococcus pneumonia, Pseudomonas aeruginosa*, and *Candida albicans.*

Electrospun fibers also provide some advantages such as cost-effective, high surface area, high loading or encapsulation capacity, and the increased bioavailability of the drug [23]. From the structural point of view, processing, solution, and environmental parameters affect the morphology of the fibers formed. The fabrication of electrospun nanofibers from biopolymers is preferred because of their biocompatibility, biodegradability, non-toxicity, and antimicrobial activity [24, 25]. PU is one of the most commonly used polymers in electrospinning because of its good barrier properties, oxygen permeability, biocompatibility, and easy availability, and it has been studied as a wound dressing material for many years [26]. The fiber scaffolds we present in this paper are electrospun from a blend of Cur and bio-based polyurethane (PU) in *N, N*-dimethylformamide (DMF) as a solvent. This study demonstrates that electrospinning provides a simple way to obtain fibrous scaffolds containing bioactive agents and can also contribute to a better understanding of the effect of process variables on the fabrication

of PU/Cur blend fibers for further use in wound healing applications.

2.   MATERIALS AND METHODS

Materials

Bio-based polyurethane (PU) with a product name of (Pearlthane® ECO D12T85, Lubrizol) was used as a raw material for biopolymer matrix and *N, N*-dimethylformamide (DMF, Sigma-Aldrich) was used as a solvent. *Curcuma longa* (Turmeric) (Cur, Sigma) was added as a bioactive agent. All the reagents were used without further purification.

Preparation of the Electrospinning Solutions

The polymer solutions were prepared by dissolving the PU in DMF at the concentrations of 5, 10, 12.5, and 15 wt% under magnetic stirring for 24 hours at room temperatue. Cur was added at the different concentrations (1, 5, and 10

wt%) into the 12.5 wt% PU solutions and left for 24 hours under stirring.

Fabrication of PU and PU/Cur Scaffolds

PU and PU/Cur fibers were fabricated via a commercial electrospinning platform (Inovenso Basic Setup) covered with a polycarbonate cabinet for safety and avoiding from air convection.

The solutions of PU and PU/Cur were filled in the 5 mL plastic syringes. The positive electrode was applied to the spinneret; a rectangular stainless-steel plate was used as a collector which was covered by an aluminum foil for counter electrode. Electrospinning of the solutions was performed with a flow rate of 1.0─1.5 mL/h, applied voltage of 10─15 kV, and tip-to-collector distance of 14─20 cm. The electrospinning parameters are given in Table 1. The working conditions were performed at ambient conditions. (55% RH, 25 ºC).

Table 1. Electrospinning parameters used to fabricate the PU and PU/Cur fibers.

Solutions (wt%)	Applied voltage (kV)	Flow rate (mL/h)	Tip-to-collector distance (cm)
PU (5, 10, 12.5, and 15)	12.5	1.00	17.0
PU (12.5) / Cur (1, 5, 10)	12.5	1.00	17.0
PU (12.5) / Cur (5)	10.0 – 12.5 – 15.0	1.00 – 1.25 – 1.50	14.0 – 17.0 – 20.0

Characterization of PU and PU/Cur Scaffolds

To determine the surface morphology of the fibers, scanning electron microscopy (SEM) was performed using Carl Zeiss 300 VP and fiber diameters were calculated by Fiji ImageJ software. In order to evaluate the hydrophilicity of the fibers, the water contact angle (CA) was measured by a Theta Lite Optical Tensiometer, (Finland). Sessile drops of 4 µL of water were deposited on the surface of the fibrous scaffolds and the measurements were conducted at least three different sample areas and averaged for each sample. X-ray diffraction (XRD) patterns of fiber samples were recorded in a Philips X'Pert Pro X-ray diffractometer using CuKα radiation (λ= 1.5418 Å). Fourier transform infrared

spectroscopy (FTIR, Thermo Scientific™ Nicolet™ iS™5) was performed for PU and PU/Cur blend fibers.

3.   RESULTS AND DISCUSSSON

The optimization of fiber fabrication by electrospinning depends on various factors which affect the formation of fibers, including solution, process, and environmental parameters. PU and PU/Cur fibrous mats were fabricated by electrospinning PU and PU/Cur solutions in DMF with different PU and Cur concentrations. The effects of solution concentrations, applied voltage, flow rate, and tip-to-collector distance on the morphology of the PU and PU/Cur fibers were investigated. The surface hydrophilicity was also

examined for further applications of the fibrous scaffolds as a wound dressing.

Effect of PU and Cur Concentration

Solvent type, solution concentration, viscosity, and conductivity are the important solution parameters for electrospinning. The stretching of a charged jet is significantly influenced by varying the electrospinning solution concentration. As a general rule, at low polymer concentration, the applied electrical field and surface tension lead to the disintegration of the entangled polymer chains and result in bead or beaded fiber formation [27]. As the concentration of the polymer in the solution increases, fiber diameter also increases. The increase in the fiber diameters can be attributed to the increase in viscosity of the electrospinning solution. When the enhanced chain entanglements overcome the surface tension of the droplet, uniformly distributed bead-free fibers can be obtained [28].

Figure 1 (a-d) shows the changes in morphology of the fibers with an increasing amount of PU in DMF. The low polymer concentration (5 wt%) resulted in the beaded fibrous structure (Figure 1a). Furthermore, the bead density decreased with the increasing PU concentration beyond 5 wt% and bead-free fibers were collected. The average diameters and surface contact angles of PU fibers were demonstrated in Figure 1(e-f). The diameters of the fibers obtained from 5, 10, 12.5 and 15 wt% PU / DMF solutions are 250 ± 80, 370 ± 130, 480 ± 150, and 850 ± 250 nm, respectively. An exponential growth with the polymer content was observed, transferred PU content from tip-to-collector was increased, and hence thicker fibers are obtained.

The wettability of the PU fibers obtained from 5, 10, 12.5 and 15 wt% PU / DMF solutions are measured as $72 \pm 7°$, $92 \pm 4°$, $94 \pm 5°$, and $96 \pm 3°$, respectively. PU fibers exhibit a hydrophilic nature when the PU content is 5 wt%. As the concentration of PU increases from 10 to 15 wt%, the water contact angle increases, indicating the hydrophobicity. This can be explained by the

changing ratio of adhesive forces (polymer-solvent) and cohesive forces (solvent-solvent). When adhesive forces are less than cohesive forces, the contact angle is higher than 90 degrees, tends not to wet the surface of the scaffold [29]. In addition, taking the diameter of the PU fibers into consideration, it has been observed that the increment in the concentration affects not only the fiber diameters but also the porosity (originated by the fiber network) which may be related to the increase in hydrophobicity.
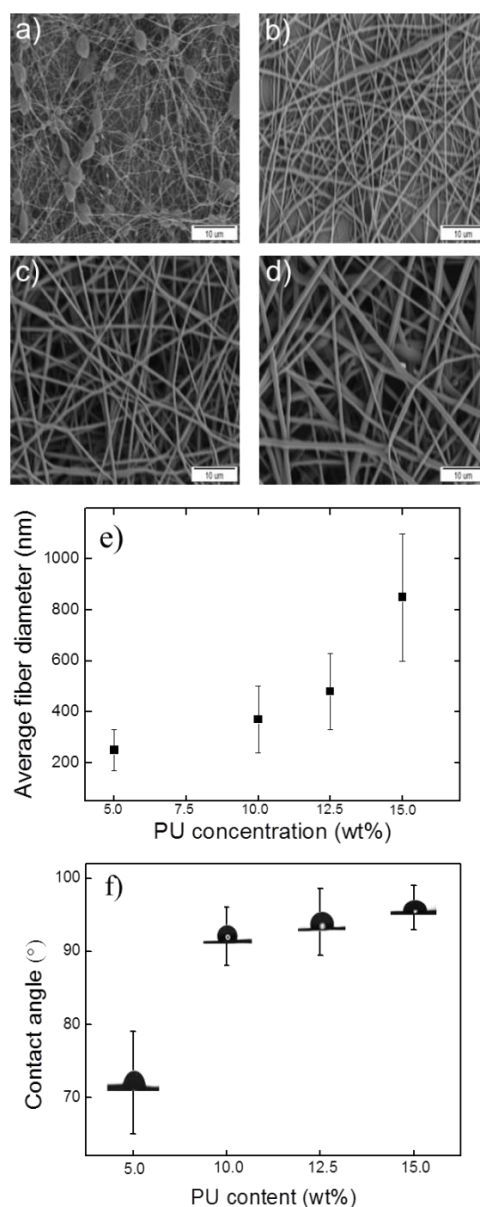
Figure 1. SEM micrographs of PU fibers obtained from electrospinning a) 5 wt% , b) 10 wt%, c) 12.5 wt%, and d) 15 wt% PU/DMF solutions. e) Average fiber diameter and f) contact angle of the fibers as functions of PU weight fraction. (Applied voltage: 12.5 kV, Flow rate: 1.00 mL/h, Distance: 17 cm).

Besides PU fibers, Cur-loaded PU fibers were also fabricated. SEM micrographs as well as photographic images, average fiber diameters, and contact angles of the fibers are shown in Figure 2. The morphology of the fibers are smooth however, as Cur content is increased, non-uniformly distributed bead-free fibers with larger diameters are obtained because of the increased viscosity. (Figure 2 (a-d)) Furthermore, higher Cur content results in fiber sticking together. The diameters of the blend fibers containing 0, 1, 5, and 10 wt% Cur are 480 ± 150, 525 ± 70, 960 ± 210, and 780 ± 155 nm, respectively. (Figure 2e) When the Cur concentration is 10 wt%, solution viscosity can be considered above the optimum value for the fiber formation that Cur is no longer able to penetrate into the fiber. As already shown in the photographic images of the blend fibers, free droplets are observed around the fiber mat containing 10 wt% Cur. A similar trend was observed for the diameter of curcumin-loaded PCL/chitosan [30], polyurethane [20] and cellulose acetate [14] fibers. The resultant thicker fibers with the addition of curcumin were attributed to the higher viscosity of the electrospinning solution and lower solvent evaporation rate. However, reduced diameter of the fibers with the increased curcumin content has also been reported by some researchers [19, 31]. The addition of curcumin leads to a decrease in the polymer concentration and enhance the conductivity of the blend solution, hence thinner fibers are obtained by overcoming the surface tension and stretching easily. This conflict may be interpreted as the differences in the used polymer/solvent combinations. Table 2 also includes the effect of curcumin addition on the properties of electrospun fibers for given system parameters.

The contact angles of the blend fibers containing 0, 1, 5, and 10 wt% Cur are $94 \pm 5°$, $90 \pm 0.5°$, $88 \pm 1.4°$, and $92 \pm 1.7°$, respectively. In general, the water contact angle relatively decreases with the addition of Cur, (Figure 2f) indicating that Cur has higher wettability than that of PU, due to the presence of hydrophilic functional groups. Fallah et al. reported that PCL/gelatin nanofibers became more hydrophilic by the incorporation of curcumin [32].

Table 2. Overview of the curcumin-loaded electrospun fibers in literature.

Samples	Curcumin content (%)	Solvent	AFD (nm)	CA (°)	Electrospinning parameters	Ref.
PLA 10% (wt/v) PLA/HPG 10/20 % (wt/v)	10.0	Chloroform /methanol	516±174 601±194	108±1 113±3	13-15 kV 0.5 mL/h 12 cm	[18]
PHBV 10 % (w/v)	0 0.1 0.3 0.5	Chloroform /DMF	519±15 304±94 215±48 207±56	-	17 kV 0.6 mL/h 20 cm	[19]
PU2000 20 (wt%) PU530 30 (wt%)	0 5.0 10.0 0 5.0	HFIP	172±64 256±110 274±107 200±80 284±112	85.8±2.6(film) 97.0±1.2(film)	20 kV 0.5 mL/h 21 cm	[20]
Almond gum/PVA 8 % (w/w) Almond gum/PVA 7 % (w/w)	1.0 2.0 3.0 4.0	Water/ethanol	169±35 151±28 121±31 127±29	-	18 kV 0.125 mL/h 15 cm	[31]
PLA 10 (wt%)	0, 1, 3, 5, 7, 9, and 11 wt%	Chloroform /acetone	1500-900	-	18 kV 0.5 mL/h 12 cm	[33]
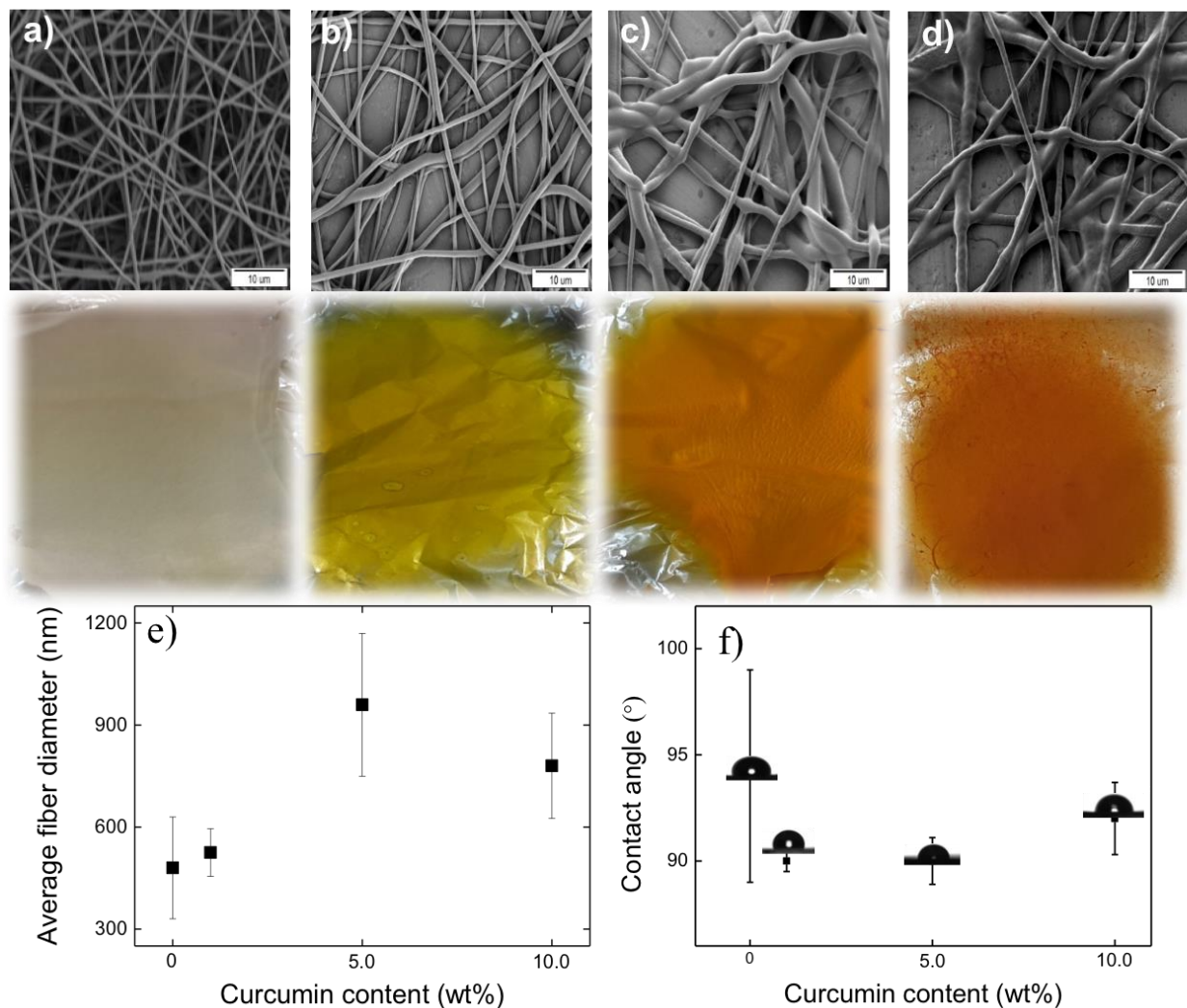
Figure 2. SEM micrographs and photographic images of the PU and PU/Cur fibers different curcumin concentrations a) 0 wt%, b) 1 wt%, c) 5 wt%, and d) 10 wt%. e) Average fiber diameter and f) contact angle of the fibers as functions of curcumin weight fraction. (Applied voltage: 12.5 kV, Flow rate: 1.00 mL/h, Distance: 17 cm, PU content in PU/Cur fibers: 12.5 wt%).

Effect of Electrospinning Parameters on the PU/Cur fibers

Processing variables such as applied voltage, flow rate, and tip-to-collector distance need to be considered for the fabrication of fibers. The size and hydrophilicity of the PU/Cur fibers are summarized in Table 3.

Applied voltage has a significant effect on the diameter of the PU/Cur fibers. The average fiber diameter increases from 730±160 to 1115±225 nm when the applied voltage rises from 10.0 to 15.0 kV, respectively. This applied electric field dependent increase can be explained as more polymer ejection and formation of large diameter fibers. Fallah et al. [32] showed that

PCL/gelatin/curcumin nanofibers have an increasing diameter with the increasing voltage ranging from 10 to 20 kV. In another example, Hoang et al. [30] reported the increased diameter of PCL/chitosan fibers with respect to the applied voltage (15, 18, and 24 kV), pointing out the higher electrostatic force results in the multi-jet formation, hence the multiple fibers can stick each other and form thicker fibers. It can be noted that applied voltage affects not only the fiber diameter but also the hydrophilicity of the fibers, as shown by the contact angle values. Fibers with larger diameter resulted in a larger contact angle. Since more uniform and the least hydrophobic fibers were obtained at 12.5 kV, this value was selected to investigate the other variables in this study.

Using different solution flow rates ranged between 1.00 and 1.50 mL/h, not any particular trend was observed in the diameter and contact angle value of the PU/Cur fibers. The diameters of the PU/Cur fibers showed first an increase then a decrease, this is probably due to the ejection of more solution from the needle, however, when the voltage is constant if electrical field is not enough for stretching of the solution, some of the solutions coming out of the needle tip drops and cannot reach the collector [32]. That is, a 12.5 kV applied voltage is not sufficient to transport all the solution moving at a rate of 1.50 mL /h to the collector. Therefore, the optimum flow rate was determined as 1.00 mL/h, at least under the ranges employed in this study.

As it is usually the case, increasing the distance between the needle tip and collector caused a decrease in the average fiber diameter. When the distance increases, the time for the formed fiber to reach the collector as well as the evaporation of the solvent increases, which leads to the elongation and thinning of the fibers [34, 35]. The average diameter of the PU/Cur fibers fabricated at an applied voltage of 12.5 kV and a flow rate of 1.00 mL/h was shown to reduce around 30% with increasing the distance. On the other hand, varying the distance did not show any obvious effect on the contact angle values of the PU/Cur fibers.

Taking the process variables employed in this study into consideration, optimum conditions for PU/Cur fibers were determined as 12.5 kV, 1 mL/h, and 17 cm. Therefore, these parameters were kept constant for further characterization of the fibers obtained from 5wt% Cur containing 12.5 wt% PU/DMF solution.

Table 3. Electrospinning parameters, average fiber diameter and contact angle values of PU/Cur fibers. (PU content: 12.5 wt%, Cur content: 5 wt%).

Parameters			AFD (nm)	Contact Angle (°)
Applied voltage (kV)	10.0	Flow rate: 1.00 mL/h Tip-to-collector distance: 17 cm	730 ± 160	91 ± 1.0
	12.5		960 ± 210	90 ± 1.1
	15.0		1115 ± 225	109 ± 2.5
Flow rate (mL/h)	1.00	Applied voltage: 12.5 kV Tip-to-collector distance: 17 cm	960 ± 210	90 ± 1.1
	1.25		1235 ± 125	91 ± 1.0
	1.50		955 ± 195	93 ± 2.0
Tip-to-collector distance (cm)	14.0	Applied voltage: 12.5 kV Flow rate: 1.00 mL/h	1390 ± 285	96 ± 1.5
	17.0		960 ± 210	90 ± 1.1
	20.0		1000 ± 215	108 ± 2.0

Structural Characterization of the PU/Cur fibers

X-ray diffraction (XRD) also proved the presence of curcumin particles in the PU fibers, as shown in Figure 3. The diffraction halo between 15° and 30° are attributed to semi-crystalline phase of the PU [36]. PU/Cur fibers have new diffraction signals at 22° and 25°, which indicates the curcumin [31, 37]. It is noteworthy to mention that although pure curcumin has a number of reflections between 10 and 30°, [31, 37] the crystalline nature of curcumin in the fibers decreases because of rapid solidification during the electrospinning preventing the stretched molecular chains to form ordered crystal structures [13, 38].
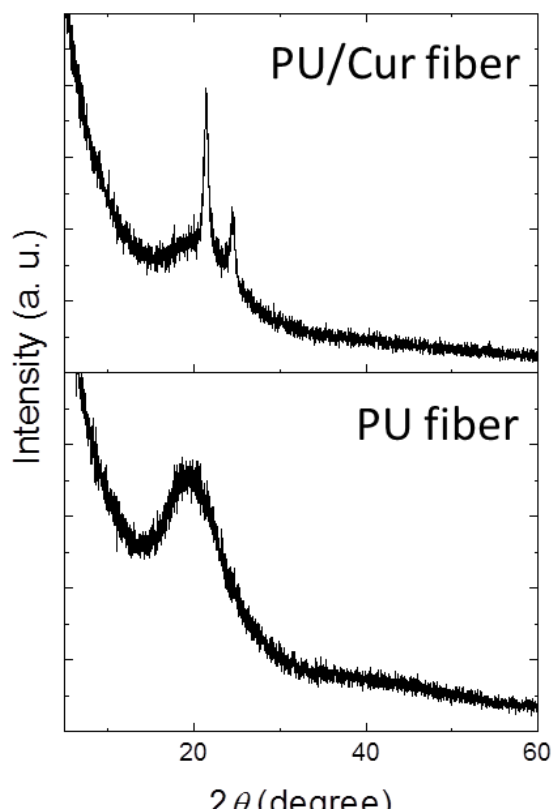
Figure 3. XRD patterns of of PU and PU/Cur fibers (PU content: 12.5 wt%, Cur content: 5 wt%, Applied voltage: 12.5 kV, Flow rate: 1.00 mL/h, Distance: 17 cm).

Figure 4 shows the FTIR spectra of the PU and PU/Cur fibers with the chemical structures of PU and Cur. The characteristic absorption bands of PU were observed. These are C = O (amide I) stretching at 1729 cm^{-1}, O─C─N (amide II) stretching at 1530 – 1595 cm^{-1}, N─H (amide III) bending at 1260 cm^{-1} and N─H stretching vibrations at 3330 cm^{-1}. The bands appeared at 2927 – 2846 cm^{-1} due to the CH$_2$ stretching, C─N and C─O stretchings at 1226 cm^{-1}, C─O─C symmetric stretching vibrations at 1166 cm^{-1} [39]. (Figure 4a) The band around 3510 cm^{-1}, which is attributed to the characteristic phenolic OH stretching vibration, was prominent in the PU/Cur (10 wt%) fibers. The disappearance of this stretching vibration with decreasing curcumin concentration and the broadening at around 3550 – 3150 cm^{-1} may be attributed to the formation of a hydrogen bond between curcumin and PU [28, 32]. (Figure 4b) Moreover, the strong stretching vibrations of the benzene ring at 1625 cm^{-1} and the olefinic C─H bending vibration at 1452 – 1420 cm^{-1} appeared in the PU/Cur (10 wt%) fibers. The bending vibrations of the enol C─O band at 1270 cm^{-1} and the C─H bond of the alkene groups at 966 cm^{-1} were detected [28]. (Figure 4c)
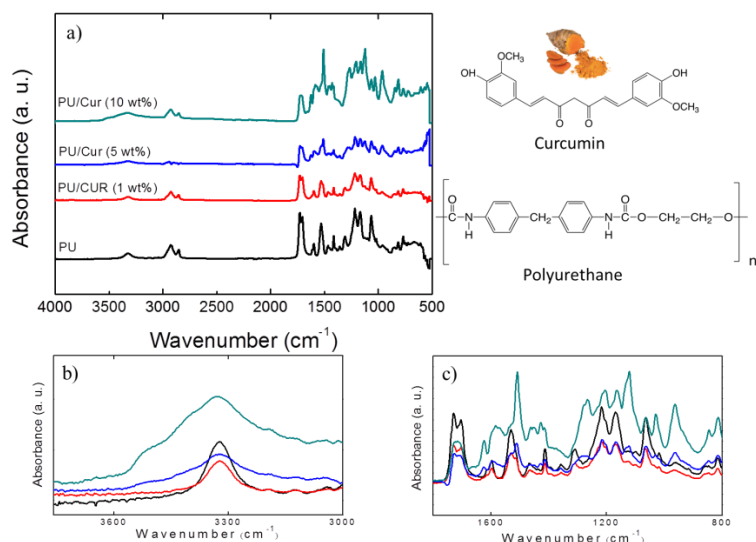
Figure 4. (a) FTIR spectra of the PU and PU/Cur fibers, (b) and (c) show the enlarged view of the spectra.

4. CONCLUSION

We have shown a simple method to fabricate curcumin-loaded polyurethane (PU/cur) fibrous scaffolds, which can be further used as a wound dressing. the fiber diameters of the pu fibers ranged from 250 to 850 nm, PU/cur fibers ranged from 525 to 960 nm. the fabrication of fibrous scaffolds containing with the desired properties is promising for the advancement of the biomaterials to be used in various biomedical healthcare sectors. ın addition, bioactive agents (such as herbal extracts, essential oils) may be good alternatives to the chemical based materials. a detailed study dealing with various essential oils, controlled bioactive agent release, cell proliferation, and cytotoxicity tests is underway.

Acknowledgements

REFERENCES

[1]. Moura, D., M.T. Souza, L. Liverani, G. Rella, G.M. Luz, J.F. Mano, and A.R. Boccaccini, Development of a bioactive glass-polymer composite for wound healing applications. Mater. Sci. Eng. C-Mater. Biol. Appl., 76 (2017) 224-232.

[2]. Regnier, T., S. Combrinck, and W. Du Plooy, Essential oils and other plant extracts as food preservatives. (2012) 539-579.

[3]. Christaki, E., E. Bonos, I. Giannenas, and P. Florou-Paneri, Aromatic plants as a source of bioactive compounds. 2 (2012) 228-243.

[4]. Sarkic, A. and I. Stappen, Essential oils and their single compounds in cosmetics—a critical review. 5 (2018) 11.

[5]. Pizzo, P., C. Scapin, M. Vitadello, C. Florean, and L. Gorza, Grp94 acts as a mediator of curcumin-induced antioxidant defence in myogenic cells. J. Cell. Mol. Med., 14 (2010) 970-981.

[6]. Aziz, M.T.A., M.F. El-Asmar, I.N. El-Ibrashy, A.M. Rezq, A.L. Al-Malki, M.A. Wassef, H.H. Fouad, H.H. Ahmed, F.M. Taha, A.A. Hassouna, and H.M. Morsi, Effect of novel water soluble curcumin derivative on experimental type-1 diabetes mellitus (short term study). Diabetol. Metab. Syndr., 4 (2012) 30.

[7]. Lee, Y.K., W.S. Lee, J.T. Hwang, D.Y. Kwon, Y.J. Surh, and O.J. Park, Curcumin Exerts Antidifferentiation Effect through AMPK alpha-PPAR-gamma in 3T3-L1 Adipocytes and Antiproliferatory Effect through AMPK alpha-COX-2 in Cancer Cells. J. Agric. Food Chem., 57 (2009) 305-310.

[8]. Jordan, W.C. and C.R. Drew, Curcumin - A natural herb with anti-HIV activity. J. Natl. Med. Assoc., 88 (1996) 333.

[9]. Wang, M.E., Y.C. Chen, I.S. Chen, S.C. Hsieh, S.S. Chen, and C.H. Chiu, Curcumin protects against thioacetamide-induced hepatic fibrosis by attenuating the inflammatory response and inducing apoptosis of damaged hepatocytes. J. Nutr. Biochem., 23 (2012) 1352-1366.

[10]. Merrell, J.G., S.W. McLaughlin, L. Tie, C.T. Laurencin, A.F. Chen, and L.S. Nair, Curcumin-loaded poly(epsilon-caprolactone) nanofibres: Diabetic wound dressing with anti-oxidant and anti-inflammatory properties. Clin. Exp. Pharmacol. Physiol., 36 (2009) 1149-1156.

[11]. Kumbar, S.G., R. James, S.P. Nukavarapu, and C.T. Laurencin, Electrospun nanofiber scaffolds: engineering soft tissues. Biomed. Mater., 3 (2008) 034002.

[12]. Rieger, K.A., N.P. Birch, and J.D. Schiffman, Designing electrospun nanofiber mats to promote wound healing - a review. J. Mat. Chem. B, 1 (2013) 4531-4541.

[13]. Horzum, N., E. Boyaci, A.E. Eroglu, T. Shahwan, and M.M. Demir, Sorption Efficiency of Chitosan Nanofibers toward Metal Ions at Low Concentrations. Biomacromolecules, 11 (2010) 3301-3308.

[14]. Suwantong, O., P. Opanasopit, U. Ruktanonchal, and P. Supaphol, Electrospun

cellulose acetate fiber mats containing curcumin and release characteristic of the herbal substance. Polymer, 48 (2007) 7546-7557.

[15]. Unnithan, A.R., P.B.T. Pichiah, G. Gnanasekaran, K. Seenivasan, N.A.M. Barakat, Y.S. Cha, C.H. Jung, A. Shanmugam, and H.Y. Kim, Emu oil-based electrospun nanofibrous scaffolds for wound skin tissue engineering. Colloid Surf. A-Physicochem. Eng. Asp., 415 (2012) 454-460.

[16]. Dhurai, B., S. Nachimuthu, Maheswaran, G. Kumar, and R. Babu, Electrospinning of Chitosan Nanofibres Loaded with Curcumin for Wound Healing. J. Polym. Mater., 30 (2013) 471-483.

[17]. Dhurai, B., N. Saraswathy, R. Maheswaran, P. Sethupathi, P. Vanitha, S. Vigneshwaran, and V. Rameshbabu, Electrospinning of curcumin loaded chitosan/poly (lactic acid) nanofilm and evaluation of its medicinal characteristics. Front. Mater. Sci., 7 (2013) 350-361.

[18]. Perumal, G., S. Pappuru, D. Chakraborty, A.M. Nandkumar, D.K. Chand, and M. Doble, Synthesis and characterization of curcumin loaded PLA-Hyperbranched polyglycerol electrospun blend for wound dressing applications. Mater. Sci. Eng. C-Mater. Biol. Appl., 76 (2017) 1196-1204.

[19]. Mutlu, G., S. Calamak, K. Ulubayram, and E. Guven, Curcumin-loaded electrospun PHBV nanofibers as potential wound-dressing material. J. Drug Deliv. Sci. Technol., 43 (2018) 185-193.

[20]. Shababdoust, A., M. Ehsani, P. Shokrollahi, and M. Zandi, Fabrication of curcumin-loaded electrospun nanofiberous polyurethanes with anti-bacterial activity. Prog. Biomater., 7 (2018) 23-33.

[21]. Sedghi, R., N. Sayyari, A. Shaabani, H. Niknejad, and T. Tayebi, Novel biocompatible zinc-curcumin loaded coaxial nanofibers for bone tissue engineering application. Polymer, 142 (2018) 244-255.

[22]. Li, J.Z., Y. Hu, T. He, M.W. Huang, X.C. Zhang, J.Y. Yuan, Y. Wei, X.M. Dong, W.

Liu, F. Ko, and W.Y. Zhou, Electrospun Sandwich-Structure Composite Membranes for Wound Dressing Scaffolds with High Antioxidant and Antibacterial Activity. Macromol. Mater. Eng., 303 (2018) 17002270.

[23]. Sedghi, R. and A. Shaabani, Electrospun biocompatible core/shell polymer-free core structure nanofibers with superior antimicrobial potency against multi drug resistance organisms. Polymer, 101 (2016) 151-157.

[24]. Reneker, D.H. and A.L. Yarin, Electrospinning jets and polymer nanofibers. Polymer, 49 (2008) 2387-2425.

[25]. Maheshwari, R.K., A.K. Singh, J. Gaddipati, and R.C. Srimal, Multiple biological activities of curcumin: A short review. Life Sci., 78 (2006) 2081-2087.

[26]. He, T., J.N. Wang, P.L. Huang, B.Z. Zeng, H.H. Li, Q.Y. Cao, S.Y. Zhang, Z.O. Luo, D.Y.B. Deng, H.W. Zhang, and W.Y. Zhou, Electrospinning polyvinylidene fluoride fibrous membranes containing anti-bacterial drugs used as wound dressing. Colloid Surf. B-Biointerfaces, 130 (2015) 278-286.

[27]. Haider, S., Y. Al-Zeghayer, F.A.A. Ali, A. Haider, A. Mahmood, W.A. Al-Masry, M. Imran, and M.O. Aijaz, Highly aligned narrow diameter chitosan electrospun nanofibers. J. Polym. Res., 20 (2013) 105.

[28]. Tsekova, P.B., M.G. Spasova, N.E. Manolova, N.D. Markova, and I.B. Rashkov, Electrospun curcumin-loaded cellulose acetate/polyvinylpyrrolidone fibrous materials with complex architecture and antibacterial activity. Mater. Sci. Eng. C-Mater. Biol. Appl., 73 (2017) 206-214.

[29]. Zhang, X., F. Shi, J. Niu, Y.G. Jiang, and Z.Q. Wang, Superhydrophobic surfaces: from structural control to functional application. J. Mater. Chem., 18 (2008) 621-633.

[30]. Hoang, M.S., D. N.H., and H. D.P., Fabrication of Curcumin Loaded Nano Polycaprolactone/Chitosan Nonwoven Fabric via Electrospinning Technique. J. Sci. Technol., 55 (2017) 99–108.

[31].Rezaei, A. and A. Nasirpour, Encapsulation of curcumin using electrospun almond gum nanofibers: fabrication and characterization. Int. J. Food Prop., 21 (2018) 1608-1618.

[32].Fallah, M., S.H. Bahrami, and M. Ranjbar-Mohammadi, Fabrication and characterization of PCL/gelatin/curcumin nanofibers and their antibacterial properties. J. Ind. Text., 46 (2016) 562-577.

[33].Moradkhannejhad, L., M. Abdouss, N. Nikfarjam, S. Mazinani, and P. Sayar, Electrospun curcumin loaded poly (lactic acid) nanofiber mat on the flexible crosslinked PVA/PEG membrane film: Characterization and in vitro release kinetic study. 18 (2017) 2349-2360.

[34].Matabola, K.P. and R.M. Moutloali, The influence of electrospinning parameters on the morphology and diameter of poly(vinyledene fluoride) nanofibers- effect of sodium chloride. J. Mater. Sci., 48 (2013) 5475-5482.

[35].Haider, A., S. Haider, and I.K. Kang, A comprehensive review summarizing the effect of electrospinning parameters and potential applications of nanofibers in biomedical and biotechnology. Arab. J. Chem., 11 (2018) 1165-1188.

[36].Maleknia, L., M. Dilamian, M.K. Pilehrood, H. Sadeghi-Aliabadi, and A.H. Hekmati, Preparation, process optimization and characterization of core-shell polyurethane/chitosan nanofibers as a potential platform for bioactive scaffolds. Res. Pharm. Sci., 13 (2018) 273-282.

[37].Sun, X.Z., G.R. Williams, X.X. Hou, and L.M. Zhu, Electrospun curcumin-loaded fibers with potential biomedical applications. Carbohydr. Polym., 94 (2013) 147-153.

[38].Zhou, Y.S., D.Z. Yang, X.M. Chen, Q. Xu, F.M. Lu, and J. Nie, Electrospun water-soluble carboxyethyl chitosan/poly(vinyl alcohol) nanofibrous membrane as potential wound dressing for skin regeneration. Biomacromolecules, 9 (2008) 349-354.

[39].Dias, R.C.M., A.M. Goes, R. Serakides, E. Ayres, and R.L. Orefice, Porous Biodegradable Polyurethane Nanocomposites: Preparation, Characterization, and Biocompatibility Tests. Mater. Res.-Ibero-am. J. Mater., 13 (2010) 211-218.

Determination of Glutathione Reductase Activity Changes Exposed to Some 2-Aminothiazole Derivatives

Hasan KARADAĞ[*] , Emine EROĞLU , Cumhur KIRILMIŞ

Adiyaman University, Science and Letters Faculty, Chemistry Department, Adıyaman, TURKEY

Abstract. In this work, effects of concentrations ranging from 0 to 500 mg/L of some 2-aminothiazole derivatives such as 4,4'-(disulfanediylbis(methylene))bis(thiazol-2-amine) dihyrochloride (DMTA) and 2-amino-4-(chloromethyl)thiazole hydrochloride (ACT) on glutathione reductase from baker's yeast *(Saccharomyces cerevisiae)* (GR) were investigated. With exposure of 25, 50, 100, 250 and 500 mg/L concentrations, % GR activity changes were calculated as -5.29 ; -3.85 ; -2.40 ; -6.73 and -10.58 in DMTA applications, while these changes were calculated as +0.98 ; 0.00 ; -0.49 ; -2.45 and 0.00 in ACT applications, respectively. This work indicated that there was a slight decrease in GR activity with the increase of DMTA concentrations and there was no significant change in GR activity with the increase of ACT concentrations. But according to control activities, no statitistical changes were observed in GR activities with exposure of these 2-aminothiazole derivatives ($p > 0.05$, n=3).

*Keywords***:** Glutathione Reductase, 2-Aminothiazole, 4,4'-(disulfanediylbis(methylene)) bis(thiazol-2-amine) dihyrochloride, 2-amino-4-(chloromethyl)thiazole hydrochloride.

Bazı 2-aminotiazol Türevlerine Maruz Kalmış Glutatyon Redüktaz Aktivitesindeki Değişimlerinin Belirlenmesi

Özet. Bu çalışmada, 2-Aminotiazol türevleri olan 4,4'-(disulfanediylbis(methylene))bis(thiazol-2-amine) dihyrochloride (DMTA) ve 2-amino-4-(chloromethyl)thiazole hydrochloride (ACT)'in 0 dan 500 mg/L ye değişen derişimlerinin ekmek mayası *(Saccharomyces cerevisiae)* glutatyon redüktazı (GR) üzerine olan etkileri araştırılmıştır. 25, 50, 100, 250 ve 500 mg/L derişimlere maruz bırakılma ile % GR aktivitesindeki değişimler, DMTA uygulamalarında sırasıyla -5,29 ; -3,85; -2,40 ; -6,73 ve -10,58 olarak hesaplanırken, ACT uygulamalarında sırasıyla +0,98; 0,00; -0,49; -2,45 ve 0,00 olarak hesaplanmıştır. Bu çalışma, DMTA derişimlerinin artışı ile GR aktivitesinde hafif bir düşüş olduğunu ve ACT derişimlerinin artışı ile GR aktivitesinde önemli bir değişimin olmadığını göstermiştir. Ancak kontrol aktivitelerine göre, bu 2-aminotiazol türevlerinin etkileştiği GR aktivitelerinde herhangi bir istatistiksel değişim gözlemlenmemiştir ($p > 0,05$, n = 3).

*Anahtar Kelimeler***:** Glutatyon Redüktaz, 2-Aminotiazol, 4,4'-(disulfanediylbis(methylene)) bis(thiazol-2-amine) dihyrochloride, 2-amino-4-(chloromethyl)thiazole hydrochloride.

1. INTRODUCTION

2-Aminothiazole derivatives have a heterocyclic ring system and have antiviral [1], antimicrobial [2], anticancer [3] and anti-inflammatory [4] activities. Recent research has shown that 2-aminothiazole derivatives act as inhibitors against kynurenine-3-hydroxylase and cyclin-dependent kinase enzymes [5].

Glutathione reductase (EC 1.8.1.7) (GR) acts an antioxidant. GR converts oxidized glutathione (GSSG) to form reduced glutathione (GSH) in the presence of NADPH (β-Nicotinamide adenine dinucleotide 2'-phosphate reduced) [6].

$$GSSG + NADPH + H^+ \xrightarrow{\text{GR}} 2\,GSH + NADP^+$$
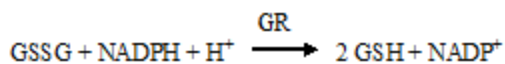
GSSG contains disulfide bridge (-S-S-) in its structure. DMTA contains disulfide bridges such as GSSG, which is the substrate of the GR enzyme. DMTA has the potential to make inhibition due to this feature. If inhibition occurs, GSH will not occur. GSH has important functions in metabolism. GSH plays a key role in maintaining proper functions in human cells and preventing oxidative stress. It neutralizes hydroxyl radicals, singlet oxygen and various electrophiles [7]. ACT is a 2-aminothiazole derivative without disulfide bridge. In this study, we investigated whether 2-aminothiazole derivative compounds containing disulfide bridge and no disulfide bridge affect on GR.

2. MATERIALS AND METHODS

2.1. Chemicals

4,4'-(disulfanediylbis(methylene))bis(thiazol-2-amine) dihyrochloride (Fig.1a) was received from Dr. Cumhur KIRILMIŞ [8]. 2-Amino-4-(chloromethyl)thiazole hydrochloride (SYX00295) (Fig.1b), L-Glutathione oxidized (G4501), β-Nicotinamide adenine dinucleotide 2'-phosphate reduced tetrasodium salt hydrate (N1630), Glutathione reductase from baker's yeast *(S. cerevisiae)* (G3664) were received from Sigma-Aldrich. Other chemicals used were analytical grade.
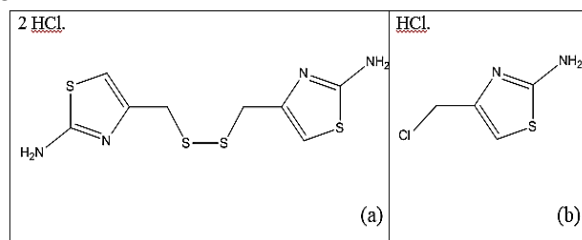
Figure 1. Structures of 4,4'-(disulfanediylbis(methylene))bis(thiazol-2-amine) dihyrochloride (a) and 2-amino-4-(chloromethyl)thiazole hydrochloride (b).

2.2. Protein determination

The protein concentration of GR was measured spectrophotometrically at 750 nm [9]. Bovine serum albumin was used as standard for the determination of GR protein concentration. For determination of protein concentration, four solutions were prepared. 1. Solution (A): 0.5 g $CuSO_4.5\,H_2O$ and 1 g sodium citrate dihydrate were dissolved at distilled water and completed to 100 mL by distilled water. 2. Solution (B): 2 g Na_2CO_3 and 0.4 g NaOH were dissolved at distilled water and completed to 100 mL by distilled water. 3. Solution (C): 2 mL solution A was added to 100 mL solution B. 4. Solution (D): 20 mL Folin-Ciocalteu was added to 20 mL distilled water. After preparation of these four solutions, 2.5 mL solution C was added to 0.5 mL of GR solution, shaked, waited for 10 minutes at room temperature, then added 0.25 mL of solution D, shaked, waited for 30 minutes and read at 750 nm for determination of GR concentration.

2.3. Glutathione reductase activitiy

The enzyme activity was measured spectrophotometrically by reading the changes in absorbance at 340 nm during oxidation of NADPH to $NADP^+$ by GSSG at 37 °C at incubated UV-1800 UV-VIS Spectrophotometer (Shimadzu Scientific Instruments) [10]. The reaction solution was contained: 1.0 mM GSSG, 0.12 mM NADPH, 0.10 M potassium phosphate buffer (pH 7.6). The oxidation of 1 μmol of NADPH/minute under these conditions was used as a Unit (U) of GR activity. Milimolar extinction coefficient of β- NADPH at 340 nm was used as 6.22. The specific activity of GR was indicated as U/mg protein.

2.4. Effect of 2-aminothiazole derivatives on enzyme activity

Solutions of 5000 mg/L DMTA and ACT in distilled water were prepared. After that, arrangement of 0, 25, 50, 100, 250 and 500 mg/L DMTA and ACT with distilled water and 700 μL GR solution were done [11]. At control or 0 mg/L, 300 μL distilled water and 700 μL GR solution were used. Solution volume of enzyme and

distilled water and 2-aminothiazole derivative was 1 mL. The mixture of GR and distilled water and 2-aminothiazole derivative was waited at room temperature for 10 minutes. Then activities of GR were determined.

2.5. Value analysis

The obtained values were shown as mean ± standard deviation. For the statistical analyses, one-way analysis of variance (ANOVA) was used, followed by the Student Newman-Keul's test using the IBM SPSS version 22 statistical software (SPSS Inc. Chicago, IL, USA). Differences were considered as significant if $p < 0.05$.

3. RESULTS AND DISCUSSION

3.1. Effect of 4,4'-(disulfanediylbis(methylene))bis(thiazol-2-amine) dihyrochloride on glutathione reductase activity

GR activities exposed to solutions of DMTA from 0 to 500 mg/L were measured. Mean of enzyme activity and standard deviation values were given in Table 1. Activity-concentration graph was shown in Fig. 2. When Table 1 and Fig.2 were examined, it was observed that there was a slight decrease in GR enzyme activity while DMTA concentration increased. However, no statistically significant changes were observed when compared to control group ($p > 0.05$, n = 3). The percent

changes in GR enzyme activities exposed to 25, 50, 100, 250 and 500 mg/L of DMTA were calculated as -5.29; -3.85; -2,40; -6.73 and -10.58 respectively.
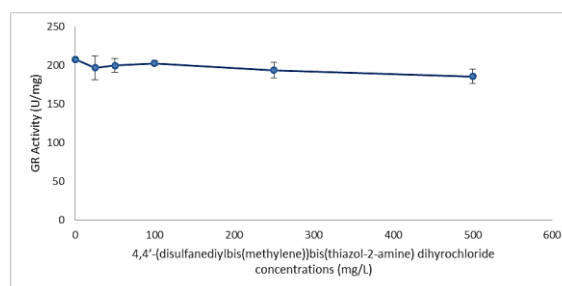
Figure 2. Effect of DMTA on GR activity.

3.2. Effect of 2-amino-4-(chloromethyl)thiazole hydrochloride on glutathione reductase activity

GR activities exposed to solutions of ACT from 0 to 500 mg/L were measured. Mean of GR activity and standard deviation values were given in Table 1. Activity-concentration graph was shown in Fig. 3. When Table 1 and Fig.3 were examined, it was seen that there were no statistically significant changes in GR enzyme activities when compared to control group while ACT concentration increased ($p > 0.05$, n = 3). The percent changes in GR activity by exposure of GR to 25, 50, 100, 250 and 500 mg/L ACT were calculated as +0.98; 0.00; -0.49; -2,45 and 0.00 respectively.

Table 1. Effect of DMTA and ACT 2-aminothiazole derivatives concentrations on GR activity.

2-Aminothiazole Derivatives Concentration (mg/L)	GR activity ± standart deviation (U/mg) for DMTA	GR activity ± standart deviation (U/mg) for ACT
0	208±3a	204±8a
25	197±15a	206±12a
50	200±9a	204±11a
100	203±3a	203±6a
250	194±10a	199±5a
500	186±9a	204±3a
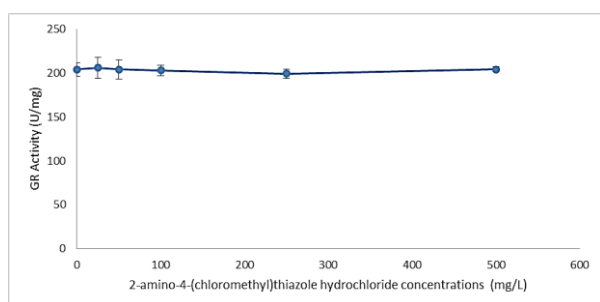
Figure 3. Effect of ACT on GR activity.

When we look at the literature, we did not find any direct studies on the effects of DMTA and ACT on GR activity. However, studies on the effects of 2-aminothiazole derivatives or thiazole derivatives on other enzyme activities were found. Such as, 2-aminothiazole derivatives act as inhibitors against kynurenine-3-hydroxylase and cyclin-dependent kinase enzymes [5]. Also, the 2-aminothiazole-4-carboxamide compound was a novel class of inhibitors of serine / threonine protein kinase (CHK1) [12]. In another study, (4 - ((4- (4-chlorophenyl) -2-thiazolyl) amino) phenol compound at a concentration of 10 µM was a moderate inhibitor (15-25% inhibition) in the experimental conditions for sphingosine kinase [13]. These result was similar like our findings about DMTA which DMTA caused a moderate inhibition (10.58 % inhibition at 500 mg/L). Another study, 3- (5- (4- (benzyloxy) -3-methoxyphenyl) -1- (4- (4-bromophenyl) thiazol-2-yl) -4,5-dihydro-1H-pyrazol-3-yl) -2H -chromen-2-one was shown to be a potential tyrosinase inhibitor [14].

4. CONCLUSION

DMTA is similar to GSSG in that it contains the disulfide bridge. DMTA may compete with GSSG to influence GR. DMTA has slightly inhibited GR (10.58 % inhibition at 500 mg/L). ACT did not have any effect on GR because it did not contain disulfide bridge. As a result, we found that DMTA caused a moderate inhibition and ACT did not cause any inhibition. But ultimately, we didn't find any statistically significant changes on GR activities in the our work.

REFERENCES

[1]. Ghaemmaghami S., May B.C.H., Renslo A.R. and Prusiner S.B., Discovery of 2-Aminothiazoles as Potent Antiprion Compounds, J. Virol., 84-7 (2010) 3408–3412.

[2]. Siddiqui H.L., Zia-Ur-Rehman M., Ahmad N., Weaver G.W. and Lucas, P.D., Synthesis and Antibacterial Activity of Bis[2-Amino-4-Phenyl-5-Thiazolyl] Disulfides, Chem. Pharm. Bull., 55-7 (2007) 1014–1017.

[3]. Kesicki E.A., Bailey M.A., Ovechkina Y., Early J.V., Alling T., Bowman J., Zuniga E.S., Dalai S., Kumar N., Masquelin T., Hipskind P.A., Odingo J.O., Parish T., Synthesis and Evaluation of the 2-Aminothiazoles as Anti-Tubercular Agents, Plos One, 11-5 (2016) e0155209.

[4]. Lin P., Hou R., Wang H., Kang I. and Chen L., Efficient Synthesis of 2-Aminothiazoles and Fanetizole in Liquid PEG-400 at Ambient Conditions, J. Chin. Chem. Soc., 56-3 (2009) 455–458.

[5]. Kim K.S., Kimball S.D., Misra R.N., Rawlins D.B., Hunt J.T., Xiao H.Y., Lu S., Qian L., Han W-C., Shan W., Mitt T., Cai Z.W., Poss M.A., Zhu H., Sack J.S., Tokarski J.S., Chang C.Y., Pavletich N., Kamath A., Humphreys W.G., Marathe P., Bursuker I., Kellar K.A., Roongta U., Batorsky R., Mulheron J.G., Bol D., Fairchild C.R., Lee F.Y. and Webster K.R., Discovery of Aminothiazole Inhibitors of Cyclin-Dependent Kinase 2: Synthesis, X-Ray Crystallographic Analysis, and Biological Activities, J. Med. Chem., 45-18 (2002) 3905–3927.

[6]. Halliwell B., Gutteridge J. M. C., Free Radicals in Biology and Medicine. 3rd ed. New York: Oxford University Press, 1999; pp 143-144.

[7]. Deponte, M., Glutathione Catalysis and the Reaction Mechanisms of Glutathione-Dependent Enzymes, Biochim. Biophys. Acta., 1830 (2013) 3217–3266.

[8]. Karabıyık H., Kırılmış C., Karabıyık H., Geometry Dependence of Electron Donating or Accepting Abilities of Amine Groups in 4,4'Disulfanediylbis(Methylene)Dithiazol-2-Amine: Pyramidal Versus Planar, J. Mol. Struct., 1141 (2017) 650-659.

[9]. Lowry O.H., Rosebrough N.J., Farr A.L., Randall R.J., Protein Measurement with the Folin Phenol Reagent, J. Biol. Chem., 193 (1951) 265–275.

[10]. Carlberg I. and Mannervik B., Purification and Characterization of the Flavoenzyme Glutathione Reductase from Rat Liver, J. Biol. Chem., 250-14 (1975) 5475–5480.

[11]. Karadag H., Bilgin R., Effect of Cyprodinil and Fludioxonil Pesticides on Human Superoxide Dismutase, Asian J. Chem., 22-10 (2010) 8147-8154.

[12]. Huang X., Cheng C.C., Fischmann T.O., Duca J.S., Richards M., Tadikonda P.K., Reddy P.A., Zhao L., Siddiqui M.A., Parry D., Davis N., Seghezzi W., Wiswell D., Shipps Jr G.W., Structure-Based Design and Optimization of 2-Aminothiazole-4-Carboxamide as a New Class of CHK1 Inhibitors, Bioorg. Med. Chem. Lett., 23 (2013) 2590–2594.

[13]. Vogt D., Weber J., Ihlefeld K., Brüggerhoff A., Proschak E., Stark H., Design, Synthesis and Evaluation of 2-Aminothiazole Derivatives as Sphingosine Kinase Inhibitors, Bioorgan. Med. Chem., 22 (2014) 5354–5367.

[14]. Saeed A., Mahesar P.A., Channar P.A., Abbas Q., Larik F.A., Hassan M., Raza H., Seo S.Y., Synthesis, Molecular Docking Studies of Coumarinyl-Pyrazolinyl Substituted Thiazoles as Non-Competitive Inhibitors of Mushroom Tyrosinase, Bioorg. Chem., 74 (2017) 187–196.

Flip Bifurcation and Stability in a Discrete-Time Prey-Predator Model with Allee Effect

Figen KANGALGİL

Sivas Cumhuriyet University, Faculty of Science, Department of Mathematics, Sivas, TURKEY

Abstract. In this paper, a discrete-time prey-predator model with Allee effect is considered. The dynamical behavior of the model is investigated. The existence and stability conditions of the coexistence fixed point of the model are analyzed. By using bifurcation theory, it is shown that the model undergoes flip bifurcation. Also, numerical simulations are presented to support the obtained theoretical results.
39A33, 37G35, 39A30.

Keywords: Flip Bifurcation; Stability, Discrete-Time Prey-Predator Model, Allee effect, Population Model.

Kesik Zamanlı Allee Etkili bir Av-Avcı Modelinin Kararlılığı ve Flip Çatallanması

Özet. Bu makalede, Allee etkili kesik zamanlı bir av-avcı modeli ele alındı. Modelin dinamik davranışları incelendi. Modelin her iki türün bir arada olduğu denge noktasının varlığı ve kararlılık şartları elde edildi. Çatallanma teorisi kullanılarak, modelin flip çatallanmaya gittiği gösterildi. Elde edilen teorik sonuçların doğruluğunu göstermek için nümerik gösterimlere yer verildi.
39A33, 37G35, 39A30.

Anahtar Kelimeler: Flip Çatallanma, Kararlılık, Kesik Zamanlı Av-Avcı Modeli, Allee etkisi, Popülasyon Modeli.

1. INTRODUCTION

The dynamics of prey-predator interaction is an important subject in bio-mathematical literature. So, many researchers studied the dynamical behavior of the prey-predator system and contributed a lot to the improvement of these models [1-21]. In literature, many species have no overlap between generations, and their population evolves in discrete-time steps. These population models are expressed by difference equations. Moreover, discrete-time models have richer dynamics than continuous models. Therefore, the researchers' interest has recently increased to discrete- time systems [1-16,25].

In [21], the author has considered the following continuous-time model with Allee effect on prey population:

$$
\frac{dx}{dt} = x(b_1 - a_{11}\, x)\frac{x}{\beta + x} + a_{12}\, x\, y)
$$

$$
\frac{dy}{dt} = y(b_2 - a_{22} y)
$$

(1)

where $x(t)$ and $y(t)$ represent population densities of prey and predator at time t, respectively. $b_i, i = 1, 2$ are the intrinsic growth rate of the prey x and predator y, $\dfrac{b_i}{a_{ii}}, i = 1, 2$ is the carrying capacity of prey and predator, respectively. a_{12} reflects the efficiency of every single population y that can contribute to population x. The term $\dfrac{x}{\beta + x}$ is Allee effect. The author investigated the local and global property of the fixed point of the system (1) with Allee effect on prey population [21].

We consider discrete- time version of the system (1) with Allee effect on predator species by applying the forward Euler scheme as follows:

$$
\begin{aligned}
x_{t+1} &= x_t + \delta(x_t(b_1 - a_{11} x_t) + a_{12} x_t y_t) \\
y_{t+1} &= y_t + \delta(y_t b_2 \frac{y_t}{m + y_t} - a_{22} y_t)
\end{aligned}
\tag{2}
$$

where $\delta > 0$ is the step size, $x(t)$ and $y(t)$ represent population densities of prey and predator at time t, respectively. All parameters are positive constants. The term $f(y) = \dfrac{y}{m + y}$ is called Allee effect where m is Allee constant [17-20]. The Allee effect is a crucial phenomenon in the biological literature. This effect describes as a positive relation between population density and the per capita growth rate. Allee function has the following property [21].

1. $f'(y) = \dfrac{y}{(m + y)^2} > 0$ for all $y \in (0, \infty)$, it means that Allee effect decreases as density increases.

2. $\lim_{y \to \infty} f(y) = 1$, that is, the Allee effect vanishes at high densities.

Many researchers have studied dynamical behavior of the predator-prey system with Allee effect [17-20].

The outline of this paper is as follows. In section 2, the stability conditions of the coexistence fixed points are discussed. In section 3, Flip bifurcation analysis is investigated by using bifurcation theory. δ parameter is selected as a bifurcation parameter. Furthermore, direction of Flip bifurcation is obtained by using normal form theory [22-24]. Moreover, some numerical simulations are presented to illustrate the analytic finding.

2. LOCAL STABILITY ANALYSIS

In this section, we discuss stability conditions of the coexistence fixed point of model (2).

Lemma 1 *Assume $F(\lambda) = \lambda^2 + p_1 \lambda + p_0$, where p_1 and p_0 are two real constants and let $F(1) > 0$. Suppose that λ_1 and λ_2 are two roots of $F(\lambda) = 0$. Then $|\lambda_1| < 1$ and $|\lambda_2| < 1$ if and only if $F(-1) > 0$ and $p_0 < 1$.*

Definition 1. A fixed point (x^*, y^*) is called sink if $|\lambda_1| < 1$ and $|\lambda_2| < 1$, and it is locally asymptotically stable.

Theorem 1. *If* $b_2 > a_{22} m$, *the system (2) has an only positive coexistence point*

$$E(x^*, y^*) = (\frac{b_1 a_{22} + a_{12}(b_2 - a_{22} m)}{a_{11} a_{22}}, \frac{b_2 - a_{22} m}{a_{22}}) \quad and \quad E(x^*, y^*) \text{ coexistence fixed point is local}$$

asymptotically stable if $0 < \delta < \min\{\delta_1, \delta_2\}$

where $\delta_1 = \dfrac{2b_2}{(b_2 - ma_{22})^2 + b_2{}^2}$ *and* $\delta_2 = -\dfrac{2a_{22}}{b_1 a_{22} + a_{12}(b_2 - ma_{22})}$.

Proof: The fixed point of the system (2) satisfy the following equations

$$x^* = x^* + \delta(x^*(b_1 - a_{11}x^*) + a_{12}x^* y^*)$$
$$y^* = y^* + \delta(y^* b_2 \frac{y^*}{m + y^*} - a_{22}y^*) \tag{3}$$

It is clear that $E(x^*, y^*) = (\dfrac{b_1 a_{22} + a_2(b_2 - a_{22} m)}{a_{11} a_{22}}, \dfrac{b_2 - a_{22} m}{a_{22}})$ is coexistence positive fixed point of the

system (2) if $b_2 > a_{22}m$. The Jacobian matrix of the model (2) at $E(x^*, y^*)$ coexistence fixed point is following form:

$$J(E) = \begin{bmatrix} 1 - \dfrac{2\delta}{\delta_2} & -\dfrac{2a_{12}\delta}{a_{11}\delta_1} \\ 0 & 1 - \dfrac{2\delta}{\delta_1} \end{bmatrix} \tag{4}$$

where $\delta_1 = \dfrac{2b_2}{(b_2 - ma_{22})^2 + b_2{}^2}$ and $\delta_2 = -\dfrac{2a_{22}}{b_1 a_{22} + a_{12}(b_2 - ma_{22})}$.

The characteristic equation of the matrix $J(E)$ is

$$\lambda^2 + (-2 + \frac{2\delta}{\delta_1} + \frac{2\delta}{\delta_2})\lambda + (1 - \frac{2\delta}{\delta_1})(1 - \frac{2\delta}{\delta_2}) = 0 \tag{5}$$

The two eigenvalues of $J(E)$ are $\lambda_1 = 1 - \dfrac{2\delta}{\delta_1}$ and $\lambda_2 = 1 - \dfrac{2\delta}{\delta_2}$. From definition 1, we get $\delta < \delta_1$ and

$\delta < \delta_2$. This completes the proof.

Example 1. For the parameter values $a_{11} = 1, a_{12} = 1, a_{22} = 1, b_1 = 1, b_2 = 2, m = 1.2, \delta = 0.5$ and initial condition $(x_0, y_0) = (1.5, 1.6)$, the positive coexistence fixed point of the model (2) is obtained as E $(x^*, y^*) = (1.8, 0.8)$. From Figure 1, the fixed point $E(x^*, y^*) = (1.8, 0.8)$ of the system (2) is local asymptotically stable for $\delta < \delta_2 = 1.11111111111$ which shows the correctness of the Theorem 1.
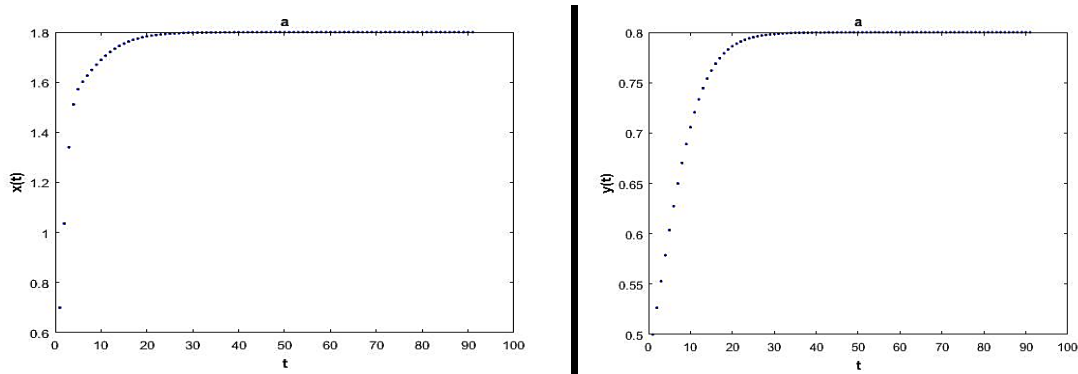
Figure1. A stable coexistence fixed point for the system (2).

3. FLIP BIFURCATION ANALYSIS

Theorem 2. [6,24] *For the system (2), one of the eigenvalues is* -1 *and the other eigenvalues lie inside the unit circle if and only if*

a) $F(1) = 1 + p_1 + p_0 > 0$

b) $F(-1) = 1 - p_1 + p_0 = 0$

c) $D_1^+ = 1 + p_0 > 0$

d) $D_1^- = 1 - p_0 > 0.$

Lemma 2. (Eigenvalue Assignment). *Let* $a_{12} > m a_{22}$ *and* $0 < \delta < 2\delta_1$. *If* $\delta_F = \delta_2$ *then the eigenvalue assignment condition of Flip Bifurcation in Theorem 2.*

Proof. From characteristic equation (5), we can write

$$p_1 = -2 + \frac{2\delta}{\delta_2} + \frac{2\delta}{\delta_1} \tag{6}$$

$$p_0 = (1 - \frac{2\delta}{\delta_2})(1 - \frac{2\delta}{\delta_1}). \tag{7}$$

Condition (a) of theorem 2 gives the inequality

$$F(1) = \frac{4\delta^2}{\delta_1 \delta_2} > 0 \tag{8}$$

which always satisfied since $\delta_1 > 0, \delta_2 > 0$ and $\delta > 0.$

$$F(-1) = 4 - \frac{4\delta}{\delta_2} - \frac{4\delta}{\delta_1} + \frac{4\delta^2}{\delta_1\delta_2} = 0 \tag{9}$$

which gives $\delta_1^* = \delta_1$ and $\delta_1^* = \delta_2$.

From condition (c) of theorem 1, we get the inequality

$$D_1^+ = \frac{2(\delta_1\delta_2 - \delta\delta_2 - \delta\delta_1 + 2\delta^2)}{\delta_1\delta_2} > 0 \ . \tag{10}$$

Eq.(10) leads to $\delta_1\delta_2 + 2\delta^2 > \delta(\delta_1 + \delta_2)$ which is always satisfied.

$$D_1^- = \frac{2\delta(\delta_1 + \delta_2 - 2\delta)}{\delta_1\delta_2} > 0 \tag{11}$$

which leads to $0 < \delta < \frac{\delta_1 + \delta_2}{2}$.

Now, it is easy to see that the Jacobian matrix J have the eigenvalues $\lambda_1 = -1$ and $\lambda_2(\delta^*) = 1 - \frac{2\delta_2}{\delta_1}$ which show the correctness Lemma 2.

To compute the coefficients of the normal form, we convert the origin of the coordinates to coexistence fixed point $E(x^*, y^*) = (\frac{b_1 a_{22} + a_{12}(b_2 - a_{22} m)}{a_{11} a_{22}}, \frac{b_2 - a_{22} m}{a_{22}})$ by the change of variables

$$\begin{aligned} x &= x^* - X \\ y &= y^* - Y \end{aligned} \ . \tag{12}$$

Then, this system can be rewritten in the form

$$X_{t+1} = JX_t + \frac{1}{2} B(X_t, X_t) + \frac{1}{2} C(X_t, X_t, X_t) + O(X_t^4)$$

where

$$J = J(\delta^*)$$

And the multilinear functions B and C are defined by

$$B_i(x, y) = \sum_{j,k=1}^{2} \frac{\partial^2 F_i(\varepsilon, 0)}{\partial \varepsilon_j \partial \varepsilon_k}\Big|_{\varepsilon=0} x_j y_k, i = 1, 2$$

and

$$C_i(\mathrm{x,y,z}) = \sum_{j,k,l=1}^{2} \frac{\partial^3 F_i(\varepsilon,0)}{\partial \varepsilon_j \partial \varepsilon_k \partial \varepsilon_l}\Big|_{\varepsilon=0} x_j\, y_k\, z_l, i=1,2$$

The values of B and C of the system can be obtained as

$$B_1(\mathrm{x,y}) = \frac{2\delta(-b_2^6 + b_2^4 a_{22}^2 m^2)}{b_2^6} x_2 y_2 \ ,$$

$$B_2(\mathrm{x,y}) = 0,$$

$$C_1(\mathrm{x,y,z}) = \left(-\frac{6\delta a_{22}^4 m^2}{b_2^3}\right) x_2 y_2 z_2$$

$$C_2(\mathrm{x,y,z}) = 0$$

and $\delta = \delta_2$.

We know that $J(\delta_2)$ has eigenvalue $\lambda_1(\delta_2) = -1$, and the corresponding eigenspace E^c is one-dimensional and spanned by an eigenvector $q \in R^2$ such that $J(\delta_2)q = -q$. Let $p \in R^2$ be the adjoint eigenvector, that is, $J^t(\delta_2)p = -p.$ By calculation we obtain

$$q \sim (1,0)^T,$$

$$p \sim (\frac{(\delta_2 - \delta_1)\,a_{11}}{a_{12}\,\delta_1}, 1)^T.$$

In order to normalize p with respect to $q,$ we denote

$$p = (1, \frac{\delta_1 a_2}{(\delta_2 - \delta_1)\,a_{11}})^T \ .$$

To determine the direction of the flip bifurcation, the sign of the critical normal form coefficient $c(0)$ is computed by the below formula:

$$c(0) = \frac{1}{6}\big\langle p, C(\mathrm{q,q,q})\big\rangle - \frac{1}{2}\big\langle p, B(\mathrm{q},(J-I)^{-1}B(\mathrm{q,q}))\big\rangle. \quad (12)$$

From the above analysis, we give below theorem.

Theorem 3. *Suppose that* $\mathrm{E(x}^*,\mathrm{y}^*)$ *is a positive coexistence fixed point of the system (2). Lemma 2 holds and* $c(0) \neq 0$, *then system (2) undergoes a flip bifurcation at the fixed point* $\mathrm{E(x}^*,\mathrm{y}^*)$ *when the parameter* δ *varies in a small neighborhood of* δ_2. *Moreover, if* $c(0) > 0$ *(respectively,* $c(0) < 0$ *), then the period-2 orbits that bifurcate from* $\mathrm{E(x}^*,\mathrm{y}^*)$ *are stable (respectively, unstable).*

Example 2. Taking parameters $a_{11}=1, a_{12}=1, a_{22}=1, b_1=1, b_2=2, m=1.2$, the coexistence fixed point of the system (2) is obtained as $(x^*, y^*)=(1.8, 0.8)$. The critical value of Flip bifurcation point is obtained as $\delta_F = \delta_2 = 1.11111111111$. The Jacobian matrix $J(\delta_2)$ of the system (2) is given;

$$J(\delta_2) = \begin{bmatrix} -1 & 2 \\ 0 & 0.6444444444 \end{bmatrix}.$$

The characteristic polynomial of the system (2) at the coexistence fixed point $(x^*, y^*)=(1.8, 0.8)$ is written by

$$F(\lambda) = \lambda^2 + 0.3555555556\lambda - 0.6444444444$$

The eigenvalues of the system (2) are $\lambda_1 = -1$ and $\lambda_2 = 0.6444444444 < 1$. Moreover, $F(1)=0.7111111116>0$, $F(-1)=0$, $D_1^+ = 0.3555555556 > 0$, $D_1^- = 1.6444444444 > 0$. This verifies Theorem 2. Also, the eigenvectors $q, p \in \mathbb{R}^2$ corresponding to $\lambda_1(\delta_2) = -1$ are

$$q \sim (1,0)^T$$

and

$$p \sim (-0.8222222222, 1)^T.$$

To achieve the necessary normalization $\langle p, q \rangle = 1$, we get

$$q = (1,0)^T,$$

$$p = (0.9999999998, -1.216216216)^T.$$

By using the formula (12), the critical norm form coefficient $c(0) = 0.36452221 > 0$. Therefore, a unique and stable period-two cycle bifurcation from $(x^*, y^*)=(1.8, 0.8)$ for $\delta > \delta_2 = 1.111111111$. In Figure 2, the phase portraits of the system (2) for different values of the δ are given. It is clear that system (2) undergoes Flip bifurcation in critical value of $\delta_F = 1.11111111$ parameter.
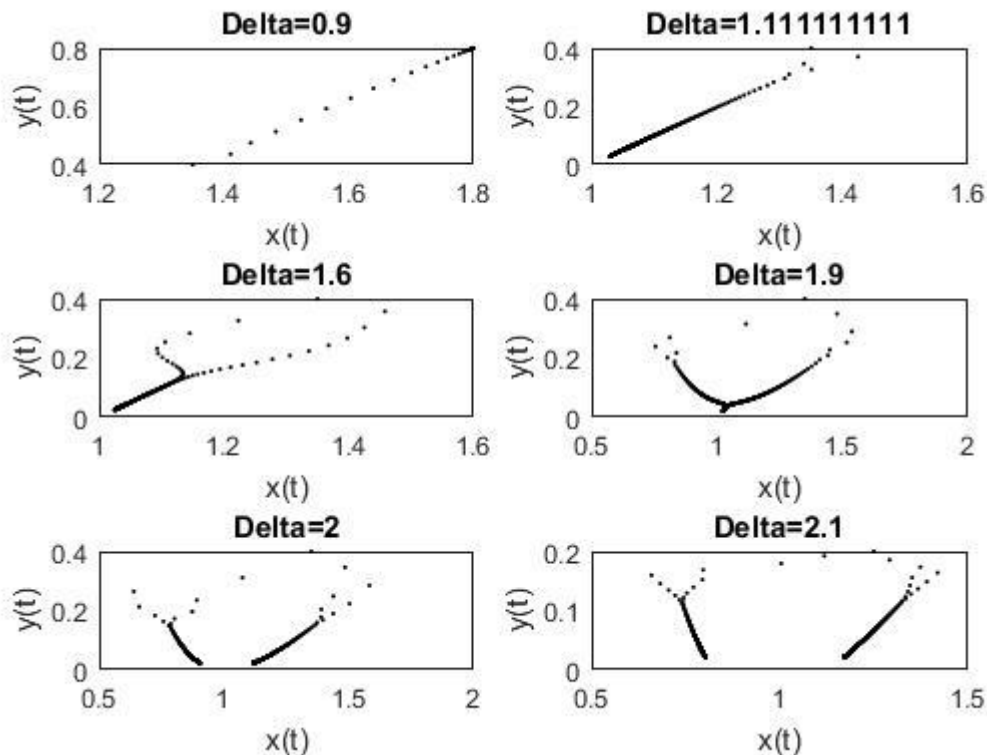
Figure 2. Phase portrait for different values of δ parameter.

4. CONCLUSION

In this study, the dynamics of a discrete-time prey-predator model with Allee effect has been investigated. Local stability conditions of the coexistence fixed point of the model are analyzed. It is shown that Flip bifurcation has been observed in the presented model. The parameter δ is selected as a bifurcation parameter. When δ reaches to $\delta_F = 1,11111111111$, the system (2) goes a flip bifurcation (see Figure 2). So, we can say that δ parameter has a strong effect on the system.

REFERENCES

[1]. He Z. and Lai X., Bifurcation and Chaotic Behavior of a Discrete-Time Predator-Prey System , Nonlinear Analysis:Real World Applications., 12 (2011) 403-417.

[2]. Salman S. M., Yousef A. M. and Elsadany A. A., Stability, Bifurcation Analysis and Chaos Control of a Discrete Predator-Prey System with Square Root Functional Response, Chaos Solitons & Fractals., 93 (2016) 20-31.

[3]. Khan A.Q., Neimark-Sacker Bifurcation of a Two-Dimensional Discrete-Time Predator-Prey Model, Springer Plus., 5 (2016) 126.

[4]. Kartal Ş., Mathematical Modeling and Analysis of Tumor-Immune System Interastion by Using Lotka-Volterra Predator-Prey Like Model with Piecewise Constant Arguments., Periodicals of Engineering and Natural Science.s, 2-1 (2014).

[5]. Kartal Ş., Dynamics of A Plant-Herbivore Model with Differential-Difference Equations, Cogents Mathematics., 3: 1136198 (2016).

[6]. Kartal Ş., Flip and Neimark-Sacker Bifurcation in a Differential Equation with Piecewise Constant Arguments Model, Journal of Difference Equations and Applications., 23-4 (2017) 763-778.

[7]. Kartal Ş. and Gurcan F., Global Behaviour of a Predator-Prey Like Model with Piecewise Constant Arguments, Journal of Biological Dynamics., 9-1 (2015) 159-171.

[8]. Elabbasy E. M., Elsadany A. A. and Zhang Y., Bifurcation Analysis and Chaos in a Discrete Reduced Lorenz System, Applied Mathematics and Computation., 228 (2014) 184-194.

[9]. Din Q., Complexity and Choas Control in a Discrete-Time Prey-Predator Model, Commun Nonlinear Sci. Numer. Simulat., 49 (2017) 113-134.

[10]. Din Q., Stability, Bifurcation Analysis and Chaos Control for a Predator-Prey System, Journal of Vibration and Control., https://doi.org/10.1177/1077546318790871 (2018).

[11]. Zhang J., Deng T., Chu Y., Qin S., Du W. and Luo H., Stability and Bifurcation Analysis of a Discrete Predator-Prey Model with Holling type III Functional Response, Journal of Nonlinear Science and Applications., 9 (2016) 6228-6243.

[12]. Liu X. and Xiao D., Complex Dynamics Behaviors of a Discrete-Time Predator-Prey System, Chaos Solitons &Fractals., 32 (2007) 80-94.

[13]. Rana S. M.,Bifurcation and Complex Dynamics of a Discrete-Time Predator-Prey System, Computational Ecology and Software., 5-2 (2015) 187-200.

[14]. Rana S. M. and Kulsum U., Bifurcation Analysis and Chaos Control in a Discrete-Time Predator-Prey System of Leslie Type with Simplified Holling Type IV Functional Response, Hindawi., Article ID 9705985 (2017).

[15]. Rana S. M., Bifurcation and Complex Dynamics of a Discrete-Time Predator-Prey System Involving Group Defense, Computational Ecology and Software., 5-3 (2015) 222-238.

[16]. Hu Z., Teng Z. and Zhang L., Stability and Bifurcation Analysis of a Discrete Predator-Prey Model with Nonmonotonic Functional Response, Nonlinear Analysis: Real World Applications., 12 (2011) 2356-2377.

[17]. Zhou S., Liu Y. and Wang G., The Stability of Predator-Prey Systems Subject to the Allee Effects, Theoretical Population Biology., 67 (2005) 23-31.

[18]. Sen M., Banarjee M. and Morozou A., Bifurcation Analysis of a Ratio-Dependent Prey-Predator Model with the Allee Effect, Ecological Complexity., 11 (2012) 12-27.

[19]. Cheng L. and Cao H., Bifurcation Analysis of a Discrete-Time Ratio-Dependent Prey-Predator Model with the Allee Effect, Communication Nonlinear Sci. Numer. Simulat., 38 (2016) 288-302.

[20]. Kangalgil F. and Ak Gumus Ö.,Allee Effect in a New Population Model And Stability Analysis, Gen. Math. Notes., 35-1 (2016) 54-64.

[21]. Lin Q., Allee Effect Increasing the Final Density of the Species Subject to Allee Effect in a Lotka-Volterra Commensal Symbiosis Model, Advance in Difference Equations., 2018-196 2018.

[22]. Kuznetsov Y. A., Elements of Applied Bifurcation Theory, Springer-Verlag, New York, NY, USA, 2nd edition, 1998.

[23]. Wiggins S., Introduction to Applied Nonlinear Dynamical System and Chaos, vol. 2, Springer-Verlag, New York, NY, USA, 2003.

[24]. Elaydi S. N., An Introduction to Difference Equations, Springer-Verlag, New York, NY, USA, 2005.

[25]. Kartal Ş., Multiple Bifurcations in an Early Brain Tumor Model with Piecewise Constant Arguments , International Journal of Biomathematics., 1-4 (2018) 1850055.

Evaluation of Kinetic Effects of Baicalein in Different Breast Cancer Cell Lines

Mehmet Rıfkı TOPÇUL [ID]

University of Istanbul, Faculty of Science, Department of Biology, Istanbul, TURKEY

Abstract. The aim of this study was to compare the antiproliferative effects of baicalein which is a flavonoide on MCF-7 and MDA-MB-231 cell line. The experiments were carried out with the evaluation of the parameters. Including cell viability, cell index, mitotic index, labelling index and apoptotic index. With the cell viability test, IC_{50} concentrations of baicalein for MCF-7 and MDA-MB-231 cells were determined as 10 μM and 30 μM, respectively and these concentrations were used in all experiments. The results showed that the IC_{50} concentrations decreased the values of cell viability, cell index, mitotic index and labelling index and increased the apoptotic index value for both cell types. These decreases and increases are statistically significant ($p<0.01$). In addition, curves of the graphs obtained from the xCelligence Real-Time Cell Analysis System showed that baicalein has cytoskeletal effects on MCF-7 cells and cytostatic effects on MDA-MB-231 cells. The results obtained from this study suggest that baicalein can be used in patients with luminal A and triple negative breast cancer in the clinic by supporting the future studies due to its antiproliferative effects on MCF-7 and MDA-MB-231 cells.

Keywords: Baicalein, Luminal A breast cancer, Triple negative breast cancer.

Baicalein'in Farklı Meme Kanseri Hücre hatlarındaki Kinetik Etkilerinin Değerlendirilmesi

Özet. Bu çalışmada, bir flavonoid olan baicalein'in MCF-7 ve MDA-MB-231 hücre hatları üzerinde meydana getireceği antiproliferatif etkilerin karşılaştırılması amaçlanmıştır. Hücre canlılığı, hücre indeksi, mitotik indeks, işaretlenme indeksi ve apoptotik indeks gibi hücre kinetiği parametrelerinin değerlendirilmesi ile deneyler gerçekleştirilmiştir.

Yapılan hücre canlılığı testi ile baicalein'in MCF-7 ve MDA-MB-231 hücreleri için IC_{50} konsantrasyonları sırasıyla 10 μM ve 30 μM olarak belirlenmiş ve tüm deneylerde bu konsantrasyonlar kullanılmıştır. Elde edilen sonuçlar kullanılan IC_{50} konsantrasyonların her hücre tipi için de hücre canlılığı, hücre indeksi, mitotik indeks ve işaretlenme indeksi değerlerini azaltırken apoptotik indeks değerini yükselttiğini göstermiştir. Bu azalma ve artışlar istatistiksel olarak anlamlıdır ($p<0.01$). Ayrıca xCelligence Gerçek Zamanlı Hücre Analiz Sisteminden elde edilen grafiklere ait eğriler, baicalein'in MCF-7 hücrelerinde sitoskeletal etkiler meydana getirirken MDA-MB-231 hücrelerinde sitostatik etki meydana getirdiğini göstermiştir. Bu çalışmadan elde edilen sonuçlar baicalein'in MCF-7 ve MDA-MB-231 hücreleri üzerine antiproliferatif etkilerinden dolayı ileride yapılacak çalışmalarla desteklenerek, klinikte luminal A ve üçlü negatif meme kanseri hastaları için de kullanılabileceğini düşündürmektedir.

Anahtar Kelimeler: Baicalein, Luminal A meme kanseri, Üçlü negatif meme kanseri.

---

1. INTRODUCTION

Recent advances in cancer diagnosis and treatment have significantly improved the prognosis of breast cancer. However, metastasis is still the main cause of cancer death [1]. Breast cancer is the most common cancer type in women worldwide and is the second leading cause of cancer death. This disease is expected to constitute 29% of all new cancer diagnoses in the next 10 years [2].

Ductal breast cancer cells are the cells that protect many ideal features of the breast epithelium. These cells are known as ER +, PR + and HER2- and are the most common type of breast cancer. It represents a group with a chance of success in treatment because of the presence of targets such as ER and PR. Triple-negative breast cancer is negative for estrogen receptors, progesterone receptors, and excess HER2 protein. Such receptors are targets in the treatment of cancer and at the same time the absence of these targets causes triple negative breast cancer to be more aggressive than other types of breast cancer [3].

Polyphenolic compounds, flavonoids, are natural products found in many fruits, vegetables and all vascular plants [4]. Some flavonoid species include anticancer and chemopreventive activities [5-7]. Baicalein, a bioactive flavonoid extracted from the root of Scutellaria baicalensis or Scutellaria radix, has antitumor activity [8-10].

In this study, we aimed to evaluate cell proliferation by comparing cell kinetics induced by baicalein in two different types of breast cancer model MCF-7 and MDA-MB-231 cell lines.

2. MATERIALS AND METHODS

2.1. Cell Culture

MCF-7 cells used as luminal A breast cancer model and MDA-MB-231 cells used as triple negative breast cancer breast cancer were grown in Dulbecco's modified Eagle's medium (DMEM, high glucose) (Gibco: Thermo Fisher Scientific, Inc., Waltham, MA, USA) supplemented with 2 mM L-glutamine and 10% fetal bovine serum (FBS; Gibco: Thermo Fisher Scientific, Inc.) plus antibiotics in a humidified atmosphere with 5% CO_2 in air. The pH of the medium was adjusted to 7.4 with $NaHCO_3$.

2.2. Baicalein Concentrations

The concentrations of baicalein (Tocris, 1761) were determined based on previous *in vitro* and clinical studies. 5 µM, 10 µM and 30 µM concentrations were prepared for both cell lines. These concentrations were prepared by dilution of the 1 µM stock solution with DMEM medium.

2.3. Cell Viability Assay (CVA)

Cell viability was examined using the MTT (Thiazolyl Blue Tetrazolium Bromide, Sigma, Missouri, USA) colorimetric assay. MCF-7 and MDA-MB-231 cells ($2x10^4$ cells per well) on logarithmic growth phase were dispensed into 96-well plate. After 24 hrs. incubation, baicalein concentrations were added to each well. At the end of the experimental period, the medium in each well was removed and 40 µl fresh MTT solution (5 mg/ml in PBS) were added into each well and cells were incubated at 37^oC for 4 hrs. After incubation, 1ml of DMSO (solublizing reagent) was added to each well and shaked thoroughly for 1 hr on a shaker. Then, the absorbance of the samples was measured against a background control as a blank using an Elisa reader (µQuant, Bio-Tek Instruments Inc Vermont, USA) at 450-690 nm.

2.4. Cell Index (CI)

Real-time cell proliferation monitoring MCF-7 and MDA-MB-231 cells were seeded at densities of 10000 and 5000 cells/well, respectively, into an E-plate 16 (ACEA Biosciences, San Diego, CA) containing 100 µL medium per well and monitored on the xCELLigence Real-Time Cell Analyzer Dual Plate (RTCA DP) instrument (ACEA Biosciences). When the cells entered log phase, the different baicalein concentrations were added to final concentrations of 5 µM, 10 µM and 30 µM. The cells were treated with baicalein for

24 h and incubated at 37°C in a 5% CO_2 atmosphere. To calculate the half maximal inhibitory concentration (IC_{50}) values and proliferation of the cells, RTCA software v. 1.2.1 was used.

2.5. Mitotic Index (MI)

After fixation with Carnoy Fixative, MCF-7 and MDA-MB-231 were hydrolyzed by Feulgen method and stained with Giemsa and MI was scored using the following formula: MI = (n/C) x100.

2.6. Labelling Index (LI)

Thirty minutes before fixation time, 1 µCi/ml ^{3}H-thymidine was applied on MCF-7 and MDA-MB-231 cells and the cells were marked. Slides were exposed at 4 °C for 3 days and then the cells were developed with D-19b. Each slide was stained with Giemsa and 3000 cells were counted to determine the LI values.

2.7. Apoptotic Index (AI)

MCF-7 and MDA-MB-231 cells were collected and then fixed with methanol: Phosphate-buffered saline (PBS) (1:1) and methanol. The cells were fixed and mounted on slides, stained with 0.5 mg/ml DAPI for 30 min and washed with PBS. Nuclear morphology of the cells was visualized using an Olympus fluorescence microscope (Olympus Corp., Tokyo, Japan). For evaluation of the AI, at least 100 cells were counted for the control and each of the experimental groups.

2.8. Statistical Analysis

All cell proliferation values (CVA, MI, LI, AI) were evaluated relative to the controls and to each other. For this reason, the values obtained from all experimental groups were analyzed using the one-way ANOVA test. The significance between the control and the experimental groups was determined by the Dunnett's test and the significance between the experimental groups was determined by the Student's t-test. P<0.01 was

considered to indicate a statistically significant result.

3. RESULTS

3.1. Cell Viability

The absorbance values of baicalein on MCF-7 cell line used as luminal A breast cancer and MDA-MB-231 cell line used as triple negative breast cancer at a concentration of 5 µM, 10 µM and 30 µM for 24 hours were decreased from 468,19 x 10^{-3} to 378,26 x 10^{-3}; 230,927 x 10^{-3} and 118,351 x 10^{-3} respectively 5 µM, 10 µM and 30 µM for MCF-7 cells (Figure 1) and decreased from 375,17 x 10^{-3} to 297,26 x 10^{-3}; 236,89 x 10^{-3} and 188,144 x 10^{-3} respectively 5 µM, 10 µM and 30 µM for MDA-MB-231 cells (Figure 2). A statistically significant decrease in absorbance values was observed as a result of baicalein application for both cell lines at 24 h. (p<0.01).
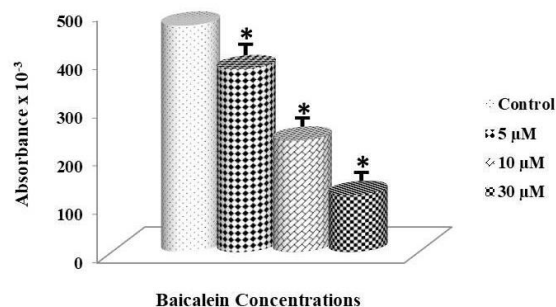
Figure 1. Absorbance values of MCF-7 cells treated with 5 µM, 10 µM and 30 µM Baicalein for 24 h (p<0.01).
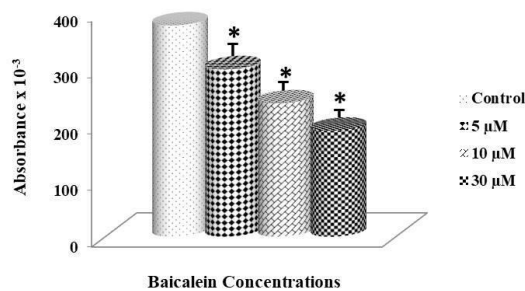
Figure 2. Absorbance values of MDA-MB-231 cells treated with 5 µM, 10 µM and 30 µM Baicalein for 24 h (p<0.01).

The results indicated that 24 hrs after the administration of baicalein concentrations to MCF-7 cells, viability values were 80,79% for 5 µM, 49,32% for 10 µM and 25,27 % for 30 µM compared to the control group which was considered as 100 % (Figure 3). For MDA-MB-231 cells, viability values were 79,23 %; 63,14 % and 50,14 % for respectively 5 µM, 10 µM and 30 µM compared to the control group which was considered as 100 % (Figure 4). When the viability % values were examined, the IC_{50} value causing half of the cells in the culture was determined as 10 µM for MCF-7 cells and 30 µM for MDA-MB-231 cells. All other experiments were performed using IC_{50} values of the cells.
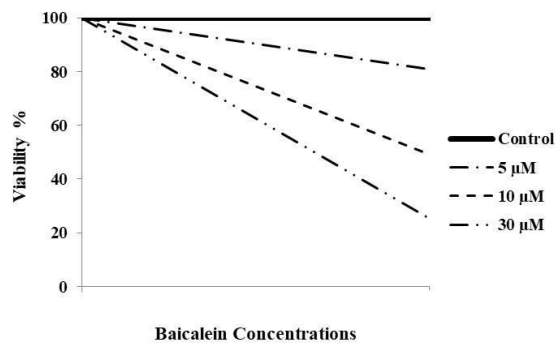
Figure 3. Percent viability values of MCF-7 cells treated with 5 µM, 10 µM and 30 µM Baicalein for 24 h (p<0.01).
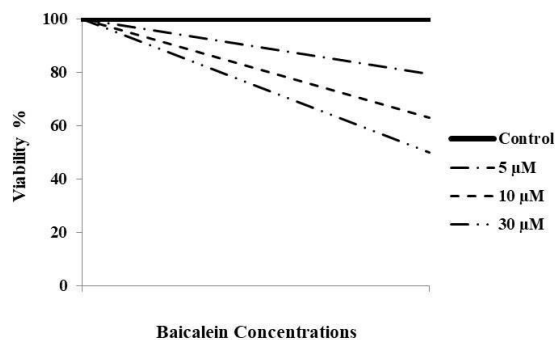
Figure 4. Percent viability values of MDA-MB-231 cells treated with 5 µM, 10 µM and 30 µM Baicalein for 24 h (p<0.01).

When cell viability of MCF-7 cells for 72 hours were examined it was seen that absorbance values decreased from 468,19 x 10^{-3} to 230,927 x 10^{-3} for 24 h; decreased from 522,367 x 10^{-3} to 193,378 x 10^{-3} for 48 h and decreased from 591,119 x 10^{-3} to

112,573 x 10^{-3} for 72 h (Figure 5). For MDA-MB-231 cell lines, these values decreased from 375,17 x 10^{-3} to 188,44 x 10^{-3} for 24 h; decreased from 401,16 x 10^{-3} to 159,38 x 10^{-3} for 48 h and decreased from 426,38 x 10^{-3} to 106,33 x 10^{-3} for 72 h (Figure 6).

It has been observed that a reduction in the rate of proliferation of both MCF-7 and MDA-MB-231 cells according to control in time dependent manner. This decrease is statistically significant at p <0.01 level.
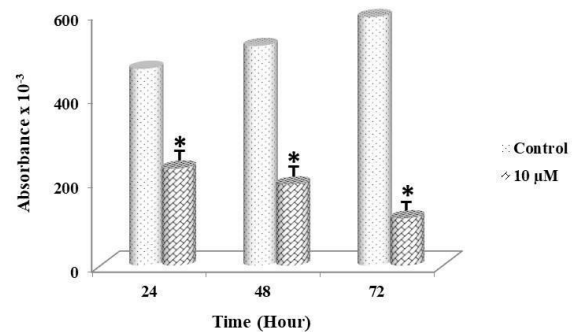
Figure 5. Absorbance values of MCF-7 cells treated with 10 µM Baicalein for 0-72 h (p<0.01).
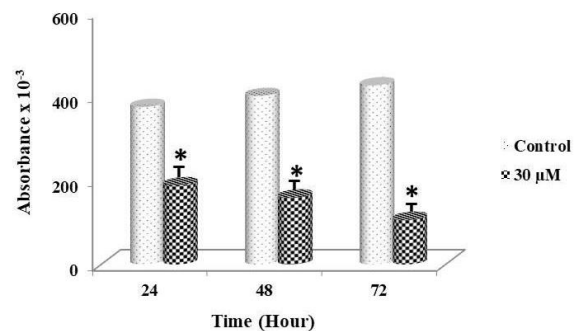
Figure 6. Absorbance values of MDA-MB-231 cells treated with 30 µM Baicalein for 0-72 h (p<0.01).

3.2. Cell Index

Cell index values obtained from xCELLigence RTCA system demonstrated that baicalein had significant anti-proliferative effects on both MCF-7 and MDA-MB-231 cell lines. Curves belong to graphics have suggested that 10 µM baicalein has cytoskeletal effect on MCF-7 cells (Figure 7) while 30 µM baicalein has cytostatic effect on MDA-MB-231 cells (Figure 8).
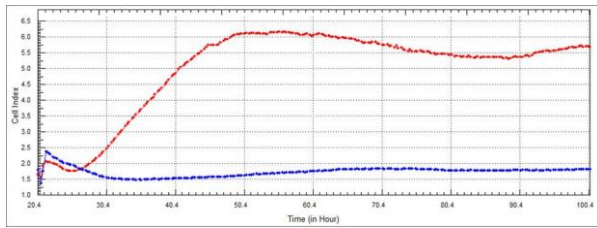
Figure 7. Cell index values of MCF-7 cells treated with 10 µM Baicalein (Red line: Control, Blue line: 10 µM).
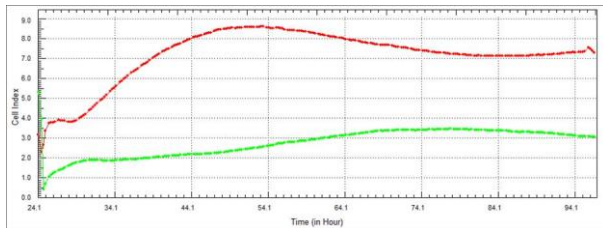
Figure 8. Cell index values of MDA-MB-231 cells treated with 30 µM Baicalein (Red Line: Control, Yellow line: 30 µM).

3.3. Mitotic Index

As a result of 10 µM baicalein application to MCF-7 cell line, mitotic index values decreased 5,12 to 2,51 at 24 h; from 6,15 to 2,08 at 48 h and from 6,18 to 1,19 at 72 h (Figure 9). As a result of 30 µM baicalein application to MDA-MB-231 cell line, mitotic index values decreased 4,21 to 2,26 at 24 h; from 4,96 to 1,89 at 48 h and from 5,18 to 1,27 at 72 h (Figure 10). The mitotic index values obtained as a result of the baicalein application in the IC_{50} concentrations to MCF-7 and MDA-MB-231 cells for 72 hours showed a statistically significant decrease ($p < 0.01$) in time dependent manner.
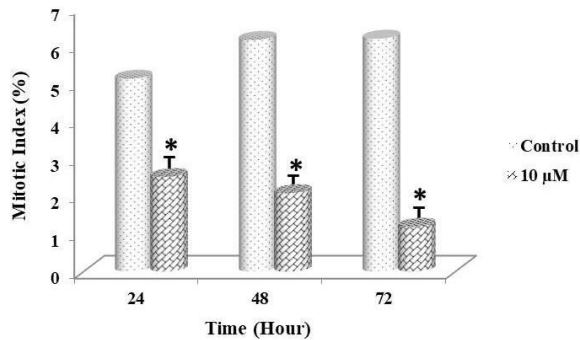
Figure 9. Mitotic index values of MCF-7 cells treated with 10 µM Baicalein for 0-72 h ($p < 0.01$).
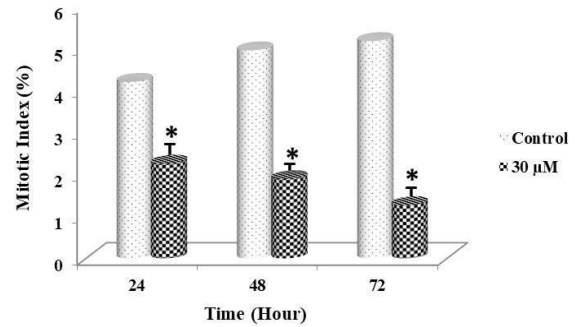
Figure 10. Mitotic index values of MDA-MB-231 cells treated with 30 µM Baicalein for 0-72 h ($p < 0.01$).

3.4. Labelling Index

The labelling index values obtained as a result of the baicalein application in the IC_{50} concentrations to MCF-7 and MDA-MB-231 cells for 72 hours showed a statistically significant decrease ($p < 0.01$) in time dependent manner. For MCF-7 cell line labelling index values decreased 4,59 to 2,97 at 24 h; from 5,21 to 2,07 at 48 h and from 5,98 to 1,16 at 72 h (Figure 11). For MDA-MB-231 cell line apoptotic index values increased from 4,29 to 2,18 at 24 h; from 4,58 to 1,57 at 48 h and from 5,11 to 1,08 at 72 h (Figure 12).
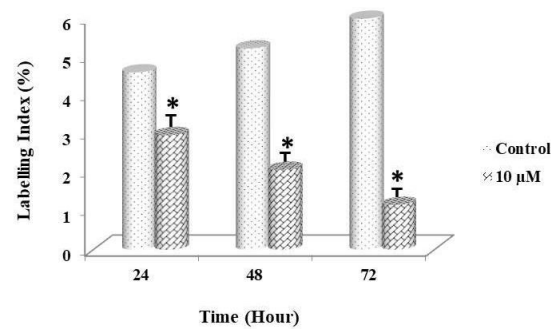
Figure 11. Labelling index values of MCF-7 cells treated with 10 µM Baicalein for 0-72 h ($p < 0.01$).
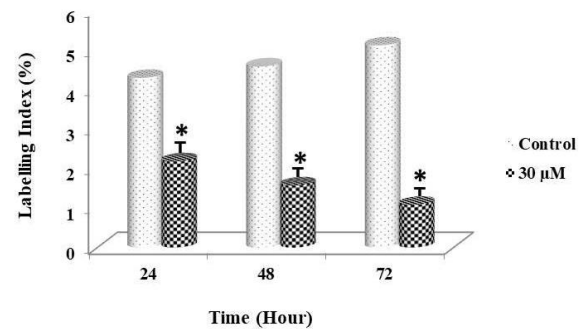
Figure 12. Labelling index values of MDA-MB-231 cells treated with 30 µM Baicalein for 0-72 h ($p < 0.01$).

3.5. Apoptotic Index

When the effects of baicalein at IC_{50} concentration on apoptotic index values of cells are evaluated, apoptotic index values of both MCF-7 and MDA-MB-231 cells showed a statistically significant increase in time dependent manner ($p < 0.01$). For MCF-7 cell line apoptotic index values increased from 1,21 to 5,53 at 24 h; from 1,18 to 9,18 at 48 h and from 2,59 to 14,29 at 72 h (Figure 13). For MDA-MB-231 cell line apoptotic index values increased from 1,92 to 4,78 at 24 h; from 2,12 to 10,19 at 48 h and from 2,37 to 16,21 at 72 h (Figure 14).
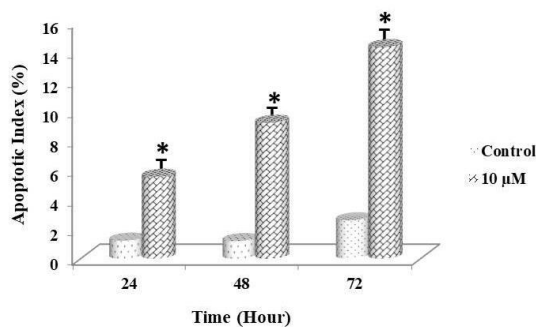
Figure 13. Apoptotic index values of MCF-7 cells treated with 10 µM Baicalein for 0-72 h (p<0.01).
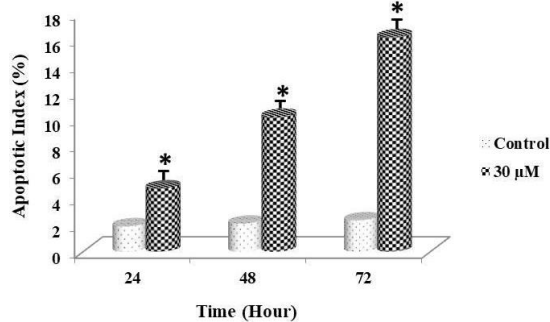
Figure 14. Apoptotic index values of MDA-MB-231 cells treated with 30 µM Baicalein for 0-72 h (p<0.01).

4. DISCUSSION

In this study evaluating the effects of baicalein on different types of breast cancer cell kinetics, results that support both previous research and new findings have been obtained. In a study evaluating the effect of baicalein on lung carcinoma cell line CH27 growth, different baicalein concentrations inhibited cell proliferation in dose and time dependent manner. Also cell cycle analysis with this cell line showed that S-phase arrest occurred as a result of 24-hour baicalein administration [11].

In a study of bladder cancer cell line BFTC 905, it was shown that baicalein inhibits cell proliferation in concentration dependent manner and high baicalein concentrations (60-80 µmol/L) completely block cell proliferation ability [12].

Studies performed with colorectal cancer cell line HCT116 showed that the cell proliferation was inhibited by the application of baicalein in a dose and time dependent manner [13].

In the gastric cancer cell line SGC7901, baicalein reduced cell proliferation in dose and time dependent manner, decreased percentage of G_1 phase cells while increased S phase. Also the increase in the number of apoptotic nuclei containing condensed chromatin as a result of the application of baicalein also showed that baicalein induced apoptosis in gastric cancer cell line SGC7901 [14].

Baicalein has been shown to be an effective inhibitor of E2/IGF-1-induced cellular proliferation and colony formation in human breast carcinoma cells [15]. The ability of baicalein to bind to ER has also been confirmed by studies [16, 17]. In particular, baicalein antagonized estradiol-dependent estrogen-sensitive element response in a dose-dependent manner [18].

As a result of the application of different concentrations of baicalein to MCF-7 cells, the cell viability decreased gradually with increasing concentration. In addition, the TUNEL test also demonstrates that baicalein has an apoptosis-enhancing effect on cells [19]. The above mentioned studies support our findings.

In a study that aimed to confirm the inhibitory effects of baicalein on MDA-MB-231 human breast cancer cells metastasis, MTT test was performed to evaluate the effect of baicalein on cell proliferation and it was observed that baicalein suppressed proliferation of MDA-MB-231 cells by

dose and time dependent manner. Also it was also determined that baicalein suppressed the migration and invasion of cells by the wound healing assay [20].

As a result, baicalein inhibits cell proliferation at different optimum doses in MCF-7 and MDA-MB-231 cells. The decrease in mitosis and synthesis phases suggests that the increase in apoptotic cells is due to different cell death mechanisms. The most important data supporting this idea is the findings obtained from the real-time cell analysis system. According to these findings, it is observed that MCF-7 cells go to death by cytoskeletal effect while MDA-MB-231 die with cytostatic effect. These data are supported by advanced studies and it is thought that Luminal A and triple negative breast cancer patients can benefit from baicalein.

Acknowledgements

REFERENCES

[1]. Xie HY, Shao ZM and Li DQ., Tumor microenvironment: driving forces and potential therapeutic targets for breast cancer metastasis. Chin J. Cancer, 36 (2017) 36.

[2]. Siegel RL, Miller KD and Jemal A., Cancer statistics, 2016. C.A. Cancer J Clin., 66 (2016) 7-30.

[3]. Çetin İ, Topçul MR., Triple Negative Breast Cancer, APJCP. 15 (2014) 2427-243.

[4]. Di Carlo G, Mascolo N, Izzo AA, Capasso F., Flavonoids: old and new aspects of a class of natural therapeutic drugs. Life Sci., 65 (1999) 337-353.

[5]. Plaumann B, Fritsche M, Rimpler H, Brandner G, Hess RD., Flavonoids activate wild-type p53. Oncogene, 13 (1996) 1605-1614.

[6]. Naasani I, Oh-Hashi F, Oh-Hara T, et al., Blocking telomerase by dietary polyphenols is a major mechanism for limiting the growth of human cancer cells *in vitro* and *in vivo*. Cancer, 63 (2003) 824-830.

[7]. Kobayashi T, Nakata T, Kuzumaki T., Effect of flavonoids on cell cycle progression in prostate cancer cells. Cancer Lett., 176 (2002) 17-23.

[8]. Bonham M, Posakony J, Coleman I, Montgomery B, Simon J, Nelson PS., Characterization of chemical constituents in Scutellaria baicalensis with antiandrogenic and growth-inhibitory activities toward prostate carcinoma. Clin Cancer Res., 11 (2005) 3905-3914.

[9]. Miocinovic R, McCabe NP, Keck RW, Jankun J, Hampton JA, Selman SH., *In vivo* and *in vitro* effect of baicalein on human prostate cancer cells. Int J. Oncol., 26 (2005) 241-246.

[10]. Ma Z, Otsuyama K, Liu S, et al., Baicalein, a component of Scutellaria radix from Huang-Lian-Jie-Du-Tang (HLJDT), leads to suppression of proliferation and induction of apoptosis in human myeloma cells. Blood, 105 (2005) 3312- 3318.

[11]. Lee HZ, Leung HWC, Lai MY, Wu CH., Baicalein induced cell cycle arrest and apoptosis in human lung squamous carcinoma CH27 cells. Anticancer Res. 25 (2005) 959-964.

[12]. Chao JI, Su WC, Liu HF., Baicalein induces cancer cell death and proliferation retardation by the inhibition of CDC2 kinase and survivin associated with opposite role of p38 mitogen-activated protein kinase and AKT. Mol Cancer Ther., 6 (2007) 3039-3048.

[13]. Chen Z, Hou R, Gao S, Song D, Feng Y., Baicalein inhibits proliferation activity of human colorectal cancer cells HCT116 through downregulation of ezrin. Cell Physiol Biochem., 49 (2018) 2035-2046.

[14]. Mu J, Liu T, Jiang L, Wu X, Cao Y, Li M, Dong Q, Liu Y, Xu H., The Traditional Chinese medicine baicalein potently inhibits gastric cancer cells. Journal of Cancer, 7 (2016) 453-461.

[15]. Lin CW, Yang LY, Shen SC and Chen YC., IGF-I plus E2 induces proliferation via activation of ROS-dependent ERKs and JNKs in human breast carcinoma cells. J Cell Physiol., 2012 (2007) 666-674.

[16].Branham WS, Dial SL, Moland CL, Hass BS, Blair RM, Fang H, Shi L, Tong W, Perkins RG and Sheehan DM., Phytoestrogens and mycoestrogens bind to the rat uterine estrogen receptor. J Nutr., 132 (2002) 658-664.

[17].Shenouda NS, Zhou C, Browning JD, Ansell PJ, Sakla MS, Lubahn DB and Macdonald RS., Phytoestrogens in common herbs regulate prostate cancer cell growth *in vitro*. Nutr Cancer, 49 (2004) 200-208.

[18].Po LS, Chen ZY, Tsang DS, Leung LK., Baicalein and genistein display differential actions on estrogen receptor (ER) transactivation and apoptosis in MCF-7 cells. Cancer Lett., 187 (2002) 33-40.

[19].An H, Yu X, Xiang C, Zhang Y, Xia J, Wang Y., Original Article Baicalein and U0126 suppress human breast cancer cell line MCF-7 through regulating MAPK signaling pathway. Int J Clin Exp Pathol., 9 (2016) 10266-10273.

[20].Ma X, Yan W, Dai Z, Gao X, Ma Y, Xu Q, Jiang J, Zhang S., Baicalein suppresses metastasis of breast cancer cells by inhibiting EMT via downregulation of SATB1 and Wnt/β-catenin pathway. Drug Design, Development and Therapy, 10 (2016) 1419-1441.

Cumhuriyet Science Journal

CSJ

Resonant Tunneling Properties of Gaussian Double Barrier Potential and Effect of the Electric Field Bias

Mehmet BATI (iD)

Recep Tayyip Erdoğan University, Department of Physics, Rize, TURKEY

Abstract. Resonant tunneling properties of finite Gaussian double quantum barrier structure are studied in the absence and presence of electric field bias. Non-equilibrium Green's function method based on the finite difference method is used. A detailed analysis of the resonant energy level is given and the importance of system parameters is discussed. The dependence of the transmission properties on the barriers and electric field bias are revealed. A comparison between different barrier shape data is presented.

*Keywords***:** Non-equilibrium Green's functions, Gaussian double barrier, Resonant tunneling, Electric field bias.

Gausyen Çift Bariyer Potansiyelinin Rezonans Tünelleme Özellikleri ve Elektrik Alan Biasının Etkisi

Özet. Gausyen kuantum çift bariyer yapısı, elektrik alan biası yokluğunda ve varlığında incelenmiştir. Sonlu farklar metodu temelli denge-dışı Green fonksiyonları yöntemi kullanılmıştır. Rezonans enerji seviyesinin ayrıntılı analizi ve sistem parametrelerinin önemi tartışılmıştır. İletim özelliklerinin bariyerlere ve elektrik alan biasına bağımlılığı incelenmiştir. Farklı bariyer şekillerinin verileri ile bir karşılaştırma sunulmuştur.

*Anahtar Kelimeler***:** Denge-dışı Green fonksiyonları, Gausyen çift bariyer, Rezonans tünelleme, Elektrik alan biası.

1. INTRODUCTION

The resonant tunneling phenomena through a one dimensional double-barrier system have enticed interest among theoretical and experimental studies [1, 2]. Electron energy spectrum of quantum wells or barriers are originated from the quantization, material compositions and geometry of structure which are adjustable parameters [3]. These structures are already used in designing in detectors, high switching devices applications and memory devices applications.

Studies of different shape of the double barriers and wells have attracted the attention of scientists since the early days of quantum mechanics. The experimental study of semiconductor barrier structures is expanding rapidly, and electric field effects are shown to be of great importance [1-3]. In recent years, various theoretical approaches such as Airy function transfer matrix method [4, 5], Wigner function method [6] and Non-equilibrium Green's function method [7, 8] have been employed to calculate the resonance energy and transmission properties of electrons in a double barrier potential. Despite several works having been devoted to the search of different shape of the double-barrier structure, to the best of our knowledge, no effort has been paid to the resonant tunneling characteristics of Gaussian double barrier (GDB).

In the present paper, resonant tunneling properties of Gaussian double quantum barrier potential are theoretically calculated in the presence of electric field bias. The reason behind the consideration of Gaussian potential profile is that it is very close to the real devices potential profile and fabrication methodologies that are available.

The outline of the rest of this paper is as follows. In Section 2, we present the model and method. Results are given in Section 3 and we finally summarize our conclusions in Section 4.

2. MODEL AND METHOD

As a model potential, we consider one dimensional Gaussian double barriers of height V_L and V_R, respectively. Double Gaussian quantum barriers can be defined as

$$U(x) = V_L e^{-\frac{(x+L_W)^2}{2\sigma^2}} + V_R e^{-\frac{(x-L_W)^2}{2\sigma^2}} \quad (1)$$

σ is the standard deviation, Lw is peak position and separation between two barrier heights is 2L$_w$ as depicted in Figure 1. The time-independent Schrödinger equation for a one dimensional potential $U(x)$ is

$$-\frac{\hbar^2}{2m^*}\frac{d^2\psi}{dx^2} + U(x)\psi = E\psi \quad (2)$$

where m^* is the effective mass of the electron, E is its energy. We assume that the electron's effective mass is constant over the entire region.
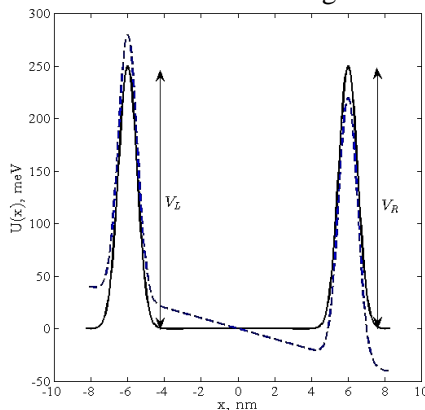
Figure 1. Potential profiles of Gaussian double barriers. The values of the parameters are given as $V_L = V_R = 250$ meV, $L_w = 6.0$ nm $\sigma = 0.05$ nm. The solid line represents the potential profile of symmetrical GDB structure without electric field bias and dashed lines stand for case when the electric field ($F = 50.0$ kV/cm) is applied.

To establish the non-equilibrium Green's function formalism based on finite difference discretization, since the formulation is given and discussed in Refs. [7, 8] in detail, we will give only definition. Retarded Green's function is defined as,

$$[G^r] = [(E + i\eta)I - H - \Sigma_L - \Sigma_R]^{-1} \quad (3)$$

where η is an infinitesimally small positive number. Σ_L and Σ_R are self-energy terms of left and right contact (see refs [7,8]). Transmission coefficient $T(E)$ can be computed as follows:

$$T(E) = Tr[\Gamma_L G^r \Gamma_R G^{r+}] \quad (4)$$

Where $\Gamma_L = i[\Sigma_L - \Sigma_L^+]$ and $\Gamma_R = i[\Sigma_R - \Sigma_R^+]$ are referred to broadening functions.

3. RESULTS

Electronic application of resonant tunneling devices can be studied from the knowledge of resonant tunneling energies and transmission coefficient $(T(E))$. Accurate estimations of these parameters play an important role in devices design. In this section, numerical calculation of resonance energy (E_{res}) and $T(E)$ has been performed by using the non-equilibrium Green's function method based on finite difference discretization.
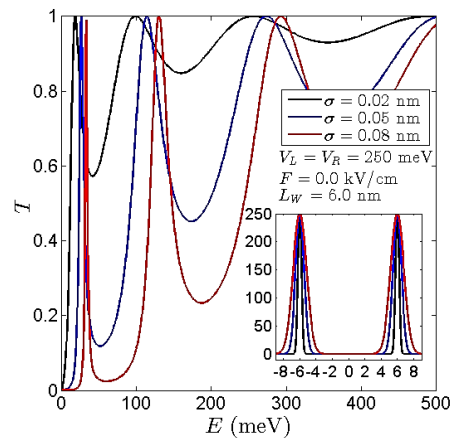
Figure 2. The transmission coefficient changes due to the chancing standard deviation of GDB.

The T versus E plots in Figure 2 show the variation of the transmission probability with the energy of an electron incident on a GDB. The results reveal that increasing of σ causes sharper unity resonant tunneling peaks and shifting to the higher energy region. Besides, the width of peak depends on the softness of the barrier structure. We can also see resonance energy levels shifting to the higher energy region with increasing standard deviation of GDB in Table 1.

Table 1. Resonance energy states of DGB with different σ for $V_L = V_R = 250$ meV, $L_w = 6.0$ nm $F = 0.0$ kV/cm.

σ (nm)	E_{res1} (meV)	E_{res2} (meV)
0.01	14.41	93.69
0.02	18.02	99.1
0.03	21.02	103.9
0.04	24.02	108.7
0.05	26.43	113.5
0.06	28.83	118.9
0.07	30.63	124.3
0.08	33.03	130.6
0.09	34.83	136.3
0.1	37.24	142.3
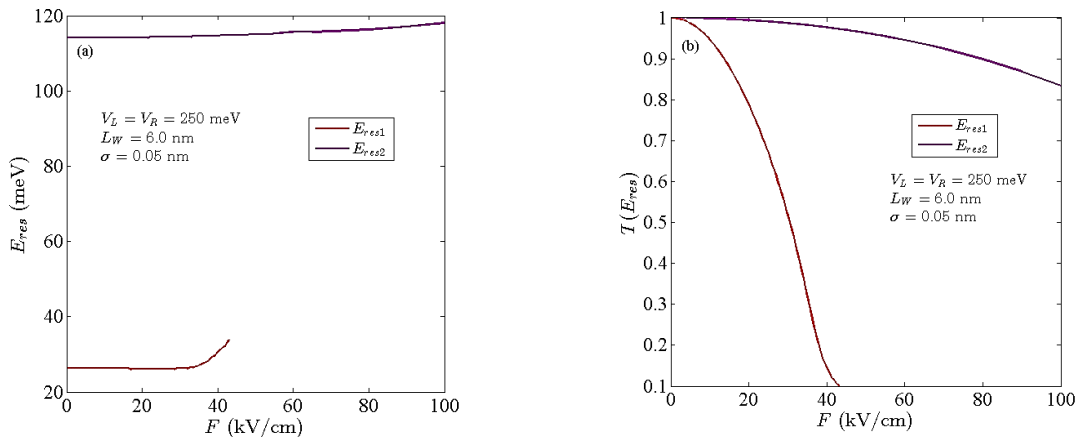
Figure 3. The variation of the (a) resonance energy and (b) amplitude of the resonant peak as a function of applied electric field bias.

Figure 3 illustrates how the resonance energy and transmission coefficient at resonance energy changes due to the chancing electric field bias. We fixed the system parameters to $V_L = V_R = 250$ meV, $L_w = 6.0$ and $\sigma = 0.05$ nm. To understand the electric field bias effect, in Fig. 3 (a) location of the resonant peak (E_{res}) and (b) the transmission probability at resonance energy ($T(E_{res})$) are

plotted, respectively. It is seen that the transmission probability at resonance energy decreases with the increasing electric field bias. Electric field bias causes an asymmetry. Asymmetry of the GDB potential is explored and is found to reduce transmission of the resonant energies. This mechanism can be used to control population trapping in the central well.
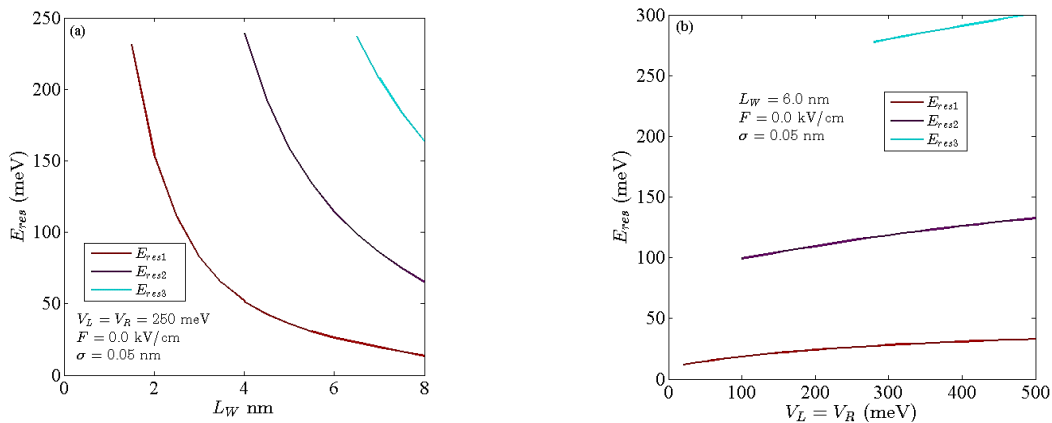
Figure 4. Dependence of the resonance energies (a) peak position (b) with respect to varying barrier heights.

The effect of the barrier separation on the transmission probability for GDB is seen from Figure 4 (a). With higher barrier separation, resonant tunneling phenomenon occurs at lower energy. We see that the resonance energies decrease exponentially with the increasing barrier separation. These findings show that the shift in the resonant energy is sensitive to the L_w . Meanwhile, crucial feature of the figure is the emergence of a third resonant energy occurred at higher energy that is a marker on the existence of third quasi-bound state. The effect of the barrier width on the resonant peak is shown in Figure 4 (b) for constant $L_w = 6.0$ nm and $\sigma = 0.05$ nm. From this figure, as expected we observe that, due to the enhanced confinement of the electron, increment in the barrier height leads to a shift in the position of the resonance energies toward a higher energy region.

The dependence of transmission coefficient on the barrier height and width makes manifest the sensitivity on the smoothness of the potential profile. When all energy range is considered, Gaussian double-barrier structures have lower resonant tunneling energy compared to rectangular double-barrier structures [9, 10]. Moreover, distinctive features of the resonant energy emerge for varying widths and heights of the potential barriers.

4. CONCLUSION

In this paper, we investigate the electric field bias and structure parameter effect in Gaussian double-barrier structure. The calculated results affirmed that the structure parameters of the systems and bias field strongly affect the resonant tunneling characteristics and thus can be controlled by these parameters. Different functional forms of the barriers may be studied to learn their characteristic features. A further challenging problem is to consider multiple barriers and external applied electric and magnetic field effects, which are necessary to model realistic devices.

REFERENCES

[1]. Chang L.L., Mendez E.E., Tejedor C., Resonant Tunneling in Semiconductors Physics and Applications, Springer US, 1991.

[2]. Harrison P., Quantum Wells, Wires and Dots: Theoretical and Computational Physics of Semiconductor Nanostructures, 3rd ed. Wiley, 2010.

[3]. Levi A.F.J., Applied Quantum Mechanics, 1st ed. Cambridge: Cambridge University Press, 2006.

[4]. Ohmukai M., Triangular double barrier resonant tunneling, Mater. Sci. and Eng. B, 116 (2005) 87-90.

[5]. Shokri A., Electrical transport engineering of semiconductor superlattice structures, Physica B, 438 (2014) 13-16.

[6]. Jiang H., Cai W., Tsu R., Accuracy of the Frensley inflow boundary condition for Wigner equations in simulating resonant tunneling diodes, J. of Comp. Phys. 230 (2011) 2031-2044.

[7]. Datta S., Quantum Transport: Atom to transistor, Cambridge: Cambridge University Press, 2005.

[8]. Batı M., Sakiroglu S., Sokmen I., Electron transport in electrically biased inverse parabolic double-barrier structure, Chin. Phys. B, 25-5 (2016) 057307.

[9]. Ohmukai M., The width ratio of two barriers in resonant tunneling, Mod. Phys. Lett. B, 17 (2003) 105-109.

[10]. Almansour S.A., Hassen D., Theoretical study of electronic transmission in resonant tunneling diodes based on GaAs/AlGaAs double barriers under bias voltage, Optics and Photonics Journal, 4 (2014) 39-45.

Sb-Contribution Influence on the Characteristics of Spray-Coated SnO₂

Güven TURGUT 🆔

Erzurum Technical University, Faculty of Sciences, Erzurum, TURKEY

Abstract. This work presents that the impact of Sb-additive on the crystalline, morphological, optical, and electrical features of SnO₂. Sb-incorporated samples were fabricated on glass substrates with spray pyrolysis. Pyramidal and polyhedron shaped tetragonal Sb-introduced SnO₂ grains were identified with XRD and SEM analysis. The degenerate n-type character for films was determined by electrical and optical characterizations. The resistivity and sheet resistance values initially decreased with Sb-content until 1.5 wt. %, then they increased with further Sb-level. However, carrier concentration increased with 2.5 wt. % Sb-contribution, then it started to goes down with 3.5 wt. %. The optical band-gap values of samples had a decreasing tendency with Sb-doping. From the results obtained in the present study, it is said that Sb-incorporated tin oxide films can be utilized in optoelectronic implements.

Keywords: Spray Pyrolysis, SnO2, Sb-doping, Electrical properties.

Isıl Püskürtme Yöntemi ile Büyütülen SnO₂ nin Karakteristik Özelliklerine Sb-Katkısının Etkisi

Özet. Bu çalışma Sb-katkısının SnO₂ nin kristal, yüzeysel, optik ve elektriksel özelliklerine etkisini sunmaktadır. Sb katkılı numuneler ısıl püskürtme yöntemi ile cam altlıklar üzerine büyütmüştür. Piramit ve çok yüzlü şekilli tetragonal Sb katkılı SnO₂ taneleri XRD ve SEM analizleri ile belirlenmiştir. Filmler için dejenere n-tipi iletkenlik özelliği elektriksel ve optiksel karakterizasyonlar ile belirlenmiştir. Özdirenç ve tabaka direnci değerleri ilk olarak ağırlıkça % 1.5 Sb içeriği ile azalmıştır ve sonra bu değerler daha fazla Sb içeriği ile artmıştır. Fakat taşıyıcı konsantrasyonu ağırlıkça % 2.5 Sb içeriği ile artmıştır, sonra ise % 3.5 Sb içeriği ile azalmaya başlamıştır. Numunelerin optik bant aralığı Sb katkılama ile azalma eğilimindedir. Bu çalışmada elde edilen sonuçlardan Sb katkılı kalay oksit ince filmlerin optoelektronik uygulamalarda kullanılabileceği söylenebilir.

Anahtar Kelimeler: Isıl püskürtme, SnO₂, Sb-katkılama, Elektriksel özellikler.

1. INTRODUCTION

Tin dioxide (stannic oxide) has excellent features of a broad band-gap of well-nigh 3.6 eV [1], high-rise optical visible transmission, infrared reflection and electrical conduction [2], small expense, superior mechanic strength and insistence under peripheral influences [3, 4]. The stannic oxide is a dielectric material, but the non-stoichiometry resulted from O vacancies or Sn interstitials brings an n-type conductivity property [2]. These features make it useful for solar cells, li-ion batteries, light emitting diodes, gas sensors, architectural windows [5, 6]. The properties of stannic oxide (SnO₂) can be tailored by doping with extrinsic atoms (Nd, W, Sb, V, Ta, Mo, Nb, F). The antimony (Sb) has 5+ oxidation state. When Sb⁵⁺ is substituted with Sn⁴⁺ or Sb⁵⁺ places on interstitial sites, it brings about an

additional free electron to tin oxide structure and it causes an increase in optical transmission and electrical conduction of SnO_2 [7]. The ionic radii of Sb^{5+} (62 Å) is close to one of Sn^{4+} (71 Å) [8], and their substitution do not bring about structural imperfections, which indicates Sb is an appropriate additive for tin oxide. Sb-incorporated stannic oxide thin layers are probably coated with many techniques such as sputtering, hydrothermal method, sol-gel coatings, chemical vapor deposition, pulsed lased deposition, and spray pyrolysis. The spray pyrolysis is an inexpensive, easy and effective [7, 9, 10]. A variety of works have been already reported on the inquiring of features of spray coated Sb-introduced SnO_2 [8, 11-21] and it was observed Sb-content greatly healed the features of stannic oxide. Although there are many studies on Sb-incorporated SnO_2, the electrical characterization results in the present study make the study very important owing to very lower resistivity and sheet resistance values than ones in the literature. For this work, the impact of Sb-content on the crystalline, surface structure, electrical and optical features of stannic oxide is inquired.

2. MATERIALS AND METHODS

0.5 wt. %, 1.5 wt. %, 2.5 wt. %, and 3.5 wt. % Sb-incorporated stannic oxide thin layers were coated on the glass substrates with spray pyrolysis. The substrate temperature (520 ºC), the nozzle and substrate distance (40 cm), the flow rate of carrier air (1.25 ml/minute), the amount of spray solution (50 ml) have been kept constant. Tin (II) chloride dehydrate ($SnCl_2.2H_2O$) and antimony (III) chloride salts solved in methanol and propane-2-ol solvents, respectively, and small amount of HCl was added into solutions. When the solutions got ready, they were pulverized on the glass substrates. The color of samples changed from light blue to dark one with Sb-content.

The crystalline structure of samples were characterized by X-Ray Diffraction (XRD) measurements with a Rigaku miniflex diffractometer with CuK_α radiation (λ=0.15418 nm). The surface of coatings was examined with Scanning Electron Microscope (Nova nano SEM)

and atomic force microscope (Nanomagnetic Instruments AFM). The thickness of films were identified to be about 1.66 µm with a cross-sectional SEM picture. The electric conductivity and optical studies were made with Hall measurements and UV–VIS (PerkinElmer, Lambda 35) spectrophotometer.

3. RESULTS AND DISCUSSIONS

3.1. Crystalline Features

The crystalline structure of Sb-incorporated SnO_2 thin films have been inquired with XRD plots shown in Fig. 1. It has been determined the whole samples are polycrystalline with SnO_2 tetragonal structure (JCPDS card no: 41-1445). The preferential orientation is (301) peak for 0.5, 1.5, and 2.5 wt. % Sb-incorporated SnO_2, and this direction changes to (200) with more Sb-content. The (301) and (200) preferential directions have been also found for undoped and Sb-incorporated SnO_2 films [13, 17]. The Sb-incorporated SnO_2 grains oriented along these directions to have minimum interfacial energy. In the present study, it can be concluded that precursor solution content affects the preferential orientation. For all samples, the observed other peaks are (110), (101), (211), (220), (310), and (321). The interplanar distance (d) values have been calculated by Bragg's law and they have been checked with the standard ones (in Table I). The lattice constants have been identified with equation [2].

$$\frac{1}{d^2} + \left(\frac{h^2+k^2}{a^2}\right) + \frac{l^2}{c^2} \qquad (1)$$
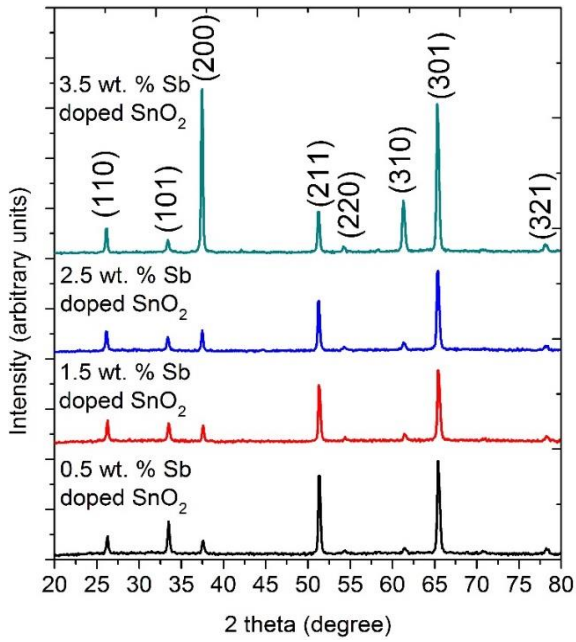
Figure 1. The XRD graphs of Sb incorporated SnO₂ thin films.

These values have been comparable with the standard ones of a=b=0.47382 nm and c=0.31871 nm. The average crystallite size of Sb-incorporated films have been determined for the most striking peak with Scherer's formula by using β − FWHM (full width at half of the peak maximum) [22].

$$D = \frac{0.9\lambda}{\beta\cos\theta} \tag{2}$$

The D values have been identified to be 30.19 nm, 28.76 nm, 29.37 nm, and 34.12 nm for 0.5 wt. %, 1.5 wt. %, 2.5 wt. %, and 3.5 wt. % Sb-incorporated SnO₂ films. The micro-strain (ε) for samples is identified by relation [7].

$$\varepsilon = \left(\frac{1}{\sin\theta}\right)\left[\left(\frac{\lambda_x}{D}\right) - (\beta\cos\theta)\right] \tag{3}$$

ε value of 0.5 wt. % Sb-incorporated stannic oxide initially increases from 3.70×10^{-3} to 3.90×10^{-3} with 1.5 wt. % Sb-content, then it decreases to the value of 3.71×10^{-3} for 2.5 wt. % Sb and then it again increases to 5.66×10^{-2} with more Sb-level. The density of dislocations (δ) for samples is estimated with relation [7].

$$\delta = 1/D^2 \tag{4}$$

δ values of 0.5 wt. %, 1.5 wt. %, 2.5 wt. %, and 3.5 wt. % Sb-incorporated SnO₂ are determined to be 1.09×10^{15} lines/m², 1.20×10^{15} lines/m², 1.16×10^{15} lines/m², and 8.59×10^{14} lines/m², respectively.

3.2. Surface properties

Figure 2. The SEM pictures of Sb-incorporated SnO₂ thin films.

The surface structures of Sb-incorporated SnO$_2$ samples are investigated with SEM and AFM studies. The SEM pictures in Fig. 2 show the particle size initially decreases with Sb level until 2.5 wt. % Sb doping content then it increases with 3.5 wt. % Sb doping. The particle structure resembles pyramidal and polyhedron shapes for 0.5, 1.5, and 3.5 wt. % Sb doped SnO$_2$. The particle structure changes to small dense shapes and also non-homogenous particle distribution forms with 2.5 wt. % Sb content. As indicated by Smith et al. [23], the change in the film surface structure may be resulted from different spraying solutions. These morphologies have been also found in earlier studies [7, 12, 24].
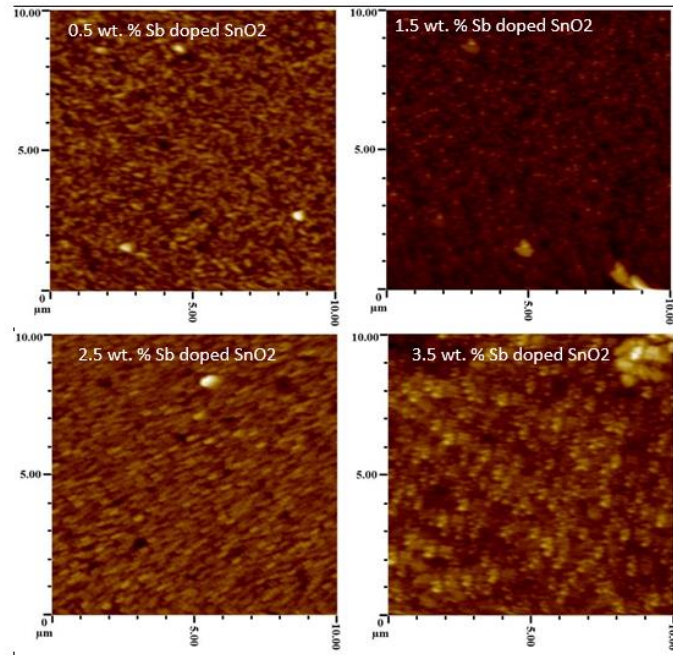
Figure 3. 2D AFM images of Sb-incorporated SnO$_2$ thin films.
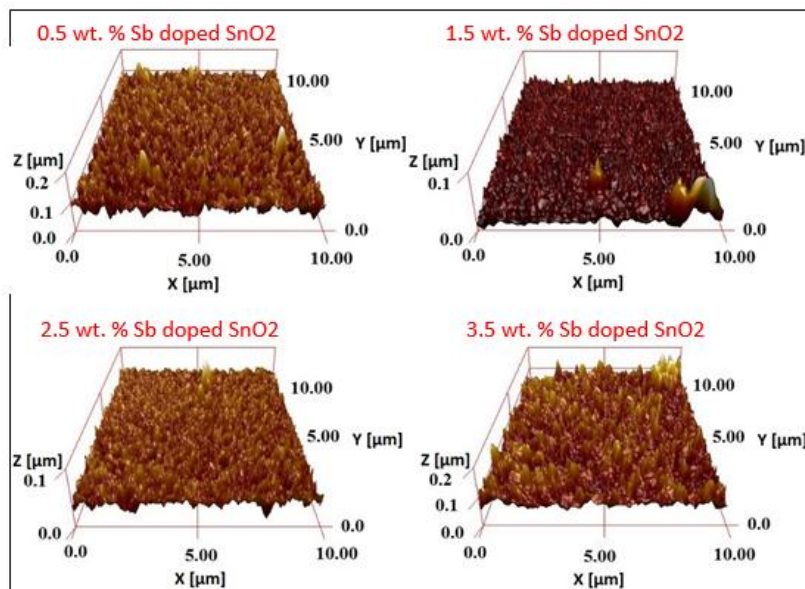
Figure 4. 3D AFM images of Sb-incorporated SnO$_2$ thin films.

The 2D and 3D AFM pictures in Fig. 3 and Fig. 4 reveals the grains are homogenously distributed on the surfaces of films. These results suggest that surface structure of films are highly influenced with Sb-contribution level.

3.3. Electrical features

The electrical features of Sb-incorporated SnO_2 samples are inquired by Hall measurements. The electrical measurements indicate n-type electrical conductivity. The resistivity (ρ), sheet resistance (R_s), carrier concentration (n), and mobility (μ) values are given in Table III. The resistivity and sheet resistance values of 0.5 wt. % Sb-incorporated SnO_2 thin film initially decrease from the values of 1.80×10^{-3} Ω.cm and 10.6 Ω to the values of 1.71×10^{-4} Ω.cm and 1.03 Ω for 1.5 wt. % Sb-contribution content. When Sb-contribution ratio is increased, the resistivity and sheet resistance values start to increase. The carrier concentration value of 0.5 wt. % Sb-incorporated sample increases from 5.81×10^{19} cm^{-3} to the values of 1.34×10^{20} cm^{-3} and 1.92×10^{20} cm^{-3} for 1.5 wt. % and 2.5 wt. % Sb-contribution levels, then decreases to the value of 5.76×10^{19} cm^{-3} with 3.5 wt. % Sb-content. The carrier mobility of 61.1 cm^2 V^{-1}s^{-1} for 0.5 wt. % Sb-contributed sample abruptly increases to the value of 266 cm^2 V^{-1}s^{-1} with 1.5 wt. % Sb-content, then it starts to decreases to the value of 150 cm^2 V^{-1}s^{-1} for 2.5 wt. % Sb-doping ratio and it again increases to 237 cm^2 V^{-1}s^{-1} for 3.5 wt. % Sb ratio. Fermi energy (E_F) of a degenerate n-type material is inside the conduction band (CB). This degeneracy is based on the energy difference of CB and Fermi level (FL). E_F values of these materials is given with equation [24].

$$E_F = \left(\frac{h^2}{8m^*}\right)\left(\frac{3n}{\pi}\right)^{\frac{2}{3}} \tag{5}$$

(m^*=0.3 m from Ref. [21]). E_F value of 0.18 for 0.5 wt. % Sb-incorporated SnO_2 initially goes up to the values of 0.32 eV and 0.40 eV for 1.5 wt. % Sb and 2.5 wt. % Sb-doped samples, then it decreases to the value of 0.18 eV with more Sb-content. Fermi energy values of Sb-incorporated SnO_2 samples are

much higher than kT (~0.03 eV), which indicates degeneracy of films.

The grain size, structural imperfections, and substitution of Sb^{5+} by Sn^{4+} can cause a change in the values of ρ, R_s, n, and μ with Sb-content. The stoichiometric stannic oxide is a good dielectric, but the valance states of 4+ and 2+ of Sn may be seen as a reason for non-stoichiometry with oxygen vacancies. An increase in the carrier concentration and easy movement of carriers causes a decrement in the values of ρ and R_s. In the variation of carrier concentration with Sb-content, it is expected that ρ and R_s values would be minimum for 2.5 wt. % Sb content. The crystalline and surface analysis indicate that films are polycrystalline and the potential obstacles occurs at grain boundaries (GBs), which they obstruct passing of carriers. From SEM pictures, the grain size of 2.5 wt. Sb contributed film is very smaller than others, and this can be seen the reason for increasing sheet resistance and resistivity. For 3.5 wt. % Sb doping content, Sb^{3+} ions is probably replaced with by Sn^{4+} and a degradation of electrical conductivity because of creation of acceptor states.

The carrier transition for a semiconductor is significant to determine scattering centers for mobility of carriers. Different scattering centers impress the mobility and the conductivity of the material. The GBs are effective for movement of carriers and negative charged GBs of SnO_2 bring about obstacles for carriers. In this model, an increment of grain size reduce GB scattering owing to a small number of GBs [25]. When the mean path (l) values of electrons are comparable with the crystalline size, GBs are very effective. The l values are identified with equation [2]

$$l = \left(\frac{h}{2e}\right)\left(\frac{3n}{\pi}\right)^{\frac{1}{3}}\mu \tag{6}$$

The mean path values of 0.5 wt. %, 1.5 wt. %, 2.5 wt. %, and 3.5 wt. % Sb-doped SnO_2 films are calculated as 42.18 nm, 24.26 nm, 15.42 nm, and 16.29 nm, respectively. The crystallite size values determined from XRD analysis are compatible

with these and the grain boundaries are effective for mobility. In addition to GBs, phonons, dopants, and structural imperfections [24] can be effective for limiting carrier movement. The resistivity and sheet resistance values are very low when they are compare with ones for spray deposited Sb doped SnO_2 films earlier studies [11, 15, 17, 19].

3.4. Optical Properties

The optical transmittance measurement of Sb-incorporated SnO_2 samples has been done with UV-VIS spectrophotometer. Transmittance (T) curves shown in Fig. 5 indicate that the transmittance values of 0.5 wt. % Sb-introduced SnO_2 thin films initially increase with 1.5 wt. % Sb content, and then continuously decrease with more Sb-level.
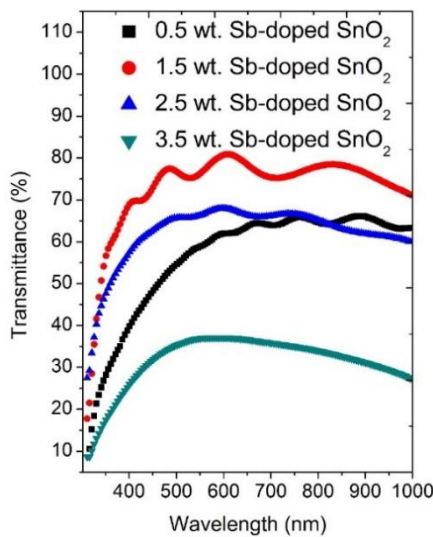
Figure 5. The optical transmittance spectra of Sb-incorporated SnO_2 thin films.

The optical band gap (E_g) has been identified with following steps; initially the absorption coefficient (α) of a film with d thickness has been determined with equation [2]

$$\alpha = \ln (1/T)/d \tag{7}$$

then E_g has been determined with equation

$$\alpha h\nu = A(h\nu - E_g)^{1/2} \tag{8}$$

where $h\nu$ and A are photon energy and the constant. By plotting $(\alpha h\nu)^2$ versus $h\nu$, the E_g values are found to be 3.94 eV, 3.88 eV, 3.80 eV, and 3.55 eV for 0.5 wt. %, 1.5 wt. %, 2.5 wt. %, and 3.5 wt. % Sb-contributed SnO_2 thin films, respectively. As seen from these values, Eg value continuously decreases with Sb content.

The optical band gap of SnO_2, which is one of degenerate semiconductors, is related to transition of electron from valance band (VB) to Fermi level (FL) by light [7]. The filled states between Fermi level and conduction band (CB) minimum prohibits inter-conduction-band absorption. Dopant atoms introduces the electrons into CB and FL rises further into CB, which is known to be Moss-Burstein (MB) sliding [26]. The alteration of n with Sb-contribution indicated that a bang gap widening would be expected with 2.5 % wt. Sb-content because of increasing the number of free carriers. But, besides the MB effect, non-stoichiometry, structural imperfections, heavy doping, and electronic transitions between Sb^{5+} and Sb^{3+} have an important effect on the changing optical band gap of SnO_2 [7, 26, 28]. In the present study, the most important effect can be an increasing density of blue color with Sb content resulted from electronic transitions between Sb^{5+} and Sb^{3+} [28], which is indicated in the experimental section.
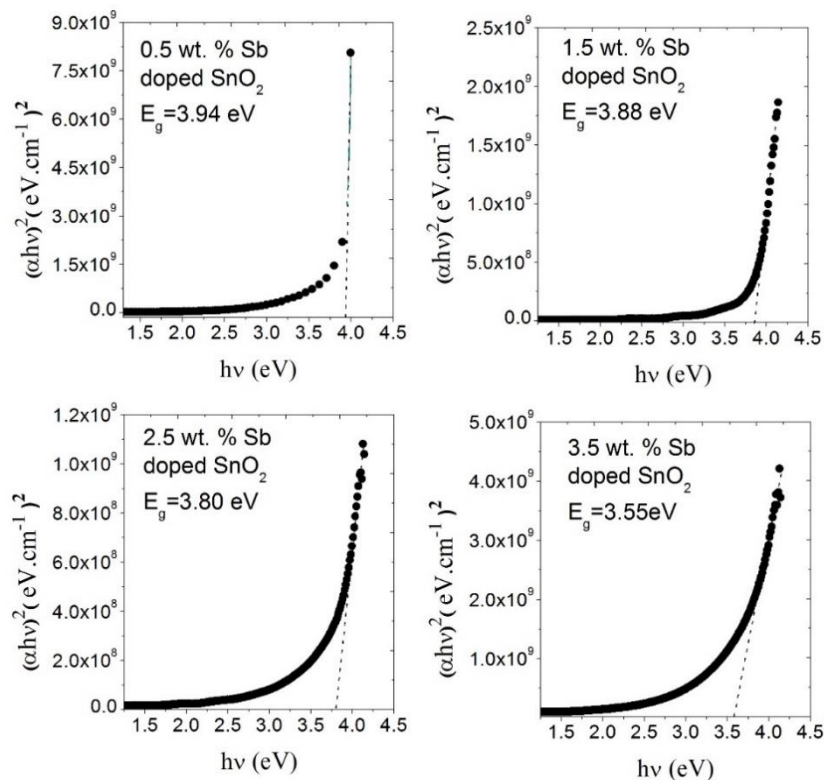
Figure 6. $(\alpha h\nu)^2$ versus $h\nu$ spectra of Sb-incorporated SnO_2 thin films.

4. CONCLUSION

The impact of Sb-contribution on the crystalline, surface morphology, electric and optic features of SnO_2 deposited with spray pyrolysis has been inquired. The characterizations have been made by means of x-ray diffraction, scanning electron and atomic force microscopes, ultraviolet/visible spectrophotometer, and Hall measurements. The XRD analysis has revealed that the films were polycrystalline tetragonal stannic oxide with (301) and (200) preferential orientations. The SEM and AFM observations have indicated the morphology of films has been changed with Sb-contribution. The electrical characterization suggested high electrical conductivity for Sb-incorporated SnO_2 films at certain-amount of Sb. The optical band gap of films has decreased with Sb-content.

REFERENCES

[1]. Babu B., Kadam A.N., Ravikumar R.V.S.S.N., Byon C., Enhanced visible light photocatalytic activity of Cu-doped SnO_2 quantum dots by solution combustion synthesis, J. Alloy. Comp. 703 (2017) 330-336.

[2]. Turgut G., Effect of Ta doping on the characteristic features of spray-coated SnO_2, Thin Solid Films 594 (2015) 56-66.

[3]. Bhatnagar M., Dhall S., Kaushik V., Kaushal A., Mehta B.R., Improved selectivity of SnO_2:C alloy nanoparticles towards H_2 and ethanol reducing gases; role of SnO_2:C electronic interaction, Sensors and Actuators B 246 (2017) 336-343.

[4]. Chandra S., George G., Ravichandran K., Thirumurugan K., Influence of simultaneous cationic (Mn) and anionic (F) doping on the magnetic and certain other properties of SnO_2 thin films, Surfaces and Interfaces 7 (2017) 39-46.

[5]. Lian X., Li Y., Tong X., Zou Y., Liu X., An D., Wang Q., Synthesis of Ce-doped SnO_2 nanoparticles and their acetone gas sensing properties, App. Surf. Sci. 407 (2017) 447-455.

[6]. Gao F., Li Y., Zhao Y., Wan W., Du G., Ren X., Zhao H., Facile synthesis of flower-like hierarchical architecture of SnO_2 nanoarrays, J. Alloy. Comp. 703 (2017) 354-360.

[7]. Turgut G., Keskenler E.F., Aydın S., Sönmez E., Doğan S., Düzgün B., Ertuğrul M., Effect of Nb doping on structural, electrical and optical properties of spray deposited SnO_2 thin films, Superlattices and Microstructures 56 (2013) 107-116.

[8]. Elangovan E., Ramamurthi K., A study on low cost-high conducting fluorine and antimony-doped tin oxide thin films, App. Surf. Sci. 249 (2005) 183-196.

[9]. Ynineb F., Attaf N., Aida M.S., Bougdira J., Bouznit Y., Rinnert H., Morphological and optoelectrical study of ZnO:In/p-Si heterojunction prepared by ultrasonic spray pyrolysis, Thin Solid Films 628 (2017) 36-42.

[10]. Menaka S. M., Umadevi G., Manickam M., Effect of copper concentration on the physical properties of copper doped NiO thin films deposited by spray pyrolysis, Material Chemistry and Physics 191 (2017) 181-187.

[11]. Babar A.R., Shinde S.S., Moholkar A.V., Bhosale C.H., Kim J.H., Rajpure K.Y., Physical properties of sprayed antimony doped tin oxide thin films: The role of thickness, Journal of Semiconductors 32 (2011) 8p.

[12]. Babar A.R., Shinde S.S., Moholkar A.V., Bhosale C.H., Kim J.H., Rajpure K.Y., Sensing properties of sprayed antimony doped tin oxide thin films: Solution molarity, J. Alloy. Comp. 509 (2011) 3108-3115.

[13]. Babar A.R., Shinde S.S., Moholkar A.V., Bhosale C.H., Kim J.H., Rajpure K.Y., Structural and optoelectronic properties of antimony incorporated tin oxide thin films, J. Alloy. Compd. 505 (2010) 416-422.

[14]. Bisht H., Eun H.T., Mehrtens A., Aegerter M.A., Comparison of spray pyrolyzed FTO, ATO and ITO coatings for flat and bent glass substrates, Thin Solid Films 351 (1999) 109-114.

[15]. Elangovan E., Ramamurthi K., Effect of substrate temperature on electrical and optical properties of spray deposited SnO_2:Sb Thin Films, J. Opt. Adv. Mater. 5 (2003) 415-420.

[16]. Elangovan E., Ramamurthi K., Studies on optical properties of polycrystalline SnO_2:Sb thin films prepared using $SnCl_2$ precursor, Cryst. Res. Cryst. Tech. 38 (2003) 779-784.

[17]. Elangovan E., Ramesh K., Ramamurthi K., Studies on the structural and electrical properties of spray deposited SnO_2:Sb thin films as a function if substrate temperature, Solid State Commun. 130 (2004) 523-527.

[18]. Elangovan E., Shivashankar S.A., Ramamurthi K., Studies on structural on structural and electrical properties of sprayed SnO_2:Sb films, J. Crys. Growth 276 (2005) 215-221.

[19]. Ravichandran K., Philominathan P., Fabrication of antimony doped tin oxide (ATO) films by an inexpensive, simplified spray technique using perfume atomizer, Mater. Lett. 62 (2008) 2980-298.

[20]. Ravichandran K., Phiominathan P., Analysis of critical doping level of sprayed antimony doped tin oxide films, J. Mater. Sci: Mater. in Elec. 22 (2011) 158-161.

[21]. Thangaraju B., Structural and electrical studies on highly conducting spray deposited fluorine and antimony doped SnO_2 thin films from $SnCl_2$ precursor, Thin Solid Films 402 (2002) 71-78.

[22]. Turgut G., Duman S., Özçelik F.S., Sonmez E., Gurbulak B., An investigation of Zn/ZnO:Al/p-Si/Al heterojunction diode by sol-gel spin coating technique, J. Sol-Gel Sci. Technol. 71 (2014) 589-596.

[23]. Smith A., Laurent J. M., Smith D. S., Bonnet J. P., Clemente R. R., Relation between solution chemistry and morphology of SnO_2-based thin films deposited by a pyrosol process, Thin Solid Films 266 (1995) 20-30.

[24]. Turgut G. and Keskenler E.F., The characteristic investigation of spray coated W incorporated in oxide thin films, Moscow University Physics Bulletin 71 (2016) 105-113.

[25]. Kazmerski L.L., Polycrystalline and Amorphous Thin Films and Devices.New York: Academic Press, 1980.

[26]. Turgut G. and, Sönmez E., Synthesis and characterization of Mo doped SnO_2 thin films with spray pyrolysis, Superlattices and Microstructures 69 (2014) 175-186.

[27]. Whitney J.E. and Davidson N., A Spectrophotometric Investigation of the Interaction between Antimony (III) and (V)[1a,b,c] in Hydrochloric Acid Solutions, J. American Chem. Soc. 71 (1949) 3809-3816.

[28]. Jung D. W. and Park D. W., Synthesis of nano-sized antimony-doped tin oxide (ATO) particles using a DC arc plasma jet, App. Surf. Sci. 255 (2009) 5409-5413.

Biosynthesis and Characterizatıon of Silver Nanopartıiles from the Lemon Leaves Extract

Gönül SERDAR[1]* , Cansu ALBAY[1], Münevver SÖKMEN[2]

[1]Karadeniz Technical University, Facult of Pharmacy, Department of Analytical Chemistry, Trabzon, TURKEY

[2]Konya Food and Agriculterl University, Faculty Engineering and Architecture, Departmen of Bioengineering, Konya, TURKEY

Abstract. The synthesis and characterization of Ag nanoparticles from *Citrus limonum* (lemon leaves) collected the Eastern Black Sea region was investigated in this study. A household microwave system device was used for microwave extraction of lemon leaves samples. The extract was prepared by taking 10g of dried lemon leaves. 10 g of sample was shaken in 100 mL of water for 90 min and extracted in a household microwave device at 4 minutes, 600 W. Ag nanoparticles were synthesized that the obtained aqueous solution was taken in different volumes by mixing 1 mM and 5mM $AgNO_3$ solution. The colloid solution was subjected to microwave in an oven 1, 3, 5, 10, 15, 20 and 30 minutes at 90, 180, 360 W. Then production of AgNPs, the mixture was watched by UV-Vis spectroscopy (Shimadzu UVP-1240 spectrophotometer) measurements at different wavelengths (300 – 800 nm) for SPR of silver nanoparticles. The transition from yellow to a dark brown, shows the synthesis of silver nanoparticles.

Keywords: Lemon leaves, Microwave Assisted Extraction, Silver nanoparticul, UV-Visible.

Limon Yaprakları Ekstraktından Ag Nanopartiküllerin Biyosentezi ve Karakterizasyonu

Özet. Bu çalışmada, Doğu Karadeniz Bölgesinde toplanan limon yapraklarından (*Citrus limonum*) Ag nanopartiküllerin sentezi ve karakterizasyonu araştırılmıştır. Limon yaprağı örneklerinin mikrodalga ekstraksiyonu için bir ev mikrodalga sistemi cihazı kullanıldı.10 g kurutulmuş limon yaprağı alınarak ekstrakt hazırlandı. Oda sıcaklığında, 10 g numune 100 mL suda 90 dakika çalkalandı ve bir ev mikrodalga cihazında, 600 W gücünde 4 dakika ekstrakte edildi, elde edilen sulu çözeltiden farklı hacimler alınarak 100 mL $AgNO_3$(1, 5 mM) çözeltisi ile karıştırılır ve karışım, 90, 180, 360 W gücünde 1, 3, 5, 10, 15, 20 ve 30 dakika boyunca mikrodalgaya maruz bırakılarak Ag nanopartikülleri sentezlendi. Daha sonra üretilen AgNP'lerin kolloid çözeltisi, AgNP'lerin yüzey plazmon rezonansı (SPR) için UV-Vis spektroskopisi ile (Shimadzu UVP-1240 spektrofotometre) farklı dalga boylarında (300 - 800 nm) ölçümleriyle izlendi. Sarıdan koyu kahverengiye renk değişimi gümüş nanopartiküllerin sentezini gösterir.

Anahtar Kelimeler: Limon yaprakları, Mikrodalga Destekli Ekstraksiyon, Gümüş nanopartikül, UV-Görünür.

1. INTRODUCTION

In recent years, nanoparticle synthesis has received great attention owing to their unequalled properties and potential applications [1]. Silver nanoparticles have been synthesized by diverse physical and chemical methods [2]. When the physical methods are costly, chemical methods

utilize toxic and hazardous chemicals which constitute significant threat to the environment and the synthesized silver nanoparticles can have reverse effects in biomedical applications due to the toxic chemicals adsorbed on their surface. The synthesis of metal nanoparticles in general and silver nanoparticles in particular exhibits a promise with potential applications in cosmetics, dermatology, pharmacology but also in catalysis and nanotechnology in general [3-5]. Especially progressive and under big expansion is the topic of green synthesis of silver nanoparticles utilizing readily available capping agents and reducing agents taken from plants and thus from renewable sources. Chemical synthesis have been shown to be simple and alternatively from green synthesis methods using either biological microorganisms or plant extracts [6].

The purpose of the work was to produce the AgNPs by exerting lemon leaves extracts which were operated in microwave assisted extraction. Microwave force is a good means for fast reduction of silver ions to silver nanoparticles at various circumtances, for example diffrerant extract volume, $AgNO_3$ concentrations, reaction time. Characterization of silver nanoparticles was using UV-Vis spectroscopy. The reaction mixture changed brown and displayed UV-Visible spectra characteristic of silver nanoparticles.

2. MATERIAL AND METHODS

2.1. Preperation of tea extract

Fresh leaves of *Citrus limonum* (lemon leaves) were collected from the Eastern Black Sea region (Trabzon, Turkey). Then, the clean and fresh *Citrus limonum* leaves were dried in an airy environment and cut into small pieces. The extract was prepared by taking 10g of dried citrus limonum leaves. 10 g of dried citrus limonum leaves and 100 mL distilled water were placed flask and then were shaken for 90 min at room temperature. After shaking, the flask was transferred in a household microwave device. Extraction was carried out under a controlled 600 W microwave power for 4 min irradiation time. After extraction, the leaf extract filtrate was

obtained by filtrating the solution through Whatman filter paper no.1. The extract is used as a reducing and stabilizing agent fort the preparation of silver nanoparticles [7].

2.2. Production and characterization of AgNP

Metal nanoparticles were synthesized by adding aqueous solution of Ag NO_3 to lemon leaf extract. 0,5, 1, 2 mL samples of Lemon leaves solution was added to 100 mL of $AgNO_3$ solution (1mM and 5 mM) in this syntheses. After the mixture was subjected to microwave in an oven 1, 3, 5, 10, 15, 20 and 30 minutes at 90, 180, 360 W. Subsequently the production of AgNPs colloid solution was watched by UV-Vis spectroscopy measurements at regular intervals of time. The UV spectral peaks for silver nanoparticles range from 400 to 480nm [8]. Absorption spectra were measured on a Shimadzu UVP-1240 spectrophotometer. Each method was repeated three times.
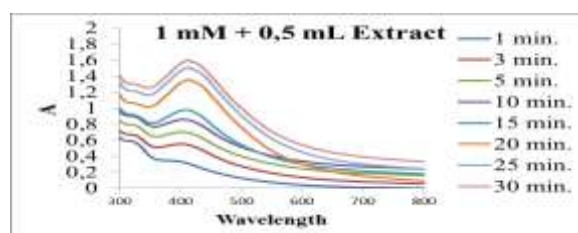
(a)
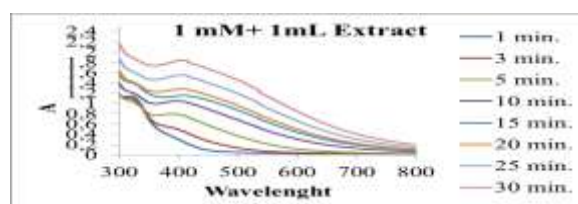
(b)
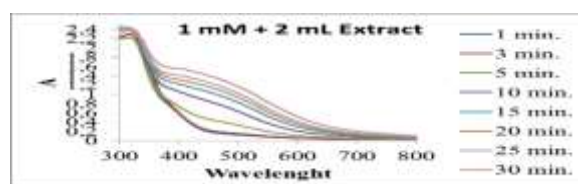
(c)

Figure 1. Uv-vis spectra of AgNPs obtained by using leaf extract of Lemon at various time (1 mM $AgNO_3$ and a)0,5 mL, b)1 mL c)2 mL Lemon leaf extract).

3. RESULTS AND DISCUSSION

Silver nitrate ($AgNO_3$) was used as sources of Ag+ ion required for that the produce of silver nanoparticles. The color of the solutions turned from yellow to dark brown is strong indication of Ag nanoparticle formation in the solution after treatment. SPR absorption spectra of silver nanoparticles produced from 1 mM (Fig.1) and 5 mM (Fig.2) $AgNO_3$ concentration.
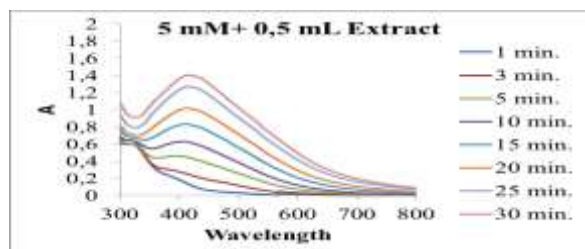
(a)
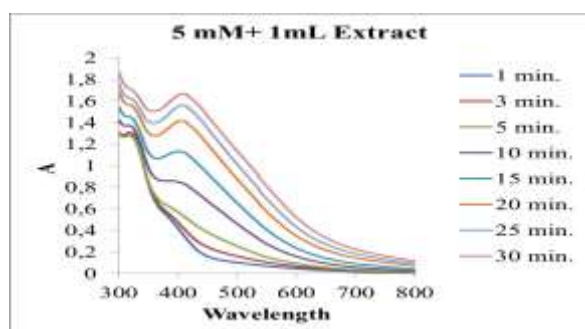
(b)
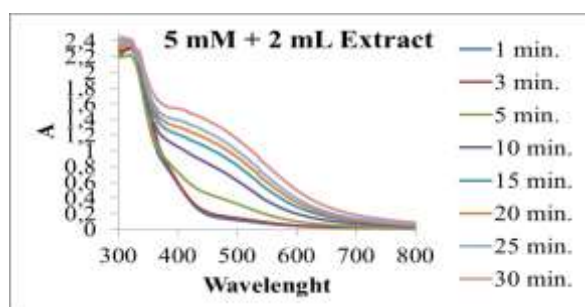
(c)

Figure 2. Uv-vis spectra of AgNPs obtained by using leaf extract of Lemon at various time (5 mM $AgNO_3$ and a)0,5 mL, b)1 mL c)2 mL Lemon leaf extract).

Silver nanoparticles were successfully generated by extracts with 0,5 mL extract volume (Fig.1a and Fig.2a). It is clear that AgNPs were successfully produced with 0,5 mLlemon leaf extract that specific resonance band surveyed around 400-460 nm then by 15 minutes subject.

The band reached to maximum height after 30 minutes (Fig.1 and Fig.2).

Economical, simple and fast production of AgNP was achieved. Using lemon leaf infusion extracts produce stable silver nanoparticles.

REFERENCES

[1]. Reenaa M., Menon A.S., Synthesis of silver nanoparticles from differant citrus fruit peel extracts and a comparative analysis on its antibacterial activity. Int. J.Curr. Microbiol. App. Sci., 6-7 (2017) 2358-2365

[2]. Mohapatra B., Kaintura R., Singh J., Kuriakose S., Mohapatra S., Biosynthesis of high concentration, stable aqueous dispersions of silver nanoparticles using Citrus limon extract, Adv. Matter. Lett., 6-3 (2015) 228-234.

[3]. Krutyakov Y.A., Kudrinskiy A.A., Olenin A.Y., Lisichkin G.C., Synthesis and properties of silver nanoparticles: Advances and prospects. Russian Chem. Rev., 77 (2008) 233-257.

[4]. Nath D.D., Banerjee P., Green nanotecnology- a new hope for medical biology. Environ. Toxicol. Pharmacol. 36 (2013) 997-1014.

[5]. Ravindron A., Chandran P.,Khan S.S., Biofunctionalized silver nanoparticles: Advances and prospects. Collids Surf. B:Biointerfaces, 105 (2013) 342-352.

[6]. El-Shishtawy R.M., Asiri A.M., Al-Otaibi M.M., Synthesis and spectroscopic studies of stable aqueous dispersion of silver nanoparticles. Spectrochimica Acta Part A: Molecular and Biomolecular Spectrosroscopy.79-5 (2011) 1505-1510.

[7]. Saxena A.,Tripathi R.M., Saxena A, Tripathi R.M, Zafer F, Singh P., Green synthesis of silver nanoparticles using aqueous solution of Ficus benghalensis leaf extract and characterization of their antibacterial activity, Mater Letters, 67 (2012) 91-94.

[8]. Praphulla R., Chandraprasad M., Lakshmi Y.N., Jahnavi R., Aishwarya P., Srinidhi S., Biosynthesis of silver nanoparticles using lemon extract and its antibacterial activity, Int. J. Multi.Curr., Research. 2 (2014) 165-169.

On the Solution of An Ill-Posed Boundary Value Problem for Second-Order Evolution Equations

İsmet GÖLGELEYEN[*] iD *, Mustafa YILDIZ* iD

Zonguldak Bülent Ecevit University, Faculty of Arts and Sciences, Department of Mathematics, Zonguldak, TURKEY

Abstract. In this work, we deal with an ill-posed boundary value problem for multidimensional second-order evolution equations with variable coefficients. By using the given data, we reduce the problem to a functional equation and we obtain a new representation for the solution by means of the Hurwitz formula.

Keywords: Second-order evolution equation, ill-posed problem, functional equation, Hurwitz's formula.

İkinci Mertebeden Evrim Denklemleri için Kötü Konulmuş Bir Sınır Değer Probleminin Çözümü Üzerine

Özet. Bu çalışmada, çok boyutlu değişken katsayılı ikinci mertebeden evrim denklemleri için bir kötü konulmuş sınır değer problemi ele alınmıştır. Veriler kullanılarak problem bir fonksiyonel denkleme indirgenmiş ve Hurwitz formülü yardımıyla bir çözüm elde edilmiştir.

Anahtar Kelimeler: İkinci mertebeden evrim denklemi, kötü konulmuş problem, fonksiyonel denklem, Hurwitz formülü.

1. INTRODUCTION

In this paper, we present a new representation for the solution of a boundary value problem for multidimensional second-order partial differential equations with variable coefficients. Our method based on the reduction of the problem to a functional equation and use of the Hurwitz formula. We first use our method for an ill-posed problem for the one-dimensional wave equation and then generalize our result for multidimensional second-order differential equations. As an example of recent studies, we refer to [1], where some new representations of the solutions and coefficients of second-order differential equations are given based on the algebraic-analytical identities.

2. AN ILL-POSED PROBLEM FOR THE ONE-DIMENSIONAL WAVE EQUATION

In this section, we shall obtain a new representation for the solution of an ill-posed problem for the one-dimensional wave equation

$$\frac{\partial^2 \omega(x,t)}{\partial t^2} = \frac{\partial^2 \omega(x,t)}{\partial x^2}, (x,t)\epsilon D \times [0,T], \tag{1}$$

with the boundary data

$$\omega(x,t)|_{t=0} = s_0(x), \omega(x,t)|_{t=T} = s_T(x), x\epsilon D, \tag{2}$$

where $D = \{x \epsilon \mathbb{R}^1 : |x| < \tau, 0 < \tau\}$. It is known that equation (1) has a general solution

$$\omega(x, t) = f(x + t) + g(x - t), \tag{3}$$

where $f(x)$ and $g(x)$ are entire functions.

We shall first consider the following boundary value problem:

Problem 1. Find the functions $f(x)$, $g(x)$, $x \epsilon D$ in (3) by data (2).

Theorem 1. Let solution (3) of equation (1) be satisfy boundary data (2). If $s_0(x)$, $s_T(x)$, $x \epsilon D$ are entire functions, then the formulas

$$f(x) = \sum_{k=0}^{\infty} s_k (2T)^k \psi_k \left(\frac{x}{2T}\right) + p(x),$$

$$g(x) = s_0(x) - f(x),$$

are valid, where s_k are the coefficients in the power series expansion of $s(x) = s_T(x + t) - s_0(x)$,

$$\psi_k(x) = \frac{k!}{2\pi i} \int_{|u|=(2k+1)\pi} \frac{e^{ux} - 1}{e^u - 1} \frac{du}{u^{k+1}}, k = 0, 1, 2, \ldots$$

and $p(x)$ is an arbitrary entire function with period $2T$.

Proof. By using data (2), (3) we can have following equations for $f(x)$ and $g(x)$

$$s_0(x) = f(x) + g(x), \tag{4}$$

$$s_T(x) = f(x + T) + g(x - T), -\infty < x < \infty. \tag{5}$$

In equation (5), we replaced x by $x + T$ to have

$$s_T(x + T) = f(x + 2T) + g(x). \tag{6}$$

Then by (4), (6) we obtain the functional equation

$$f(x + 2T) = f(x) + s(x) \tag{7}$$

for $f(x)$, where $s(x) = s_T(x + T) - s_0(x)$.

On the other hand, from Section 8 of Chapter 2 in [2], we know the following result for the functional equations of type (7):

Let the function $f(z)$ be an entire function with $z = x + iy$, $i^2 = -1$ such that

$$f(z + h) = f(z) + a(z), h = h_1 + ih_2 \neq 0, \tag{8}$$

where $a(z)$ is a given entire function. Moreover, we set $a(z) = \sum_{k=0}^{\infty} a_k z^k$. Then the function

$$f_0(z) = \sum_{k=0}^{\infty} a_k h^k \psi_k \left(\frac{z}{h}\right) \tag{9}$$

satisfies equation (8), where

$$\psi_k(z) = \frac{k!}{2\pi i} \int_{|u|=(2k+1)\pi} \frac{e^{uz} - 1}{e^u - 1} \frac{du}{u^{k+1}}, k = 0, 1, 2, \ldots. \tag{10}$$

To obtain the general solution of functional equation (8) in terms of entire functions, it is sufficient to add an arbitrary entire function $p(z)$ with period h, that is, $f(z) = f_0(z) + p(z)$.

Remark 1. In the special case, if $f(z + 1) = f(z) + z^k$, then it is easy to find a particular solution of this equation in the form of a polynomial of degree $k + 1$. This is the Bernoulli polynomial $B_{k+1}(z)$ which is determined up to a constant term, i.e., $f(z) = B_{k+1}(z)$ and

$$\frac{e^{uz}-1}{e^u-1} = \sum_{k=0}^{\infty} \frac{B_{k+1}(z)}{k!} u^k, |u| < 2\pi.$$

Now, let us return to our problem. By Hurwitz's formula (9), the entire particular solution of equation (7) is obtained as follows:

$$f_0(x) = \sum_{k=0}^{\infty} s_k (2T)^k \psi_k\left(\frac{x}{2T}\right), T > 0, \tag{11}$$

provided that $s(x)$ in (7) is an entire function, $s(x) := \sum_{k=0}^{\infty} s_k x^k$, where the functions ψ_k are defined in (10). Hence, the general solution of (7) can be written as

$$f(x) = f_0(x) + p(x),$$

where $p(x)$ is an arbitrary entire function with period $2T$.

Moreover, the entire function $g(x)$ can be determined from relation (4):

$$g(x) = s_0(x) - f(x),$$

and so entire solution (3) of equation (1) is obtained.

It is worth noting that we have equations for $f(x), g(x)$ when $x \epsilon D$ only but we can also find $f(z), g(z), z\epsilon\mathbb{C}^1$ because $f(z), g(z)$ are entire functions and then $x = z|_{y=0}$.

Remark 2. Problem 1 is ill-posed, because

a) The entire data $s_0(x), s_T(x)$ are determined by only $x\epsilon D$, but in the Hurwitz's formula and formula for the solution $\omega(x,t)$, the continuous extension of these entire data from domain D to the complex space is necessary.
b) The function $p(z)$ is arbitrary periodic and we have nonstability and nonuniqueness.

3. NEW REPRESENTATION FOR THE SOLUTION OF A GENERAL SECOND-ORDER DIFFERENTIAL EQUATION

Let D be an open domain in $\mathbb{R}^n$, for example $D = \{x: |x| < \tau, 0 < \tau\}$. We assume that $a_{ij}(x)$, $a_{ij} = a_{ji}, i, j = 1,2,,...,n$, are fixed complex valued continuous functions, $v(x)\epsilon C^2(D)$ is fixed complex valued function such that

$$v(x) \neq const, \sum_{i,j=1}^{n} a_{ij}(x) \frac{\partial v}{\partial x_i} \frac{\partial v}{\partial x_j} \neq 0, B - Cv(x) \neq 0, x\epsilon D,$$

B, C are constants.

In the future, we shall consider the second-order equation with known complex valued coefficients

$$\lambda(x)\frac{\partial^2 \omega}{\partial t^2} = \sum_{i,j=1}^{n} a_{ij}(x)\frac{\partial^2 \omega}{\partial x_i \partial x_j} + \mu(x) \sum_{i,j=1}^{n} a_{ij}(x)\frac{\partial \omega}{\partial x_i}\frac{\partial v}{\partial x_j} \equiv L\omega, \tag{12}$$

where

$$\lambda(x) = \sum_{i,j=1}^{n} a_{ij}(x) \frac{\partial v}{\partial x_i} \frac{\partial v}{\partial x_j}, \ \mu(x) = -\frac{1}{\lambda(x)} \left[\frac{2C\lambda(x)}{(B-Cv(x))} + \sum_{i,j=1}^{n} a_{ij}(x) \frac{\partial^2 v}{\partial x_i \partial x_j} \right].$$

If the coefficients in (12) are real and $\lambda(x) > 0, \sum_{i,j=1}^{n} a_{ij}(x)\xi_i\xi_j \geq K|\xi|^2, K > 0$, then (12) is a hyperbolic equation.

In the case of $n = 1$ and $a_{11}(x) = a(x)$, equation (12) has a form

$$a(x)\big(v'(x)\big)^2 \frac{\partial^2 \omega}{\partial t^2} = \frac{\partial^2 \omega}{\partial x^2} - \frac{1}{a(x)\left(\frac{\partial v}{\partial x}\right)^2} \left[\frac{2Ca(x)\big(v'(x)\big)^2}{(B-Cv(x))} + a(x)v''(x) \right] \frac{\partial \omega}{\partial x} v'(x), a(x)\big(v'(x)\big)^2 > 0$$

and if all functions are real, then $\frac{1}{c^2(x)} = a(x)\big(v'(x)\big)^2$ is velocity and $p(x) =$

$$-\frac{v'(x)}{a(x)\left(\frac{\partial v}{\partial x}\right)^2} \left[\frac{2Ca(x)\big(v'(x)\big)^2}{(B-Cv(x))} + a(x)v''(x) \right] \text{ is pressure.}$$

Then we have the following lemma.

Lemma 1. Let $f(z), g(z), z\epsilon\mathbb{C}^1$ be arbitrary entire functions. Then the solution $\omega(x,t)$ of (12) has a form

$$\omega(x,t) = \frac{1}{(B-Cv(x))} [f(v(x) + t) + g(v(x) - t)] + \widetilde{\omega}(x,t), \tag{13}$$

where $\widetilde{\omega}(x,t)$ is a common solution for $n > 1$, that is, $\lambda(x) \frac{\partial^2 \widetilde{\omega}}{\partial t^2} = L\widetilde{\omega}$ and $\widetilde{\omega}(x,t) = 0$ for $n = 1$.

Proof. By relation (13), we have

$$\frac{\partial^2 \omega}{\partial t^2} = \frac{1}{(B-Cv(x))} [f''(v(x) + t) + g''(v(x) - t)] + \frac{\partial^2 \widetilde{\omega}}{\partial t^2}, \tag{14}$$

$$\frac{\partial \omega}{\partial x_i} = \frac{C\frac{\partial v}{\partial x_i}[f(v(x)+t)+g(v(x)-t)]}{(B-Cv(x))^2} + \frac{1}{(B-Cv(x))} \frac{\partial v}{\partial x_i} [f'(v(x) + t) + g'(v(x) - t)] + \frac{\partial \widetilde{\omega}}{\partial x_i} \tag{15}$$

and

$$\frac{\partial^2 \omega}{\partial x_i \partial x_j} = \frac{2C^2(f+g)}{(B-Cv(x))^3} \frac{\partial v}{\partial x_i} \frac{\partial v}{\partial x_j} + \frac{C(f+g)}{(B-Cv(x))^2} \frac{\partial^2 v}{\partial x_i \partial x_j} + \frac{2C(f'+g')}{(B-Cv(x))^2} \frac{\partial v}{\partial x_i} \frac{\partial v}{\partial x_j} + \frac{(f''+g'')}{(B-Cv(x))} \frac{\partial v}{\partial x_i} \frac{\partial v}{\partial x_j}$$

$$+ \frac{(f'+g')}{(B-Cv(x))} \frac{\partial^2 v}{\partial x_i \partial x_j} + \frac{\partial^2 \widetilde{\omega}}{\partial x_i \partial x_j}. \tag{16}$$

By (14)-(16), we can see that identity (12) holds.

Now, we shall consider the following boundary value problem.

Problem 2. Find the functions $f(z), g(z), z\epsilon\mathbb{C}^1$ in (13) if the data

$$\omega|_{t=0} = \omega_0(x), \omega|_{t=T} = \omega_T(x), \widetilde{\omega}|_{t=0} = \widetilde{\omega}_0(x), \widetilde{\omega}|_{t=T} = \widetilde{\omega}_T(x) \tag{17}$$

are known for $n > 1$.

In (17), $\widetilde{\omega}_0(x), \widetilde{\omega}_T(x), x\epsilon D$, can be regarded as noises. It is clear that $\widetilde{\omega}_0(x) = \widetilde{\omega}_T(x) = 0$ for $n = 1$.

Next, we introduce the functions

$$S_0(x) = \omega_0(x) - \widetilde{\omega}_0(x), S_T(x) = \omega_T(x) - \widetilde{\omega}_T(x), x \epsilon D,$$

where

$$\widetilde{\omega}|_{t=0} = \widetilde{\omega}_0(x) = \omega_0(x) - \frac{1}{(B - Cv(x))}\left[f(v(x)) + g(v(x))\right],$$

$$\widetilde{\omega}|_{t=T} = \widetilde{\omega}_T(x) = \omega_T(x) - \frac{1}{(B - Cv(x))}\left[f(v(x) + T) + g(v(x) - T)\right].$$

Moreover, we set

$$S(v(x)) = (B - C(v(x) + T))S_T(v(x) + T) - (B - Cv(x))S_0(v(x)) := \sum_{k=0}^{\infty} S_k z^k\big|_{z=v(x)}.$$

Hence, we have the following theorem.

Theorem 2. Let solution (13) of equation (12) satisfy data (17). Then the formulas

$$f(z) = \sum_{k=0}^{\infty} S_k (2T)^k \, \psi_k \left(\frac{z}{2T}\right) + P(z), \tag{18}$$

$$g(z) = (B - Cz)S_0(z) - f(z), \tag{19}$$

are valid, where $P(z)$ is an arbitrary entire function with period $2T$.

Proof. By using (13), (17) we can write

$$(B - Cv(x))S_0(v(x)) = f(v(x)) + g(v(x)), \tag{20}$$

$$(B - Cv(x))S_T(v(x)) = [f(v(x) + T) + g(v(x) - T)]. \tag{21}$$

In the last equality, we replace $v(x)$ by $v(x) + T$ to have

$$(B - C(v(x) + T))S_T(v(x) + T) = [f(v(x) + 2T) + g(v(x))]. \tag{22}$$

Then from (20), (22) we obtain

$$f(v(x) + 2T) = f(v(x)) + S(v(x)),$$

where

$$S(v(x)) = (B - C(v(x) + T))S_T(v(x) + T) - (B - Cv(x))S_0(v(x)).$$

Finally, taking $v(x) = z$ yields the functional equation

$$f(z + 2T) = f(z) + S(z)$$

for $f(z)$ and then by Hurwitz's formula we obtain (18). The entire function $g(z)$ can be calculated by the formula

$$g(z) = (B - Cz)S_0(z) - f(z).$$

Thus, Theorem 2 is proved.

Example 1. If $n = 1, a_{11}(x) = 1, v(x) = x, B = 1, C = 0, \widetilde{\omega}_0(x) = 0, \widetilde{\omega}_T(x) = 0$ in (12), (13), then we have

$$\frac{\partial^2 \omega}{\partial t^2} = \frac{\partial^2 \omega}{\partial x^2},$$

and

$$\omega_0(x) = f(x) + g(x), \omega_T(x) = f(x + T) + g(x - T), x \epsilon D \subset \mathbb{R}^1,$$

for the entire functions $f(z), \ g(z), z\epsilon\mathbb{C}^1$.

Example 2. If $n = 3, a_{ij}(x) = \delta_{ij} = \begin{cases} 1, & i = j \\ 0, & i \neq j \end{cases}, v(x) = |x|, x \neq 0, B = 0, C = -1$, then we have

$$\frac{\partial^2 \omega}{\partial t^2} = \Delta\omega,$$

and (13) has the following form

$$\omega(x, t) = \frac{1}{|x|}[f(|x| + t) + g(|x| - t)] + \widetilde{\omega}(x, t),$$

where $\frac{\partial^2 \widetilde{\omega}}{\partial t^2} = \Delta\widetilde{\omega}$, that is, $\widetilde{\omega}$ is a common solution. Here the boundary value problem is to find the entire functions $f(z), \ g(z), \ z\epsilon\mathbb{C}^1$ for $S_0(x) = \omega_0(x) - \widetilde{\omega}_0(x) = \frac{1}{|x|}[f(|x|) + g(|x|)], S_T(x) = \omega_T(x) - \widetilde{\omega}_T(x) = \frac{1}{|x|}[f(|x| + T) + g(|x| - T)]$.

Here we note that, in the complex case, all the functions including $v(x)$ are complex and the solution, data and the other functions should be entire. Example 2 is not correct in this case. But in the real case, all the functions are real and in the special hyperbolic case we have different variants. It is clear that f and g must be entire. Example 2 is correct in this case without $x = 0$.

Acknowledgments

REFERENCES

[1]. Anikonov, Yu. E., Neshchadim, M. V. Representations for the Solutions and Coefficients of Second-Order Differential Equations, Journal of Applied and Industrial Mathematics, 7-1 (2013) 15-21.

[2]. Markushevich, A. I. Introduction to the classical theory of Abelian functions, Translations of Mathematical Monographs, 96, American Mathematical Society, Providence, R. I., 1992.

Recovery of Zinc from Zinc Oxide Ore by Sulfuric Acid Leaching

*Özlem KAYA** iD *, Funda SERİN ÇAKIR* iD

Sivas Cumhuriyet University, Department of Mining Engineering, Sivas, TURKEY

Abstract. This study investigates the extraction from zinc oxide ore by leaching using sulfuric acid. Effects of some parameters such as leaching time, acid concentration, leaching temperature, particle size and solid/liquid ratio were studied for maximum zinc extraction and minimum acid consumption. Optimum leaching conditions were determined to be 120 minutes of leaching time, 55 g/L H_2SO_4 of acid concentration, 25 ˚C of leaching temperature, -780 μm of particle size and a solid/liquid ratio of 1/10. In these optimum conditions, 93.42% of zinc extraction and 1.58 (ton H_2SO_4/dissolved ton Zn) of acid consumption were achieved.

Keywords: Zinc oxide ore, acid leaching, sulfuric acid.

Sülfürik Asit Liçi ile Çinko Oksit Cevherinden Çinko Geri Kazanımı

Özet. Bu çalışmada sülfürik asit kullanılarak liç ile çinko oksit cevherinin kazanımı araştırılmıştır. Liç süresi, asit konsantrasyonu, liç sıcaklığı, partikül boyutu ve katı/sıvı oranı gibi bazı parametrelerin etkileri maksimum çinko ekstraksiyonu ve minimum asit tüketimi için araştırılmıştır. Optimum liç koşulları 120 dakika liç süresi, 55 g/L H_2SO_4 asit konsantrasyonu, 25 ˚C liç sıcaklığı, -780 μm partikül boyutu ve 1/10 katı/sıvı oranı olarak belirlenmiştir. Bu optimum koşullarda, %93.42 çinko ekstraksiyonu ve 1.58 (ton H_2SO_4/ çözünen ton Zn) asit tüketimi elde edilmiştir.

Anahtar Kelimeler: Çinko oksit cevheri, asit liç, sülfürik asit.

1. INTRODUCTION

Zinc is one of the three most important metals after aluminum and copper among non-ferrous metals in terms of utilization. In the past year, as other metals, the increasing demand for zinc in the world has required intensive studies for extraction of metals from zinc oxide ores. Zinc production can be achievable by both hydrometallurgical and pyrometallurgical processes. The hydrometallurgical process mainly contains acid leaching, alkaline leaching and ammonia leaching.

The term "oxide zinc ores" covers all of the oxide, carbonate and silicate of zinc minerals. Main zinc minerals are smithsonite ($ZnCO_3$), zincite (ZnO), hemimorphite ($Zn_4Si_2O_7(OH)_2$ $2H_2O$) and

willemite (Zn_2SiO_4). Leaching of these zinc oxide minerals by sulfuric acid can be described by Eqs. 1-4 [1-3].

$$ZnCO_3 + H_2SO_4 \rightarrow ZnSO_{4(aq)} + H_2O + CO_2 \qquad (1)$$

$$ZnO + H_2SO_4 \rightarrow ZnSO_{4(aq)} + H_2O \qquad (2)$$

$$Zn_4Si_2O_7(OH)_2.H_2O + 4H_2SO_4 \rightarrow 4ZnSO_{4(aq)} + Si_2O(OH)_6 + 3H_2O \qquad (3)$$

$$Zn_2SiO_4 + 2H_2SO_4 \rightarrow 2ZnSO_{4(aq)} + Si(OH)_{4(aq)} \qquad (4)$$
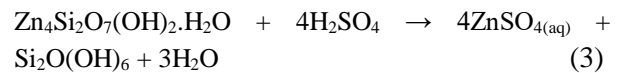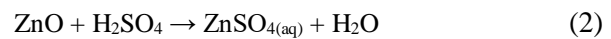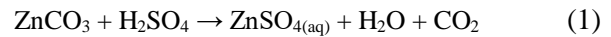
Hematite (Fe_2O_3), limonite ($FeO(OH).nH_2O$), dolomite ($CaMg(CO_3)_2$), calcite ($CaCO_3$) and quartz (SiO_2) are common gangue minerals in zinc oxide ores. Leaching of zinc oxide ores consumes

a great deal of acid because of the presence of large amounts of these gangue minerals. Therefore, it is of great significance to effectively achieve beneficiation by leaching these zinc oxide ores.

Sulfuric acid leaching of zinc ores has been studied by many researchers: Abdel-Aal [1] studied the kinetics of sulfuric acid leaching of low-grade zinc silicate ore, and the results showed that leaching of about 94% of zinc was achieved using a -200+270 mesh ore particle size at a reaction temperature of 70 °C for 180 minutes of reaction time with 10% sulfuric acid concentration and a solid:liquid ratio of 1:20 g/mL. Bodas [4] performed leaching of zinc silicate ore by sulfuric acid and found that the maximum zinc extraction (95% Zn) was obtained at a 4.5 M concentration of sulfuric acid in 3 h of leaching at 70 °C, keeping the solid:liquid weight ratio at 1:5. Canbazoğlu et al. [5] investigated dissolution of zinc in sulfuric acid solution from low-grade lead&zinc ore, and they reported that leaching of zinc could be achieved with 90% of zinc extraction with a consumption of 5607 kg of acid in the optimum leaching conditions as; leaching temperature: 60 °C, leaching time: 60 minutes, acid concentration: 100 g/L; particle size: 83.27% below 45 µm and stirring speed: 350 rpm. Uysal [6] studied evaluation of low-grade zinc oxide ore using sulfuric acid leaching, and the best leaching conditions were obtained to be 350 rpm of stirring speed, 60 minutes of leaching time, 75 g/L of acid concentration, 80 °C of leaching temperature, particle size of 80% below 60 µm and solid/liquid ratio of 1/10.

As known, zinc is produced mostly from zinc sulfide ores because sulfides are easy to separate from gangue. With declining reserves of zinc sulfides, there is an increasing focus on processing zinc oxide ores. Extensive studied have been performed to upgrade zinc ores by flotation, but this method had limited effect on their qualities. Many studies focused on using the hydrometallurgical route for zinc oxide ores in sulfuric acid or alkaline. The aim of this study is to achieve the maximum zinc extraction and minimum acid consumption from zinc oxide ore by leaching using sulfuric acid. Effects of several

parameters such as leaching time, acid concentration, leaching temperature, particle size and solid/liquid ratio on zinc leaching were investigated.

2. MATERIALS AND METHODS

The zinc oxide sample for the leaching study was obtained from Hakkari in Turkey. The results of the chemical analysis of the ore sample are shown in Table 1. X-ray diffraction (XRD) spectra of the sample were obtained using a Rigaku DMAX IIIC model X-ray diffractometer using CuKά radiation at 35 kV and 15 mV. X-ray diffraction analysis indicated that the mineralogical constituents were smithsonite ($ZnCO_3$), cerussite ($PbCO_3$) and goethite (FeOOH) (Figure 1).

In order to prepare the sample for experiments, the following steps were pursued: crushing (-2.8 mm), grinding (-250 µm) and sieving. H_2SO_4 from Merck, with an analytical purity of 95-98% was used in all leaching experiments. The leaching experiments were performed in a 1 L glass beaker that was placed in a thermostatically controlled water bath. The beaker was covered with a plastic cap that contained four holes for placing the mechanical stirrer, thermometer, pH meter or condenser and for taking samples. After leaching, the leach residue filtered from the leach solution, then washed with distilled water and dried at 105 °C to obtain total dissolved weight values. At the end of each experiment, the leach solution was analyzed by atomic adsorption spectrometry (AAS) to determine the degree of zinc extraction. The amount of sulfuric acid in the pregnant leach solution was determined by NaOH titration in order to determine the amount of consumed acid in the leaching experiments.

Zinc extraction and acid consumption were calculated using following equations (5-6):

$$ZE\,(\%) = \frac{\left[V1\,(mL)\; x\; S\; x\; \frac{1}{1000}\; x\; \frac{D\,(mg/L)}{1000}\right]\; x\; N\,(g)}{100} \tag{5}$$

ZE: Zinc extraction (%)
V1: The volume of H_2SO_4 used in leaching experiments (mL)
S: Dilution factor
D: Value of read in AAS (mg/L)
N: Amount of solid used in leaching experiments (g)

$$AC\,(g) = \left[LA\,(M)\; x\; V1\,(mL) - \frac{\left(\frac{M\,(mol)\; x\; T1\,(mL)}{T2\,(mL)}\right)\; x\; S}{2}\; x\; V1\,(mL)\right]\; x\; H\,(g/mol) \tag{6}$$

AC (g): Acid consumption (g)
LA: The molarity of H_2SO_4 used in leaching experiments (M)
V1: The volume of H_2SO_4 used in leaching experiments (mL)
M: The molarity of NaOH (M)
T1: The volume of NaOH spent in titration (mL)
T2: The volume of leaching solution used in titration (mL)
S: Dilution factor
H: Molecular weight of H_2SO_4 (g/mol)

Table 1. Chemical analysis of ore sample.

Component	Weight (%)
Zn	25.44
Fe	21.20
Pb	4.20
Cu	<0.01
Mn	0.17
Ca	0.47
Cd	0.09
Ni	<0.01
SiO_2	3.68
S	0.18
As	0.28
K	<0.10
Na	<0.10
Moisture	0.51
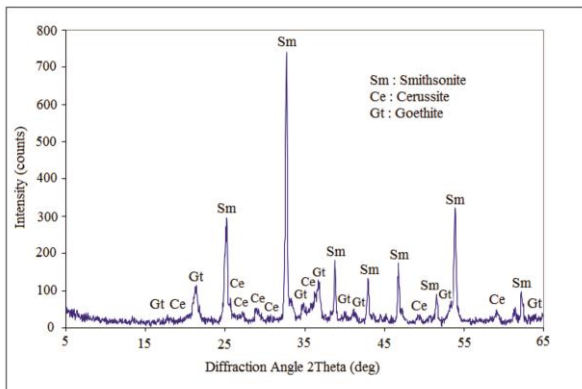
Figure 1. XRD pattern of the zinc oxide ore used in the experiments.
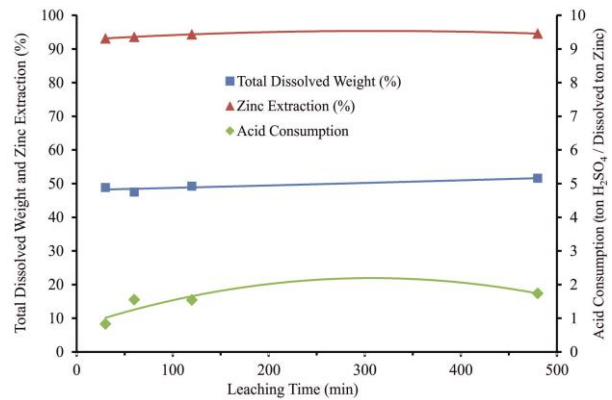
Figure 2. Effect of leaching time on the extraction of zinc.

3. RESULTS AND DISCUSSION

3.1. Effect of Leaching Time

The effect of leaching time was studied under the conditions that H_2SO_4 concentration was 75 g/L, leaching temperature was 40 ˚C, ore particle size was -250 µm and ratio of solid/liquid was 1/10. The results are shown in Figure 2. When the leaching time increased from 30 to 480 minutes, zinc extraction (%) increased from 93.16% to 94.58%, while total dissolved weight (%) only increased from 48.85% to 51.62%. It was seen that zinc extraction (%) and total dissolved weight (%) were not affected much by increasing the leaching time. Similarly, Xu et al. [3] observed that leaching time had no remarkable effects on the percentage of zinc extraction. On the other hand, acid consumption (ton H_2SO_4/dissolved ton Zn) increased by increasing the leaching time. As seen in Figure 2, 93.60% zinc was extracted in 60 minutes by 1.55 (ton H_2SO_4/dissolved ton Zn) acid consumption. Based on experimental results the leaching time of 60 minutes was chosen as the most suitable leaching time.

3.2. Effect of Acid Concentration

The experiment for the effect of acid concentration was carried out in the range of 25-125 g/L H_2SO_4 (Figure 3). The effect of acid concentration was investigated for a leaching time of 60 minutes at the temperature of 40 ˚C, particle size of -250 µm and solid/liquid ratio of 1/10. As observed in Figure 3, by increasing acid concentration, the amount of total dissolved weight (%) increased, and consequently, zinc extraction (%) increased. This behavior was previously observed by Abdel-Aal [1] and Bodas [4] in sulfuric acid media. However, increase in acid concentration causes an increase in acid consumption (ton H_2SO_4/dissolved ton Zn). Figure 3 shows that the total dissolved weight was 47.50%, and zinc extraction of 93.60% could be achieved at 75 g/L of H_2SO_4 concentration. For this reason, the acid concentration value was selected as 75 g/L in the experiments. Additionally, for economic reasons, the acid consumption was kept constant at 75 g/L.
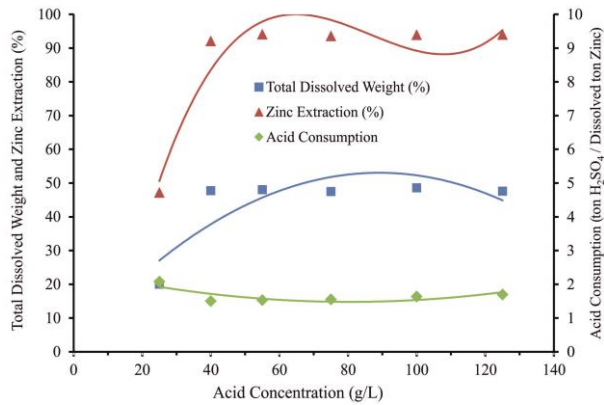
Figure 3. Effect of acid concentration on the extraction of zinc.

3.3. Effect of Leaching Temperature

The results that were obtained in the leaching experiments under different temperatures at the leaching time of 60 minutes using the 75 g/L H_2SO_4 concentration, the particle size of -250 µm and the 1/10 solid/liquid ratio are presented in Figure 4. The effect of temperature was investigated in the range of 25-90 ˚C. The leaching temperature did not have a significant effect on total dissolved weight (%) and zinc extraction (%). Moreover, acid consumption (ton H_2SO_4/dissolved ton Zn) increased as temperature increased. It seems that higher values of total dissolved weight (%) and zinc extraction (%) and a lower value of acid consumption (ton H_2SO_4/dissolved ton Zn) are achieved by lower temperatures. Consequently, the best results were obtained with the leaching temperature of 25 °C.

3.4. Effect of Particle Size

Effect of particle size on leaching was studied in the range of 90 µm to 1050 µm using ASTM standard sieves. The experiments were performed with different particle sizes for 120 minutes using 55 g/L H_2SO_4 at 25 ˚C temperature and 1/10 solid/liquid ratio. The results are given in Figure 5. As seen in Figure 5, total dissolved weight (%) and zinc extraction (%) increased with a decrease in particle size. Usually, the literature shows that the smaller the particle size, the faster the leaching of zinc, as observed by Souza et al. [7] and Wang et al. [8]. When the initial particle size (-1050 µm) of the ore decreased to -90 µm, zinc extraction (%) increased from 71.90% to 94.02%. However, the decrease in particle size did not affect total dissolved weight (%) and acid consumption (ton H_2SO_4/dissolved ton Zn) positively. The best results were obtained with the particle size of -780 µm because of the high total dissolved weight (46.34%) and high zinc extraction (93.42%) and low acid consumption (1.58 (ton H_2SO_4/dissolved ton Zn)) values.
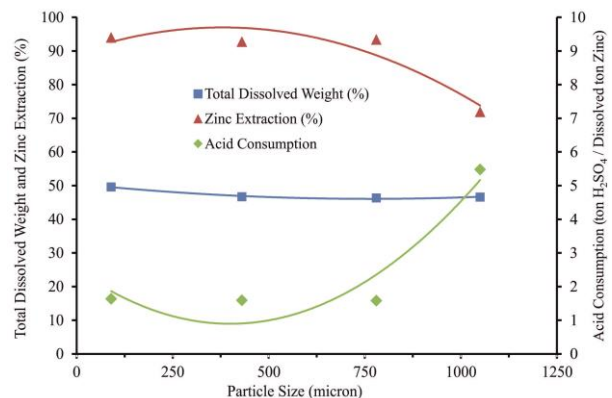
Figure 5. Effect of particle size on the extraction of zinc.

3.5. Effect of Solid/Liquid Ratio

Figure 6 presents the results of leaching with different solid/liquid ratios that was studied in the range of 1/4 to 1/10. The effect of solid/liquid ratio was investigated for a leaching time of 120 minutes at the temperature of 25 ˚C using 55 g/L H_2SO_4 and -780 µm of particle size. Figure 6 shows that the decrease in solid/liquid ratio increased total dissolved weight (%) and zinc extraction (%). Zinc

Figure 4. Effect of leaching temperature on the extraction of zinc.

extraction (%) increased from 50.09% at solid/liquid = 1/4 to 93.42% at solid/liquid = 1/10. Lower acid consumption by the 1.58 (ton H_2SO_4/dissolved ton Zn) value was obtained at the solid/liquid ratio of 1/10, too. Thus, it was determined to keep the solid/liquid ratio at 1/10. When the solid/liquid ratio was increased, the amount of dissolved per unit liquid increases, and hence, the rate of leaching decreases [9]. This is consistent with the result of Espiari et al. [10] in the treatment of zinc oxide ore by acidic leaching.
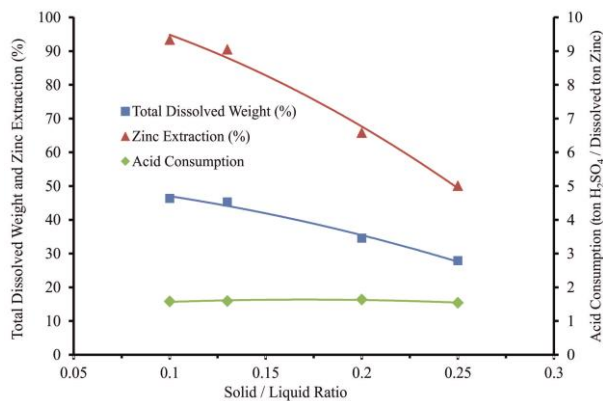
Figure 6. Effect of solid/liquid ratio on the extraction of zinc.

4. CONCLUSIONS

By optimizing the leaching parameters as summarized in Table 2, the experiments showed that it was possible to extract 93.42% of zinc with 46.34% total dissolved weight by 1.58 (ton H_2SO_4/dissolved ton Zn) acid consumption.

Table 2. The results of sulfuric acid leaching under optimum process conditions.

Leaching Time (minute)	120
Acid Concentration (g/L)	55
Leaching Temperature (ºC)	25
Particle Size (μm)	-780
Solid/Liquid Ratio	1/10

It was observed that the following conclusions could be drawn:

- Leaching time and leaching temperature did not have significant effects on leaching recovery of zinc oxide ore,
- Zinc extraction (%) increased gradually with sulfuric acid concentration,
- With decrease in particle size of zinc oxide sample, zinc extraction (%) increased,
- Zinc extraction (%) decreased as the solid/liquid ratio increased.

This study demonstrated that zinc oxide ore from Hakkari in Turkey could be successfully processed to recover zinc by sulfuric acid leaching.

Acknowledgement

REFERENCES

[1]. Abdel-Aal E.A., Kinetics of Sulfuric Acid Leaching of Low-Grade Zinc Silicate Ore, Hydrometallurgy, 55 (2000) 247-254.

[2]. Havlik T., Turzakova M., Stopic S., Friedrich B., Atmospheric Leaching of EAF Dust with Diluted Sulphuric Acid, Hydrometallurgy, 77 (2005) 41-50.

[3]. Xu H., Wei C., Li C., Fan G., Deng Z., Li M., Li X., Sulfuric Acid Leaching of Zinc Silicate Ore Under Pressure, Hydrometallurgy, 105 (2010) 186-190.

[4]. Bodas M.G., Hydrometallurgical Treatment of Zinc Silicate Ore from Thailand, Hydrometallurgy, 40 (1996) 37-49.

[5]. Canbazoğlu M., Kaya Ö., Kulaksız M.I., Nizamoğlu Y.S., Sulphuric Acid Leaching of Zinc from Low Grade Lead&Zinc Ores, Proceedings of the XIII Balkan Mineral Processing Congress, 2 (2009) 587-593.

[6]. Uysal G., The Evaluation of Low Grade Zinc Oxide Ore of Niğde Öküzgönü Tepe Using Sulfuric Acid Leaching and Solvent Extraction, MSc thesis, Cumhuriyet University, Department of Mining Engineering, (2011) Sivas, Turkey.

[7]. Souza A.D., Pina P.S., Lima E.V.O., Silva C.A., Leão V.A., Kinetics of Sulfuric Acid Leaching of a Zinc Silicate Calcine, Hydrometallurgy, 89 (2007) 337-345.

[8]. Wang R.X., Tang M.T, Yang S.H, Zhagn W.H, Tang C.B., He J. Yang J.G., Leaching Kinetics of Low-Grade Zinc Oxide Ore in NH_3-NH_4Cl-H_2O System, J. Cent. South Univ. Technol., 15 (2008) 679-683.

[9]. Bayrak B., Laçin O., Saraç H., Kinetic Study on the Leaching of Calcined Magnesite in Gluconic Acid Solutions, J. Ind. and Eng. Chem., 16 (2010) 479-484.

[10].Espiari S., Rashchi F., Sadrnezhaad S.K., Hydrometallurgical Treatment of Tailings with High Zinc Content, Hydrometallurgy 82 (2006) 54-62.

WOA-Miner: Classification Rule Discovery Using Whale Optimization Algorithm

Ufuk ÇELİK ⓘD

Bandirma Onyedi Eylul University, Omer Seyfettin Applied Science Faculty, Management Information Systems Department, Balikesir, TURKEY

Abstract. This paper proposes a rule discovery tool for classification by using whale optimization algorithm that simulates the foraging behavior of humpback whales. Rule extraction is based on the optimization of randomly selected attributes according to rule fitness value. Algorithm were implemented and tested the most known 13 datasets and the results were compared with other known data mining algorithms including Decision Tree, Naïve Bayes, J48, JRip, Artificial Bee Colony and Ant Colony Optimization. The obtained results showed that whale optimization algorithm proved an appropriate candidate for classification processes.

Keywords: Data mining, Classification, Rule discovery, Whale optimization algorithm.

Balina Optimizasyonu Algoritması Kullanarak Sınıflandırma Kuralları Keşfi: WOA-Madenci

Özet. Bu çalışma, kambur balinaların yiyecek arama davranışını simüle eden balina optimizasyonu algoritmasını kullanarak sınıflandırma için bir kural bulma aracı önermektedir. Kural çıkarımı, kural uygunluğuna göre rastgele seçilen niteliklerin optimizasyonuna dayanır. Algoritma en bilinen 13 veri setini uygulayarak test etmiş ve sonuçlar Karar Ağacı, Naive Bayes, J48, JRip, Yapay Arı Kolonisi ve Karınca Koloni Optimizasyonu dâhil diğer bilinen veri madenciliği algoritmalarıyla karşılaştırılmıştır. Elde edilen sonuçlar balina optimizasyon algoritmasının sınıflandırma süreçleri için uygun bir aday olduğunu kanıtlamıştır.

Anahtar Kelimeler: Veri madenciliği, Sınıflandırma, Kural keşfi, Balina optimizasyonu algoritması.

1.   INTRODUCTION

Classification rule discovery is one of the crucial algorithms in the rising field of data mining, which operates to extract a set of rules from a training dataset [1]. Therefore, any user can easily apply these classification rules to test dataset in order to make an intelligent decision. Classification needs labelled data for model building. Each instance of training dataset is allocated to one class, which is represented by some specific attributes, and a class label attribute. The classification model that is built from this allocation is then used to extract valuable information, discover patterns or predict the trends by classifying new dataset without class label attribute.

Classification rule discovery can be achieved with many different methods such as decision trees, artificial neural network, Naïve-Bayes or association rules [2, 5]. In this manner, optimization algorithms are widely used for rule extracting because of that they rely on basic concepts and are easy to develop [6]. Meta-heuristic optimization algorithms have capabilities

of solving many different problems from wide range of disciplines [7, 12]

Whale optimization algorithm (WOA) shown in Figure 1 is a new meta-heuristic optimization algorithm which mimics the foraging behavior of humpback whales [13].

Figure 1. Bubble-net feeding of humpback whale*.

*Whale Behavior (2013). Department of Marine and Coastal Ministry of Natural Resources and Environment, Available at: http://km.dmcr.go.th/th/c_1/s_209/d_9927 Retrieved November 12, 2018.

This algorithm is inspired from humpback whales' hunting tactic by using a spiral to simulate bubble-net attacking method in order to encircle their prey. In this concept, WOA-Miner creates classification rules by simulating this hunting behavior.

2. METHOD

Humpback whales have a special foraging mechanism. This hunting system that is called bubble-net feeding method [14] is done by creating specific air bubbles along a circle or spiral shape as shown in figure 1. This movement is the pattern maneuver, which starts from nearly 12 meters' down by creating bubbles in spiral shape around the prey and then finishes at the surface by

swimming up while encircling prey through the surface. The last maneuver consists of three different phases: coral loop, lob tail and capture loop. This phase is not included in WOA but more information about this stage is explained in detail by Goldbogen et al. [15]. Thus, WOA is a mathematical modelling of this unique behavior's first phase (spiral bubble-net feeding movement) that can only be observed in humpback whales.

2.1 Mathematical model of whale optimization algorithm (WOA)

WOA contains 4 phases called initialization, encircling prey, bubble-net feeding behavior and search for prey. In this section, mathematical models of these four stages are explained.

Initialization is about creating a search space of food source (FS) for the whales. This space consists of W for whales and N for parameters to be optimized. W is the total number of whales and N is the size of solution vector which is dimension of FS. Each value of N is limited with lower and upper bounds. In this phase, randomly selected attributes are defined as $X_{wd} = (X_{1,1}, \ldots, X_{WD}) \in FS$, $w = 1, \ldots, W$, $d = 1, \ldots, D$ and they are calculated the equation (2.1) below within the range [0,1].

$$(2.1) \quad X_{w,1} = lb + rand(0,1) \times (ub - lb)$$

Encircling prey is to define the position of forage and covering in a circle by whale. The ideal position in the search space is not known at the beginning. Therefore, WOA accepts that this new candidate solution is the target forage or close to the best. The best position is calculated in initialization according to fitness value first time. After that, the other agents try to update new position according to the best search agent. This model is formulated by the equations below:

$$(2.2) \quad \vec{D} = \left| \vec{C} \times \overrightarrow{X_{best}}(t) - \vec{X}(t) \right|$$

$$(2.3) \quad \vec{X}(t + 1) = \overrightarrow{X_{best}}(t) - \vec{A} \times \vec{D}$$

In this equation $|\ldots|$ is for absolute value, and $\times$ is element-by-element multiplication, where t represent the current iteration, $\vec{A}$ and $\vec{C}$ are coefficient vectors, $\overrightarrow{X_{best}}$ is the best solution and $\vec{X}$

is the position vector. Search agents changes their positions by adjusting the value of $\vec{A}$ and $\vec{C}$ vectors. By the way, $\overrightarrow{X_{best}}$ is updated if there is a better solution in each iteration. The formulation of $\vec{A}$ and $\vec{C}$ is given below:

(2.4) $\vec{A} = 2a \times r - a$

(2.5) $\vec{C} = 2 \times r$

where a is decreased from 2 to 0 linearly in each iteration and r is random value within [0,1]. Decreasing value of a in the equation (2.4) is one of the mechanism called *shrinking encircling* in *bubble-net feeding behavior (exploitation)*. Another approach for bubble-net feeding is named as *spiral updating position*, which mimics the helix-shaped movement of humpback whales. This spiral equation given in (2.6) is created between the positon of whale and forage.

(2.6) $\vec{X}(t + 1) = \overrightarrow{D'} \times e^{bl} \times \cos(2\pi l) + \overrightarrow{X_{best}}(t)$

In this equation, $\overrightarrow{D'} = \left|\overrightarrow{X_{best}}(t) - \vec{X}(t)\right|$ represents the absolute distance between the best position of whale and the current position of forage, b is a constant value in order to define the shape of spiral, l is a random value between -1 and 1.

Humpback whales swim around the forage in a shrinking circle and a spiral-shaped concurrently. It is assumed that there is a probability of 50% to choose one of this mechanism in order to change position of search agents during optimization. Mathematical model of this selection is given in equation (2.7) below.

(2.7) $\vec{X}(t + 1) =$
$$\left\{ \begin{array}{ll} \overrightarrow{X_{best}}(t) - \vec{A} \times \vec{D} & if\ p < 0.5 \\ \overrightarrow{D'} \times e^{bl} \times \cos(2\pi l) + \overrightarrow{X_{best}}(t) & if\ p \geq 0.5 \end{array} \right\}$$

A random number p between 0 and 1 is used to select movement. Foraging process of whales continue with *search for prey (exploration)* mechanism additionally bubble-net feeding behavior. This is a random search mechanism, which uses $\vec{A}$ vector if $\vec{A} > 1$. Then WOA performs a global search with the mathematical model as given below.

(2.8) $\vec{D} = \left|\vec{C} \times \overrightarrow{X_{rand}} - \vec{X}\right|$

(2.9) $\vec{X}(t + 1) = \overrightarrow{X_{rand}} - \vec{A} \times \vec{D}$

In this model, $\overrightarrow{X_{rand}}$ is a randomly selected position vector (a random whale) from the current population. In focus to exploitation stage, this randomly selected agent instead of best position is used by WOA in the exploration stage to perform a global search.

The WOA, which its pseudo code was presented in figure 2, has as a global optimization capability because of its exploration and exploitation futures. The algorithm takes some input parameters such as W for total number of whales, D for total number of parameters in solution, MaxCycle for maximum number of iterations, ObjFunc is for objective function for fitness calculation.

After taking input parameters, the algorithm sets random solutions (determines whale population) and finds the X_{best}. WOA takes parameter p for bubble-net attacking method and decides spiral or circular movement according to the value of p. If $\left|\vec{A}\right| \geq 1$, a random agent is selected for global search whereas best solution is found if $\left|\vec{A}\right| < 1$ for position updates.

Figure 2. Pseudo-code of the WOA.

```
Inputs:
W: total number of whales (search agents)
D: total number of parameters to be optimized
MaxCycle: the total number of iteration
ObjFunc: fitness function
Outputs:
X_best: optimum values of D to discover best prey
[best_solution] = WOA (W, D, MaxCycle, ObjFunc) {
    // Initialization phase:
    for each W {
        for each D {
            Determine random values of whale population X_{wd} = (X_{1,1}, ..., X_{W,D})
        }
    }
    while (t < MaxCycle) {
        Find X_best according to ObjFunc for each search agent
        Decrease a linearly from 2 to 0 in equation (2.4)
        for each W {
            // shrinking encircling mechanism phase:
            Update A, C, l and p
            for each D {
                if (p < 0.5) {
                    if (|A⃗| < 1) {
                        // encircling prey phase:
                        Update agent's position by the equation (2.2)
                    } else if (|A⃗| ≥ 1) {
                        // search for prey phase:
                        Choose a random agent (X_rand)
                        Update agent's position by the equation (2.9)
                    }
                } else if (p ≥ 0.5) {
                    // spiral updating position phase:
                    Update agent's position by the equation (2.6)
                }
            }
        }
        Avoid the out of bound if agent goes beyond
        Calculate each agent's fitness value according to ObjFunc
        Update X_best for a better solution
        t = t +1
    }
    return X_best
}
```

After taking input parameters, the algorithm sets random solutions (determines whale population) and finds the X_{best}. WOA takes parameter p for bubble-net attacking method and decides spiral or circular movement according to the value of p. If $|\vec{A}| \geq 1$, a random agent is selected for global search whereas best solution is found if $|\vec{A}| < 1$ for position updates.

2.2 Classification performance

Classification rules has two parts namely antecedent and consequent. First part includes some conditions in a conjunction form of "IF attribute$_1$ = value$_1$ and ... attribute$_n$ = value$_n$". Consequent part includes the prediction class in the form of "THEN class=Class$_x$". Briefly, classification rule discovery is to assign a relevant class for a rule while adding attributes to its antecedent part if the conditions match with

attributes. The quality of the rule can be calculated several fitness measures such as entropy or gini index.

In this study, ROC analysis approach was used as fitness function (f-measure) formulated in equation (2.10) for the rule quality [16,17]. This is a harmonic mean of precision and recall (sensitivity) in order to seek a balance between them. Additionally, accuracy value was obtained for the classification performance by using 10-fold cross validation method.

$$(2.10) \quad F = 2 \times \frac{precision \times recall}{precision+recall} = 2 \times \frac{\frac{TP}{TP+FP} \times \frac{TP}{TP+FN}}{\frac{TP}{TP+FP} + \frac{TP}{TP+FN}} = \frac{2TP}{2TP+FP+FN}$$

In order to determine rule fitness, each instance must be calculated according to prediction and the actual result. There are four groups called true positive (TP), false positive (FS), false negative (FN) and true negative (TN). All instances fall into one of these groups in this approach, which was shown in table 1.

Table 1. ROC analysis of Rule Test against Training Set.

	Actual	
Prediction	True	False
True	TP	FP
False	FN	TN

- TP is the number of instances whose attributes are covered by the rule and class is same as prediction
- FP is the number of instances whose attributes are covered by the rule but the class is different from prediction
- FN is the number of instances whose attributes are not covered by the rule, but the class is same as prediction
- TN is the number of instances whose attributes are not covered by the rule and the class is different form prediction.

In ROC analysis, precision as positive predictive value shows how many of the prediction are actual positive by division of true positive predictions in total predictive positives. Recall also named sensitivity or true positive rate identifies actual positive by division of true positives in total of true positive and false negatives. Finally, AUC stands for "Area Under the ROC Curve". If the AUC is higher, model prediction is closer to the 100%.

2.3 WOA-Miner algorithm

WOA-Miner algorithm which its pseudo-code is presented in figure 3 takes some input parameters additionally to the WOA such as TS for training set, MICR for minimum instances which is the number of instances that must be covered by the rule and MUI for the maximum uncovered instances which is used for stopping new rule discovery.

WOA-Miner consists of three important mechanisms namely, rule discovery, removing unnecessary conditions, default rule determining. WOA-Miner initializes a whale population as food source, which is created from randomly selected values of attributes between the lower and the upper boundaries of dataset. Rule discovery phase takes best solution from the dimension using by WOA and constructs the rule adding by each attribute. WOA-Miner determines the rule consequent for that rule and eliminates unnecessary conditions by removing each attribute recursively. Then it calculates the rule quality using equation (2.10). If the rule quality is a better than the best quality, it inserts the rule into ruleset and removes classified examples from dataset using by this ruleset. For the uncovered instances, the most frequent class is selected as consequent part of the default rule without antecedent part. Finally, algorithm returns the ruleset.

3. DATASETS

To evaluate the performance of WOA-Miner algorithm, several datasets from UCI Machine Learning Repository were used [18]. Dataset that has numerical attributes was normalized and converted to nominal values because of the rule-

based algorithm has only nominal attributes capability in the terms of rule discovery process.

Table 2 shows the properties of datasets used in the study.

```
Inputs:
TS: training dataset
MICR: minimum instances covered by the rule
MUI: maximum uncovered instances
Outputs: significant classification rules
Variables:
CovAtt = number of attributes that is covered by rule
// rule discovery phase
while (MUI < Number of Instances) {
    X[D] = WOA (W, D, MaxCycle, ObjFunc)
    while (MICR > CovAtt) {
        Rule = ConstructRuleAddingByEachAttribute (X, DefaultClassIndex)
        CovAtt++
    }
    Rule = DetermineRuleConsequent (Rule)
    Rule = RemoveUnnecessaryConditions (Rule) // attribute pruning
    Rule = CalculateRuleQuality (Rule)
    if (RuleQuality > BestQuality) {
        RuleSet = AddRule (Rule)
        DataSet = RemoveClassifiedExamples (Rule)
    }
}
// find default class of uncovered instances
FreqClass = DefineMostFrequentClass (DataSet)
RuleSet = AssignClass(FreqClass)
return RuleSet
```

Figure 3. Pseudo-code of WOA-Miner algorithm.

Table 2. Properties of the datasets used in the study.

Datasets	Samples	Attributes	Attribute Type	Classes
Breast Cancer	286	9	Nominal	2
Breast Cancer Wisconsin (Original)	699	9	Nominal, Numerical	2
Chess (King-Rook vs. King-Pawn)	3196	35	Nominal	2
Dermatology	366	34	Nominal, Numerical	6
Diabetes	768	8	Numerical	2
Lymphography	148	18	Nominal, Numerical	4
Mushroom	8124	22	Nominal	2
Nursery	12960	8	Nominal	5
Soybean (Large)	683	35	Nominal	19
Molecular Biology (Splice-junction Gene Sequences)	3190	60	Nominal	3
Tic-Tac-Toe Endgame	958	9	Nominal	2
Congressional Voting Records	435	16	Nominal	2
Zoo	101	17	Nominal	7

4. RESULTS AND DISCUSSION

In this study, experiments were conducted by using WEKA workbench machine learning software with the usage of experimenter module [19]. This module allows experimenting each dataset recursively running one-by-one under the selected algorithms. The experiment result of algorithms was shown in Table 3.

Table 3. Analysis experiments result.

Data	Algorithms	Average Accuracy	Average Precision	Average Recall	Average F Measure	Average ROC
breast-cancer	DT	73.473	0.758	0.925	0.831	0.668
	J48	75.542	0.759	0.960	0.847	0.628
	JRip	70.948	0.766	0.855	0.802	0.612
	NB	71.700	0.781	0.836	0.806	0.715
	ACO	76.576	0.785	0.925	0.848	0.657
	ABC	74.483	0.761	0.935	0.837	0.617
	WOA	**74.137**	**0.776**	**0.892**	**0.827**	**0.639**
wisconsin	DT	92.851	0.930	0.965	0.947	0.973
	J48	94.420	0.962	0.954	0.957	0.961
	JRip	94.422	0.961	0.954	0.957	0.951
	NB	97.280	0.992	0.967	0.979	0.992
	ACO	89.128	0.869	0.985	0.922	0.849
	ABC	91.128	0.896	0.980	0.936	0.880
	WOA	**89.256**	**0.872**	**0.982**	**0.923**	**0.852**
chess_kr-vs-kp	DT	97.216	0.978	0.968	0.973	0.986
	J48	99.437	0.993	0.996	0.995	0.999
	JRip	99.187	0.991	0.993	0.992	0.994
	NB	87.891	0.876	0.895	0.885	0.952
	ACO	92.773	0.891	0.984	0.935	0.925
	ABC	59.448	0.642	0.505	0.565	0.599
	WOA	**93.849**	**0.915**	**0.974**	**0.943**	**0.937**
dermatology	DT	86.869	0.864	1.000	0.925	0.976
	J48	94.550	0.966	0.964	0.964	0.982
	JRip	89.047	0.967	0.964	0.964	0.982
	NB	97.267	1.000	1.000	1.000	1.000
	ACO	92.620	0.872	1.000	0.929	0.964
	ABC	89.910	0.937	0.964	0.948	0.967
	WOA	**93.252**	**0.938**	**0.981**	**0.958**	**0.975**
diabetes	DT	64.973	0.693	0.834	0.756	0.619
	J48	65.106	0.651	1.000	0.789	0.500
	JRip	65.752	0.683	0.888	0.771	0.555
	NB	67.840	0.753	0.754	0.753	0.740
	ACO	0.000	0.000	0.000	0.000	0.000
	ABC	65.236	0.658	0.970	0.784	0.515
	WOA	**65.444**	**0.657**	**0.983**	**0.787**	**0.512**
lymphography	DT	78.286	0.100	0.100	0.100	0.518
	J48	79.714	0.500	1.000	0.833	0.982
	JRip	74.905	0.000	0.000	0.000	0.357
	NB	85.667	0.667	1.000	1.000	1.000
	ACO	77.000	0.000	0.000	0.000	0.482
	ABC	71.524	0.000	0.000	0.000	0.500
	WOA	**73.633**	**0.000**	**0.000**	**0.000**	**0.495**
mushroom	DT	100.000	1.000	1.000	1.000	1.000
	J48	100.000	1.000	1.000	1.000	1.000
	JRip	100.000	1.000	1.000	1.000	1.000
	NB	95.827	0.932	0.992	0.961	0.998
	ACO	84.404	0.793	0.971	0.870	0.839
	ABC	90.965	0.890	0.968	0.922	0.907
	WOA	**92.926**	**0.905**	**0.980**	**0.938**	**0.927**
nursery	DT	94.699	1.000	1.000	1.000	1.000
	J48	97.052	1.000	1.000	1.000	1.000
	JRip	96.836	0.975	1.000	0.988	0.994
	NB	90.324	1.000	1.000	1.000	1.000
	ACO	86.566	1.000	1.000	1.000	1.000
	ABC	63.912	1.000	0.734	0.801	0.867
	WOA	**57.106**	**0.738**	**0.172**	**0.251**	**0.580**
soybean	DT	84.312	0.619	1.000	0.735	1.000
	J48	91.509	0.967	0.950	0.947	0.974
	JRip	92.236	1.000	1.000	1.000	1.000

	Algorithm				
	NB	92.965	1.000	1.000	1.000	1.000
	ACO	70.727	0.967	1.000	0.980	0.999
	ABC	64.572	1.000	1.000	1.000	1.000
	WOA	**67.967**	**0.944**	**0.920**	**0.965**	**0.959**
splice	DT	78.809	0.567	0.919	0.701	0.972
	J48	94.075	0.911	0.961	0.935	0.971
	JRip	93.981	0.926	0.937	0.931	0.969
	NB	95.298	0.938	0.936	0.937	0.995
	ACO	0.000	0.000	0.000	0.000	0.000
	ABC	74.514	0.666	0.729	0.656	0.793
	WOA	**85.978**	**0.776**	**0.926**	**0.835**	**0.919**
tic-tac-toe	DT	73.388	0.619	0.632	0.622	0.802
	J48	84.546	0.783	0.768	0.773	0.898
	JRip	97.808	0.980	0.958	0.968	0.978
	NB	69.616	0.586	0.428	0.493	0.747
	ACO	72.546	0.821	0.472	0.499	0.666
	ABC	70.764	0.569	0.692	0.608	0.704
	WOA	**71.398**	**0.574**	**0.785**	**0.653**	**0.731**
vote	DT	94.947	0.954	0.966	0.959	0.979
	J48	96.332	0.971	0.970	0.970	0.980
	JRip	95.412	0.974	0.951	0.962	0.955
	NB	90.143	0.945	0.892	0.917	0.971
	ACO	95.867	0.961	0.974	0.967	0.954
	ABC	92.632	0.940	0.940	0.939	0.922
	WOA	**95.539**	**0.975**	**0.952**	**0.963**	**0.956**
zoo	DT	86.273	0.893	1.000	0.938	0.996
	J48	92.182	1.000	1.000	1.000	1.000
	JRip	87.273	0.860	0.975	0.903	0.936
	NB	95.091	1.000	0.950	0.971	1.000
	ACO	91.182	0.873	1.000	0.927	0.943
	ABC	85.273	0.940	0.950	0.938	0.950
	WOA	**91.555**	**0.870**	**0.998**	**0.925**	**0.942**

In this table, WOA-Miner significant classification capability over all the datasets. The algorithm obtained the results by employing 10 whales, adjusting 3 for the parameter minimum cases per rule, 10 for maximum uncovered cases, 10 for convergence of rules with the implementation of 100 iterations and 0.5 for shape spiral parameter. The classification performance of WOA-Miner was compared with the other meta-heuristic algorithms such as Artificial Bee Colony (ABC) and Ant Colony Optimization (ACO), decision tree algorithms such as Decision Table (DT), JRip and other classification algorithms such as J48 and Naïve Bayes (NB).

For the "Breast Cancer" dataset experiment, ACO obtains the best result for average accuracy [20]. Although WOA has the best maximum accuracy among the algorithms, it has a very low result for min-accuracy, which decreases the average. ABC algorithms is also better than WOA.

"Breast Cancer Wisconsin (Original)" dataset has numeric attributes; therefore, it was normalized in scale of 0 to 1 before the classification [21,22]. This situation results a low classification performance for the WOA as well as ACO and ABC. In this experiment, NB algorithm has the best performance for all accuracy types.

"Chess (King-Rook vs. King-Pawn)" dataset was classified by using WOA with the results of 93.849% average accuracy, which is near to ACO and it is better than ACO, NB and ABC [23].

Experiment for the "Dermatology" dataset shows a remarkable classification performance for all algorithms used [24]. According to maximum accuracy rates, each algorithm reached the 100% maximum average classification performance except the DT. WOA is on the third rank and it is better than ACO and ABC. Another point for this dataset is that it has both numerical and nominal attributes.

"Diabetes" dataset contains only numerical attributes; therefore, it has a low classification performance for all algorithms when it is compared the other datasets. In addition, even the ACO algorithm cannot build the classifier for this dataset because of the wide range of numerical attributes cannot be calculated with the entropy equation. In this experiment, WOA obtained the better results than ABC and ACO as it was placed in third rank.

"Lymphography" dataset has both numerical and numerical attributes and it was normalized before the experiment [25]. WOA has a very low level for the minimum accuracy which decreases the average performance same as "Breast Cancer" dataset. However, WOA is better than ABC in this experiment. In this dataset, NB has the best performance with the result of 85.667% accuracy.

"Mushroom" is a well-balanced dataset for the class attribute [26]. Hence, it has a great classification capability for the algorithms. However, WOA gives a 92.926% average accuracy but it is better than ABC and ACO in this experiment.

WOA is the worst algorithm for the "Nursery" dataset with the result of 57.106%. which is near to the ABC algorithm [27, 28].

"Soybean (Large)" dataset is not a well-balanced dataset with 19 different class attribute [29]. This can be a reason for bad classification performance of WOA as well as ABC and ACO algorithm. However, WOA obtained a better result than ABC.

"Molecular Biology (Splice-junction Gene Sequences)" dataset has a wide range of attributes as well as instances [30]. Actually, all attributes in this dataset are nominal but it is also an unbalanced class dataset. However, WOA is better than ABC, DT and ACO algorithm with the result of minimum, maximum and average accuracies are 67.712%, 92.476% and 85.978% respectively. In this experiment, ACO could not build the classifier.

"Tic-Tac-Toe Endgame" dataset experiment showed a low performance when it is compared with the other datasets [31]. JRip is the best

algorithm. WOA has gathered better result than ABC and NB.

"Congressional Voting Records" dataset has the 100% maximum accuracy for all algorithms [32]. However, when the performance is compared according to the average accuracy. WOA is placed in third rank and it is better than JRip, DT, ABC and NB.

Although, all algorithms have 100% maximum accuracy rate in the "Zoo" dataset, WOA is worse than J48 and NB algorithms according to average accuracy [33]. However, it was placed in third order and it is better than ABC and ACO, DT and JRip.

5. CONCLUSION

In this article, a new approach for rule-based classification by using meta-heuristic algorithm called WOA-Miner has been represented. Developed and coded algorithm by author was experimented using Weka benchmark software. According to the results obtained from experiments, the algorithm mostly produces better accuracy or sensitivity performance results in datasets taken from real life examples when it is compared to the similar rule-based algorithms. Regarding predictive accuracy, WOA-Miner significantly outperformed when it is compared to the other meta-heuristic algorithms such as ABC and ACO in most datasets. On the other hand, classical rule-based classification methods like DT, J48 or NB have the better performance than WOA-miner in most datasets.

In addition, this algorithm generates the rules after a pruning mechanism, which eliminates the unnecessary and repeated rules. WOA-miner is also a good classifier for the datasets that have numeric attributes. Because, the algorithm search mechanism is not based on the information theory, which is used in many meta-heuristic algorithms like ACO used in this study. Therefore, it can be concluded that the proposed WOA-Miner algorithm can be considered as another beneficial and accurate classifier among the rule-based

classification methods for numerical and nominal values.

Of course, algorithm still needs to be improved in order to increase the accuracy performance in some datasets such as cancer or nursery. WOA also should be tested on some newly created datasets from different concepts especially for big data. This is another subject of the future work.

REFERENCES

[1]. Cano A., Zafra A. and Ventura S., An Interpretable Classification Rule Mining Algorithm, Inf Sci (Ny), 240 (2013) 1–20.

[2]. Wang J.L. and Chan S.H., Stock Market Trading Rule Discovery Using Two-Layer Bias Decision Tree, Expert Syst Appl, 30-4 (2006) 605–611.

[3]. Shukla A., Tiwari R., Ranjan R.A. and Kala R., Multilingual Character Recognition Using Hierarchical Rule Based Classification and Artificial Neural Network, Lect. Notes Comput. Sci. (including Subser. Lect. Notes Artif. Intell. Lect. Notes Bioinformatics), 5552-2 (2009) 821–830.

[4]. Sharawi M., Zawbaa H.M. and Emary E., Feature Selection Approach Based on Whale Optimization Algorithm, Ninth Int. Conf. Adv. Comput. Intell., (2017) 163–168.

[5]. Canayaz M. and Demir M., Feature Selection with the Whale Optimization Algorithm and Artificial Neural Network, Int. Artif. Intell. Data Process. Symp., IEEE, (2017) 1–5.

[6]. Khan S.A., Nazir M. and Riaz N., Optimized Features Selection for Gender Classification Using Optimization Algorithms, Turkish J Electr Eng Comput Sci, 21-5 (2013) 1479–1494.

[7]. Rodrigues D., Papa J.P. and Adeli H., Meta-Heuristic Multi and Many Objective Optimization Techniques for Solution of Machine Learning Problems, Expert Syst, 34-6 (2017) e12255.

[8]. Diao R. and Shen Q., Nature Inspired Feature Selection Meta-Heuristics, Artif Intell Rev 44-3 (2015) 311–340.

[9]. Celik M., Karaboga D. and Koylu F., Artificial Bee Colony Data Miner (ABC-Miner), Int. Symp. Innov. Intell. Sys. App. (INISTA), (2011) 96–100.

[10]. Michelakos I., Mallios N., Papageorgiou E. and Vassilakopoulos M., Ant Colony Optimization and Data Mining, Next Gener. Data Technol. Collect. Comput. Intell., N. Bessis and F. Xhafa, (Eds). Berlin: Springer Heidelberg, 352 (2011) 31–60.

[11]. Parpinelli R.S., Lopes H.S. and Freitas A.A., Data Mining with an Ant Colony Optimization Algorithm, Evol Comput IEEE Trans, 6-4 (2002) 321–332.

[12]. Shunmugapriya P. and Kanmani S., A Hybrid Algorithm Using Ant and Bee Colony Optimization for Feature Selection and Classification (AC-ABC Hybrid), Swarm Evol Comput, 36 (2017) 27–36.

[13]. S. Mirjalili and Lewis A., The Whale Optimization Algorithm, Adv Eng Softw, 95 (2016) 51–67.

[14]. Wiley D., Ware C., Bocconcelli A., Cholewiak D., Friedlaender A., Thompson M., et al., Underwater Components of Humpback Whale Bubble-Net Feeding Behaviour, Behaviour, 148-5 (2011) 575–602.

[15]. Goldbogen J.A., Friedlaender A.S., Calambokidis J., McKenna M.F., Simon M., Nowacek D.P., Integrative Approaches to the Study of Baleen Whale Diving Behavior, Feeding Performance and Foraging Ecology, BioScience, 63-2 (2013) 90–100.

[16]. Gribskov M. and Robinson N.L., Use of Receiver Operating Characteristic (ROC) Analysis to Evaluate Sequence Matching, Comput Chem, 20-1 (1996) 25–33.

[17]. Fawcett T., An Introduction to ROC Analysis, Pattern Recognit Lett, 27-8 (2006) 861–874.

[18]. Dheeru D. and Taniskidou E.K., (UCI) Machine Learning Repository, Available at: http://archive.ics.uci.edu/ml. Retrieved November 7, 2018.

[19]. Witten I.H., Frank E., Hall M.A. and Pal

C.J., (Eds). Appendix B - The WEKA Workbench in Data Mining 4th Edition Practical Machine Learning Tools and Techniques, USA: Morgan Kaufmann, 2017.

[20]. Zwitter M. and Soklic M., Breast Cancer Data Set, University Medical Centre, Institute of Oncology, Ljubljana, Yugoslavia, 1998, Available at: https://archive.ics.uci.edu/ml/datasets/brea st+cancer. Retrieved November 7, 2018

[21]. Wolberg W.H. and Mangasarian O.L., Multisurface Method of Pattern Separation for Medical Diagnosis Applied to Breast Cytology, Proc Natl Acad Sci, 87-23 (1990) 9193–9196.

[22]. Mangasarian O.L., Street W.N. and Wolberg W.H., Breast Cancer Diagnosis and Prognosis Via Linear Programming, Oper Res, 43-4 (1995) 570–577.

[23]. Shapiro A.D., Structured Induction in Expert Systems. Boston: Addison-Wesley Longman Publishing Co, 1987.

[24]. Güvenir H.A., Demiröz G. and İlter N., Learning Differential Diagnosis of Erythemato-Squamous Diseases Using Voting Feature Intervals, Artif Intell Med, 13-3 (1998) 147–165.

[25]. Zwitter M. and Soklic M., Lymphography Data Set, University Medical Centre, Institute of Oncology, Ljubljana, Yugoslavia, 1988, Available at: http://archive.ics.uci.edu/ml/datasets/Lymp hography. Retrieved November 7, 2018.

[26]. Schlimmer J., Mushroom Data Set, National Audubon Society Field Guide to North American Mushrooms. USA: National Audubon Society, 1988.

[27]. Zupan B., Bohanec M., Bratko I. and Demsar J., Machine Learning by Function Decomposition, ICML, (1997) 421–429.

[28]. Olave M., Rajkovic V. and Bohanec M., Chapter 10: An Application for Admission in Public School Systems, Expert Systems in Public Administration, USA: Elsevier Science Ltd., 1989; pp 145–160.

[29]. Michatski R.S., Michalski R.S. and Chilausky R.L., Knowledge Acquisition by Encoding Expert Rules Versus Computer Induction' From Examples: A Case Study Involving Soybean Pathology, 51-1 (2002) 63–67.

[30]. Noordewier M.O., Towell G.G. and Shavlik J.W., Training knowledge-based neural networks to recognize genes in DNA sequences, NIPS'90 Proceedings of the 3rd International Conference on Neural Information Processing Systems, San Francisco: Morgan Kaufmann Publishers Inc., 1990; pp 530–536.

[31]. Aha D.W., Tic-Tac-Toe Endgame, UCI Machine Learning Repository, Available at: http://archive.ics.uci.edu/ml/datasets/Tic-Tac-Toe+Endgame. Retrieved November 7, 2018.

[32]. Schlimmer J., Congressional Voting Records Data Set, 98th Congress, 2nd session 1984, Washington, D.C.: Volume XL: Congressional Quarterly Inc., 1985.

[33]. Forsyth R., Zoo Data Set, UCI Machine Learning Repository, Available at: http://archive.ics.uci.edu/ml/datasets/Zoo. Retrieved November 7, 2018.

Cumhuriyet Science Journal

CSJ

Comprehension of Road Traffic Signs by Various Road Users in Kano City

Ibrahim Khalil UMAR[*] , *Samir BASHIR*

Kano State Polytechnic, Department of Civil Engineering Technology, Kano, NIGERIA

Abstract. Human perception of the information on the road signs is a critical factor in determining the safe use of both the vehicle and the interacting environment. A total of 30 road traffic signs which includes10-warning, 10-regulatory and 10-informatory signs were evaluated using 190 questionnaires to determine comprehension level of road users in Kano. The questionnaire was administered to both private and commercial drivers of trucks, cars, tricycle, motorcycle, and bicycle. Majority of the respondents are male (91.6%) which is due to the disproportionate ratio between male and female drivers in Kano city and 90% of them are youth below the age of 40 years showing that majority of the state drivers are young people. The comprehension level was found to be good 79%. The least comprehended signs in Kano are "park and ride" with comprehension level of 54.7%, followed by "Narrow bridge" (60%), "line merge ahead" (62.1%), "slippery road" (63.2%), "No entry for all vehicles" (70.5%). The signs with up to 90% recognition were "fuel station", "stop sign" and "school crossing". Sex, education, driving experience and type of vehicle used seems to affect the comprehension level of drivers in Kano. Truck drivers have a poor understanding of the traffic signs lower than all other classes of road users (65%).

*Keywords***:** Comprehension, road signs, driving experience.

Kano Şehrindeki Çeşitli Yol Kullanıcıları Tarafından Yol Trafik İşaretlerininin Bilinirliği

Özet. Yol işaretlerinin insanlar tarafından algılanabilirliği hem araçların hemde etkileşimindeki çevrenin güvenilir olarak kullanılabilmesi için kritik bir faktördür. Bu çalışmada 190 anket kullanılarak Kano şehrindeki yol kullanıcılarının 10 adet uyarı, 10 adet trafik tanzim ve 10 adet trafik bilgi işareti olmak üzere toplam 30 trafik işaretini kavrama seviyeleri değerlendirilmiştir. Anketler hem şahsi hem de ticari kamyon, otomobil, triportör (üç tekerlekli bisiklet), motorsiklet ve bisiklet sürücülerine yöneltilmiştir. Kano şehrindeki erkek ve bayan sürücü orantısızlığına bağlı olarak ankete katılanların çoğunluğu erkektir (91.6%) ve 90%'ı 40 yaşın altındadır, bu durum bölgedeki sürücülerin birçoğunun genç olduğunu göstermektedir. İşaretlerin bilinirlik seviyesi 79% olarak bulunmuştur. Kano'daki en az kavranan işaretler 54.7% bilinirlik seviyesi ile "Park et devam et" işaretidir. Bunu "Daralan köprü" (60%), "İleride birleşen şerit" (62.1%), "Kaygan yol" (63.2%) ve "Araç giremez" (70.5%) işaretleri takip etmektedir. Bilinirliği 90%'a varan işaretler, "Benzin istasyonu", Dur işareti" ve "Okul geçidi" dir. Cinsiyet, eğitim, sürüş tecrübesi ve kullanılan araç tipi Kano'daki sürücülerin işaretleri kavrama seviyelerini etkileyen parametreler olarak görünmektedir. Kamyon sürücüleri trafik işaretlerini diğer tüm sınıflardaki yol kullanıcılarından daha zayıf algılamaktadır (65%).

*Anahtar Kelimeler***:** Bilinirlik, yol işaretleri, sürüş tecrübesi.

1.   INTRODUCTION

Road signs, traffic lights, and other traffic control devices are used to regulate, warn, guide or inform road users. An acceptable level of road traffic quality and safety is achieved with the orderly and predictable movement of traffic and pedestrian, by helping drivers to be aware of the road condition ahead [1]. Human perception of the information on road signs is a critical factor in determining the safe use of both the vehicle and the interacting environment [2].

Research conducted in Canada and USA by Dewar, Kline, & Swanson, (1994) using 480 volunteer licensed drivers evaluated age differences in comprehension of traffic sign symbols. The result shows that older drivers had poorer understanding than younger ones in 39% of the symbols examined. [3]

Unsatisfactory comprehension of traffic signs is a common problem for drivers in many countries. The unsatisfactory comprehension is related to the characteristics of the traffic control devices themselves.   Research concerning traffic sign comprehension dates back to 1966 and that early studies focused on evaluating user understanding levels of local traffic signs and most of the results indicated that the general comprehension performance was far from satisfactory [4].

Generally,   drivers   have   problems   in comprehension of traffic control devices. Drivers' personal   characteristics   control   drivers' comprehension   abilities   with   educational background as a major factor affecting the understanding of traffic control devices [5]. The overall comprehension of the 15 traffic signs of the 202 respondents in Soloraya area, Central Java Province is 67% [6].

There   is   a   serious   problem   in   drivers' understanding of existing traffic signs. only 50–60% of the traffic signs were identified correctly by the drivers. However, drivers' years of education, gender, monthly income, and nationality have a significant effect on their understanding of traffic signs. A quadratic term involving income had a significant negative effect. In the presence of the

above variables age, marital status, drivers experience and accident experience ratio proved to be unstable. In fact, it is the drivers' personal characteristics   which   control   the   drivers' understanding abilities and not their accident involvement rates. Male drivers with over ten years of driving experience are significantly better than less experienced male drivers. Male drivers are better than female drivers in all experience categories. Single and married drivers understand the signs equally well [7].

Drivers age, education and driving experience played prominent roles in the understanding of traffic signs while marital status and age had no effect on the understanding [8].

In a study in Israel, 48 undergraduate students were tested with 30 different traffic signs. The comprehension of traffic signs between symbolic and text displays was examined. Results indicated that text signs were better comprehended and the reaction time was improved for the symbolic signs with added text, especially for less familiar signs. [9]. However, another study argued that the addition of text can only improve comprehension of signs for local drivers but in foreign settings, text traffic signs in local language would worsen driver's comprehension. In the study, the text traffic signs such as stop sign and yield sign seem to be relatively difficult to understand from tourist's perspectives [10].

Research conducted in Turkey found that many traffic signs were not well known to the drivers. Only 12 signs were identified correctly by 70% or more of the participants. Some researches further investigated individual differences in performance on comprehension test and suggested that user characteristics   significantly   influence comprehension [11].

The understanding of traffic signs was found be statistically related with drivers' level of education, gender, monthly income and nationality using 28 posted signs with participants from Bahrain, Kuwait, Oman, Qatar, and the United Arab

Emirates. The findings, also show that only 56% of the posted signs could be comprehended [12].

The percentage of correct responses for all signs combined was only around 49% - 50% for regulatory signs, 52% for warning signs, and 55% for informatory signs. Out of the 42 signs evaluated, only four traffic signs were understood by more than 80 percent of the respondents. These signs are "No Overtaking", "No Use of Horn", "Pedestrian Crossing", and "Road Works". Twelve other signs were understood by more than 60% (but less than 80%) of the respondents-"Roundabout", "Side Road Right", "Road Hump", Railway Level Crossing with Gate or Barrier", Stop", "No Rickshaws", "No Left Turn", "No U-Turn", One Way Traffic", "Hospital and Fire Station". Based on analyses of demographic and driving characteristics of the respondents, it would be reasonable to assume that the results of the understanding of traffic signs presented here are applicable to male professional drivers of ages between 25 and 44 years. [13]

It is believed that there is a low level of comprehension of road signs by road users in Nigeria which in turn results to increased accident rates. This study assesses the level of comprehensibility of some road signs by drivers in Kano city with the aim of proposing ways to increase the level of understanding of the road signs.

2. METHODOLOGY AND DATA COLLECTION

A questionnaire survey was used for data collection in this study. The questionnaire was distributed randomly to drivers in Kano city. A total of 190 questionnaires were administered in schools, motor parks and around parking lots of some shopping centers amongst commercial and private drivers of cars, trucks, tricycle, motorcycle, and bicycle. The questionnaire was divided into 2-sections. The first section comprises of demographic characteristics which include sex, age, level of education, type of vehicle driven, driving experience and license category (private or commercial). The second section comprises of 10-warning signs, 10-

regulatory signs and 10-informatory signs making a total of 30 road signs. The signs were carefully selected to capture the most important traffic signs in the state with higher association with safety issues. Each of the signs was given a code WS1-WS10 for warning signs, RS1-RS10 for regulatory signs and IS1-1S10 for informatory signs and respondents were given a multiple choice under each sign. The responses were classified as "0" for incorrect response and "1" for a correct response for all the signs.

Twenty (20) of the selected traffic signs were obtained from the previous studies and remaining ten (10) road signs are local signs. Ben-Bassat and Shinar have used the road Signs WS3, WS5, WS8, WS9, IS6, RS1, RS3, RS6 and RS9 in a study to test the effect of context and drivers' age on highway traffic signs comprehension [14]. The use of road signs WS1, WS10, IS1, IS2, 1S5, 1S6, RS1, RS2, RS5, RS8, and RS9 was employed in a study to study the correlation between drivers' personal characteristics and their familiarity/comprehensibility with some traffic signs [15]. Other traffic signs that were used in previous research include WS7 [9] and IS7 [16].

Figure 1. Warning Signs.

Figure 1 shows the warning signs evaluated in the study. The signs have the following meaning: WS1 = Narrow bridge ahead, WS2= falling rock, WS3= school crossing, WS4=Y-ıntersection, WS5= Narrow road, WS6= Line merge ahead, WS7= Rail line, WS8= slippery road, WS9=Road work, WS10= traffic light.

Figure 2. Informatory Signs.

Figure 2 shows the informatory signs used in the study. The meaning of the signs is IS1= Gasoline station, IS2=Hospital, IS3= one-way, IS4= rest area, IS5= Restaurant, IS6= Parking, IS7= park and ride, IS8= Train station, IS9= Airport, IS10= Bus station.

Figure 3. Regulatory signs.

The regulatory signs used were presented in figure 3, the signs have the following meanings: RS1= stop, RS2=yield, RS3= maximum speed of 50kph, RS4= All vehicles prohibited, RS5= No overtaking, RS6= No parking, RS7= Tricycle prohibited, RS8= Height limit of 3.5m, RS9= No Entry for all types of vehicles, RS10= Pass either.

3. RESULTS AND DISCUSSIONS

3.1 Demographic characteristics of respondents

Table 1 shows the demographic profile of the respondents. Majority of the respondents are male (91.6%) which is due to the disproportionate ratio between male and female drivers in Kano city. Almost 90% of the respondents are youth below the age of 40 years showing that majority of the state drivers are young people. This is as a result of the

country's population where 82% of the population were below 40-years age [17]. The educational level of the drivers shows that 37.9% have up to SSCE level, 33.7% have OND, 14.7% have BSC degree, 4.2% have MSC degrees and 8.4% have primary education and only 1.1% had an informal education. 62% of the respondents have driving experience of 5-15 years, 11.6 % have over 20 years of experience. 63.2% of the respondents are private drivers and 36.8% are commercial drivers. 63.2% are Car and truck drivers which are believed to be more concerned with the road signs.

3.2 Comprehension of road signs

A total of 30 road signs were evaluated, the result in table 2 shows that informatory signs were more comprehended (83.2%), followed by regulatory signs (79.5%) then Warning signs (74.8%). The overall comprehension of the signs is good which may be related with education level (90% have at least to SSCE education) and experience of drivers (85.3% at least 5 years of driving experience). The warning signs with less than 75% comprehension are WS1= "Narrow bridge" (60%), WS6= "line merge ahead" (62.1%), WS8= "slippery road" (63.2%), WS5= "narrow road" (71.6%) and WS2= "falling rock" (72.6%). Three regulatory signs have a comprehension level of less than 75%; RS9= "No entry for all vehicles" (70.5%), RS8= "height limit of 3.5m" (72.6%) and RS10= "pass either" (73.7%). Only IS7 = "park and ride" (54.7%) has a comprehension level of less than 75% among the informatory signs evaluated and it's the least comprehended sign of all signs evaluated Only IS1 = "fuel station", RS1= "stop sign" and WS3 = "school crossing" out of the total signs evaluated were comprehended by more than 90% of the respondents.

Table 1. Respondent's Profile.

Characteristics of Respondents			
Characteristics		**Number**	**Percentage %**
Gender	Male	174	91.6
	Female	16	8.4
Age	<20	14	7.4
	20-30	104	54.7
	30-40	54	28.4
	40-50	14	7.4
	>50	4	2.1
Education Level	Primary	16	8.4
	SSCE	72	37.9
	OND	64	33.7
	BSc.	28	14.7
	MSc.	8	4.2
	Informal	2	1.1
Type of Vehicle	Bicycle	20	10.5
	Motorcycle	40	21.1
	Tricycle	10	5.3
	Car	110	57.9
	Truck	10	5.3
Category of Licence	Private	120	63.2
	Commercial	70	36.8
Driving Experience	<5	28	14.7
	5-10	68	35.8
	11-15	50	26.3
	16-20	22	11.6
	>20	22	11.6

Table 2. Comprehension of Road Sign on Profile of Respondents.

Profile of Correspondents		Average Comprehension (%)
GENDER	Male	79.0
	Female	76.0
AGE	<20	76.0
	20-30	81.8
	30-40	78.0
	40-50	65.2
	>50	90.0
EDUCATION LEVEL	Primary	80.0
	SSCE	77.0
	OND	80.2
	BSc	81.0
	MSc	84.2
TYPE OF VEHICLE	Bicycle	78.0
	Motorcycle	82.2
	Tricycle	66.0
	Car	81.0
	Truck	65.0
DRIVING EXPERIENCE	<5	74.0
	5-10	75.2
	11-15	78.0
	16-20	80.5
	>20	87.0

4. CONCLUSIONS

From the analysis of the result, it can be concluded that the comprehension level of road signs in Kano is good as the average comprehension level is 79%. The least comprehended signs in Kano is "park and ride" with comprehension level of 54.7%, followed by "Narrow bridge" (60%), "line merge ahead" (62.1%), "slippery road" (63.2%), "No entry for all vehicles" (70.5%). The low comprehension of the "park and ride" traffic sign is as a result of its low familiarity among the drivers since its installed in few places in the city and most of the installed signs were damaged due to road accidents or covered with posters of politicians which a common practice in the state. The "line merge ahead", "narrow bridge" and "slippery road" are mostly seen on interstate highways and only drivers that travel more often are mostly familiar with the signs and low level of comprehension of the signs may be attached to the fact that the study was conducted within the metropolis without considering that the drivers traveled out of the city or not. The signs with up to 90% recognition were "fuel station", "stop sign" and "school crossing" which corroborates with research conducted in Jordan [15]. These traffic signs are the most common and familiar to all road users due to their high frequency on the roads. The message on the signs is very clear and easy to comprehend its meaning even on seeing it for the first time.

Male drivers seem to comprehend road signs more than the female drivers. Driving experience shows a positive effect on the driver's response, drivers with over 20 years' experience comprehend 87% of all the signs as against 74% for less than 5-years' experience. Truck drivers and tricycle drivers are the least in the signs understanding having 65% and 66% respectively while car divers comprehend up to 81% of the signs. The low comprehension level among truck drivers and tricycle users may be associated with their low education level as the majority of road users in this category hardly make it to the high school. Another factor is the manner in which driver's license are issued in Nigeria as most drivers do not undergo the required training before obtaining the license.

The relationship between a driver's level of comprehension and involvement in a traffic accident which has not been considered in this research should be studied in the future. Future research should also focus on obtaining the correlation between response time and comprehension level among various road users in Kano state. The comprehension level among the road users can be improved by sanitizing the license issue procedure in such a way that, all prospective drivers must undergo training through which they will learn a lot and be familiarized with all necessary traffic signs before been issued with a driving license.

REFERENCES

[1]. Panoiu M., Rat C. L., and Panoiu C., Study on Road Sign Recognition in Labvıew, in International Conference on Applied Sciences 2015 (2015) 1–10.

[2]. Bezuidenhout U., Road Sign Conspicuity And Memorability : What We See And Remember, in IPENZ Transportation Group Conference, March 2014 (2014) 1–6.

[3]. Dewar R. E., Kline D. W., and Swanson H. A., Age differences in Comprehension of Traffic Sign Symbols, J. Transp. Res. Board (TRR 1456), 1994 1–10,

[4]. Zhang T. and Chan A. H., Traffic Sign Comprehension: A Review of İnfluential Factors and Future Directions for Research, in International Multi Conference of Engineers and Computer Scientists (IMECS), 2013.

[5]. Makinde O. O. and Oluwasegunfunmi V., Comprehension of Traffic Control Devices Amongst Urban, Eur. J. Eng. Technol., 2-1 (2014) 9–19.

[6]. Munawar A. and Setiadji B. H., Drivers ' Comprehension of the Traffic Signs, Int. J. Sci. Res., 5-2 (2016) 534–538.

[7]. Al-madani H., Assessment of Drivers Comprehension of Traffic Signs Based on Their Traffic, Personal And Social Characteristics, Transp. Res. Part F, 5 (2002).

[8]. Makinde O. O. and Opeyemi D. A., Understanding of traffic Signs By Drivers – A Case of Akure City, Ondo State, Nigeria,

ARPN J. Sci. Technol., 2-7 (2012) 608–612.

[9]. Shinar D. and Vogelzang M., Comprehension of Traffic Signs With Symbolic Versus Text Displays, Transp. Res. Part F, 18 (2013) 72–82.

[10]. Choocharukul K. and Sriroongvikrai K., Road Safety Awareness and Comprehension Road from International Tourist's Perspectives : A Case of Study of Thailand, in Transportation Research Procedia, 25 (2017) 4518–4528.

[11]. Kirmizioglu E. and Tuydes-Yaman H., Comprehensibility of Traffic Signs among Urban Drivers İn Turkey, Accid. Anal. Prev., 45 (2012) 131–141.

[12]. Al-Madani H. and Al-Janahi A., Assessment of Drivers Comprehension of Traffic Signs Based on their Traffic, Personal and Social Characteristic, Transp. Res. Part F, 5 (2012) 63–76.

[13]. Razzak A. and Hasan T., Motorist Understanding of Traffic Signs : A Study in Dhaka City, J. Civ. Eng., 38-1 (2010) 17–29.

[14]. Ben-Bassat T. and Shinar D., The Effect of Context and Drivers' Age on Highway Traffic Signs Comprehension, Transp. Res. Part F Traffic Psychol. Behav., 33 (2015) 117–127.

[15]. Taamneh M. and Alkheder S., Traffic Sign Perception among Jordanian Drivers: An Evaluation Study, Transp. Policy, 66 (2018) 17–29.

[16]. Shinar D., Dewar R. E., Summala H., and Zakowska L., Traffic Sign Symbol Comprehension: A Cross-Cultural Study, Ergonomics, 46-15 (2003) 1549–1565.

[17]. National Bureau of Statistics, National Population Estimates, Abuja, Nigeria, 2016.

Effect of Ambient and Cryogenic Milling on the Microstructure and Properties of Tungsten Matrix Composites Fabricated by Activated Sintering

Özge BALCI[1]* , Duygu AĞAOĞULLARI[2] , Mehmet Suat SOMER[1] , M. Lütfi ÖVEÇOĞLU[2]

[1]Koç University, Department of Chemistry, İstanbul, TURKEY

*[2]İstanbul Technical University, Department of Metallurgical and Materials Engineering, Particulate Materials
Laboratories (PML), İstanbul, TURKEY*

Abstract. Tungsten matrix composites reinforced with TiB_2 and Y_2O_3 particles were fabricated by milling under ambient/cryogenic conditions and Ni activated sintering. Powder blends constituting the W - 1 wt. % Ni - 2 wt. % TiB_2 - 1 wt. % Y_2O_3 composition were mechanically milled for 12 h under ambient condition or cryomilled for 10 min or sequentially milled under ambient and cryogenic conditions. Milling was carried out in a high-energy ball mill under ambient condition whereas cryogenic milling was conducted in externally circulated liquid nitrogen. Milled powders were compacted using a hydraulic press and the pellets were sintered at 1400°C for 1 h under Ar / H_2 gas flowing conditions. The effects of different milling types on the microstructural and mechanical properties of the sintered composites were investigated. After sintering, in addition to dominant W phase, small amounts of WB and NiW phases were detected in all sintered samples. The application of cryomilling after milling at ambient condition provided the disappearance of the clustered TiB_2 and Y_2O_3 particles in the sintered sample: They were located at the grain boundaries of W1Ni matrix and homogeneously distributed through the microstructure. Sequentially milled and sintered composite had the highest relative density (95.77 %) and the highest microhardness (7.23 GPa) values among the samples. Nano-indentation tests showed that there was an improvement in the hardness and elastic modulus of W matrix phase, which yielded the values of 8.9 and 373.7 GPa, respectively.

Keywords: Tungsten matrix composites, Cryomilling, Activated sintering, TiB_2, Y_2O_3.

Normal ve Kriyojenik Şartlarda Öğütmenin Aktive Edilmiş Sinterleme Süreçleri ile Geliştirilen Tungsten Esaslı Kompozitlerin Mikroyapı ve Özellikleri Üzerindeki Etkisi

Özet. Bu çalışmada, Ni ile aktive edilerek sinterlenen tungsten esaslı matrisin TiB_2 ve Y_2O_3 partikülleri ile takviye edilmesiyle, tungsten esaslı kompozit malzeme üretimi gerçekleştirilmiştir. W - % 1 ağ. Ni - % 2 ağ. TiB_2 - % 1 ağ. Y_2O_3 kompozisyonundan oluşan toz harmanları, normal koşullarda 12 sa mekanik olarak öğütülerek ya da 10 dk kriyojenik ortamda öğütülerek ya da normal ve kriyojenik şartlarda ardışık olarak öğütülerek hazırlanmıştır. Normal şartlarda öğütme yüksek enerjili bir değirmende uygulanırken; kriyojenik şartlarda öğütme sıvı azot ile dışarıdan çevrelenen bir sistemde yapılmıştır. Öğütülmüş tozlar hidrolik pres kullanılarak preslenmiş ve pekiştirilen bünyeler Ar/H_2 gazaltı şartlarında 1400°C'de 1 sa sinterlenmiştir. Farklı öğütme koşullarının sinterlenen kompozit malzemelerin mikroyapısı ve özellikleri üzerindeki etkisi incelenmiştir. Sinterlenme sonrasında, baskın W fazına ek olarak düşük mikarda WB ve NiW fazları oluşumu gözlemlenmiştir. Normal şartlarda öğütme sonrası uygulanan kriyojenik öğütme, sinter malzemelerin

mikroyapısındaki TiB$_2$ ve Y$_2$O$_3$ partiküllerin topaklanmasının yok olmasına neden olmuştur: Partiküllerin W1Ni matrisinin tane sınırlarında ve homojen olarak mikroyapıda dağılması sağlanmıştır. Ardışık olarak öğütülmüş ve sinterlenmiş kompozitler, numuneler arasında en yüksek rölatif yoğunluk (% 95,77) ve mikrosertlik değerlerini (7,23 GPa) sunmuştur. Nano-indentasyon testleri sayesinde, W matris fazının sertlik ve elastisite modül değerlerinin sırasıyla 8,9 ve 373,7 GPa değerlerine kadar iyileştirildiği kanıtlanmıştır.

Anahtar Kelimeler: Tungsten esaslı kompozitler, kriyojenik öğütme, aktive edilmiş sinterleme, TiB$_2$, Y$_2$O$_3$.

1. INTRODUCTION

Tungsten (W) and its composites are candidate materials for important structural applications at high temperatures due to their excellent properties such as high melting point, high elastic modulus, high thermal shock resistance, low thermal expansion coefficient, good corrosion resistance and good high-temperature strength and stiffness [1-2]. However, the densification of W is very difficult due to its high melting point and low ductility [3-4]. In recent years, fully dense W composites have been fabricated at much lower temperatures by utilizing powder metallurgy and advanced sintering techniques or the addition of some transition elements or their compounds [4-5]. Activated sintering of W and W matrix composites with the small amounts of metallic additives (such as Ni, Co, Fe, etc.) resulted in highly densified sintered bodies [6-7]. Furthermore, high-temperature materials such as borides, nitrides, carbides or oxides have been also added to tungsten to enhance the mechanical properties at elevated temperatures [4, 8-12].

Therefore, activated sintering of W and W matrix composites reinforced with different carbide, nitride and oxide phases have been attracted great attention in the current literature [5, 12-16]. Among the boride reinforcement particles, titanium diboride (TiB$_2$) is an important ultra-high temperature ceramic with excellent properties such as high melting point, high temperature strength and good chemical resistance [17]. There are several researches reporting the fabrication and characterization of tungsten matrix composites reinforced with TiB$_2$ and/or Y$_2$O$_3$ particles [18-20]. Furthermore, Ni powders added into the W by mechanical alloying process enables a rapid solid-state incorporation of the sintering aid into the matrix with an enhanced activation as well as

particle size reduction [21]. Generally, mechanical milling under ambient condition has been used as powder preparation technique of W-based powders [14-16]. However, milling under different conditions and its effects on the microstructure and final properties of the W sintered bodies are not a considerably discussed topic [22]. The addition of transition metal diborides as well as oxide particles and milling of these powders under cryogenic conditions can be suggested as an alternative powder preparation technique for tungsten matrix composites [22-23].

The aim of the present study is to report the effects of milling under ambient and/or cryogenic conditions on the microstructural and mechanical properties of the Ni activated sintered tungsten matrix composites reinforced with TiB$_2$ and Y$_2$O$_3$ particles.

2. EXPERIMENTAL PROCEDURE

2.1. Fabrication of the composites

Elemental tungsten (W, Eurotungstene™, 99.9 % purity, 4-7 µm particle size range) and nickel (Ni, ABCR™, 99.9 % purity, 3-7 µm particle size range) powders were used as the matrix metal and as the activated sintering agent, respectively. Titanium diboride (TiB$_2$, Alfa Aesar™, 99.5 % purity, 40-44 µm particle size range) and yttrium oxide (Y$_2$O$_3$, Alfa Aesar™, 99.99 % purity, 8-10 µm particle size range) powders were utilized as reinforcement and dispersoid materials, respectively. The content of Ni activated sintering aid was selected as 1 wt. % of W matrix: Previous studies carried out in our laboratory facilities revealed that 1 wt. % Ni is an adequate agent amount for the activated sintering of W [12, 14]. Thus, 1 wt. % Ni added W powders were mechanically milled for 6 h and they are hereafter

referred to as W1Ni pre-alloy. In order to compensate for the size ranges of the reinforcement and dispersoid particles, TiB_2 and Y_2O_3 powders were pre-milled separately for 6 h. W1Ni pre-alloy, pre-milled TiB_2 and pre-milled Y_2O_3 powders were blended to constitute the composition of W1Ni-2 wt. % TiB_2-1 wt. % Y_2O_3 (referred to as-blended W1Ni-2TiB_2-1Y_2O_3).

Mechanical milling under ambient condition was carried out in a Spex™ 8000D Mixer/Mill (at a rate of 1200 rpm) for 12 h using a tungsten carbide-cobalt (WC-Co) vial (50 ml capacity) and WC-Co balls (ϕ 6.5 mm) with a ball-to-powder weight ratio (BPR) of 7:1 (total powder amount: 7 g). Pre-alloying of W1Ni and pre-milling of TiB_2 and Y_2O_3 were also conducted at the same conditions with those used in mechanical milling experiments. Cryomilling was conducted in a Spex™ 6870 Freezer/Mill (at a rate of 900 collisions/min) for 10 min using a cylindrical polycarbonate vial and stainless steel rods. Before milling processes, the vials were evacuated and back-filled with Ar gas (Linde™, 99.999 % purity) in a Plaslabs™ glove box. Vials were soaked into liquid nitrogen (Linde™, refrigerated) without a direct powder-nitrogen contact. After milling processes, powders were unloaded under Ar atmosphere. Hereafter, as-blended W1Ni-2TiB_2-1Y_2O_3 powders milled for 12 h under ambient condition is referred to as S1, cryomilled for 10 min in the presence of externally circulated liquid nitrogen around vial is referred to as S2 and sequentially milled for 12 h under ambient condition and cryomilled for 10 min is referred to as S3. All powders were compacted to obtain cylindrical specimen with a diameter of 6.5 mm: Uni-action hydraulic press was used under a uniaxial pressure of 400 MPa (10 ton capacity MSE™ MP-0710). The pressed samples were sintered at 1400 ºC for 1 h in a high-temperature controlled atmosphere furnace (Linn™ HT-1800) under Ar/H_2 gas flowing conditions with a heating and cooling rate of 10 ºC/min.

2.2. Characterization studies

X-ray diffraction (XRD) investigations were carried out using a Bruker™ D8 Advanced Series powder diffractometer with CuK_α (λ=1.5406 Å) radiation incremented at a step size of 0.02° at a rate of 2°/min. The International Center for Diffraction Data® (ICDD) powder diffraction files were utilized for the identification of crystalline phases. The average crystallite sizes and lattice strains of the W phase in the milled powders were determined using a Bruker™-AXS TOPAS V3.0 software based on the modified Scherrer's formula. The most intense XRD diffraction peaks with (110), (200) and (211) reflections were fitted according to the Lorentzian profile by applying fundamental parameters approach. Particle size measurements of the milled powders were conducted using a Microtrac™ Nano-flex particle size analyzer (PSA) equipped with a Bandelin Sonopuls™ ultrasonic homogenizer using distilled water as the aqueous media.

Densities of the sintered composites were determined by Archimedes method using ethanol and the result of each sample was reported as the arithmetic mean of five different measurements. Microstructures of the samples were examined using a Hitachi™ TM-1000 scanning electron microscope (SEM) operated at 15 kV. A series of metallographic treatments including grinding and polishing were applied and the polished samples were coated by gold to provide electrical conductivity during SEM analysis. Vickers microhardness measurements of the sintered samples were conducted using a Shimadzu™ HMV Microhardness Tester under a load of 100 g for 10 s and the result of each sample includes the arithmetic mean of twenty successive indentations with a standard deviation. Nano-indentation measurements were performed at a peak load of 50 mN using an Agilent G200 nano-indenter. Load-displacement curve of the sintered sample was obtained from the matrix and reinforcement/dispersoid phases with a holding time of 5 s. In addition, the nanohardness and elastic modulus values obtained from nano-indentation tests were reported.

3. RESULTS AND DISCUSSION

Figure 1 illustrates the XRD patterns of the milled W1Ni-2TiB_2-1Y_2O_3 powders using different milling types under ambient and/or cryogenic

conditions (S1, S2 and S3). As shown in Figure 1, all milled powders contain only the W phase (ICDD Card No: 04-0806, Bravais lattice: body-centered cubic, a=b=c=0.316 nm). No peaks belonging to the Ni, TiB_2 and Y_2O_3 phases were identified in the XRD patterns after milling under ambient and/or cryogenic conditions. The absence of these phases was probably due to their very small amounts in the total powders and/or peak broadening caused by the continuous deformation during milling. Furthermore, any diffraction peak belonging to a secondary phase was not detected after milling at different conditions, indicating that no reaction took place between W, Ni, TiB_2 and Y_2O_3 particles. WC contamination was previously observed for the W composites mechanically alloyed for 24 h using a high energy ball mill (1200 rpm) in a WC vial with WC balls with a BPR of 10:1 [20]. However, the XRD patterns in Figure 1 do not show the emergence of WC phase in the broad W peaks after milling at different conditions, most likely due to its very small content in the W matrix. Therefore, milling for 12 h is a sufficient milling time without any WC contamination in visible amount, considering the milling times in literature [20, 24].
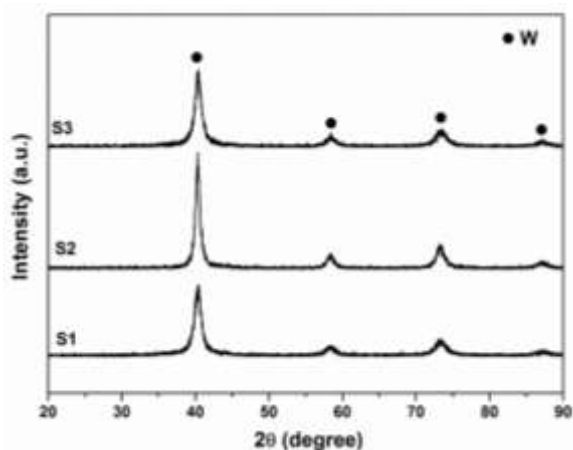
Figure 1. XRD patterns of the milled powders.

To reveal the effect of different milling types under ambient and/or cryogenic condition on the composite powders, the average crystallite sizes and lattice strains of the W phase in the milled powders (S1, S2 and S3) were determined (Table 1). The average crystallite size and lattice strain of the W phase in the S1 sample were found as 10.2

nm and 2.50 %. The small crystallite size is a result of continuous fracturing and welding mechanism triggered by the high impact energy released from the collisions of powders with vial and balls during milling under ambient condition. In the cryomilled powders (S2); however, the average crystallite size of the W phase is higher (16.4 nm) and the lattice strain is lower (1.54 %) than those of the S1 sample. This issue is also observable in the XRD peaks in Figure 1 supporting that higher broadening of the W peaks results in higher decrease in the average crystallite size and increase in the lattice strain. Furthermore, the average crystallite size (9.3 nm) and lattice strain (2.77 %) values of the W phase in the sequentially milled powders (S3) are similar to those of the S1 sample.

Table 1. Average crystallite sizes and lattice strains of the milled powders.

Sample Name	Crystallite Size (nm)	Lattice Strain (%)
S1	10.2	2.50
S2	16.4	1.54
S3	9.3	2.77

Figure 2(a) shows the average particle sizes of the milled powders. Considering the initial average particle sizes of the powders, it can be said that milling of the $W1Ni-2TiB_2-1Y_2O_3$ powders under ambient condition for 12 h resulted in a significant decrease in the average particle size of the S1 powders (282.3 nm). SEM image of the milled S1 powders is given in Figure 2(b), showing the agglomeration of the powder particles during high-energy ball milling. The average particle size of S2 sample is lower (270.8 nm) than that of S1, indicating that cryomilling enables the prevention of agglomeration. The repeated fracturing and welding mechanism in the presence of an amount of temperature increase during high-energy ball milling could result in a higher average particle size value in the S1 sample than that of S2, even if longer milling time was used. On the other hand, cryomilling has the advantage of hindering rewelding mechanism thanks to the externally circulated liquid nitrogen. The combined process of milling under ambient and cryogenic conditions

should be more beneficial for particle refinement and prevention of agglomeration. Thus, there is a remarkable decrease in the average particle size of S3 (215.7 nm), compared to that of S1 (282.3 nm). This means that subsequent 10 min of cryomilling provided breaking down of the agglomerated particles.
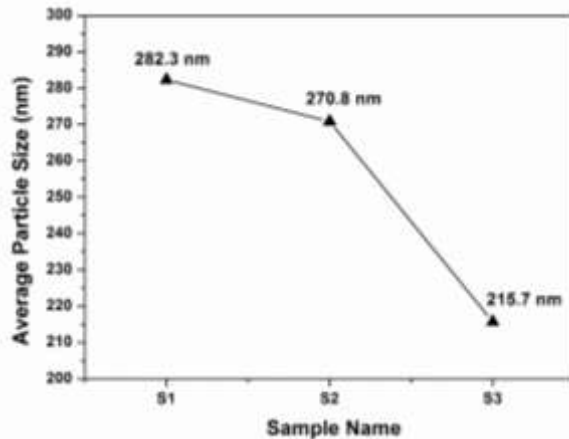
(a)
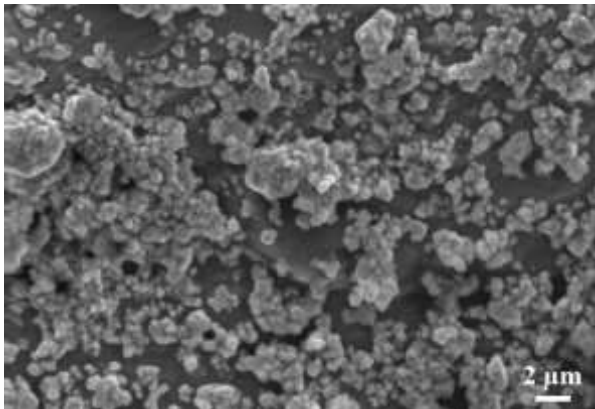
(b)

Figure 2. **(a)** Average particle sizes of the milled powders and **(b)** SEM image of the milled S1 powders.

Figure 3 shows the XRD patterns of the bulks samples sintered from the S1, S2 and S3 powders. High temperature during sintering resulted in an increase in the XRD peak intensities as compared with those of powders illustrated in Figure 1, that this indicated improved crystallinity (Figure 3). As seen from Figure 3, all sintered samples contain the peaks of WB and NiW phases in addition to the major W phase which was already present in the

milled powders (Figure 1). Small amount of Ni (1 wt. %) went into the W solid solution and caused the emergence of Ni(W) solid solution phase. Furthermore, no diffraction peaks of TiB_2 and Y_2O_3 were observed after sintering, most likely due to their small amounts and broad peaks dominated by the intense peaks of the W phase. Similarly, the characteristic peaks of the boride, carbide and oxide phases have not been observed in the W matrix composites reported in literature [12, 16, 22]. Additionally, the formation of WB compound is due to the diffusion of decomposed TiB_2 into the W1Ni matrix. On the other hand, W or Ni based intermetallic compound (such as W_5Si_3, NiTi etc.) or WC contamination was not identified after sintering at 1400 ºC, as shown in Figure 3: These phases have been already reported for the sintered W matrix composites reinforced with carbide/boride and oxide particles [12, 19, 20]. The present result can be attributed to the proper amount of the reinforcement (2 wt. % in the total composition) which does not cause emergence or enhancement of the contamination and intermetallics.
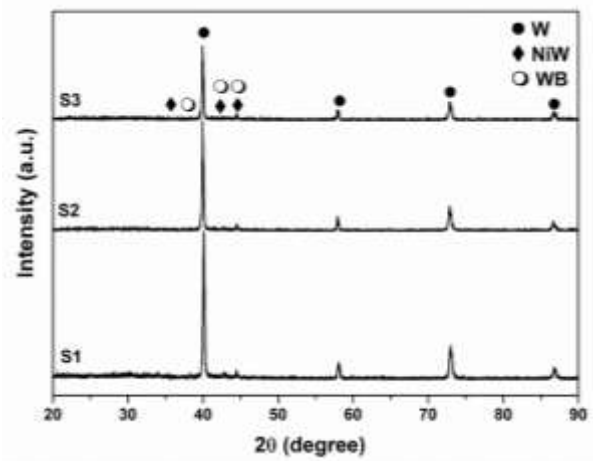
Figure 3. XRD patterns of the sintered samples.

Figure 4 shows the BSE/SEM images of the sintered samples taken from the polished surfaces. TiB_2 and Y_2O_3 particles (dark contrast) which are located both at the grain boundaries and at the grain interiors of W1Ni matrix (light contrast) are representatively signed in the SEM image of S1 sample. Some clustered areas of the TiB_2 and Y_2O_3 particles are detected through the microstructures

of both S1 and S2 samples. The pores are observable in the SEM image of S2 sample, indicating the insufficient sintering process of the cryomilled powders. As the microstructural differences resulted from different milling types are compared to each other, it is evident that boride reinforcement and oxide dispersoid have a homogenous distribution throughout the surface of the S3 sample: These homogenously distributed particles having sizes between 1-2 μm are located majorly at the grain boundaries and hence inhibit the grain growth and coarsening during sintering [25]. Furthermore, unlikely the S1 and S2 samples, no pores or particle clustering are present in the SEM image of the S3 sample, indicating the positive effect of sequential milling process on the sintering ability of the composites. Thus, 10 min of cryomilling followed by high-energy ball milling provided the disappearance of the clustered areas of TiB_2 and Y_2O_3 particles, in comparison with the SEM images of S1 and S3 samples.
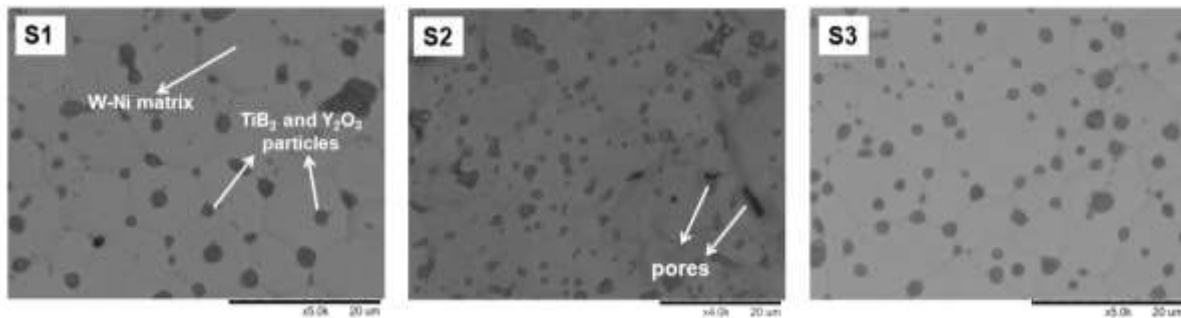
Figure 4. BSE/SEM images of the sintered samples taken from the polished surfaces.

According to the Archimedes density measurements, the relative densities of S1, S2 and S3 sintered samples were calculated as 90.79, 88.29 and 95.77 %, respectively. The lowest density was found in present study for the sample sintered from the cryomilled powders, whose SEM image also showed the presence of pores in the microstructure (Figure 4). On the other hand, S3 sample has the highest relative density which indicates the significant effect of sequential milling process on the densification rate, conforming well to the SEM image in Figure 4. Similar relative density (~93 – 97 %) values were reported for the Ni activated sintered W matrix composites reinforced with boride and oxide particles [12, 15, 19].

Figure 5 shows the average microhardness variation of the sintered samples in relation to different milling types. S2 sample sintered from the cryomilled powders has the lowest microhardness value (5 GPa), in compliance with the lowest value of relative density among the samples. As seen from Figure 5, the application of cryomilling after milling under ambient condition results in a significant increase in the microhardness value from 6.04 to 7.23 GPa (S1 and S3). The evolution of average crystallite sizes of the powders (Table 1) and density/microhardness values (Figure 5) of the all sintered samples are in great consistency with each other, in which the decrease in average crystallite size corresponds to an increase in density/microhardness. The measured relative density and microhardness values of the sequentially milled and sintered sample are effectively high considering the powder metallurgy methods and sintering temperature (1400 °C) used in the present study.
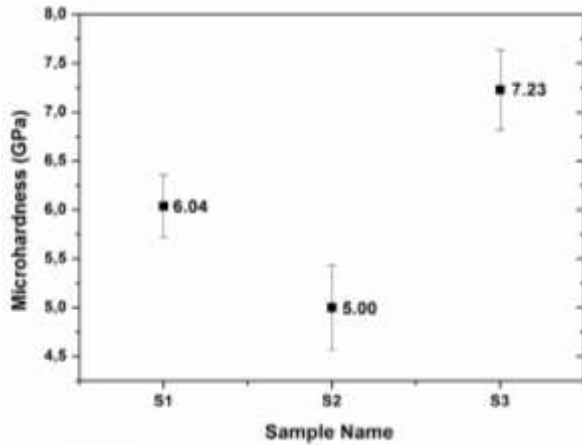
Figure 5. Average microhardness variation of the sintered samples in relation to different milling types.

Nano-indentation tests were performed individually on the W phase and the reinforcement/dispersoid particles in the sintered S3 sample to compare the hardness and elastic modulus values with those of pure W. Figure 6 show the load – displacement curves of the constituents in the sintered S3 sample, obtained from nano-indentation tests under maximum load of 50 mN. The curve of W matrix slightly shifts to smaller indentation depths for the reinforcement/dispersoid particles, indicating an increase in the indentation stiffness. The maximum penetration depths in the matrix and particles were found to be approximately 522.1 and 497.2 nm, respectively. Thus, there is a slight difference between the amount of plastic deformation dissipated during indentation on the W matrix and reinforcement/dispersoid particles.
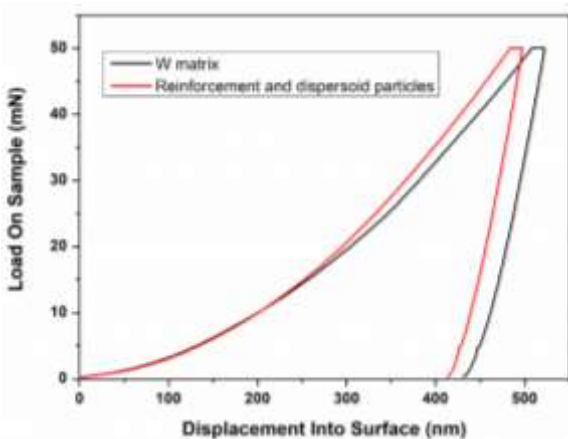
Figure 6. Load – displacement curves of the sintered S3 sample, obtained from nano-indentation tests.

The nanohardness and elastic modulus values for the constituents of S3 sample, obtained according to the Oliver-Pharr method, are listed in Table 2 [26]. The hardness (3.4 – 4.6 GPa) and elastic modulus (~300 GPa) of pure tungsten is significantly improved to 8.9 and 373.7 GPa, respectively. The presence of TiB_2 particles along with Y_2O_3 ones (dark contrast in the microstructure in Figure 3) resulted in a nanohardness and elastic modulus of 9.7 and 424.5 GPa, respectively. Improved nano-mechanical properties of the S3 sample having high relative density (95.77 %) can be attributed to the strengthening by the reinforcement particles distributed homogenously in the W matrix phase.

Table 2. Nanohardness and elastic modulus values for the constituents of S3 sample.

	W matrix	**TiB_2 reinforcement/ Y_2O_3 dispersoid**
Nanohardness (GPa)	8.9	9.7
Elastic modulus (GPa)	373.7	424.5

Consequently, the evaluation of present results showed that sequential milling under ambient and cryogenic conditions could be a beneficial powder preparation process to improve the microstructural and final properties (e.g. density, microhardness, elastic modulus) of the W-based composites.

4. CONCLUSIONS

The following conclusions can be drawn based on the results reported in the present study:

- The fabrication of tungsten matrix composites reinforced with TiB_2 and Y_2O_3 particles were achieved by milling under ambient/cryogenic conditions and Ni activated sintering method.

- Only W phase was detected in all milled powders and the lowest crystallite size of 10.2 nm was obtained in the sequentially milled powders. After sintering, in addition to dominant W phase, small amounts of WB and

NiW phases were detected in all sintered samples.

- Micron-scale TiB_2 and Y_2O_3 particles were homogenously distributed in the microstructures of the bulk samples sintered from the sequentially milled powders. The application of 10 min of cryomilling after high energy ball milling for 12 h provided the disappearance of the clustered areas of TiB_2 and Y_2O_3 particles which were located at the grain boundaries of W1Ni matrix.

- Sequentially milled and sintered sample had the highest relative density (95.77 %) and the highest microhardness (7.23 GPa) values.

- Nano-mechanical properties of the tungsten phase were improved due to the strengthening by the reinforcement particles distributed homogenously in the W matrix phase. W matrix phase in the sequentially milled and sintered sample yielded a nanohardness and elastic modulus of 8.9 and 373.7 GPa, respectively.

Acknowledgements

REFERENCES

[1]. Lassner E., Schubert W.D., Tungsten: Properties, Chemistry, Technology of the Element, Alloys and Chemical Compounds, Kluwer Academic, New York, 1999.

[2]. Caldwell S.G., Tungsten heavy alloys, in: Lee P.W., Lacocca R. (Eds.), Powder Metal Technologies and Applications, ASM Handbook (v. 7), ASM International, Materials Park, Ohio, (1998) 914–921.

[3]. Arshad K., Wang J., Yuan Y., Zhang Y., Zhou Z.-J. and Lu G.-H., Development of tungsten-based materials by different sintering techniques, Int. J. Refract. Met. Hard Mater., 50 (2015) 253–257.

[4]. Wei B., Wang Y., Zhao Y., Wang D., Song G., Fu Y. and Zhou Y., Effect of NbC content on microstructure and mechanical properties of W-NbC composites, Int. J. Refract. Met. Hard Mater., 70 (2018) 66–76.

[5]. Li Y., Zhang J., Luo G., Shen Q., and Zhang L., Densification and properties investigation of W-Cu composites prepared by electroless-plating and activated sintering, Int. J. Refract. Met. Hard Mater., 71 (2018) 255–261.

[6]. German R.M. and Munir Z.A., Enhanced low-temperature sintering of tungsten, Metall. Mater. Trans., A 7 (1976) 1873–1877.

[7]. Hayden H.W. and Brophy J.H., The activated sintering of tungsten with group VIII elements, J. Electrochem. Soc., 110 (1963) 805–810.

[8]. Song G.M., Wang Y.J. and Zhou Y., The mechanical and thermophysical properties of ZrC/W composites at elevated temperature, Mater. Sci. Eng. A-Struct., 334 (2002) 223–232.

[9]. Kim Y., Lee H.K., Kim E., Cheong D. and Hong S.H., Fabrication of high temperature oxides strengthened tungsten composites by spark plasma sintering process, Int. J. Refract. Met. Hard Mater., 27 (2009) 842–846.

[10]. Chen Y., Wu Y.C., Yu F.W. and Chen J.L., Microstructure and mechanical properties of tungsten composites co-strengthened by dispersed TiC and La_2O_3 particles, Int. J. Refract. Met. Hard Mater., 26 (2008) 525–529.

[11]. Liu W., Xue L. and Yan Y., Microstructure and mechanical properties of W-Cr-TiN composite by spark plasma sintering, Fusion Engineering and Design, 125 (2017) 503–509.

[12]. Ağaoğulları D., Balcı Ö., Gökçe H., Öveçoğlu M. L. and Duman I., Comparative investigations of the activated sintered W–1wt.% Ni composites reinforced with various oxide and boride particles, Int. J. Refract. Met. Hard Mater., 41 (2013) 577–584.

[13]. Li B., Sun Z., Hou G., Ding F., Hu P. and Yuan F., The effects of alumina reinforcement and nickel activated sintering on nanosized tungsten matrix, J.Alloy. Compd., 692 (2017) 420–426.

[14].Genç A., Çoşkun S. and Öveçoğlu M.L., Microstructural characterizations of Ni activated sintered W-2 wt % TiC composites produced via mechanical alloying, J.Alloy. Compd., 497 (2010) 80–89.

[15].Gökçe H., Balcı Ö., Ağaoğulları D., Demirkan Ö., Genç A., Öveçoğlu M.L. and Duman I., Characterization Investigations of W-Ni Matrix Composites Reinforced with TiB_2 and La_2O_3, Acta Physica Polonica A, 123-2 (2013) 309–312.

[16].Balcı Ö., Demirkan Ö. U., Ağaoğulları D., Gökçe H., Genç A., Öveçoğlu M. L. and Duman I., Effects of La_2O_3 Addition on the microstructure and properties of activated sintered W-Ni Compacts, Solid State Phenomen., 194 (2012) 217–221.

[17].Munro R.G., Material properties of titanium diboride, J. Res. Natl. Inst. Stan., 105 (2000) 709-720.

[18].Battabyal M., Schäublin R., Spätig P. and Baluc N., W–2wt. %Y_2O_3 composite: Microstructure and mechanical properties, Mat. Sci. Eng. A, 538 (2012) 53–57.

[19].Genç A., Coşkun S. and Öveçoğlu M., Fabrication and properties of mechanically alloyed and Ni activated sintered W matrix composites reinforced with Y_2O_3 and TiB_2 particles, Mater. Charact., 61-7 (2010) 740–748.

[20].Çoşkun S. and Öveçoğlu M.L., Effects of Y_2O_3 additions on mechanically alloyed and sintered W-4 wt% SiC composites, Int. J. Refract. Met. Hard Mater., 29 (2011) 651–655.

[21].Gupta V.K., Yoon D.H., Meyer H.M. and Luo J., Thin intergranular films and solidstate activated sintering in nickel-doped tungsten, Acta Mater., 55 (2007) 3131–3142.

[22].Ağaoğulları D., Balcı Ö. and Öveçoğlu M. L., Effect of milling type on the microstructural and mechanical properties of W-Ni-ZrC-Y_2O_3 composites, Ceram. Int., 43-9 (2017) 7106–7114.

[23].Back S.H., Lee G.H. and Kang S., Effect of cryomilling on particle size and microstrain in a WC-Co alloy, Mater. Trans., 46-1 (2005) 105–110.

[24].Veleva L., Oksiuta Z., Vogt U. and Baluc N. Sintering and characterization of W–Y and W–Y_2O_3 materials. Fusion Eng. Des., 84 (2009) 1920–1924.

[25].Suryanarayana C., Mechanical alloying and milling, Prog. Mater. Sci., 46 (2001) 1–184.

[26].Oliver W.C. and Pharr G.M., An improved technique for determining hardness and elastic modulus using load and displacement sensing indentation experiments, Journal of Materials Research 7-6 (1992) 1564–1583.

Cumhuriyet Science Journal

CSJ

Design of Reversed-Phase Chromatography Column Packing Material for Protein Separation: Part 2- Chromatographic Performance

*Berna SARAÇOĞLU KAYA** iD *,Ebru SAĞ* iD

Sivas Cumhuriyet University, Faculty of Engineering, Chemical Engineering Department, Sivas, TURKEY

Abstract. In the second part of the two-part study, monodisperse and porous poly(vinyl acetate-co-divinylbenzene) [poly(VAc-co-DVB)] and poly(divinylbenzene) [poly(DVB)] column packing materials synthesized in the first part of the study were tested in Reverse Phase Chromatography (RPC) under different conditions. The investigation of column performances concluded that columns packed with poly(VAc-co-DVB) (2500 plate/m) and poly(DVB) (1500 plate/m), showed high and stable theoretical plate number and high peak resolution values compared to literature values. Protein recovery data in RPC column, poly(VAc-co-DVB) (93-99%), were determined as similar as quantitative values for all proteins. Reproducibility tests of analytes of poly(VAc-co-DVB) column were assessed "run to run" and "day to day" Relative Standard Deviation (RSD) values were determined under 2.8%.

Keywords: Monodisperse-Porous Particle, Column Packed Material, Reversed-Phase Chromatography (RPC), Protein Separation.

Proteinleri Ayırmak İçin Ters Faz Kromatografisi Kolon Dolgu Materyali Tasarımı: Bölüm 2- Kromatografik Performans

Özet. İki bölümden oluşan çalışmanın ikinci bölümünde çalışmanın ilk bölümünde sentezlenmiş olan eş boyutlu ve gözenekli poli(vinil asetat-co-divinilbenzen) [poli(VAc-co-DVB)] ve poli(divinilbenzen) [poli(DVB)] kolon dolgu materyalleri Ters Faz Kromatografisi (Reversed Phase Chromatography, RPC) için farklı koşullarda test edilmiştir. Sentez sonrası elde edilen partiküllerle doldurulan kolonların kromatografik performansları incelediğinde, poli(VAc-co-DVB) (2500 tabaka/m) ve poli(DVB) (1500 tabaka/m) kolon için literatürdeki değerlerden daha yüksek ve kararlı teorik tabaka sayısı değerleri elde edilirken pik çözünürlük değerlerinin de kabul edilen değerlerin üstünde olduğu görülmüştür. Poli(VAc-co-DVB) (%93-99) ulaşılan protein geri kazanım değerleri ise bütün proteinler için kantitatife yakın değerler olarak belirlenmiştir. Üretilen kolonlar için analitlerin, analizden analize ve günden güne tekrarlanabilirlik testleri yapılmış, hem "analizden analize " hem de "günden güne" Bağıl Standart Sapma (BSS) değerleri % 2,8'in altında bulunmuştur.

Anahtar Kelimeler: Eşboyutlu-Gözenekli Partikül, Kolon Dolgu Materyali, Ters Faz Kromatografisi (RPC), Protein Ayırma.

1. INTRODUCTION

Chromatography, one of the most common analytical techniques used today, began to be used as separation technology in the 20th century [1-9]. Chromatograph is a separation method based on the differential migration of analytes in a mobile phase as they move along a stationary phase. The diversity and development of the technique used have led to the discovery of various principles, the

expansion of the target and application areas of the technique [10]. Chromatography types can be categorized as Partition Chromatography, Paper Chromatography, Thin Layer Chromatography, Gas Chromatography and High-Performance Liquid Chromatography. High-Performance Liquid Chromatography (HPLC) is the most widely used analytical method among these chromatographic methods. [11]. It has wide applications in many fields such as chemistry, biology, genetics, food processing, medical and medicine [12]. HPLC is divided into subheadings such as Normal Phase Chromatography (NPC), Size Exclusion Chromatography (SEC), Ion Exchange Chromatography (IEC) and Reverse Phase Chromatography (RPC), which are developed around different separation processes according to their application area. Among these separation processes, Reverse Phase Chromatography is an analytical method that is used effectively to purify, isolate or separate biomolecules. The main reasons for the preference of RPC are the stability of the system, separation in short-time, serial and high efficient analysis and microscale analysis. Columns developed for reverse phase HPLC systems are mostly silica-based commercial columns. The polydisperse structure of the packed materials used in these columns leads to irregular pressure regimes, whereas nonporous structures lead to inefficient protein separations. The chemical and mechanical strength of these columns, which are very low reusability, is also low. [2-4]. Commonly encountered problems in HPLC columns designed up to now; the long analysis period, the difficulty of some analytes to leave the column, and the difficulty of chromatographic separation due to non-specific interactions. [1, 5-9].

In the first part of the study, we have developed reverse phase packing materials for protein separation, which are highly efficient in chemical and mechanical strength and capable of separating protein mixtures in a short time. In this part of the study, it is aimed to test the suitability of polymeric particles with a uniform size and porosity as a column packing material.

2. MATERIALS AND METHODS

2.1. Column Packed Materials Produced for RPC

The production of polystyrene (PS) particles used as seed latex in the synthesis of poly(vinyl acetate-co-divinylbenzene) [poly(VAc-co-DVB)] and poly(divinylbenzene) [poly(DVB)] column materials, and the synthesis of uniform-porous poly(VAc-co-DVB) and poly (DVB) particles and the characterization of the resulting particles are described in detail in the first part [13].

2.2. Preparation of RPC Columns

Poly(vinyl acetate-co-divinylbenzene) [poly(VAc-co-DVB)] and poly(divinylbenzene) [poly(DVB)] particles which are designed as column packing material form columns with DVB2 and DVB3 codes respectively. Particles were packed into 100 mm x 4.6 mm ID. stainless steel HPLC columns (Schimadzu, Japan) using water as mobile phase at 20 MPa (200 atm) pressure and room temperature. After the filling process, the column was washed with the mobile phase used in the analyzes for about 1 hour. Figure 1 gives a schematic representation of column filling.
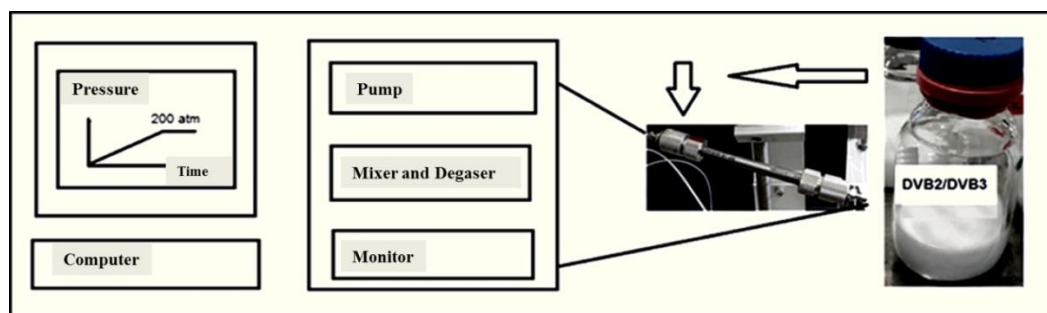
Figure 1. HPLC column filling.

2.3. Chromatographic Performance of RPC Columns

In this section, Shimadzu Gradient Liquid Chromatograph, LC-10 ADVP and SPD-10 AVVP UV detector were used as HPLC for the chromatographic performance tests. The sample mixture containing 4 different proteins (Sigma) as analytes: Bovine Serum Albumin (BSA, Cat No. A-2153, Fraction V, MA 67,000), Lysozyme (Cat No. L- 6876, MA 14,600), Ribonuclease -A (Cat No: R-5503, MA: 13,700) and Cytochrome-C (Cat No. C-2037, MA: 12,327). As understood from the molecular weights of these proteins, it is aimed that the prepared columns can perform chromatographic separation as wide as possible in the polarity range. In the experiments performed in the RPC mode, different acetonitrile (AcN, purity suitable for HPLC, Aldrich) -water mixtures were used under isocratic conditions as the mobile phase and trifluoroacetic acid (TFA, Aldrich) was added into these mixtures (0.15% v/v).

Experiments on protein separation by RPC in HPLC system were carried out under gradient conditions. Chromatograms were recorded at 280 nm with a UV-detector. In the chromatographic tests performed for protein separation, a protein mixture containing Ribonuclease A, Cytochrome C, Lysozyme and Bovine Serum Albumin was used. This mixture is a standard mixture which is widely used in the literature to determine the chromatographic performances of Reversed Phase (RP) columns [14-16]. In chromatographic experiments on gradient conditions, the mobile phase gradient was varied between 0.5-2.0 units of AcN/min. It was used as the mobile phase A in chromatographic experiments carried out on gradient conditions of AcN containing 5% (v/v) water and 0.15% (v/v) TFA. Mobile phase B was formed with water and 0.15% TFA. The gradient was applied linearly at 30% to 60% mobile phase A, depending on the column type, on a selected gradient run. This time period was chosen as 30 minutes in the flow rate scan. All chromatographic studies were carried out at room temperature.

2.4. Determination of Chromatographic Parameters

The parameters determining the column performances were calculated from the chromatograms obtained in the specified conditions. In each analysis, for all components in the sample mixture injected into the system, variables such as peak width and peak width at half-height were measured, and column performance parameters such as theoretical plate number and peak resolution were calculated, respectively.

The peak resolution for a given protein in the resulting chromatograms is calculated according to Equation [1]. To observe that the two peaks are separated from each other, it is necessary that R = 1 and this resolution value means that the two bands overlap each other by 2%. If this value is greater than 1.5, the peaks are completely separated and a good resolution is obtained.

$$R_{B/A} = 2 \times \frac{(t_B - t_A)}{(W_A + W_B)}$$
[1]

Where: $R_{(B/A)}$ refers to the resolution between the selected peak B and the previous peak A. t_B and t_A indicate the retention times for peak B and peak A, respectively, from the injection point. W_B and W_A represent the peak width for peak B and peak A, respectively.

Theoretical plate number (N) values were calculated according to Equation [2] using chromatograms obtained in isocratic mode, resulting in chromatographic experiments in which cytochrome C was used as the analyte.

$$N = 5.54 \times \left(t/W_{1/2} \right)^2 \qquad [2]$$

Where: t refers to the retention time, $W_{(1/2)}$ is the peak width at half-height. Theoretical plate number increases with column efficiency.

The protein recovery experiments with the column packed with DVB2 particles were performed under a linear gradient of AcN/water at room temperature with a flow rate 0.75 mL/min and a protein concentration of 1 mg/mL. In each run, a single protein was injected into the column. The recovery ratio (% w/w) was calculated as the ratio of peak area obtained with the column to that with the same injection performed into the closed loop. In order to obtain run-to-run and day-to-day reproducibities, the analyte mixture containing each protein at a concentration of 1 mg/mL was injected into the column 10 times/day for one week.

3. RESULTS AND DISCUSSION

In the study, the polymeric microspheres in the monodisperse porous structure synthesized in the first part were designed as reverse phase chromatography column packing material with a structure suitable for the proteins to be separated and characterized by Fouirer Transform Infrared Spektrofotometre (FTIR), Scanning Electron Microscopy (SEM) and Brunauer-Emmett-Teller (BET) surface area and porosity measuring device [13,17]. The relationship between the back pressure of the HPLC columns obtained with these particles and the mobile phase flow rate was investigated. In subsequent chromatographic analyzes, the effect of these changes on the column separation ability was observed by changing gradient conditions and flow rate.

3.1. Chromatographic Performance of DVB2 and DVB3 RPC Columns

The synthesized particles were filled into HPLC columns under high pressure and tested for their suitability in the HPLC system. The behavior of the back pressure flow rate of the columns is shown in Figure 2. As can be seen, the backpressure values obtained with the particles are low compared to the common RPC column materials. It is seen as an advantage because the separation in HPLC columns is carried out in a shorter time at higher flow rates. Compared to the DVB2 column, the rigid pore structure in the

DVB3 column [13] creates a high resistance to flow and this leads to a higher backpressure value.
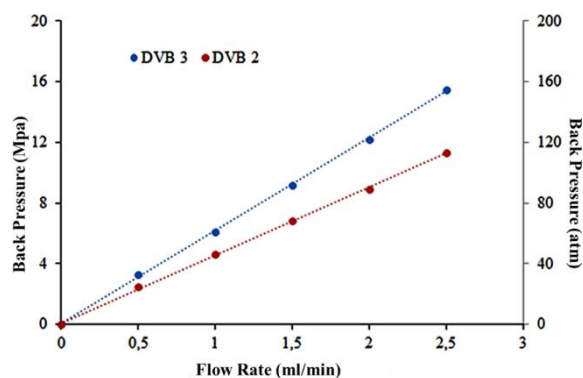
Figure 2. Back pressure-flow rate behavior of RPC columns with DVB2 and DVB3 codes. Mobile phase: AcN/Water Column: 100 x 4.6 mm ID.

The chromatographic performance of RPC columns encoded as DVB2 and DVB3 were investigated for protein separation under gradient conditions. For this purpose, a mixture of Ribonuclease A, Cytochrome C, Lysozyme and BSA was used. In the first part of the chromatographic studies, the gradient slope was varied in the range of 0.5-2.0 and the best chromatographic separation was determined for the protein mixture used (Figure 3). In Figure 3, it has been found that both of the columns perform separation, additionally, the DVB2 column performs better than the DVB3 column and the gradient slope is 1.0 unit of AcN/min, the better the protein peaks are separated. The chromatographic behaviors of the two designed columns are consistent with the results in the literature [14-16]. It appears that each of the proteins in the mixture of proteins given to the column emerged sequentially according to the polarity of the column, and none of them adhered to the column. This result shows that the columns perform the separation.
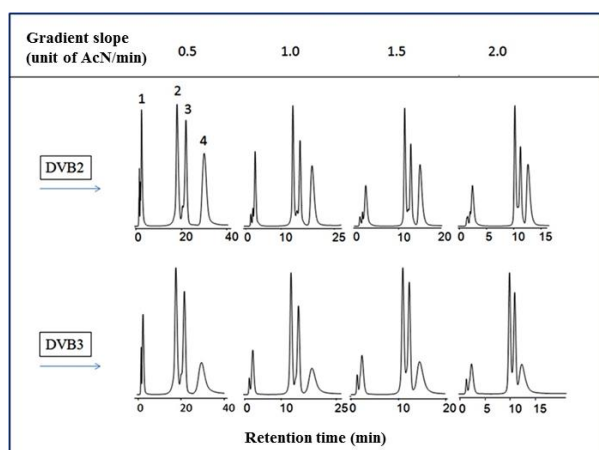
Figure 3. Sample chromatograms showing the effect of gradient slope on protein separation gradient conditions with RPC using DVB2 and DVB3 columns Flow rate (mL/min): 0.75 mL/min. Mobile phase A: AcN + 5% water + 0.15% TFA, Mobile phase B: Water + 0.15% TFA, Gradient conditions: 30% mobile phase A, 60% mobile phase B in linear form. Column dimensions: 100x4.6 mm ID., UV-detector 280 nm. Peak order: (1) Ribonuclease A, (2) Cytochrome C, (3) Lysozyme, (4) BSA.

The peak resolution values calculated using the chromatograms obtained at different gradient slopes are given in Table 1. When the slope was 1.0 unit of AcN / min, resolution values were obtained indicating that the peaks completely separated from each other on the HPLC chromatogram. For this reason, in the next section of the chromatographic studies it was decided to use 1.0 unit AcN / min of the gradient slope.

Table 1. Effect of gradient slope on the chromatographic behavior of DVB2 and DVB3 columns. (Flow rate (mL / min): 0.75, Mobile phase: A: AcN + 5% water + 0.15% TFA B: Water + 0.15% TFA, Gradient conditions: 30% mobile phase A to 60% mobile phase B in linear form. Column dimensions: 100x4.6 mm ID).

Column: DVB2			
Gradient slope	R(2/1)	R(3/2)	R(4/3)
0.50	11.26	2.22	3.05
1.00	11.64	2.12	2.26
1.50	9.60	1.80	1.84
2.00	10.40	1.47	1.43
Column: DVB3			
Gradient slope	R(2/1)	R(3/2)	R(4/3)
0.50	9.06	1.86	2.07
1.00	9.29	1.76	1.64
1.50	8.00	1.45	1.23
2.00	7.41	1.27	0.92

In the second part, the effect of the mobile phase flow rate on the chromatographic behavior of the columns was investigated. Chromatograms obtained at different flow rates for both columns are given in Figure 4. When these chromatograms are examined, it is seen that column performance is good in the range of flow rate studied.
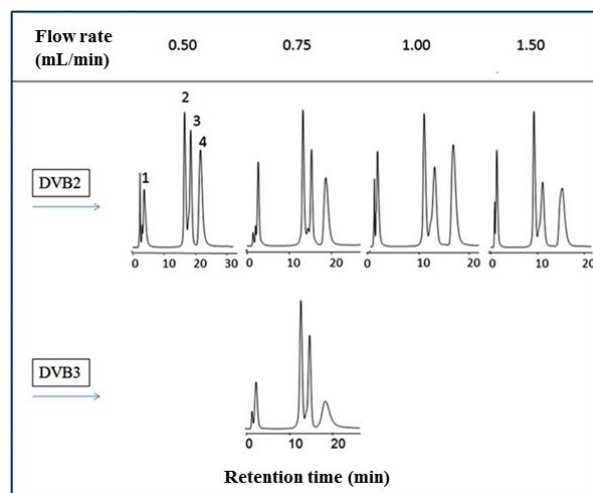
Figure 4. Sample chromatograms showing the effect of mobile phase flow rate on chromatographic separation of DVB2 and DVB3 columns in gradient conditions with RPC Flow rate (mL / min): 0.50, 0.75, 1.00, 1.50 Mobile phase: A: AcN + 5% water + 0.15% TFA B: Water + 0.15% TFA, Gradient conditions: 30% A to 60% B in 30 minutes in linear form. Column dimensions: 100x4.6 mm ID., UV-detector 280 nm. Peak order: (1) Ribonuclease A, (2) Cytochrome C, (3) Lysozyme, (4) BSA.

As shown in Figure 4, the analysis time in the DVB2 column decreased with the increasing flow rate of the column. At the highest flow rate, the column is able to successfully dissociate all analytes in 14 minutes. In the DVB3 column, the high back-pressure values and the narrow range of the column's operable flow rate are a limiting feature in terms of chromatographic use.

The peak resolution values obtained at different flow rates for the columns are given in Table 2. Resolution values indicate that the protein mixture can be chromatographically separated at all flow rates. Also, the peak resolution values do not change significantly with flow rate. This means that the analysis time is shortened with increasing flow rate.

Table 2. Effect of mobile phase flow rate on the chromatographic behavior of DVB2 and DVB3 columns. (Gradient time (min): 30, Mobile phase: A AcN + 5% water + 0.15% TFA B: Water + 0.15% TFA, Gradient conditions: 30% A to 60% B in linear form Column dimensions : 100x4.6 mm ID)

Column: DVB2			
Flow rate (mL/min)	R(2/1)	R(3/2)	R(4/3)
0.50	9.77	1.58	1.87
0.75	11.64	2.12	2.26
1.00	9.59	1.63	2.23
1.50	10.85	2.31	3.14
Column: DVB3			
Flow rate (mL/min)	R(2/1)	R(3/2)	R(4/3)
0.75	9.26	1.76	1.64
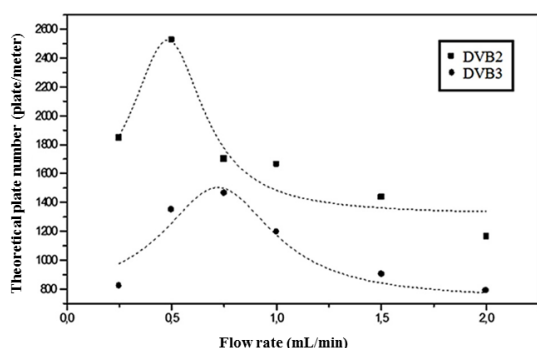
Figure 5. Variation of the theoretical plate number of the DVB2 and DVB3 columns with the flow rate (van Deemter diagram). Mobile phase: A: AcN / water. Analyte: Cytochrome C (0.25 mg / mL), Column dimensions: 100x4.6 mm ID., UV-VIS detector, 280 nm.

The relationship between the theoretical plate number indicating the column efficiency and the flow rate is given in Figure 5 for DVB2 and DVB3 columns. As seen here, the highest plate number (highest separation yield) values were obtained with the DVB2 column at a flow rate of 0.5-0.75 mL / min between 2000-2600 plate / m.

The protein recovery values obtained for this column are given in Table 3. Protein recovery is important for repeated use for a column using RPC. If the recovery is low, the analyte supplied to the column is adsorbed by the column material, and regeneration of the column becomes difficult due to the conditioning, which leads to column clogging by increasing the back pressure of the column. Protein recovery of commonly used commercial columns is usually above 90%.

Table 3. Protein recovery values for the DVB2 column. Mobile phase: AcN / water. Protein concentration: 1 mg / mL (protein solution injected into the column, 10 µL) Flow rate: 0.75 mL / min.

Protein	Protein recovery %
Ribonuclease A	95
Cytochrome C	99
Lysozyme	94
BSA	93

In the last part of the chromatographic studies, the reproducibility tests of the analytes for the DVB2 column were made "run to run" and "day to day". For reproducibility tests, each sample of protein concentration 1 mg / mL (injection volume, 10 □L) was injected into the column 10 times a day for one week and the retention times of the analytes were recorded. Relative Standard Deviation (RSD) values of "run to run" and "day to day" values obtained as a result of the analyzes made in the gradient conditions vary between 1.2 - 2.8%. These results show that the synthesized column packing material can be used repeatedly for RPC.

4. CONCLUSIONS

- Optimum operating conditions for the columns DVB2 and DVB3, respectively, formed with monodisperse and porous apolar poly(VAc-co-DVB) and poly(DVB) particles for RPC were 0.75 mL / min mobile phase flow rate and 1 unit AcN / min gradient slope has been identified.
- The performance of the DVB2 column in protein separation was observed to be better than the DVB3 column due to its higher resolution and theoretical plate number.
- Protein recovery values for the DVB2 column are quantified for all proteins.
- Analytes for the DVB2 column were tested for reproducibility and Relative Standard Deviation (RSD) values were found in the range of 1.2-2.8%. These results show that the synthesized column material can be successfully used for RPC.

- The DVB2 column synthesized in the study was exhibited a chromatographic performance similar to the columns used commercially for protein separation in gradient conditions. In addition, the high chemical and mechanical strength, protein recovery, theoretical plate number, reproducibility and low back pressure of DVB2 column packing materials are superior to commercial columns.

REFERENCES

[1]. Camlı, S.T., Şenel, S., Tuncel, A., Cibacron Blue F3G-A Attached Uniform and Macroporous Poly(styrene-divinlybenzene) Particles For Specific Albumin Adsorption. J. Biomater. Sci. Polym., 8 (1999) 875-889.

[2]. Ellingsten, T., Aune, O., Ugelstad, J., Hagen, S., Mono-sized Stationary Phases for Chromatography, Journal of Chromatography A, 535 (1990) 147-161.

[3]. Galia, M., Svec, F. , Fréchet, J.M.J., Monodisperse Polymer Beads as Packing Material for High-performance Liquid Chromatography. Effect of Divinylbenzene Content on the Porous and Chromatographic Properties of Poly(styrene-co-divinylbenzene) Beads Prepared in Presence of Linear Polystyrene as a Porogen, J. Polym. Sci., Polym. Chem., 32 (1994) 2169-2175

[4]. Hossoya, K., Teramachi, M., Tanaka, N., Kobayashi, A., Kanda, T., Ohtsu, Y., Preparation Strategy for Uniformly Sized, Polymer-Beads HPLC Packing Materials Having Practically Acceptable Column Efficiency. 1. Copolymerization Technique, Anal. Chem., 73(24) (2001) 5852-5857

[5]. Lewandowski, K., Svec, F., Frechet, J.M.J., Polar, A Novel Polar Seperation Medium For The Size Exclusion Chromatography of Small Molecules: Uniformly Sized, Porous Poly(vinylphenol-co-divinylbenzene) Beads, J. Liq. Chrom. & Rel. Technol., 20 (1997) 227-243

[6]. Smigol, V., Svec, F., Frechet, J.M.J., 2-Dimensional High-Performance Liquid-Chromatography Using Monodisperse Polymer Beads Containing Segregated Chemistries Prepared By Pore-Size Specific Functionalization - Single-Column Combinations of Size Exclusion Or İon-Exchange With Reversed-Phase Chromatography, Analytical Chemistry, 66 (23) (1994) 4308- 4315

[7]. Smigol, V., Svec, F., Frechet, J.M.J., High-Performance Liquid Chromatography of Complex mixtures Using Monodisperse Dual-Chemistry Polymer Beads Prepared by a Pore-Size-Specific Functionalization Process. A Single Column Combination of Hydrophobic Interaction and Reversed-Phase Chromatography, Analytical Chemistry, 66 (13) (1994) 2129-2138

[8]. Unsal, E., Durdu, A., Elmas, B., Tuncel, M., Tuncel, A., A New Affinity-HPLC Packing For Protein Separation: Cibacron Blue Attached Uniform-Porous Poly(HEMA-co-EDM) Beads, Analytical and Bioanalytical Chemistry, 383 (2005) 930-937

[9]. Unsal, E., Irmak, T., Durusoy, E., Tuncel, M., Tuncel, A., Monodisperse porous particles with polyionic ligands for ion exchange separation of proteins, Analytical Chimica Acta, 570 (2006) 240-248

[10]. Ettre, L.S., Chromatography: the Separation Technique of the 20th Century. Chromatographia, 51 (1/2) (2000) 7-17

[11]. Engelhardt, H., One century of liquid chromatography from Tswett's columns to modern high speed and high performance separations, Journal of Chromatography B, 800 (1-2) (2004) 3-6

[12]. Zhang, Y. W., Yao, S., Zeng, H., Song, H., Chiral Separation of Pharmaceuticals by High Performance Liquid Chromatography, Current Pharmaceutıcal Analysıs, 6 (2) (2010) 114-130

[13]. Saraçoğlu Kaya, B., Sağ, E., Design of Reversed Phase Chromatography (RPC) Column Packing Material for Protein Separation: Part 1- Synthesis and Characterization, Cumhuriyet Science Journal, 38 (4) (2017) 788-797

[14]. Unsal, E., Camli, S. T., Irmak, T., Tuncel, M., Tuncel, A., Monodisperse poly(styrene-co-divinylbenzene) particles (3.2 μm) with

relatively small pore size as HPLC packing material, Chromatographia, 60 (2004) 553–560

[15]. Unsal, E., Camli, S.T., Senel, S., Tuncel, A., Chromatographic Performance of Monodisperse–Macroporous Particles Produced by "Modified Seeded Polymerization." I: Effect of Monomer/Seed Latex Ratio, Journal of Applied Polymer Science, 92 (2004) 607–618

[16]. Unsal, E., Elmas B., Camli, S.T., Senel, S., Tuncel, A., A Uniform Particles For The Reversed Phase Separation of Proteins With High Resolution and High Column Efficiency, Separation Science and Technology, 40 (2005) 1425-1438

[17]. Çağlayan, B., Unsal, E., Çamlı, T., Tuncel, M., Tuncel, A., Monodisperse Porous Poly(Vinyl Acetate-Codivinylbenzene) Particles By Single-Stage Seeded Polymerization: A Packing Material For Reversed Phase HPLC. J. Sep. Sci., 29 (2006) 936 – 944

Pavement Management System Investigation in Case of Afghanistan

Sepanta NAIMI [ID] *, Mohammad Ali KARIMI* [ID]

Istanbul Aydin University, Faculty of Engineering, Department of Civil Engineering, Istanbul, TURKEY

Abstract. Afghanistan is encountering a massive compete in arrangement of old infrastructure. Specially for roads structure, it is found that many roads pavements built 30 to 40 years ago and now it is the end of their life. Other roads had been deteriorated because of misuse, overuse and mismanagement and also after more than 3 decades of conflict Afghanistan encountered keen challenges in rehabilitation and reconstruction of the roads. In addition, present and future threats influence the wished mission of these pavements for fast, safe and comfort transportation of people and goods. Moreover, the current management shows that the system is being used now is not flexible enough to consider on the changing conditions and is poor to assist in making decisions.

This study aims to initiate a Pavement Management System by providing an organized procedure of maintaining, reconstructing, and operating the roads pavements and to utilize in a better flexible strategy that can enable this research to perform better tasks, more economically, higher quality and do it such a manner to achieve a desired result.

A system has been also presented to help and make easier the decision making process. It is Micro PAVER pavement software. Micro PAVER is a Pavement Management System developed by the US Army Corps of Engineers. Micro PAVER provides pavement management capabilities to:

- Organize and develop the pavement list.
- Analyze the running condition of pavements.
- Develop methods to forecast future conditions report on past and future pavement execution; and
- Develop plots for pavement maintenance based on condition needs or budget.

Therefore, in order to have a good management system, this system will be preferred which provide an organized method of maintenance, reconstruction and operation of the roads pavements. And the system will be flexible enough and assists in making decisions.

Keywords: Pavement management system, Micro PAVER, pavement maintenance, flexible strategy, pavement execution.

Afganistan'da Yol Kaplaması Yönetim Sistemi Araştırması

Özet. Afganistan, eski altyapı düzenlemesinde önemli bir sorunla karşı karşıyadır. Özellikle yolların yüzeyi sözkonusu olduğunda, birçok yol kaplamasının 30-40 yıl önce yapıldığı ve şimdi ömrünü tamamladığı görülmektedir. Bazı yollar da kötü kullanım, aşırı kullanım ve yanlış yönetim nedeniyle ve ayrıca 30 yıllık savaştan sonra Afganistan'ın yolların iyileştirilmesi ve yenilenmesi bakımından ciddi zorluklarla karşılaşılması nedeniyle kötüleşmiştir. Bunun yanısıra, mevcut ve gelecekteki tehditler de insanların ve ürünlerin hızlı, güvenli ve rahat ulaşımını sağlamak için arzu edilen bu yol kaplamaları işini etkilemektedir. Bunun yanısıra, mevcut yönetim şu anda kullanılmakta olan sistemin değişen koşullarını hesaba katmaya yetecek kadar esnek değil ve kararlar verilmesine yardımcı olmakta zayıf kalıyor.

Araştırma, yol kaplamalarının bakımına, yeniden yapımına ve işletilmesine ilişkin bir organize prosedürün sağlanmasına yönelik bir Yol Kaplama Yönetim Sistemi başlatmak ve daha iyi görevleri daha ekonomik şekilde ve daha yüksek kaliteyle gerçekleştirmemizi ve bunları arzu edilen sonuca ulaşacak şekilde yapabilmemizi sağlayacak daha esnek bir stratejiyle kullanmayı amaçlamaktadır.

Ayrıca, karar verme sürecine yardımcı olacak ve bunu kolaylaştıracak bir sistem de sunuldu: Micro PAVER yol kaplama yazılımı. Micro PAVER, ABD Mühendisler Kolordusu tarafından geliştirilen bir Yol Kaplama Yönetim Sistemidir. Micro PAVER:

- Yol kaplama listesini organize etmeye ve geliştirmeye;
- Yol kaplamalarının çalışma koşulunu analiz etmeye;
- Geçmişteki ve gelecekteki yol kaplama icraatına yönelik gelecekteki koşulları tahmin etmeye yönelik yöntemler geliştirmeye ve
- Koşullara, ihtiyaçlara veya bütçeye dayalı olarak yol kaplama bakımına planlar geliştirmeye yönelik yol kaplama yönetimi becerileri sağlıyor.

Bu nedenle, iyi bir yönetim sistemine sahip olmak için yol kaplamalarının bakımına, yeniden yapımına ve işletilmesine ilişkin bir organize yöntem sağlayan bu sistem tercih edilecektir. Bu sistem, yeterince esnek olacak ve kararlar alınmasına yardımcı olacaktır.

Anahtar Kelimeler: Yol kaplama yönetim sistemi, Micro PAVER, yol kaplama bakımı, esnek strateji, yol kaplama icraatı.

1. INTRODUCTION

A Pavement Management System (PMS) is an important tool in order to manage a road system appropriately. AASHTO regulations are used by road agencies which are dealing with maintenance and evaluation of road systems in a long service condition. PMS analyzes the most advantageous maintenance strategies and aids to apply and execute them. It relates to all occupations involved in a procedure of making a great road system. These occupations are such as, planning, initial information acquisition, maintenance, rehabilitation and construction [1].

Maintenance for the pavement network is one of the most significant and a vital duty to ensure that goods and people are carried and transported in a safe, fast, relax, and economic way. Witnesses in improved countries has proved that lack of proper maintenance would cause into a serious increasing vehicle operating cost, travel period and untrustworthy road transportation service.

It is known that the quality and effectiveness of roads boosts the health of social system quality of life and the durability of business and economic

activities. Reasons for collapse and baleful failure of these roads may happen due to overuse, aging, and wrong management. Therefore, the maintenance and protection of such roads can take a great national notice [2].

Engineers and Managers, who have created and used pavement technology, can feel that pavement management has a matter of "Pay less now" or pay much more later [3]. All agencies working in this field find it out that they may not afford to pay later; it is more costly to reconstruct and rehabilitate badly damaged pavements. Unfortunately, there are agencies not paying attention to the pavement infrastructure maintenance, however, when the pavement is in the failure stage due to deterioration, large amount of money are spent for restoration. Agencies blessed with a good pavement infrastructure need to start a pavement management system as soon as possible. They have to make a complete list of the pavement infrastructure, evaluate its current and projected condition and specify the budget required to maintain the pavement condition higher than acceptable level. They must clarify the

condition for the work requirements, concentrate on projects, and maximize spending of maintenance funds [4].

In Afghanistan, pavement infrastructure plays an important role in the development of the country and therefore, Afghanistan pavement projects and their threats are chosen in this research to be investigated. [1].

- **Current Threats**:

Afghanistan's infrastructures reach to their end of economic life and challenges with old structure. In particular, there are road pavements found that were built 30 or 40 years ago and some are recently built with low quality, which are already about reaching to the end of their service life. [5] Afghanistan pavements have the below current threats:

- Increased rate of failure. (pavements damages fast)
- Vehicles overloading on the pavement.
- Fast traffic increase.
- Poor maintenance. (improper and not standard materials, wrong implementation)
- Bad design and implementation.
- Taliban (Terrorist groups who put the bombs beside the road or under the bridge)
- Restricted resources (funds, equipment, materials ...)
- Not enough data to make decision.
- Improper management system.

The traditional maintenance system which is currently used in Afghanistan municipality indicates:

- Lack of documentation. (no Maintenance Repair and Reconstruction (MRR) history, no periodic inspections ……)
- Lack of usage of structured set of data to save and process the system data in the Required Minimum Distribution (RMD).
- Systems being used are not enough flexible in setting work plans and timetables in order to monitor variable conditions.
- System is substandard in how to make decisions.

From above mentioned matters, the lack of extensive Pavement Management System (PMS) is considerably felt [6].

- **Future Threats:**

Future economy growth and the need to have fast, secure and relax transportation in order to move people and goods can put further pressure on already stressed pavement system. Adding to the equation, the growth of weighty loading generation and the shadow of continuing conflicts is not forecasting a bright future at this section.

The aim of this study is to expand a Pavement Management System that makes a regular procedure of protecting, rehabilitating, raising and utilizing Afghanistan's pavements. This is to facilitate a better and more flexible approach in making decisions, which are required to earn the wishes of road user's. To achieve this aim, the fallowing points should be considered:

- Building up a satisfactory data to maintain road pavements.
- Choosing and constructing an evaluation system for pavements.
- Developing computer program to facilitate the management process of road pavements.

In the following sections, we will define the pavement distresses, the index of international roughness and pavement conditions. It will be followed by the elaborating the maintenance strategies and highlighting the ones that are specifically applicable to the Afghanistan's roads requirement.

2. PAVEMENT DISTRESSES

Pavement distress involves distortion, disintegration, rutting, cracking, and other kinds of surface damages that shows a devaluation in the pavement's surface condition.

The deterioration of pavements is a result of weather or environmental factors, traffic, pavement and some other reasons [7]. The factors mentioned result in an increase on the shear in sub base, surface and subgrade, surface fatigue and

consolidation. Traffic factors are acceleration and deceleration which is done by heavy axle load repetition, while pavement factors include excess asphalt, poor subgrade drainage and insufficient particle interlock. Temperature changes and rainfall are types of climatic factors that may result deterioration to pavements [3, 8].

3. INTERNATIONAL ROUGHNESS INDEX (IRI)

International Roughness Index is used to determine the quality of the running lengthwise profile of a passed track and organize a systematize roughness scale. Often units used are millimeters per meter (mm/m) or meters per kilometer (m/km) [9, 10]. The IRI is found in the average corrected slope (ACS), that is a filtrated proportion of a typical vehicle's gathered pendency movement (in m, inch, etc.) apportioned by the distance passed by the carrier with the measurement (mile, km, etc.). IRI is then equal to ACS times 1,000. as shown in Figure 1
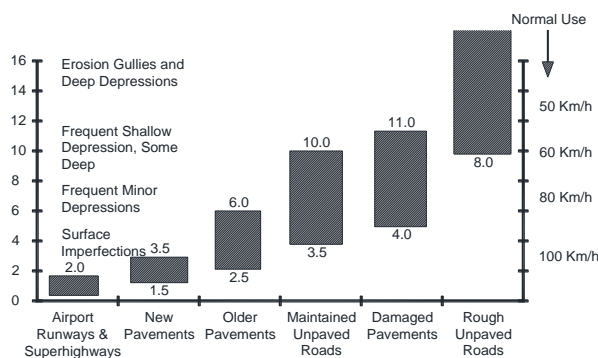
Figure 1. International Roughness Index.

4. PAVEMENT CONDITION INDEX (PCI)

The PCI arranges a numerical rating for the situations of road branches of road network, which 0 represents the worst condition and 100 represents the best condition [11]. This process is used worldwide to create a measurement of the condition of pavements which are taken into account for the functional performance beside the structural performance [12, 13]. The PCI measures two conditions:

1. Type, severity of pavement surface distresses and extent (like distortion, cracks and rutting).
2. The fluency and drive comfort of the road.

The PCI explains to public works organizers,

*   The current condition of the road segments
*   The size and rate of deterioration of the road segment and network by passing the time.

A PCI benefit;

*   Determine maintenance and rehabilitation requirements
*   Observe pavement condition over the time.
*   Provide a strategy for the network preventive maintenance
*   Develop budgets for the road maintenance.
*   Analyze pavement design and materials

Figure 2. Pavement Condition Index (Cost Saving + Higher Service Level).

There are some steps to perform the condition and identifying the PCI rating criteria manually as described below: [14]

Road Pavements are divided into branches and sections.

*   Every pavement section also is divided into units.
*   Units are evaluated where distress conditions, severity and density are specified.
*   Deduct value is specified for each type of distress.
*   Total Deduct Value (TDV) should be computed.

- Total Deduct Value is computed to obtain Corrected Deduct Value (CDV).
- Pavement Condition Index for each sample unit evaluated is computed from the bellow equation.

$$PCI = 100 - CDV$$

The PCI of the total section is computed by taking the average of PCI's of all sample units.

5. MAINTENANCE STRATEGIES

Engineering scientists specified strategies for the different levels of pavement deterioration and condition [15]. Whenever the pavement is in its good condition, inexpensive preventive maintenance therapies are cost-effective, but when the pavements reach to the end of their design life, relatively expensive reconstruction will be needed [16]. Maintenance types versus pavement conditions are shown as Figure 3
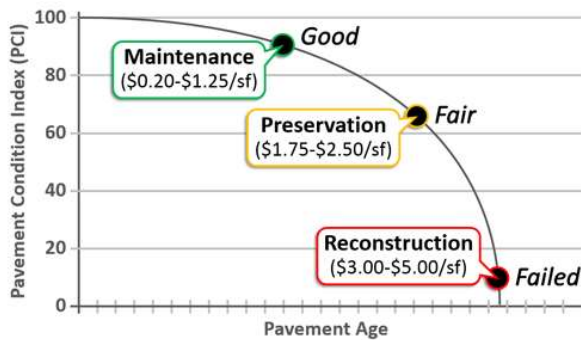
Figure 3. Maintenance Strategies.

5.1. Determining Strategies

At first pavement condition data should be collected. It has to be evaluated to determine the rehabilitation and maintenance requirements [17, 18]. This evaluation should use special standards, with engineering arbitration. The induction must look at the determined status of sections and specify the cause of the detected distress and how it could be best corrected [12].

There can be are five strategies that considered for paved surfaces:
- A- Routine Maintenance
- B- Preventive Maintenance
- C- Deferred Action
- D- -Rehabilitation
- E- Reconstruction
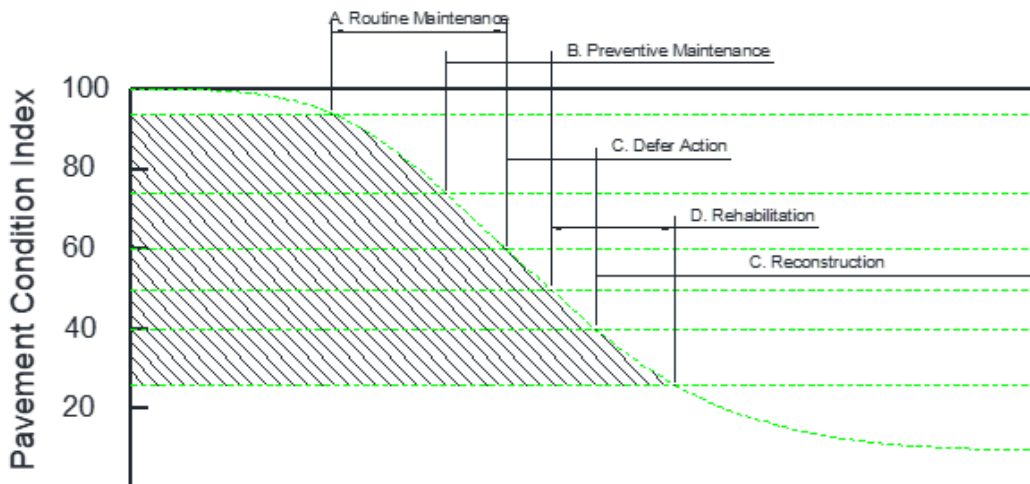
Figure 4. Five Strategies of the Paved Surfaces.

Typical Actions

The appropriate maintenance and repair strategies are best chosen using a life-cycle cost analysis. This action can be time consuming if attempted for every decision on every pavement section [19]. If a detailed economic analysis is not used, the most proper strategy can be selected using a logic scheme as suggested in Table 1 and Table 2. Such a scheme, of course, can be refined with a life-cycle analysis using average costs for typical actions, then using the resulting decision criteria as the standard for all sections. If such an approach is taken, different criteria for each pavement type can be chosen [8].

It should be considered that there is considerable overlap of possible strategies on the PCI performance curve [20]. In the example shown in Table 1, there are two or three possible strategies

for any PCI value from 25 to 15. This leads to a realistic approach because the collapse of pavements is a gradual process. A change in just a few PCI points will not usually make one strategy preferred over another.

Within specific ranges of condition, one must look at the factors that went into the overall condition rating [21]. Predominately surface distress such as weathering, raveling, or bleeding would show a need for preventive maintenance over other strategies. On the other hand, if most of the condition rating is a result of structural distress such as alligator cracking, potholes, or failed patches, then it may be best not to expend preventive maintenance funds and plan a rehabilitation effort. Roughness can also help specify strategy decisions [13].

Table 1. Typical Actions Flexible Pavements.

Strategy	Recommended Actions
A-Routine Maintenance	1- Crack sealing 2-Skin patching 3-Local repairs 4-Strategy C actions as necessary
B- Preventive Maintenance	1-Strategy A and C actions as necessary 2-Surface seals 3-Thin overlays
C-Deferred Action	1-Patching of high severity potholes, shoving, corrugations and rutting
D- Rehabilitation	1- Strategy A, B, and C actions as necessary 2- Removal of a portion of the surface if necessary 3- Structural overlay
E- Reconstruction	1- Strategy D actions as necessary 2- Removal and replacement of the entire Pavement structure 3- Geometric, safety and traffic improvements as necessary

5.2. Comparing Condition Assessment and Strategy

The all rating, actual distresses and their causes, and performance of the surface over a time should be examined to determine the most proper strategy [22, 23]. A strategy

should be thought of as an overall approach at this point rather than specific decisions about where to patch or how many inches of overlay to apply [24].

Table 2. Matching Condition Assessment and Strategy.

PCI	Other Consideration	Strategy
76-95	None (Excellent / Very good)	A
61-75	Normal or Small Amount of Surface distress	A
	Mostly Surface Distress	B
51-60	Mostly Surface Distress	B
	Distress Evenly Balanced	C
	Mostly Structural Distress very Rough (PSI < 2.0)	D
41-50	Relatively Smooth (PSI $\geq$ 2.5)	C
	Rough (PSI < 2.5)	D
26-40	Relatively Smooth to Rough (PSI $\geq$ 2.5)	D
	Very Rough (PSI < 2.5)	E
0-25	None(Very Poor / Failed)	E

A- Routine Maintenance
B-Preventive Maintenance
C-Deferred Action
D-Rehabilitation
E-Reconstruction

5.3. Evaluation the condition of Herat pavement

Evaluating the condition of Herat pavement network will be based on detailed visual inspection survey. It deals with the identification of pavement distress type, its extent and the level of severity of each type and it is also based on PCI criteria. Although, other methods including automated data collection, hand held computers, tablet computers or pocket inspectors may be developed to facilitate inspection and to eliminate data entry errors.

Table 3. Major Branch Data in Herat Pavement Network.

Branch ID	Branch Name	Number of Sections	True Area (SM)
100	Walayat Str	8	8832
150	64 Metra Str	9	25920
200	Spin Adi Str	6	10065.6
250	Farqa Str	14	34904.8

A pavement condition inspection form was prepared for this purpose. This form containing for example the condition data of Walayat Street is shown in Table 5.

Not all parameters need to be inspected every year, but an inspection scheduling procedure should be developed to assist in determining which sections should be re-inspected. There are commended pavement condition inspection policies minimizing the overall inspection effort of the city. A 2-3-year inspection interval at maximum is recommended.

Table 4. Part of Section Data in Herat Pavement Network.

Branch ID	Branch Name	Section ID	Inspection Date	Surface	Lanes	True Area (SM)
100	Walayat St	A/100	10/12/2015	AC	4	1104
100	Walayat St	B/100	10/12/2015	AC	4	1104
100	Walayat St	C/100	10/12/2015	AC	4	1104
100	Walayat St	D/100	10/12/2015	AC	4	1104
100	Walayat St	E/100	10/12/2015	AC	4	1104
100	Walayat St	F/100	10/12/2015	AC	4	1104
100	Walayat St	G/100	10/12/2015	AC	4	1104
100	Walayat St	H/100	10/12/2015	AC	4	1104
150	64 Metra St	1L/150	3/10/2015	AC	2	2880
150	64 Metra St	2R/150	3/10/2015	AC	2	2880
150	64 Metra St	3L/150	3/10/2015	AC	2	2880
150	64 Metra St	4R/150	3/10/2015	AC	2	2880
150	64 Metra St	5L/150	3/10/2015	AC	2	2880
150	64 Metra St	6R/150	3/10/2015	AC	2	2880
150	64 Metra St	7L/150	3/10/2015	AC	2	2880
150	64 Metra St	8R/150	3/10/2015	AC	2	2880
150	64 Metra St	9L/150	3/10/2015	AC	2	2880
200	Spin Adi St	AR/200	5/11/2011	AC	2	1677.6
200	Spin Adi St	BR/200	5/11/2011	AC	2	1677.6
200	Spin Adi St	CR/200	5/11/2011	AC	2	1677.6
200	Spin Adi St	DR/200	5/11/2011	AC	2	1677.6
200	Spin Adi St	ER/200	5/11/2011	AC	2	1677.6
200	Spin Adi St	FR/200	5/11/2011	AC	2	1677.6
250	Farqa Str	1R/250	4/8/2012	AC	2	2493.20
250	Farqa Str	1L/250	4/8/2012	AC	2	2493.20
250	Farqa Str	2R/250	4/8/2012	AC	2	2493.20
250	Farqa Str	2L/250	4/8/2012	AC	2	2493.20
250	Farqa Str	3R/250	4/8/2012	AC	2	2493.20
250	Farqa Str	3L/250	4/8/2012	AC	2	2493.20
250	Farqa Str	4R/250	4/8/2012	AC	2	2493.20
250	Farqa Str	4L/250	4/8/2012	AC	2	2493.20
250	Farqa Str	5R/250	4/8/2012	AC	2	2493.20
250	Farqa Str	6R/250	4/8/2012	AC	2	2493.20
250	Farqa Str	7R/250	4/8/2012	AC	2	2493.20
250	Farqa Str	8R/250	4/8/2012	AC	2	2493.20
250	Farqa Str	9R/250	4/8/2012	AC	2	2493.20
250	Farqa Str	10R/250	4/8/2012	AC	2	2493.20

Table 5. condition data of Walayat Street.

INVENTORY INFORMATION		Date: 12.02.2017	
Street Name : Walayat Str	Street ID : 100A	Section ID : 100/A	
From : Section 1	To : Section 2	Number of lanes : 0	
Section Length : 120 m	Zone : 01	Section Wide : 9.20 m	

Distress Information

1- Alligator Cracking	8- Reflection Cracking	15- Rutting
2- Bleeding	9- Lane/Shoulder Drop Off	16- Shoving
3- Block Cracking	10- Long and Trance	17- Slippage Cracking
4- Bumps and Sags	11- Patching & Util. Cut	18- Swell
5- Corrugation	12- Polished Aggregate	19- Weathering & Raveling
6- Depression	13- Potholes	
7- Edge Cracking	14- Rail Road crossing	

Distress Type	1	7	12	17	3	13	10
Severity	6 L	22 M	11	7 M	14 L	2	16 M
	13 L	16 L	8		11 L		
	6 M	14 L	29				

Total Severity	Low	19	30			25	2	
	Medium	6	22	48	7			16
	High							

Comments:

Notes: 1. Distress (13) is counted as number of potholes.
2. Other distress types are measured in m2 except (4 − 7 − 8 − 9 − 10) in m.

consequently, the current condition can be identified. Table 6 shows the condition of the case study zone sections as calculated by Micro PAVER.

Table 6. The PCI Values of the Case Study Zone Sections.

Section Condition Report									
Date: 02/04/2018			Pavement Database				Network ID : WS1		
Branch ID	Section ID	Last Construction date	Surface	Use	True Area (sqm)	Last Inspection Date	Age at Inspection	PCI	
100A (Walayat Str	100/A	2/3/2016	AC	ROADWAY	1104	9/20/2017	1	75	
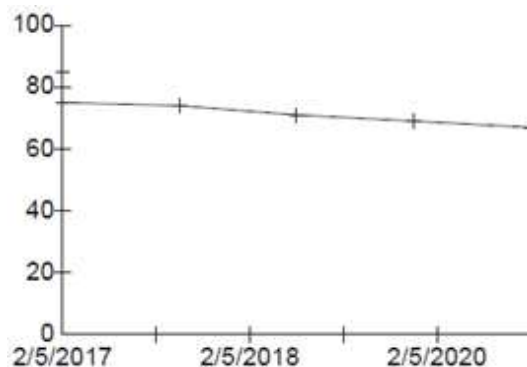
Graph 1. Section Condition Plot (Year vs. PCI).

that predict how a certain type of pavement will perform based on its performance in the past.

6. REQUIRED ROAD MAINTENANCE IN AFGHANISTAN

The main aim of this research is to develop a methodology for analysis of maintenance needed for Afghanistan roads. In this research, some structural arrangements proposed for the condition analysis of roads to plan and preform effective maintenance remedy for the enhancement of roads in Afghanistan. Maintenance is serious phase of road activity to maintain the original finance. So this is important to develop strategies for road maintenance condition and the condition of roads depending upon sectional area condition and sectional area significance [25]. The condition itself depends on functional and structural condition and functional condition is heavily pertinent to the available traffic condition and safety of the roads.

6.1. Maintenance Types

The type of maintenance and terminology, which relate to the highway maintenance, differs for each country [26]. It also differs from each urban area to others and from one highway authorization to another highway authorization and also, time is considered as another critical factor for performance of maintenance [27, 28]. Therefore, according to the time of performing, the maintenance can be categorized as below;

- Routine Maintenance
- Periodic Maintenance
- Extraordinary Maintenance
- Emergency Maintenance (According to Condition in Afghanistan)
- Winter Maintenance (According to Climate in Afghanistan)

7. CONCLUSIONS AND RECOMMENDATIONS

The current PMS in Afghanistan is in its traditional method and even it is not considered in many pavements. This entails the lack of accurate decision making to optimize the maintenance activities in most cities to match the road user's expectations. In this research, we could identify a serious and strong gap for comprehensive PMS. It can be concluded by this research with the following recommendations:

1. A PMS should be launched to service and work for to maintain Afghanistan pavements and enhance the management process and optimize the benefits to the society through a concentrate PMS.
2. Future enhancement should be considered to include all elements of roads maintenance management system.
3. Pavement Condition Index (PCI) to be chosen as a tool for Afghanistan pavements network condition analysis.
4. Micro PAVER caters for developing the management process of Afghanistan Pavement Roads Network.
5. Micro PAVER can be also utilized to help and find an easier way for the decision making process to manage Afghanistan Road Pavements.
6. In Afghanistan Maintenance Department staff have to be educated and trained to know the correct ways of carrying out the PMS tasks and the department should be equipped with the updated tools.

REFERENCES

[1]   Molenaar A. A. A., Pavement Management Systems. TUDelft, Delft University of Technology, Delft, Netherland, (2002) 50-148.

[2]   AASHTO. 2018. AASHTO T 222 and ASTM D 1196: Nonrepetitive Static Plate Load for Soils and Flexible Pavement Components, for Use in Evaluation and Design of Airport and Highway Pavements. Address: https://www.aashtofree.com/aashto-t-222-

81-pdf-free-download/. Retrieved: Febuary 2 (2018).

[3] Shahin M.Y., Pavement Management for Airport, Roads, and Parking Lots, Chapman & Hall, New York, USA, (1994) 396-416.

[4] The Pavement Management System Guide Book Review Team, Washington State Department of Transportation: A Guide for Local Agency Pavement Managers, The Northwest Technology Transfer Center, Olympia, (1994) 18-50.

[5] Affleck RT. and Freeman R., Engineering Research Center Development. Challenges for Engineering Design, Construction and Maintenance of Infrastructure in Afghanistan ERDC/CRREL Special Report 10-2 (2010).

[6] Government of Afghanistan, The Afghanistan Road Toll Gazette Publication, 6 (2012) 1091-1391.

[7] Roberts F L., Kandhal P S., Brown E R., Lee D-Y. and Kennedy T W., Hot Mix Asphalt Materials, Mixture Design, and Construction, Second Edition. National Asphalt Paving Association Education Foundation: Lanham, MD., USA, (1996) 7-10.

[8] USAID., Final Road Fund Study (Component 3), Technical Assistance to the Ministry of Public Works; and Asian Development Bank, Strategic Roadmap for Development Partner Support to O&M of Afghanistan Roads, December 9 (2015) 26.

[9] Islamic Republic of Afghanistan, Transport and Civil Aviation Strategy 1387–1391 (2007/08–2012/13), Pillar III, Infrastructure, Afghanistan National Development Strategy, 2008.

[10] Danial L. and Stacks P.E., Texas Department of Transportation Glossary; by Texas Department of Transportation, (2018) 38-135.

[11] National Cooperative Highway Research Program Report 626, NDT Technology for Quality Assurance of HMA Pavement Construction, Washington DC, USA, (2009) 16-20.

[12] Shahin M.Y., Pavement Management for Airports, Roads, and Parking Lots: Second edition, Published by Springer, (2005) 43-61.

[13] UFC 3-270-08. Unified Facilities Criteria Unified Facilities Criteria, Washington, USA, (2004) 77-89.

[14] Sarsam S. I., Pavement Maintenance Management System: A Review. Trends in Transport Engineering and Applications, 3-2 (2016) 19–30.

[15] Narasimha, V.L., Sundararajan T. and Raja M., Subjective Rating Technique- a tool for Prioritizing Roads in a Network for Periodic Maintenance, Highway Research Bulletin, The Indian Road Congress, 69 (2003) 1-14.

[16] The World Bank. European Union TACIS Program and GTZ, Proceedings of the Highway Policy Seminar for Countries of the Former Soviet Union, 15-19 May, Moscow, (1995) 207–216.

[17] Ahmed A., Recycled bassinet for Enhancing the Stability of Poor Sub Grades Clay Soil in Road Construction Projects, Construction and Building Materials, 48 (2013) 151–159.

[18] USAID., Evaluation of the Ministry of Public Works Capacity to Conduct Roadway Operations and Maintenance, (2012) 9-15.

[19] Sarsam SI., Razzoki SI. and Najim SH. Implementation of Decision Support System (DSS) in Pavement Maintenance Management, International Journal of Economics and Business Administration, 1-2 (2015) 71–81.

[20] Federal Aviation Administration (FAA.), Airport Pavement Management Program, Advisory Circular AC 150/5380-7B, FAA Washington, D.C., USA, (2014) 6-13.

[21] Garber NJ. and Hoel LA., Traffic and Highway Engineering, Fourth edition, United State Copyright, Cengage Learning, Canada, (2009) 1025-1033.

[22] The World Bank. Selecting Road Management Systems, DOC1101, Washington DC, (1997) 2-8.

[23] Swarup A., Agarwal P.K. and Khan A. B., Strategies for Economical Construction Of Rural Roads, Civil and Environmental Research, 7-7 (2015) 79-85.

[24] USAID., Final Closeout Report, TO 14 – Road Operations and Maintenance and Capacity Building Program, (2011) 4-6.

[25] SIGAR., Commander's Emergency Response Program in Laghman Province Provided Some Benefits, but Oversight Weaknesses and Sustainment Concerns Led to Questionable Outcomes and Potential Waste, SIGAR Audit 11-7 (2011) 1-5.

[26] Misra A., Roohanirad A. and Somboonyanon P., Guidelines for a Roadway Management System (RMS) for Local Governments, U.S. Department of Transportation Research and Special Programs Administration, Washington DC, USA, (2003) 947-954.

[27] Zeng S. and Ouyang XY., Study on Frame Design of Highway Pavement Maintenance Management System, Proceeding, Second International Conference on Intelligent Computation Technology and Automation, 4: 10-11. October, Hunan, China, (2009) 438–441.

[28] Broten M. Local Agency Pavement Management Application Guide, The Northwest Technology Transfer Center, Washington State Department of Transportation, Olympia, (1996) 15-17.

Usage of β_V Seeds as an Alternative Pre-crystallization Technique in Production of Synbiotic Sugar-free Dark Chocolate: Effect of Quality Characteristics

Ömer Said TOKER[1] [iD], Derya GENÇ POLAT[2] [iD]*

[1]Yildiz Technical University, Chemical and Metallurgical Engineering Faculty, Food Engineering Department, Istanbul TURKEY

[2]Tayaş Gıda A.Ş., Gebze, Kocaeli, TURKEY

Abstract. Pre-crystallization process in chocolate production requires high investment cost and it is employed with multistage thermal processes. Improper tempering process results in fat bloom main quality defect of the chocolate products. Seeding is an alternative tempering process and it is performed by addition of β_V and/or β_{VI} seeds, extracted by chocolate or cocoa butter, to chocolate or chocolate products. In the present study, synbiotic dark chocolate was produced by inulin (DP<10) used as a prebiotic fiber at concentarion of 9.00 g / 100 g and probiotic *L. acidophilus*. Effect of different β_V concentrations (0.50-1.50 g/100 g) on the quality parameters and viability of probiotics was observed. Probotic enrichment (9.0 log cfu/25 g) was performed after conching process. During production process, 0.50-1.50 log cfu/25 g vitality loss was observed and application of seeding technique caused to decrease in probiotic level (*P*<0.05). The other quality parameters, namely, water activity, water content, colour properties (*L**, *C**, *h°*, *WI*), hardness, rheological parameters (yield stress and plastic viscosity) and sensory properties were not negatively affected by seeding technique. Higher vitality level can be obtained by optimization of seeding process such as shear rate.

Keywords: Functional, Prebiotic, Probiotic, Tempering.

Sinbiyotik Şekersiz Bitter Çikolata Üretiminde Alternatif Pre-Kristalizasyon Tekniği Olarak β_V Tohum Kristali Kullanımı: Kalite Parametrelerine Etkisi

Özet. Çikolata üretiminde pre-kristalizasyon prosesi, konvansiyonel olarak yüksek sabit yatırım maliyeti gerektiren ekipmanlar kullanılarak çok aşamalı ısıl işlemler ile yürütülmektedir. Uygun olmayan temperleme işlemi başlıca çikolata kalite kusurlarından olan yağ çiçeklenmesi ile sonuçlanmaktadır. Tohumlama adı verilen alternatif temperleme işlemi ise, çikolata ve/veya kakao yağından elde edilen β_V ve/veya β_{VI} kristal tohumların çikolataya ilave edilmesi sonucu gerçekleştirilebilir. Bu çalışmada, prebiyotik lif olarak 9.00 g/100 g düzeyinde inulin (DP<10) ve probiyotik aktiviteye sahip *L. acidophilus* içeren bitter çikolatalarda farklı düzeylerde (0,50-1.50 g/100 g) tohum kristal (β_V) kullanımının başlıca kalite parametreleri ve probiyotik canlılıktaki proses stabilitesi üzerine etkisi incelenmiştir. Konçlama prosesi sonrası 9.00 log CFU/25 g düzeyinde probiyotik ilavesi gerçekleştirilmiştir. Probiyotik canlılık düzeyinde proses kaynaklı yaklaşık 0.50 – 1.50 log cfu/25 g aralığında kayıp olduğu, prekristalizasyon tekniği olarak tohumlama tekniği uygulamasının, kullanılan tohum kristal miktarından bağımsız olarak probiyotik canlılık düzeyi üzerinde olumsuz etkisi belirlenmiştir (*P*<0.05).

Ancak çalışma kapsamında yeralan başlıca çikolata kalite parametrelerinden su aktivitesi, nem, renk (*L**, *C**, *h°*, *WI*), tekstür (sertlik), reolojik özellikler (akma basıncı (yield stress) ve plastik viskozite) ve duyusal profil için tohumlama tekniği uygulamasının avantaj unsuru olabileceği belirtilmiştir. Probiyotik ve/veya sinbiyotik bitter çikolata geliştirilmesinde tohum kristal ilavesi aşamasında karıştırma süresi optimizasyonu ile daha yüksek probiyotik canlılık düzeyine ulaşılması mümkün olabilir.

Anahtar Kelimeler: Fonksiyonel, Prebiyotik, Probiyotik, Temperleme.

1. INTRODUCTION

Chocolate is a product which is widely consumed throughout the world by people of all ages. The change in consumer preferences observed in recent years is also seen in chocolate or chocolate products, high sugar and fat composition of chocolate products gives people worry due to health conscious of them. Therefore, production of sugar-free products by substituting sugar with alternative compounds is major efforts of the food industry in order to achieve consumer desire.

However, different quality defects can be observed when alternative compounds, especially bulk sweeteners, are used in chocolate products; indicating that process and formulation optimization studies are required to obtain the products with desired quality level. For example, substituting of sucrose with bulk sweeteners influenced the rheological parameters; thereby quality of the products [1]. Isomalt, maltitol, xylitol [2-6], lactitol [7], sorbitol and mannitol [8] are major ingredients used in development of sugar-free chocolate products.

General production of chocolate is generally composed of mixing, refining, conching and tempering steps. Pre-crystallization process is conventionally performed by multi-stage heat processes [9, 10]. This process is reqired for obtaining the most stable polymorph of cacao butter (β_v) [11]. Cacao butter can be crystallised into six different polymorhic forms; which are named as form I-VI or form sub-α, α, β_2', β_1', β_2, β and this gradation is done according to increasing melting point and stability [12]. Tempering process is employed for the formation of β_v crystals, the most stable form among six polymorphs, by controlled heating and cooling cycle [13].

There are four important stages of tempering process: complete melting occured at 50°C, cooling to crystallization temperature (32°C), crystallization (27°C) and transformation of unstable-crystals (29-31°C) [14]. Conventional pre-crystallization is performed by pumping of melted chocolate through different tempering zones [15]. Conventional tempering method perfomed by adjusting temperature requires significant energy and production time. Therefore, alternative tempering methods were investigated to overcome disadvantages of the conventional process. Alternative tempering process is achived by addition/inoculation of form β_v and/or β_{vi} crystal seeds, extracted from cacao butter and/or solid chocolate, to melted chocolate for formation of stable crystals in chocolate. This process is known as "seeding" and crystal seeds are designated as "seed".

Enrichment of chocolates with several bioactive compounds as well as reducing sugar level or substituting the sugar completely is also ranked among consumer expectations. Probiotics and prebiotic fibers are of capital importance and food products including both of them are defined as synbiotics [16]. Previous studies were conducted to enrich dark chocolate products with probiotics for improving functionality of the products [17-22]. However, in these studies, dark chocolate samples were produced with conventional formulations and production processes. In the study carried out by Konar at al. [23], the chocolate products were manufactured by traditional tempering technique and inulin with different polymerisation degrees (DP>23 and DP<10), *Lactobacillus paracasei* and *L. acidophilus* probiotics were incorporated to chocolate products prepared by sucrose or maltitol and some quality parameters of chocolates and

vitality level of probiotics were investigated. Findings of the research showed that usage of inulin with DP lower than 10 and *L. acidophilus* was suggested for both sweetener types considering vitality of probiotic level.

In the present study, the effect of usage of β_V crystal seeds at different concentations on the main quality characterictics of dark chocolate sapmles including inulin with DP lower than 10 as a prebiotic fiber and *L. acidophilus* as a probiotic was investigated.

2. MATERIAL AND METHOD

2.1. Materials

Regarding production of dark chocolate samples, maltitol (Roquette Frenes, Lestres, Fransa), cacao butter, natural and alkalized cacao liquor (Altinmarka, Istanbul, Turkey), inulin (Beneo-Orafti, Belgium), soy lecithin (Brenntag Chemistry, Istanbul, Turkey), polyglycerol polyricinoleate (PGPR) (Palsgaard, Zierikzee, Holland), cacao butter-based β_V seed crystal (SEED100, Uelzena, Uelzen, Germany) and lyophilised *L. acidophilus* (LOT No 41127003932) (Danisco, Niebüll, Germany) were used.

2.2. Production of Dark Chocolates and Inocculation of Probiotics

Maltitol (32.5 g), cacao butter (13.0 g), natural cacao liquor (28.0 g), alkalized cacao liquor (17.0 g), soy lecithin (0.35 g), PGPR (0.15 g) and inulin (DP<10, 9 g) were present in formulation of dark chocolate with 100 g. Batches of 10 kg were prepared for each sample group. For this aim, melted cacao butter (20% of the total cacao butter in the formulation) and maltitol, natural cacao liquor and alkalized cacao liquor were heated to 40°C and mixed until uniformity was obtained. At the end of the mixing and heating process, chocolate mass was pre-refined by three roll refiner (Lehmann, Aaelen, Almanya) and it was heated to 50°C by mixing. Gap of three rolls and pressure leveles were adjusted to achieve desired particle size ranged between 20-25 µm. D_{90} values were controlled by measusing with micrometer (Mitutoyo, Manufacturing Co. Ltd., Japan, 0.001

mm accuracy). After reaching desired particle size, dry-conching process was performed at 70°C for 80 min. After that the residual cacao butter (80% of the total cacao butter), soy lecithin and PGPR were added and wet conching process was conducted. Total conching period lasted 480 min.

Following the conching process, *Lactobacillus acidophilus* (9 log cfu/25 g) was inoculated to chocolate samples cooled to 35°C. After inoculation, mixing process was performed approximately 5 min. For production of control sample, conventional tempering process with 3 stages was employed (33-35°C, 24-25°C and 25-26°C). Suitability of tempering process was checked by temper index values (TI) measured using temper meter (Chocometer, Aasted Farum, Denmark). Tempering process was terminated when TI value of the sample reached to between 5.5-6.0. Regarding pre-crystallization process as an alternative to conventional tempering, seeding technique was performed at 32°C. For this aim, several levels of β_V seeds (0.50, 0.75, 1.00 and 1.50 g seed/100 g chocolate) were added and mixing process was applied for 10 min. Afterwards, moulding and vibration processes (Aasted Farum, Denmark) were carried out at 27-30°C for all sample groups. Later, cooling step was employed at temperature level ranged between 12-14°C for 20 min in cooling tunnel (Aasted Farum, Denmark). The prepared samples were packaged with aluminium foil and stored at 20±2°C until analyses.

Particle size of the chocolate samples produced was measured using micrometer (Mitutoyo, Manufacturing Co. Ltd., Japan, 0.001 mm accuracy). Acquired value represents the largest particle size present in the samples [24]. Particle size of the produced chocolate samples was found to be 20.33 ± 0.58 µm.

2.3. Determination of Vitality of Probiotic Level

Vitality level of probiotics were determined after 1 day of production according to the method reported by Konar et al. [23]. For this aim melted chocolate samples were plated on convenient media (De

Man, Rogosa and Sharpe Agar (Oxoid CM 361)) and after incubation at 37.5 ºC for 48 h, LAB were counted.

2.4. Texture Analyse

Hardness parameter of chocolates was determined by texture analyser equipment (Stable Micro Systems, TA-XT Plus, UK) depending on the method described by Toker et al. [25]. The force required to break chocolate sample was determined using time versus distance graph. Hardness values of the chocolate samples was measured 7 times for each sample.

2.5. Rheological Analyses

Rheological properties of the chocolate samples were determined using stress/strain controlled rheometer Çikolata (Antonpaar MCR 302, Australia). Rheological analyses were conducted at 40°C according to the method described by ICA (International Confectionery Association). The method is composed of 4 steps as the following:

1. Step: Shear rate at 5 s^{-1} was applied for 500 s to homogenise the samples and to equilibrate the temperature
2. Step: Shear rate increased from 2 s^{-1} to 50 s^{-1} within 180 min.
3. Step: The chocolate samples were sheared at for 60 s.
4. Aşama: Sheared rate decreased from 50 s^{-1} to 2 s^{-1} within 180 s.

Casson model parameters (yield stress and plastic viscosity), seen in Eq. 1, were calculated using the data obtained from analyses.

$$\tau^{0.5} = \tau_0{}^{0.5} + \eta_{pl}\, \dot{\gamma}^n \tag{1}$$

where τ is shear stress; $\dot{\gamma}$ is shear rate, τ_0 is yield stress and η_{pl} is plastic viscosity

2.6. Moisture Content

Moisture content of the produced chocolate samples was determined by the method described by Lonchampt and Hartel [26].

2.7. Water Activity

Water activity values of the samples were determined using a_w-meter (Novasina, Switzerland) depending on the method reported by Konar [4].

2.8. Color Measurement

Color parameters (*L*: brightness, *a*: ±red-green and *b*: ±yellow-blue) of the chocolates were measured by colorimeter (Chroma Meter CR-400, Konica Minolta, Japonya). Chroma (*C**), hue angle (*h°*) and whiteness index (*WI*) were calculated using the following equations (Eq. 2-4) [27]:

$$C* = \sqrt{a*^2 + b*^2} \tag{2}$$

$$h° = \arctan\,(b*/a*) \tag{3}$$

$$WI = \sqrt{(100 - L)^2 + a*^2 + b*^2} \tag{4}$$

2.9. Sensory Analyses

Sensory properties of the chocolate samples were investigated by multiple-comparison technique [28]. For this aim, 8 trained panelists were evaluated the effect of β_v seed concentration on the sensory parameters of synbiotic chocolates. The evaluated parameters are sweetness, bitterness, fattiness, cacao taste, particle size, lightness, end taste present in mouth, first bite, color, melting in mouth, smootness and apperance which were scored to between 1 (very bad) and 10 (very good).

2.10. Statistical Analyses

All of the results were expressed as average ± standard deviation. The results were analysed with ANOVA and the significance level between samples were determined by Tukey's Test.

Statistical analyses were performed by MINITAB-Express (Minitab Inc., State College, PA, ABD) and MSTAT (Michigan State University, East Lansing, MI, ABD) software programs ($p<0.05$).

3. RESULTS AND DISCUSSION

Spesific surface area and D_{90} values are critical parameters of particle size analyses which are related with the quality characteristics of chocolates. Beckett [29] reported that these two parameters are also important in production process. Particle size affects the sensory, textural and rheological properties of chocolates. In addition, it also plays an important role in pumping, mixing, transportation and stability of solid-liquid mixtures [30].

In the present study, in order to clearly observe the effect of β_v seed concentration on the quality properties of the samples, the other factors such as particle size was standardized for abolishing its effect. D_{90} parameter of chocolate samples was found to be 20.33 and addition level of β_v did not significantly influence this parameter ($P>0.05$) since very low amount of seed was added to the formulation, which did not result in remarkable differences in the D_{90} value. Similar particle size of the chocolates prepared with conventional and seeding tempering methods is important for the desired quality of the samples. In addition, similar production process can be used for the chocolates be manufactured by seeding technique.

3.1. Probiotic Vitality Level

As mentioned above, *L. acidophilus* was inoculated at concentration of 9.0 log cfu/25 g to dark chocolate samples including maltitol and inulin. There are different views for definition of probiotic foods. For example in Canada and Italy, for probiotic statement in label, the probiotic level should be 9.0 log cfu/serving size or day and general acceptance for serving size of the chocolate is 25 g [16]. However, Maragkoudakis et al. [31] reported that 5 – 8 log cfu/g probiotic load can be acceptable for dairy products. In the present case,

stability of probiotics during process and shelf life as well as inoculation level is of capital importance.

In this study, regarding for all chocolate groups, the loss of probiotic vitality due to production process was found to be approximately 0.50 – 1.50 log cfu/25 g (Table 1). This loss level is consistent with the previous studies where different probiotics were used in chocolate or chocolate-based products [21, 23, 32]. According to the results, pre-crystallization technique also influenced the probiotic vitality level ($P<0.05$). Highest vitality level was observed in dark chocolate sample prepared with conventional tempering process and application of seeding technique resulted in decrease in vitality level of probiotics.

In the production process of the chocolate tempered with β_v seed crystals, mixing process required after seed addition should be optimized depending on formulation of the products or ingredinets present in the media [33]. Mechanical force applied during mixing process can adversely affect the vitality level of probiotics. Change percentage of vitality level due to applied process is shown in Table 1. Probiotic dark chocolate production can be achieved by adjusting inoculation level considering the losses observed during manufacturing. In conventional tempering, flow is conducted at different temperature zones without mechanical forces; therefore there is no mechanic stress for probiotics. However, production of synbiotic or probiotic chocolate with β_v seeding technique, probiotic loss can be decreased by optimizing mixing process employing for achievement of desired TI values (4.0-6.0 TI).

Table 1. Vitality level of *Lactobacillus acidophilus* in dark chocolate samples and loss of them during processes.

β_V Crystal Amount	*L. acidophilus* enumaration (log cfu/25 g)	Loss in Probiotic Level (%)
0.00 g/100g (Control)	8.556 ± 0.126 [a]	4.93
0.50 g/100g	7.543 ± 0.034[c]	16.18
0.75 g/100g	7.992 ± 0.131[b]	11.20
1.00 g/100g	7.964 ± 0.099[b]	11.51
1.50 g/100g	8.042 ± 0.187[b]	10.64

Different letters show significant differences between corresponding quality parameters of the sample (*p*<0.05).

3.2. Moisture Content and Water Activity

Water activity can provide information about microbiological, physical and chamical stability of the food products. This crucial parameter is also taken into consideration for controlling of raw materials used in the product and for determining production process effects. Water activity and content of the chocolates are influenced by raw material, specific surface are of the products and temperature levels which applied during refining and conching processes [34, 35]. In addition water activity affects the storage stability of the products especially the fat bloom observed.

As water activity of the dark chocolates including maltitol veried between 0.182-0.212, moisture content was between 0.79 g/100 g – 0.86 g/100 g (Table 2). Generally, chocolate products have water activity lower than 0.40. Also, it is aimed for all chocolate samples with water content lower than 1.5 g/100 g. Chocolates produced with polyols instead of sucrose had lower water activity values [36], which can associated with hydrophilic characteristics of ingredients. In addition, using inulin in chocolate also resulted in decrease in water activity [4].

Regarding β_v seeding technique, remarkable reduction was observed in the chocolates especially for the ones prepared by 1.00 and 1.50 % seeds, no significant differences was found between water content of the samples (*P*<0.05). After proper tempering, fat crystal network is fimly packed in chocolate, which reduces water and fat transportation [37]. The results showed that seeding technique is a good alternative to conventional method for synbiotic dark chocolate production in terms of water activity and moisture content parameters.

Table 2. Rheological parameters, water activity, water content and textural properties of dark chocolate samples.

β_V Crystal Amount	Yield stress (σ_0, Pa)	Plastic viscosity (Pa.s)	a_w	Water content (%)	Hardness (g)
0.00 g/100g	31.20 ± 2.95[a]	3.050 ± 0.341[a]	0.212 ± 0.005[a]	0.81 ± 0.05[a]	8526 ± 796[a]
0.50 g/100g	27.87 ± 2.98[a]	2.724 ± 0.217[ab]	0.212 ± 0.009[a]	0.86 ± 0.02[a]	8665 ± 381[a]
0.75 g/100g	26.49 ± 3.17[a]	2.590 ± 0.198[ab]	0.206 ± 0.004[a]	0.80 ± 0.03[a]	8804 ± 361[a]
1.00 g/100g	26.09 ± 4.21[a]	2.551 ± 0.201[ab]	0.195 ± 0.010[ab]	0.79 ± 0.03[a]	8826 ± 414[a]
1.50 g/100g	24.05 ± 3.76[a]	2.351 ± 0.119[b]	0.182 ± 0.006[b]	0.81 ± 0.05[a]	7594 ± 640[a]

Different letters show significant differences between corresponding quality parameters of the sample (*p*<0.05).

3.3. Textural Properties

Texture is another quality parameter for chocolate and its derivatives, the snap sound formed during breaking of chocolate is related with textural characteristics. Hardness is important textural parameter for chocolate which is equal to the required force necessary for penetrating of probe into chocolate at desired level or for breaking of the sample. Product formulation, production process and parameters affect hardness of the end product [14, 23, 29, 33]. Generally, sugar-free chocolates had lower hardness values when compared with the ones including sucrose [38].

Hardness values of the synbiotic chocolate produced in the study were found to between 7595 g and 8826 g (Table 2). Applied pre-crystalization technique and seeding level did not significantly affect hardness value (*P*>0.05). Fatty acids crystallise as binary or tertnary chain depending on the triglyceride composition and position. β_V crystal form enables ternary closed packaging system; therefore, thermodynamic stability increases [8]. Therefore, there can be relation between hardness and fatty acid composition [39]. In addition, hardness is an important indicator of tempering efficiency and formation of fat crystal network. Hardness value of chocolate depends on crystallization of cacao butter, crystal size and morphology and polymorphic behavior [38]. According to the results, seeding technique can be satisfactorily used in production of synbiotic bitter chocolates including maltitol.

3.4. Rheological Properties

Flow behavior of melted chocolates takes part among main quality parameters. Rheological parameters of chocolate influence designing of production process (temperature level of processes, mixing, transporation, pumping), and removal of water and air during production. Therefore, these quality characteristics direclty affects the quality parameters. Applied shear rate versus shear stress data for chocolate were modelled with Casson (especially), Herschel-Bulkley and Bingham models. Yield stress and plastic viscosity parameters were evaluated for rheological characterization. Importance of rheological parameters in sensory charactersistics and designing of production process is forced to be considered them during the manufacturing of the products with desired quality [4].

Slight but not significantly important decreased was observed in yield stress values of the synbiotic chocolate including maltitol as a result of β_V seed used for pre-crystallization purpose (*P*<0.05). This result can be seed as an advantage for seeding technique since no significant production process change is required. Plastic viscosity values also decreased with increasing β_V seed concentration (Table 2) (*P*<0.05). Texture analysis results are in accordance with rheologica parameters [4]. Deviations of these parameters from suitable ones can be eliminated by increasing PGPR level to decrease yield stress and change in lecithin level for modifying viscosity of samples [23].

3.5. Color Properties

Visual characteristics such as brightness, roughness, turbidity, transparency and color properties can be used for defining of chocolate appearance [39]. The preliminary parameter being associated with the food quality is visual characteristics, mainly color, affect positively or negatively consumer acceptability of the products. Regarding chocolate, color and lightness are the most important quality parameters. For this aim, in the study, brightness (*L**), chroma (*C**), hue angle (*h*°) and whiteness index (WI) values were investigated (Table 3).

Table 3. Color properties of synbiotic dark chocolates.

β_V Crystal Amount	*L**	*C**	*h*°	*WI*
0.00 g/100g	26.9 ± 0.21[b]	7.31 ± 0.25[a]	0.72 ± 0.03[a]	73.4 ± 0.19[a]
0.50 g/100g	27.2 ± 0.13[ab]	7.61 ± 0.10[a]	0.72 ± 0.02[a]	73.2 ± 0.12[ab]
0.75 g/100g	27.2 ± 0.25[ab]	7.28 ± 0.45[a]	0.73 ± 0.05[a]	73.2 ± 0.23[ab]
1.00 g/100g	27.8 ± 0.20[a]	7.33 ± 0.19[a]	0.69 ± 0.01[a]	72.6 ± 0.21[b]
1.50 g/100g	27.2 ± 0.48[ab]	7.65 ± 0.13[a]	0.70 ± 0.01[a]	73.2 ± 0.47[ab]

Different letters show significant differences between corresponding quality parameters of the sample (*p*<0.05).

For all chocolate types, surface brightness positively affected consumer perception [4]. Chocolate brightness increased with seed usage (*P*<0.05); however, concentration is not significantly affect this parameter. Precrystlization technique and seed concentration did not significantly influence *C** and *h°* parameters (*P*>0.05). WI is included in the scope of this study since it is correlated with fat and sugar bloom, main quality defects of chocolate. Conducting precrystallization with seeding technique resulted in reduction of WI values (*P*<0.05). No regular trend was observed between *WI* values and seed concentration; however, using seed at 1.00 g/100 g level is the most suitable level regarding all the color parameters analysed.

Moisture content, pH, ingredients of chocolate as well as tempering process also affect the color parameters [40]. Color of foods gives clues about various factors such as poperties of raw materials, applied production technology, storage conditions and period. Regarding chocolate, color change is generally resulted from variation in formulation and process conditions [38]. Proper tempering of chocolate improves brightness, color and moulding properties of chocolates [40]. The results of the present study implied that employind seeding technique can provide advantage in production of synbiotic dark chocolate including maltitol in terms of color parameters.

3.6. Sensory Properties

Chocolate quality is also determined by subjective evaluaitons such as sensory characteristics in addition to objective analyses such as texture, rheology and color measurements. Chocolate quality can be defined by appearance, taste, texture, last taste perception in mouth and satisfaction level of consumers. Origin, variety, harvesting and processing conditions of cacao as well as chocolate production steps can generate variation in sensory properties of chocolates such as taste, texture and appearance. Preference of conscious/unconscious consumers is based on the sensory characteristics of the products [28, 32]; therefore, it is inevitable part of product development process.

In the present study, sensory evaluation was performed by research and development experts using multiple comparision technique. Sweetness, bitterness, cacao taste, fattiness, particle size, lightness, last taste in mouth, first bite, color, melting in mouth, roughness, texture and appearance properties were scored with high points (Figure). Generally, no significant difference was observed between sensory results for all parameters evaluated (*P*>0.05). Sensory analysis results also indicated that seeding technique can be used as an alternative method in synbiotic dark chocolate production as well as in other quality parameters considered.
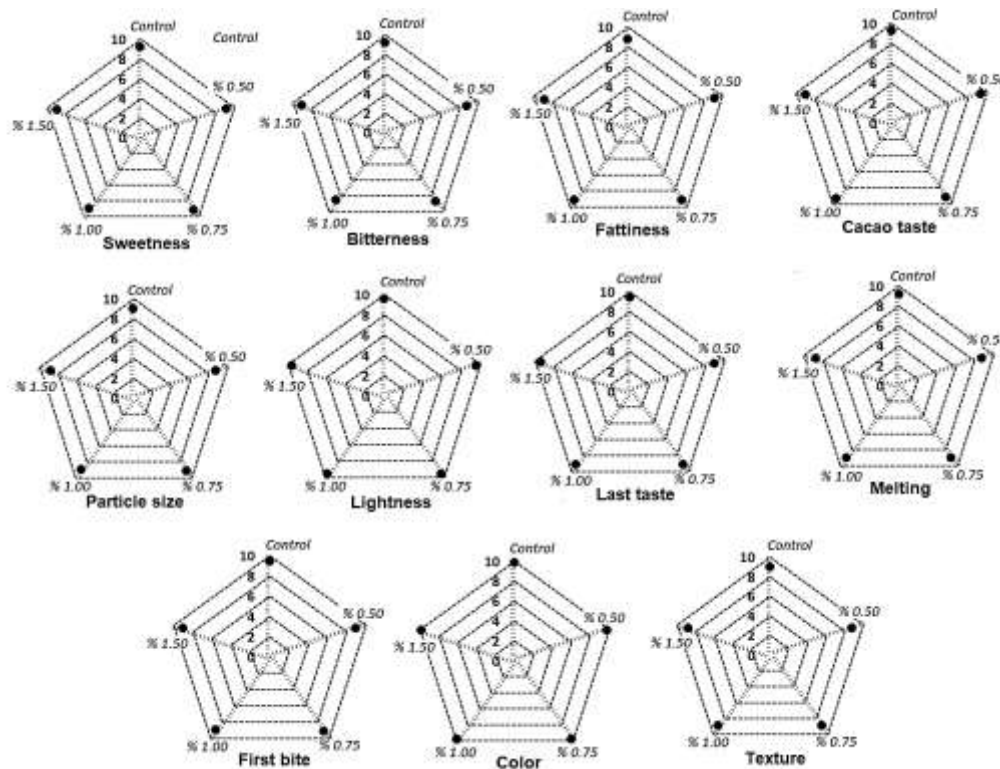
Figure. Sensory properties of synbiotic dark chocolate including βV seeds at different concentrations.

4. CONCLUSIONS

In functional food development studies, the improvement of products having similar quality characteristics with conventional ones is of great importance for consumer acceptance. At the same time, the consumers' expectation is that the bioactive components of these foodstuffs have stability over their shelf life and have the potential to show potential effects, especially those declared by the label. As a result of this study, probiotic and synbiotic chocolate development studies, the effects of the changes tending to process optimization or using alternative technologies on the viability of probiotics have been demonstrated. Although there are no negative changes in quality characteristics, the determination of higher probiotic viability in the products manufactured with conventional tempering may be indicated as a disadvantage for the use of seeding techniques in functional chocolate development studies. However, this effect needs to be examined in different chocolate matrices. In addition, researches aimed at eliminating this disadvantage are particularly important with the optimization

studies carried out in the application of seeding for pre-crystallization process. This is because the use of alternative pre-crystallization techniques has the potential to significantly increase the availability of chocolate production with improved storage stability as well as high efficiency production at low energy costs. Depending on the seeding level, production process (mixing time and rate) should be optimized. The results of the present study also indicated that faster production is possible by using seeding technique, which can provide advantage to the manufacturers.

Acknowledment

REFERENCES

[1]. Belscak-Cvitanovic A., Komes Dujmovic M., Karlovic S., Biskic M., Brncic M. and Jezek D., Physical, bioactive and sensory quality parameters of reduced sugar chocolates formulated with natural sweeteners as sucrose

alternatives, Food Chemistry, 167 (2015) 61-70.

[2]. Olinger P.M., New options for sucrose-free chocolate. The Manufacturing Confectioner, 74(5) (1994) 77–84.

[3]. Sokmen A. and Gunes G., Influence of some bulk sweeteners on rheological properties of chocolate, LWT-Food Science and Technology, 39 (2006) 1053–1058.

[4]. Konar N., Influence of conching temperature and some bulk sweeteners on physical and rheological properties of prebiotic milk chocolate including containing inulin, European Food Research and Technology, 23 (2013) 135-143.

[5]. Konar N., Ozhan B., Artik N. and Poyrazoglu E.S., Using polydextrose as a prebiotic substance in milk chocolate-Effects of process parameters on physical and rheological properties, CyTA Journal of Food, 12-2 (2014) 150-159.

[6]. Konar N., Ozhan B., Artik N., Dalabasmaz S. and Poyrazoglu E.S., Rheological and physical properties of ınulin-containing milk chocolate prepared at different process conditions. CyTA Journal of Food, 12-1 (2014) 55-64.

[7]. Melo L.L.M.M., Bolini H.M.A. and Efraim P., Storage time study of sugar-free and reduced calorie milk chocolates. Department of Food and Nutrition FEA, UNICAM Campinas, Brazil, CEP (2008) 13083-130862.

[8]. Afoakwa E.O., Paterson A. and M. Fowler M., Factors influcing rhelogical and textural qulities in chocolate- a review, Trend in Food Science and Technology, 18 (2007) 290-298.

[9]. Dhonsi, D. and Stapley A.G.F., The effect of shear rate, temperature, sugar and emulsifier on the tempering of cocoa butter, Journal of Food Engineering, 77 (2006) 936-942.

[10]. Glicerina V., Balestra F., Rosa M.D. and Romani S., Rheological, textural and calorimetric modifications of dark chocolate during process, Journal of Food Engineering, 119-1 (2013) 173-179.

[11]. Afoakwa E.O., Paterson A., Fowler, M. And Vieira J., Particle size distribution and compositional effects on textural properties and appearance of dark chocolates, Journal of Food Engineering, 87 (2008) 181-190.

[12]. Dahlenborg H., Millqvist-Fureby A. and Bergenstahl B. Effect of shell microstructure on oil migration and fat bloom development in model pralines, Food Structure, 5 (2015) 51-65.

[13]. Debaste F., Kegelaers Y., Liegeois S., Ben Amor H. and Halloin V., Contribution to the modeling of chocolate tempering process, Journal of Food Engineering, 88 (2008) 568-575.

[14]. Afoakwa E.O., Paterson A., Fowler M. and Vieira J., Effects of tempering and fat crystallization behaviour on microstructure, mechanical properties and appearance in dark chocolate systems, Journal of Food Engineering, 89 (2008) 128-136.

[15]. Bolliger S., Breitschun B., Stranzinger M., Wagner T. and Windhab E.J., Comprasion of precrystallization of chocolate, Journal of Food Engineering, 35 (1998) 281-297.

[16]. Konar N., Toker O.S., Oba S. and Sagdic O., Improving functionality of chocolate: A review on probiotic, prebiotic, and/or synbiotic characteristics, Trends in Food Science & Technology, 49 (2016) 35-44.

[17]. Maillard M. and Landuyt A., Chocolate: an ideal carrier for probiotics. Agro Food Industry Hi-Tec, 19-3 Suppl. (2008) 13–15.

[18]. Coman M.M., Cecchini C., Verdenelli M.C., Silvi S., Orpianesi C. and Cresci A., Functional foods as carriers for SYNBIO, a probiotic bacteria combination, International Journal of Food Microbiology, 157 (2012) 346-352.

[19]. Erdem O., Gultekin-Ozguven M., Berktas I., Ersan S., Tuna H.E., Karadag A., Ozcelik B., Gunes G. and Cutting S.M., Development of a novel synbiotic dark chocolate enriched with Bacillus indicus HU36, maltodextrin and lemon fiber: Optimization by response surface methodology, LWT – Food Science and Technology, 56 (2014) 187-193.

[20]. Champagne C.P., Raymond Y., Guertin N. and Belanger G., Effects of storage conditions, microencapsulation and inclusion in chocolate particles on the stability of

probiotic bacteria in ice cream, International Dairy Journal, 47 (2015) 109-117.

[21].Lalicic-Petronijevic J., Popov-Raljic J., Obradovic D., Radulovic Z., Paunovic D., Petrusic M. and Pezo L., Viability of probiotic strains *Lactobacillus acidophilus* NCFM[®] and *Bifidobacterium lactis* HN019 and their impact on sensory and rheological properties of milk and dark chocolates during storage for 190 days, Journal of Functional Foods, 15 (2015) 541-550.

[22].Raymond Y. and Champagne C.P., The use of flow cytometry to accurately ascertain total and viable counts of *Lactobacillus rhamnosus* in chocolate, Food Microbiology, 46 (2015) 176-183.

[23].Konar N., Palabiyik I., Toker O.S., Genc Polat D., Sener S., Akcicek A. and Sagdic O., Effect of Inulin DP on various properties of sugar-free dark chocolates containing *Lactobacillus paracasei* and *Lactobacillus acidophilus*. International Journal of Food Engineering, doi: 10.1515/ijfe-2017-0045 (2017).

[24].Beckett S.T. The science of chocolate (2nd Ed.) London, Cambridge, UK: Royal Society of Chemistry (2008).

[25].Toker O.S., Sagdic O., Konar N., Zorlucan T. and Dağlıoğlu O., Some physicochemical, rheological and melting properties and volatile compound profile of compound chocolate and cocolin samples: Effect of particle size, European Food Research and Technogy, 242-8 (2016) 1253-1266.

[26].Lonchampt P. and Hartel R.W., Surface bloom on improperly tempered chocolate, European Journal of Lipid Science and Technology, 108-2 (2006) 159-168.

[27].Periche A., Heredia A., Escriche I., Andrés A. and Castelló M.L., Potential use of isomaltulose to produce healthier marshmallows, LWT - Food Science and Technology, 62 (2015) 605-612.

[28].Shah A.S., Jones G.P. and Vasiljevic T., Sucrose-free chocolate sweetened with Stevia rebaudiana extract and containing different bulking agents effects on physicochemical and sensory properties, International Journal of Food Science and Technology, 45 (2010) 1426-1435.

[29].Beckett S.T. Industrial chocolate manufacture and use, (3rd Ed.). Blackwell, Oxford, 1999.

[30].Ziegler G. and Hogg R., Particle size reduction, In: Industrial chocolate manufacture and use, Beckett ST. (Ed.), Chapman § Hall, New York, USA, (1999) 182-199.

[31].Maragkoudakis P.A., Miaris C., Rojez P., Manalis N., Magkanari F. and Kalantzopoulos G., Production of traditional Greek yoghurt using *Lactobacillus* strains with probiotic potential as starter adjuncts, International Dairy Journal, 16 (2006) 52-60.

[32].Zaric D.B., Bulatovic M.L.J., Rakin M.B., Krunic T.Z., Loncarevic I.S. and Pajin B.S., Functional, rheological and sensory properties of probiotic milk chocolate produced in a ball mill, RSC Advances, 6 (2016) 13934-13941.

[33].Konar N., Oba S., Toker O.S., Palabiyik I., Goktas H., Artik N. and Sagdic O., Rapid tempering of sucrose-free milk chocolates by β_V seeding: textural, rheological and melting properties, European Food Research and Technology, 243 (2017) 1849-1860.

[34].Vercet A. 2003. Browning of white chocolate during storage, Food Chemistry, 81 (2003) 371-377.

[35]. Rossini, K., Norena C.P.Z. and Brandelli A., Changes in the colour of white chocolate during storage: potential roles of lipid oxidation and non-enzymatic browning reactions, Journal of Food Science and Technology, 48-3 (2011) 305–311.

[36].Shadwell, N., Villalobos F., Kern M. and Hong M.Y., Blooming reduces the antioxidant capacity of dark chocolate in rats without lowering its capacity to improve lipid profiles, Nutrition Research, 33 (2013) 414-421.

[37].Afoakwa, E.O., Paterson A., Fowler M. and Vieira J., Microstructure and mechanical properties related to particle size distribution and composition in dark chocolate, International Journal of Food Science and Technology, 44-1 (2009) 111–119.

[38].Aidoo R.P., Afoakwa E.O. and Dewettinck K., Rheological properties, melting

behaviours and physical quality characteristics of sugar-free chocolates processed using inulin/polydextrose bulking mixtures sweetened with stevia and thaumatin extracts, LWT - Food Science and Technology, 62 (2015) 592-597.

[39].Aidoo R.P., De Clerq N., Afoakwa E.O. and Dewettinck K., Industrial manufacture of sugar-free chocolates- applicability of alternative sweeteners and carbohydrate polymers as raw materials in product development, Trends in Food Science and Technology, 32 (2013) 84-96.

[40].Lindecrantz A. Investigation of seedpowder technology for pre-crystallization processing for dark chocolate- Effect on fat crystal structure and storage stability. Master of Science Thesis in the Master Degree Program Biotechnology, Chalmers University of Technology, Gothenburg, Sweden, 2014.

A Geographical Information System (GIS) Based Traceability System Suggestion for a Pastry Firm Operating Nationwide

Evren GÖLGE[1*] iD *, Tarık TÜRK*[2] iD

¹Sivas Cumhuriyet University, Food Engineering Department, Sivas, TURKEY

²Sivas Cumhuriyet University, Engineering Faculty, Geomatics Engineering Department, Sivas, TURKEY

Abstract. Logistics and traceability are important issues for big scale firms. Traceability is primarily viewed as a tool for the food safety by providing a mean for recall as well as proof for the authenticity of food, but it is also related to food quality. Maintaining the cold chain not only effecting the customer's preference and satisfaction but also the profitability, production and logistic costs for big scale firms especially producing perishable food products. Recently, the trend of utilizing GIS based traceability systems is increasing, which facilitates to minimize the production and distribution of unsafe and low quality food products. This paper presents a GIS based system enabling network analysis, which might be efficiently and effectively used in the firms operating in ready-to-eat pastry sector, intended to be used for full-automation through all the stages from production to retail was developed and a partial application was performed.

Keywords: GIS, Traceability, Food Safety.

Ulusal Çapta Faaliyet Gösteren Tatlı Firması için Coğrafi Bilgi Sistemi (CBS) Tabanlı İzleme Sistemi Önerisi

Özet. Lojistik ve izlenebilirlik büyük ölçekli firmalar için önemli konulardır. İzlenebilirlik öncelikle gıda güvenliği için gıdaların orijinalliğini ispatlamanın yanı sıra geri çağırma olanaklarını da sağlayan bir araç olarak görülmekle birlikte gıda kalitesiyle de doğrudan ilgilidir. Soğuk zincir sadece müşterilerin tercih ve memnuniyetini etkilemekle kalmayıp özellikle bozulabilir gıda ürünleri üreten büyük ölçekli firmaların kârlılık, üretim ve lojistik giderlerini de etkilemektedir. Son zamanlarda, CBS tabanlı izlenebilirlik sistemlerini kullanma eğilimi giderek artmakta ve bu da düşük kaliteli gıda ürünlerinin üretimini ve dağıtımını en aza indirmeyi kolaylaştırmaktadır. Bu çalışmada, üretimden perakendeye kadar tüm aşamalarda tam otomasyona yönelik hazır pasta ve tatlı sektöründe faaliyet gösteren firmalarda etkili ve etkin bir şekilde kullanılabilecek ağ analizinin kullanıldığı CBS tabanlı bir sistem geliştirilerek kısmi bir uygulama yapılmıştır.

Anahtar Kelimeler: CBS, İzlenebilirlik, Gıda Güvenliği.

1. INTRODUCTION

Food products require cautious and strategic handling procedures because they have a short life span. Food-borne illnesses and microbiological contamination can easily occur if food is improperly handled during production, storage, or distribution. The food industry is continuously susceptible to the outbreak of illnesses such as *Salmonella*, *Campylobacter* and *Escherichia coli* O157:H7, etc. Outbreaks focus consumer concern on the safety and quality of food [1, 2].

In national and international food companies and the global food trade, food chain integrity concerns

safety as well as origin fraud and quality concerns. It appears to be a great problem for many firms to ensure the integrity of the cold chain as well as address customer preferences and satisfaction in addition to profitability, production, and logistic costs, especially for perishable food products managed by large companies. Consumers demand verifiable evidence of traceability to ensure food quality and safety. To respond to these demands, a traceability system is needed that provides information on the origin, processing, retailing, and final destination of foodstuffs.

In general terms, quality can be defined as "conformance to requirement" or "fitness for use or consumption". According to the ISO definition, "quality is the totality of features and characteristics of a product that bear on its ability to satisfy stated or implied needs" [3]. However, food quality is very general, implying that expectations of individual consumers may differ dramatically. Quality includes attributes that influence a product's value to the consumer. A product can appear to be of high quality (i.e. well-coloured, appetizing, and flavourful, etc.), but it can be unsafe because of undetected pathogenic organisms, toxic chemicals, or physical hazards [4]. The CAC (2003) defines food safety as an assurance that food will not cause harm to the consumer when it is prepared and/or eaten according to its intended use [5]. Food safety refers to all hazards, whether chronic or acute, that may make food injurious to the health of the consumer. It is a non-negotiable, global issue affecting billions of people who suffer from diseases caused by contaminated food. In ensuring food safety, Hazard Assurance Critical Control Point (HACCP) is regarded as the best method. In addition, it is the best way to demonstrate commitment to food safety [6].

Effective logistics management requires delivering the right product, in the right quantity, in the right condition, to the right place, at the right time, and for the right cost [7]. Logistics greatly affect profit, price, and the consumer satisfaction, so logistics management is important to the success of food producers [8]. In the process of improving logistics, detailed location analysis (mapping and clustering of raw material suppliers, production and retail sites, etc.) and route analysis (creating optimal routes for product collection and distribution, simulating route distance and delivery time) are essential.

According to ISO 9000 (2005) standards, traceability is defined as: "the ability to trace the history, application or location of that which is under consideration". ISO guidelines further specify that traceability may refer to the origin of materials and parts, the processing history, or the distribution and location of the product after delivery. The European Union (EU) regulation 178/2002 [9] narrows the definition to the food industry by defining traceability as the ability to trace and follow a food, feed, food-producing animal or substance intended to be, or expected to be incorporated into a food or feed, through all stages of production, processing, and distribution. The Codex Alimentarious Commission [5] defines a more concise definition of traceability as the ability to follow the movement of a food through specified stages of production, processing, and distribution.

According to Golan et al. (2004) the three main objectives of food traceability systems are 1) to improve supply management, 2) to facilitate back-tracing for food safety and quality, and 3) to differentiate and market foods with subtle or undetectable quality attributes [10]. The benefits of these objectives appear as lower-cost distribution systems, reduced recall expenses, and expanded sales of products with attributes that are difficult to discern. It was also suggested that an efficient traceability system should be characterized by breadth (i.e. the amount of information collected), time depth (i.e. tracking information forward and backward in time) and precision (i.e. degree of assurance to pinpoint a particular movement of a food product in order to evaluate costs and benefits).

Consumers are increasingly concerned about food safety and the properties of the food they buy and eat. It has been recognized that there is an increasing need for transparent information on the

quality of the entire food chain supported by modern tracing methods [11, 12]. Moe (1998) mentioned that traceability is an essential subsystem of quality management [13]. A well-developed internal traceability system would improve data collection efficiency, production flow control, and quality assurance.

Geographical Information Systems (GIS) are information systems that can integrate geographical data during data acquisition, storage, processing, inquiry, analysis, and certification steps. It is used in many areas including the food sector [14-18].

This study's objective is to propose a GIS-based control system for efficient and safe product transportation for ready-to-eat desserts in Turkey.

For this reason, a nationwide firm that excels in various milk and dough desserts was selected as a case study.

2. MATERIALS AND METHODS

The national company STP Gıda A.Ş. has been chosen for the proposed GIS based system in this study. It has four production facilities (two in İstanbul, one in İzmir and one in Ankara) and 190 retail outlets [19]. The total number of outlets and their locations are presented in Table 1. The firm has the most outlets in the Marmara and Aegean regions and the fewest in the Eastern and South Eastern Anatolia regions. This is quite understandable because the company is based in the Aegean region, which is also where its highest-capacity production facility is located.

Table 1. The location of the firm's subsidiaries.

Region	Provinces and the number of the retail outlets									of retail outlets	Percent
Marmara	Bursa	Çanakkale	İstanbul	Kırklareli	Kocaeli	Tekirdağ					
	5	2	48	1	3	2				61	32,1
Aegean	Afyon	Aydın	Balıkesir	Denizli	İzmir	Manisa	Muğla	Uşak			
	2	5	3	3	28	1	4	1		47	24,7
Central Anatolia	Aksaray	Ankara	Eskişehir	Kayseri	Kırıkkale	Kırşehir	Konya	Niğde	Sivas		
	1	13	1	3	1	1	3	1	1	25	13,2
Mediterranean	Adana	Antakya	Antalya	Isparta	Mersin	Osmaniye					
	3	1	9	2	2	1	18			36	18,9
Black Sea	Bolu	Düzce	Ordu	Samsun	Sinop	Tokat	Trabzon	Zonguldak			
	1	1	1	4	1	1	1	2		12	6,3
South Eastern Anatolia	Batman	Diyarbakır	Gaziantep	Mardin	Şanlıurfa						
	1	1	1	1	1					5	2,6
Eastern Anatolia	Elazığ	Erzurum	Malatya	Van							
	1	1	1	1						4	2,1
										190	100

The whole range of products produced by the firm both milk and dough type of desserts have been selected as the material of the study. The product names are listed in Fig. 1 under the title "Product Sell Number". Milk desserts constitute the great portion of the products of the firm. Apparently, milk products are perishable type of foods. Parallel to the scope of this study, these type of products must be swiftly transported to subsidiaries and customers following their production. From this point of view the strategies in the process of product delivery followed by the firm are strictly critical for the profitability and hence implicating a great risk.

In creation of the proposed GIS based system, the first step was the random formation of the retail

data of each 190 retail outlets of the firm. The daily retail data for each product in each retail outlet of the firm was randomly formed between 1 to 100 retails daily for 365 days through three consecutive years (2013-2015) by random data generation function of the Excel programme in Microsoft Office Professional Plus.

A GIS based system was established considering all the steps in the transportation of each of the products produced by the firm. In this system both geographical and non-geographical data exist. While creating the system, the firm's product tree were formed first. Then, the geographical locations of the subsidiaries were transferred the created system by detecting on the satellite view and on the map considering the data exist on the website of the

firm. Turkey's transportation web and province border data was used as exist geographical data (Fig. 1).

On the other hand, a database including the parameters for the retail of the products of the firm and the cold chain was designed (Fig. 1). This database was integrated in ArcGIS10.1 GIS software environment. Besides a user-interface program was developed to facilitate the interaction between the software and the user that enables the utilization of the software without requiring software background [20, 21]. In result, the user can reach and query the desired data for all the production facilities and subsidiaries of the firm in which retail process occur (Fig. 1 and Fig. 2).
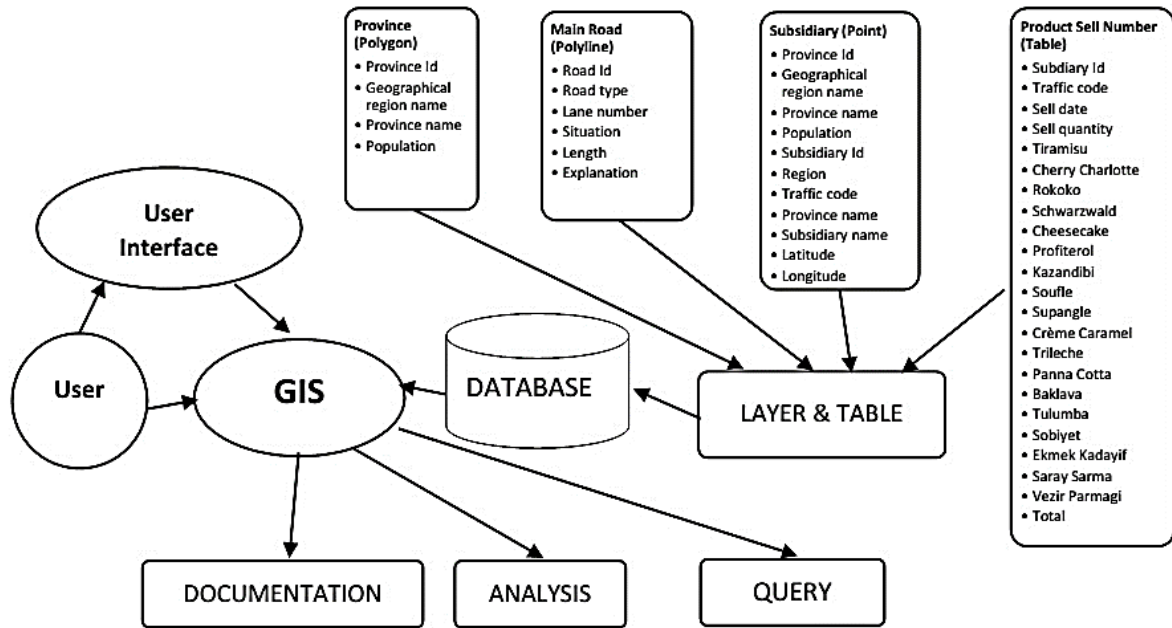
Figure 1. Schematic description of the created system.
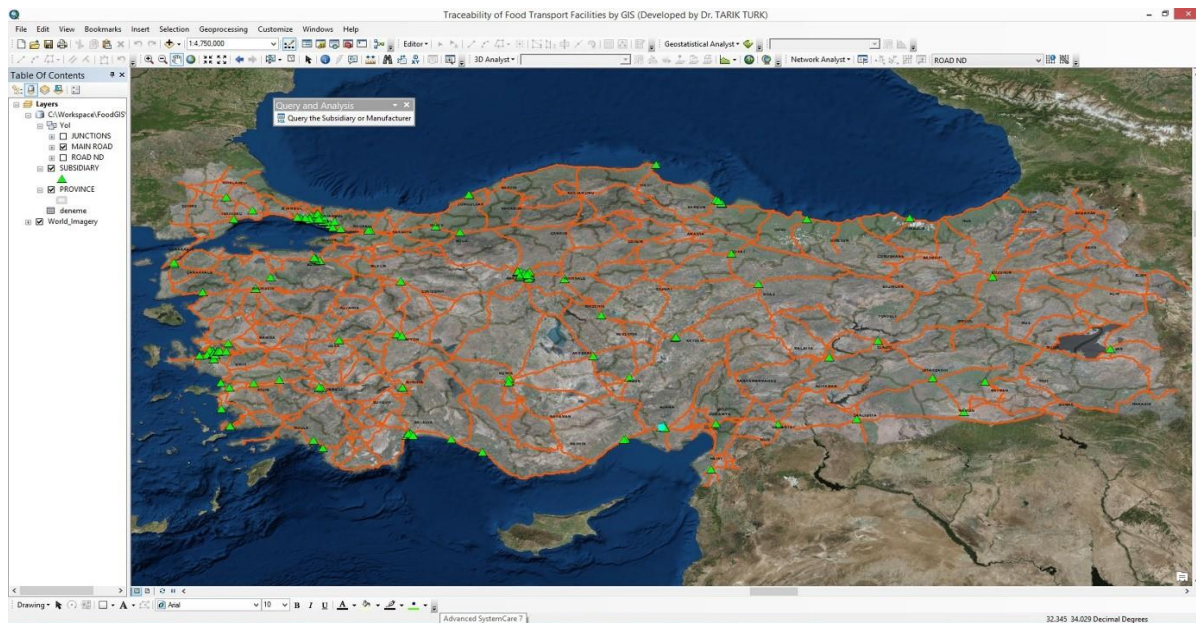
Figure 2. General view of the created system and user interface program developed on ArcGIS Software environment.

3. RESULTS AND DISCUSSION

In this study, a GIS based system established aiming to maintain full automation of the operations from production stage to retail stage in subsidiaries of a selected nationwide operating model firm in ready-to-eat pastry sector in Turkey. The capability of the established system was as follows:

- Monitoring by a GIS based system,
- Accessing the geographical location and the detailed information of the production sites and the subsidiaries of the firm (Fig . 2 and 3),
- Requirement of the new production sites or subsidiaries in the strategic planning of the firm, and if necessary with the help of geographical analysis (Buffer Analysis, Density Analysis, Clustering Analysis, Network Analysis etc.) the determination of the geographical location of the new production site to be installed,
- Determination of retail statistics of any product type produced by the firm with respect to subsidiaries and profitability of any subsidiary with one click (Fig. 3),
- Selection of the production site for any random subsidiary to be supplied from (Fig. 4)

The difference and originality of the system proposed in this paper from similar previous systems could be listed as many operations executed by the firm are GIS based and performed with the help of the user interface program developed in the frame of this study [14, 22]. Besides the retail statistics of the firm's products can be obtained with one click through the created system (Fig. 3). In addition a wide perspective was presented for the profitability of the firms operating in this sector by performing Network Analysis applications in a GIS based system.

As the firm is operating nationwide, the 4 production facilities and 190 subsidiaries have been dispersed all over Turkey. The locations of each 4 production facilities and each 190 subsidiaries have been shown on the map of the created system using ArcGIS10.1 software (Fig. 2). With the help of these programs not only the statistical data on the product retail of the firm but also the geographical locations of the subsidiaries on the map could be selected and all the data on the selected subsidiary is obtainable with one click (Fig. 3).

In this paper it is not possible to present most of the query and geographical analysis that could be accessed provided by the system. For this reason some of these were presented in the following scenarios.

Scenario 1

In this scenario, all the retail information of the selected product type "Tiramisu" for the subsidiary selected "Adana Real" can be queried on day, month and annual basis with one click by the user interface program developed (Fig. 3).
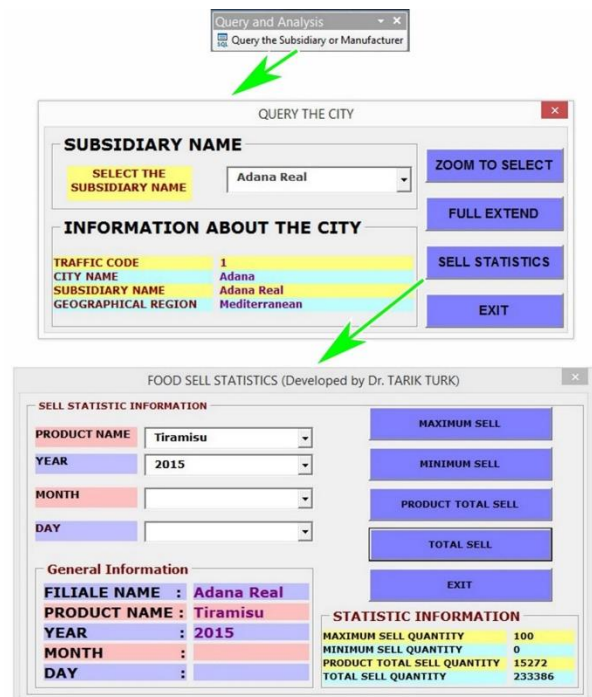
Figure 3. The user interface programs developed.

Figure 4. Route map according to the subsidiaries and production places.

Alongside the optimum route determination, regarding to the position of the subsidiary and the effective utilization of the sources, the address matching and resource allocation and similar applications of network analysis the production, retail and logistic activities of the firm can be executed swiftly, effectively and efficiently. In addition, with the help of buffer analysis or network service area analysis the location of the newly formed production sites could be determined by the established GIS based system.

4. CONCLUSIONS

A GIS based system, which might be efficiently and effectively used in the firms operating in ready-to-eat pastry sector, intended to be used for full-automation through all the processes from production stage to retail stage was developed and a partial application was performed within the scope of this study. Thus, all the activities of the firm was stored in a geographical database and all kind of information is instantly reachable by inquiry. Furthermore, differing from the classical database in addition to geographical analysis operations, the implemented system can answer geographical based questions such as, considering the costs from which present production site the

product must be transported to the retail subsidiaries as well as the determination and optimization of the geographical site of the potently established production sites. By this means the implemented system have a potential to increase the profit of the firms and facilitates the delicate products of the ready-to-eat pastry sector be transported safely to consumers situated far away.

Product-tracing systems are essential for food safety and quality control. Traceability systems help firms isolate the source and extent of safety or quality control problems. The more precise the tracing system, the faster a producer can identify and resolve food safety or quality problems. Quality and safety are both linked to traceability whereas safety is implicated by traceability more often.

Traceability is primarily viewed as a tool for the food safety by providing a means for recall as well as proof for the authenticity of food, but it is also related to food quality. Since both quality and safety were shown to be related to confidence, traceability may indeed boost consumer confidence through quality and safety assessments.

Cold chain is a critical issue for food sector. It has direct and indirect effects on human health, company profitability, etc. In the present study the system was designed both considering the production and expiry date and time of the product. As if the production and expiry data for each product would have been entered into the database and the vehicle tracking and navigation systems would have been integrated with the system established, the process from production stage to final user could be easily tracked on real-time basis.

On the other hand, different from the other systems presented in literature, when the desired retail prices of the products are set to the established system, the retail revenues of each individual subsidiary could be calculated on daily, monthly and annual basis for each different product type.

In result GIS based control systems certainly help a food firm especially operating with perishable products in resource allocation, route optimization, product traceability, etc. As the technology develops with the use of sophisticated sensors (e.g. RFID technology, nanosensors), the control parameters of the food product will increase which directly effects the level of real-time monitoring and efficiency of the GIS control systems. Thus, food safety management will be promoted and gain much more flexibility and accuracy.

Acknowledgements

REFERENCES

[1] Bertolini M., Bevilacqua M., Massini R. Approach To Product Traceability In The Food Industry. Food Control, 17 (2006) 137-145.

[2] Trienekens J., Zuurbier P. Quality And Safety Standards In The Food Industry, Developments And Challenges. International Journal Of Production Economics, 113-1 (2008) 107-122.

[3] Guidelines for quality management in soil and plant laboratories. Address: http://www.fao.org/3/W7295E/W7295E00.htm. Retrieved July 2, 2017.

[4] Safety and quality of fresh fruit and vegetables: A training manual for trainers. United Nations. Address: https://unctad.org/en/docs/ditccom200616_en.pdf. Retrieved July 24, 2017.

[5] Codex Alimentarius Commission. Basic Texts On Food Hygiene. Address: http://www.fao.org/docrep/012/a1552e/a1552e00.htm. Retrieved September 25, 2017.

[6] International Organization for Standardization. ISO 22000 Food Safety Management. Address: https://www.iso.org/obp/ui/#iso:std:iso:22000:ed-2:v1:en. Retrieved September 25, 2017.

[7] Aghazadeh, S. Improving Logistics Operations Across The Food Industry Supply Chain. International Journal of Contemporary Hospitality Management, 16-4 (2004) 263-268.

[8] Brimer R.C. Logistics Networking: A Consideration Of The Components Essential To An Integrated Logistics Support Network. Logistics Information Management 8-4 (1995) 8-11.

[9] EU. Regulation (EC) No 178/2002 Of The European Parliament And Of The Council. Address: https://www.ecolex.org/details/legislation/regulation-ec-no-1782002-of-the-european-parliament-and-of-the-council-laying-down-the-general-principles-and-requirements-of-food-law-establishing-the-european-food-safety-authority-and-laying-down-procedures-in-matters-of-food-safety-lex-faoc034771/. Retrieved September 25, 2017.

[10] Golan E., Krissoff B., Kuchler F., Calvin L., Nelson K., Price G. Traceability In The U.S. Food Supply: Economic Theory And Industrial Studies. Agricultural Economic Report. Address: https://ageconsearch.umn.edu/bitstream/33939/1/ae040830.pdf. Retrieved September 20, 2017.

[11] Beulens A.J. M., Broens D.F., Folstar P., & Hofstede, G. J. Food Safety And

Transparency In Food Chains And Networks. Food Control, 16-6 (2005) 481-486.

[12] Rijswijk W.V., Frewer L.J. How Consumers Link Traceability To Food Quality And Safety: An International Investigation. Address: http://ageconsearch.umn.edu/bitstream/10061/1/sp06va02.pdf. Retrieved September 22, 2017.

[13] Moe T. Perspectives On Traceability In Food Manufacture. Trends In Food Science & Technology, 9-5 (1998) 211-214.

[14] Bosona T., Gebresenbet G. Cluster Building And Logistics Network Integration Of Local Food Supply Chain. Biosystems Engineering, 108 (2011) 293-302.

[15] Bosona T., Gebresenbet G. Food Traceability As An Integral Part Of Logistics Management In Food And Agricultural Supply Chain. Food Control, 33 (2013) 32-48.

[16] Eckert J., Shetty S. Food Systems, Planning and Quantifying Access: Using GIS To Plan For Food Retail. Applied Geography, 31 (2011) 1216-1223.

[17] Mcmeekin T.A., Baranyi J., Bowman J., Dalgaard P., Kirk M., Ross T., Schmid S., Zwietering, M.H. Information Systems In Food Safety Management. International Journal Of Food Microbiology, 112 (2006) 181–194.

[18] Suprem A., Mahalik N., Kim K. A Review On Application Of Technology Systems, Standards And Interfaces For Agriculture And Food Sector. Computer Standards & Interfaces, 35 (2013) 355–364.

[19] Özsüt Company Website. Address: http://en.ozsut.com.tr/. Retrieved September 1, 2015.

[20] Turk T., Gumusay U., Tatar O. Creating Infrastructure For Seismic Microzonation By Geographical Information Systems (GIS): A Case Study In The North Anatolian Fault Zone (NAFZ). Computers & Geosciences, 43 (2012) 167–176.

[21] Turk T. Investigating Health Studies Using Geographical Information Systems: Cancer Case Study. Polish Journal Of Environmental Studies, 22-5 (2013) 1505-1517.

[22] Hashemi Beni L., Villeneuve S., Leblanc D.I., Côté K., Fazil A., Otten A., Mckellar R., Delaquis P. Spatio-Temporal Assessment Of Food Safety Risks In Canadian Food Distribution Systems Using GIS. Spatial And Spatio-Temporal Epidemiology, 3 (2012) 215–223.

Selecting Smart Strategies Based on Big Data Techniques and SPACE Matrix (FASE model)

Mohammad Ali FARAJIAN[1], Shahriar MOHAMMADI[2], Bahram Sadeghi BIGHAM[3] *,
Farhad SHAMS*

[1]*Department of Computer Science and Information Technology, Institute for Advanced Studies in Basic Sciences
(IASBS), Zanjan, IRAN*

[2]*K.N.Toosi University of Technology, Faculty of Industrial Engineering, Tehran, IRAN*

[3]*Associate Professor of Computer Science and Information Technology, Institute for Advanced Studies in Basic
Sciences (IASBS), Zanjan, IRAN*

Abstract. One of the most important questions for managers of corporations is how they select a smart strategy for their corporations. To answer this question, Managers should consider some dimensions witch impact on the future of the corporation, and then they select a suitable strategy for their corporations. This paper presents a novel model (FASE model) for evaluating strategic position and choosing smart strategy based on Big Data techniques and SPACE matrix. In order to achieve the best position in the market, FASE model facilitates selecting the best strategy among: aggressive, conservative, defensive, and competitive strategies. FASE model consists of three main processes namely Fuzzy-Cmeans, Apriori association rule inducer, SPACE matrix. Fuzzy-Cmeans algorithm is used for clustering customers based on RFM values and behavioral scoring. The results of the clustering were then profiled on customers' attributes using Apriori association rule inducer. A SPACE matrix was used to evaluate the strategic position and to choose smart strategy. To get a better understanding of the FASE model, the banking case has been selected and FASE model is applied over that.

*Keywords***:** Big Data, smart strategy, Fuzzy-Cmeans, Apriori algorithm, SPACE matrix.

Big Data ve SPACE Matris Yöntemlerine Dayalı Akıllı Stratejiler Belirlenmesi (FASE Model)

Özet. Şirket yöneticileri için en önemli sorulardan biri, şirketleri için akıllı bir stratejiyi nasıl seçtikleridir. Bu soruyu cevaplamak için yöneticiler, kurumun geleceği üzerinde etkisi olan bazı boyutları göz önünde bulundurmalı ve ardından şirketleri için uygun bir strateji seçmelidir. Bu makale, stratejik pozisyonu değerlendirmek ve Büyük Veri teknikleri ve UZAY matrisini temel alan akıllı bir strateji seçmek için yeni bir model (FASE modeli) sunmaktadır. Piyasadaki en iyi pozisyonu elde etmek için FASE modeli, en iyi stratejiyi seçmeyi kolaylaştırır: saldırgan, muhafazakâr, savunmacı ve rekabetçi stratejiler. FASE modeli, Fuzzy-Cmeans, Apriori birlik kural uyarıcısı, UZAY matrisi olmak üzere üç ana işlemden oluşur. Fuzzy-Cmeans algoritması, müşterileri RFM değerlerine ve davranışsal puanlamaya dayalı olarak kümelemek için kullanılır. Kümelenmenin sonuçları daha sonra Apriori birlik kural uyarıcısı kullanılarak müşterilerin özelliklerine göre şekillendirilir. Stratejik pozisyonu değerlendirmek ve akıllı bir strateji seçmek için UZAY matrisi kullanılır. FASE modelini daha iyi anlamak için, bir bankacılık vakası seçildi ve bunun üzerine FASE modeli uygulandı.

*Anahtar Kelimeler***:** Büyük veri, akıllı strateji, Fuzzy-Cmeans, Apriori algoritması, UZAY matrisi.

1. INTRODUCTION

The concept of competition is vital and decisive for corporations that offer goods and services to customers in the oligopoly market. Any competitive corporation that has perfect connectivity with its market has to choose favorable competitive strategy to attain sustainable competitive position in the market. Competitive strategy can be understood as the collection of decisions and actions strategic managements undertake to lead corporations to gain a sustainable competitive advantage in a particular industry [1]. Many techniques and tools were developed for strategic management, e.g. Chen et al proposed analytical SWOT method that used strength, weakness, opportunity, and threats dimensions [2], Kangas et al. have used AHP technique to SWOT analysis [3], Paiva et al proposed a framework of manufacturing strategy process from a resource-based view [4], Yüksel and Dagdeviren utilized ANP to SWOT analysis to solve complex problems [5]. Aslan et al proposed SWOT can be applied to create TOWS (Threats-Opportunities-Weaknesses-Strengths) matrix in order to deploy strategies [6], A PEST analysis political, economic, social and technological dimensions [7], PESTLE model classifies issues as political, economic, social, Technological, legal and environmental [8], Zalengera et al implement PESTLE analysis for sustainable development of renewable energy [9]. All of the mentioned models should identify various dimensions that impact on strategic management. Due to the fact that identifying various dimensions that impact on corporation's strategy is so challenging, selecting favorable competitive strategy is very difficult for managers. As competitive conditions grow ever more turbulent, the importance of developing and using Big Data techniques appears to be increasing exponentially. The most important question for firm managers is that how they can make a connection between the Big Data technique and strategy. This paper presents a novel model for evaluating strategic position and choosing smart strategy (ESP&CSS) based on Big Data techniques and SPACE matrix. The proposed model has two main parts: Big Data techniques and SPACE matrix.

In this decade, Big Data technology has not only a great popularity in the research area but also in business world. This technology supports manager for A better understanding of business environment. Big Data technology can help corporations to demystify meaningful trends, patterns, relationships and correlations in their customers' behavior, products, services, and data. It also can support managers to evaluate strategic position and then selecting favorable competitive strategy. The Big Data techniques include classification, clustering, Sentiment analysis, association rules, Social network analysis, regression analysis, rule-based reasoning approach, genetic algorithms, decision trees, etc. The proposed model gets benefit from the advantages of Fuzzy-Cmeans algorithm and Association rules method.

There are many methods for developing organizational strategies that were formed based on the matrixes. For instant the strength, weakness, opportunity, and threats (SWOT) matrix or Boston Consulting Group (BCG) method that is a portfolio planning model, GE Matrix that is an extension of the BCG-matrix, or Growth-share matrix which involves portfolio decisions about priority and resources [10, 11, 12]. The Strategic Position & Action Evaluation (SPACE) matrix [13] is one of the most popular methods that can be considered as a supportive dimension in strategies development trend because of its speed in finding the competitive position of an corporation to determine what type of a strategy it should undertake. The proposed model uses Fuzzy-Cmeans algorithm, Association rules method, and SPACE matrix that is called FASE model.

To gain a better understanding of FASE model, this study is organized as follows. Section 2 explains the proposed novel model that is an integrated Big Data techniques and SPACE matrix. Section3 exhibits four processes of FASE model: first,

explains how to make a preprocessing on data and after that how to extract RFM values and CBT value, Second, gives a thorough illustration of Fuzzy-Cmeans as a tool for clustering the customer using CBT value and RFM scoring variables, third, presents processes of creating cluster profiles using Apriori association rule inducer, fourth, explicates processes of evaluating strategic position and choosing smart strategy using SPASE matrix. Finally, conclusions are made in section 4.

2. RESEARCH MODEL

This research presents the FASE model for evaluating strategic position and choosing suitable strategy based on Big Data techniques and SPACE Matrix. As showed in Fig. 1; FASE model can be divided into five processes: (1) selecting the customer's dataset and data preprocessing (2) extracting RFM values as some of the input attributes for Big Data clustering algorithms (3) clustering customers based on c-means algorithm (4) Finding frequent patterns, associations, correlations, or causal structures from a cluster of customers using the Apriori algorithm. (5) Finally, determining what type of strategy a company should undertake using SPACE matrix method; Input of this process is the outcome of the analysis of strategic managers and Big Data mining methods. The details of the FASE model process are presented step by step as follows:

Process 1: selecting the customer's dataset and data preprocessing: At first, we select the customer's dataset and then preprocess the data to put it in a form that is most useful to the clustering algorithm. Thus, firstly we remove the attributes which include missing values or inaccurate values, eliminate the redundant attributes, normalize all numeric values in the dataset and transform the raw data into a format that will be more effectively processed for clustering customer.
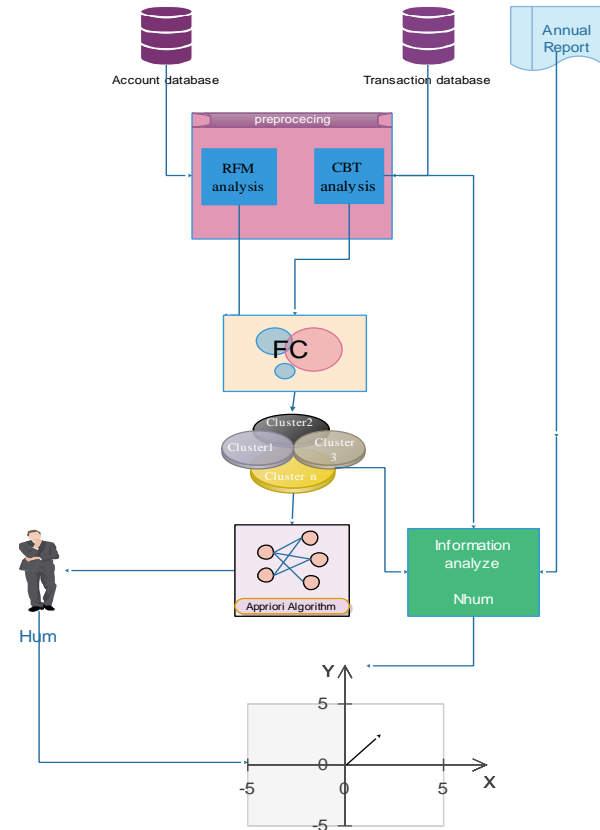
Figure 1. FASE model for evaluating a strategic position and selecting a smart strategy.

Process 2: extracting RFM values: RFM values are defined as follow: recency (R) of the last purchase, frequency (F) of the purchases over a specific time and Monetary (M) value of the purchases in a specific period time. RFM values are calculated for every customer as one of the behavioral scoring elements affecting customer segmentation.

Process 3: clustering customers. Customers are divided to clusters by Fuzzy-Cmeans method. Input of this method involves RFM values and some important attributes that impact on strategic decisions. Output of this process is membership values that indicate the degree to which every customers belong to each cluster.

Process 4: Finding association rules. FASE model finds association rules from clusters of customers by Apriori algorithm. This algorithm applies on each cluster and Inputs of this algorithm are RFM values and some important attribute values of each

cluster. Also, the MinConf element and MinSup element determine the accuracy of the required rules. The extracted association rule is used to create profile of each cluster. These created profiles are used by strategic managers to realize their customer's behaviors.

Process 5: determining strategy: in final process, FASE model evaluates strategic position and chooses high performance strategy for a corporation based on SPACE matrix method. SPACE analysis matrix is a super technique for assessing the sense and wisdom in a particular strategic plan. The SPACE matrix contains the internal dimensions (Competitive Advantage (CA) and Financial Strengths (FS)) and external dimensions (Industry Strengths (IS) and Environmental Stability (ES)). In this process, internal dimensions and external dimensions are evaluated to find the strategic position of the corporation and then select smart strategy.

3. DETAILS OF THE RESEARCH MODEL

3.1. Data preprocessing

In this study we do not only describe the FASE model in detail but also, we apply our model on a banking dataset (Fig. 2). Banking datasets were provided by an Iranian debit card issuer. These datasets contain customers transaction dataset, customers profile dataset and financial annual reports data set. Customers profile dataset consists of effective debit card account information of 85,341 customers until November 2014. Customers transaction dataset consists of over than 64.32 million individual transaction records from September 2012 to November 2014. Obviously, all of data are not related to the chosen object, so extraction of knowledge from the banking datasets included the following three sub-processes. In the first sub-process, two datasets are integrated on a column to create a single dataset. Then the second sub-process was intended to extract only that data useful for the big data algorithms. Dataset contains unnecessary data fields and records which are removed. The next sub-process, the raw data, is transformed into a numeric format and then all of

data in the dataset are normalized to a constant scale which will be more effectively processed.

Data preprocessing is a Big data technique that involves transforming raw data into an understandable format. This process prepared data to extract RFM values. RFM analysis [14] model is a marketing model that provides effective variables for customer segmentation. The model consists of three variables that are customer recent consumption, frequency and money amount. The definition of RFM analysis model is described as follows:

1) R represents recency of the last purchase that refers to the time interval between the last customer consumption and current.
2) F represents frequency of the purchases that refers to the number of transactions over a specific period of time.
3) M represents monetary value of the purchases that refers to the cumulative total of money spent for products by a particular customer in a specific period.

Recently, researches have proposed WRFM, RFMTC and LRFMC instead of RFM. WRFM model is a novel method that allocated weights to RFM variables using natural characteristics of an industry; Therefor disparate weights should be assigned to RFM variables. For instance, Stone [15] suggested that ordered weights should be assigned to RFM variables. he suggested highest weighting on the Frequency, followed by the Recency, with the lowest weighting on the Monetary variable. However Chuang et al. suggested that Recency had the least value and then Frequency higher value and Monetary had the most value [16]. Farajian suggested that Monetary and Frequency have more value than Recency [17]. In some researches, weights of RFM variables were ascertained by analytic hierarchy process (AHP) [18]. RFMTC model used to develop RFM model and added two parameters to these three parameters [19]. These parameters are "time since first purchase" and "churn probability" that are exploited using Bernoulli sequence in probability theory. LRFMC model expanded RFM model to two more parameters, length of customer

relationship and cost of a customer [20]. Hu and Yeh proposed the RFM-pattern that can approximate the set of RFM-customer-patterns without customer identification information by a novel algorithm to ascertain complete set of RFM-patterns [21].

This process tries to extract RFM values from banking dataset where R is a value measure that is reverse of the date of the time distance between the date of user's last transaction and the date of last transaction on the dataset[1]. For example, if the time distance related to the customer equals to 30, the value of the R equals to $\frac{1}{30}$. The value measure F is the average number of transactions per month. The value measure M is the average amount of financial transactions the user made per month.

Table 1. Score of Customer for evaluating of CBT factor.

Amount of Transaction During a Month (ATDM)	Score of Customer (SC)
0< ATDM <800	1
800<= ATDM <1800	2
1800<= ATDM <2900	3
2900<= ATDM	4

Another important variable, we need to cluster the Customer's Transactional Behavior (CBT). It is an implicit variable which cannot be retrieved directly from the data base. We needed to develop a method to extract the CBT. As shown in the following equation, this study employs CBT to extract customer's transactional behavior:

$$CBT = \frac{\sum_{i=1}^{j} w_i sc_i}{j} \quad \text{where} \quad w_i = \frac{2(j-i+1)}{j*(j+1)} \quad (1)$$

The w_i indicates the degree of importance of SC; The recent SC is more important than other SCs. Where sc_i indicates the score of the customer during a month i, and the month j is the whole period of observation. Using table 1 values, Score of each customer during a month was calculated.

3.2. Clustering the Customers

Clustering is the process of grouping a set of various objects into groups of similar objects. A cluster is a collection of data objects that have high similarity in comparison to one another within the same cluster and are dissimilar to the objects in other clusters. There are a lot of algorithms for clustering the set of various objects, for instance neural network, Kmeans, Kmediod and so on. FASE model uses the customers' dataset to analyze the customer behaviors. Hence, we study algorithms that is used in this area. Many researches presented various methods for customers clustering such as Panel Data Clustering, support vector regression analysis, logistic regression analysis , linear discriminate analysis (LDA), multiple discriminate analysis (MDA), neural networks and so on [22, 25]. Baesens and et al. presented a purchase behavior modeling based on Bayesian neural networks [26]. Farajian utilized K-means to cluster the banking customer and predicted the customer behavior by Apriori algorithm [17]. Dasgupta et al. predicted market response using neural network models [27]. Davies examined how a variety of bank customer groups represent different expectations of the automatic teller machines service. Kim & Sohn managed customer loans using neural networks [28]. Nan-Chen [29] proposed an integrated model to manage existing credit card customers in a bank using self-organizing map(SOM). Chan used self-organizing map (SOM) and back propagation network (BPN) to perform data clustering, price prediction, and error prediction after information is crawled and stored into a dataset [30]. Yong used fuzzy clustering algorithm based on Axiomatic Fuzzy Set to cluster the customers [31]. Dibya mentioned FCM is suitable for overlapping clustering task while data belongs to more than one cluster [32]. The advantage of using fuzzy theory in customer clustering and CRM is that the business analyst can gain in-depth understanding into the data mining model [33]. Base on that FASE-model used the fuzzy C-mean algorithm to

---

[1] there is a constraint if this number is more than 300,R value equals with zero

clustering customers. This algorithm is described as follow:
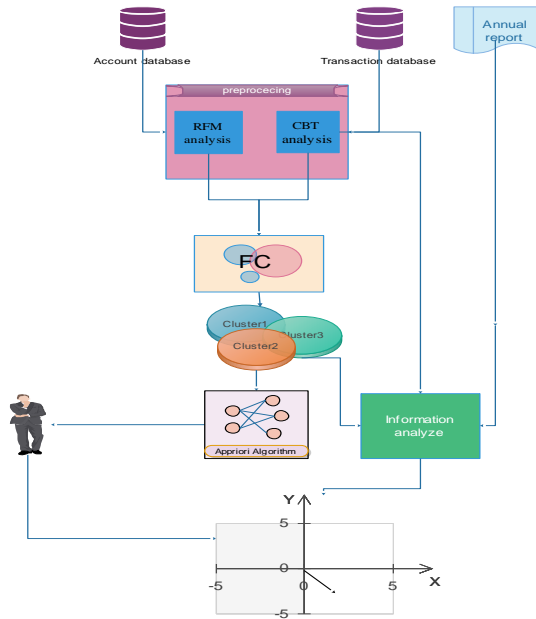
Figure 2. Result of FASE model on the national Iranian's debit card issuer.

Fuzzy clustering methods are based on fuzzy logic, while it permits an object to be assigned to different clusters. Fuzzy-CMeans (FCM) is a fuzzy clustering method which is based on K-means clustering concepts to partition collection of objects into clusters, i.e. FCM iteratively determines the cluster centers and updates the memberships of objects [34]. In the FCM clustering method, each object is belonged to clusters with a value of membership by membership function. Hence, every object may belong to several clusters with diverse membership values that are between 0 and 1. Moreover, there is a fuzzy rule that states the sum of the membership values of an object to all clusters must be 1. Let $O = (O_1, O_2, \dots, O_N)$ indicates an object with N attributes to be partitioned into a list of c cluster centers $C = (c_1, c_2, \dots, c_M)$ where O_i denotes value of attribute i belongs an object O. FCM attempts to determine the most characteristic point in each cluster then FCM computes the membership value for each object in the clusters to minimize the cost function defined as follows:

$$J = \sum_{x=1}^{N} \sum_{y=1}^{M} \varphi_{xy}^{\gamma} \left\| O_x - c_y \right\|^2 \tag{2}$$

Table 2. Input variable for Apriori Algorithm.

Variable Name	Comments
Days–segments	Days segment of a month for each transaction 1, <11; 2, 11-20; 3, 21-30.
Month-segment	Month segment of a year for each transaction 1, <3;2,4-6;3,7-9;4,10-12.
Times-Segment	Times segmentation of a day for each transaction 1, <8; 2,8-16; 3, 16-24;
Education	2010, Elementary; 2020; middle school; 2030, high school; 2040Undergraduate; 2050, graduate; 2060, Postgraduate; 2070, Dr
Age-code	1, <20; 2, 20-40; 3, 40<.
Amount of transaction	Monthly amount of transaction 1, <200; 2,200-700; 3, 700-1200; 4,1200-2500;5,2500-4000; 6,4000<
Transaction type	for example: 1100,P-Payment;1110, Deposit; 1115, Transfer in; 1116,Transfer Out;….
Sex	0, men; 1, women.
Terminal type	Code of terminal type
Occupation	Encoded field
Block code	Card usage:1, limit;2, not limit

Where φ_{xy} $\left(0 \le \varphi_{xy} \le 1\right)$ indicates the value of membership O_x in the ith cluster, c_y is the yth cluster center, γ $(1 \le \gamma)$ ascertain the degree of cluster fuzziness. The membership value is computed by using membership function that is defined as follows:

$$\varphi_{xy} = \frac{1}{\sum_{k=1}^{M} \left(\frac{\left\| O_x - c_y \right\|}{\left\| O_x - c_k \right\|} \right)^{2/(\gamma-1)}} \tag{3}$$

Every object O has a set of membership values that denoted degree of being in the yth cluster. The highest membership value is the most likely object belonging to that cluster. The cluster centers are updated by following function:

$$c_y = \frac{\sum_{x=1}^{N} \varphi_{xy}^{\gamma} O_x}{\sum_{x=1}^{N} \varphi_{xy}^{\gamma}} \tag{4}$$

FCM method, at first step, starts with Chose M centers randomly, second step Computes a set of membership values, third step updates the clusters center, forth step Computes objective function J, fifth step Repeats steps second to forth until convergence $\|\varphi^{(k)} - \varphi^{(k-1)}\| \leq \varepsilon$ termination tolerance, ε.
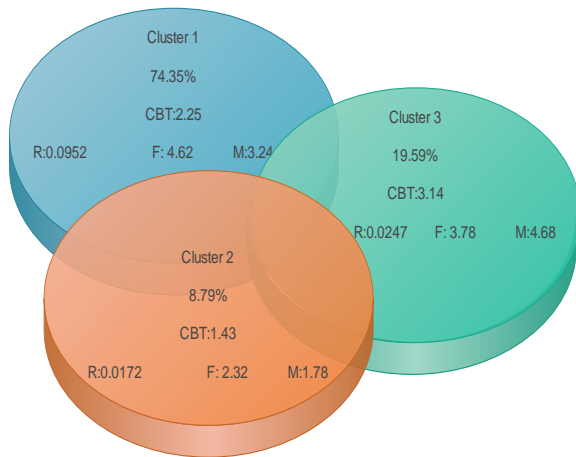
Figure 3. Statistical summarized data of clusters after customer 's clustering.

FASE model uses Fuzzy-CMeans method to cluster the bank dataset after integrating information in a single dataset. The attributes are used for clustering contains RFM values and CBT value as predicated variables to classify each customer into several homogenous clusters. In this experimental dataset, FASE model supposes N=4 and M=3 for Fuzzy-CMeans method. Result of Fuzzy-CMeans method executed on all existing customer's data arranges three profitable groups of customers. As showed in Fig. 3, the number of customers, ratio of number of customers relative to the overall customers, average RFM and to the overall customers was 74.35% and the number of customers is 63,452. The next clusters include 7504 and 16726 customers in order. The next major step is to choose the target cluster of customers, so FASE model selects clusters which have ratio of number of customers relative to the overall customers greater than 15%. All customers who belong to selected clusters become candidates for conducting suitable strategies for a bank.

3.2. Creating cluster Profiles by Association rule mining

Once the customers' clusters are created, FASE model tries to understand practical patterns in bank customers' clusters so that it could better figure out behaviors of various customers. The association rule inducer is a rule-based machine learning method to generate the customers' profiles that contain practical patterns and important information. The bank dataset after Data preprocessing contained 27 attributes. Some of these attributes are un-important or irrelevant which must be ignored for the purpose of more accuracy customer profiles. Association rule mining is a method for discovering relationships between a set of items that occur frequently together in a dataset [35, 37]. In the following we describe the concept of association rules mining: Let $I = \{i1, i2, \ldots, im\}$ be a set of items in which each item denotes a particular literal. Let BD= {t1, t2, . . ., tn} be a big dataset of transactions, where each transaction T is a non-empty subset of items that $T \subseteq I$. Suppose W is an item set $W \subseteq I$, a transaction T contains W only and only if $W \subseteq T$. Support (W, BD) indicate the present of iteration W in BD. The association rule is a denotation of the form W$\Rightarrow$Z (s%, c%), where $W \subseteq I$, $Z \subseteq I$ and $W \cap Z = \varnothing$. The support of rule W$\Rightarrow$Z is percent of transactions contain both W and Z in BD (i.e. Support(W$\cup$Z,BD)=s%), The confidence of rule W$\Rightarrow$Z is percent of a transaction in DB which contains W.

Table 3. Result of executing Apriori Algorithm on Cluster-1.

Rule ID	Association rules	Support	Confidence
1.	Transaction type =1100← Days–segments=1&sex=0& Times-Segment=3	6.1%	84%
2.	Terminal type =3020← Days–segments=1&sex=1& Times-Segment=3	16.2%	86%
3.	Transaction type =1100← Days–segments=2&sex=1	26.2%	94%
4.	Transaction type =1100← Month-segment=2& sex=0	17.6%	93%
5.	Transaction type =1100← Month-segment=2& sex=0& Days–segments=2	10.4%	82%
6.	Terminal type =3010← Days–segments=1&sex=1& Transaction type=1117	12.3%	85%
7.	Terminal type =3020← Days–segments=1&sex=1& Transaction type=1100	9.8%	84%
8.	Terminal type =3020← Times-Segment=2&sex=1& Transaction type=1110	6.3%	87%
9.	Terminal type =3020← Days–segments=1&sex=1& Transaction type=1110	11.8%	84%
10.	Terminal type =3020← Days –segments=1&sex=1& Transaction type=1120	21.4%	91%
11.	Terminal type =3030← Days–segments=1&sex=1& Transaction type=1120& Times-Segment=2	12.6%	87%
12.	Terminal type =3030← Days –segments=1&sex=1& Transaction type=1120& Times-Segment=3	14.0%	93%
13.	Terminal type =3040← Days –segments=1&sex=0& Transaction type=1115	11.6%	83%
14.	Terminal type =3010← Days –segments=1&sex=0& Transaction type=1116	15.1%	85%
15.	Terminal type =3010← Days –segments=1&sex=1& Transaction type=1116	7.3%	87%
16.	Terminal type =3020← Age-Segments=2&sex=1& Times-Segment=2	10.7%	83%
17.	Terminal type =3020← Age-Segments=2&sex=1& Times-Segment=3	15.8%	87%
18.	Terminal type =3030← Age-Segments=2&sex=0&Transaction type=1121& Marital Status=1	7.3%	83%

Apriori algorithm is one of most successful algorithms was proposed for mining association rules in a transaction dataset by Agrawal and et al [38, 39]. This algorithm contains two essential steps which are 1) Support Satisfaction 2) confidence satisfaction. The first step is detecting all the association rules whose support is greater than a minimum support (MinSup); and the second step evaluates association rules to have confidence greater than minimum confidence (MinConf). In this process for explanation, we chose only cluster-1 for mining association rules. Table 2 lists the input variable for creating cluster profiles by Apriori algorithm. Criterions were set up to recognize association rules that had at least 80% confidence and 6% support. Table 3 shows the profile of cluster-1 in the form of association rules, where each rule represents customers' behavior in different conditions that strongly associated with the customers. These rules can be guidelines for managers to learn more about their corporation's customer behavior to make more accuracy decisions about strategy of corporation.

3.4. SPACE Matrix

SPACE matrix [13] includes four-quadrant which indicates aggressive, conservative, defensive or competitive strategies. The SPACE matrix analysis functions upon two internal and two external strategic dimensions in order to determine the organization's strategic posture in the market environment. This matrix has been improved during years by some researchers for instance Tuncay and Jelena [10, 40]. The axes of the SPACE Matrix represent horizontal and vertical dimensions of a firm. The horizontal dimension shows financial strength (FS) and competitive advantage (CA). The vertical dimension shows environmental stability (ES) and industry strength (IS). These dimensions are the most important determinants of an overall strategic position of corporation in the market environment. Each of dimensions in the SPACE matrix has its own specific measures that is shown Table 5. The following are a few technical assumptions of SPCSE matrix:

- The domain for CA and IS values in the SPACE matrix are plotted on the X axis.
   CA values can range from -1and -5
   IS values can range from +1and +5
- The domain for the FS and ES values of the SPACE matrix are plotted on the Y axis.
   ES values can take -1 to -5

FS values can take +1 to +5

The SPACE matrix is erected by a point contain X and Y. X is calculated by average score of environmental stability and financial strength dimensions. Y is calculated by the average score of industry strength and competitive advantage dimension.

After evaluating the company across four dimensions, SPACE matrix can recommend four different strategies: aggressive strategy, conservative strategy, competitive strategy, or defensive strategy.

Table 4. Formulas and expected min and max scale for factors.

Factors	Formula	Min	Max	score
Return on investment	(gain from investment – cost of investment) / cost of investment	1.25	2.35	3.61
Leverage (debt to equity ratio)	total liabilities / total shareholders' equity	1.35	2.20	3.78
Liquidity ratio	LR = liquid assets / short-term liabilities	1.5	2.9	2.62
Capital required versus capital available	capital available/ Capital required	0.9	1.9	3.24
The bank's revenue	revenue in the current year/ revenue in the last year	1.0	1.3	2.93
Customer loyalty	Loyal customer /total customers	0.12	0.19	2.12
Data processing services in the bank	Total tools use for analyzing bank data / Total Standard tools used for analyzing bank data	0.2	0.5	3.72
Market share	(Bank's Revenue in Specific Time) / (Relevant Market's Total Revenue in Specific)	0.10	0.23	2.52
The bank has a large customer base	Total customer of the bank / Total customer of banking in Iran	0.08	0.18	2.86

FASE model evaluating factors can be methodologically grouped into two group: Nhum factor and Hum factor. Nhum computes score of factors related to each dimension by analyze the banking dataset, dataset of financial annual reports and result of clustering customers. Hum calculates the scores of factors by managers of bank.

Table 5. Score of important factors for evaluating strategic dimensions.

Factors Determining Environmental Stability-		
Factors	Score of factor	Nhum/ Hum
1.Technological changes of banking	4	Hum
2. Less-developed countries have rate of inflation	5	Hum
3.Demand variability (much to little)	3	Hum
4.Barriers to entry into market	1	Hum
5.Competitive pressure/rivalry	2	Hum
6.Price range of competing service	2	Hum
Impact of International Economic Sanctions	5	Hum
Average	-3.14	
Competitive Advantage-		
1. Market share	2.52	Nhum
2. Services quality	5	Hum
3. Data processing services in the bank	3.72	Nhum
4.bank service replacement cycle	4	Hum
5.Customer loyalty	2.12	Nhum
6.Competition's capacity utilization	3	Hum

7.Technological know-how	2	Hum
8. The bank has a large customer base.	2.86	Nhum
9. Speed of new service introductions	1	Hum
Average	-2.91	
Industry Attractiveness+		
1. Growth potential	5	Hum
2. Profit potential	5	Hum
3. Financial stability	4	Hum
4.Technological know-how	3	Hum
5.Resource utilization	3	Hum
6.Capital intensity	4	Hum
7.Ease of entry into the market	3	Hum
8.Productivity; capacity utilization	2	Hum
Average	3.62	
Financial Strength+		
1. Return on investment	3.61	Nhum
2. Leverage (debt to equity ratio)	3.78	Nhum
3. Liquidity	2.62	Nhum
4. Capital required versus capital available	3.24	Nhum
5. Cash flow	4	Hum
6. Ease of exit from market	1	Hum
7. Risk involved in the business	3	Hum
8. Inventory turnover	4	Hum
9. The bank's revenue	2.93	Nhum
Average	2.81	

Nhum utilizes table 4 to estimate some factors of each dimension[41, 43]. FASE model determine amount of each Nhum factor utilize the precise

formula and then result of each factor compares with the expected value (min and max values) of each factor in the corporation's strategy. Score of each factor is calculated by normalizing the score between 1 and 5. For instance, the scale of Liquidity ratio calculated by above formula equals 2.42 and the score for this factor 2.62. After calculating all factors of each dimension, then Find the average scores for FS, CA, IS and ES and then Plot the average score for each dimension on the appropriate axis in the SPACE Matrix. The Result of directional vector in the banking case equals [0.71, -0.33].

[3.62, -2.91], [2.81, -3.14] = [0.71, -0.33]

Calculations are summarized in the Fig. 4.
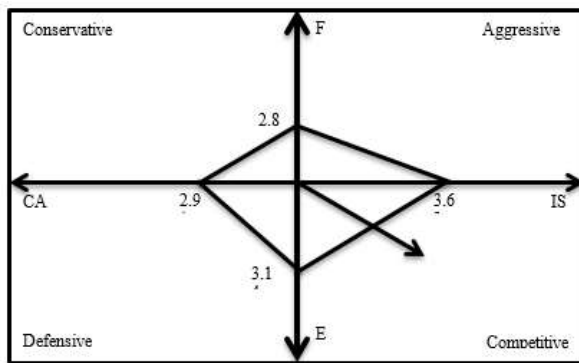
Figure 4. Result of performing SPACE Matrix the national Iranian's debit card issuer.

According to Fig. 4 showed the strategic position of the bank is competitive. Therefore, the bank can follow a competitive strategy which is characteristic of an attractive industry in a relatively unstable environment. SPACE analysis recommends that bank in such position take the following actions: 1. Obtain financial resources to increase customers thrust. 2.cooperate with a special bank that is looking for opportunities to expand. 3. Reduce its variable and fixed costs to improve or extend the service line. 4. invest in differentiation competitive advantages.

4. CONCLUSION

The Strategic management science propose for managers to find the proper orientation in order to lead their corporations. Since market environments

change constantly and corporations face the new situations, knowing the strategic position of corporations can be a good solution to overcome these changes. We have presented FASE model to be a semi-automatic selecting smart strategy for all corporations. FASE model consist of Fuzzy-Cmeans clustering algorithm, Apriori rule inducer, and SPACE matrix for evaluating strategic position and selecting smart strategy. Using Big Data mining is one of the novelties of FASE model; Therefore, managers have comprehensive analysis of factors that relate to dimensions of the strategic. At end of this research, the FASE model applied over the Iran bank institute. The results reveal that the strategic position of the bank is competitive position and the bank can follow a competitive strategy.

REFERENCES

[1]. Fazlollahtabar H. and Abbasi A., Applying Integrated Strategic Planning and RADAR Technique to Find Optimal Course Delivery Policy in a Virtual Learning System. In: The 3rd International Conference on Virtual Learning, ICVL., (2008) 169–176.

[2]. Chen S-JJ., Hwang, C. L./Beckmann MJ and Krelle W., Fuzzy Multiple Attribute Decision Making: Methods and Applications. New York; Springer-Verlag New York. Inc. doi:10.1007/978-3-642-46768-4.

[3]. Kangas J., Pesonen M., Kurttila M. and Kajanus M., A' WOT : Integrating The AHP With SWOT Analysis. ISAHP, (2001) 189–198.

[4]. Paiva E.L., Roth A.V., Fensterseifer J.E., Organizational Knowledge and The Manufacturing Strategy Process: A Resource-Based View Analysis, Journal of Operations Management, 26-1 (2008) 115–132.

[5]. Yüksel İ., Dagdeviren M., Using The Analytic Network Process (ANP) in a SWOT Analysis - A Case Study for a Textile Firm, Inf. Sci. (Ny), 177-16 (2007) 3364–3382.

[6]. Aslan I., Çınar O. and Özen Ü., Developing

Strategies for The Future of Healthcare in Turkey by Benchmarking and SWOT Analysis. Procedia – Soc. Behav. Sci., 150 (2014) 230–240.

[7]. Law J., Managing Change and Innovation in Public Service Organisations - Edited by Stephen P. Osborne and Kerry Brown, Public. Adm., 84 (2006) 794–796.

[8]. Basu R., Tools for analysis-Pestle analysis in implementing quality: a practical guide to tools and techniques. Fisrt. Thomson Learning: London, (2004) 98-100.

[9]. Zalengera C., Blanchard R.E., Eames P.C., et al. Overview of the Malawi energy situation and A PESTLE analysis for sustainable development of renewable energy, Renew. Sustain. Energy Rev., 38 (2014) 335–347.

[10]. Gürbüz T., A Modified Strategic Position and Action Evaluation (SPACE) Matrix Method, International MultiConference of Engineers and Computer Scientists, (2013) 13–16.

[11]. Shen L., Zhou J., Skitmore M. and Xia B., Application of a Hybrid Entropy–McKinsey Matrix Method in Evaluating Sustainable Urbanization: A China Case Study, Cities, 42 (2015) 186–194.

[12]. Decuseara N.R., Using The General Electric / Mckinsey Matrix In The Process Of Selecting The Central And East European Markets, Manag. Strateg., 19 (2013) 59–66.

[13]. Radder L. and Louw L., The SPACE matrix: A tool for calibrating competition, Long Range Plann, 31-4 (1998) 549–559.

[14]. Hughes A., Strategic Database Marketing. 4th ed. McGraw-Hill Education, (2012) 598

[15]. Stone B. and Jacobs R., Successful Direct Marketing Methods. McGraw-Hill, 2001.

[16]. Chuang H.-M. and Shen C., A Study on The Applications of Data Mining Techniques to Enhance Customer Lifetime Value - Based on The Department Store Industry, 2008 International Conference on Machine Learning and Cybernetics. IEEE, (2008) 168–173.

[17]. Farajian M.A. and Mohammadi S., Mining the Banking Customer Behavior Clustering and Association Rules Methods Using Clustering and Association Rules Methods, Int. Journal Ind. Eng. Prod. Res., 21 (2010) 239–245.

[18]. Wei-Jiang L., Shu-Yong D., Xue Y., Xiao-Feng W., Determination of Customer Value Measurement Model RFM Index Weights, African Jour. Bus. Manag., 15 (2011) 5567–5572.

[19]. Yeh I.-C., Yang K.-J. and Ting T.-M., Knowledge Discovery on RFM Model Using Bernoulli Sequence, Expert Syst. Appl., 36 (2009) 5866–5871.

[20]. Soeini R. and Fathalizade E., Customer Segmentation Based on Modified RFM Model in The Insurance Industry, Int. Proc. Comput. Sci. Inf. Tech. 25 (2012) 101–104.

[21]. Hu Y.H. and Yeh T.W., Discovering Valuable Frequent Patterns Based on RFM Analysis Without Customer Identification Information, Knowledge-Based Syst., 61 (2014) 76–88.

[22]. Malhotra R. and Malhotra D., Evaluating Consumer Loans Using Neural Networks, Omega, 31 (2003) 83–96.

[23]. Levis A.A. and Papageorgiou L.G., Customer Demand Forecasting Via Support Vector Regression Analysis, Chem. Eng. Res. Des., 83 (2005) 1009–1018.

[24]. Zheng T., Zhu D., Wang X. and Yu B., Panel Data Clustering and Its Application to Discount Rate of B Stock in China. In 2009 Second International Conference on Information and Computing Science, IEEE, (2009) 163–166.

[25]. Nie G., Chen Y., Zhang L., and Guo Y., Credit Card Customer Analysis Based on Panel Data Clustering, Procedia Comput. Sci., 1 (2010) 2489–2497.

[26]. Baesens B., Viaene S., Van den Poel D., Vanthienen, J. and Dedene G., Bayesian Neural Network Learning for Repeat Purchase Modelling in Direct Marketing, Eur. Jour. Oper. Res., 138 (2002) 191–211.

[27]. Dasgupta C.G., Dispensa G.S., Ghose S., Comparing The Predictive Performance of a Neural Network Model with Some Traditional Market Response Models, Int.

Jour. Forecast, 10 (1994) 235–244.

[28]. Davies F., Moutinho L., Curry B., ATM User Attitudes: a Neural Network Analysis, Mark. Intell. Plan., 14 (1996) 26–32.

[29]. Hsieh N.C., An Integrated Data Mining and Behavioral Scoring Model for Analyzing Bank Customers, Expert Syst. Appl., 27 (2004) 623–633.

[30]. Chan C.-C.H., Intelligent Spider for Information Retrieval to Support Mining-Based Price Prediction for Online Auctioning, Expert Syst. Appl., 34 (2008) 347–356.

[31]. Wang Y., Ma X., Lao Y. and Wang Y., A Fuzzy-Based Customer Clustering Approach with Hierarchical Structure for Logistics Network Optimization. Expert Syst. Appl., 41 (2014) 521–534.

[32]. Bora D.J., A Comparative Study Between Fuzzy Clustering Algorithm and Hard Clustering Algorithm, IJCTT, 10 (2014) 108–113.

[33]. Wong K.W., Data Mining Using Fuzzy Theory for Customer Relationship Management, WAWISR, 2001.

[34]. Bezdek J.C., Pattern Recognition with Fuzzy Objective Function Algorithms, Springer Science & Business Media, 2013.

[35]. Calders T, Dexters N, Gillis J.J.M. and Goethals B., Mining Frequent Itemsets in A Stream, Inf. Syst., 39 (2014) 233–255.

[36]. Tan P.-N., Steinbach M. and Kumar V., Introduction to Data Mining, Boston (2006) (First Edition).

[37]. Vimieiro R. and Moscato P., A New Method for Mining Disjunctive Emerging Patterns in High-Dimensional Datasets Using Hypergraphs, Inf. Syst., 40 (2014) 1–10.

[38]. Agrawal R., Imielinski T. and Swami A., Mining Association Rules Between Sets of Items in Large Databases, SIGMOD Conference, 22 (1993) 207-216.

[39]. Agrawal R. and Srikant R., Fast Algorithms for Mining Association Rules in Large Databases, Ailamaki, (1994) 487–499.

[40]. Borocki J., Process Of Applying Modified Space Model For Defining Company ' s Strategy, Appl. Modif. Sp. Model Defin. Co., 2 (2011) 61–68.

[41]. Mailvahanan R., Performance Evaluation of Printed Circuit Board Manufacturing Maquiladoras: A Return on Investment Approach, J. Oper. Manag., 9 (1990) 437–438.

[42]. Pizzica A.J. and Rist M., Financial Ratios for Executives: How to Assess Company Strength (2015)

[43]. Menezes M.B.C., Kim S. and Huang R., Return-on-Investment (ROI) Criteria for Network Design, Eur. Jour. Oper. Res., 245 (2015) 100–108.

Investigation of Surface Temperature Differentiation of Fagus and Quercus Stands by Using Landsat Images

Çağdaş KUŞÇU ŞİMŞEK[*] [ID], Osman DOĞAN [ID]

Sivas Cumhuriyet University, Faculty of Engineering, Geomatic Engineering, Sivas, TURKEY

Abstract. While climatic features of regions affect the variety of tree species and their structures, the vegetation structures of the regions are effective on micro climate. In this study, thermal differentiations in the *Fagus* and *Quercus* stands which are homogenous in structure and are found within the boundaries of Mercanköşk Forest Sub-District Directorate in Şile are presented.

The surface temperature data which is obtained by Landsat TM-5 and Landsat 8 - ETM thermal images during 2011, 2013, 2014 and 2015 is compared statistically in relation to data obtained from the stand. According to the results obtained, it has been found out that there is a difference of surface temperature up to 2.4°C among tree types. This surface temperature difference which is within the boundaries of forest sub-district directorate having similar regional features has an undeniable effect in terms of climate. It has been thought that using this information as a regional inventory in the preparatory studies within the scope of tackling with global warming will be effective on the success to be achieved.

Keywords: Landscape Planning, Micro climate, Remote Sensing, Fagus, Quercus.

Landsat Görüntüleri Kullanılarak Kayın ve Meşe Meşcerelerinin Yüzey Sıcaklığı Farklılığının İncelenmesi

Özet. Bölgelerin iklimsel özelliklerinin, ağaç türlerinin çeşitliliğini ve yapısal özelliklerini etkilemesine karşın bitki örtüsü yapısı da mikro iklim üzerinde etkili olmaktadır. Bu çalışmada, bu bilgiye dayanarak, Şile'nin Mercanköşk Orman İşletme Şefliği sınırı içerisinde kalan ve homojen yapı sergileyen kayın ve meşe meşcereleri ele alınarak yüzey sıcaklığı farklılıkları ortaya konulmaya çalışılmıştır

2011 Landsat TM-5 ve 2013, 2014 ve 2015 yıllarına ait Landsat 8 - ETM termal görüntüleri üzerinden elde edilen yüzey sıcaklığı bilgileri, meşcere verisi ile ilişkilendirilerek istatistiksel olarak karşılaştırılmıştır. Elde edilen sonuçlara göre, iki ağaç türüne ait homojen meşcere alanları arasında 2.4°C'ye varan yüzey sıcaklığı farklarının oluştuğu tespit edilmiştir. Bölgesel özelliklerin hemen hemen benzer olduğu şeflik sınırları içerisinde oluşan bu sıcaklık farkı, iklimsel açıdan gözardı edilemeyecek bir etki yaratmaktadır. Özellikle küresel ısınmayla mücadele kapsamında yapılan hazırlık çalışmalarında, bu bilgilerin bölgesel envanter olarak kullanılmasının, elde edilecek başarı üzerinde etkili olacağı düşünülmektedir.

Anahtar Kelimeler: Peyzaj Planlama, Mikro iklim, Uzaktan Algılama, Kayın, Meşe.

1. INTRODUCTION

Recently, the world of science has focused on the anticipated destructions emerging as a result of the global climate changes and has concentrated on developing action plans and adaptation strategies to struggle with probable scenarios. The issue, which is debated on global warming in the macro scale, is debated on the combined effects of global climate changes and urban climates, which change due to urbanization, and anthropogenic effects in the micro scale. Globally, the factors which have an influence on global climate changes, locally

have an influence on urban climate and these factors increase the climatic comfort conditions of the cities especially which are on the tropical and mid-latitudes above the critical level [1]. Thus, man who is not in the scope of climatic comfort criteria may encounter with fatal consequences frequently. When current examples are examined, the seriousness of the situation becomes more obvious. Heat waves which are encountered more frequently due to global climate changes have caused the death of 70.000 people in Europe in the summer of 2003 [2], almost 2500 people in 15 days in India in 2015 [3] and 700 people in a week in France in 2015 [4]. Such circumstances have led this issue to be handled under the scope of natural disaster. Besides, the temperatures' increasing above the seasonal normals causes an increase in electric consumption together with agricultural irrigation. For instance it was stated that the increasing electric consumption due to extremely hot weather conditions all over Turkey on 28th July 2015 reached to 866,653 MWh and broke a record and that the electric bill for a day was nearly 333 million lira [5, 6]. That is, increasing human population with its anthropogenic effects together with increasing climatic pressure pose a threat both for health and economy.

Today, humankind is under the pressure of both global climate changes and anthropogenic effects especially in the big cities in the mid latitude. These two incidents have an interdependent and transitive nature; not only they are influenced by the same factors but also they cause pressure on each other. As stated in the abovementioned examples, the incidents, which are not in the scope of comfort criteria, may have fatal dangers. During this process, while man is struggling with global climate changes in the macro scale, he has to struggle with protecting climatic structures of the cities in the micro scale. Heat waves, which are considered as natural disasters by most developed countries, have led to the development of strategies and the preparation of action plans. The preparation process is supported by many scientific studies.

Turkey, where is situated in the mid latitude, is rather unprepared for this problem. Each region has its own climatic characteristics with its geographical location, wind direction and speed, topography, ecological features, surface elements, land use, urban features, population etc. Thus, the strategies, which will be developed, should be prepared by taking the inner dynamics of that region into consideration. This increases the need for regional studies, which will evaluate various factors on climate. Besides, this complex structured problem brings along the need for multidisciplinary studies.

While climatic features of a district have an influence on the vegetation, vegetation also has an influence on the climatic features. The vegetation climate relationship, which influences each other and has a dual interaction, necessitates the development of dual strategies.

In the upcoming years, considering droughts and natural deteriorations when predicting how the climate change in the new climate scenarios will affect forest dynamics and tree adaptations it has become necessary to identify the growth patterns and dispositions of trees under the stand or tree scale [7]. On the other hand, to obtain more fruitful results in the struggle with macro and micro climate changes, conscious forestation efforts which considers structural features of the vegetation have become more important. For instance, the areas covered by leaves from different types of trees can create a temperature differences up to 4°C - 5°C in the micro climate [8].

On the other side, green spaces contribute to the reduction of greenhouse effects by cooling the weather, increasing relative humidity, providing clean air, filtering the air and producing oxygen. The soil and the vegetation first absorb the heat and then send it away by vaporization [9]. These features increase the adaptation ability to climatic changes. Perspiration of the vegetation that retains water or the vaporization in the soil are important factors to cool the air and they can create a difference in temperature up to 1°C – 5°C. The air

stream moving above the trees contribute to cooling the environment by carrying the cool air to the treeless districts [10].

Vegetation, which is used as a natural source to cool the cities decreases the energy amount necessary to cool the air therefore, decreases the use of fossil fuels necessary for electric production. The studies conducted in Atlanta (USA) reveal that in 1975 trees sent 13,6 million tonnes of pollutant away from the atmosphere in one year and made a contribution of 75 million dollars and in 1996 these values were limited to respectively 8,6 million tonnes and 47 million dollars [11]. According to the same study, thanks to the advantages provided by the trees, energy worth 2,8 million dollars is saved. When the issue is dealt with from the point of view of utility theory of value it is obvious that making use of green spaces effectively to struggle with macro and micro climate changes provides great benefits economically.

Today, the importance of conscious forestation is increasing gradually to make the most of forests and green spaces which are necessary natural sources against CO_2 emission speed because of rapidly increasing population, urbanization, consumption and anthropogenic effects.

In the current study, thermal differences are tried to be investigated by examining *Fagus* and *Quercus* stands in the same closeness and growth age, and which have a homogeneous structure in the Şile Mercanköşk Forest Sub-district Directorate, by using remote sensing techniques. The obtained results are aimed to be used in the forestation of both city centres and urban periphery which has an important role in minimizing the temperature rise occurring in the micro climatic structures of the cities and forestation of the district.

2. MATERIALS AND METHODS

2.1. Study Area

The study was carried out within the borders of İstanbul Şile Mercanköşk Forest Sub-district

Directorate. It's neighbours are Yeşilvadi in the east, Ağva in the west, Şile Forest Sub-district Directorate in the North. Within the borders of the directorate there are 9460 ha *Quercus*, 2470 ha *Fagus*, 130 ha carpinus, 201 ha pinus pinea homogenous stands. Together with the other stands there are nearly 12458.3 ha forest areas in sum (Figure 1).

Figure 1. The study area.

Setting is important in certain aspects to reach a reliable result. First of all overall climate features should not have a lot of difference depending on sub-factors and secondly climatic features between homogenous stands of different types should be revealed. In this context, the directory is preferred because the borders of the directory consist of small units and regional characteristics do not have a lot of differences. Besides, anthropogenic effects are decreased by choosing the setting somewhere far away from the city centre.

A district within the borders of the metropolitan İstanbul which has the 1/5 population of the country is preferred as the setting because the study is thought to be a preparation for the landscape practices against increasing climatic brittleness due to the city's rapid growth.

2.2. Data

In the study, satellite imaging and data from the stand are used. In the selection of satellite images, the images from the summer period are used because heat islands are detected more easily then. Besides, since the stand data belongs to 2012, four

years when change of area usage is in the acceptance boundary is preferred. Accordingly, 19.07.2011 Landsat 5-TM and 30.07.2013, 10.07.2014, 29.07.2015 LANDSAT 8 OLI/TIRS data belonging to the area is used. Landsat 2012 image belonging to the area is not used since it could not be found.

As the stand data, data from 2012 belonging to Mercanköşk Forest Sub-district Directorate is used. However, since it is thought that the differentiation of closeness and growth age may create a difference micro-climatically, the areas which have similar closeness and growth age are used together. As a result of this elimination, homogenous *Fagus* and *Quercus* stands which have similar closeness and growth age are used.

2.3. Method

The basic hypothesis of the study is that different tree species have different thermal characteristics which can affect the micro-climatic structure. Climate studies are both multi-parameter studies, which evaluate issues using different scales and details, and have time and period differences. In the climatic studies which have a complex structure, the selection of scale, parameter and period have a great importance for the accuracy of the analysis. Besides, the analysis method of this complex structure is also an important factor influencing the accuracy of evaluation.

In the studies, it is necessary to approach the topic with a far-reaching point of view and to create real-like modelling with up-to-date data. In this respect, geographical information systems (GIS) and remote sensing methods are important tools of the processes such as analysis, evaluation, decision-making and developing strategies. They are necessary tools for climatic studies because they not only pave the way for observing very large areas and identifying problematic points but also they have features such as proving a holistic approach for planning, enabling the integration of multiple data, being updatable and enabling time changes [12]. Especially in the climate studies another adavantage of remote sensing is that it

enables visualizing heat on large areas and obtaining a great amount of thermal data at a sitting [9]. Furthermore it also enables measuring many factors about vegetation such as perspiration, vegetation stress, NDVI and canopy temperature [8]. In the light of this information, in this study, which used GIS and remote sensing effectively the workflow, consisted of image processing, arrangement of the stand data on the database, association of thermal images with the stand data, statistical analysis, results and forming planning suggestions.

The study is carried and discussed on the basis of surface temperatures. Surface temperatures are different from air temperatures in terms of measurement techniques. Remote sensing techniques are used as the most effective method for determining surface temperatures [13, 14]. However, there are also many studies that show the high correlation between air temperatures and surface temperatures which are obtained from remote sensing techniques [15-18].

On the other hand, this study is mandatorily handled in this context, because it involves the period between the years 2011-2015 and because we can't make any measurements parallel to past with terrestrial measurements. So, the use of remote sensing techniques have been deemed suitable for this study taking support from researches both mentioned and not mentioned above.

Before image processing, calibrations of the images of Landsat TM-5 and Landsat-8 OLI were made according to the landsat parameters which were given in metadata. By this way, spectral radiance values L_λ (W/(m^2 * sr * μm)) were obtained [19].

In order to calculate surface temperature, emissivity and NDVI values, which highlight reflection characteristics of surface elements, are used. Emissivity emerges with the electromagnetic wave releasing ability of the objects. The emissivity value is not only dependent on the creation of objects but also to

the surface roughness, physical properties of the object, and angle and wavelength. On the large scale, it is very difficult to calculate surface emissivity values, and this process is usually achieved based on certain hypothesis. Van de Griend and Owe [20] by doing a series of thermal band emissivity and normalized vegetation index (NDVI) calculations (eq. 1) in the natural environment, have found that there is a high correlation logarithmic connection between them (eq. 2). Generally the emissivity value of the dry soil is lower since the vegetation is more humid. The ε value is calculated based on Van's formula. Then, according to the radiative transfer equation

(eq. 3) given by Jiménez-Muñoz et al. [21], the radiation brightness values were calculated. Then by using eq. 4, the land surface temperature (T_s) values were calculated and land surface temperature images (Figure 2) were obtained.

$$NDVI = (Band4-Band3)/(Band4+Band3) \qquad (1)$$

$$\varepsilon = 1.0094 + 0.047 \, Ln(NDVI) \qquad (2)$$

$$L_\lambda = [\varepsilon_\lambda \, L_\lambda(T_s) + (1- \varepsilon_\lambda) \, L_{\lambda \, atm}\downarrow]\tau + L_{\lambda \, atm}\uparrow \qquad (3)$$

$$T_s = K_2 / \ln((K_1/ L_\lambda)+1) \qquad (4)$$
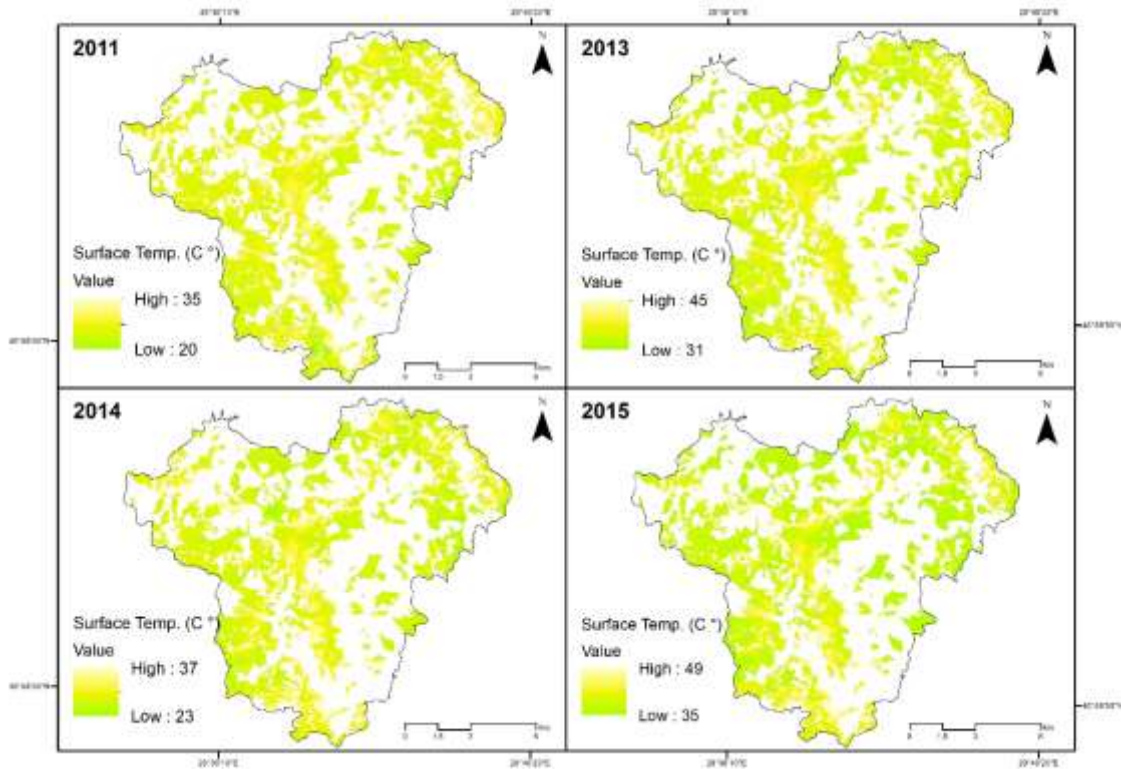
Figure 2. Years of surface temperature images.

In this study, the possible changes in surface temperatures are considered due to the instantaneous meteorological situations or different exogenous factors by using the images of 4 different years and by examining the correlations of these images with each other. Between the surface temperatures of these images, high correlations were determined in the range from 0.701 to 0.866 at 0.01 significance level.

These high correlations show that the images can be evaluated together.

Subsequently, the effects of the elevation, slope and the aspect values on surface temperatures are examined by regression analysis. The results show that, the topographic factors have no significant effect on surface temperatures. So, based on these results, topographic factors are not used as parameters.

As stand data, homogenous structured areas, which are obtained by making use of stand codes in the database are used (Figure 3).
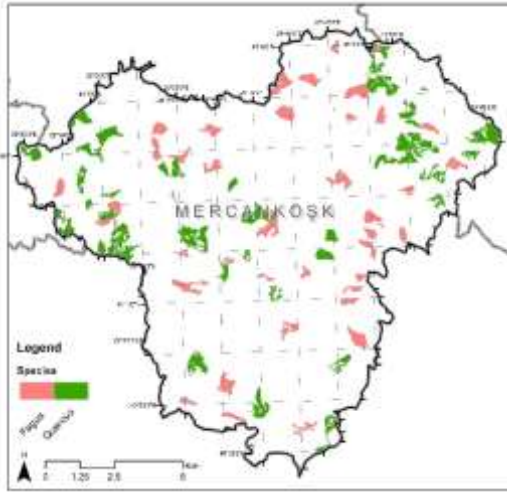
Figure 3. *Fagus* and *Quercus* stands which are used.

In this area, homogenous stands of *Pinus Pinea, Carpinus*, *Fagus* and *Quercus* are observed. However, in order to identify the climatic effect created by the vegetation better, taking closeness and growth age, which will make a difference into consideration, *Fagus* and *Quercus* stands with a similar structure, are assessed. In the area the closeness in *Fagus* stands is 3, growth ages are 0-1-2-3; the closeness in the *Quercus* stands is 0-2-3, growth ages are 0-1-2-3-4. Therefore, the study is conducted by taking closeness 3 and growth ages 1-2-3, which are common values in both vegetation species. Since the area proportion of *Fagus* stands is rather lower than the area proportion of *Quercus* stands, areas with a similar size near the *Fagus* stands are selected as sample *Quercus* areas. In this study, which is evaluated based on pixels, data base is formed by associating thermal images belonging to 4 different years to the stand data and surface temperature differentiation of *Fagus* and *Quercus* stands is examined by using independent variables t test with a confidence interval of % 95.

3. RESULTS AND DISCUSSION

According to the results obtained from T tests, the average surface temperature of *Quercus* and *Fagus* stands differentiate from each other within all years of the study. The comparison table which

is prepared based on the results of the T test ($t_{0,05:df}$ = t) conducted to compare the surface temperature grades of *Quercus* and *Fagus* stands can be seen below (Table 1). When the significance level of the results are examined, the *Quercus* and *Fagus* stands have significantly differentiated from each other in terms of thermal structure in all years except for the 2013 year which have a closeness level of 3 and growth age level 3 (Table 2). Average surface temperature values of the years 2011 - 2013 - 2014 and 2015 can be seen in Table 2 and surface temperature differences between the two species and their graphical illustrations are shown in Table 3.

When the average temperature values and the temperature differences between the two groups are examined it has been identified that the growth ages of the trees are influential on the thermal characteristics of tree species; the *Fagus* stands are nearly 0.7°C – 1.6°C cooler than the *Quercus* stands in the 1st and 2nd growth ages however the *Quercus* stands are 1.1°C – 2.4°C cooler than the *Fagus* stands in the 3rd growth age.

Different plant species exhibits different thermal characteristics that can be used to control and regulate indoor and outdoor thermal comfort [22], [23]. In recent years, researches on this subject have gained importance. Some of these studies applied with terrestrial measurements and some of them applied with thermal cameras. For instance, a study conducted by Leuzinger and Körner [8] which compared the surface temperatures measured with thermal cameras, the maximum difference was found 4.5°C between *Larix* and *Tilia* species. In the same study, 2.2°C mean temperature difference was found between *Quercus* and *Fagus* species. According to Lin and Lin's [24] research results, Elastic being the most effective tree in the sense of cooling effect, followed by *Parvifolia* and *Microcarpa*. The results of analysis revealed that there were significant differences in the magnitude of temperature reduction, which ranged from 0.64 °C to 2.52 °C, under different tree groups. In another study by Abreu-Harbich et al. [25], a cluster of *S. Siamea, C. Pluviosa* and *T.Tipu* trees had the best

cooling effects with their shading reducing the air temperature by 5.9°C – 11.5°C was found.

According to the results obtained from this study, it has been identified that the Quercus and Fagus species in the 3rd growth age can create 1.1°C – 2.4°C surface temperature difference which can also effect the micro-climate. This range is compatible with the results of Leuzinger and Körner's [8] study where *Quercus* stands mean surface temperature was 2.2°C cooler than *Fagus* stands. On the other hand, 1st and 2nd growth ages results were found different from the 3rd growth age (Table 3). According to this, *Fagus* stands are nearly 0.7°C – 1.6°C cooler than the *Quercus*

stands. This dual result can be caused by the soil effect which increases if the plants have not reached sufficient growth level. But, more detailed studies supported by terrestrial and remote sensing measurements are needed to clarify the causes of this dual situation.

In addition, it must be mentioned here that the stand data used in the study was accepted as correct due to it was obtained via the Forest Directorate. Therefore, it should be noted that possible errors in stand data will affect the results of the study.

Table 1. Descriptive statistics.

Closeness / Growth Age	Year	Species	N	Mean	Std. Deviation	Std. Error	95% Confidence Interval for Mean		Minimum	Maximum
							Lower Bound	Upper Bound		
Closeness: 3 / Growth Age: 1	Ts 2015	Fagus	4233	37.8240	1.48307	.02279	37.7793	37.8687	35.62	48.83
		Quercus	6157	38.6111	1.43125	.01824	38.5754	38.6469	36.01	46.61
		Total	10390	38.2905	1.50313	.01475	38.2616	38.3194	35.62	48.83
	Ts 2014	Fagus	4233	29.5603	1.50698	.02316	29.5149	29.6057	23.97	38.96
		Quercus	6157	30.5653	1.72338	.02196	30.5223	30.6084	24.34	39.00
		Total	10390	30.1558	1.71140	.01679	30.1229	30.1888	23.97	39.00
	Ts 2013	Fagus	4233	37.3802	2.02782	.03117	37.3191	37.4413	32.16	49.04
		Quercus	6157	39.0060	1.87797	.02393	38.9591	39.0530	33.74	49.01
		Total	10390	38.3436	2.09836	.02059	38.3033	38.3840	32.16	49.04
	Ts 2011	Fagus	4233	27.2850	1.79389	.02757	27.2309	27.3391	24.02	39.31
		Quercus	6157	28.7610	2.37858	.03031	28.7016	28.8204	21.51	40.16
		Total	10390	28.1597	2.27801	.02235	28.1159	28.2035	21.51	40.16
Closeness: 3 / Growth Age: 2	Ts 2015	Fagus	762	38.3181	2.28832	.08290	38.1553	38.4808	36.00	47.52
		Quercus	860	39.4200	2.43673	.08309	39.2569	39.5831	35.67	46.04
		Total	1622	38.9023	2.43052	.06035	38.7839	39.0207	35.67	47.52
	Ts 2014	Fagus	762	29.7377	2.06851	.07493	29.5906	29.8848	27.37	38.79
		Quercus	860	31.2395	1.91890	.06543	31.1111	31.3679	28.15	37.46
		Total	1622	30.5340	2.12652	.05280	30.4304	30.6375	27.37	38.79
	Ts 2013	Fagus	762	37.5456	2.27976	.08259	37.3835	37.7078	35.16	46.22
		Quercus	860	38.5041	2.44960	.08353	38.3402	38.6681	34.35	48.29
		Total	1622	38.0538	2.41841	.06005	37.9361	38.1716	34.35	48.29
	Ts 2011	Fagus	762	27.3950	2.08832	.07565	27.2465	27.5435	24.06	35.86
		Quercus	860	28.1542	2.35573	.08033	27.9965	28.3118	22.99	37.05
		Total	1622	27.7975	2.26534	.05625	27.6872	27.9078	22.99	37.05
Closeness: 3 / Growth Age: 3	Ts 2015	Fagus	56	41.0003	2.69988	.36079	40.2773	41.7234	37.22	46.31
		Quercus	69	38.5774	1.15182	.13866	38.3007	38.8541	37.23	42.74
		Total	125	39.6629	2.32899	.20831	39.2506	40.0752	37.22	46.31
	Ts 2014	Fagus	56	32.1892	2.44994	.32739	31.5331	32.8453	29.40	37.65
		Quercus	69	30.6534	.94139	.11333	30.4273	30.8795	29.22	33.25
		Total	125	31.3414	1.93294	.17289	30.9992	31.6836	29.22	37.65
	Ts 2013	Fagus	56	39.4941	2.40828	.32182	38.8491	40.1390	36.37	44.03
		Quercus	69	39.1819	1.40033	.16858	38.8455	39.5183	37.20	43.49
		Total	125	39.3218	1.91628	.17140	38.9825	39.6610	36.37	44.03
	Ts 2011	Fagus	56	29.3145	2.39596	.32017	28.6729	29.9561	26.60	32.73
		Quercus	69	28.1235	1.43669	.17296	27.7784	28.4687	25.77	32.06
		Total	125	28.6571	2.00792	.17959	28.3016	29.0126	25.77	32.73

Table 2. Average surface temperature values and average differences of *Fagus* and *Quercus* stands by years, closure groups and growth ages.

Closeness / Growth Age	Year	Mean		Mean Difference	Sig. (2-tailed)	% 95 Confidence Interval of the Difference	
		Fagus T(°C)	Quercus T(°C)	Quercus – Fagus ΔT(°C)		Lower	Upper
Closeness: 3 Growth Age: 1	Ts 2015	37.8240	38.6111	0.7871	0.000	0.7160	0.8344
	Ts 2014	29.5603	30.5653	1.0050	0.000	1.0935	0.9701
	Ts 2013	37.3802	39.0060	1.6258	0.000	1.4457	1.5909
	Ts 2011	27.2850	28.7610	1.4760	0.000	1.4357	1.2785
Closeness: 3 Growth Age: 2	Ts 2015	38.3181	39.4200	1.1019	0.000	0.8708	1.3330
	Ts 2014	29.7377	31.2395	1.5018	0.000	1.3075	1.6960
	Ts 2013	37.5456	38.5041	0.9585	0.000	0.7271	1.1899
	Ts 2011	27.3950	28.1542	0.7592	0.000	0.5411	0.9772
Closeness: 3 Growth Age: 3	Ts 2015	41.0003	38.5774	-2.4229	0.000	-3.1344	-1.7115
	Ts 2014	32.1892	30.6534	-1.5358	0.000	-2.1701	-0.9015
	Ts 2013	39.4941	38.1819	-1.3122	0.367	-0.9950	-0.3705
	Ts 2011	29.3145	28.1235	-1.191	0.000	-1.8765	-0.5054

Table 3. Surface temperature difference charts of fagus and quercus stands by years, closeness groups and growth ages.
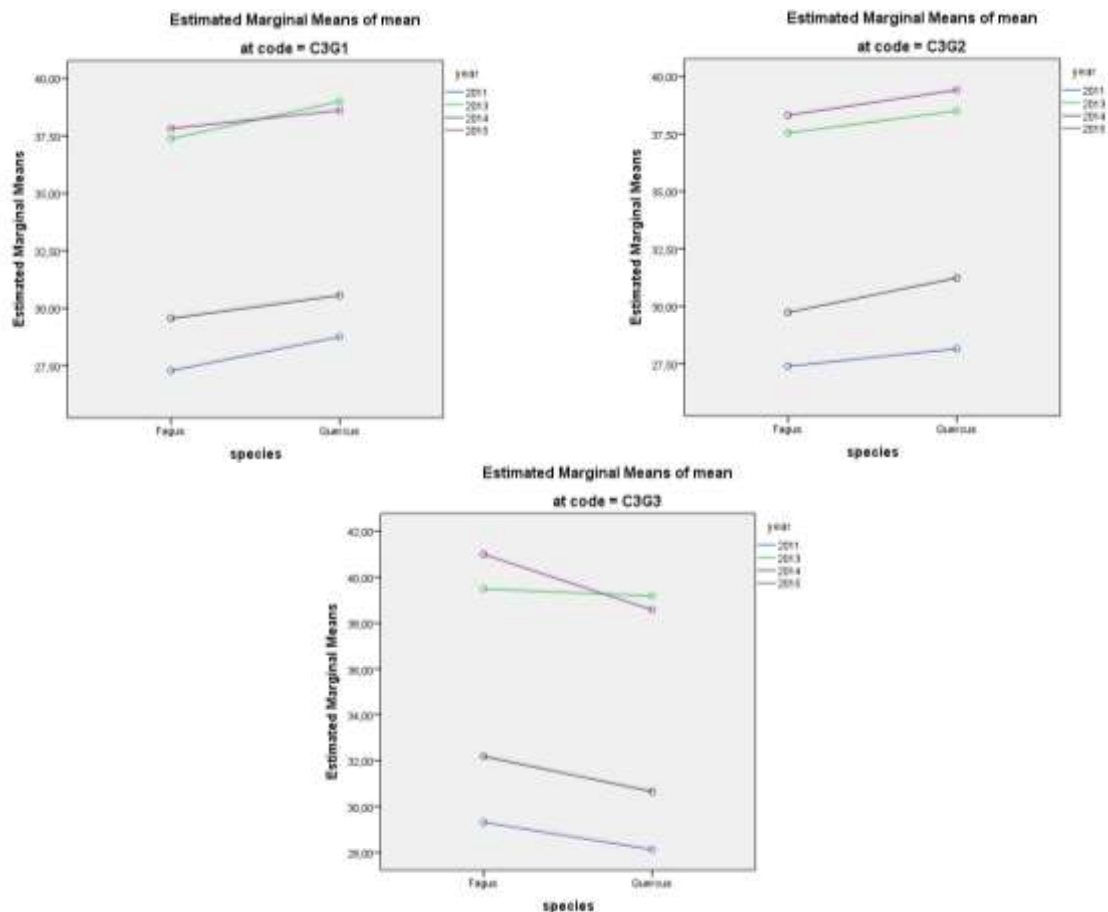
4. CONCLUSION

Along with the increasing urbanization, the structure of vegetation, which emerges to be a factor in the solution of many physical and ecological problems, is one of the emphasized issues of recent years. It is considered as a parameter in many topics such as improvement of the urban climate, decreasing air pollution, absorption of noise and productive energy usage. Today many of the urban governments carry out studies of landscape planning and city forestry by making use of biological features of the vegetation with a more conscious approach in order to benefit from the urban vegetation more effectively in their studies.

Green spaces have a great role in the regulation of urban climate. Shading and perspiration and vaporization processes of the vegetation have a natural cooling mechanism function in the urban areas [1]. Many studies conducted in various cities in the world have shown that urban parks and park areas in the city centers create a surface temperature difference of 2°C – 8°C [26]. In this era when we feel the effects of global climate change more day by day, the necessity of creating future-proof plans and strategies is inevitable. In this context, the maximum advantage principal should be taken into account in the forestation practice as one of the most effective tools of the struggle. So, not only natural stands but also in the green spaces and parks which are created artificially; the species, their closure levels, growth ages, and landscaping should be tackled in a planned way.

In this article, it has been emphasized that climatic efficiency should be featured and put on the agenda in the forestation practices and regional inventories should be formed. A meticulous study is necessary for the attempt to associate the climate factor which is a far-reaching and complex issue with forest ecology which also has a complex structure. Therefore, in the study which is conducted within the scope of the information which is obtained by the available data in order to decrease the effects of various factors, the areas with similar features in the homogenous stands are compared within the borders of the directory. In this study, only Quercus and Fagus trees are compared since only these trees are found suitable to the study when certain features such as homogenous structure, closeness and growth age are evaluated together. However, in Turkey where there are essentially 37 tree species [27], it is necessary to evaluate other tree species in order to develop future-proof and serious strategies. It is obvious that an inventory which will be prepared in this respect will contribute to urban landscape practices.

REFERENCES

[1]. Kuşçu Şimşek Ç, Anthropogenic Effects Heat on Urban Climate in Istanbul: Investigation of Urban Heat Islands, Phd. Thesis, Yıldız Technical University, Graduate School of Natural and Applied Sciences, 2013.

[2]. Robine J.M, Cheung S.L, Roy S.L, Oyen H.V and Herrmann F.R, Report on Excess Mortality in Europe During Summer 2003. EU Community Action Programme for Public Health, Grant Agreement, 2007.

[3]. CNN (2015). URL:http://edition.cnn.com/2015/06/01/asia/india-heat-wave-deaths/ Retrieved June 1, 2015.

[4]. AA (2015). URL: http://www.aa.com.tr/tr/dunya/557235--fransada-sicak-hava-bir-haftada-700-can-aldi Retrieved July 16, 2015.

[5]. İmar Panosu (2015). URL: http://imarpanosu.com/sicak-havanin-bir-gunluk-elektrik-faturasi-333-milyon-tl/ Retrieved June 31, 2015.

[6]. Hürriyet Newspaper (2015). URL: http://www.hurriyet.com.tr/ekonomi/29688051.asp Retrieved July 31, 2015.

[7]. Aitken S.N, Yeaman S, Holliday J.A, Wang T and Curtis-McLane S., Adaptation, Migration or Extirpation: Climate Change Outcomes for Tree Populations. Evolutionary Applications 1(2008) 95–111.

[8]. Leuzinger S and Körner C., Tree Species Diversity Affects Canopy Leaf Temperatures

in a Mature Temperate Forest. Agricultural and Forest Meteorology 146 (2007) 29-37.

[9]. Sabnis G.M., Green Building with Concrete Sustainable Design and Construction. CRC Press, (2011) 175-226.

[10]. Manning M.J, Plants in Urban Ecosystems: Essential Role of Urban Forests in Urban Metabolism and Succession Toward Sustainability. International Journal of Sustainable Development and World Ecology 15 (2008) 362-370.

[11]. Barış M.E., Kent planlaması, kent ekosistemleri ve ağaçlar (Urban planning, urban ecosystems and trees). Planlama Dergisi TMMOB Şehir Plancıları Odası Yayını, 4 (2005) 156-163.

[12]. Weng Q and Quattrochi D.A., Urban Remote Sensing, CRC Press, Taylor&Francis Group, 2007, ISBN: 0-8493-9199-7.

[13]. Coll C, Caselles V, Galve J.M, Valor E, Niclo`s R, Sa´nchez J.M and Rivas R., Ground Measurements for the Validation of Land Surface Temperatures Derived from AATSR and MODIS Data, Remote Sensing of Environment 97 (2005) 288 – 300

[14]. Trigo I.F, Monteiro I.T, Olesen F and Kabsch E. An Assessment of Remotely Sensed Land Surface Temperature. Journal of Geophysical Research, 113 (2008) 1-12, D17108, doi:10.1029/2008JD010035.

[15]. Prihodko L. and Goward S.N., Estimation of Air Temperature from Remotely Sensed Surface Observations. Remote Sensing of Environment 60 (1997) 335-346.

[16]. Kawashima S, Ishida T, Minomura M and Miwa T., Relations between Surface Temperature and Air Temperature on a Local Scale during Winter Nights. Journal of Applied Meteorology 39 (2000) 1570-1579.

[17]. Unger J, Gál T, Rakonczai J, Mucsi L, Szatmári J, Tobak Z, Leeuwen B and Fiala K., Air Temperature Versus Surface Temperature in Urban Environment. In: The seventh International Conference on Urban Climate, 29 June - 3 July, Yokohama, Japan, 2009.

[18]. Mutiibwa D, Strachan S and Albright T., Land Surface Temperature and Surface Air Temperature in Complex Terrain. IEEE

Journal of Selected Topics in Applied Earth Observations and Remote Sensing 8-10 (2015) 4762-4773.

[19]. USGS (2016). Landsat Handbook URL: http://landsat.gsfc.nasa.gov/wp-content/uploads/2016/08/Landsat7_Handbook.pdf, https://landsat.usgs.gov/landsat-8-l8-data-users-handbook Retrieved September 16, 2016.

[20]. Van De Griend A.A and Owe M., On the Relationship between Thermal Emissivity and the Normalized Difference Vegetation Index for Natural Surfaces. International Journal of Remote Sensing 14-6 (1993) 1119-1131.

[21]. Jiménez-Muñoz, Cristóbal, J., Sobrino J. A., Sòria G., Ninyerola M. and Pons X., Revision of the Single-Channel Algorithm for Land Surface Temperature Retrieval from Landsat Thermal-Infrared Data, IEEE Transactions on Geoscience and Remote Sensing, vol. 47-1 (2009) 339-349.

[22]. Abreu-Harbich L.V, Labaki L.C and Matzarakis A., Different Trees and Configuration as Microclimate Control Strategy in Tropics. In: Proceedings of the ICUC8 – 8th International Conference on Urban Climates, 6-10 August, UCD, Dublin Ireland, 2012

[23]. Leuzinger S, Vogt R. and Körner C., Tree Surface Temperature in an Urban Environment. Agricultural and Forest Meteorology, 150 (2010) 56-62

[24]. Lin B.S and Lin Y.J., Cooling Effect of Shade Trees with Different Characteristics in a Subtropical Urban Park. Hort Science 45-1 (2010) 83-86.

[25]. Abreu-Harbich L.V, Labaki L.C and Matzarakis A., Effect of Tree Planting Design and Tree Species on Human Thermal Comfort in the Tropics. Landscape and Urban Planning 138 (2015) 99-109.

[26]. Kuşçu Şimşek Ç., An Analysis of Micro Climatic Influences of Middle-scale Urban Parks: The Case of Gezi Park, Maçka Park and Serencebey Park, Metu JFA 33-2 (2016) 1-17.

[27]. OGM, Orman atlası [Forest atlas]. Orman Genel Müdürlüğü Yayını, 2013.

AUTHOR GUIDELINES

Thank you for choosing to submit your paper to Cumhuriyet Science Journal. The following instructions will ensure we have everything required so your paper can move through pre-evaluating, peer review, production and publication smoothly. Please take the time to read and follow them as closely as possible, as doing so will ensure your paper matches the journal's requirements.

Submission

Cumhuriyet Science Journal is an international, peer-reviewed, free of charge journal covering the full scope of both natural and engineering sciences. Manuscripts should be submitted by one of the authors of the manuscript as online submission after registration to the Cumhuriyet Sciences Journal. Microsoft Word (.doc, .docx), files can be submitted. There is no page limit. If there is a problem while uploading the files of manuscript, please try to reduce their file size, especially manuscripts including embedded figures. Submissions by anyone other than one of the authors will not be accepted. The submitting author takes responsibility for the paper during submission and peer review. If for some technical reason submission through the online submission systme is not possible, the author can contact csj@cumhuriyet.edu.tr for support.

Submission or processing charges

Cumhuriyet Science Journal does not charge any article submission, processing charges, and printing charge from the authors.

Terms of Submission

Papers must be submitted on the understanding that they have not been published elsewhere (except in the form of an abstract or as part of a published lecture, review, or thesis) and are not currently under consideration by another journal. The submitting author is responsible for ensuring that the article's publication has been approved by all the other coauthors. It is also the authors' responsibility to ensure that the articles emanating from a particular institution are submitted with the approval of the necessary institution. Only an acknowledgment from the editorial office officially establishes the date of receipt. Further correspondence and proofs will be sent to the author(s) before publication unless otherwise indicated. It is a condition of submission of a paper that the corresponding author permit editing of the paper for readability. All enquiries concerning the publication of accepted papers should be addressed to csj@cumhuriyet.edu.tr. Please note that Cumhuriyet Science Journal uses iThenticate software to screen papers for unoriginal material. By submitting your paper to Cumhuriyet Science Journal are agreeing to any necessary originality checks your paper may have to undergo during the peer review and production processes. Upon receiving a new manuscript, the Editorial office conducts initial pre-refereeing checks to ensure the article is legible, complete, correctly formatted, original, within the scope of the journal in question, in the style of a scientific article and written in clear English. Any article that has problems with any of the journal criteria may be rejected at this stage.

Peer Review

This journal operates a double-blind review process. All contributions will be initially assessed by the editor for suitability for the journal. Papers deemed suitable are then typically sent to a minimum of two independent expert reviewers to assess the scientific quality of the paper. The author is required to upload the revised article to the system within 15 days by making the corrections suggested by the referee. The article will be rejected if there are no fixes in it. The Editor is responsible for the final decision regarding acceptance or rejection of articles. The Editor's decision is final.

Title and Authorship Information

The following information should be included

Paper title

Full author names

Full institutional mailing addresses

Corresponding address

Email address

Orcid numbers of all authors

Abstract

The manuscript should contain an abstract. The researchers who are native speakers of Turkish have to add Turkish title and abstract as well. The abstract should be self-contained and citation-free and should be 250-300 words.

Keywords

Keywords of the scientific articles should be selected from the web address of www.bilimadresleri.com

Introduction

This section should be succinct, with no subheadings.

Materials and Methods

This part should contain sufficient detail so that all procedures can be repeated. It can be divided into subsections if required.

Conflicts of interest

Sample sentence if there is no conflict of interest: The authors stated that did not have conflict of interests.

Acknowledgements

References

References to cited literature should be identified by number in the text in square brackets and grouped at the end of the paper in numerical order of appearance. Each reference must be cited in the text. Always give inclusive page numbers for references to journal articles and a page range or chapter number for books. References should be styled and punctuated according to the following examples

[1] Keskin B. And Ozkan A.S., Inverse Spectral Problems for Dirac Operator with Eigenvalue Dependent Boundary and Jump Conditions, Acta Math. Hungar., 130-4 (2011) 309– 320.

[2] National Cancer Institute, Surveillance Epidemiology and End Results. Cancer of the Corpus and Uterus, NOS. Available at: http://seer.cancer.gov/statfacts/html/corp.html?statfacts_page=corp. Retrieved March 2, 2008. (Sample reference of website)

[3] Isaacson K.B., Endometrial ablation. In: UpToDate, Basow, DS (Ed), UpToDate, Waltham, M.A., 2008. (Sample reference of Uptodate topics)

[4] Speroff L., Fritz M.A., Anovulation and The Polycystic Ovary. In. Speroff L., Fritz M.A., (Eds). Clinical Gynecologic Endocrinology and Infertility. 7th ed. Philadelphia, Pa: Lippincott Williams and Wilkins; 2005: chap 12. (Sample reference of online book chapters found in websites).

[5] Mazur M.T., Kurman R.J., Dysfunctional Uterine Bleeding. In: Mazur M.T., Kurman R.J., (Eds). Diagnosis of endometrial biopsies and curettings. A practical approach. 2nd ed. Berlin: Springer, 2005; pp 100-120. (Sample reference of printed book chapters)

Preparation of Figures

Each figure can be integrated in the paper body or separately uploaded and should be cited in a consecutive order. Figure widths can be 4-6 inch as 300 dpi. The labels of the figures should be clear and informative. The name and the subtitles of the figures must be 9-point font.

Preparation of Tables

Tables should be cited consecutively in the text. Every table must have a descriptive title and if numerical measurements are given, the units should be included in the column heading. Tables should be simple with simple borders and text written as left text. The name and the subtitle of the tables must be 9-point font

Proofs

Corrected proofs must be returned to the publisher within 2 weeks of receipt. The publisher will do everything possible to ensure prompt publication. It will therefore be appreciated if the manuscripts and figures conform from the outset to the style of the journal.

Copyright

Ethical Guidelines

New methods and ethically relevant aspects must be described in detail, bearing in mind the following:

Human Experiments. All work must be conducted in accordance with the Declaration of Helsinki (1964). Papers describing experimental work on human subjects who carry a risk of harm must include:

A statement that the experiment was conducted with the understanding and the consent of the human subject.

A statement that the responsible Ethical Committee has approved the experiments.

Animal Experiments. Papers describing experiments on living animals should provide:

A full description of any anaesthetic and surgical procedure used.

Evidence that all possible steps were taken to avoid animal suffering at each stage of the experiment. Papers describing experiments on isolated tissues must indicate precisely how the donor tissues were obtained.

Submission Preparation Checklist

As part of the submission process, authors are required to check off their submission's compliance with all of the following items, and submissions may be rejected that do not adhere to these guidelines.

The submission has not been previously published, nor is it before another journal for consideration (or an explanation has been provided in Comments to the Editor).

The submission file is in Microsoft Word document file (Times New Roman) format.

Where available, URLs for the references have been provided.

The text is single-spaced; uses a 11-point font; employs italics, rather than underlining (except with URL addresses); and all illustrations, figures, and tables are placed within the text at the appropriate points, rather than at the end.

The text adheres to the stylistic and bibliographic requirements outlined in the Author Guidelines, which is found in About the Journal.

If submitting to a peer-reviewed section of the journal, the instructions in Ensuring a Double-Blind Review have been followed.